HAL
open science

Investigation of a Chemical Looping Combustion (CLC) Configuration with Gas Feed

Mohammad Mahdi Yazdanpanah

To cite this version:

Mohammad Mahdi Yazdanpanah. Investigation of a Chemical Looping Combustion (CLC) Configuration with Gas Feed. Other [cond-mat.other]. Université Henri Poincaré - Nancy 1, 2011. English. NNT : 2011NAN10118 . tel-01746270

HAL Id: tel-01746270

https://hal.univ-lorraine.fr/tel-01746270

Submitted on 29 Mar 2018

HAL is a multi-disciplinary open access archive for the deposit and dissemination of scientific research documents, whether they are published or not. The documents may come from teaching and research institutions in France or abroad, or from public or private research centers.

L'archive ouverte pluridisciplinaire **HAL**, est destinée au dépôt et à la diffusion de documents scientifiques de niveau recherche, publiés ou non, émanant des établissements d'enseignement et de recherche français ou étrangers, des laboratoires publics ou privés.

UNIVERSITÉ DE LORRAINE

AVERTISSEMENT

Ce document est le fruit d'un long travail approuvé par le jury de soutenance et mis à disposition de l'ensemble de la communauté universitaire élargie.

Il est soumis à la propriété intellectuelle de l'auteur. Ceci implique une obligation de citation et de référencement lors de l'utilisation de ce document.

D'autre part, toute contrefaçon, plagiat, reproduction illicite encourt une poursuite pénale.

Contact : ddoc-theses-contact@univ-lorraine.fr

LIENS

Code de la Propriété Intellectuelle. articles L 122. 4
Code de la Propriété Intellectuelle. articles L 335.2- L 335.10
http://www.cfcopies.com/V2/leg/leg_droi.php
http://www.culture.gouv.fr/culture/infos-pratiques/droits/protection.htm

THÈSE

Université Henri Poincaré, Nancy 1

École Doctorale Énergie, Mécanique et Matériaux (EMMA)

Spécialité « Mécanique et Energétique »

Sujet du mémoire:

Etude de la combustion de gaz en boucle chimique

Investigation of a Chemical Looping Combustion (CLC) Configuration with Gas Feed

par:

Mohammad Mahdi YAZDANPANAH

Soutenue le 20 Décembre 2011

à IFP Énergies nouvelles, Lyon, France, devant le jury composé de:

Tobias PRÖLL	Pr., Technische Universität Wien, Vienne, Autriche	Rapporteur
Joachim WERTHER	Pr., Universität Hamburg, Hambourg, Allemagne	Rapporteur
Pascal BOULET	Pr., Université Henri Poincaré, Nancy, France	Examinateur
Arnaud DELEBARRE	Pr., Université Henri Poincaré, Nancy, France	Directeur de thèse
Frédéric FEBVRE	Ing., Manager R&D, TOTAL, Paris, France	Examinateur
Ann FORRET	Ing. docteur, IFP Énergies Nouvelles, France	Examinateur
Thierry GAUTHIER	Ing. docteur (HDR), IFP Énergies Nouvelles, France	Examinateur
Pierre GUIGON	Pr., UT de Compiègne, Compiègne, France	Président

Abstract

Chemical looping combustion (CLC) is a promising novel combustion technology involving inherent separation of carbon dioxide with minimum energy penalty. An oxygen carrier is used to continuously transfer oxygen from the air reactor to the fuel reactor where the oxygen is delivered to burn the fuel. Consequently, direct contact between the air and the fuel is prevented. The resulting flue gas is rich in CO_2 without N_2 dilution. The reduced oxygen carrier is then transported back to the air reactor for re-oxidation purposes, hence forming a chemical loop.

This dissertation presents studies conducted on a novel 10 kW_{th} CLC configuration built to investigate a wide range of conditions. The system employs concept of interconnected bubbling fluidized beds using L-valves to control solid flow rate and loop-seals to maximize gas tightness.

Hydrodynamics of solid circulation was investigated with a cold flow prototype and a high temperature pilot plant in a wide temperature range. A solid circulation model was developed based on the experimental results using the pressure balance principle.

Hydrodynamic of the gas phase in the reactors was investigated through RTD studies. A hydrodynamic model was then developed based on the two phase model of bubbling fluidized beds. Methane Combustion was experimentally studied in the pilot plant using $NiO/NiAl_2O_4$ oxygen carriers. Good combustion performances and CO_2 capture efficiency were achieved. A reactor model was finally developed using the previously developed hydrodynamic model of bubbling fluidized bed and adapting a reaction scheme.

Key words: CO_2 Capture, Chemical Looping Combustion (CLC), Modeling, Fluidized Bed, L-valve, Loop-seal.

Résumé

La combustion en boucle chimique (CLC) est une nouvelle technologie prometteuse, qui implique la séparation inhérente du dioxyde de carbone (CO_2) avec une perte minimale d'énergie. Un transporteur d'oxygène est utilisé pour le transfert de l'oxygène en continu du "réacteur air" vers le "réacteur fuel" où l'oxygène est apporté au combustible. Ainsi, le contact direct entre l'air et le combustible est évité. Le gaz résultant est riche en CO_2 et n'est pas dilué avec de l'azote. Le transporteur d'oxygène réduit est ensuite transporté vers le "réacteur air" afin d'être ré-oxydé, formant ainsi une boucle chimique.

Ce manuscrit présente des études conduites en utilisant une nouvelle configuration de CLC de 10 kW_{th} construite pour étudier une large gamme de conditions opératoires. Cette unité met en œuvre le concept des lits fluidisés interconnectés en utilisant des vannes-en-L pour contrôler le débit de solide et des siphons pour minimiser les fuites de gaz. L'hydrodynamique de la circulation de solide a été étudiée sur une maquette froide et un pilote chaud. Un modèle de la circulation du solide a ensuite été développé sur le principe du bilan de pression.

L'hydrodynamique de la phase gaz dans le réacteur a été étudiée expérimentalement en utilisant la distribution des temps de séjour (DTS). Un modèle hydrodynamique a été développé sur le principe du lit fluidisé bouillonnant à deux phases. La combustion du méthane a été étudiée avec $NiO/NiAl_2O_4$ comme transporteur d'oxygène. De bonnes performances de combustion et de captage de CO_2 ont été atteintes. Un modèle de réacteur a été finalement mis au point en utilisant le modèle hydrodynamique du lit fluidisé bouillonnant développé précédemment et en adaptant un schéma réactionnel à cette configuration.

Mots clés: Captage CO_2, Combustion en boucle chimique, Modelisation, Lit fluidisé, Vanne-en-L, Siphon.

… to my beloved family..

… and to my uncle, Reza, who left to let us be …

Acknowledgement

This research project would not have been possible without the support of many people. First and foremost, thoughts of sincere gratitude and respects goes to my supervisors at IFPEN; Ann Forret, Thierry Gauthier, and Ali Hoteit. Their encouragements, helps, and criticisms have made a profound impact on my scientific and engineering approach towards problem solving and project development. I deeply appreciate their assistances which were extended to personal supports and sympathy during all these three years. In this context, I would like to express my sincere gratitude to prof. Arnaud Delebarre who had the role of scientific supervision of this work. His professional contributions have profoundly enriched this thesis.

I would like to extend my acknowledgement and recognition to my very distinguished thesis comette memebrs: Prof. Boulet, Mr. Febvre, Prof. Guigon, Dr. Pröll, and Prof. Werther. Their comments and suggestions have been a great benefit to this dessetation.

I owe my sincere thanks to R. Beaumont and W. Pelletant for their valuable professional assists in progression of this work. Further, I am pleased to extend my appreciation to, Process Design and Modeling Division at IFPEN; L. Nougier, J. C. Viguie, C. Barrere-Tricca. Particularly, I like to express my gratitude to all of my colleagues in the CLC project at IFPEN; A. Lambert, K. Surla, F. Guillou, F. Salvatori, T. Sozinho and at TOTAL S. A.; S. Riflfart, and H. Stainton. Furthermore, I am truly indebted and thankful to R. Andreux, J. M. Schweitzer, C. Plais, D. Pavone, D. Guiillaume for their invaluable technical advises and clues.

My special recognitions go to all of friends and PhD students at IFPEN with whom I shared these three years, particularly; Marc, Ghislain, Javad, Pierre, Marie, Luis, Alberto, …

Last but definitely not the least, I wishes to express my love and gratitude to my beloved family; for their understanding and endless love, through the duration of my studies.

List of Symbols

A: Surface area, m².
A_0: cross sectional area of valve opening, m².
A_b: bed surface area, m².
AI: Attrition index, %.
Ar: Arrhenius number.
A_R: Reactor area, m².
A_{Sp}: Surface area of the standpipe, m².
C_0: Tracer concentration in the reactor at time zero, ppmv.
C_∞: Tracer concentration in the reactor at the final steady state condition, ppmv.
C_D: valve aperture discharge coefficient, ppmv.
C_i^b: Concentration of species i in the bubble phase, mol/m^3.
C_i^d: Concentration of species i in the emulsion phase, mol/m^3.
C_{out}: Tracer concentration at the exit of the reactor, ppmv.
CSTR: Continuous stirred tank reactor.
D: Diameter, m.
Daxg: Axial dispersion coefficient for gas phase, m²/s.
DaxL: Axial dispersion coefficient in liquid phase, m²/s.
Daxs: Axial dispersion coefficient in the solid phase, m²/s.
D_b: Cyclone barrel diameter, m.
$d_{b,max}$: Maximum bubble diameter, m.
d_b: Equivalent volume diameter of a bubble, m.
d_{b0}: Initial bubble size, near the bottom of the bed, m.
d_{bm}: Limiting bubble size, m.
$d_{eq,s}$: Equivalent volume diameter of a bubble at the bed surface, m.
$d_{h,Cyc-i}$: Cyclone inlet hydraulic diameter, m.
d_{hi}: Hydrodynamic diameter, calculated as 4(Inlet area)/(Inlet perimeter), m.
D_L: Lift diameter, m
D_o: Diameter of the outlet tube of cyclone, m.
dp: Particle Sauter diameter, m.
D_P: Pipe diameter, m
dz: Height of the descritized cell, m.
E: Activation energy, J/mol.
E(t): Fraction of particles that remained in the system for a time between t and t+dt
F(t): Fraction of particles that remained in the system for a time less than t.
G_s: Solid flux , kg/m².s
H_R: Height of fluidized bed, m.
H_{det}: Height of the detector tube in the reactor, m.
H_{mf}: Height of the bed in minimum fluidization condition in the reactor, m
H_R: Height of solid bed in the reactor, m.
ID: Inner Diameter, m
k: Reaction rate constant, $mol^{1-n} \cdot l^{n-1} \cdot s^{-1}$.
K_{bc}: Gas exchange coefficient between the bubble and the cloud phase, 1/s.
K_{be}: Gas exchange coefficient between the bubble and the emulsion phase, 1/s.
K_{ce}: Gas exchange coefficient between the cloud and the emulsion phase, 1/s.
K_d: Gas exchange coefficient by mass transfer between bubble and emulsion phase, 1/s.
K_{fi}: Contraction coefficient in entrance of cyclone

k_t: Avrami rate constant, s^{-m}.
LHV: Lower Heating Value, J/kg.
$L_{lv,H}$: Length of horizontal section of the l-valve, m.
l_{or}: Spacing between adjacent holes, m.
L_{RP}: Length of recycle pipe of loop-seal, m.
L_{SPs}: Height of solid in the standpipe of the loop-seal, m
M: Mass of particles in a system element, kg
m: Actual mass of oxygen carrier, kg.
m_{ox}: Mass of fully oxidized oxygen carrier, kg.
m_{red}: Mass of fully reduced oxygen carrier, kg.
m_t: Slope of temperature variation in the reactor, °C/s.
M_{tl}: Quantity of the solid transport lines, kg.
M_{TR}: Total injected mass of solids in each reactor, kg.
M_{ts}: Mass of the solid in transport lines, kg.
M_yO_x: Oxidized oxygen carrier.
M_yO_{x-1}: Reduced oxygen carrier.
Nf: fluidization number, i.e. the ratio of the gas velocity to minimum fluidization velocity.
N_{or}: Number of orifices per unit area.
N_r: Fluidization number, U/U_{mf}.
P: pressure, Pa.
Pe: Peclet number.
Pg: Gage pressure, mbar.
ppmv: Part per million in volume.
Q: Gas flow rate, Nm^3/h.
Q_0: Reference air flow rate, Nm^3/h.
Q_{air}: Inlet aeration rate in the air reactor, Nm^3/h.
Q_{ent}: Gas entrainment rate, Nm^3/h.
$Q_{g,H}$: Horizontal gas flow rate, Nm^3/h.
Q_{SR}: Aeration rate into the loop-seal below recycle chamber, Nm^3/h.
Q_{Ss}: Aeration rate in the loop-seal below the standpipe, Nm^3/h.
Q_t: Total aeration rate, Nm^3/h.
r: Reaction rate, $mol/m^3/s$.
R: Gas constant, $J.mol^{-1}.K^{-1}$.
R_0: Oxygen transfer capacity.
Re_P: Pipe Reynolds number for interstitial gas velocity.
Re_R: Reynolds number for reactor.
RT: Residence time, s.
RT_{det}: Residence time of the Helium detector device and detection lines, s.
RT_{in}: Residence time of the gas injection line and distributor of the reactor, s.
RT_R: Residence time of the empty space between the solid bed and the sniffer of the detector, s.
RT_t: Total residence time, s.
s: Slip factor for calculation of solid particles velocity.
T: Temperature, °C.
t: Time, s.
$\bar{t}$: Mean residence time, s.
t_{first}: First appearance time, s.
U: Superficial gas velocity, m/s
U_o: Gas velocity in cyclone outlet tube, m/s
$U_{air,in}$: Air injection velocity in the air reactor, m/s.

U_{bm}: Assumed constant mean bubble velocity in the bed, m/s.
U_{br}: Bubble raise velocity, m/s.
U_{ch}: Chocking velocity, m/s.
U_e: Gas flow rate in the emulsion phase, m/s.
U_f: Gas velocity in freeboard of fluidized bed, m/s
U_{ft}: Gas flow through velocity, m/s.
U_{HP}: Superficial gas velocity in the horizontal section of the loop-seal, m/s
$U_{lv,H}$: Superficial gas velocity in the horizontal pipe of the l-valve, m/s
U_{gb}: Bubble velocity, m/s.
U_{gd}: Gas velocity in the emulsion phase, m/s.
U_i: Cyclone inlet gas velocity, m/s
U_{mb}: Minimum bubbling velocity, m/s
U_{ms}: Minimum slugging velocity, m/s
U_{pf}: Particle velocity in freeboard of fluidized bed before entrance into the cyclone, m/s
U_{pi} : Particle velocity at solids inlet of cyclone, m/s
U_R: Gas flow rate in the reactor, m/s.
$U_{s,HP}$: Superficial solid velocity in the horizontal pipe of the loop-seal, m/s
$U_{s,lv,H}$: Solid velocity in the horizontal section of the l-valve, m/s
Uss: Superficiel gas velocity of the first loop-seal aeration, m/s.
U_t: Terminal velocity of the particles, m/s.
v: Interstitial velocity, m/s.
v_g: Interstitial velocity of gas, m/s.
Vol: Volume of element, m^3.
v_r: Interstitial relative solid – gas velocity, m/s.
v_s: Interstitial velocity of solid particles, m/s.
Vsg: Superficial gas velocity in the reactor, m/s.
X: Oxidation degree, %.
W(t): Fraction of particles that remained in the system for a time greater than t.
W_s: Solid flow rate, kg/h.
Y_i: Mole fraction of component i in the gas phase.

Greek Symbols

α: Avrami nuclei growth rate.
β: Angle of repose.
γ: gas yield, %.
δ: Bed fraction in the bubble phase.
ΔH_{det}: Difference of the two different detector positions heights, m.
ΔH_{det}: Difference of the two different detector positions heights, m.
δ_{lv}: Gas fraction factor in the L-valve.
$\Delta P_{(f-i)g}$: Contraction pressure drop, Pa.
$\Delta P_{(f-i)p}$: Acceleration of solids pressure drop, Pa.
$\Delta P_{(f-i)p}$: Barrel friction fressure drop, Pa.
ΔP_{acc}: Pressure drop due to acceleration, Pa.
$\Delta P_{Cyc,g}$: Pressure drop in the cyclone, between gas entry and exit, Pa.
ΔP_{DR2}: Pressure drop in the reactor for the section above the entrance of the loop-seal into the reactor, Pa.
ΔP_f: Pressure drop causes by friction, Pa.
ΔP_g: Pressure drop due to static head (gravity) , Pa.

ΔP_{ls}: Pressure drop across the whole loop-seal, Pa.
ΔP_{lv}: Pressure drop across the whole l-valve, Pa.
ΔP_o: Outlet exit contraction pressure drop, Pa.
ΔP_{piping}: Pressure drop in the discharge line of gas exit of cyclone to atmosphere, including piping and filtration, Pa.
ΔP_r: Gas reversal pressure Drop, Pa.
$\Delta RT_{R\ empty}$: Residence time between two determined heights in the empty reactor, s.
Δt_{lag}: Lag time of the analyser response, s.
ε: Voidage of solid bed.
ε_0: Voidage for vertical gravity moving bed without interstitial fluid flow.
ε_{gb}: Fraction of the bed voidage in the bubble phase versus total bed volume.
ε_{gd}: Fraction of the bed voidage in the emulsion phase versus total bed volume.
ε_{gdt}: Total fraction of the bed voidage in the emulsion phase versus total bed volume.
ε_s : Free settled voidage of solid bed.
ε_{st}: Voidage of tapped solid bed
η_c: Combustion efficiency, %.
η_{cO2}: Capture efficiency, %.
θ: Angle of the recycle pipe with horizontal axis
μ: Mathematical moment.
μ_g: Gas viscosity, Pa.s.
μ_{ij}: Stoichiometric constant of element i in reaction j.
μ_L : Solid loading, kg solid/kg gas.
ρ_b: Bulk density free settled solids, kg/m^3
ρ_g: Gas density, kg/m^3.
ρ_s: Solid density, kg/m^3.
ζ^2: Dimensionless variance.
ΣP: Sum of pressure drops, Pa.
η_p: Tubularity parameter.
ζ_t: Second moment of the RTD respond function, variance, s^2.
η: Ideal residence time in a vessel, s.
θ: Spherecity of solid particles.

Subscripts and abbreviations

0: Input into the reactor.
Ar: Arrhenius Number.
AR: Air Reactor.
av: Average.
b: Bubble phase.
BFB: Bubbling fluidized bed.
c: Cloud phase.
CCS: Carbon capture and storage.
CFB: Circulating fluidized bed.
CLC: Chemical looping combustion.
CLH: Chemical Looping Hydrogen.
CLR: Chemical Looping Reforming.
CLOU: Chemical Looping Oxygen Uncoupling.
CSTR: Continuous stirred-tank reactor.
Cyc: Cyclone.

DCFB: Dual Circulating Fluidized Bed.
DP: Detector position.
det: Gas detector (analyzer).
dis: Distributor.
DR: Reactor section above the solid entrance point in the loop-seal.
e: Emulsion phase.
ECBM: CO2 Enhanced Coal Bed Methane recovery.
EOR: Enhanced Oil Recovery.
EU: European Union.
FCC: Fluid catalytic cracking.
Fr: Fraud number.
FR: Fuel Reactor.
g: Gas.
GHG: Green House Gas.
HC: Horizontal dilute phase pneumatic conveying line.
HP: Horizontal pipe of the loop-seal.
i: Chemical species i.
IEA: International Energy Agency.
in: Gas injection line, including the valve, injection tubes and gas distributor.
IP: Helium tracer gas injection position.
IPCC: Intergovernmental Panel on Climate Change.
L: Lift, pneumatic dilute solid conveying line.
LH–HW: Langmuir–Hinshelwood–Hougen–Watson.
ls: Loop-seal.
lv,A-H: L-valve section between the aeration point and the discharge point into the lift.
lv,H: Horizontal section of the L-valve.
lv,v : The vertical arm of the l-valve above the aeration point.
lv: L-valve.
mf: Minimum fluidization.
OC: Oxygen carriers.
PF: Plug flow.
R: Reactor.
R1:Reactor 1.
R2:Reactor 2.
RC: Recycle chamber of the loop-seal.
Re: Reynolds number.
RP: Recycle pipe of the loop-seal.
RTD: Residence time distribution.
s: Solid.
SC: Supply chamber.
SEM: Scanning electron microscope.
SP: Stand pipe.
SS: First gas injection point in the loop-seal below the recycle chamber.
Tb: T-bend.
TGA: Thermogravimetric Analysis.
UNFCCC: United Nations Framework Convention on Climate Change.
w: Wake phase.
YSZ: Yttria-Stabilized Sirconia.

Contents

ABSTRACT ..... **III**

RESUME ..... **V**

ACKNOWLEDGEMENT ..... **IX**

LIST OF SYMBOLS ..... **XI**

GREEK SYMBOLS XIII
SUBSCRIPTS AND ABBREVIATIONS XIV

CONTENTS ..... **XVII**

INTRODUCTION **3**

THESIS FRAMEWORK 4

1. LITERATURE REVIEW **9**

1.1 GLOBAL WARMING 9
1.2 CARBON DIOXIDE EMISSION MITIGATION, CARBON CAPTURE AND STORAGE 11
1.3 CHEMICAL LOOPING COMBUSTION 15
1.4 CLC DESIGNS 17
1.5 SOLID CIRCULATION 19
1.5.1 Non-mechanical Pneumatic L-valve *19*
1.5.2 Loop-Seal *23*
1.5.3 Stand Pipe Solid Flow *25*
1.5.4 Solid Circulation Modeling *26*
1.5.5 Solid Flow Rate Measurement *26*
1.6 BUBBLING FLUIDIZED BED REACTOR 27
1.6.1 Residence time distribution *27*
1.6.2 Hydrodynamic Model of Bubbling Fluidized Bed (BFB) *29*
1.6.3 Multi-Phase Models *31*
1.7 KINETICS OF CHEMICAL LOOPING COMBUSTION 33
1.8 CONCLUSION 37

2. MATERIALS AND METHODS **41**

2.1 EXPERIMENTAL INSTALLATIONS 41
2.1.1 Cold Flow Prototype (Maquette) *41*
2.1.2 High Temperature Prototype (Pilot Plant) *43*
2.1.3 Gas Analyzing Devices *46*
2.2 PARTICLE PROPERTIES 48
2.3 TRACING AND RTD TESTS IN THE COLD PROTOTYPE 49
2.4 PNEUMATIC CONVEYING GAS VELOCITY 50
2.5 SOLID FLOW RATE 51

2.5.1 Solid Flow Rate Measurement Methods *51*
2.5.2 Solid Flow Rate Measurement, Demonstration Methods *54*
2.6 OPERATIONAL PROCEDURES 56
2.7 ELECTROSTATICS EFFECT 57
2.8 CONCLUSION 57

3. SOLID CIRCULATION INVESTIGATIONS: EXPERIMENTAL RESULTS 61

3.1 L-VALVE OPERATION 61
3.1.1 Standpipe of the L-valve *62*
3.1.2 Gas Flow in the Standpipe of the L-valve *64*
3.1.3 Solid Flow Control Mechanism in the L-valve *67*
3.1.4 Calculation of Pressure Drop in the Standpipe Using Ergun Equation *69*
3.1.5 Average Voidage of the Moving Solid Bed in the Standpipe *69*
3.1.6 Effect of Gas Properties on the L-valve Operation *72*
3.1.7 Effect of Particles Properties on the L-valve Operation *73*
3.1.8 L-valve High Temperature Operation *75*
3.1.9 L-valve Limiting Operation *77*
3.2 LOOP-SEAL OPERATION 80
3.2.1 Pressure Drop in the Loop-Seal *81*
3.3 LOOP-SEAL GAS TRACING STUDY 83
3.3.1 Effect of the Loop-seal Aeration, Qss *83*
3.3.2 Effect of Loop-Seal Aeration, Qsr *85*
3.3.3 Effect of Solid Flow Rate *86*
3.3.4 Effect of the Pressure Drop across the Supply Chamber *87*
3.3.5 Flow in the Horizontal Pipe of the Loop-seal *90*
3.4 GLOBAL GAS TIGHTNESS BETWEEN THE REACTORS 93
3.5 STEADY STATE OPERATION 94
3.6 GEOMETRICAL PARAMETERS OF THE LOOP-SEAL AND THE L-VALVE 97
3.7 CONCLUSION 98

4. SOLID CIRCULATION INVESTIGATIONS: MODELING 101

4.1 MODELLING APPROACH 101
4.2 FIRST MODEL SECTION 103
4.3 SECOND MODEL SECTION 104
4.4 PRESSURE DROP MODELLING 105
4.4.1 Pressure Drop in the Reactor *106*
4.4.2 Pressure Drop in the Standpipe of the L-valve *106*
4.4.3 Pressure Drop in the Lift *107*
4.4.4 Pressure Drop in the Horizontal Conveying Line and the Blinded Tee Bend *109*
4.4.5 Cyclone Pressure Drop *110*
4.4.6 Pressure Drop in the Supply chamber of the Loop-Seal *111*
4.4.7 Recycle Chamber Pressure Drop *112*
4.4.8 Recycle Pipe Pressure Drop *114*
4.4.9 Solid Flow in the L-valve and the Loop-Seal *115*
4.4.10 Pressure Drop in Horizontal Flow *118*
4.5 MODEL VALIDATION 119
4.5.1 Model Results, Solid Flow Rate *119*

4.5.2 Model Results, Height of Solid Column in the Supply Chamber of the loop-seal *121*
4.5.3 Model Results, Pressure Variation Loop *122*
4.6 SENSITIVITY ANALYSIS 126
4.7 CONCLUSION 127

5. REACTOR STUDY: HYDRODYNAMICS 131

5.1 EXPERIMENTAL RTD INVESTIGATION 131
5.2 RTD MEASUREMENT INPUT FUNCTION 132
5.3 GAS SAMPLING 135
5.4 RTD SIGNAL TREATMENT 136
5.4.1 Linear Residence Time (RT) Treatment *136*
5.4.2 Analysis of Signal Dispersion *137*
5.5 INTERFERING SIGNALS MEASUREMENT 137
5.6 EFFECT OF OPERATING PARAMETERS ON RT 138
5.6.1 Effect of the Fluidized Bed Height *138*
5.6.2 Effect of the Gas Velocity on the Residence Time (RT) *139*
5.6.3 Effect of Solid Flow Rate on Residence Time (RT) *140*
5.7 BUBBLING FLUIDIZED BED MODEL 140
5.8 MODELING OF THE SYSTEM COMPONENTS 145
5.9 MODEL RESULTS 147
5.9.1 Bubble Size Correlations *147*
5.9.2 Gas Dispersion in Emulsion Phase *148*
5.9.3 Model Validation *150*
5.9.4 Sensitivity Analysis *153*
5.10 CONCLUSION 155

6. REACTOR STUDY: METHANE COMBUSTION 159

6.1 EXPERIMENTAL RESULTS 159
6.1.1 Data Evaluation *159*
6.1.2 Continuous and Transitional Steady State Test *161*
6.1.3 Batch tests *167*
6.1.4 Oxidation Reactor *170*
6.1.5 CO_2 Capture Efficiency *172*
6.1.6 Attrition and Particle Aging *173*
6.1.7 Agglomeration *177*
6.2 REACTOR MODEL 178
6.2.1 Modeling of the System Components *178*
6.2.2 Reaction Mechanism *180*
6.2.3 Kinetic Rate Equations *181*
6.2.4 Heat Transfer *183*
6.2.5 Gas Phase Reaction and Expansion *184*
6.2.6 Solid Phase Material Balance *185*
6.3 MODEL VALIDATION 186
6.4 CONCLUSION 189

CONCLUSIONS 193

REFERENCES 197

APPENDIXES **213**

1. PHOTO OF THE CLC COLD FLOW PROTOTYPE 213
2. PARTICLES PROPERTY MEASUREMENT METHODS 215
   2.1. Density Measurement *215*
   2.2. Sphericity *216*
   2.3. Minimum Fluidization Velocity *216*
   2.4. Particle Size Distributions *218*
3. HELIUM DETECTOR CHARACTERISTICS 221
4. CALIBRATION OF ROTAMETERS 222
5. BUBBLING FLUIDIZATION REGIME 223
6. CALCULATION OF THE SOLID BED HEIGHT AND VOIDAGE IN THE REACTOR 224
7. CYCLONE PRESSURE DROP TERMS 225
8. LIST OF EXPERIMENTAL RTD RESULTS 226

RESUME ETENDU **229**

1. INTRODUCTION 229
2. LES INSTALLATIONS 231
   2.1. Maquette froide *231*
   2.2. Le pilote chaud *233*
3. LA CIRCULATION DES PARTICULES 235
   3.1. Opération du siphon *238*
4. MODELE DE CIRCULATION 239
   4.1. La premier section du modèle *240*
   4.2. La deuxième section du modèle *241*
   4.3. Validation du modèle *242*
5. HYDRODYNAMIQUE DU REACTEUR 244
   5.1. La validation du modèle *245*
6. LA COMBUSTION DU METHANE 246
   6.1. La modélisation du réacteur *249*
7. CONCLUSIONS 249

RESUME **251**

Introduction

Introduction

The global temperature of the earth is generally a function of the energy difference received from the sun, and the reflected energy into the surrounding space. The atmosphere of the earth acts as a covering shield to capture a part of this radiative energy and maintain a temperature high enough for the life on the earth. This effect is called greenhouse effect which exists thanks to the presence of some naturally occurring atmospheric gases as H_2O, CO_2, CH_4, O_3 and N_2O. However, since the industrial revolution, human has been exploiting the fossil fuels which have been reserved under ground for millions of years, burning them and emitting them into the atmosphere. As a result, billions of tons of greenhouse gases, notably CO_2, has been emitted into the atmosphere from under ground sources. Moreover, mankind has been continuously affecting the natural sinks of these gases especially through deforestation. These manmade actions have added a considerable additional stress on climate of the earth, causing a great life threat called "global warming".

Different measures have been proposed to fight against the undesirable effects of the global warming. Carbon capture and storage (CCS) has been widely considered as a mid to long term mitigating measure against emission of the greenhouse gases. Moreover, the carbon capturing can have double advantages, both environmental and economic. This can be achieved if CO_2 be used in some industrial applications after being captured. CO_2-EOR (Enhanced Oil Recovery by injecting CO_2 into oil reservoirs) is one of the potential industrial usages of CO_2 to increase petroleum production. This process has been commercially in use for about 40 years (with CO_2 mostly from natural sources) and its feasibility has been well recognized in terms of transportation and injection of CO_2. The main missing part of the chain is low cost feasible carbon capturing system. In this case, the fossil fuel is exploited from the underground reservoirs, its energy is used, and the undesirable greenhouse gases are being re-injected into its initial place where it has been for millions of years.

In the human circulatory system, red blood cells act as intermediate oxygen transporters between the air and the body cells. Therefore, the energy production in body cells happens without direct contact between the air and the cells. Similar system is being used in the chemical looping combustion (CLC). An oxygen carrier (mostly a metal oxide) transports air oxygen to a combustion reactor where it delivers the oxygen to a fuel. Therefore, the produced flue gas is free of Nitrogen and rich in CO_2. In other words, CO_2 is an intrinsic product of the CLC, resulting in a cost effective carbon separation process.

Chemical looping combustion has received an increasing attention since the beginning of the current century. Several academic and industrial groups are currently working in this domain world wide. Research and development in the CLC field can be generally divided in to two main categories. First is the development of effective oxygen carriers regarding the economical, technical, environmental and safety aspects. Several hundreds of oxygen carriers have been already investigated including various natural minerals, industrial wastes, and synthetic materials.

Development of industrially reliable CLC process is the second axis of research and development in chemical looping combustion. Several laboratory pilot plants have been developed with capacities ranging from 0.3 kW_{th} to 1 MW_{th}. Circulating fluidized bed combustion (CFB) and fluid catalytic cracking (FCC) are two of the main mature industrial process involving circulation of fluidized particles. These systems, especially CFB, have been a basis for the development of CLC process. However, the development of a reliable commercial CLC process requires more efforts to be dedicated to the research and development particularly in the scale up and design of higher capacity systems.

Chemical looping combustion has the advantage of being flexible in terms of the feed. Different types of gas, liquid and solid fuels have been tested in this system. The gas feeds have received more

attentions and have been the first challenge being addressed. However, more investigations are still required both in terms of materials and process development into the larger scales adapted for each type of feed.

Solid circulation is a key factor in the chemical looping combustion process development. Solids transport the oxygen necessary for combustion of fuel. In addition, circulation of solids is a vital parameter for thermal heat balance in the overall system especially in the case of significant reaction heat difference between the oxidation and reduction reactions. Accordingly, capacity of adequate solid circulation and possibility of the control of the circulation rate between the reactors is an important development point. Control of solid circulation permits to adjust properly the solid circulation, and achieve required heat integration. This also brings about flexibility in terms of the energy production capacity, possible change of oxygen carriers or feed.

Gas tightness is another important factor in CLC process design. Circulating particles between the reactors can entrain some gases between them and result in gas leakage between the reactors. Gas leakage out of the fuel reactor results in loss of produced CO_2, i.e. reduction of capture efficiency. Moreover, the leakage of the unreacted gases from the fuel reactor into the air reactor can result in the direct contact between the air and fuel. This brings about a vigorous exothermic combustion which may result in safety problems and material damages. The gas leakage into the fuel reactor can cause dilution of the produced CO_2 stream with Nitrogen which reduces the separation efficiency. This problem can be addressed through proper design of the system and employment of gas tightening devices such loop-seals discussed above.

Different solid flow rate controlling approaches have been employed in the existing CLC pilots. A common approach is use of non-mechanical pneumatic valves such as loop-seal and L-valve. Despite the wide spread use of this kind of devices in various industrial CFB combustion systems, still some investigations are required for an optimum use of these devices in CLC system. Of particular interest in this regard is the effect of temperature and gas properties on the operation of this devices and possible operational limits.

Modeling of the CLC system is an important tool both for better understanding of the system and also for scale up of the system into the superior scales. The modeling can be divided into two interconnected stages. First is modeling of the solid circulation and pressure drop variation across the CLC system. This model permits to better understand the solid circulation phenomena. Moreover, it provides a tool to predict the effect of main operation parameters on the solid circulating operation including effect of temperature and size. The second modeling stage is the modeling of the hydrodynamics and kinetics inside the CLC reactors. This is an important modeling stage which helps to verify the developed reaction schemes and employed hydrodynamic model. Moreover, it is a useful tool for scale up purposes.

An important point to be considered in modeling of fluidized bed is the level of empiricalness involved in the model. This may limit the use of the model into some determined size and temperature ranges. In addition, the scaling may have some effects on the change, appearance or disappearance of some phenomena. Accordingly, it is always recommended to joint together both experimental and modeling investigations in development of a process. Evidently, this involves comprehensive scientific investigations in each development stage both in terms of experimental and modeling studies.

Thesis Framework

IFP Energies nouvelles and Total S.A. are currently working on a common development project on the chemical looping combustion. The main purpose of the project is to develop a commercial scale CLC process. It involves CLC investigations in different stages from TGA to 1 MW_{th} scale involving gas, liquid and solid feeds. The current thesis has been defined in the framework of the stated project including experimental and modeling study in a cold flow prototype and a high temperature comprehension pilot plant of 10 kW_{th} capacity. The aim of the pilot plant is to investigate CLC reactions in well defined and controlled conditions, in order to test various oxygen carrier systems.

The pilot is originally designed to address different kinds of gas feeds (CH_4, CO, H_2) with a further development possibility to test different liquid and solid feeds.

The 10 kW_{th} system is designed based on the interconnected bubbling fluidized bed system. Bubbling fluidized bed reactors are used as air and fuel reactors. The solids are circulated between the reactors through identical solid conveying lines. Each line is composed of a series of solid conveying elements to lead the particles into the succeeding reactor. Solid flow rate is controlled by use of L-valves installed at bottom exit of each reactor. Solids at the exit of each L-valve are conveyed vertically through a riser. A Blinded T-bend diverts solid flow into a horizontal dilute phase solid conveying pipe which leads the particles into a cyclone. The separated solids leave the cyclone into a loop-seal which transport particles into the next reactor. Loop-seals are used to ensure gas tightness of each reactor.

The current study can be divided into two main parts including: solid circulation at ambient temperature and overall CLC studies at high temperatures involving reactions. Hydrodynamic investigations of solid circulation have been carried out in a cold flow prototype at ambient conditions. The operation of the L-valve and loop-seal in control of solid circulation and gas tightness were the main investigation aims. A solid circulation model was then developed based on the experimental results using the conventional pressure balance principle. The hydrodynamics of the bubbling fluidized bed reactors were experimentally studied by aid of residence time distribution (RTD) in the cold flow prototype.

The second part of the study was constituted of the chemical looping combustion investigation in the high temperature pilot plant with $NiO/NiAl_2O_4$ oxygen carriers and CH_4 feed. The main reason for this selection was existence of various literatures on that. This helps to better understand and verify the functioning of the current CLC system. The solid circulation at high temperature and oxidation and reduction reactions were studied in this phase. The results were then used to confirm the solid circulation mode at high temperature. Moreover, a combustion model was developed to predict the gas conversion in the fuel reactor based on the existing reaction schemes in the literature.

The current dissertation is composed of six chapters. A brief review of the existing relevant literature is presented in Chapter 1. The necessity of carbon capture and storage as a global warming mitigation measure is discussed first. In this context, various existing carbon capture technologies are briefly presented. Chemical looping combustion is demonstrated to be a promising carbon capture technology regarding the economical aspects. The chapter is then followed by presentation of the L-vale and loop-seal as two non-mechanical pneumatic conveying devices employed in conventional circulating fluidized bed systems. A survey is carried out through the existing hydrodynamic models of the bubbling fluidized bed. The chapter ends with a review of the kinetics of the chemical looping combustion reactions including different employed oxygen carriers, kinetic models and reaction schemes.

Chapter 2 presents the experimental installations and materials used in the current study. The cold flow prototype and the high temperature pilot plant are presented in detail. The employed gas analyzers and their operational principles are briefly discussed. Properties of different particles employed in the current study and associated measurement or calculation methods are detailed. Solid flow rate measurement is a vital point in the current investigation. The principal measurement technique of solid flow rate is therefore presented. Finally, the experimental operation procedures are detailed both for the cold flow prototype and high temperature pilot plant.

Chapter 3 present solid circulation investigations carried out in the cold flow prototype. L-valve is a critical element in the current CLC system. Use of more than one L-valve permits control of both the solid flow rate and inventory repartition between different reactors. L-valve operation and associated solid and gas flow across it are discussed in this chapter. The main investigated parameters include: voidage of the solid moving bed in the standpipe, impact of gas properties on the L-valve operation, effect of temperature and limiting L-valve operation. Loop-seal operation is then investigated in terms of impact of various operating conditions including: effect of different loop-seal aerations, solid flow rate, and pressure drop down stream of the device. The steady state solid circulation and geometrical parameters are briefly discussed at the end of the Chapter 3.

Chapter 4 presents the solid circulation model developed based on the experimental solid circulation results from of cold flow prototype and high temperature pilot plant. The modeling approach is based on the pressure balance across the circulation loop. The application of this method to the current study is first discussed. The employed procedures to calculate pressure drop in each section of the model is then explained. Results for each section are compared with the experimental data to select the best available relation. The model is then verified against the experimental results at ambient and high temperatures.

Chapter 5 presents the hydrodynamic investigations of the fluidized bed reactors of the current system. The results from the experimental residence time distribution study of the gas phase is first discussed. A hydrodynamic model based on the bubble – emulsion two phase theory is developed. The experimental results are used to choose the relations from the existing literature best adapted to the current CLC design. The experimental and modeling results are finally compared to verify the validity of the model in different conditions.

Chapter 6 presents the experimental and modeling results from the combustion of methane at the high temperature pilot plant. The presented experimental results are constituted of three sorts of tests including: batch, transitional and continuous steady state combustion runs. The state of oxygen carriers after the long term experimental tests is then analyzed. The main examined parameters are: attrition, agglomeration and particle aging. The hydrodynamic model developed previously is then modified to take into consideration reaction effects. The modeling results are then compared with the experimental finding to validate the selected kinetic scheme.

Current work is to provide an understanding of the CLC system in hand both in terms of solid circulation, combustion, and oxidation reactions. This provides a kind of reference for further development with alternative kinds of oxygen carriers and feeds.

Chapter 1.

Literature Review

1.1 GLOBAL WARMING 9
1.2 CARBON DIOXIDE EMISSION MITIGATION, CARBON CAPTURE AND STORAGE 11
1.3 CHEMICAL LOOPING COMBUSTION 15
1.4 CLC DESIGNS 17
1.5 SOLID CIRCULATION 19
1.5.1 Non-mechanical Pneumatic L-valve 19
1.5.2 Loop-Seal 23
1.5.3 Stand Pipe Solid Flow 25
1.5.4 Solid Circulation Modeling 26
1.5.5 Solid Flow Rate Measurement 26
1.6 BUBBLING FLUIDIZED BED REACTOR 27
1.6.1 Residence time distribution 27
1.6.2 Hydrodynamic Model of Bubbling Fluidized Bed (BFB) 29
1.6.3 Multi-Phase Models 31
1.7 KINETICS OF CHEMICAL LOOPING COMBUSTION 33
1.8 CONCLUSION 37

1. Literature Review

This chapter makes a brief survey of the existing literatures relevant to the current study. The essay starts with a discussion on the global warming and its connections to the greenhouse gases. Carbon capture and storage (CCS) is then discussed as a potential solution to the stated problem. The carbon capturing is then shown to be the main economical and technological challenge of CCS development. Different existing carbon capture technologies are then briefly presented. Chemical looping combustion is presented as a promising carbon separation process. The existing developed CLC pilot systems are briefly discussed. Solid circulation in circulating fluidized beds is briefly surveyed including a discussion on the L-valve and the loop-seal as the pneumatic non-mechanical valves. Measurement and modeling approaches employed in the existing literatures for the solid circulation are presented next.

The hydrodynamics of the bubbling fluidized bed is discussed in the second part of the current chapter. Residence time distribution (RTD) is presented as a conventional experimental hydrodynamic investigation technique. Different possible hydrodynamic modeling approaches are then discussed showing the diverse possibilities in hydrodynamic modeling of bubbling fluidized beds. The chapter ends with a short presentation of the kinetics of reactions and effect of oxygen carriers in chemical looping combustion.

1.1 Global Warming

Global warming and its consequent effect on climate change is one of the major overriding environmental, social and economical threats facing mankind. Scientific studies have demonstrated that the global surface temperature has increased in the past century by more than 0.5°C [1,2]. Moreover, global average sea level rose at an average rate of 1.8 mm per year over 1961 to 2003 with a similar reduction in the snow converge of the northern hemisphere [3]. This warming is, at least in part, a result of anthropogenic climate-forcing agents [4], a burst of warming that has taken the global temperature to its highest level in the past millennium [5].

The surface temperature of the earth is a consequence of the thermal energy balance between the sun as energy source, earth's surface, atmosphere and outer space as the ultimate energy sink. Greenhouse effect is the energy capture and recycling effect due to the atmosphere of the earth. Thanks to this effect, the average temperature of the earth is about 15 °C which is 33 °C above the temperature of an identical black body of identical radiation [6]. This difference permits current diversity of life on the earth.

A comparison of sun radiative activity and climate over the past 1150 years illustrates a close match between the earth's temperature and solar activity [7]. However, this relation has been disturbed in last decades. Figure 1.1 illustrates evolution of temperature and the main temperature contributing elements in the past century. Solar radiation and volcanic abruption are the main natural forcing elements while the GHGs have both anthropogenic and natural sources. Comparison of data since 1975 shows that temperatures rises while solar activity show little to no long-term trend [8]. Figure 1.2 illustrates the estimated contribution of radiative climate forcing elements since the industrial revolution, for period of 1750 to 2000. These data demonstrate that long lived greenhouse gases (GHG) are the principal responsible for the observed warming. Among the greenhouse gases, increase of CO_2 concentration has caused the largest forcing over this period. Increase of tropospheric ozone has also contributed to warming, while stratospheric ozone decrease has contributed to cooling [9]. The altered greenhouse gas emission imposes a positive perturbation on the Earth's energy balance with space [10]. This interpretation is supported by similar observation on positive heat storage in the ocean [11] and the magnitude of energy imbalance estimated from climate forcing for recent decades [12,13].

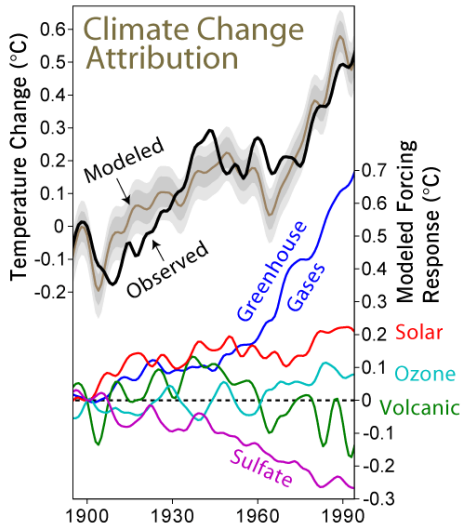

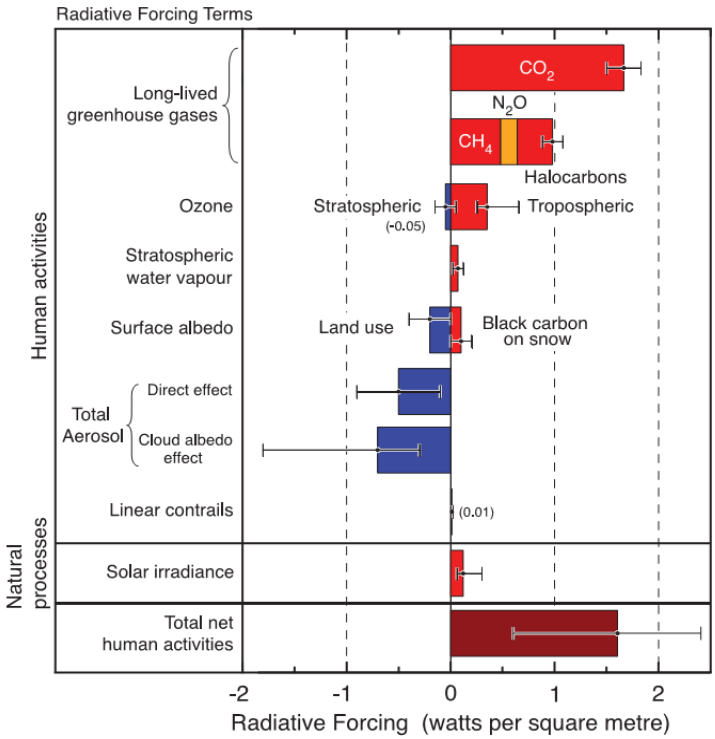

Figure 1.1: Trend of climate change attributing elements in the 20 century [14,15].

Figure 1.2: Estimated effect of various radiative climate forcing elements between 1750 and 2000 [9].

Global greenhouse gas emissions due to human activities have grown since pre-industrial times, with a sharp increase of 70% between 1970 and 2004 [16]. Carbon dioxide is the most important anthropogenic GHG. The global atmospheric concentration of carbon dioxide has increased from a pre-industrial value of about 280 ppm [16] to 390.02 ppm in August 2011 [17]. Its annual emissions have grown between 1970 and 2004 by about 80%, from 21 to 38 giga-tons, and represented 77% of total anthropogenic GHG emissions in 2004 [18].

Figure 1.3 illustrates flow diagram of anthropogenic greenhouse gas emission in 2005. It shows that carbon dioxide is the principal greenhouse gas with four main sources of: electricity and heat production, industrial usages, transportation and change of land usage. Methane and Nitrogen Oxide are respectively the second and the third important greenhouse gas which are principally produced by agriculture sources and waste disposal.

Concerns about the danger of climate change were raised in early 1980s by scientific community. As a result, the Intergovernmental Panel on Climate Change (IPCC) was created in 1988 by United Nations to assess the question of climate change. Its first major report in 1990 showed that there was broad international consensus that climate change was human-induced [19]. This report served as the basis of the United Nations Framework Convention on Climate Change (UNFCCC). UNFCCC is an international environmental treaty developed at the United Nations Conference on Environment and Development conference (Earth Summit) held at Rio de Janeiro, June 1992. The objective of the treaty is to stabilize greenhouse gas concentrations in the atmosphere at a level that would prevent dangerous anthropogenic interference with the climate system [20]. UNFCCC has no mandatory limits for the certified countries (194 countries plus European Union). Instead, the treaty provides for protocols that would set mandatory emission limits. The principal protocol ratified to date is the well-known Kyoto protocol.

The Kyoto Protocol was adopted in 1997 [21], recognizing the developed countries as the main responsible for the current high level of the GHG in the atmosphere. The protocol sets binding targets for 37 industrialized countries and the European community for reducing greenhouse gas emission. This amounts to an average of five percent against 1990 levels over the five-year period 2008-2012.

The last UNFCCC conference was held in December 2010 in Cancún, Mexico. The outcome of the summit was an agreement adopted by the states parties that called for a large "Green Climate Fund", and a "Climate Technology Center" and network. It looked forward to a second commitment period for the Kyoto Protocol.

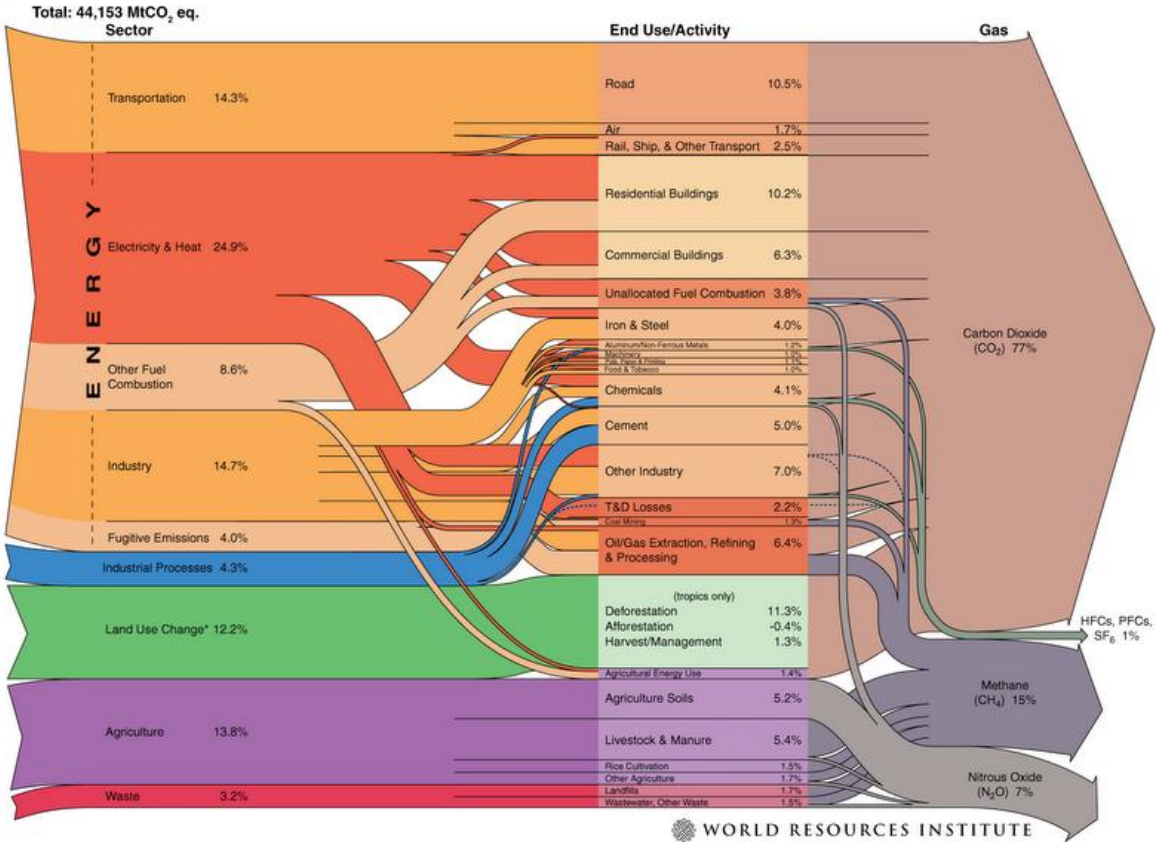

Figure 1.3: Global greenhouse gas emission flow diagram, based on the 2005 data. Dotted lines represent flows of less than 0.1% percent of total GHG emissions [22].

In addition to the international treaties listed above two other levels of climate protection legislation / agreements have been already developed. The EU climate and energy package is a European program adopted by European Parliament in 2008 [23]. It set a series of environmental and energetic targets known as the "20-20-20" including 20% reduction in GHG emission, 20% use of renewable energies, and 20% increase in energy efficiency by 2020. The third level of the existing environmental legislations on climate change is those ratified by individual countries and regions.

1.2 Carbon Dioxide Emission Mitigation, Carbon Capture and Storage

Energy sector CO_2 emissions will increase by 130% by 2050 in the absence of new policies or supply constraints as a result of increased fossil fuel usage, as projected by IEA [24]. Fossil fuels are the primary source of anthropogenic carbon dioxide emission by human activities. Reduction of CO_2 emission could be achieved through different measures. Development of alternative renewable energy sources and improvement of energy efficiency are the most effective measures for this purpose. However, regarding the current industrial state and existing energy infrastructure, a rapid change in energy source away from fossil fuels with current share of more than 85% [4] seems impossible. The latest energy outlooks published by IEA indicates that fossil fuels will continue to be the dominant energy source in the future [25]. Their future projection shows that oil remains the dominant fuel in the primary energy mix with demand increasing from 85 million barrels per day (mb/d) in 2008 (84 mb/d in 2009) to 99 mb/d in 2035. Demand for coal increases from 4 736 million tonnes of coal

equivalent (Mtce) in 2008 to just over 5 600 Mtce (1 Mtce is equal to 0.7 Mtoe) in 2035, with most of the growth before 2020 [25].

Carbon capture and storage (CCS) is a midterm solution to the stated problem, permitting reduction of CO_2 emission with minimum change in current energy sources. Carbon dioxide (CO_2) capture and storage is a process consisting of the separation of CO_2 from industrial and energy-related sources, transport to a storage location and long-term isolation from the atmosphere [26]. IPCC third assessment report indicates that no single technology option will provide all of the emission reductions needed to achieve stabilization, but a portfolio of mitigation measures will be needed [27]. IEA has stated that to meet global emissions reduction goals at lowest cost, extensive deployment of CCS is required [25]. They propose a roadmap called "BLUE map" to decrease CO_2 emission by 50% in 2050 compared to the 2005 emissions. Figure 1.4 illustrates the resulting deployment of CCS projects by different sectors in this road map. Accordingly, around 100 large scale CCS projects will be needed by 2020 to meet the BLUE map goal, and over 3000 by 2050. This represents a significant scale up from the five large scale CCS projects that are in operation today. The coal power stations and syngas production by biomass represent the most potential sectors for the upcoming development.

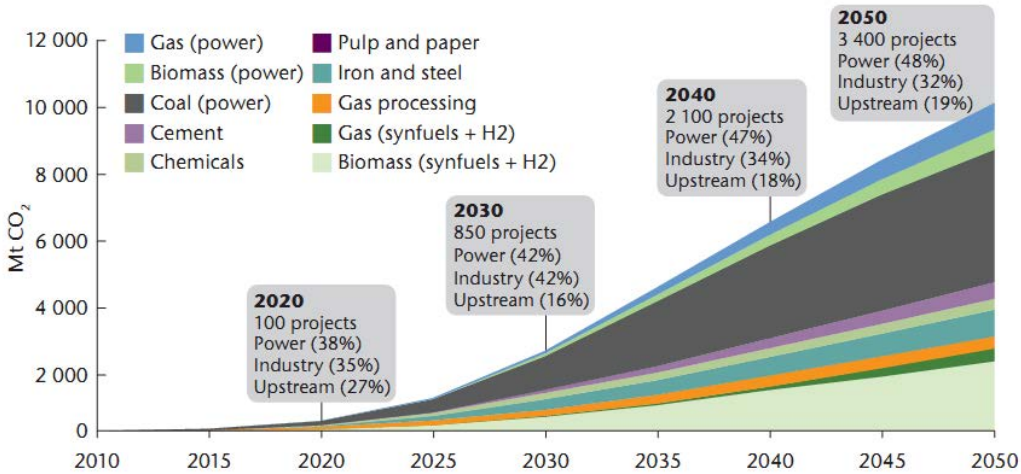

Figure 1.4 : Global deployment of CCS in the period of 2010 – 2050 by sector [25].

Carbon Capture and Storage (CCS) is divided into three main sections including: carbon dioxide capturing, transportation, and storage. Theoretically, carbon capturing is possible from any type of source even ambient air [28]. However, regarding the technical and financial constraints stationary point sources with concentrated CO_2 flue gas are of utmost interest. A closer look to the existing CO_2 sources in Figure 1.3 illustrates that the heat and electricity production cites and industrial units account for about 40 % of total CO_2 production while being a point source. Therefore, most of the capturing research and developments are being carried out in this domain. The capturing processes can be classified into three major categories including:

- Pre-combustion; which is separation of carbon in the form of CO_2 from the fuel before final usage and conversion of the fuel to a carbon free energy vector. The most common configuration involves gasification of fossil fuel with air or oxygen. The products undergo a water-gas shift to a high-concentration stream of CO_2 and H_2. The CO_2 is then captured and the H_2 is reacted with air [29].
- Oxy-fuel combustion; which is combustion of a fossil fuel with pure oxygen. The flue gas in this combustion process includes essentially CO_2 and water. The main separation step in this system is oxygen separation from air while control of the combustion temperature is the principal technological challenge [30,31].
- Post-combustion; in which CO_2 separation happens after combustion process from effluent exhaust gases. A chemical or physical solvent is normally used in this process to capture CO_2

the concentration of which is rarely above 15%. The main advantage of post combustion methods is that they can be directly employed to capture CO_2 from existing units. The main technology used in this category is carbon capture scrubbing particularly Amine absorption which is a well-known process.

The technological maturity and actual know-how of the stated carbon capturing processes varies significantly from one process to other. Figure 1.5 illustrates some of the existing technologies with the required commercialization date from today. It covers a large area from the ready to use processes such as Amine scrubbing to technologies in early development phase like biological capturing processes [32]. The main axis of development in this regard is the cost reduction and reliability.

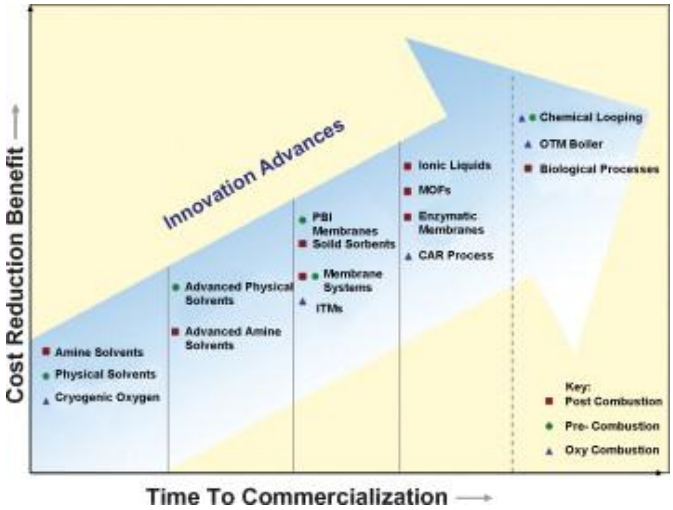

Figure 1.5 : Innovative CO2 capture technologies—cost reduction benefits versus time to commercialization [32].

The captured CO_2 is not necessarily stored near the capture point. Therefore, it has to be transported from capture to storage site by pipeline, ship or trucks. To transport the large amount of CO_2, pipelines are the most practical mean. CO_2 transportation by pipelines has been well developed to date and used since 1972 in USA over very long distances. An example is the Cortez pipeline with a transportation capacity of 19.3 Mt/yr along 808 km operated by Kinder Morgan since 1984 [33]. Similarly, Statoil has been transporting CO_2 extracted from natural gas along a 160 km subsea pipeline in north Norway. Carbon dioxide is preferably transported in supercritical condition (T>31 °C and P > 74 bar) for ease of operation and minimization of the corrosion problems [34].

The final step of the CCS is long term storage of carbon dioxide away from the atmosphere. Some important aspects should be respected including: safety, minimal environmental impact, verifiability, and liability [35]. IPCC has recognized three groups of storage options as: ocean storage, mineralization and industrial usage, or geological storage [36]. The ocean storage involves injection of CO_2 deep into the water where it dissolves or forms hydrates or heavier-than water plumes that sinks at the bottom of the ocean [37]. However, the increase of CO_2 concentration in the ocean can have serious consequences in marine life. It increases acidity of the water, can affect growth of corals, and may finally go back to atmosphere through equilibrium of water and atmosphere (this take a very long time) [38]. Mineralization involves chemical conversion of CO_2 to solid inorganic carbonates. Despite its interesting potential in safe CO_2 storage, high cost remains the main disadvantage of this process [37]. The geological CO_2 storage includes: oil and gas reservoirs; saline aquifers; and unminable coal seams (in combination with enhanced coal bed methane recovery) [39].

CO_2 storage in the depleted or operating oil reservoirs appeals as an interesting option. These reservoirs have a good sealing ability as they have retained liquid and gas hydrocarbons for millions of years. Moreover, this can result in some financial returns in case of CO_2 – EOR where CO_2 is injected into the oil reservoir to increase or maintain the pressure for higher hydrocarbon production [40]. CO_2 EOR has been largely studied and is commercially pursued since 1970 [41]. Most CO_2 used for EOR

is coming from naturally occurring sources [42]. More recently, some demonstration projects has been started to demonstrate aspects of CO_2 EOR chain as example [26,43]:

- Sleipner operated by Statoil in Norway since 1996 with storage rate of 1 Mt/yr of Co_2 with CO_2 injection in saline aquifer above natural gas reservoir.
- In Salah operated by BP and Statoil in Algeria since 2004 storage with storage rate of 1 Mt/yr into the saline aquifer.
- Weyburn operated by Encana in Canada for injection and CO_2 capturing by Dakota Gas from coal gasification in USA. The injection has been started in 2000 with 1 Mt/yr of CO_2 injection.

The CO_2 storage capacity of a reservoir include the CO_2 remained in the reservoir at the end of EOR operation and any extra CO_2 that can be injected after the EOR project [42]. The US experience indicated that approximately 40% of the originally injected CO2 is being produced in the producer wells and can be reinjected [44]. This suggests a CO_2 retention efficiency of approximately 60% at CO_2 breakthrough if separation and reinjection is not considered after the breakthrough [42]. Figure 1.6 illustrates schematically a CO_2 EOR process with CO_2 recycling.

It is estimated 130 billion tons of CO_2 worldwide could potentially be captured through the use of CO_2-EOR [45]. Therefore, CO_2-EOR presents a major economical and environmental interest. As example, in Texas, EOR now accounts for 20% of its oil production. It is estimated the benefits of EOR production will result in additional revenue of $200 billion and will create 1.5 million jobs [45].

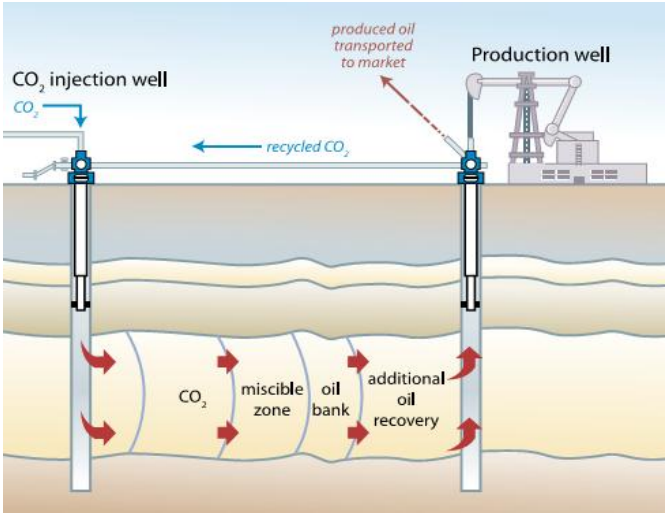

Figure 1.6: Injection of CO_2 for enhanced oil recovery (EOR) with some storage of retained CO_2. The CO_2 that is produced with the oil is separated and re-injected back into the formation [26].

Additional energy consumption for carbon capture and storage process (CCS) results in added costs of produced energy. A power plant equipped with a CCS system (with access to geological or ocean storage) would need roughly 10–40% more energy than a plant of equivalent output without CCS [26]. Table 1.1 lists the thermal efficiency and costs associated with two conventional power plants with and without CCS. Accordingly, CCS decreases the thermal efficiency by 15% – 26 % with a significant effect on the capital cost of 29% to 206% and electricity cost increase of 29% to 61%. Regarding the CO_2 EOR process, the cost and benefits of the project depends highly on the oil and gas price in the market. However, the anticipated performance of the Weyburn demonstration project shows that it is favorable even with available CO_2 at a cost of $35/t [42]. The financial studies are variable due to different hypotheses and variation of markets. Carbon capturing stands for principal part of the total cost for 70 % to 80%, transportation for 2 % to 5% and storage for 10 to 20% [46]. Accordingly, proper selection of carbon capturing technology can result in considerable cost saving in a CCS system. This shows the importance of the research and development studies on the capturing technology.

Table 1.1: Comparison of power stations with and without CO2 capture [47]. Capture cost include CO_2 compression to 110 bar but not storage and transport costs.

Technology	Thermal efficiency (% LHV)		Capital Cost ($/kW)		Electricity Cost (c/kWh)		Cost of CO_2 avoided ($/tCO2)
Gas fired plants							
No capture	55.6		500		6.2		
post-combustion capture	47.4	-15%	870	74%	8	29%	58
pre-combustion capture	41.5	-25%	1180	136%	9.7	56%	112
Oxy-combustion	44.7	-20%	1530	206%	10	61%	102
Coal fired plants							
No capture	44		1410		5.4		
post-combustion capture	34.8	-21%	1980	40%	7.5	39%	34
pre-combustion capture	32.5	-26%	1820	29%	6.9	28%	23
Oxy-combustion	35.4	-20%	2210	57%	7.8	44%	36

1.3 Chemical Looping Combustion

Chemical looping processes involve continuous circulation of a specie (Oxygen) from a source medium (Air reactor) to a reaction region (Fuel reactor) by aid of carrier particles (oxygen carrier). Various kinds of chemical looping processes have been developed to date. The main technologies developed based on this principle are:

- Chemical Looping Combustion (CLC): An oxygen carrier is used to transfer oxygen from air to a fuel (gas, liquid, or solid). The output is combustion heat and flue gas contains CO_2 and water vapor.
- Chemical Looping Reforming (CLR): Oxygen carrier transport oxygen to the fuel only for partial oxidation and steam reforming. The system output in this case is a syngas rich of H_2 and CO which is not diluted with Nitrogen [48].
- Chemical Looping Hydrogen (CLH): Water vapor is injected into the oxidation reactor in place of air. The oxygen carrier then decomposes water to hydrogen and oxygen. Hydrogen is the product of the system. Oxygen is then transported to the reduction reactor to burn the fuel and complete the loop [49].
- Chemical Looping Oxygen Uncoupling (CLOU): In this process, oxygen carriers transport oxygen to fuel reactor. Oxygen is then released into the gas phase from the particles to react with solid fuel [50].

Chemical Looping Combustion involves indirect combustion of fuel without any direct contact between air and fuel. The resulting flue gas is a ready to capture CO_2 stream diluted only with water vapor which can be easily condensed out of the stream. Therefore, CO_2 is an inherent product of CLC process and Nitrogen does not dilute the produced flue gas. This is the main advantage of CLC as minimum extra energy is required to capture CO_2. Therefore, the overall combustion efficiency is comparable with the conventional combustion processes, i.e. minimum energy penalty for CO_2 capturing [51] estimated for only 2 – 3% efficiency lost [52]. Moreover, NO_x formation reduces in this process as oxidation happens in air reactor in absence of fuel in temperatures below 1200 °C above which NO_x formation increases considerably [53].

Principle of CLC process is based on the use of an oxygen carrier to act as an intermediate transporter of oxygen between the air and the fuel. Therefore, direct contact of the air and the fuel is inhibited. A solid oxygen carrier (mostly metal oxide) is used to oxidize fuel stream. This results in production of CO_2 and H_2O as:

$$C_nH_{2m} + (2n+m)M_yO_x \rightarrow nCO_2 + mH_2O + (2n+m)M_yO_{x-1} \qquad \Delta H_{red} \qquad \textbf{Eq. 1.1}$$

Heat of this reaction (ΔH_{red}) depends on the nature of the oxygen carrier and its reaction with the fuel. However, this reduction reaction is mostly endothermic. The reduced form of the oxygen carrier, M_yO_{x-1}, is then transferred to the air reactor where in contact with the air the particles are reduced to their initial state of M_yO_x, as:

$$M_yO_{x-1} + \frac{1}{2}O_2 \rightarrow M_yO_x \qquad \Delta H_{ox} \qquad \textbf{Eq. 1.2}$$

Oxidation reaction is always an exothermic reaction [54]. The overall heat of CLC process will be sum of the two heats state above and this is equal to the heat released in a conventional combustion reaction. Figure 1.7 presents schematically the overall concept of this indirect transfer of oxygen between air and fuel.

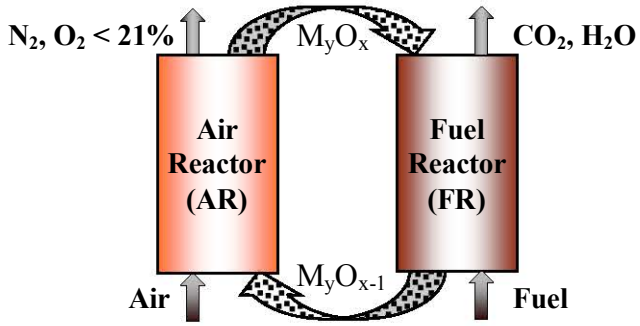

Figure 1.7: Principle of chemical looping combustion (CLC). M_yO_{x-1} and M_yO_x indicate oxygen carrier in reduced and oxidized states.

There exist some important challenges in CLC research and development. These could be considered in two general categories of material and process development. Oxygen carrier is an essential element which should meet some important criteria including: high oxygen transport capacity, high reaction rate, long life time, mechanical resistance, resistance in high temperature, no toxicity, being environmentally friendly, availability and affordable cost. Numerous studies have been carried out on development of oxygen carrier particles [55-57]. Regarding the process development, there exist different criteria to be met including:

- Proper selection of the oxygen carrier inventory in reactors to ensure maximum reaction conversion [58].
- Sufficient particle circulation between the fuel and air reactors to achieve sufficient oxygen transfer for complete combustion of the fuel. Moreover, circulation rate should be adjusted to meet necessary energy transfer to keep the system thermally balanced. The recirculation rate also affects the solids inventory in the reactors needed to convert the fuel. Thus, a decrease in the recirculation rate increases the minimum mass of solids needed in the system [59].
- High pressure operation to provide higher overall efficiency of the power generation, with high pressure being also favorable for the downstream CO_2 sequestration [54].
- Minimization of gas leakage between the reactors to prevent dilution of the produced CO_2 stream and to prevent leakage of the captured CO_2 out of the reactor which reduces the efficiency of the capturing process [60].

Chemical looping combustion represents a major economical interest regarding the minimum energy lost in this process. However, the process is currently in early development and demonstration phase as illustrated in Figure 1.5. Therefore, 10 to 15 years of extra research and development is required before final commercialization step of this process.

Ekström et al. [52] have carrier out an economical analysis for a series of available carbon capture processes in framework of European ENCAP project. Considering a 445 MW bench-scale CLC with bituminous coal, they have found a 13 % to 22 % cost increase in electricity production (compared to 31% to 41% for conventional oxyfuel) and a CO_2 avoidance cost of 6 – 13 € (14 – 30 € for oxyfuel). Similarly, they have found that CLC results in minimum additional electricity cost for a 393 MW natural gas unit with electricity cost increase of 15 – 31% (for three tested CLC systems) while other examined technology range from 29 to 61% increase. Their final conclusion states that ~~of~~ the evaluated more new, and therefore less validated technologies, CLC (Chemical Looping Combustion) for coal, petcoke and natural gas appear promising, with potentially higher electric efficiencies and lower costs, but need more research and development."

1.4 CLC Designs

Principle of chemical looping combustion was invented by Lewis and Gilliland [61] as a way to produce pure Carbon Dioxide in 1954. In 1983, Richter and Knoche [62] suggested this system to increase efficiency of combustion reaction through reduction in irreversible entropy production. About 10 years later, Ishida and Jin [63] developed the application of CLC as a promising method for CO_2 capturing. Since then, mostly in recent years, many researches have been devoted to chemical looping systems not only for carbon capture but also to produce high quality syngas.

Chemical looping combustion system can be designed in various ways. Different designs have already been proposed for CLC process. These could be classified into two general categories: interconnected fluidized bed designs and fixed bed processes. The latter category includes some innovative design as: packed bed CLC [64], packed bed membrane assisted chemical looping reactor [65] and rotating bed reactor [66]. However, most of the existing systems are designed based on the circulating fluidized bed system. Fluidized bed system provides a good contact between gas and solid phases and continuous smooth flow of solid materials between the two reactors [67,68].

The most common fluidized bed design is based on the conventional circulating fluidized bed (CFB) systems with addition of a second reactor as fuel reactor [69-71]. Lyngfelt et al. developed first system of this kind with gaseous feed in 2004 [69] (see Figure 1.8.a). Since then, various similar CLC configurations were constructed worldwide [70-73]. In these systems a low velocity bubbling fluidized bed reactor is dedicated to fuel combustion reaction and a high velocity riser is considered as air reactor. The advantage of this design is the fact that due to its similarity with conventional CFB combustion process, it is best adapted with existing power generation units and its phenomena have been subject of many investigations to date. Studies reveal that solid flow control can be achieved in this configuration [74,75], however it is a function of gas flow in the reactors and solid inventory in each reactor. In other words, solid flow could not be adjusted independently from other parameters of fluidization. In order to improve solid circulation control and achieve proper residence time in the reactors different modified designs are developed to date. Forero et al. [76] have added a bubbling fluidized bed as air reactor (AR) just below the riser. De Diego et al. [73] have also used a bubbling fluidized bed as AR while separating the riser and the AR using a loop-seal.

A promising design have been developed by Kolbitsch et al. [77] based on Dual Circulating Fluidized Bed (DCFB) concept (see Figure 1.8.h). In this system, Fuel reactor (FR) is in turbulent regime forming a second loop inside the overall system. They have accordingly succeeded to control the solid flow rate just based on the aeration rate in AR, independent from the gas rate in FR. Ryu et al [78] have developed a 50 kWth pressurized CLC design for pressures up to 6 atm. They have used bubbling fluidized bed reactors with circulation of solids by aid of small diameter risers placed inside the bed feed through orifices at the bottom of the risers. Alstom Power [79] has developed a series of novel system based on the limestone where calcium sulfide (CaS/CaSO4) is used as oxygen carrier (see Figure 1.8.m). Regarding their rich background in CFB combustion units they have developed different sizes with possibility of retrofitting of some existing CFB systems. Calcium based designs have been pursued by some other research groups [80,81] including University of Stuttgart for a post combustion CO2 capture system [80].

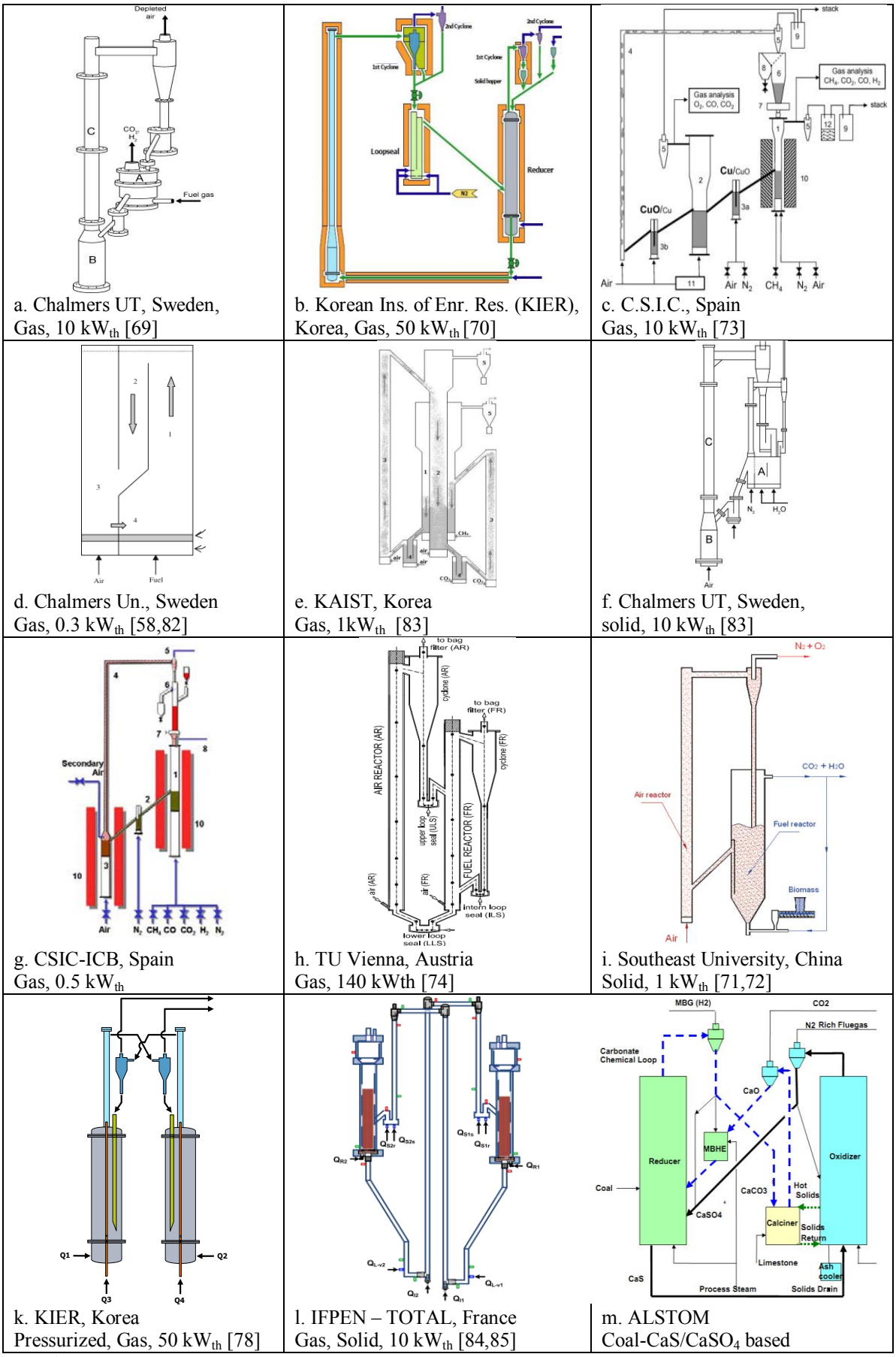

a. Chalmers UT, Sweden, Gas, 10 kW_{th} [69]

b. Korean Ins. of Enr. Res. (KIER), Korea, Gas, 50 kW_{th} [70]

c. C.S.I.C., Spain Gas, 10 kW_{th} [73]

d. Chalmers Un., Sweden Gas, 0.3 kW_{th} [58,82]

e. KAIST, Korea Gas, 1kW_{th} [83]

f. Chalmers UT, Sweden, solid, 10 kW_{th} [83]

g. CSIC-ICB, Spain Gas, 0.5 kW_{th}

h. TU Vienna, Austria Gas, 140 kWth [74]

i. Southeast University, China Solid, 1 kW_{th} [71,72]

k. KIER, Korea Pressurized, Gas, 50 kW_{th} [78]

l. IFPEN – TOTAL, France Gas, Solid, 10 kW_{th} [84,85]

m. ALSTOM Coal-CaS/$CaSO_4$ based

Figure 1.8: Scheme of existing CLC systems around the world as pilot units.

In addition, some novel designs have been proposed mostly dedicated to laboratory tests. Kronberger et al. [58] have developed an alternative design, two compartment fluidized bed reactor, with simplified configuration resulting in smaller installations requirement and lower cost for experimental studies (Figure 1.8.d). Son et al. [86] have proposed an annular fluidized bed CLC reactor in order to provide sufficient reaction time and optimize heat transfer between the reactors (Figure 1.8.e).

CLC design adapted for used of solid fuels was pioneered by research team at Chalmers University [87]. Their design is based on the previously developed gas feed 10 kWth CLC system with CFB working principle (Figure 1.8.f). The main modification was in the fuel reactor. The reactor was divided into two compartments to create a narrower residence time to decrease leakage of chars into air reactor. Oxygen carriers were then lead into a carbon stripper adjacent to the fuel reactor where an increased Nitrogen velocity was applied to strip out ashes and unreacted solids from the main oxygen carrier flow. The oxygen carriers are then lead into the air reactor through a loop-seal. The unreacted separated particles are conveyed back into the fuel reactor. Shen et al. [71,72] developed a 10kWth CLC system with coal and biomass feed (Figure 1.8.i). They have employed a circulating AR leading into the FR which operates in spoted bed regime. The solid is introduced into the system through a bottom feeder together with fluidization gas. Recently, they have developed a similar CLC system of 1 kWth with the difference of a loop-seal added to the fuel reactor exit into the air reactor. Regarding the industrial R&D and scale-up, Alstom power has developed a 1 MW_{th} solid fuel auto-thermal CLC installed at TU Darmstadt, Germany, in the framework of EU-funded ECLAIR project [88]. The operation and results of this pilot will be an important step toward industrial CLC process.

1.5 Solid Circulation

Solid circulation is an essential parameter in fluidized bed processes with solid recirculation system. It is known that the major operational problems in these processes is failure of solid circulation and feeding systems [89,90]. This fact demonstrates importance of a good comprehension and mastery of solid circulation. This is of even more vitality in chemical looping combustion due to: oxygen transfer, gas tightness and thermal balance. In CLC process, the oxygen necessary for combustion is supplied by solid circulation. Consequently, higher solid circulation is desired to achieve higher combustion capacity. Moreover, an appropriate control of solid circulation is of great interest both for proper control of combustion conversion, and flexibility of operation in terms of fuel input and power output. In addition, solid circulation is essential to achieve a desired thermal equilibrium between air and fuel reactors especially in case with endothermic reactions like reduction of Nickel based oxygen carriers.

Solids in circulation entrain some interstitial gas resulting in leakage problem. Gas leakage out of the fuel reactor reduces the quantity of the carbon dioxide captured and therefore, reduces the capture efficiency. Moreover, this can cause safety problems if the combustible gas leaks into the air reactor. A direct contact between oxygen of air and combustible gas results in a violent combustion which can cause significant problems. On the other hand, gas leakage into the fuel reactor can cause dilution of the flue gas and increase of the impurities in the captured CO_2. Accordingly, control and minimization of gas leakage is another essential operational parameter in CLC.

The solid circulation and possible control measures are discussed in the following sections. Non-mechanical L-valve is presented first as an efficient device to control solid circulation. Loop-seal is a typical element used in circulating fluidized bed systems. This device is briefly discussed and the related existing literatures on its operation are reviewed. Standpipes have an important role in operation of both L-valve and loop-seal. Therefore, a section is dedicated to this element. Measurement of solid circulation and modeling of circulating fluidized bed systems are finally discussed very briefly.

1.5.1 Non-mechanical Pneumatic L-valve

Solid circulation control could be best achieved through use of the mechanical valves as in some mature catalytic processes like FCC [91]. High temperature however limits the use of mechanical valves for CLC applications. Non-mechanical pneumatic valves (loop-seals, L-, J- and V-valves) do

are a category of flow rate controlling devices does not employ any moving mechanical part. These are considered as an interesting solid flow controlling device for these operating conditions. L-valve is a common non-mechanical valve with some design and operational advantages as: simplicity in design, low cost, effective in solid flow control, small air flow requirement and long operational life time [90,92].

Solid flow rate in the L-valve is a function of the aeration gas injected into the L-valve. Knowlton and Hirsan [93] explained that the total aeration which causes the solids to flow in the L-valve is not only the external aeration, but the total gas flow around the elbow of the L-valve. The total gas flow is sum of the external gas injection and the gas flow in the standpipe (vertical arm of the L-valve). They then use the modified Ergun equation [94] for the interstitial relative velocity of the gas and solid, to predict gas flow across the L-valve. The pressure drop in the standpipe of the L-valve is a dependent parameter [93], which is an intrinsic property of non-fluidized standpipes [95]. Pressure drop in this section adjusts to balance pressure drop over the entire elements of the system. Accordingly, pressure drop in this element can be calculated from the overall pressure balance over the entire solid circulation loop [90,92]. The total gas flow can then be calculated taking into account the gas flowing down the standpipe with solids or leaving upwards through the particles in the standpipe.

Various researches have already been carried out on L-valve operation. Table 1.2 presents a brief list of the existing understanding on the effect of different parameters on the L-valve operation. The parameters are divided into some categories including; effect of geometry of the L-valve, particles properties, gas properties, flow rates, pressure, temperature and observed limits of L-valve operation.

The geometry of L-valve is an important parameter in its efficiency in solid flow control. Various studies have been conducted to investigate effect of L-valve geometry on its operation [90,92,93,96,97]. Table 1.2 lists the main investigation results on the L-valve and effect of various geometrical and operating parameters. An important point to be mentioned about L-valve is the fact that it is not a suitable device to control solid flow rate of small group A particles. The slope of solid flow rate versus external gas injection increases as particle size increases. For small group A particles it becomes a very sharp line, making it difficult to control the flow [92]. Moreover, it may be impossible to stop solid flow with these particles due to the high quantity of gases entrained in the standpipe compared to the required gas flow around the elbow to maintain solid circulation [90].

Different correlations have been developed in the literature to predict solid flow rate for a determined gas injection into the L-valve [92,97-102]. Some existing solid flow rate correlations are listed in

Table 1.3 Pioneered by Geldart and Jones [92] the correlations mostly relate solid flux divided by valve diameter (G_s/D) to superficial velocity of the injected air into the L-valve divided by minimum fluidization velocity (U/U_{mf}). The idea of correlating Gs/D is to take into account the effect of pipe diameter based on the work carried out by Geldart and Ling on dense phase conveying of fine coals [103]. Daous and Al-Zahrani [99] however use velocity over the solid particles diameter to correlate their data. A different approach presented by Yang and Knowlton [102] uses the equations of mechanical slide valves to correlate solid flow rate W_s of the L-valve and the pressure drop across the valve.

Pressure drop in the horizontal section of the L-valve has been correlated by various researchers. Some of the correlations available in the literature are listed in Table 1.4. Most of the researches have correlated the pressure drop per unit length to the solid flux in the section using empirical dimensional correlations [92,97,99,100,104,105]. However, Lae [105] has used a modified form of the Ergun correlation to predict the pressure drop. The author has then developed a correlation, describing the average voidage in the section based on dimensionless numbers. Ergun equation [94] is originally developed for a fixed bed of solids. It has been also used for a moving non-fluidized solid bed confirmed by Yoon and Kunii [106] in their experiments with moving beds of glass beads. However special aspect of horizontal solid flow in the L-valve mostly non-equivalent voidage distribution and high relative solid velocity in the moving solid bed requires this relation to be verifies with more experimental results.

Table 1.2: Different investigation results on the L-valve operation.

Category	Element	Comment
Geometry	Length of standpipe	$H_{lv,v}$ ↑ ➔ W_{max} ↑ & influences Q(Ws)[1] [93] ΔP/L = linear in the standpipe
	Diameter of standpipe	As $D_{lv,v}$ ↑ ➔ Ws_{max} ↑ & $Q_{lv,min}$[2] ↑ & η_{lv}[3] ↓[93]
	Aeration point	To be placed close to the bottom of downcomer but not below elbow [93] No of aeration points ↑ ➔ Q(Ws) ↑ Point of max Pressure [92]
	Elbow	Elbow geometry from sharp to gradual ➔ Q(Ws) ↓ [92] & sensitivity of control near the Ws_{min} ↑ [92]
	Length of horizontal pipe	$L_{lv,H}$ ↑ ➔ to some extent $\Delta P_{lvH}/L$ ↑ [93] & $\Delta P_{lvH}/L$ ↓ [97]
	Diameter of horizontal pipe	D_{lvH} ↑➔η_{lv} ↓ at small Ws & η_{lv} ↑ at higher Ws & $\Delta P_{lvH}/L$ ↓ (for a given Ws)[93]& Ws_{max} ↑[92]& controllability at low Ws ↓[92]
	Angel of horizontal pipe	θ [4] ↑ ➔ Q(Ws) ↓ & flow stability and control at low Ws ↑[92] θ >106°➔gas bypassing➔Ws_{max}↓ (≈ 2/3 of Ws_{max} at 90°) [92]
	size of L-valve	If D_{lv} < 0.2 m : D_{lv} ↑ ➔ Q(Ws) ↑ [97] If D_{lv} > 0.25 m : D_{lv} ↑ ➔ Q(Ws) = cte [97] D_{lv} ↑ ➔ Q(Ws) ↑ [92]
Particles	Density	ρ_P ↑ ➔ Ws_{max} ↑ & Q(Ws) ↑ [93,104] & $\Delta P_{lvH}/L$ ↑ [93,104] & Ws_{max} ↓[6] [104]
	Diameter	dp ↑ ➔ $Q_{lv,min}$ ↑ & $\Delta P_{lvH}/L$ = cte [93] & Q(Ws) ↑ [92,104] & Ws,max ↓[6] [104] & $\Delta P_{lvH}/L$ ↓ [104] & δ_{lv} [5] [92]
	Sphericity	ϕ ↑ ➔ Ws ↑ [100]
	Classification	Group C: impossible flow Group A: Very narrow Q_{lv} ➔ very difficult Ws control Group B: Best suited in the L-valve Group D: possible but high Q_{lv} requirements and limited D_{lv}
Gas flow rate	External aeration rate	Q_{lv} min (at Ws_{min}) ≈ Q_{mf} (= A×U_{mf}) [92]
	in the standpipe	$Q_{lv,v}$= up/downward [104]=function of pressure loop[93,107] dp ↑ ➔ Ws,critical at which direction of $Q_{lv,v}$ changes ↑ [92]
	Around the elbow	$Q_{lv,H}$ = Q_{lv} + $Q_{lv,v}$ & Ws = f ($Q_{lv,H}$) [104]
Gas	Gas density	-
	Gas viscosity	-
	Pressure	-
Temperature		T ↑ ➔ Q(Ws) ↓ (The effect is more than what expected only by expansion due to viscosity increase) [108]
Limit		Hopper discharge [92,97], solid height in the downcomer [104] $H_{lv,v}$ [109], Height of the downcomer [109]

[1] Q(Ws) = the required Q_{lv} to achieve a certain Ws.
[2] $Q_{lv,min}$: the minimum required external gas flow rate for the solid to start flowing.
[3] η_{lv}: The achieved solid flow rate for an external L-valve aeration.
[4] θ: the downward angel of the horizontal pipe of L-valve with horizontal line.
[5] δ_{lv} = $Q_{lv,v}$ / Q_{lv}.
[6] Due to the increase of solid hold up in the elements downstream of the L-valve and reduction of height of solid bed in the downcomer.

Table 1.3: Some existing correlations for prediction of the solid flow rate in the L-valve.

Correlation	Condition	Ref
$\frac{G_s}{D_{lv}} = 3354\frac{U_{lv}}{U_{mf}} - 2965$	$D_{lv} \geq 0.025$ d_p (280 μm – 790 μm)	[92]
$\frac{G_s}{D_{lv}} = 780\left(\frac{U}{U_{mf}}\right)^2$		[98]
$\frac{G_s}{D_{lv}} = 79600\left(\frac{U}{U_{mf}}\right)^2 d_p^{0.6}$	D_{lv} (0.02 m – 0.04 m) d_p (137 μm – 1490 μm) atm discharge, hopper feed	[97]
$\frac{G_s}{D} = -5450 + 1.08\frac{U_{lv}}{d_p}$	D_{lv} (0.025, 0.036 & 0.05 m) d_p (470 – 3000 μm) ρ_P (2680 kg/m^3)	[99]
$\frac{G_s}{D_{lv}} = 1.758\left(\frac{U}{U_{mf}}\right)^{1.95} Ar^{1.27}\phi_s^{6.9}$	D_{lv} (0.05 m) 4 solids of Geldart group B d_p (55 μm - 440 μm)	[100]
$\Delta P_{lv} = \frac{1}{2\rho_p(1-\varepsilon_{mf})}\left[\frac{W_s}{C_D A_o}\right]^2$ $C_D = 0.5$ To find A_0: $Q_t = 0.177(\pi/4)D_h^2 L_h + 0.710 U_t A_o$ $Q_t = Q_{lv} + Q_{lv,v}$ And $Q_{lv,v} = \frac{W_s \varepsilon_{mf}}{\rho_p(1-\varepsilon_{mf})}$	Dlv (38 mm – 152 mm) dp (175 μm – 509 μm) ρ_p (1230 – 4150 kg/m^3) θ (0.56 – 0.915) Developed from equation for slide valves considering non slip condition (valid for high solid flux):	[102]

Table 1.4: Pressure drop correlations existing in literatures for L-valve.

Correlation	Conditions	Ref
$\frac{\Delta P_{lvH}}{L_{lv,H}} = 216\frac{G_s^{0.17}}{D_L^{0.63} d_p^{0.15}}$	Group B particle $D_{lv} \geq 0.025$ d_p (280 μm – 790 μm)	[92]
$\frac{\Delta P_{lvH}}{L_{lv,H}} = 3500 G_s^{0.30}\frac{d_P^{0.10}}{L_h^{0.70}}$	D_{lv} (0.02 – 0.04 m) d_p (137 – 2000 μm) ρ_P (2600 kg/m^3)	[97]
$\frac{\Delta P_{lvH}}{L_{lv,H}} = 0.0649\frac{G_s^{0.178}\rho_b^{0.996}}{D_{lv}^{0.574} d_p^{0.237}}$	D_{lv} (0.027 m) Group A and B particles d_p (45-630 μm) ρ_P (1770 – 4460 kg/m^3)	[104]
$\frac{\Delta P_{lvH}}{L_{lv,H}} = 9.13\left(\frac{D}{d_p}\right)^{1.4}(G_s)^{-0.10} U_{g,lvH}$	D_{lv} (0.025, 0.036 & 0.05 m) d_p (470 – 3000 μm) ρ_P (2680 kg/m^3)	[99]

$\frac{\Delta P_{lvH}}{L_{lv,H}} = 150 \frac{(1-\varepsilon_H)^2}{\varepsilon_H^{\ 2}} \frac{\mu_g}{(d_{sv})^2} \left(\frac{U_{gH}}{\varepsilon_H} - \frac{G_s}{(\rho_s(1-\varepsilon_H))} \right)$ $\varepsilon_H = 2.964\,\mathrm{Re}^{0.239}\, Ar^{-0.318} Mv^{0.05}$	Group B sands d_p (145 – 395 μm) ρ_P (2600 kg/m^3) $Mv = \frac{\rho_s - \rho_g}{\rho_g}$	[105]
$\frac{\Delta P_{lvH}}{L_{lv,H}} = 0.115 \frac{G_s^{\ 0.137}}{\rho_b^{\ 0.131} d_p^{\ 0.64}}$	D_{lv} (0.050 m) d_P (80 – 190) ρ_P (2660 – 4000 kg/m^3)	[100]

1.5.2 Loop-Seal

Loop-seals are mostly used to buildup the necessary pressure in a solid circulation loop so that particles could flow from a zone of low pressure (e.g. a cyclone) to a high pressure zone (e.g. a furnace or a riser) [110] without undesirable inverse gas flow. Loop-seals are extensively used in fluidized bed systems. A typical loop-seal is made of three main components: supply chamber (SC), recycle chamber (RC), and recycle pipe (RP) [111]. Different configurations exist for loop-seals based on the connection of SC and RC including: the use of a simple slit opening between the chambers [112] or a horizontal pipe connection between two sections [113]. The refractory walls and insulation around the standpipe and loop-seal recycle chamber would typically require a thickness well exceeding 250–500 mm[112]. Therefore, loop-seals usually have a horizontal pipe unless they are specifically designed to have no external wall between these two chambers. In some industrial high solid flow units, two recycle pipes could be used to increase the maximum solid flow rate in the loop-seal. This technology is called twin-exit loop-seal [111]. Another possible modification in the loop-seal is development of specific design dedicated to especial applications such as employment of a heat exchanger inside the loop-seal [110] or solid feeding into the system in industrial applications.

Particles flow through a standpipe into the supply chamber and then lead into the recycle chamber. Solids are in fluidized state in the recycle chamber and overflow through a horizontal passage or weir into the recycle pipe where they are conveyed to the following element which could be a riser or a reactor. Various studies have been carried out on hydrodynamics of solid and gas flow in a loop-seal [110-122]. Horizontal solid flow between two chambers of loop-seal is critical both for understanding and modeling of loop-seal operation. Some correlations have been already developed in literature works on solid flow [120,123,124] and pressure drop [119,121,122,125] in this section. Table 1.5 and Table 1.6 list some of the existing correlation in the available literature on the loop-seal.

Flow in the recycle chamber has been also studied in different works [111,112,119,123,126]. Cheng and Basu [119] have reported that aeration in the recycle chamber should pass a critical value for the solid flow to start. In atmospheric pressure this corresponds to the U_{mf} which decreases as pressure rises. Above this critical value, solid flow rate increases as U_{RC} increases however the solid flow levels off beyond a certain value above which solid flow remains constant, as observed by various researchers [111,112,119,124]. A smooth operation of loop-seal, requires the aeration of the recycle chamber to be above the U_{mf} of largest particles [118]. Pressure drop in RC is mostly calculated using the conventional pressure drop equation in a fluidized bed. However, Monazam et al. [123] have correlated the pressure drop in this section and solid flux through the loop-seal. Botsio and Basu [117] have studied the solid overflow out of the recycle chamber into the recycle pipe in a CFB system. They have developed a correlation based on the sharp-crested orifice theory of water flow relating pressure drop and solid flux in this section. Pressure drop in recycle pipe of the loop-seal is described similar to the conventional pneumatic conveying lines pressure drop including the terms of gas and solid friction, static head and kinetic acceleration head [119].

Higher pressures have been reported to increase the solid flow rate through the loop-seal [119]. It is reported that aeration requirement to obtain the same solid flux (G_s) increases with increasing particle size [116,119,122]. However, the obtained maximum G_s is almost the same regardless of particle diameter (d_p) [122]. Kim and Kim [122] have compared solid flow results for particles of similar size and different densities. They have concluded that the maximum obtainable solid flow rate is higher for particles with higher density.

Table 1.5: Solid flow rate correlations developed for solid flow in the loop-seal.

Correlation	Installations	dp (µm)/ρs (kg/m³)	ref
$\frac{W_s D_r}{M U_t} = 0.00192 \left(\frac{U_g^2}{g D_r}\right)^{0.323} \left(\frac{U_{move}}{U_{mf}}\right)^{1.27} \left(\frac{U_{ls}}{U_t}\right)^{0.18}$	CFB, 0.25 m ID of ls, 15.45 m riser with 0.3 m ID	Cork (1007/189) (Group B)	[123]
$G_s = C_D \left(\frac{A_0}{A}\right) \sqrt{2\rho_s (1-\varepsilon_{mf}) \Delta P_v}$ $C_D\left(\frac{A_0}{A}\right) = 0.130 \left(\frac{U_{BA}}{U_{mf}}\right)^{0.200} \left(\frac{U_A}{U_{mf}}\right)^{0.372} \left(\frac{L_h}{D_d}\right)^{-0.458} \left(\frac{U_g}{U_t}\right)^{-1.102}$ based on mechanical valves correlation of [127]	Riser: 0.1 m i.d. , 5.3 m high Downcomer: 0.08 m i.d., 4.0 m high ls: 0.08 m i.d.	FCC (65/1720)	[120]
$G_s = 3.96 \left(\frac{U_A}{U_{mf}}\right)^{0.70} Ar^{0.36}$ $G_s = 0.10 \left(\frac{U_A}{U_{mf}}\right)^{2.23} Ar^{0.90}$	CFB, ls: 0.08 m i.d. riser: 0.08 m i.d., 4.0 m high vertical aeration: $L_h/D_d = 2.5$ $L_h/D_d = 3.5$	FCC (65/1720) Sands (125/3055), (239/3120), (350/2382)	[124]

Table 1.6: Pressure drop correlations developed in different researches for solid flow in the horizontal passage of the loop-seal.

Correlation	Section	Installation	dp (µm)/ρs (kg/m³)	Ref
$0.66 \left(\frac{A_g}{A_{sp}}\right)^{-1.2} G_s$	Across the weir	ls: 0.09 m i.d. downcomer: 0.026 m i.d.	90 /2365 and 232 /2730 and 503/2818	[119]
$\Delta P_{ls} = \frac{(G_s A_{sp})^2}{(C_{D0} A_{ls})^2} 2\rho_s (1-\varepsilon_{mf})$ $C_{D0}A_0 = 11\times10^{-6}$ m² ± 30 % A_0: effective valve flow area, m²	DP_{ls} Solids mechanical valve corr. adopted from [119]	0.04m i.d. ls 0.08m i.d. downcomer 1.9 m long /0.04 m i.d.	alumina (70 / 2800) with helium and nitrogen mineral sand (130/4400) with nitrogen	[125]
$\left(\frac{\Delta P}{L}\right)_{va} = 1.8\times10^{-5} \left[\frac{(G_s/\rho_s)^2}{d_p g}\right]^{0.40} \left[\frac{G_s d_p}{\mu}\right]^{-0.36} \left[\frac{\rho_s}{\rho_g}\right]^{2.88}$	Vertical section below aeration, horizontal section to the weir	0.08 m i.d. ls 0.08 i.d. downcomer 5.3 m high and 0.1 i.d. m	sand 78, 101, 157, 239 / 3120 kg/m³ FCC : 65 / 1720	[122]
$\Delta P_{ls} = \Delta P_w + \Delta P_{va}$ $\left(\frac{\Delta P}{L}\right)_w = \rho_s (1-\varepsilon) g$ in weir section which is fluidized $\varepsilon = \frac{1}{2.1}\left\{0.4 + \left\{4\left[\frac{\mu \rho_g U_0}{d_p^2 (\rho_g (\rho_s - \rho_g) \phi_s^2 g)}\right]^{0.43}\right\}^{1/3}\right\}$ $\left(\frac{\Delta P}{L}\right)_{va} = 0.0056 G_{sd}^{0.51} \rho_{bulk}^{2.01} d_p^{-0.97} D_{ls}^{-0.76}$ Downcomer and supply chamber	Across the ls	riser: 0.1m i.d. / 7.6 m high Downcomer: 0.1m i.d. 5.62 m ls: 0.1 m i.d.	Silica sand 240µm 2582 kg/m³ Air	[121]

1.5.3 Stand Pipe Solid Flow

The purpose of a standpipe is to transfer solids from a region of lower pressure to a region of higher pressure [95] by gravity force of particles. The vertical section of the L-valve above the aeration point and the recycle chamber of the loop-seal below the cyclone dipleg can be considered as standpipes based on this definition. The gas-solid flow in a standpipe is largely divided into non-fluidized, fluidized and streaming flows. The non-fluidized bed flows are divided into packed bed and transitional packed bed flows by slip velocity [128,129]. Packed bed flow often occurs when the gas flow is assisting solids flow, with the gas pressure higher at the top of the downcomer than at the bottom. In this case, the voidage of the bed is constant equal to voidage of a non-fluidized vibrated solid bed. Transitional packed bed flow usually occurs when the gas flow is upward relative to the downward solids flow, with the gas pressure at the bottom of the standpipe higher than that at the top, i.e., at the negative pressure gradient condition [129]. Bed voidage in this region is variable as a function of relative gas – solid slip velocity [130]. Knowlton T. M. [95] has explained that for a particle velocity above 0.3 m/s slip-stick flow happens. Regarding the oscillatory aspect of this flow operation with solid velocities less than 0.3 m/s are recommended.

Solid flow in standpipes of both L-valve and loop-seal is in downwards cocurrent or counter current solid and gas flow. Particles flow in dense phase mode by the gravity force of the solids. Pressure drop in this section is developed through the relative movement of solid and gas. As the solids are not fluidized, change in relative solid –gas velocity can change the pressure drop across the solid bed. This type of solid flow has been investigated by different researchers [128,131,132]. Ergun equation [94] used with relative solid–gas velocities is used to calculate pressure drop in standpipe of both L-valve [92,93,97] and loop-seal [112,116,119,120,122]. A critical parameter in dense phase solid flow is the change of bed voidage for different solid velocities. Different equations and correlations have been developed for the solid voidage in this section versus solid flow rate [93,132-134]. Table 1.7 lists some of the existing correlation of the voidage of the moving solid bed in a standpipe.

Table 1.7: Correlations of solid bed voidage in a standpipe/ downcomer (ε_{sp}).

Correlation	Condition	Ref
$\varepsilon_{SP} = \varepsilon_{st} + \frac{(\varepsilon_{mf} - \varepsilon_{st})}{v_{mf}} v_{sl}$	linear relation between gas velocity and voidage	[135]
$\varepsilon_{SP} = 1 - \frac{1-\varepsilon_s}{R}$ $R = 3.1(d_p \rho_s)^{0.5} \quad for \quad \frac{U}{U_t} < 0.0168\left(\frac{U}{U_t}\right)^{-0.6}$ $R = 23.94(d_p \rho_s)^{0.3}\left(\frac{U}{U_t}\right) \quad for \quad \frac{U}{U_t} > 0.0168\left(\frac{U}{U_t}\right)^{-0.6}$	Sand particles d_p (503, 232, 90) µm ρ_s (2818,2730,2365) kg/m3	[119,136]
$\varepsilon_{sp} = 0.6953\left(\frac{Ar}{18\,\mathrm{Re}_s + 2.7\,\mathrm{Re}_s^{1.687}}\right)^{-0.054}$ $\mathrm{Re}_s = \frac{d_p \rho_g}{\mu_g}\left(\pm\frac{Q_{sp}}{A} + \frac{\varepsilon_{sp}}{1-\varepsilon_{sp}} v_s\right)$	Geldart group A Alumina/Hydrated alumina/ FCC catalyst d_p (34.11,46.66, 54) µm ρ_s (2770.4, 2037.4, 1760.9) kg/m^3	[131]
$\frac{\varepsilon_{sp}}{D^{0.4}} = 2.25\left(\frac{Ar}{18\,\mathrm{Re}_s + 2.7\,\mathrm{Re}_s^{1.687}}\right)^{-0.2}$	Sand particles d_p (95) µm ρ_s (2260) kg/m^3	[132]
$\varepsilon_{sp} = \frac{\varepsilon_{mf} - \frac{\varepsilon_{mf} - \varepsilon_S}{1-\varepsilon_S}(1 - \frac{\Delta P}{\rho_p g.\Delta z})}{1 - \frac{\varepsilon_{mf} - \varepsilon_S}{1-\varepsilon_S}}$	Sand/ resin d_p (260.9, 605) µm ρ_s (2611,1392) kg/m^3	[137]

1.5.4 Solid Circulation Modeling

Solid circulation in fluidized bed systems has been subject of many modeling researches to date [74,107,125,138-142]. Circulating fluidized beds (CFB), due to a wide spread use in industry; have been subject of many investigations in this field [107,139,140]. Pressure and material balances are commonly used to predict the solid circulation rate and the pressure drop variation in fluidized bed systems. Pressure is balanced over solid circulation loop in a stable operation. Based on this principle, pressure balance of the solid circulation loop is to be formed around the circulation loop using the proper pressure drop equations in each section. Consequently, proper selection of the solid circulation and pressure drop correlations in each part of the circulation loop is essential in this type of modeling.

The use of non-mechanical valves is a common solid flow control measure in high temperature operations such as combustion systems. Two common elements used for this purpose are L-valve [93,143,144] and loop-seal [114-116,120,124]. There exist different similarities between these elements. Both are consisted of a dependent standpipe (supply chamber in loop-seal), a critical aeration and horizontal section. The main difference is existence of a second aeration in loop-seal a shorter length of the horizontal pipe in the loop-seal compared to L-valve. Moreover, the standpipe of the L-valve is mostly filled with solids while in loop-seal this element is not filled with solids particularly if it is placed below a cyclone.

1.5.5 Solid Flow Rate Measurement

Solid circulation is a critical element in the chemical looping combustion process as discussed above. Consequently, solid flow rate measurement is an essential task to be carried out. Various techniques have been used to measure solid flow rate in circulating fluidized bed systems. The ideal measurement system for the solid circulation rate should be reliable, online, non-interfering and operational in high temperature and pressure conditions if the case [125]. Burkell et al. [145] assessed a range of measurement techniques for solid circulation rate in the circulating fluidized beds. These methods can be broadly classified into two groups, namely direct and indirect methods. The direct methods include:

- Timing the solid accumulation in the return leg by closing a permeable valve [145].
- Timing the descent of identifiable particles in the standpipe walls [145].
- Sampling of bed solids using insertion probe [146].

And the indirect methods include:

- Measuring the pressure drop in a particular section of the riser [142,147,148].
- Measuring the force imparted by returning particles as they fall downward from the cyclone [145].
- Measuring the pressure drop across a constriction in the return loop [145].
- Performing a heat balance on a calorimetric section in the standpipe [146].
- Measuring the weight of solids accumulating in a specially designed chamber with lateral vertical slots [149].
- Cross correlating the tribo-electric signals in suspensions [150].

Although the direct methods are easily calibrated, they are limited for online application and impractical in large industrial scale units operating at elevated temperatures. The indirect methods, on the other hand, provide adequate online measurement, but careful calibrations are necessary and have the disadvantage of being equipment dependent [125].

Measurement of pressure drop in a particular section of the riser is a simple and practical indirect measurement method used in various studies [142,147,148,151]. The pressure drop in a pneumatic conveying line is consisted of three main parameters of acceleration, gravity, and friction [152] which are function of solid velocity. Therefore, a correlation can be developed between the solid flow rate and pressure drop in this section. Pressure drop due to acceleration is depends not only on the velocity but also different particles and system properties which can have different behaviors. Therefore, the solid flow rate correlation should be developed above the initial acceleration region in a riser [151].

1.6 Bubbling Fluidized Bed Reactor

The reactors employed in the current study are bubbling fluidized beds. Fluidized bed reactors have some advantages including: homogeneous temperature across the reactor, possibility to handle catalyst de-activation due to homogeneity of the reactor, operation with high gas flow rate with reasonable pressure drops, operation with wide range of particle size, and ease of solid circulation in and out of the reactor [153]. These make the fluidized bed to be an interesting choice in CLC system with: high isothermal reaction, high gas flow rates, and required solid circulation [67,68]. A fluidized bed has some disadvantages compared to a fixed bed reactor including poorer conversion performance due to the mixing of the reactants and gas bypassing through bubbles, particles lost through attrition and elutriation, and complexity of design and operation [153].

Development of a model helps in better understanding of a system while providing a useful tool for further investigation and scale-ups. A reactor model can be principally divided into three interconnected sections including: hydrodynamics, kinetics, and heat. The hydrodynamics describes the dynamic of materials in the reactor through balance of momentum and mass. Kinetic section of the model takes into account the reactions dynamic in the system while a heat balance stands for thermal behavior of the system.

In the following sections, the Residence Time Distribution (RTD) measurement technique is first discussed as a useful experimental tool to investigate hydrodynamics of a reactor. Next, different modeling approaches used to describe the hydrodynamics of a bubbling fluidized bed are briefly reviewed. Multiphase hydrodynamic models are then developed in more details as an appropriate modeling approach for a bubbling fluidized bed.

1.6.1 Residence time distribution

The total time spent within the boundaries of a reactor is known as the exit age, or residence time (RT) [154]. The residence time distribution (RTD) of a chemical reactor is a probability distribution function that describes the amount of time a fluid element could spend inside the reactor. The residence time distribution measures features of ideal or non-ideal flows associated with the bulk flow patterns in a reactor or other process vessel [155]. Residence time experiments have been used to explore the hydrodynamics of many chemical processes. Transient experiments with inert tracers are used to determine residence time distributions. The main types of RTD functions that can be measured using tracer experiments are listed in Table 1.8.

Table 1.8: List of residence time distribution functions [155].

Symbol	Input Signal	Output Signal	Physical Interpretation	Properties
F(t)	Positive step change of tracer concentration	$F(t) = C_{out}(t)/C_{\infty}$	F(t) is the fraction of particles that remained in the system for a time less than t.	F(0)=0 F(∞)=1 dF/dt ≥ 0
E(t)	Sharp impulse of tracer (Dirac)	$E(t) = \frac{C_{out}(t)}{\int_0^{\infty} C_{out}(t)dt}$	E(t) is the fraction of particles that remained in the system for a time between t and t+dt	E(t) ≥ 0 $\int_0^{\infty} E(t)dt = 1$
W(t)	Negative step change in tracer concentration (Wash out)	$W(t)=C_{out}(t)/C_0$	W(t) is the fraction of particles that remained in the system for a time greater than t.	W(0)=1 W(∞)=0 dW/dt ≤ 0

In a theoretical ideal tank with one input and one output, the average residence time is defined as the volume of the tank divided by the total volumetric flow rate (assuming no volume change due to reaction):

$$\tau = \frac{V}{Q} \qquad \textbf{Eq. 1.3}$$

τ is commonly called the time constant of the tank. It should be noted that the Eq. 1.3 is valid only for the systems that behave ideally with uniform, additive flow. It does not account for possible non-ideal deviations, such as bypassing (or stagnation) where some fluid elements travel at significantly different velocities than others (e.g. bubbles typically travel faster than the gas in the dense phase), and it assumes that there is no back-flow. In the heterogeneous reaction systems, such as fluidized beds, gas-solid contact time is needed to predict the conversion [156,157]. However, residence time distribution gives useful information on the gas holdup and macromixing characteristics of the reactor. The RTD can be characterized by its moments. The most important moment is the first moment about the mean, known as the mean residence time:

$$\bar{t} = \int_0^\infty tE(t)dt = \int_0^\infty W(t)dt = \frac{mass\ inventory\ in\ the\ system}{mass\ flow\ rate\ through\ the\ system} = \frac{hold-up}{throughput} \qquad \textbf{Eq. 1.4}$$

Higher moments of the RTD function measure its shape and help to understand better the system behavior. The nth moment about the origin can be calculated as:

$$\mu_n = \int_0^\infty t^n f(t)dt = n\int_0^\infty t^{n-1}W(t)dt \qquad \textbf{Eq. 1.5}$$

The second moment of the RTD respond function is called variance ($\mu_2=\zeta_t^2$) and gives useful information once calculated about the mean. ζ_t^2 has dimension of squared time and is mostly expressed as dimensionless variance, ζ^2, as:

$$\sigma^2 = \frac{\mu_2'}{\bar{t}^2} = \frac{\int_0^\infty (t-\bar{t})^2 f(t)dt}{\bar{t}^2} = \frac{2\int_0^\infty tW(t)dt}{\bar{t}^2} - 1 \qquad \textbf{Eq. 1.6}$$

The variance is a measure of the spread of the data around the mean, which is a characteristic of the macromixing phenomena occurring within the bed. Table 1.9 presents a summary of the information which can be gained directly from the ζ^2 value.

Table 1.9: Reactor characteristics from dimensionless variance, ζ^2 [154].

Dimensionless variance	Reactor
$\zeta^2=0$	Plug flow
$0<\zeta^2<1$	Well designed turbulent flow reactor
$\zeta^2=1$	Ideal continuous flow stirred tank reactor (CSTR)
$1<\zeta^2$	Laminar flow reactor

Overall reactor Peclet number (Pe_r) can be calculated from the mean residence time and the variance. Pe_r is the ratio of the rate of transport by convection to the rate of transport by diffusion or dispersion. Therefore, high Pe_r numbers signify plug flow-like behavior, while very low Pe_r is associated with well mixed behavior. According, to the dispersion model with closed–closed boundary conditions (i.e., no dispersion across the system boundaries), Pe_r can be calculated as [154]:

$$\sigma^2 = \frac{\sigma_t^2}{\bar{t}^2} = \frac{2}{Pe_r} - \frac{2}{Pe_r^2}(1-e^{-Pe_r}) \qquad \textbf{Eq. 1.7}$$

Closed–closed boundary conditions are a reasonable assumption since gas is not expected to back-diffuse across the porous distributor plate due to the associated pressure drop, while the return of gas from the freeboard should be minimal because the particle concentration is very low [158].

Bubbles carry a large portion of the gases to the bed surface in a fluidized bed. Moreover, bubbles are known to behave chaotically, i.e. bubbles erupt at different locations and different times. Therefore, the gas flow analysis can result in a signal with considerable noise. The output signal could also vary

considerably between different measurements for identical conditions. This indicates importance of cautious on reproducibility of the RTD experimental results. Christensen et al. [158] illustrate such a behavior in a fluidized bed. They measure up to 200 points for each experimental condition to achieve an averaged general behavior of their system. Moreover, at high gas velocities, non-uniformities can occur because the large bubbles tend to migrate towards the middle of the bed. Thus, a probe position at the wall could miss the tracer in the bubble.

Another measured characteristic of RTD is first appearance time, t_{first}, where the washout function first falls below 1.0 or a step function starts to rise. An important use of t_{first} is to model the real reactors with a series configuration of an ideal piston flow reactor and a stirred tank reactor. This model is called fractional tubularity model and uses a fractional tubularity parameter, $\tau = t_{first} / \bar{t}$ [154]. This is mostly used for systems with a sharp first appearance time and $\zeta^2 < 1$ like fluidized bed reactors [155]. Moreover, t_{first} presents the shortest residence time of particles in a bed.

1.6.2 Hydrodynamic Model of Bubbling Fluidized Bed (BFB)

The modeling of fluidized beds has been subject of many studies to date. Different approaches have been adopted to mathematically describe behavior of these reactors. Table 1.10 lists the main modeling approaches already developed. The developed models can be classified globally into the pseudo-homogeneous models and the multiphase flow models. The reaction conversion in a fluidized bed varies from plug flow to well below mixed flow reactor [153]. Therefore, the pseudo-homogeneous approaches have limited application scope. Multiphase modeling approaches are being developed since early 1960th thanks to better understanding of the flow in a fluidized bed. Two scientific developments have been of remarkable importance in this regard. Davidson and Harison [159] discovered the single bubble rise velocity and its effect on the gas flow in vicinity of the bubble. Rowe and Partridge [160] completed this investigation by discovering that any single raising bubble drags behind it a wake of solids.

A bubbling fluidized bed reactor can be divided into three axial zones with different solid–gas flows [161]. These zones, schematically illustrated in Figure 1.9, are:

- The jet zone: is the bed region just above the gas distributor. Injected gas forms a jet penetrating into the fluidized bed with a complicated hydrodynamic behavior.
- The bubbling fluidized region: where gas bubbles are formed.
- The solid disengagement zone: which is the region above the bed surface where the particles are projected by burst of the bubbles in the surface.

This illustrates the complexity of the hydrodynamic of gas and solid flow in bubbling fluidized bed and vast variety of the possible modeling procedures. The choice of proper model depends mostly on the nature of the reactor. Reaction conversion in a fluidized bed can be generally limited by two phenomena: material transfer between different phases or the reaction rate. Accordingly, the importance of the hydrodynamic increases as the reaction rate increases. In case of very fast reactions, the conversion is limited by mass transfer between the bubble and the emulsion phase and a considerable part of the reaction happens in the interface of the bubble and the emulsion phase (the cloud region). Moreover, the gas jet zone plays a decisive role in these kind of systems [161].

Solid mixing in a fluidized bed occurs mostly due to the effect of bubbles movement in the bed. Bubbles displace solids due both to wake carried by them and to drift effect (net particles motion). As a result, particles are displaced rapidly upwards, with some wake shedding along the bubbles way. The bulk of the particles then have a slow compensatory downward motion, often stick-slip flow [162]. The main approaches used in the literature to model the solids mixing in the bubbling fluidized bed are use of axial dispersion, CSTR or the counter current mixing models. The axial dispersion is mostly adoptable to the systems with high aspect ration (H_R/D_{bed}) with small scale mixing. This is characteristic of fine particles (group A) with mild gulf streams or turbulent fluidized beds [153]. Some of the existing D_{axs} are listed in Table 1.12. Grace [162] explains that the particle mixing in a bubbling fluidized bed is neither random nor in small steps due to the bubbles effect. As a result, axial dispersion is not a good representation of vertical mixing in bubbling fluidized bed. CSTR model is

another common approach used in the literature to model the solid phase in a bubbling fluidized bed [163,164]. The counter current mixing model as the other alternative, views the solids moving in two streams, one rising and the other descending with a cross flow or interchange between streams [153]. K-L model [153] is an example of this kind of approaches used in some literatures to model bubbling fluidized bed systems [165].

Table 1.10: Various approaches employed to model hydrodynamics of solid and gas flow in a fluidized bed reactor.

Model	Formalism	Potentials/ limits	Ref.
Ideal reactor Models	BFB considered as an ideal reactors: CSTR, PF reactor, tank in series	Estimation for a limited operating conditions Unreliable in scale up and new operating conditions No flow pattern considerations (bubbling, solid flow...)	
Dispersion and Tank in Series Models	Simple one parameter model	Conversion well below mixed flow cannot be accounted for	[155]
RTD Models	Conversion calculated based on the RTD results of solid/gas phase	No distinction between the bubble and emulsion phase contacts	[166]
Contact time distribution model	Based on the RTD results Distinction of different gas velocity in bubble and emulsion Definition of effective rate constant	Problem in defining a meaningful contact time distribution function to take into account considerable back mixings	[167, 168]
Two region Model	Separation of the bubble and emulsion phase into two parallel reactors with 6 adjustable parameters: 1. Gas velocity in bubble and emulsion phase 2. Volume of gas in each reactor 3. Gas dispersion in bubble reactor 4. Gas dispersion emulsion reactors 5. solid repartition between reactors 6. cross flow between reactors Different modeling hypotheses have been developed	▪ Proper fitting of the experimental results ▪ A curve fitting model which brings no understanding of the reactor phenomena ▪ Limited application in scale up and prediction for new operating conditions	see Table 1.11
Hydrodynamic Flow Models	Considers hydrodynamic behavior of bubble in the fluidized bed (rise velocity, diameter...) Considers effect of bubble on the emulsion phase: formation of bubble cloud and wake Different modeling approaches are developed base on these findings, e.g. K-L BFB model.	▪ Proper fitting of the experimental results ▪ Reliable scale up and prediction of new conditions with proper selections of the modeling strategy ▪ Brings about better understanding of the physical phenomena in the reactor	see Table 1.11
Computational Fluid Dynamic (CFD)	Euler – Euler	▪ High level of modeling is required ▪ Simulation of large systems	
	Euler – Lagrange	▪ Low – medium level of model is required ▪ Numerical experimentation is possible ▪ Simulation of small- medium systems	

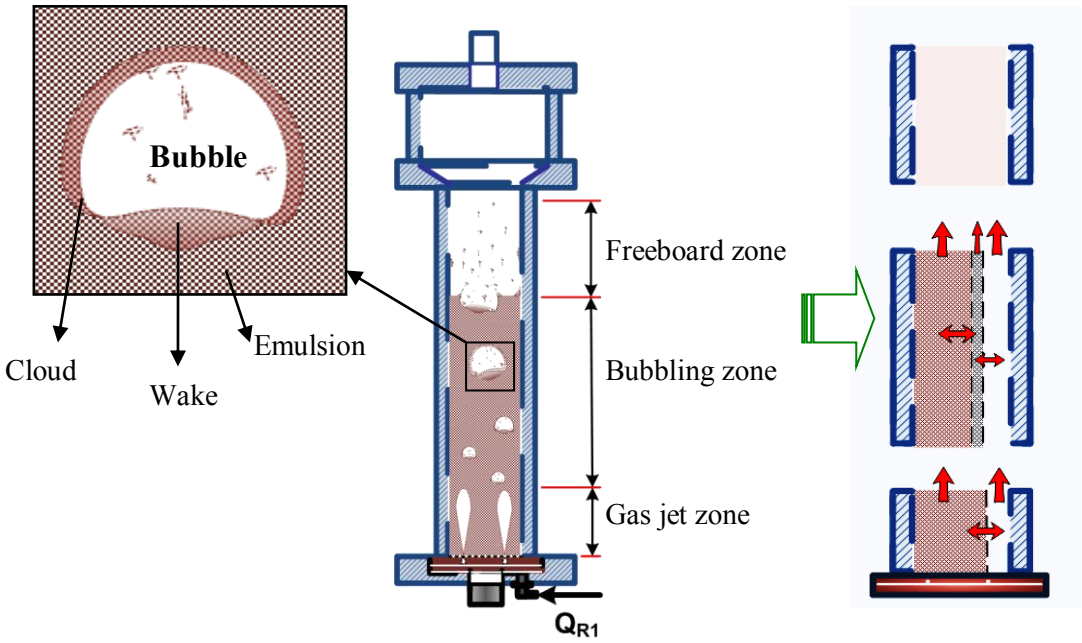

Figure 1.9: Characterization of a bubbling fluidized bed.

1.6.3 Multi-Phase Models

Multi-phase models divide the gas and solid in the fluidized bed into distinct phases such as: bubble, cloud, wake and emulsion phases. The most common method is the two phase theory. It considers that all gas in excess of minimum fluidization passes across the bed in form of bubbles. Toomy and Johnstone [169] proposed initially this model. Since then, a broad range of models have been developed based on this theory. The main difference between the models is in definition of the governing equation in each phase, particle fraction in each phase and the gas interchange between them. Wen and Fan [170] have developed the general material balance equations in the bubble and the emulsion phase respectively as:

$$F\left(\frac{\partial C_i^b}{\partial t}\right) - FD_b\left(\frac{\partial^2 C_i^b}{\partial z^2}\right) + FU\left(\frac{\partial C_i^b}{\partial z}\right) + K_{be}(C_i^b - C_i^d) + F_s k C_i^b = 0 \qquad \textbf{Eq. 1.8}$$

And

$$f\left(\frac{\partial C_i^e}{\partial t}\right) - fD_e\left(\frac{\partial^2 C_i^e}{\partial z^2}\right) + fU\left(\frac{\partial C_i^e}{\partial z}\right) + K_{be}(C_i^e - C_i^b) + f_s k C_i^b = 0 \qquad \textbf{Eq. 1.9}$$

Where f and F respectively stand for volumetric fraction of gas in the emulsion and bubble phase. Ho [171] has compared some of the existing two phase models in the literature. He concludes that most of the studies assume steady state conditions ($\partial C_i^b/\partial t = \partial C_i^b/\partial t = 0$), either PF ($D_e$=0) or CSTR ($D_e$=∞), PF in the bubble phase (D_b = 0), and $U_e = U_{mf}$. Table 1.11 lists some of the bubbling fluidized bed models existing in literature and the corresponding hypothesis.

A review of the existing models suggests that the hydrodynamic model of a bubbling fluidized bed have to consider the effect of bubbles and associated mixing phenomena. Therefore, a two phase model is the simplest reasonable modeling approach. This requires appropriate selection of the hydrodynamic equations to well describe the bed behavior. In the other hand, choice of material balance models is equally important. The gas phase in the bubbles can be considered as a plug flow regarding the fast bubble rise velocity (in case of the current system) and negligible reaction due to lack of catalysts (oxygen carriers in CLC system). However, the gas flow in the emulsion phase has a different behavior regarding the slow gas movement in this phase, high back mixing imposed by bubble and solids movements and reaction effect due to the presence of the catalysts. Accordingly, the

axial dispersion model seems to be a reasonable choice as the gas governing equation in the emulsion phase.

Table 1.11: Some of the models used in the literature for a bubbling fluidized bed.

Model	Bubble phase	Cloud	Emulsion phase	Scheme	Ref.
Wen & Fan (1975)	Axial dispersion model	non	▪ Axial dispersion model		[170]
Orcutt & Davidson (1962)	▪ Plug flow ▪ $\varepsilon_b = 1$ (no solid) ▪ No reaction	non	▪ CSTR ▪ Ue = Umf	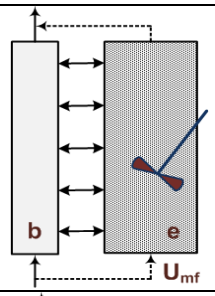	[172]
Davidson & Harrison (1963)	▪ d_b = cte ▪ $Q_b = Q - Q_{mf}$ ▪ no solid ▪ no reaction ▪ Plug flow	non	▪ Steady state model ▪ Reaction ▪ Either CSTR or PF	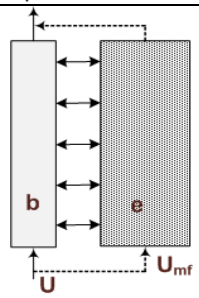	[159]
Werther (1980)	▪ Plug flow ▪ Variable d_b along the bed	non	▪ Concentration profile film around the bubble, adopted from gas- liquid systems ▪ negligible gas flow ▪ Interesting for fast reactions	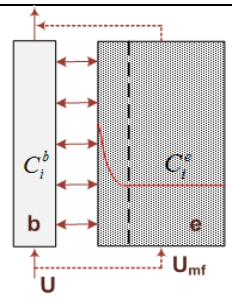	[173]
Kunii & Levenspiel (1968)	▪ All flow passes in bubble zone ▪ Bubble wake drag solid upward in the bed ▪ Plug flow ▪ no solid ▪ Davidson model used for bubble size [159]	▪ Thin layer around bubbles including bubble wake ▪ Reaction	▪ Reaction ▪ at minimum fluidization condition ▪ Downward solid flow ▪ Exchange coefficients based on the ref. [159,174]	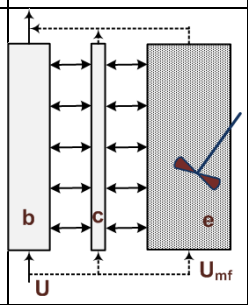	[153, 175]
Kato & Wen (1969, Bubble assemblage model)	▪ Bed is divided to n compartments height of each is equal to the bubble size at that height ▪ CSTR ▪ consisted of spherical bubbles ▪ db raise to maximum calculated by Harrison relation [176]	▪ Spherical cloud around the bubble ▪ $\varepsilon_c = \varepsilon_e$	▪ CSTR ▪ $\varepsilon_e = \varepsilon_{mf}$	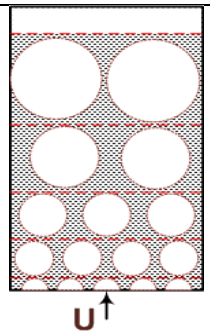	[177]

Axial dispersion coefficient (D_{ax}) is a key parameter in the axial dispersion material balance equation. This coefficient is mostly developed in liquid–gas bubbling columns. Some of the existing D_{ax} correlations in the literature are listed in Table 1.12. The results in bubble column demonstrate that the D_{ax} is a function of the bed diameter and the gas flow rate. Gas dispersion in the bubble phase ($D_{ax,b}$) is reported to be dependent of the bubble size. Small sized bubbles have a dispersion close to that of liquid phase [178], suggesting that the small bubbles are entrained with the liquid phase. The dispersion of large bubbles is reported to be very small, indicating that large bubbles rise relatively undistributed through the reactor and can be described by a plug flow model [179]. In case of the fluidized bed applications, the dispersion approach is mostly used in turbulent bed reactors. Since, mixing occurs by much smaller step compared with the bubbling fluidized bed. Some of the existing correlations developed for fluidized beds are listed in Table 1.12.

Table 1.12: Axial dispersion relations in the literature for bubble column or fluidized beds.

Equation	Application	Ref.
$D_{axL} = 0.31 V_L(0) D_T$	$V_l(0)$: centerline velocity D_T: column diameter	[180]
$D_{axL} = 0.35 g^{1/3} D_T^{4/3} U_g^{1/3}$	the authors extended the correlation to fluidized beds Making use of Kolmogoroff's theory of isotropic turbulence	[181]
$D_{axL} = 0.065 g^{1/2} d_t^{3/2} \left(\frac{U_g^3}{g v_L} \right)^{1/8}$	Liquid phase gas dispersion	[182]
$D_{axL} = 5 \times 10^{-4} U_g^3 d_t^{3/2}$	Gas phase dispersion	[183]
$Pe_{axg} = \frac{UH}{D_{ax,g}} = 3.47 Ar^{0.149} \mathrm{Re}^{0.0234} Sc^{-0.231} \left(\frac{H}{D} \right)^{0.285}$ $D_{radg} \approx 0.1 D_{axg}$	gas in a turbulent fluidized bed	[184]
$Pe_{axg} = \frac{UH}{D_{axs}} = 4.22 \times 10^{-3} Ar$	group B particles, turbulent regime	[185]
$Pe_{axg} = 9.454 \times 10^{-1} Fr_t^{0.653} Ar^{0.368}$ $Fr_t = (Vsg - U_{mf}) / (g D_t)^{1/2}$	Group A particles $8.0 \times 10^{-4} < Fr_t < 0.91$ $6.9 < Ar < 72.4$	[186]
$D_{axs} = 0.365 \mathrm{Re}_D^{-0.368} \left[g (Vsg - U_{mf}) D^4 \right]^{1/3}$	group A particles, turbulent regime	[187]
$D_{axs} = 0.06 + 0.1 Vsg$ $D_{axs} = 0.30 D_{bed}^{0.65}$	small beds large diameter beds	[153]
$D_{axs} = 12 Vsg^{1/2} D_{bed}^{0.9}$	group A, vigorously fluidized bed	[188]

1.7 Kinetics of Chemical Looping Combustion

Kinetics of chemical looping combustion reactions have been investigated by various researchers. Fuel type and oxygen carrier are the main influencing parameters in this regard apart from the hydrodynamics which determines the contact time. Numerous oxygen carriers have been already tested [55,189]. The studies have been mostly focused on the transitional metal oxides namely nickel, copper, iron and manganese and cobalt [54,189]. Availability and low cost are the main advantages of copper and iron. On the other hand, nickel has the best reactivity, thermal and reaction stability with CH_4. Natural ores and industrial wastes are the most interesting source of oxygen carriers regarding the financial aspects. However, majorities of the tested particles have been manufactured by different technologies such as: freeze granulation, spin flash drying, spray drying, and impregnation [55]. In

order to improve mechanical properties, the active metal oxides are usually deposited on supporting materials such as: SiO2, TiO2, ZrO2, Al2O3, YSZ and bentonite [68].

A support is supposed to provide a base surface for dispersing the catalytically active metal in order to obtain a stable and high activity metal surface. Support plays an important role since it determine the final particle size, available surface by its pore structure, morphology, and phase transitions that it can undergo. However, supports play an additional direct or indirect role in reaction of a catalyst. The same active metal on different support produces different conversion and yields [190,191]. As example, ZrO_2 is known to oxidize deposited carbon, hence, avoiding catalyst deactivation.

Nickel has received a particular attention due to its high reactivity and durability in chemical looping combustion systems. Both bulk and supported Ni/NiO have been tested [54]. However, bulk nickel oxide has shown poor oxidation performance over repeated reduction – oxidation cycles which is due to agglomeration [192]. Consequently, supported nickel is preferred. Alumina (Al_2O_3) has been the support most employed [193-196] due to its favorable fluidization properties and thermal stability. However, in presence of nickel oxide and alumina, the nickel aluminate ($NiAl_2O_4$) can be formed which results in reduction of active nickel phase in the oxygen carrier [197]. Therefore, reducing the support and metal contact can reduce this probability [54]. Another proposed solution is to employ an excess amount of nickel in OC preparation to compensate this activity lost [197,198]. An alternative is to use the nickel aluminate as the support in place of Alumina [199-201]. This brings some advantages including: stability of the $NiAl_2O_4$ in high temperatures (up to 1200 °C), good reactivity of Ni/$NiAl_2O_4$ with CH_4, CO and H_2, prevention of agglomeration, reduction of carbon deposition, and no evidence of nickel carbide formation. However, Ni/$NiAl_2O_4$ requires more quantity of nickel in fabrication which increases the manufacturing cost.

Nickel based oxygen carriers have also been tested using some other common supporting materials. Ni/$MgAl_2O_4$ system has shown to limit sintering and stabilize the structure of the oxygen carrier to higher temperatures [199,200,202]. Ni/YSZ (Yttria-stabilized zirconia) has been found to have a very good reactivity and regenerability given the abundant availability of NiO sites with no metal support complexes [192,203,204]. NiO/bentonite has displayed a promising activity and stability in oxidation – reduction cycles with limited performance at high temperatures [83,205]. Ni/TiO has shown coke formation and conversion of Ni to less active $NiTiO_3$ species [83,206]. Ni/SiO_2 and Ni/ZrO_2 have resulted in formation of nickel complexes resulting in activity reduction above 900 °C [207,208].

Reduction of the oxygen carriers by fuel involves various catalytic and non-catalytic reactions in solid phase. In case of gas and liquid phase reactions; the initial reaction rate is the highest as it is the time when the highest reactant concentration exists. In contrast, many reactions in the solid phase do not start with maximum rate. These reactions involve participation of some active sites (nuclei) which may require time to be developed in the particle [209]. Figure 1.10 illustrates a typical reaction path in solids where α stands for reaction advancement between 0 and 1. It illustrates that the reaction in solid phase can have a complex behavior in terms of advancement. Accordingly, there have been numerous models developed to date for this purpose.

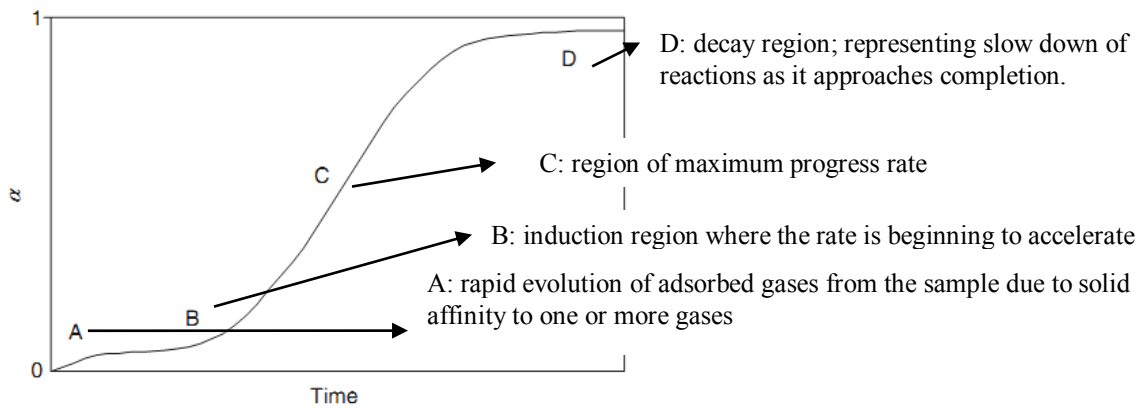

Figure 1.10: A general reaction progress versus time plot for a reaction in the solid state [209].

The combustion of gases on the NiO based catalyst has been widely studied in the steam reforming [210-213] and CLC process [86,196,214,215]. The variation of the reactions behavior for nickel based catalyst has been well observed. For instance, Richardson et al. [210] used X-ray diffraction to study nickel oxide reduction by hydrogen. They found that the reduction follows a series of steps: (1) initial induction period with formation of Ni metal clusters; (2) acceleration of reduction rate as size of clusters increase; and (3) pseudo-first-order advance of reaction. The kinetic models employed for chemical looping can be divided into two major categories. This includes nucleation growth models based on the Avrami Erofeev models or shrinking core models [165,216].

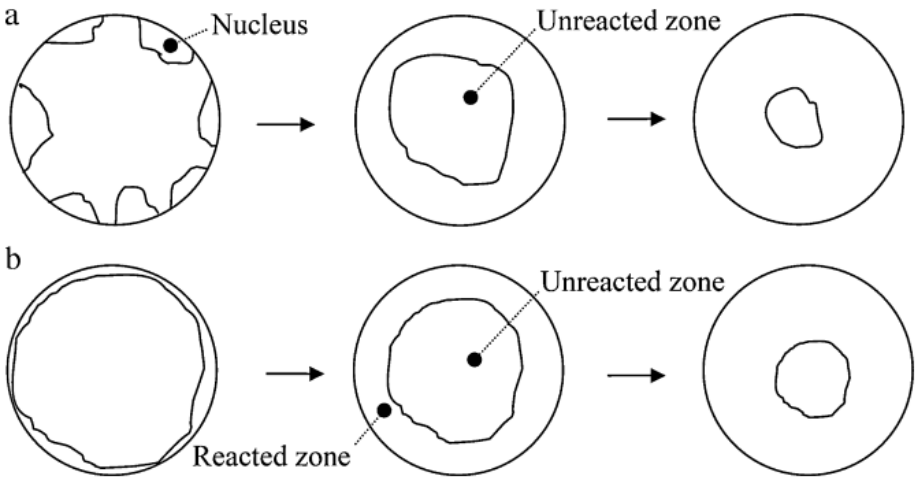

Figure 1.11: (a) Avrami Erofeev nucleation growth model and (b) shrinking core model [216].

The shrinking core model relates the available reactive sites on the particle to the reaction progress. Here, the reaction occurs first at the outer skin of the particle. The zone of reaction then moves into the solid, leaving behind completely converted material and inert solid. Thus, at any time there exists an unreacted core of material which shrinks in size during reaction [217]. Shrinking core models are defined based on the particle shape (spherical, flat plate, or cylindrical) and the governing mechanism (external or internal mass transfer, and reaction) [209]. Models are written in the conversion rate being dependent on the temperature T, the gaseous reactant concentration C and the conversion. The conversion is defined as the unreacted solid volume divided by the overall reactive particle volume [216].

The nucleation model considers the chemical mechanism and kinetics of the gas–solid reactions only. This model does not include morphological factors, which may be equally important in determining the kinetics. Specifically for the porous particles, the effect of particle size and its state in the course of the reaction is very important in determining reaction rates [54].

Some issues should be taken into consideration regarding the limits of the classical models presented above. First, regarding the complexity of the reaction behavior in the solid, the simple reaction models are not sufficient to explain whole pathway. Accordingly, Kruggel-Emden et al. [216] have proposed use of empirical equations which are sum of different exponential and polynomial terms to cover variation of the behavior through whole reduction path. An additional point is the fact that the behavior of the catalysts (oxygen carriers) depends strongly on their production methods. Therefore, a model which predicts well for an especial oxygen carrier may not be the best adapted for similar cases. Therefore empirical expressions obtained are always only valid for a certain carrier material/gas combination. Therefore, it does not worth to highly optimize equations as done for those used in hermodynamics, simply adjusted equations should be reasonable to be used [216].

The reduction of CH_4 on the oxygen carrier can be divided into catalytic and non-catalytic reactions. Non-catalytic reactions involve those between NiO and reducing gases of CH_4, CO and H_2 as [165,218-220]:

$$CH_4 + NiO \rightarrow Ni + 2H_2 + CO \qquad \textbf{Eq. 1.10}$$

Reduction of NiO by CO:

$$CO + NiO \rightarrow Ni + CO_2 \qquad \textbf{Eq. 1.11}$$

Reduction of NiO by H_2:

$$H_2 + NiO \rightarrow Ni + H_2O \qquad \textbf{Eq. 1.12}$$

These reactions involve transfer of oxygen from the NiO to the reacting gases and are considered thermodynamically irreversible for practical purposes. The main catalytic reactions [165,214,219,220] are consisted of methane reforming with steam:

$$CH_4 + H_2O \xleftrightarrow{Ni} CO + 3H_2 \qquad \textbf{Eq. 1.13}$$

And methane reforming with carbon dioxide:

$$CH_4 + CO_2 \xleftrightarrow{Ni} 2CO + 2H_2 \qquad \textbf{Eq. 1.14}$$

Methanation of carbon monoxide:

$$CO + 3H_2 \xleftrightarrow{Ni} CH_4 + H_2O \qquad \textbf{Eq. 1.15}$$

Water gas shift (WGS) reaction:

$$CO + H_2O \xleftrightarrow{Ni} CO_2 + H_2 \qquad \textbf{Eq. 1.16}$$

And the oxidation reaction:

$$2Ni + O_2 \xleftrightarrow{Ni} 2NiO \qquad \textbf{Eq. 1.17}$$

Carbon deposition by methane (pyrolysis):

$$CH_4 \xleftrightarrow{Ni} C + 2H_2 \qquad \textbf{Eq. 1.18}$$

Or through carbon deposition by CO (Boudouard reaction):

$$2CO \xleftrightarrow{Ni} CO2 + C \qquad \textbf{Eq. 1.19}$$

The carbon deposited may be gasified through:

$$C + CO_2 \xleftrightarrow{Ni} 2CO \qquad \textbf{Eq. 1.20}$$

And

$$C + H_2O \xleftrightarrow{Ni} CO + H_2 \qquad \textbf{Eq. 1.21}$$

Formation of carbon deposit is a possible undesirable side reaction in CLC. Boudouard reaction and pyrolysis are the main reactions leading to the coke formation [199]. Transitional metals like Ni favor these reactions through catalytic effects. Increase of temperature favors endothermic pyrolysis reaction while hindering the exothermic Boudouard reaction. Moreover, oxygen availability, fuel composition and pressure affect the carbon deposition [204,221]. Sufficient oxygen availability in fluidized bed reactors has been reported to prevent the carbon formation while reduced particles with $\Delta X > 80$ % result in rapid coking [206,221]. Water presence has an important role in carbon formation. Ishida et al. [206] have demonstrated negligible coke formation with H_2O to CO ratio of above 1 with nickel based oxygen carrier.

Various reactor models have been already developed for chemical looping combustion processes. Illiuta et al. [165] have developed a model based on the three phase theory of bubbling fluidized beds for nickel based oxygen carriers. They have employed a detailed reaction scheme including 4 non-catalytic and 7 catalytic reactions. The model predicted well experimental results from the fixed and fluidized beds. Abad et al. [163] developed a steady state reactor model for bubbling fluidized of Cu based oxygen carriers bed including the bottom zone and freeboard. They employed the two phase theory of bubbling fluidized bed using plug flow material balance in both phases. The model prediction illustrated a good agreement with the experimental results from a 10 kW_{th} CLC pilot plant.

It was determined from their results that the reaction in the freeboard had a deceive importance to get high combustion efficiency. They found that the most important model parameters affecting the combustion efficiency were: bubble-emulsion gas exchange coefficient, decay factor for solid concentration in the freeboard, and contact efficiency between solid and gas in freeboard.

Kramp et al. [164] developed a steady state CLC reactor model based on the two phase theory for gas feed CLC systems of 50 kW_{th} and 100 MW_{th}. They employed plug flow material balances for gas in both bubble and emulsion phase. CSTR model was used to model the material balance for solid particles. Attrition and oxygen carrier loss have been modelled using the model derived from small scale laboratory experiments. They have found that the large scale units result in lower fuel conversion due to higher gas bypassing through the bed in the form of bubbles. They concluded that the similar performance is not guaranteed between pilot scale and large scale process due to scale-up effects on hydrodynamics. Moreover, it has been shown that the large scale processes involve a significantly higher lose of oxygen carrier based on the same amount of thermal energy produced. Addition of a second stage cyclone at the exit of air reactor was demonstrated to decrease particle loss in larger units. However, adding a secondary cyclone after fuel reactor did not result a significant improvement.

Bolhàr-Nordenkampf et al [222] have developed a model based on the conservation of mass and energy, including thermodynamic equilibrium. The model permits investigation of complex power plant configurations as well as optimisation of parameters. They have figured out that an air/fuel ratio of 0.9 and below results in total fuel conversion and the equilibrium state. Above this ratio a deviation from the calculated heat extraction for maximum conversion to equilibrium is observed due to decrease in fuel conversion and deviation from equilibrium. They have compared different oxygen carrier materials finding the highest potential with Ni, Co, Cu, Fe, and Mn based materials. Accordingly, Cu based carrier have the highest fuel conversion potential with CO concentration below 1 vppm. Moreover, they have used the model library for design of a 120 kW pilot including associated downstream facilities [223,223].

Kolbitsch et al. [224] have developed a model based on the dual circulating fluidized bed (DCFB) reactor system. The plug flow reacting gas is only in contact with a defined fraction of well mixed particles along the height of the reactor. An nth order kinetic model is used for Ni-based oxygen carriers based on the literature [225] using shrinking core model for active OC surface. They have found an important influence of fuel reactor temperature on the system performance. The air/fuel ratio and solid circulation rate have found to have a minor effect as long as they are not limiting. Moreover, they have shown that the oxidation of particles in the air reactor requires a much larger inventory in the air reactor compared to the fuel reactor or both reactors have to be very large.

1.8 Conclusion

A brief survey of the existing literatures was carried out in this chapter. Global warming threat and its root cause on the greenhouse gases emission was demonstrated. The gravity of this menace in addition to the scarcity of the energy sources necessitates employment of a series of diverse mitigation measures. Carbon capture and storage (CCS) is a promising mid and long term solution to address these problems. CCS abates the negative greenhouse impact associated with use of fossil fuels. Moreover, it can be used in some industrially appealing processes such as amelioration of energy production through CO_2-EOR (Enhanced oil production by aid of CO_2), and ECBM (CO_2 Enhanced Coal Bed Methane recovery). Chemical looping combustion (CLC) was shown to be an appealing carbon capture method regarding minimum energy penalty for CO_2 separation. Different existing designs around the world have been briefly presented in this chapter.

Solid circulation has been shown to be a key element in the CLC systems. It determines the oxygen transfer rate in addition to keeping the overall energy balance of the system. On the pilot plant, emphasis was made on control of solid circulation using L-Valves. Accordingly, a brief survey was carried out on the solid circulation control methods in circulating fluidized bed system notably pneumatic non-mechanical L-valves. The available published works on the L-valve operation was

therefore discussed. Despite the existing knowledge on this device, more investigations are required to best make use of this device in CLC systems. Additional researches on the effect of temperature on the L-valve operation in terms of gas and particles properties variation are required.

Gas leakage has been illustrated to be an undesirable phenomenon in the CLC. Therefore, maximum gas tightness especially for the fuel reactor is desired in the chemical looping applications. Loop-seals were presented to be an interesting device to minimize this negative effect in addition to the careful system design and operation. Loop-seals have been in used in the circulating fluidized beds in commercial scales. However, gas leakage has not really been an important issue of concern in these cases. Therefore, some additional investigations should be carried out to discover the best operational and design measures to minimize gas leakage not only in the loop-seal but also L-valves.

The existing hydrodynamic models for bubbling fluidized bed reactors were also presented in the current chapter. The survey illustrates a vast existing possibility to model these reactors. The main parameters to be chosen in this field are selection of the most adapted modeling approach, selection of the governing equations in each phase including; material balance models, bubble diameter and rise velocity, gas exchange coefficients, etc. Accordingly, an experimental investigation dedicated to hydrodynamic may be an interesting model selection approach. Residence time distribution (RTD) was hence presented as an experimental tool for this purpose.

The chemical reaction aspects involved in chemical looping combustion were finally presented in this chapter. A brief literature survey was carried out through the various oxygen carriers already used in this system, the solid phase reaction complexity and existing reaction models. A reaction scheme for combustion of methane on the nickel based oxygen carrier was presented based on the existing literature. An additional scheme refinement and selection of appropriate reaction rate equation is required in this regards.

Chapter 2
Materials and Methods

2.1 EXPERIMENTAL INSTALLATIONS 41

2.1.1 Cold Flow Prototype (Maquette) 41

2.1.2 High Temperature Prototype (Pilot Plant) 43

2.1.3 Gas Analyzing Devices 46

2.2 PARTICLE PROPERTIES 48

2.3 TRACING AND RTD TESTS IN THE COLD PROTOTYPE 49

2.4 PNEUMATIC CONVEYING GAS VELOCITY 50

2.5 SOLID FLOW RATE 51

2.5.1 Solid Flow Rate Measurement Methods 51

2.5.2 Solid Flow Rate Measurement, Demonstration Methods 54

2.6 OPERATIONAL PROCEDURES 56

2.7 ELECTROSTATICS EFFECT 57

2.8 CONCLUSION 57

2. Materials and Methods

IFP Energies nouvelles and TOTAL have a joint project for development of CLC technologies. One of the goals of the program was to study CLC performances in a wide range of operating conditions to achieve a deep understanding of the process at small scales. As a part of this program, a novel 10 kW_{th} CLC design was developed based on the principle of interconnected bubbling fluidized bed reactors. The purpose of this system was to achieve maximum operation flexibility through control of solid flow rate by use of L-valves and minimization of gas leakages by use of loop-seals. The current study has been carried out within framework of this project to study different process aspects associated with this design in cold and high temperature conditions. This chapter presents different devices, materials and procedures employed in the current study.

A cold flow prototype was constructed to study solid circulation and hydrodynamic of fluidized beds. The prototype is composed of two bubbling fluidized beds connected to each other by two identical conveying lines. Each line is composed of a series of elements including: an L-valve, a lift (vertical dilute phase pneumatic conveying line), a T-bend followed by a horizontal conveying line connected to a cyclone and a loop-seal lead to the second reactor. Ilmenite and two sand particles were used in this system with air as principal fluidization gas. A gas tracer and residence time distribution study was carried out in this prototype by use of Helium as the tracing gas. All operations were carried out at the ambient temperature and pressure conditions.

A high temperature pilot plant was designed based on the same principle and dimensions. The pilot is composed of three bubbling fluidized beds; a fuel reactor and two air reactors connected to each other through a conveying line similar to the cold flow prototype. Methane was used as the combustion feed with $NiO/NiAl_2O_4$ particles as the oxygen carriers.

This chapter presents the cold prototype and high temperature pilot plant and the gas analyzing devices employed in each system. Physical properties of the particles used in this study are presented next. Measurement of solid flow rate is an important investigation element in the current study. Different direct and indirect techniques employed in the current study for solid flow rate measurement are discussed in this chapter. The experimental procedures followed in operation of each system are presented next. Some interfering electrostatic effects were observed in the cold flow prototype. These are briefly discussed as the last part of the current chapter.

2.1 Experimental Installations

The current work has been carried out in two comprehension CLC set-ups designed for the purpose of laboratory scales experimental investigations. A cold flow prototype (also called "maquette") was used to investigate in details solid circulation and hydrodynamic properties of the system at ambient temperature. Effect of temperature on the hydrodynamics and reactions were then studied in a second prototype (called "high temperature pilot plant" in this essay) operating at high temperatures. Both cold flow prototype and high temperature pilot plant were constructed using the same concepts with similar designs and dimensions. The main design difference between the systems is the number of interconnected reactors. The cold prototype is consisted of two interconnected reactors while the pilot plant is constructed of three interconnected reactors. The principles and concept of the design used in these equipments is explained in the following sections.

2.1.1 Cold Flow Prototype (Maquette)

The cold flow prototype was used to investigate solid circulation and the fluidization hydrodynamics in the reactors. The prototype was made of transparent Plexiglas which enables visual observation of different phenomena in the system. Moreover, this facilitates modifications if required. Figure 2.1

illustrates the scheme of the cold flow prototype with indication of main system elements and corresponding abbreviations used in this report.

The cold flow prototype is composed of two interconnected bubbling fluidized bed reactors, R1 and R2 with circular cross section of 0.1 m. The bed height in these reactors can be adjusted up to 1 m. Bubbling beds were chosen to provide sufficient contact time between solid and gas (air in the cold flow model) to achieve optimum reaction conversion. Beside, this will result in higher flexibility of the system and permits use of various oxygen carriers with different oxygen transfer capabilities, and reaction rates. Gases (Q_{R1} and Q_{R2}) are injected at the bottom of the reactors through a staggered perforated plates with four identical injection holes with a hole density of 509 orifice/m². In the cold flow model, air is used as a gas in both reactors. The superficial gas velocity in the bottom part of the fluidized beds ranges from 0.035 m/s to 0.35 m/s. In the top of the reactor, cross section increases in order to reduce gas velocity and to trap the entrained solids back to the reactor.

The gas out flows from the reactors and cyclones are conducted into an empty cylindrical barrel of 0.5 m i.d. and 1 m height. This is to collect the fine particles, as well as a safety separation – storage device to collect the particles leaving the system during possible instable operations. Connection of all gas exits to the same barrel resulted in identical exit pressures at all these elements. The gas outflow from the collection barrel was then led to an electrostatic filter before release into atmosphere.

The fluidized beds are interconnected with two identical circulation lines composed of an L-valve, a blind tee, a cyclone and a loop-seal. The cold flow prototype is schematically presented in Figure 2.1. Pneumatic L-valves with 0.017 m i.d. and 1 m height are used to control solid flow rate. L-valves are composed of hybrid standpipes with 30° inclined sections in order to convey the solids horizontally. This inclined section is implemented to simulate the lateral spacing imposed by the thickness of the thermal insulations used in the pilot plant. Aerations (Q_{lv1} and Q_{lv2}) located 1.5 D_{lv} above the centerline of the horizontal section. Solids at the exit of the L-valves are transported through a vertical dilute phase conveying line (lift or riser) with 0.021 m i.d. and 2.25 m height. Gas superficial velocity in the lift ranges from 1.5 to 8.0 m/s. A blind tee bend is used to divert flow to a horizontal dilute phase conveying line with 0.017 m i.d. and 0.365 m length. Solid gas separation is performed in a cyclone (Cyc 1, Cyc2) where separated solids are lead to a loop-seal located in the bottom of the cyclone dipleg. The cyclone geometry used in the cold flow model is described in appendix 1. Loop-seals are used to ensure gas tightness between air reactor and fuel reactor. Solid particles are then circulated back to the first reactor through an identical second circulation line.

Different designs are available for loop-seal [112,113,226]. The configuration used in the current system is illustrated in the Figure 2.1. Main elements of the Loop-seal are supply chamber (SC) which is the bottom section of the cyclone dipleg, horizontal pipe (HP), recycle chamber (RC) and recycle pipe (RP). Two aerations are used in the loop-seal, Q_{Sr} and Q_{Ss}. Q_{Sr} is to fluidize the solids in the RC and supply minimum pressure drop required for the solids to flow into the reactor. Q_{Ss} is the critical aeration of the loop-seal, and serves for two purposes: first to convey the solids horizontally into the RC through the HP and second to facilitate the solid flow in the SC. Dimensions of the different sections presented above can be found in the appendixes.

Experiments were carried out in ambient temperature and pressure conditions using dry air as fluidization gas. Air is supplied from a compressed air network with constant pressure (6 bars) and dried with absorption. Gas inflow for L-valves and loop-seals are controlled using specific mass flow rate controllers connected to a computer for data collection. Gas flow into the lifts and reactors were controlled with manual valves and flow rates are measured using rotameters with constant pressure. Pressure drops were measured by digital pressure transducers and were automatically registered on a computer with adjustable frequency. Several pressure taps were located all over the installation to measure pressure drop in different sections of the circulation loop. Locations of pressure taps are illustrated in Figure 2.1 (green taps). All instrumentation (pressure taps and flow meters) were calibrated using available internal IFP Energies nouvelles quality standards.

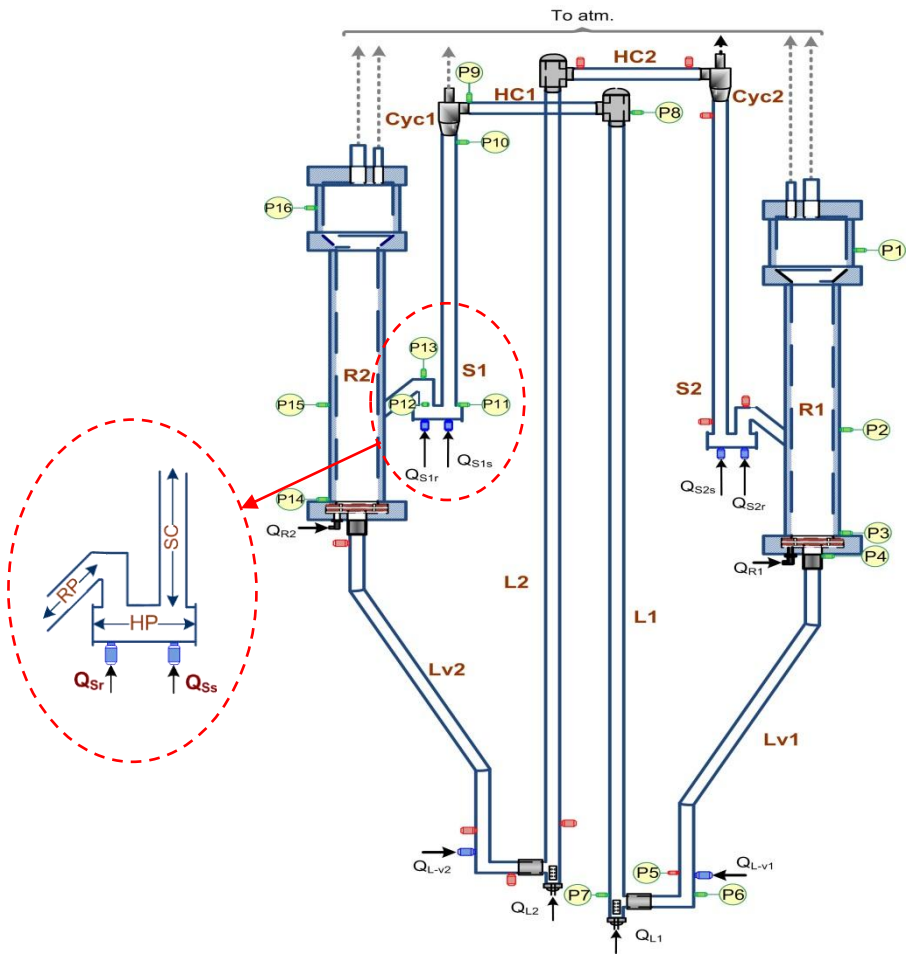

Figure 2.1 : Schema of the CLC cold prototype installations at IFP EN. Blue taps represent aeration points and red colored taps are the real taps used on the installation for pressure measurement. These are identical in both lines however in the figure it is illustrated just on line 2. Green numbered taps indicate the pressure drop notations used in this report. Abbreviations used in the figure stand for: R: reactor, lv: L-valve, lvH: horizontal section of the L-valve, L: lift, HC: horizontal conveying, Cyc: cyclone, DR: reactor bed above the loop-seal entry. The photo of the installation and the dimension of different section can be found in the appendixes 1.

2.1.2 High Temperature Prototype (Pilot Plant)

The high temperature pilot was constructed based on the same design as the cold flow prototype, with dimensions close to the cold flow model dimensions. The hot pilot plant configuration is illustrated in Figure 2.2. The main difference between cold flow prototype and the hot pilot plant relays on the number of interconnected reactors which is three in the pilot versus two for the prototype. One of the reasons for the pilot plant to have three reactors is related to the need to collect data in the oxidation reactor at intermediate oxidation states in order to study oxidation kinetics, while feeding the reduction reactor with fully oxidized material. Therefore, two oxidation reactors were implemented in the pilot plant. In the current operating mode, reactor R1 (0.13 m i.d., and 1 m high) is the fuel reactor with possibility of injection of CH_4 and/or N_2. Two other reactors, R2 and R3 (0.1 m i.d., and 1 m high each), are the oxidation reactors with possibility of Air and/or nitrogen injection. The 10 $_{kWth}$ prototype has been constructed with specific alloy HR-120 which provides excellent strength at elevated temperature up to 1095°C combined with very good resistance to carburizing and sulfidizing environments. Gases are injected at the bottom of the reactors through staggered perforated plates through four identical holes resulting in a hole density of 509 orifice/m².

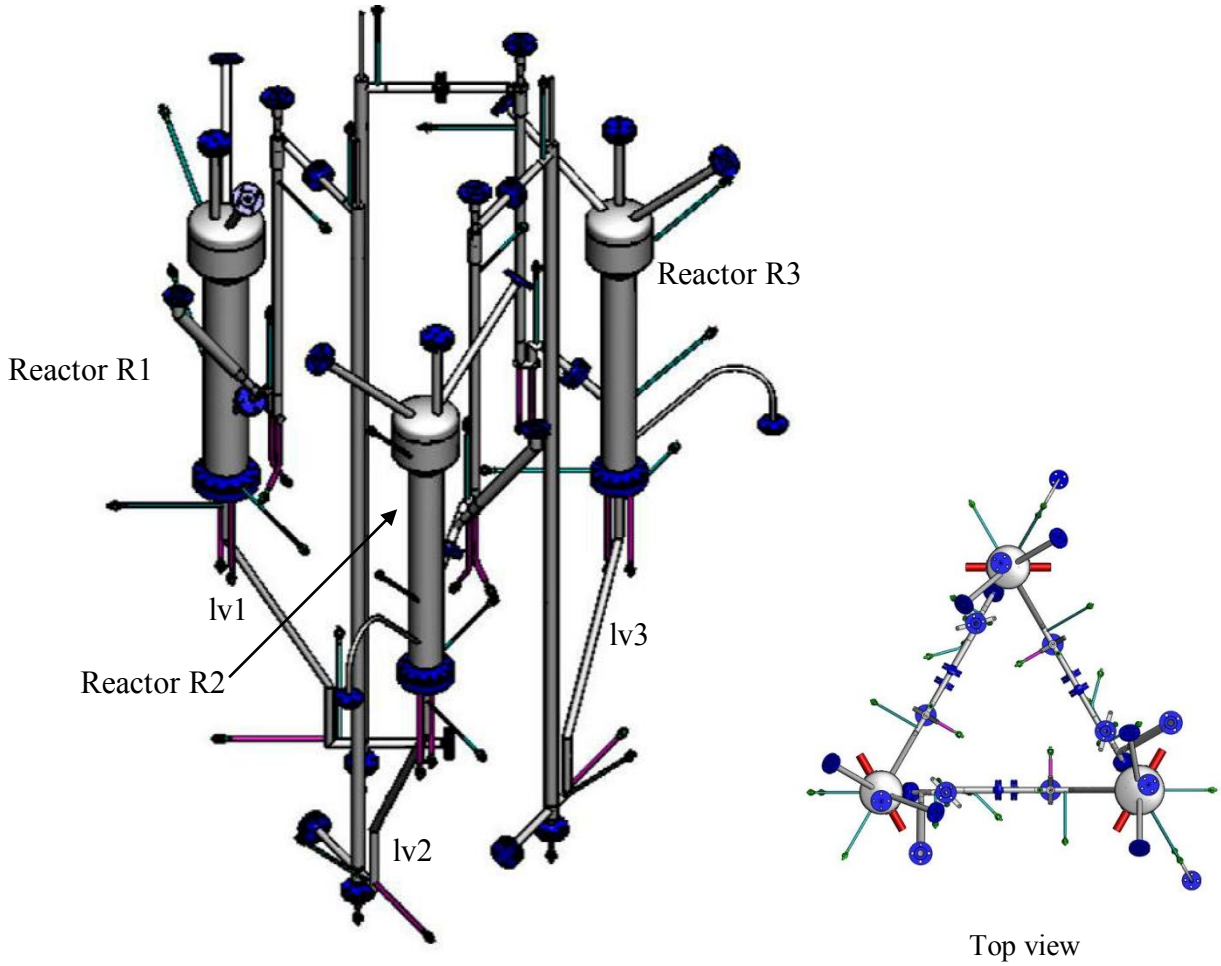

Figure 2.2: Scheme of the hot pilot plant configuration with three interconnected reactors.

The hot pilot plant employs identical solid circulation system as cold flow prototype. The system is composed of three interconnected bubbling fluidized bed reactors. The fuel reactor (R1) has an internal diameter of 0.13m while the air reactors have identical diameters of 0.1m. Solids leave the FR through a bottom connected standpipe to a pneumatic L-valve of 0.017 m i.d. and 1.1 m height (with a 0.635 m high 30° inclined line). Solids at the exit of the L-valves are transported through a lift with 0.02 m i.d. and 2.25 m height. A blinded tee bend is employed to divert solid flow to a horizontal dilute phase conveying line. Solid – gas separation is performed in a cyclone where separated solids are lead to a loop-seal located in the bottom of the cyclone dipleg. Loop-seal is used to ensure gas tightness between fuel reactor (R1) and air reactor (R2). Solid particles are then transferred to the second air reactor (R3) through an identical second circulation line. The same description is adapted to the circulation between R3 back to the first reactor R1. The entire reactor system is hanging on a scaffold and guided vertically using rails below the air and fuel reactors.

A Kammer™ valve is used to control the pressure inside the fuel reactor. The valve is installed at the gas exit of the reactor upstream of the solid filter. The opening of the valve was controlled automatically from the unit computer with adjustable opening between 0 – 100 %. Manual valves were installed at the gas exit of the R2 and R3, permitting the control of the pressure inside the reactors. Moreover, manual valves were installed at the gas exit of the cyclones permitting pressure control at each cyclone. The pressure at the cyclones and the reactors were critical parameters regarding the pressure balance and solid circulation around the system. The valves openings were adjusted in the beginning of the test (100% open in most cases) and remained unchanged through the test period. However, the Kammer™ valve was more frequently used to adjust the pressure inside the R1 to maintain a constant reactor pressure. This was necessary due to the molar expansion happening during

the gas combustion. The pressure control in the R1 was especially critical as the stability of the Loop-seal was dependent on this parameter. Moreover, a safety system was controlling the pilot operation based on the pressure drop across the loop-seals (ls1 and ls2). In the case that the pressure drop across the loop-seals passed a minimum value, the safety system was designed to replace the combustion gas with inert gas (N_2) to avoid direct contact of the combustion gas with air.

Dry air is supplied from a compressed air network of constant pressure. Nitrogen was used as the buffering fluidization gas when reactive gases are not injected into the system. Nitrogen and methane (CH_4) are supplied from bottles furnished by Air Liquide™. The fluidization gas in each system component and corresponding flow rate limit is listed in the Table 2.1. Gas flow rate into the system is controlled by means of specific mass flow rate controllers piloted from a computer. Gases were preheated by means of electrically heated exchangers to 350 °C before injection into the system. Pressure drops were measured by digital pressure transducers and were automatically registered on a computer with adjustable frequency. Several pressure taps were located all over the installation to measure pressure drop in different sections of the circulation loop. The pressure gauges installed at the pilot plant are illustrated in Figure 2.3 for a transportation line between two reactors. The locations of pressure gauges are identical for all three lines.

In a small pilot plant, heat losses can be very significant. Therefore, it was chosen to control temperatures in each part of the pilot plant and not to operate adiabatically. Temperature of the system was then controlled by use of electrical heaters installed around the reactors and solid transfer lines. The system was covered with a layer of thermal insulation (mineral wool) to minimize thermal lost. The heating system was working based on feed back control with adjustable temperature set point piloted from the unit control computer. Temperature of the system is measured by use of thermocouples of type K. Four thermocouples are installed inside each reactor in different heights on a descending internal measurement bar. The thermocouples are installed at heights of 0.1, 0.325, 0.450 and 0.750 m from the bottom of the reactors (distributor). Two additional thermocouples are installed at the external surface of the reactors at 0.11 and 0.7 m from the bottom of the reactor. Additional thermocouples measure temperature in the transfer lines on each L-valve, 1 in each lift, 1 in the blinded T-bends and 2 on the loop-seals.

Entrained solids were gathered by means of six filters installed separately at the gas exit of each reactor and each cyclone. Separated fine particles were then gathered in specific reservoirs installed below each filter. The reservoirs were systematically emptied at the end of each test to analyze the particles. The particles were then weighted and sieved at 100 µm and the large particles were reintroduced into the pilot plant. Existence of particle filters at the gas exits of the cyclone and reactors imposed an additional pressure drop at the exit of these elements. This pressure drop is a function of gas flow rate passing through each filter.

Table 2.1: Gas injection in different section of the high temperature pilot plant.

Element	Fluidization gas	Flow rate range (Nm^3/h)
Fuel reactor (R1)	Nitrogen CH4	0 – 0.5 0 – 1.0
Oxidation reactor (R2)	Air Nitrogen	0 – 3.5 0 – 0.5
Oxidation reactor (R3)	Air Nitrogen	0 – 2.5 0 – 0.5
Lift (L1, L3)	Nitrogen	0 – 3.0
Lift (L2,)	Air Nitrogen	0 – 3.0 0 – 3.0
Loop-seal (1, 2, 3)	Nitrogen	0 – 0.5

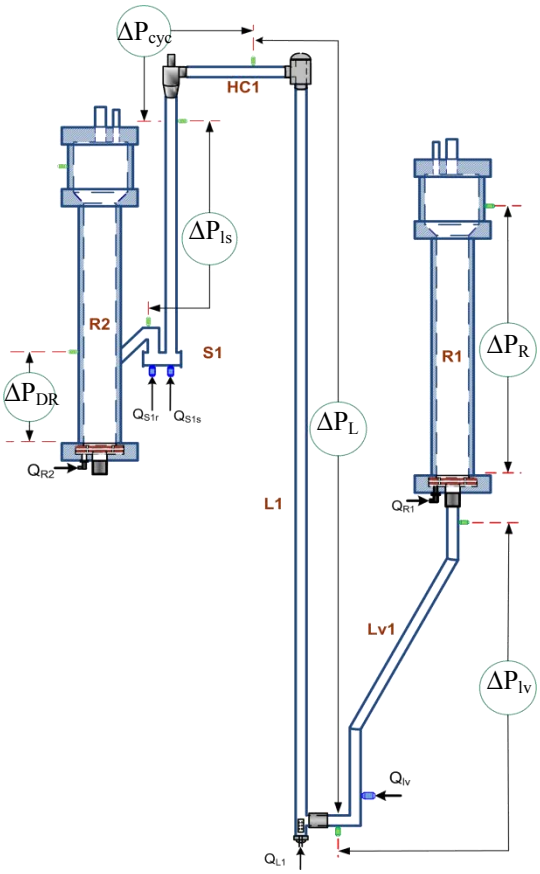

Figure 2.3: Scheme of the pilot plant pressure drop measurement gauges.

The combustion gas at the exit of the fuel reactor was dehumidified through water cooled condensers. The flow rate of the dry air was measured by a gas flow meter and registered in the system computer. A constant fraction of the flue gas is then sampled to the gas analyzers. Flue gas from fuel reactor is then analyzed to determine H_2, CO, CO_2, CH_4 and N_2 contend. Depleted air from air reactors, R2 and R3, is analyzed to determine CO, CO_2 and O_2 content. The principles of the employed analyzers are presented in section 2.1.3.

2.1.3 Gas Analyzing Devices

Protec™ Helium Detector was used as the Helium measurement device in the gas tracer study performed in the cold flow prototype. The device is capable of detecting Helium sucked into the device though a sniffer line. The device works based on the mass spectrometry principle. The main aspects of the device and the calibration result of the apparatus are listed in the appendixe 3. The Helium detector and on/off control valve were connected to a computer permitting online registration of the measurements results with adjustable frequency. The sampling/detector system consisted of a 1 mm i.d. 2.5 m long sampling tube leading to the Helium detector.

High temperature pilot plant is equipped with two set of online gas analyzing systems for the combustion fuel gas (measuring CO, CO_2, H_2, and CH_4) and the depleted air at the exit of oxidation reactors (measuring O_2 and CO_2). The fuel reactor exit gas is led to a water seal, where most of the steam condenses. After cooling, a fraction of each gas leaving the air reactors and the fuel reactor is led first through a small filter, where any entrained fines are removed. The sampled gas is then passed through a second gas condenser working with a refrigerator cooled with the Peltier effect to reduce the dew point of the sampled gas to about 3 °C. A diaphragm pump sucks the gases into the analyzers by passing it across a filter with water detector which stops the pump in the case of water presence. A scheme of the gas injection and detection system of the fuel reactor is illustrated in Figure 2.4.

CO, CO_2, and CH_4 are simultaneously measured by non-dispersive infrared (NDIR) detectors (wavelength range λ = 2.5 - 8 µm) provided by ABB™. This apparatus is calibrated by ambient air sampled by an electro-valve representing zero set point. The maximum measurement scale is calibrated against a gas mixture of known composition. Hydrogen is measured by means of a thermal conductivity analyzer provided by ABB™. These kinds of devices are mostly used for measurement of binary gases based on the thermal conductivity of each gas. The current analyzing system includes an integrated function that corrects the measurements for the CO, CO_2 and CH_4 measured previously by NIDR analyzer. This device is calibrated in two points against Hydrogen and Nitrogen.

A separate set of gas analyzers are installed to measure O_2 and CO_2 content of the depleted air at the exit of the oxidation reactors (R2 and R3). The gas is sampled from the cooled gas stream at the exit of R2 and R3 downstream of particle filters. A three ways vale permits to select the gas stream into the analyzer from either R1 or R2. An assembly of rotameter and vacuum pump permits to control the gas inflow into the analyzing system. A scheme of the gas flow system of the oxidation reactors is illustrated in Figure 2.5. The CO and CO_2 analyzers work with the same principle as described above. Oxygen is measured by a paramagnetic analyzer. The device has good measurement stability in time.

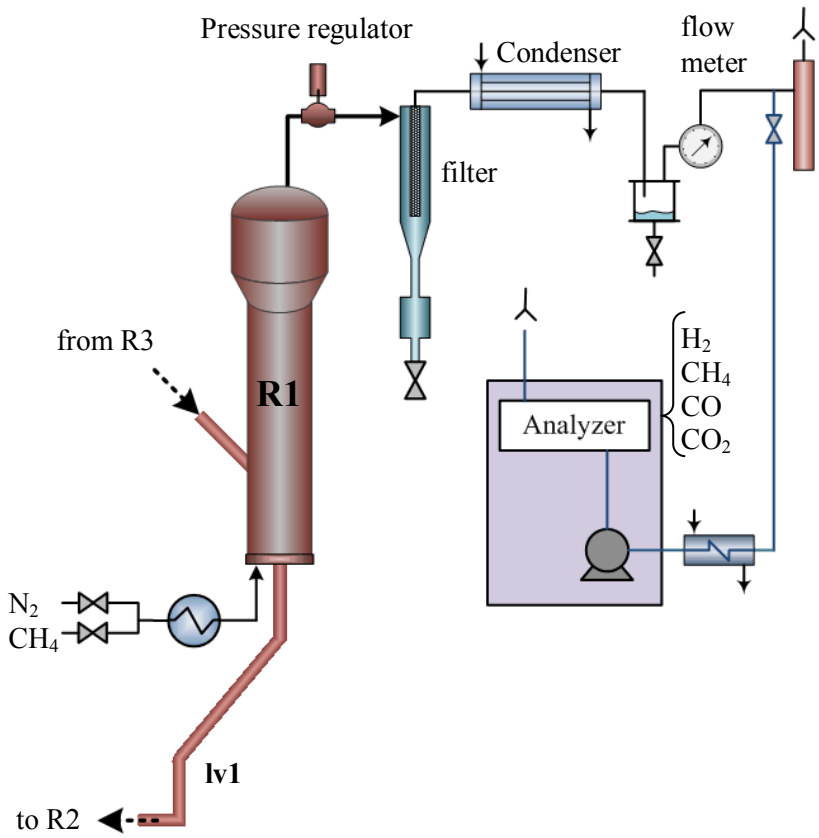

Figure 2.4 : Scheme of the gas flow around the fuel reactor in the high temperature pilot plant.

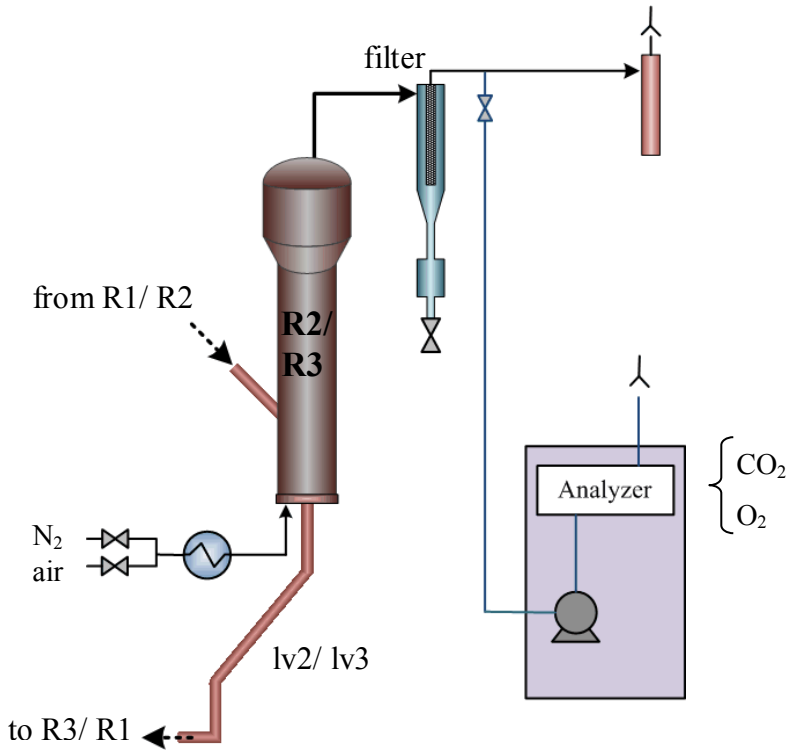

Figure 2.5: Scheme of the gas flow around the oxidation reactors (R2 / R3) in the high temperature pilot plant.

2.2 Particle Properties

Particles properties are one of the most influencing parameters in fluidized bed and solid circulation operation. Therefore, proper characterization of the particles used is essential for understanding and modeling of the current system. Hydrodynamic study in the cold flow prototype was carried out using three solids named: sand I, sand II, and ilmenite. Sand was obtained from a local supplier (SIKA). Ilmenite was obtained from a Namakwa sand concentrate supplied from South. Ilmenite particles used in the RTD test were sieved to a particle diameter of 50 µm. This modified particles diameters to 127.6 µm as presented in the appendixes.

$NiO/NiAl_2O_4$ (60/40) particles are used as the oxygen carrier in the hot pilot plant. This Ni-based oxygen carrier has been manufactured by Marion Technologies (France) and prepared by precipitation. The main properties of these solid particles and corresponding experimental methods used for characterization are listed in Table 2.2. The experimental procedure and detailed results for different particles are reported in appendix 0. The theoretical oxygen transfer capacity (R_0) is 12.8%, corresponding to reduction of NiO to Ni. This value will be used for the calculation of oxidation degrees, even if we have to notice that some authors, have measured oxygen transfer capacity up to 14.5 wt% according to thermogravimatric tests [14] for the same particles. This difference is mainly due to the slower reduction of $NiAl_2O_4$ to Ni and Al_2O_3. The oxygen carrier used in the combustion tests and solid circulation at 700 °C was sieved to a particle diameter of 100 µm. This modified the particles to a Sauter diameter of 201 µm. The particle size distributions of these particles are illustrated in the appendix 2.4.

Table 2.2: Properties of solid particles used in the cold flow prototype and high temperature pilot plant. The properties are reported based on the experimental method (unless mentioned) at ambient temperature. The experimental methods in each case are presented in the appendixes 0.

Property	Value			
Solid	**Sand I**	**Sand II**	**ilmenite**	**OC1**
ρ_s (kg/m^3)	2650	2650	4750	3250
d_p (µm)	253	368	107 [c]	168 [d]
d_{50} (µm)	268	384	132	201
U_{mf} (m/s)	0.038	0.068	0.0147	0.03 [b]
U_t (m/s)	1.37 [a]	1.95 [a]	0.82 [a]	1.22 [a]
U_{ch} (m/s)	3.8 [e]	4.4 [e]	3.4 [e]	3.6 [e]
ε_{mf}	0.513	0.514	0.455	0.48
ε_s (free settled)	0.463	0.457	0.434	
ε_{st} (tapped)	0.398	0.404	0.396	
Φ	0.86	0.76	0.64	

[a] **Calculated by correlation developed by Haider and Levenspiel [227].**
[b] **Calculated by Wen and Yu correlaton [228]**
[C] **The particle used in the gas tracer and RTD study were sieved for 50 µ with d_p shifted to 128 µm.**
[d] **The particles used in the circulation test at 700 °C and combustion tests were sieved for 100 µm with d_p shifted to 201 µm (OC2).**
[e] **Calculated by PSRI correlation [229].**

2.3 Tracing and RTD Tests in the Cold Prototype

Gas tracer study was carried out in the CLC cold flow prototype. Dry air was used as the main fluidization gas with Helium as tracing gas. Tracer gas was injected either in steady state or transitional mode based on the study purpose. Steady state Helium injection was to investigate the gas flow repartition between different sections of the system mainly L-valve and Loop-seal. The transitional tracer injection was used in case of residence time distribution measurements in the reactor R1. Different configurations used in the current study and the aimed investigation purposes are listed in Table 2.3. The corresponding positions are illustrated in the Figure 2.6.

Helium was used in the gas tracer and RTD studies as the tracer gas. Helium was supplied from a bottle of 9 Nm^3 with a purity of 99.999% (impurities of 2 ppm of O_2, 0.5 ppm of C_nH_n and 3 ppm of H_2O). Helium flow rate was controlled by means of a Rotameter at fixed pressures. The device operating range and calibration results are presented in appendixes, Figure 15. For the residence time measurements, an on/off control valve was used to control the start and stop of the Helium gas flow. The tracer gas (Helium) was injected into the reactor fluidization line just upstream of the windbox. A static mixer was used in the air injection tube to ensure proper mixing of the Helium and the air.

Table 2.3: Different injection – detection positions used in the current study, corresponding to Figure 2.6.

No.	injection position	Detection position	Purpose
1	IP1	DP1	RTD measurements
2	IP1	DP2	L-valve vertical section flow
3	IP1	DP3	Leakage between two reactors
4	IP2	DP3	Loop-seal standpipe flow
5	IP3	DP2	Effect of gas on L-valve
6	IP4	DP2	Loop-seal standpipe flow
7	IP4	DP3	Horizontal gas flow in the Loop-seal

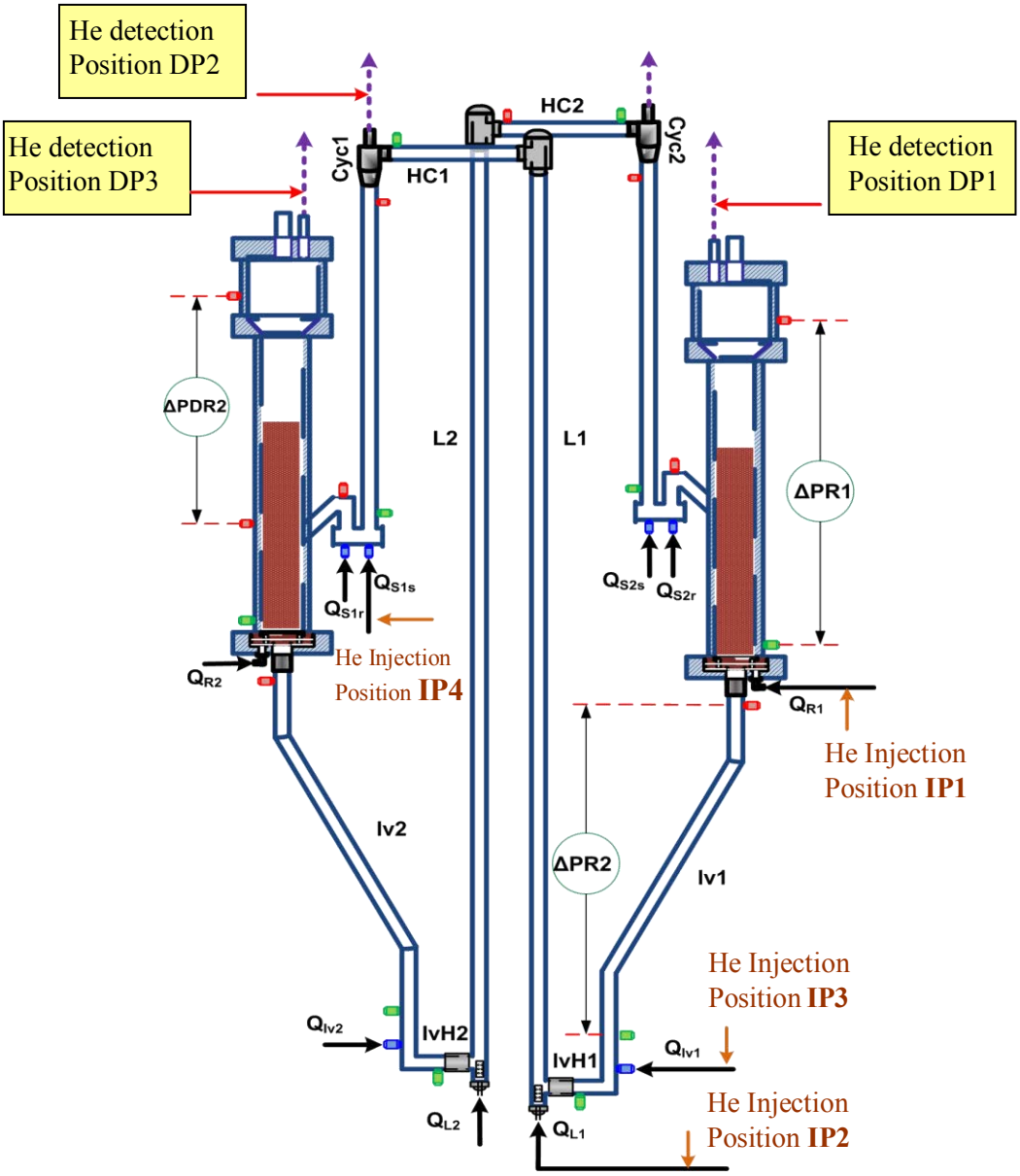

Figure 2.6: Scheme of the CLC cold flow prototype. Different Helium tracer injection – detection configurations used in the study are indicated in the figure.

2.4 Pneumatic Conveying Gas Velocity

The lifts used to pneumatically convey particles between reactors in the current design. The lifts are operated at constant gas velocity in order to estimate solid circulation through lift pressure drop measurement. Proper selection of the gas velocity is an important parameter in the pneumatic conveying of solids. Operation slightly above the minimum pressure gradient point is mostly desired in the pneumatic transport lines [230]. Chocking and saltation phenomena should be avoided in vertical and horizontal conveying. These critical velocities were calculated from the correlations in the literature [231] as presented in Table 2.2. Moreover, Zenz-type diagram [152] of pressure drop per unit length versus gas velocity was drawn in Figure 2.7 from experimental results for three solids used in cold flow. The pressure drop decreases when gas velocity increases due to the decreasing solid hold-up. In the range of operating conditions tested, it was not possible to reach the minimum pressure drop point where pressure drop increases due to increasing friction. The selected gas velocities for lift

operation were thus 6.5 m/s for sand I, and 8 m/s for sand II and ilmenite which is close to the minimum pressure gradient according to Figure 2.7.

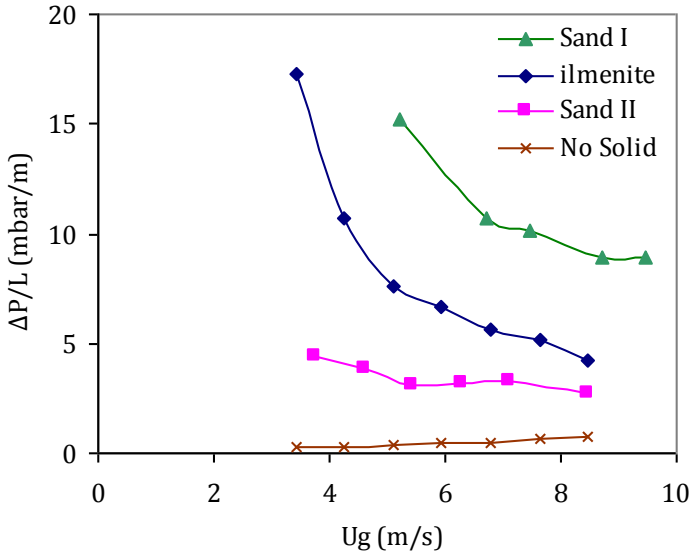

Figure 2.7: Vertical pressure gradient for three solids with solid flow rate of 170 kg/h of ilmenite, 65 kg/h of sand II and 88 kg/h of sand I. The pressure drop values are normalized based on the solid flow rate for each data series.

2.5 Solid Flow Rate

Measurement of solid flow rate is an important parameter in the current study. This section presents the employed measurement techniques as well as demonstration methods.

2.5.1 Solid Flow Rate Measurement Methods

Indirect method of pressure drop measurement across a particular section of the riser [147,148,232] was adopted in the current study. A 2 meter section of the riser was selected with visual uniform axial solid profile (not including the visual dense initial phase of the riser). Direct measurement methods were then used to correlate pressure drop and the solid flow rate across this section, as:

$$G_s = f(\Delta P / L) \qquad \textbf{Eq. 2.1}$$

The correlation was then used in the steady state solid circulation test to measure the solid flow rate. This procedure was used both in the cold flow model and in the hot pilot plant.

The solid flux correlation was developed in batch solid flow rate measurement tests. Solids were circulated in a batch operation from a reactor (e.g. R1) to the following reactor (e.g. R2) while using a constant aeration rate into the L-valve. The other L-valve was not operating; therefore, the solid inventory was reducing in R2 and increasing in R2. The solid accumulation was then measured in both of the reactors by different means. First method was measurement of the variation of the height of the solid bed in the reactor (ΔH_R) during time intervals, Δt. The variation of the mass of the solid inventory was then calculated and plotted versus time. The average solid flow rate is then the slope of the mass variation curve versus time. An example of this calculation procedure is illustrated in the Figure 2.8.

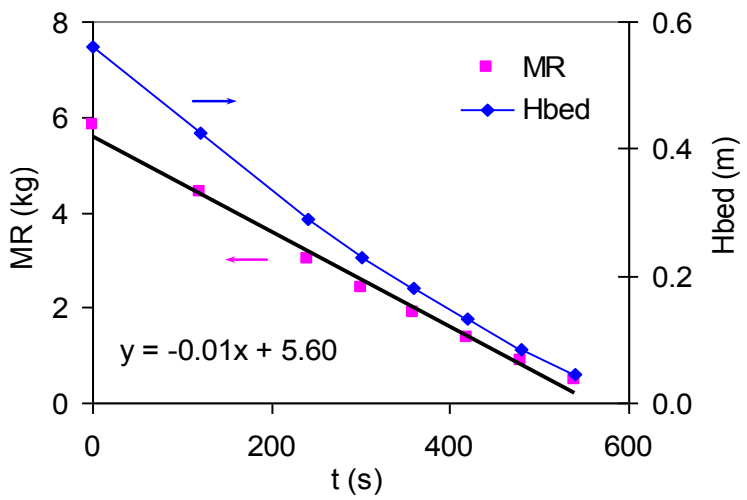

Figure 2.8: Variation of solid height and the mass of the solid in the reactor for Sand I in the cold flow model with Q_{lv}=0.07 Nm^3/h for sand I. The resulting slope of the line is the solid flow rate, 0.01 kg/s or 36 kg/h .

The other measurement method was based on the variation of the pressure drop in the reactor. The instantaneous solid flow rate could be calculated also from the evolution of the pressure drop across the reactors as:

$$W_s = \frac{dM_{s,R}}{dt} = \frac{A_R}{g} \cdot \frac{dP_R}{dt} \qquad \textbf{Eq. 2.2}$$

Where $M_{S,R}$ is the solid mass in the reactor, A_R the reactor surface area and P_R is the pressure drop across the reactor. Figure 2.9 illustrates an example of solid flow rate measurement based on the variation of the pressure drop.

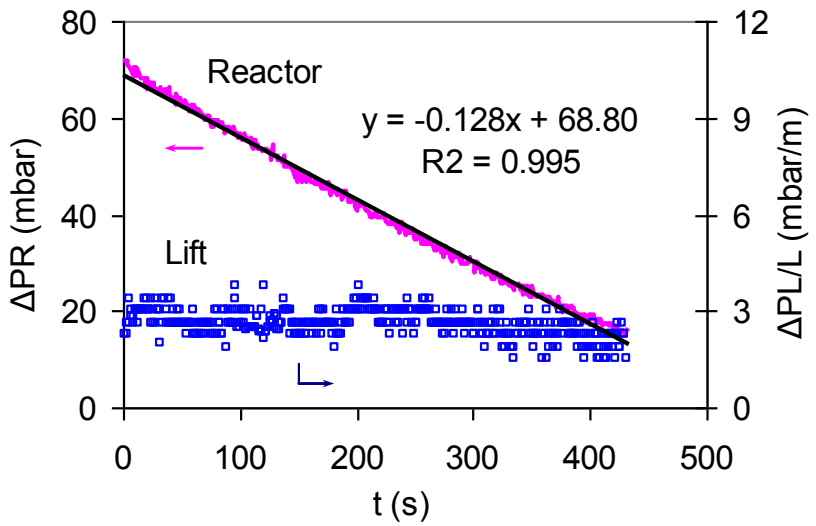

Figure 2.9: Pressure drop in the reactor and the lift for constant aeration in the L-valve in a batch process with Q_{lv}=0.07 Nm^3/h in the cold flow prototype for sand I particles. The resulting solid flow rate was 37 kg/h and average lift pressure drop per length was 2.6 mbar/m.

Figure 2.8 and Figure 2.9 present measurement of solid flow rate with these two techniques in the cold flow model with sand I and identical operating conditions. The result is 37 kg/h as average solid flow rate calculated from H_R variation method and 36 kg/h obtained from the pressure evolution curve calculated with Eq. 1.7. This demonstrates a very close value calculated with these two different methods. Accordingly, the pressure evolution method has been used as principal method in the course of batch circulation solid flow measurement tests. This choice brings about some advantages. It can be used both in cold flow model and hot pilot plant. Then, automatic data acquisition on a computer reduces the possible human errors. Moreover, solid flow measurement with this method could be carried out for different solid heights. Accordingly, one can prevent the effect of reactor pressure drop on solid flow rate by setting a determined minimum and maximum reactor pressure drop in the reactor during the measurement process. Solid flow rate measured in the direct batch method was then plotted versus the pressure drop across the lift. Figure 2.10 illustrates the resulting curve for three solids in the cold flow prototype.

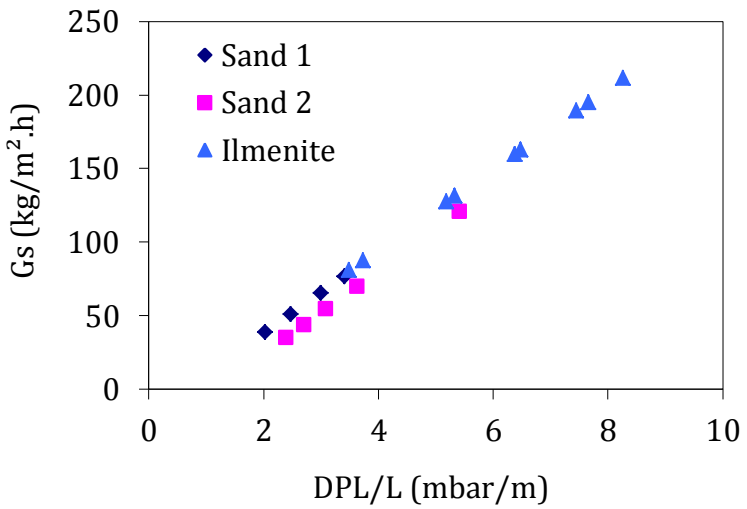

Figure 2.10: Solid flux variation versus associated pressure drop in the lift for three solids. These curves are used to measure the solid flow rate in the continuous operations. Gas velocity in the lift was 5.4 m/s for sand I, 8 m/s for sand II, and 6.8 m/s for ilmenite particles.

The solid flow rate measurement in the high temperature pilot was measured with the same principle but some modifications in the measurement procedure. As the pilot was operating in high temperatures, uniformity of the temperature across the system was important to ensure control of superficial gas velocity in the lifts and L-valves. Therefore, to ensure the uniform temperature and constant conditions, the measurement was carried out in two steps. First solids were circulated in steady state between three reactors. Once the steady state condition was attained, one of the L-valves (lv1), was stopped. Therefore, solids started to accumulate in R1 and inventory of R3 was decreasing. The solid flow rate was then calculated from the pressure drop variation as explained above. Moreover, at the end of each steady state operation with pilot plant, this operation was repeated to measure the solid flow rate more precisely.

Figure 2.11 illustrates the plot of solid flux versus pressure drop for a temperature range of 345 °C to 560°C. The results illustrate that the pressure drop is the same for two cases with different temperatures but similar gas flow rate. Accordingly, the main influencing parameter in the pressure drop in the lift is the gas flow rate and the temperature changes the pressure drop indirectly through variation of the gas flow rate.

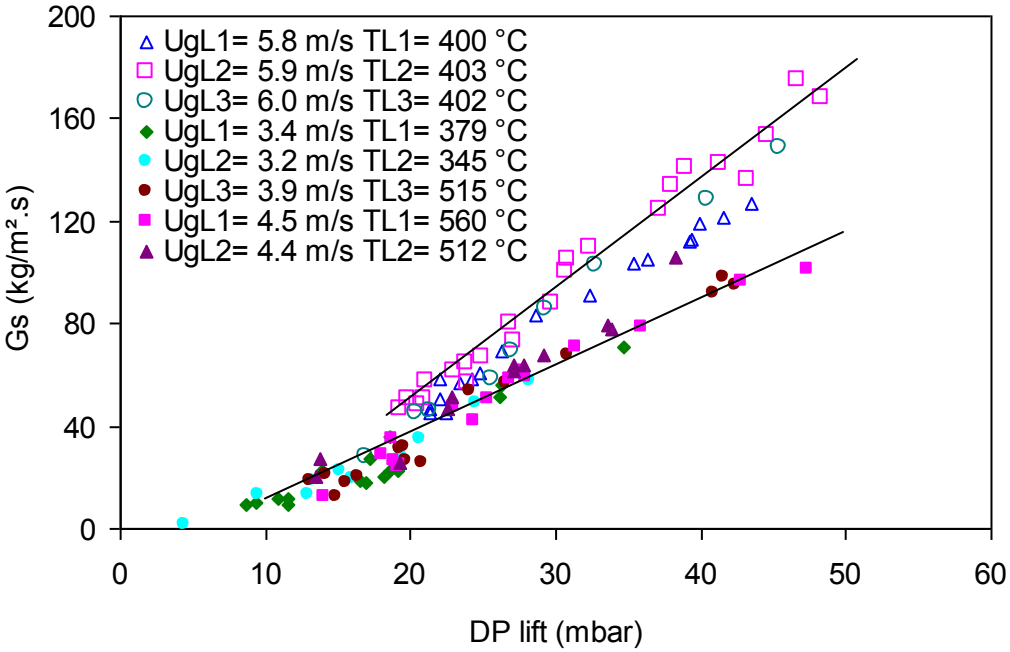

Figure 2.11: Solid flux versus pressure drop in three lifts of the high temperature pilot plant. The average velocities and temperatures are listed in the figure.

2.5.2 Solid Flow Rate Measurement, Demonstration Methods

The pressure drop-solid flow rate correlations (Gs – ΔP_{lift} curves) were obtained from the measurement in batch operations. In order to verify validity of the relation in continuous operation, three series of validation tests were carried out in cold flow prototype.

First, a series of successive batch-continuous-batch tests was carried out in the cold prototype with a constant aeration rate in the L-valves. Solid inventory was set to 0.7 m in R1 and 0.3 m in R2. A constant aeration was adopted in the L-valve lv1 resulting batch circulation of the solids to the reactor 2. Once the solid level reached 0.5 m in both reactors, the second L-valve was actuated with the same aeration rate as the other. Continuous stable operation was continued for a determined time interval. Aeration was then stopped in lv2, resulting in a batch operation till R1 reaches 0.3 m. Pressure drop in different elements of the system was observed to investigate variation of condition between continuous and batch operation.

Figure 2.12 illustrates the results for a batch-continuous-batch circulation test. The pressure drops in the critical sections of the installation dealing with solid flow rate are presented including the horizontal section of the L-valve and the lifts. The pressure drop in the lift 1 shows a stable behavior regardless of batch or continuity of the operation. Pressure drop in the Lift 2 also reaches the same value as the pressure drop in the lift 1 during stable operation. Moreover, pressure drop in the reactors remains constant when demonstrating a stable circulation process during the continuous circulation. This illustrates that pressure drops of the solid flow in the L-valve and in the lift are identical regardless of batch or continuity of the operation.

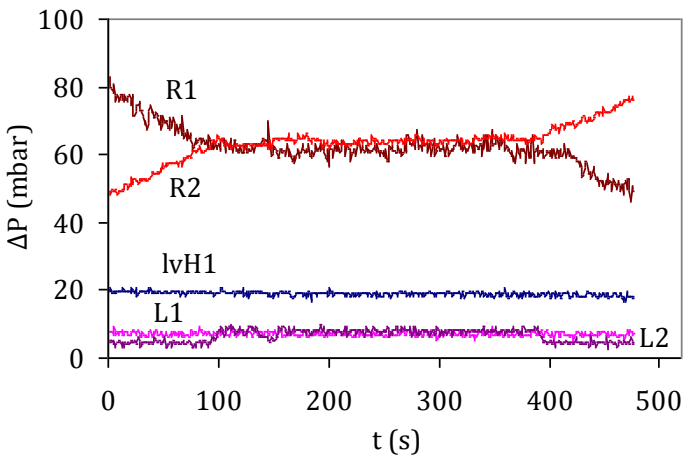

Figure 2.12 : Pressure drop variation across the main solid circulation elements in a consecutive batch – continuous – batch operation with aeration rate of 0.08 m^3/h for sand I.

Alternatively, another kind of experiment was conducted in the cold flow prototype. The aeration flow rates in the L-valves were set differently in the two L-valves, resulting in a different solid flow rate in each direction. The difference of solid flow rate was measured experimentally (from $d\Delta P_R/dt$) and calculated from the pressure drop in the lifts. Figure 2.13 illustrates an example of this kind of tests. Experimentally measured solid flow rate difference was 40 kg/h versus calculated value from the pressure drop curves of 44 kg/h. This demonstrates 10 % difference between the values which is acceptable regarding the possible experimental errors.

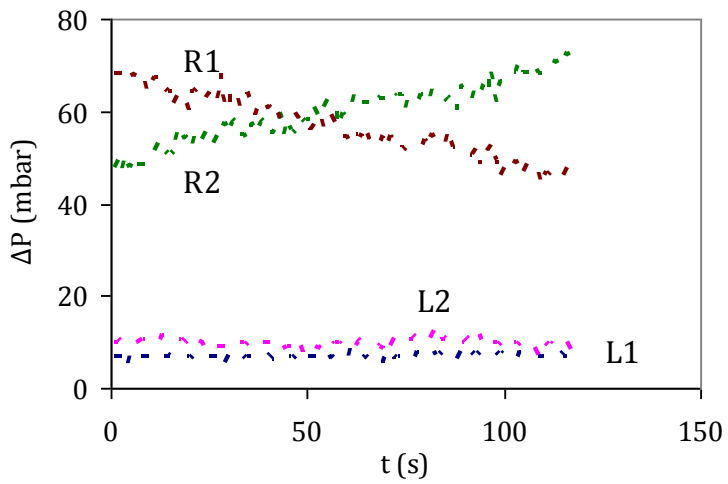

Figure 2.13: Pressure drop variation in a continuous operation of sand I with Q_{lv1} = 0.13 and Q_{lv2} = 0.08 in the cold flow prototype. The resulting measured solid flow rate is 40 kg/h calculated from the slop of the reactors pressures from Eq. 1.7.

Finally, a butterfly valve was employed at the dipleg of the cyclone (Cyc 2) of the cold flow model, to redirect solids into an accumulation reservoir for a determined time interval. The solid weight was then measured using a balance. The average solid flow rate was therefore calculated. The resulting solid flow rate was 66 kg/h for sand I with Q_{lv} = 0.1 Nm^3/h. Solid flow correlation of Figure 2.10 results in 69 kg/h for the same test. Therefore, this method also provided another validation result on the method of online solid flow rate measurement used in this study.

The results from the batch calibration method and demonstrative continuous tests illustrate an acceptable agreement in both cases. Therefore, the resulting curves illustrated in the Figure 2.10 were used in the course of experimentations to measure solid flow rate on the cold flow prototype.

The experimental results presented in this section compared the solid flow rate measurement results obtained with different possible techniques in the current system. Accordingly, the selected solid flow rate measurement method was based on the measurement of the pressure drop across a fixed section of the lift. A correlation was developed between the solid flow rate and pressure drop in this section in batch solid circulation from one reactor to the other. The results were then used in the continuous tests to measure the solid flow rate. This method was used in both the pilot plant and the cold prototype. In the operations at the pilot, due to the effect of temperature on the gas velocities, the solid flow rate was measured at the end of each continuous operation to obtain more precise measurements.

2.6 Operational Procedures

Cold flow prototype has the advantage of being transparent which brings about possibility of visual observations in addition to the conventional measurements such as pressure drop and gas analysis. In a normal operation, the solid inventory inside the reactors was adjusted to the desired quantity. The operation was conducted through the following steps as:

1. Fluidizing the solids in the reactors.
2. Adjusting the gas flow rate in the lifts.
3. Opening the gas inflow into the loop-seals to the required flow rates.
4. Start-up of circulation as last step by adjusting the external gas injection in the L-valves.

In the steady state solid circulation operations, the external gas flow rate in the L-valves were adjusted in a manner to attain constant pressure drops in the reactors. Once the system reached the steady state, the desired measurements were carried out.

The experimental operation in the high temperature pilot plant was different and more complex regarding addition of temperature and reactions control. First, the system temperature was set to the desired condition. Once the temperature was attained, the gases were adjusted in the lifts and then in the loop-seals similar to the cold prototype. It is also important to point out that in the pilot plant; the reactors remain always fluidized with inert gas (N_2) to avoid particles agglomeration. In order to start up a run in the pilot plant, the following procedure is carried out:

1. Solid circulation: The solid circulation is first started from R1 to R2 by injecting an initial low gas flow rate in the lv1. Next, identical gas injection is applied in lv2 and then lv3 to get solids circulating between three reactors. The external L-valve aeration was then set to the flow rates necessary to reach the planned solid flow rate. The level of the external L-valve aerations are then adjusted to have constant pressure drop in each reactor, indicating steady state identical solid flow between the reactors.
2. Air injection: The nitrogen was replaced by air in the reactors R2 and R3.
3. Loop-seal stabilization: The pressure drops in the loop-seals were then adjusted and stabilized by use of the height of the fluidized bed in each reactor. In the case of high pressure drop down stream of the loop-seals a Kammer^{TM} valve at the gas exit of the reactor R1 permitted control of the pressure drop downstream of the loop-seal more precisely in this reactor. Regarding the air reactors, R1 and R2, the pressure drop was adjusted not only by height of the fluidized bed in the reactors but also by aid of the pressure drop in created in the particle filters at the exit of the reactors. Higher air flow rate in the reactors resulted in higher pressure drop in the filters, easing the stabilization of the loop-seals. In addition, there was possibility of pressure control by manual valves at the R2 and R3 flue gas line. However, pressure drop adjusting through air flow rate was preferred in most cases due to the ease and flexibility of the control. Therefore, in the cases where the set up values of Q_{R2} and Q_{R3} were not critical for experiments, these flow rates were used to control the pressure drop ΔP_{R2} and ΔP_{R3}. It should

be mentioned that in most of the experiments there was no need to add additional measures for loop-seal stabilization as the normal operating conditions were sufficient for a stable steady state operation.

4. Analysis start up: The gas analyzers are then set up on line. The oxygen concentration in the reactor R3 is checked carefully to ensure that oxygen carriers are fully oxidized.
5. Combustion: Finally, the nitrogen is replaced by the desired CH_4 flow rate in the fuel reactor R1 to start the combustion in the fuel reactor.

Once the experimental test was completed, the combustion gas was replaced by nitrogen. The solid circulation was continued to ensure full oxidation of oxygen carrier. One of the L-valves (mostly lv1) was then stopped to measure the solid flow rate. Afterwards, the air was replaced by Nitrogen in R2 and R3. The L-valves were then stopped and the system was put into standby mode while the reactors and loop-seals remained fluidized by Nitrogen and other gas flow rates were stopped. After each run, the 6 flue gas filters were cleaned by use of back pressure and the solid recovery reservoirs downwards filters were emptied to gather the particles.

2.7 Electrostatics Effect

Electrostatic effects were observed during the experimental tests in the cold flow prototype. These effects had a variable nature depending on the operating conditions. The main effects of the electrostatic charge accumulation in the system were production of electrical arcs inside the system and sticking of the particles on the interior surface of the reactor and conducting tubes which some time altered the solid circulation.

The electrostatic effects had an accumulative nature. It was negligible at the beginning of experimental tests, while its effects increased progressively along the experimental test period. After a period of about 3 to 4 hours of solid circulation, considerable effects were observed. Moreover, the solid properties play an important role. Experiments with Sand 1 particles with smallest size and density were the most altered by electrostatic. In some cases, L-valve and loop-seal flow were blocked due to the particles stuck on the tube walls. The electrostatic effects had very little influence in case of sand 2 and negligible with ilmenite particles.

To reduce the impact of electrostatics, some measures were employed in the cold flow prototype. First, electrical charges accumulating at the external surface of the system were discharged by aid of a conducting mesh and wire system connected to a neutral ground source. The use of an antistatic compound called Larostat (quaternary ammonium salt) was also tried but no significant improvement was noticed, contrary to the benefits found by Herbert [233] and Aubert [234] with FCC powders. Electrostatic effects were not observed in the high temperature pilot plant due to the conductive nature of the system.

2.8 Conclusion

The experimental setups and measurement methods used in the current study were presented in this chapter. A novel CLC design was developed to study the chemical looping combustion process in small scale of 10 kW_{th} as a part of a joint project lead by IFP Energies nouvelles and TOTAL S.A.. The system is composed of interconnected bubbling fluidized beds as fuel and air reactors with L-valves to control solid circulation flow rate and inventory level in each reactor. Moreover, loop-seals are employed to guarantee gas tightness of the reactors.

The cold flow prototype used in the current study was presented in this chapter. The prototype was used to investigate the solid circulation control (actuated by L-valves), gas-tightness (obtained by loop-seals), gas tracer investigation, and fluidized bed hydrodynamics (DTS study). The cold flow prototype is an essential device for better understanding the CLC process and scale up purposes both regarding construction of the high temperature pilot plant of similar size and also development of CLC systems of higher capacities. For this purpose this device was used to develop a solid circulation model and a hydrodynamic fluidized bed model.

The 10 kW_{th}, high temperature pilot plant and the associated measurement devices and methods were presented next. The pilot plant was built with similar dimension as cold flow prototype. This device was used to investigate effect of temperature on solid circulation by comparison of the results with cold flow prototype. Moreover, it permitted to study CLC reactions at high temperatures. Nickel based oxygen carriers ($NiO/NiAl_2O_4$) with methane as the combustion feed were used in the framework of this study. The pilot is an important tool for scale-up purposes by addition of temperature and reaction effects to what found by cold flow prototype. For this purpose, the experimental results from the pilot plant permit to develop and validate a reactor model by addition of the reaction kinetics to the hydrodynamic model developed by aid of residence time distribution studies in the prototype.

The experimental data obtained from the cold flow prototype and the high temperature pilot plant permit to study CLC system in different hydrodynamic and reaction aspect necessary for understanding and development of this process. This is best illustrated in development of a CLC model including both solid circulation and reaction presented in the following chapters.

Chapter 3

Solid Circulation Investigations: Experimental Results

3.1 L-VALVE OPERATION 61

3.1.1 Standpipe of the L-valve 62

3.1.2 Gas Flow in the Standpipe of the L-valve 64

3.1.3 Solid Flow Control Mechanism in the L-valve 67

3.1.4 Calculation of Pressure Drop in the Standpipe Using Ergun Equation 69

3.1.5 Average Voidage of the Moving Solid Bed in the Standpipe 69

3.1.6 Effect of Gas Properties on the L-valve Operation 72

3.1.7 Effect of Particles Properties on the L-valve Operation 73

3.1.8 L-valve High Temperature Operation 75

3.1.9 L-valve Limiting Operation 77

3.2 LOOP-SEAL OPERATION 80

3.2.1 Pressure Drop in the Loop-Seal 81

3.3 LOOP-SEAL GAS TRACING STUDY 83

3.3.1 Effect of the Loop-seal Aeration, Qss 83

3.3.2 Effect of Loop-Seal Aeration, Qsr 85

3.3.3 Effect of Solid Flow Rate 86

3.3.4 Effect of the Pressure Drop across the Supply Chamber 87

3.3.5 Flow in the Horizontal Pipe of the Loop-seal 90

3.4 GLOBAL GAS TIGHTNESS BETWEEN THE REACTORS 93

3.5 STEADY STATE OPERATION 94

3.6 GEOMETRICAL PARAMETERS OF THE LOOP-SEAL AND THE L-VALVE 97

3.7 CONCLUSION 98

3. Solid Circulation Investigations: Experimental Results

The solid circulation investigations were mainly focused on the operation of the L-valve and the loop-seal as the critical elements of the system. L-valves enable control of solid flow rate between different reactors in the current configuration. Accordingly, a sufficient understanding of L-valve operation is essential in operation of the CLC system. Loop-seals guarantee gas tightness of the reactors by preventing free gas entry into the reactors. Therefore, current investigation was aimed to figure out the optimal loop-seal operation in terms of gas leakage and design requirement. Regarding the gas leakage, gas flow rate out of the reactors through the L-valves is another important parameter to be investigated and minimized if possible. This was investigated through the pressure drop and gas tracer study for the out leakage from one reactor and the leakage from one reactor to the other.

Solid circulation and hydrodynamic studies were mainly carried out in the cold flow prototype regarding the ease of operation, possibility of visual observation and ease of modifications if required. The current chapter includes L-valve investigation in terms of solid circulation control, pressure drop, and gas repartition measured by aid of gas tracer study. The voidage of the moving solid bed in the standpipe of the L-valve was then calculated based on the experimental for two operating regimes of packed bed and transitional packed bed flow. Loop-seal operation was then investigated including the pressure drop variation across different elements of the loop-seal. Gas tracer study was then used to measure the gas repartition in different sections based on the operating conditions. The high temperature pilot plant was then used to complete the study by taking into account the effect of the temperature and to verify the previous findings in conditions of elevated temperatures.

3.1 L-valve Operation

Control of solid flow rate is an important parameter in the chemical looping combustion process. L-valves are used in the current installation to control solid flow rate. Concept of L-valve operation was briefly reviewed in the literature review section. L-valve is principally composed of four main parts: vertical section above the external aeration point (standpipe, or downcomer), the vertical section below the aeration point and the elbow, the horizontal section and the external aeration point. A hybrid standpipe with vertical and inclined sections was employed in the current design. This was to convey solids horizontally to the lift entry while keeping a minimum length in the horizontal section of the L-valve. The total horizontal distance between the reactor and the lift was imposed by the thickness of the thermal insulations used around the reactor and the lifts.

L-valve controls solid flow rate through variation of the external gas injection ($U_{lv} = Q_{lv}/A_{lv}$). Solid flux variations as function of the external aeration rate of the L-valve are plotted in Figure 3.1. As expected, results demonstrate that solid flux can be varied in a wide range with different solids in the current system. According to these results, the required aeration rate varies considerably depending on solid properties. Smaller sized particles require less aeration for the same solid flow rate. Moreover, in the case of ilmenite with higher solid density, considerably higher solid flow rates were achieved. It can also be pointed out that solid circulation at high temperatures requires much less external gas flow rate.

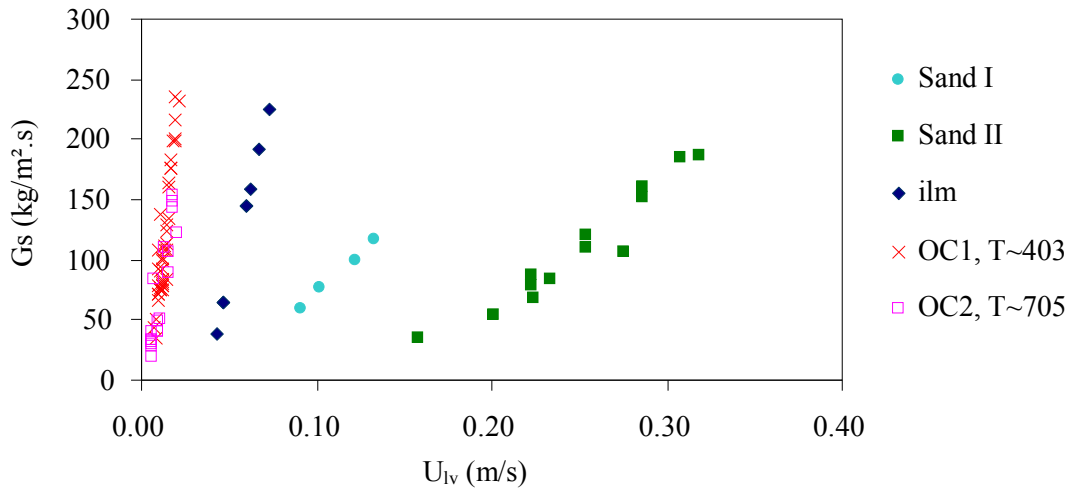

Figure 3.1: Solid flux control in the CLC cold flow prototype for three solids in ambient temperature and Nickel based oxygen carriers at high temperature pilot plant at 403 °C and 705 °C.

Regarding the importance of the solid flow control and associated gas leakages in the CLC system, more detailed investigations were conducted to understand L-valve operation as a function of pressure balance, gas and particle properties.

3.1.1 Standpipe of the L-valve

Pressure drop across the standpipe of the L-valve (upper vertical pipe) is a dependent parameter varying to adjust overall pressure balance across the solid circulation loop [93,235]. The pressure balance loop around the L-valve in the cold flow prototype, starting from the atmospheric pressure above the reactor R1 to the cyclone exit (Cyc1), is:

$$\Sigma\Delta P = \Delta P_{R1} + \Delta P_v + \Delta P_{lvH} + \Delta P_L + \Delta P_{Tb} + \Delta P_{HC} + \Delta P_{Cys,g} = 0 \qquad \textbf{Eq. 3.1}$$

Three sorts of pressure drop elements can be distinguished in this equation. First, ΔP_v, (standpipe pressure drop) is a variable parameter and its value depends on the other components. Second category includes those elements which depend on the solid and gas flow rates including: ΔP_{lvH}, (pressure drop in the horizontal section of the L-valve) ΔP_L (in the lift), ΔP_{Tb} (in the T-bend), ΔP_{HC} (horizontal conveying), and $\Delta P_{Cyc,g}$.(cyclone). The third category includes the pressure drop in the reactor ΔP_{R1} which depends only on the solid inventory in the reactor. ΔP_{R1} can be adjusted separately from other system variables. It should be mentioned that solid flow rate have a minor effect on the pressure drop of the reactor in the sense that higher solid flow rate reduces slightly the reactor inventory. However, this effect is not significant and can be adjusted by controlling the solid inventory in the second reactor R2. This results in a unique feature of the current system which is the possibility to adjust ΔP_v independently from the external L-valve aeration by variation of the solid inventory in the reactor R1.

In order to investigate the pressure drop in the L-valve, pressure drop variation in the standpipe of the L-valve was measured during a batch experiment in the cold flow prototype. Solids were circulated with constant L-valve aeration from R1 to R2 while opposite circulation was stopped (Figure 3.2 and Figure 3.3).

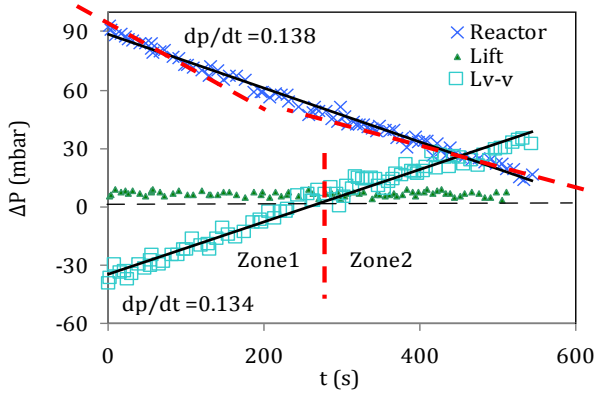

Figure 3.2 : Pressure drop evolution in the standpipe of the L-valve for a batch solid circulation from R1 to R2 with Q_{lv} = 0.08 Nm^3/h, and G_s = 49 kg/m².s.

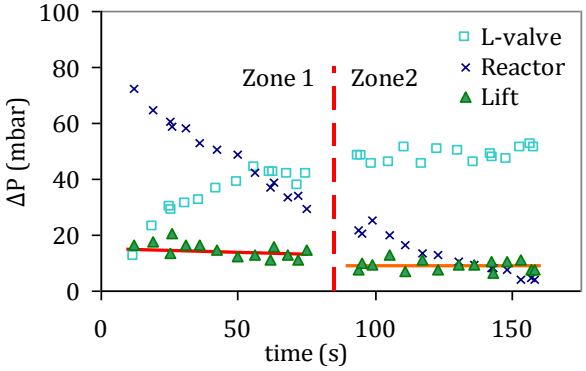

Figure 3.3: Pressure drop evolution in the standpipe of the L-valve for a batch solid circulation from R1 to R2 with Q_{lv} = 0.18 Nm^3/h, G_s = 196 kg/m².s in zone 1 and 98 kg/m².s in zone 2 (right).

As illustrated in the Figure 3.2, pressure variation in the standpipe follows the pressure variation of the reactor but in opposite direction. The pressure drop variation in the standpipe suggests different operation regimes in the standpipe of the L-valve, listed in Table 3.1. This can briefly be explained as:

- Regime 1: Pressure drop in the standpipe is negative in the case of high pressure drop in the reactor.
- Regime 2: Decrease of the pressure drop in the reactor (or any other independent pressure element in the pressure loop) causes the pressure drop in the standpipe to increase. Below a certain pressure drop in the reactor, the ΔP_v turns to positive.
- Regime 3: corresponds to the condition where the pressure drop in the standpipe is high enough to impose a relative gas – solid velocity higher than the solid velocity. In this case gas starts to rise along the standpipe countercurrent of solid flow direction. It should be noted that the regime 3 could happen after regime 4 or 5 based on the properties of the particles.
- Regime 4: Pressure across the standpipe can increase until a limit which is fluidization of the L-valve, corresponding to a slip velocity exceeding minimum fluidization velocity [235]. Thereafter, pressure drop remains constant and standpipe can not absorb more pressure.
- Regime 5: Transition to the bubbling regime can cause a considerable solid flow perturbation. In this condition, solid flow rate decreases due to formation of gas bubbles which increases the voidage of solid flow. Therefore, the solid quantity in the L-valve decreases causing reduction of the total pressure drop of the solid column in the standpipe. This phenomenon is well demonstrated in Figure 3.3 where solid flux drops suddenly from 196 kg/m².s to 98 kg/m².s. Therefore, operating an L-valve with a fluidized standpipe is not recommended.

The other associated solid and gas flow fluctuations in this condition are discussed in the section 3.1.9.

As listed in Table 3.1, there exist different regimes of solid – gas flow in the standpipe of the L-valve. The flow regime can be deduced from the solid flow rate and the standpipe pressure drop. Regimes 1 - 3 with non-fluidized moving solid bed in the standpipe are the most common operating zones in the standpipe of the L-valve as explained above. Accordingly, solid and gas flow behavior in theses regimes were investigated in more details as presented below.

Table 3.1: Various operation regimes in the standpipe of the l-valve based on the pressure drop across the section.

Regime	ΔP_v = P5-P4	$V_r = V_s - V_g$	U_g	Scheme	Reference	Comment
1	negative	negative	descending	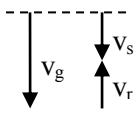	Figure 3.2 – Zone 1	Packed bed moving solid bed in the standpipe
transition	0	0	$U_g = U_s$			
2	positive	positive	descending	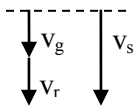	Figure 3.2 – Zone 2	Transitional packed bed solid flow in the standpipe
transition	positive	$v_r = v_s$	$v_g = 0$			
3	positive	$v_r > v_s$	ascending	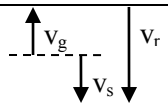	Figure 3.3 – Zone 1	This step may happen after step 4 or 5 or never happen based on the solid properties
transition	$\Delta P_{SP} = \Delta P_{mf}$	$v_r = v_{mf}$	asc. / des.			
4	$\Delta P_{SP} = \Delta P_{mf}$ = cte	$v_r > v_{mf}$	asc. / des.		Figure 3.3 – Zone 2	Fluidized solid flow in the standpipe
transition	$\Delta P_{SP} = \Delta P_{mb}$	$v_r = v_{mb}$	asc. / des.			
5	$\Delta P_{SP} < \Delta P_{mf}$	$v_r > v_{mb}$	asc. / des.			$W_s \downarrow$ as $v_g \uparrow$ due to bubble formation
	$\Delta P_{SP} = \Delta P_t$	$v_r = v_t$	asc.			Solid flow stops

3.1.2 Gas Flow in the Standpipe of the L-valve

Gas flow rate in the standpipe of the L-valve is a function of solid flow, pressure balance, and solid and gas properties. Downward solid movement tends to drag gases from the reactor along the standpipe of the L-valve. Effect of solid flow rate on the quantity of gas dragged down in the standpipe was investigated through series of experiments with ilmenite and sand II particles. Helium was injected into the reactor and detected at the cyclone exit according to the configuration 2 of (Table 2.3). This configuration permits to measure downwards gas flow rate in the standpipe. Solid flow rate was changed for each test by changing the external L-valve aeration while other operating parameters were kept constant, including height of solid in the reactor and different external aerations.

Variation of superficial gas flow velocity from tracer measurement in the vertical section of the L-valve ($U_{lv,v}$) versus solid flux (Gs) are presented in Figure 3.4. Each point in the graph corresponds to a steady state solid circulation between two reactors. Resulting curves demonstrate that downward gas flow increases with a linear tendency according to the increase of solid flow rate. These results are compared with the associated pressure drop variation illustrated in the Figure 3.5 for a better understanding of the solid flow rate effect. Indeed, when solid circulation increases, the downcomer pressure drop also increases due to the increase of the transfer line pressure drop.

Standpipe pressure drop variation due to the raise of solid flow rate is illustrated in Figure 3.5 for the experimental results presented above. Pressure drop increases linearly as solid flow rate increases for both solids. However, pressure drop in the standpipe is positive for sand particles while ilmenite has negative pressure drop. The reason for this difference is higher solid density of the ilmenite (4750

kg/m^3) compared to the sands (2650 kg/m^3). Accordingly, ilmenite imposes a reactor pressure drop about two times higher compared to the sand particles for the same solid height in the reactor. Comparison of Figure 3.4 and Figure 3.5 demonstrates that for the same gas flow rate in the standpipe, ilmenite has a pressure drop of about 50 mbar less than sand particles. This difference is equivalent to difference in the pressure drop of the reactor for ilmenite (110 mbar) and sand particles (54 mbar). Despite this difference in pressure drop, both solids impose similar gas flow rates in the standpipe for the same solid flux as in the Figure 3.4. This difference can be explained based on the particle size difference between two solids. Smaller size of ilmenite particles increases the pressure drop developed across the solid bed for the same gas flow rate compared to sand particles. The effect of particle diameter on the pressure drop can be deduced from the Ergun equation where ΔP is proportional to inverse of particles diameter. Accordingly, smaller sized particles develop higher pressure drop for the same gas flow rate. In other words, same pressure drop imposes smaller gas flow rate for smaller particles.

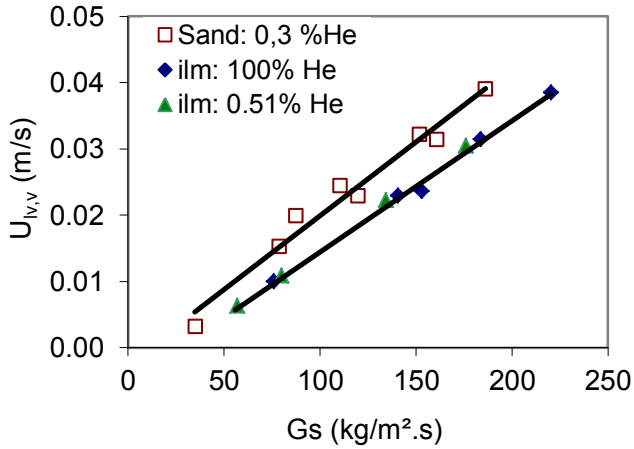

Figure 3.4: Measured downward gas flow rate through the vertical section of the L-valve with different tracer gas injection concentrations and solid height of 0.5 m in the reactor for both ilmenite and sand particles. Pressure drop variations for the presented experimental results are presented in the Figure 3.5.

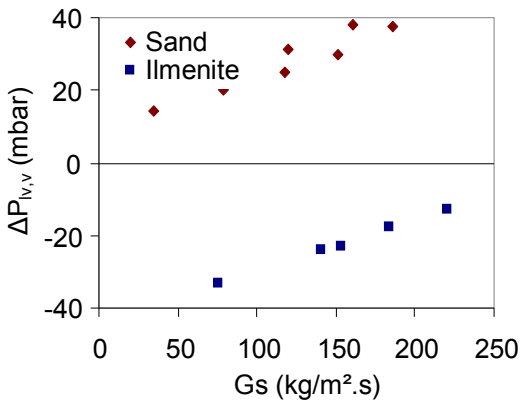

Figure 3.5: Pressure drop variation along the standpipe of the L-valve due to the variation of the solid flow rate through the L-valve for sand and ilmenite particles. Solid height in the reactor was 0.5 m in both cases which is equivalent to a pressure drop of 110 mbar for ilmenite and 54 mbar for sand particles.

Pressure drop across the vertical section of the L-valve ($\Delta P_{lv,v}$) is a dependant variable parameter. It varies to balance the overall pressure balance across the solid circulation loop [93]. Therefore, variation of pressure drop across an individual element in the system can change the pressure drop in this section. Variation of $\Delta P_{lv,v}$ changes the quantity of gas passing through this section ($Q_{lv,v}$). A feature of the current CLC installation is the possibility to adjust $\Delta P_{lv,v}$ by changing pressure drop across the reactor (ΔP_R) by change of solid height in the reactor. This permits control of pressure drop across the standpipe, independently from the L-valve external aeration. Using this feature, series of tracer tests were conducted where gas flow rate in the vertical section of the L-valve was measured for different pressure drops across the element. Measurements were conducted during steady state solid circulation with different solid heights in the reactor, while external aeration rate into the L-valve (Q_{lv}) was maintained constant. Pressure drop and gas flow rate in the vertical section of the L-valve are illustrated in Figure 3.6 as a function of reactor pressure drop ΔP_R for sand II particles. An increase in ΔP_R of about 90 mbar causes the pressure drop in the standpipe ($\Delta P_{lv,v}$) to reduce from +60 mbar to –30 mbar. Consequently, gas flow rate changes due to pressure drop variation across the standpipe. Two zones can be distinguished in Figure 3.6 based on the gas flow in the standpipe:

- High pressure drops region (zone I): gas flows upwards in the standpipe; consequently, no Helium is detected in the gas exit of the cyclone.
- Low pressure drop region (zone II): below a critical value, gas starts flowing downwards in the standpipe and progressively increases as the pressure drop reduces further in the standpipe.

The pressure drop change and associated $Q_{lv,v}$ variation affect the solid flow rate effectuated in the L-valve. This phenomenon is discussed below.

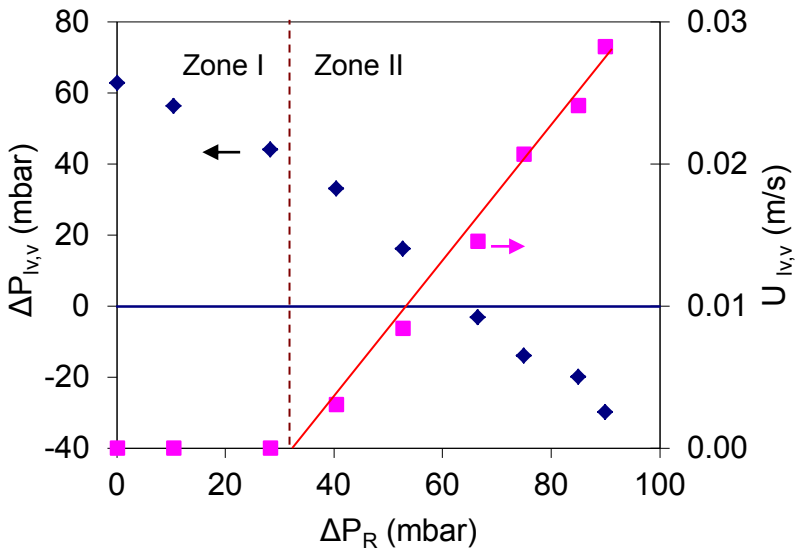

Figure 3.6: Effect of reactor pressure drop on the pressure drop and gas flow in the vertical section of the L-valve with Q_{lv} = 0.16 Nm^3/h and G_s varies from 64 to 35 kg/m².s (see Figure 3.9) for sand particles.

Figure 3.7 illustrates similar investigations conducted with ilmenite particles. Variation of pressure drop in standpipe from 60 mbar to -35 mbar increases downwards gas flow rate in the standpipe similar to the behavior observed with sand particles. However, in the case of the ilmenite particles gas flow in the standpipe remains always downwards even with high pressure drops in the downcomer of 60 mbar. This difference is a consequence of diameter and density of ilmenite particles.

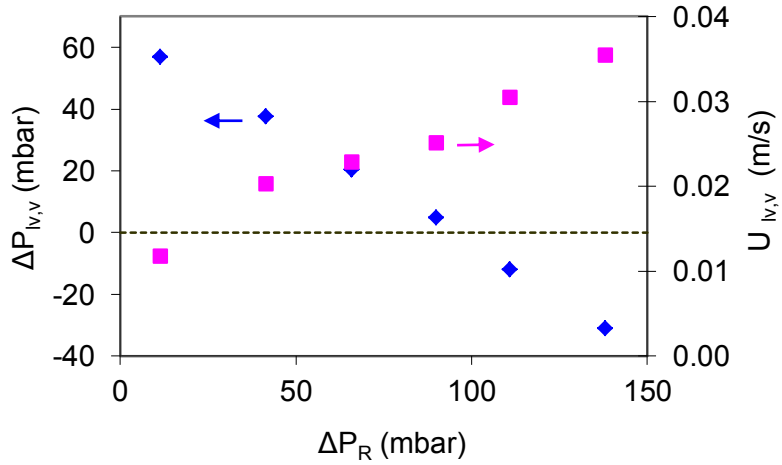

Figure 3.7: Effect of the reactor pressure drop on the quantity of gas passing through the vertical section of the L-valve with Q_{lv} = 0.033 Nm^3/h and Gs varies from 203 to 133 kg/m².s (see Figure 3.9) for ilmenite particles.

Ergun equation is considered as the governing relation between pressure drop and gas flow in the standpipe. This relation suggests that the only particle property affecting pressure drop is the particle diameter and not the density. Pressure drop is then related to the gas flow rate with an inverse factor of particle diameter. Consequently, smaller particle sizes decrease the gas flow rate for a given pressure drop.

Particle density does not have a direct effect on the pressure drop of non-fluidized moving solid bed in

the standpipe. However, it can change the pressure through an indirect influence. For identical solid height in the reactor, solids with higher density impose higher pressure drop in the reactor. Consequently, standpipe of the L-valve must absorb less pressure to balance the pressure drop across the circulation loop for the same solid flow rate. Therefore, pressure drop across the standpipe reduces as pressure drop in the reactor increases. This favors downward gas flow rate in the standpipe. This can be observed in Figure 3.7.

3.1.3 Solid Flow Control Mechanism in the L-valve

Knowlton [93,144] has pointed that the solid flow rate in the L-valve is controlled by the total amount of gas passing through the elbow of the L-valve. This includes the external aeration (Q_{lv}) and the gas flow in the standpipe ($Q_{lv,v}$). Therefore, change in either of these gas flow rates affect solid flow actuated in the L-valve. The dependency of solid flow rate in the L-valve to different operating parameters in the current system is illustrated in the Figure 3.8.

$$G_s \propto Q_H \propto \begin{cases} Q_{lv} \\ Q_{lv,v} \propto \Delta P_{lv,v} \propto \Sigma\Delta P \propto \begin{cases} \Delta P_R \propto M_R \\ \Delta P_{lvH} \propto G_s \\ \Delta P_L \propto G_s, Q_L \\ \Delta P_{HC} \propto G_s, Q_L \\ \Delta P_{Cyc} \propto G_s, Q_L \end{cases} \end{cases}$$

Figure 3.8: Dependence of the solid flow rate in the L-valve to different operating parameters of the system.

Solid flow rate and superficial gas velocity in the elbow of the L-valve were measured for the experimental tests presented above. Figure 3.9 illustrates the variation of downward gas flow rate across the standpipe imposed by change of the reactor pressure drop. Results demonstrate that the increase in the reactor pressure drop increases the downward gas flow rate through decrease of the standpipe pressure drop. Accordingly, the total gas flow around the elbow increases which in turn augments the solid flux actuated in the L-valve. The observed variation is higher in the case of ilmenite particles compared to the sand particles. This is mainly due to the fact that the ratio of the flow in the standpipe to the flow in the horizontal section (Q_v/Q_H) is more important for ilmenite compared to sand.

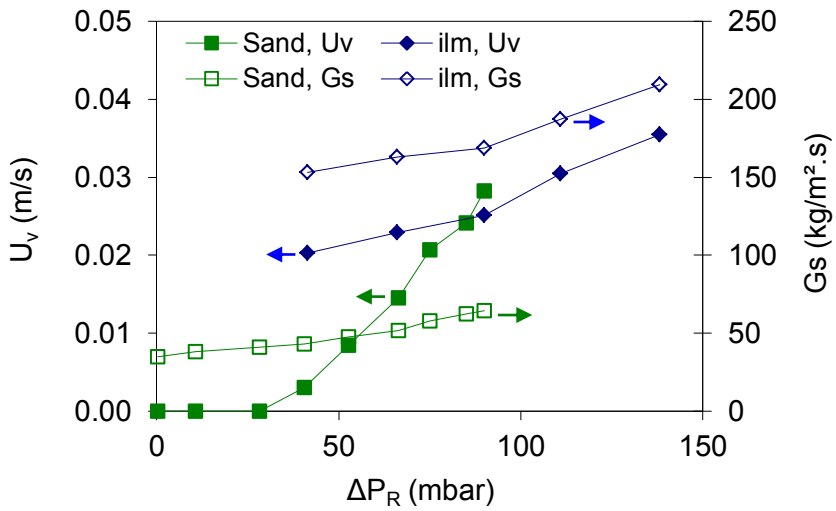

Figure 3.9: Effect of the reactor pressure drop on the gas flow rate in the standpipe and the solid flow rate effectuated in the L-valve for sand II particles with Q_{lv} = 0.15 Nm^3/h and ilmenite particles with Q_{lv} = 0.055 Nm^3/h. $\Delta P_{lv,v}$ is controlled through change of solid inventory in the reactor (see Figure 3.6 and Figure 3.7).

The internal and the external L-valve air flow rates versus the solid flux in the L-valve are presented in Figure 3.10 for two test series with sand II particles. In the first series, the solid flow rate was controlled through the variation of the external L-valve aeration (U_{lv}). As expected, increase in U_{lv} increases the solid flux. Moreover, the gas flow rate in the standpipe increases as solids entrain more gases downwards in the standpipe. Gas flow velocity in the horizontal section of the L-valve $U_{lv,H}$, which is sum of U_{lv} and U_v, increases in the same order.

The external L-valve aeration (U_{lv}'), was kept constant in the second series of experiments presented in Figure 3.10. The standpipe gas flow rate was then varied by adjusting the pressure drop across the standpipe through changes in the reactor pressure drop. Accordingly, for a constant external aeration, horizontal gas flow rate in the L-valve increases as $U_{lv,v}'$ increases. This demonstrates that for a constant external aeration of the L-valve, the solid flow rate can be varied through variation of the $U_{lv,v}$ imposed by change of the pressure drop across the standpipe. These experimental results confirms the conclusion of Knowlton and Hirsan [236] on the importance of the total gas flow of $Q_{lv,v}$ and Q_{lv} as the solid flow rate controlling parameter in the L-valve. This is well illustrated in Figure 3.10 where the gas flow in the horizontal section (represented by the velocities U_{lvH} and $U_{lv,H}'$) lay on the same line for both of the experimental series. Standpipe gas flow variation is steeper in case of pressure drop change compared to the external aeration change for unit change of the solid flux (Figure 3.11). This is due to the fact that Q_v must compensate required Q_H variation for a unit change of solid flux while external aeration is constant.

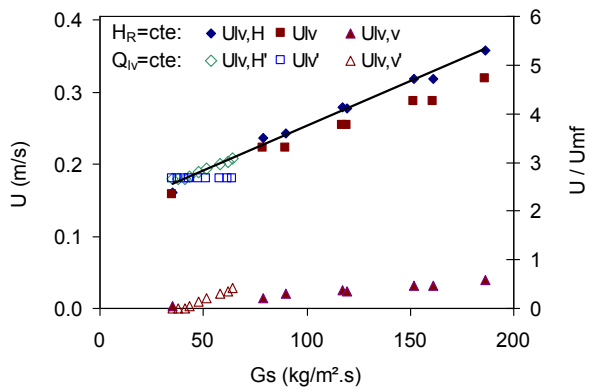

Figure 3.10: Variation of solid flow rate versus measured gas flow rate in the horizontal section of the L-valve ($Q_{lv,H}$), gas flow rate in the standpipe ($Q_{lv,v}$) and external L-valve gas injection, Q_{lv} for sand particles for two experimental series with change in external L-valve aeration (♦,■,▲) and variation of pressure drop in the standpipe (◊, □, Δ). Results are plotted in terms of both gas velocity and fluidization number (U/U_{mf}).

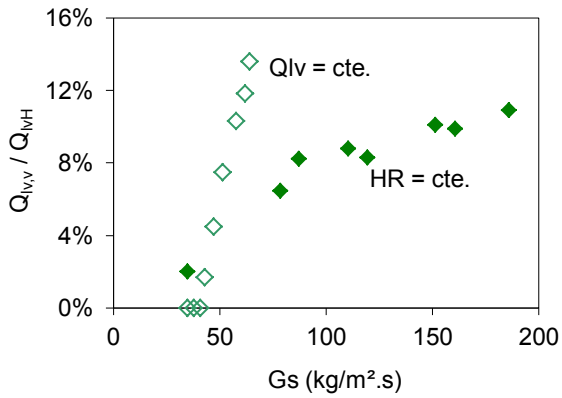

Figure 3.11: Ratio of the gas flow rate in the vertical section of the L-valve versus gas flow rate in the horizontal section of the L-valve for two operational conditions: constant external L-valve aeration (Q_{lv} = cte), and constant height of solid bed in the reactor (H_R = cte).

These results illustrate that a desired solid flow rate in the L-valve can be achieved by different repartitions of the external aeration and the gas flow in the standpipe. This is of particular interest in case of some processes like CLC where the gas flow out of the reactor is considered as a leakage and should be minimized. Therefore, a proper control of pressure drops across the system (resulting from pressure balance and design aspects) together with appropriate external aeration, helps to optimize this gas leakage out of the reactor.

3.1.4 Calculation of Pressure Drop in the Standpipe Using Ergun Equation

Ergun equation [94] modified for slip velocities can be used to calculate pressure drop in the standpipe of both L-valve [92,93,237] and loop-seal [112,116,119,120,122]. To examine the validity of this equation in the L-valve, pressure drop was calculated using the Ergun equation. Gas – solid slip velocity was estimated separately, based on the tracing experimental results:

$$V_{sl} = V_g - V_s = \frac{Q_g}{A_{sc}.\varepsilon} - \frac{W_s}{A_{sc}.(1-\varepsilon)} \qquad \textbf{Eq. 3.2}$$

Linear relation of Knowlton and Hirsan [93] was used to estimate the voidage of the moving solid bed. Results are presented in the Figure 3.12 for calculated and measured pressure drop. Figure 3.12 illustrates that the Ergun equation using Knowlton voidage equation [93] predicts well the trend of the experimental results. The comparison between experimental and measured results shows that this method underestimates the experimental results by less than 15%. This difference probably relies on the prediction of bed voidage which is discussed in the section 3.1.5.

These results illustrate that the Ergun equation can be reliably employed for the pressure drop calculation in the standpipe of the L-valve. However, a better precision can be achieved in case of use of a more sophisticated bed voidage relation or consideration of other influencing phenomena like wall effect.

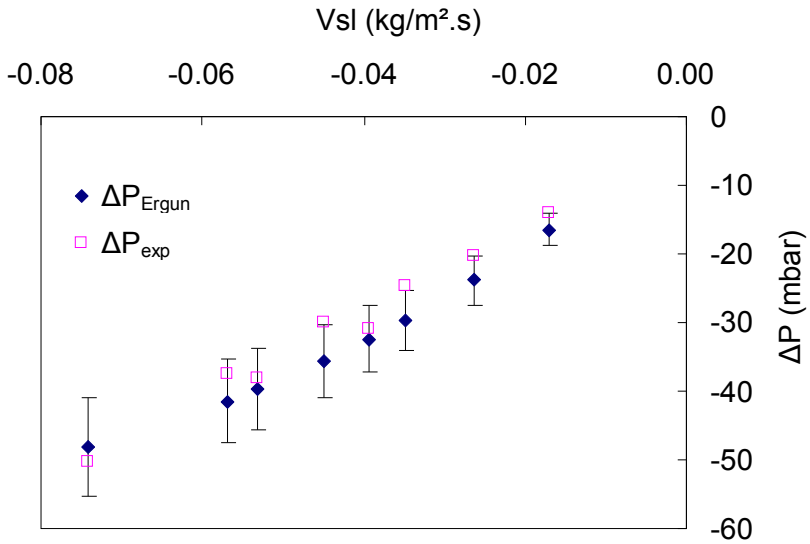

Figure 3.12: Comparison of experimental Pressure drop and calculated pressure drop variation ion the standpipe of the L-valve versus gas – solid slip velocity. Ergun equation was used to calculate the pressure drop in the standpipe based on the experimentally measured gas and solid flow rates. Knowlton relation [93] was used to calculate the variation of voidage of the moving solid bed. Error bars illustrate ± 15% error for measured pressure drop.

3.1.5 Average Voidage of the Moving Solid Bed in the Standpipe

Experimentally measured pressure drop, gas flow rate and solid flow rate values were used to calculate average voidage of the moving solid bed (ε_{sp}) based on the Ergun equation. Voidage was calculated using an iterative procedure as illustrated in the Figure 3.13. Current installation permits control of pressure drop across the standpipe independently from external L-valve aeration (Q_{lv}). Using this feature, voidage of the solid bed was measured for two non-fluidized solid flows regimes, as shown in Figure 3.14.

$$\left.\begin{array}{l} W_{s,\exp} \rightarrow V_s = \dfrac{W_s/A}{\varepsilon} \\ Q_{g,\exp} \rightarrow V_g = \dfrac{Q_g/A}{\varepsilon} \end{array}\right\} \longrightarrow \left.\begin{array}{l} V_{sl} \\ \Delta P_{\exp} \end{array}\right\} \xrightarrow{\text{Ergun}} \varepsilon$$

Figure 3.13: Procedure of the calculation of the voidage of the moving bed from the experimental results and Ergun equation. An iterative procedure was used to calculate the voidage.

Packed bed solid flow regime is reached when pressure drop $\Delta P_{lv,v}$ across the standpipe is negative. Slip velocity is positive in this regime, as gas downward flow is faster than solids as illustrated in Figure 3.9. Bed voidage variation versus slip velocity in this regime is illustrated in zone II of Figure 3.14. The resulting moving bed voidage in this case is constant and corresponds roughly to the tapped bed voidage. In other words, one can imagine that gas flow pushes to pack moving solids tighter together in this regime.

Transitional packed bed solid flow was obtained by imposing positive pressure drop in the standpipe, resulting in negative slip velocities (Figure 3.9, zone I). In this case, reactor pressure drop was kept constant and solid flow rate and pressure drop variations were adjusted through changes of the external gas flow in the L-valve (Q_{lv}). Resulting variation of average voidage is illustrated in Figure 3.14. Slip velocity is negative in this region, meaning either upward gas flow or downward gas flow slower than solid flow. As slip velocity increases in value, voidage of solid bed expends from tapped bed voidage toward bed voidage at minimum fluidization condition.

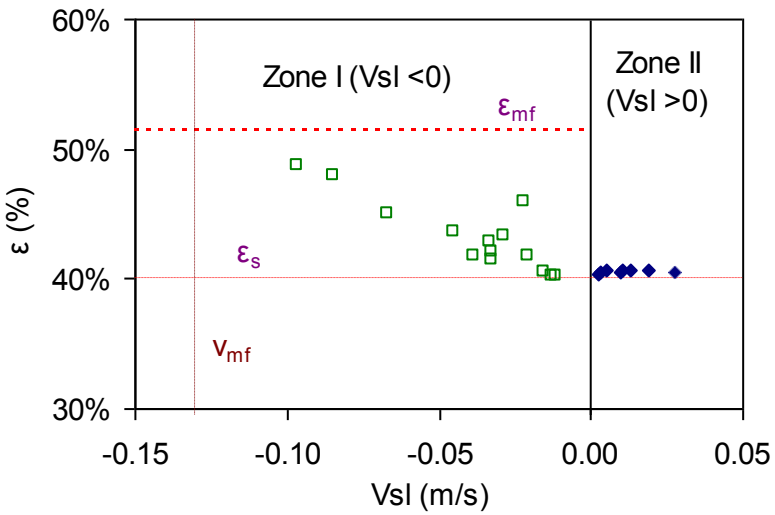

Figure 3.14: Variation of voidage of the moving solid bed in the standpipe of the L-valve versus interstitial solid flow rate for sand particles.

The voidage of moving solid bed in the standpipe of the L-valve was similarly calculated for the ilmenite particles. The resulting voidage is plotted in Figure 3.15 versus slip velocity. Transitional packed bed flow regime (V_{sl}<0) was experimentally more restricted to attain for ilmenite particles due to the higher grain density of the particles which imposes negative pressure on the standpipe. The moving bed in the standpipe has a voidage close to the tapped bed voidage in the packed bed regime similar to sand particles. As discussed before, ilmenite particles were more sensitive toward variation of gas flow rate in the L-valve. Accordingly, the experimental results show more dispersion in case of the ilmenite particles compared to the sand particles. Sensitivity of the calculated bed voidage for different experimentally measured parameters was calculated (Table 3.2). Results demonstrate that

sensitivity of the calculated voidage remains reasonably low compared to the measured parameters. This illustrates reliability of the calculated voidage values.

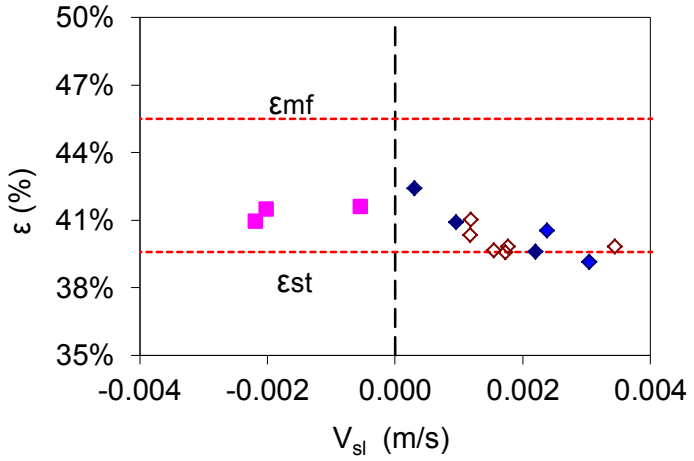

Figure 3.15: The voidage of the moving solid bed in the standpipe of the L-valve versus interstitial solid flow rate for ilmenite particles.

Table 3.2: Sensitivity in the estimation of moving bed voidage based on the procedure of Figure 3.13.

Parameter	Reference value	Variation	Resulting ε sensitivity
ΔPlv,v	21 mbar	10% / -10%	-0.22 / 0.22 %
Qlv,v	16.4 Nl/h	10% / -10%	-5.45 / 5.96 %
Gs	141 kg/m².s	10% / -10%	-5.21 / 5.78 %

Correlations listed in the Table 1.7 were then compared with experimental results obtained above. Linear correlation proposed by Knowlton and Hirsan [93] results in the closest prediction. Correlation of Li et al. [131] gives a good estimate of voidage variation trend, however, it overestimates voidage values. This difference may be due to the fact that the correlation was developed with group A particles.

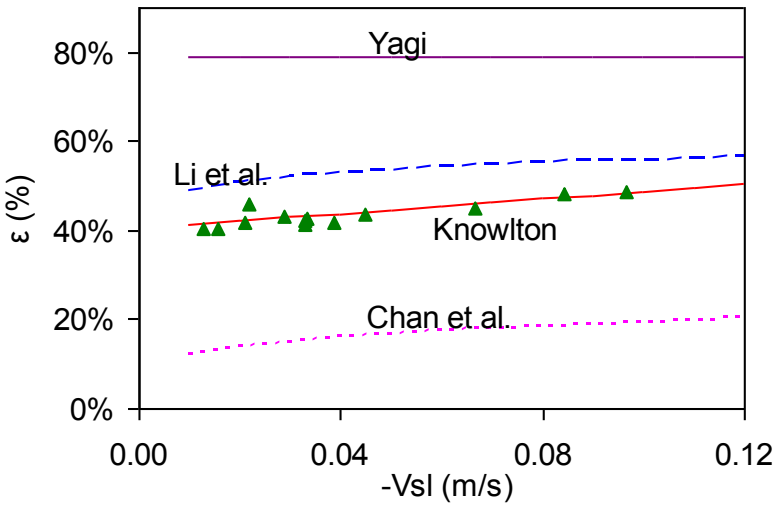

Figure 3.16: Comparison of the experimental results with the correlations developed by Yagi [136], Li [131], Chan et al. [132], and Knowlton and Hirsan [93].

3.1.6 Effect of Gas Properties on the L-valve Operation

The impact of gas properties on the solid circulation in the L-valve is not very much discussed in the open literature. Smolders and Baeyens [97] have investigated L-valve operation with CO_2 as external injection gas (Q_{lv}). Their system was composed of an L-valve charged from a hopper. They reported lower solid flux actuated by CO_2 compared to Air due to higher upward flow of CO_2 in the downcomer compared to Air. In the current study, the L-valve was operated using alternatively Helium and air. Properties of these gases are listed in Table 3.3. Both gases have similar viscosity while air density is 86% higher than Helium. This permits to study the effect of gas density on solid and gas flow in the L-valve. Gas flow in the downcomer was downwards in all of the tests in this section. Therefore, the gas in the downcomer was identical with the fluidization gas of the reactor.

Table 3.3: Properties of Air and Helium at 20 °C and 1 bar.

Property	Molecular mass (g/mol)	ρ (Kg/m3)	μ (Pa.s)
Air	28.96	1.205	1.81e-05
Helium	4.002	0.164	2.00e-05
CO_2	44.009	1.815	1.47e-5

The solid fluxes in the L-valve were measured for ilmenite and sand particles alternatively with Helium and air. Figure 3.17 and Figure 3.18 illustrate successively the solid flux in terms of the external L-valve aeration (U_{lv}) and the gas flow rate around the L-valve bend ($U_{lv,H}$). With both gases, the trend is similar and the resulting solid flux is similar. Considering the fact that the gas density is the main difference between two gases, it can be deduced that gas density is not a decisive parameter in solid flow control in the L-valve.

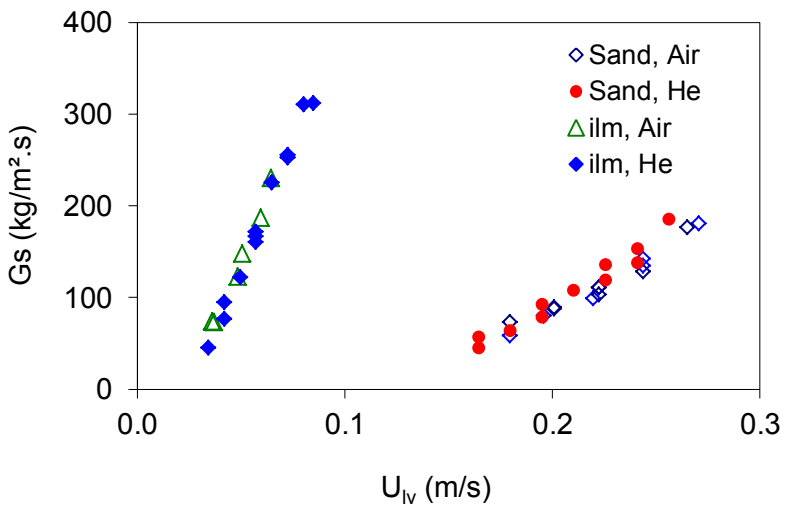

Figure 3.17: Solid flux versus the external L-valve aeration for ilmenite and sand particles alternatively with air and Helium.

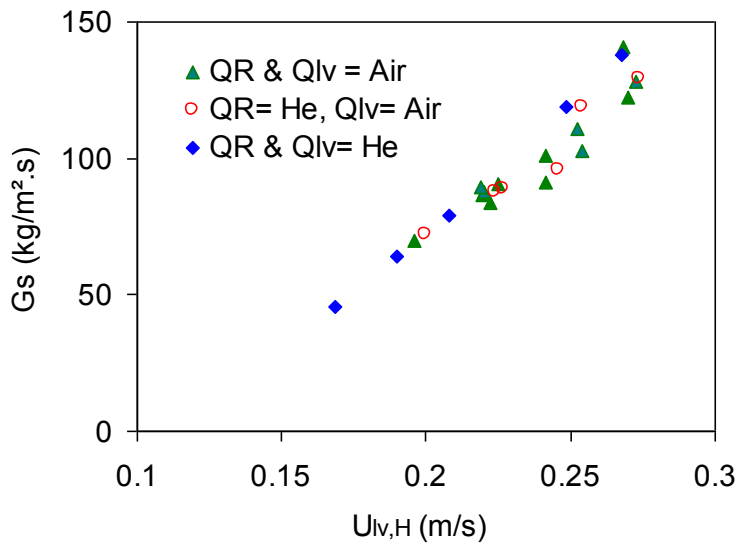

Figure 3.18: Solid flux effectuated in the L-valve versus gas superficial velocity in the horizontal section of the valve for sand particles. Each point corresponds to a steady state circulation between two reactors with H_R = 0.5 m.

These results can help to anticipate the effect of temperature on the solid flow rate in the L-valve. Based on the current results, it can be concluded that the effect of the temperature through gas density will be negligible in high temperatures for air. This results confirm the Knowlton's statement [95] that the gas viscosity variation is the main reason why less gas is required at high temperatures in the L-valve compared to the low temperature operations.

3.1.7 Effect of Particles Properties on the L-valve Operation

Effects of solid properties on the L-valve operation have been studied in various researches [93,104,238]. Figure 3.19 illustrates solid flux versus external L-valve gas injection ($U_{lv}= Q_{lv} /A_{lv}$) and the gas flow around the elbow of the L-valve ($U_{lvH} = Q_{lvH}/A_{lv}$) for three solids in the cold flow prototype. Comparison of the experimental results illustrates that the difference between the U_{lv} and U_{lvH} increases as solid flow rate increases or particles size decreases. This difference relies on the gas flow across the standpipe of the L-valve ($Q_{lv,v}$). As discussed previously, these two terms are related as $Q_{lvH} = Q_{lv} + Q_{lv,v}$. Therefore, it can be concluded that the contribution of the $Q_{lv,v}$ in solid flow rate increases as solid flow rate increases or particle size decreases.

Comparison of the solid circulation results in Figure 3.19 illustrates considerable difference in terms of the solid flow effectuated for different particles in the current study. Particle size shows an important influence on the required gas flow rate to achieve a solid flow rate. Decrease of particle size reduces both minimum required gas injection to start the solid circulation and also increases the slope of the solid flux versus gas injection. Similar results have been observed by other researches [93,104,238]. Effect of particle density can not be directly deduced form the graph as ilmenite has higher density but smaller particle size. However, comparison of these results implies that increase of particle density increases the solid flow rate similar to the literature results [93,104,238]. Particle density has an additional indirect effect on the solid circulation flow rate as discussed in section 3.1.2. Particle with higher density results in higher pressure drop in the reactor for a given height of the fluidized bed. Accordingly, pressure drop in the standpipe of the L-valve decreases, resulting in higher downward gas flow across the standpipe. Therefore, more gas will be available around the elbow of the L-valve, resulting in higher solid flow rate.

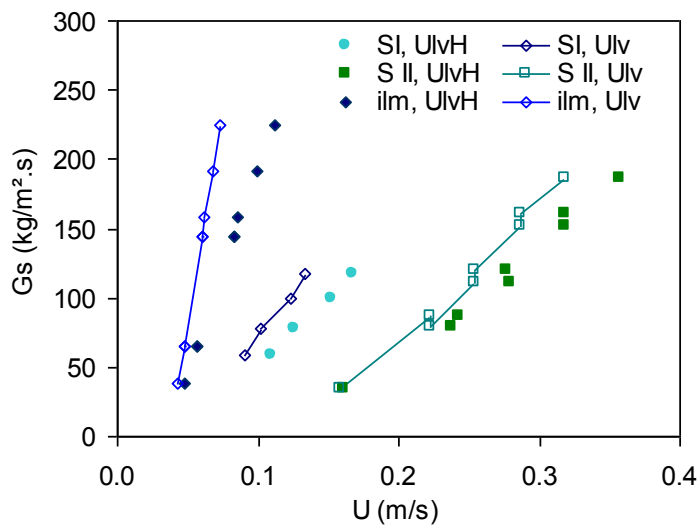

Figure 3.19: Solid flow rate versus the gas flow rate in the horizontal section of the L-valve for three solid particles in the cold flow prototype with H_R = 0.5 m, U_L = 6.8 m/s for ilmenite and sand II and U_L = 5.4 for sand I particles. Gas flow rates in case of sand I are calculated based on the procedure in the section 3.1.4.

The solid flux effectuated in the L-valve is plotted versus the fluidization number (U_{lvH} /U_{mf}) of the gas flow rate around the elbow of the L-valve. Results show that all curves shrink on an identical curve plotted in terms of the fluidization number. Similar behaviour is observed in terms of fluidization number in the literature findings [92,97,100,239]. These results will be discussed in more details in Chapter0 4 for selection of the solid flow control relation in the L-valve.

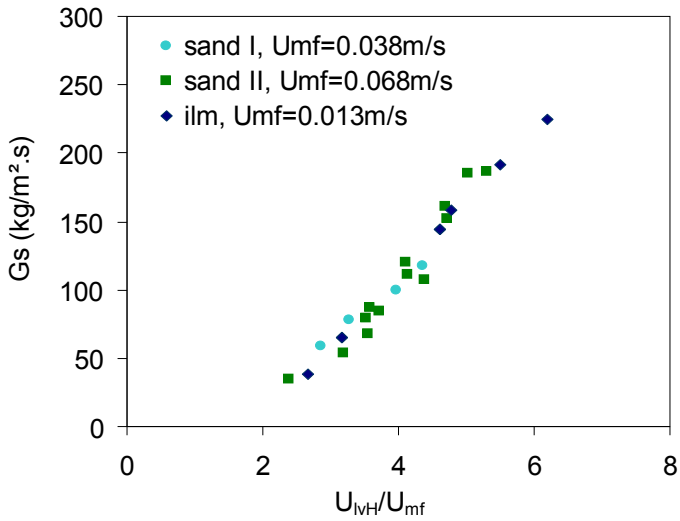

Figure 3.20: The solid flux effectuated in the L-valve versus fluidization number around the elbow of the L-valve for the experimental results of Figure 3.19.

Effect of particles properties on the solid circulation flow rate was discussed. Particles size had a considerable effect on the solid flow rate. As size of the particles decreases, higher solid flow rate is achieved for identical gas flow rate. Moreover, higher particle density results in higher solid flow rate especially through the effect on the pressure drop across the solid circulation loop. Minimum fluidization velocity was then shown to be a good indicator of the solid flow control in the L-valve. Solid flux results shrink on the identical curve versus fluidization number in an L-valve of given geometry.

3.1.8 L-valve High Temperature Operation

Results obtained at high temperature pilot plant can be used to evaluate the impact of temperature on the L-valve operation. As presented above, gas flow velocity around the elbow of the L-valve is the main solid flow controlling parameter. However, lack of sufficient pressure measurement gauges on the high temperature pilot plant in the current study, makes the calculation of the Q_{lvH} unreliable. On the other hand, comparison of the results in Figure 3.19 illustrates that solid flux variation demonstrates similar trend in terms of U_{lvH} or external gas flow ($Q_{lv} = U_{lv}A_{lv}$). The main difference is that the results shrink on a single curve in terms of U_{lvH}/U_{mf} but not for U_{lv}/U_{mf}. Due to this lack of information, the effect of temperature discussed in the current section is based on the external gas injection into the L-valve. The experimental conditions including height of the solid column in the reactor were maintained constant for different tests.

Figure 3.21 illustrates the solid flux actuated in the L-valve of the cold flow prototype and the high temperature pilot plant for three temperatures. The results illustrate that the required gas flow rate (on normal basis) at high temperature decreases significantly. At high temperature gas viscosity increases while gas density decreases. Decrease of gas density results in increase of gas flow rate due to the gas expansion. This increased solid flow rate effectuated in the L-valve by increase of the drag force on the particles.

Ideal gas law was used to calculate the gas expansion and real gas velocity based on the temperature in the L-valve (Figure 3.21). It shows that the solid flow rate have similar behaviour in terms of real gas velocity at different temperatures. A closer observation of the results in the Figure 3.21 illustrate that the pilot results at 403 °C have the same behaviour as ilmenite particles in the ambient condition. Ilmenite particles have an average diameter of 107 µm while the oxygen carriers (OC1) are of 168 µm diameter. Therefore, based on the discussions of the section 3.1.7, OC1 results should be in right of the ilmenite curve as higher gas flow velocity is required to achieve identical solid flow rate for bigger particles. This illustrates that the effect of temperature on the solid flow rate is more than the effect anticipated by gas expansion due to the density variation. Operation of the L-valve with Helium presented in section 3.1.6 illustrated that gas density does not have a significant effect on the solid flow rate in the L-valve for identical real gas velocity (at the real operation temperature). Accordingly, it can be deduced that the gas viscosity is the parameter affecting solid flow rate in this case. These results are in agreement with Knowlton's statement on the temperature effect on the L-valve operation [95].

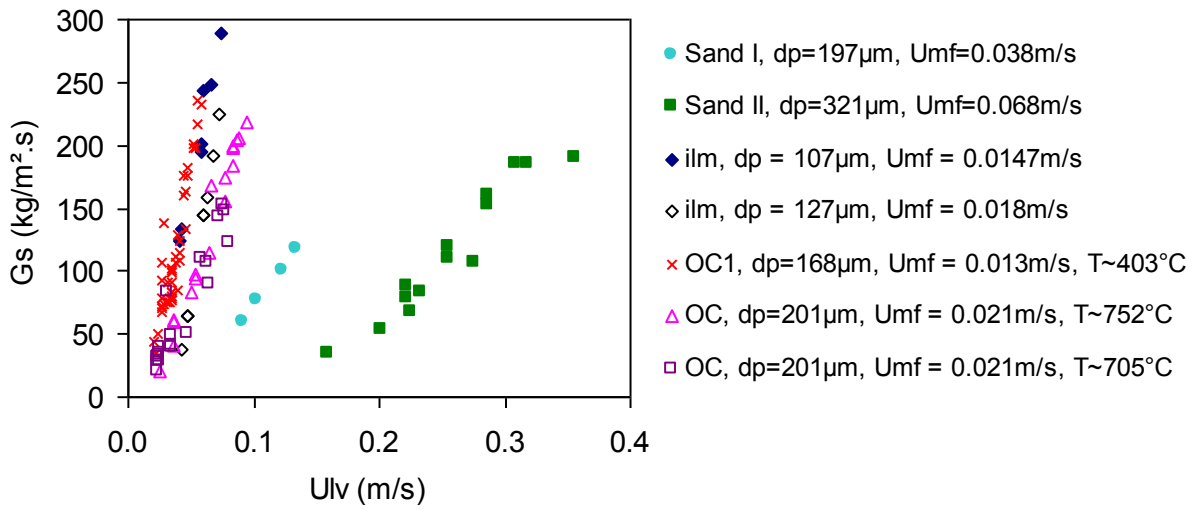

Figure 3.21: Solid flow rate versus velocity of the external gas injection into the L-valve in the cold flow prototype and high temperature pilot plant for different particles listed. The solids in the hot pilot plant were modified between two tests. The particles with diameter below 100µm were screened out of the system in the 705°C and 752°C operations.

As discussed above, the gas flow rate in the horizontal section of the L-valve in the pilot plant can not be exactly calculated. Therefore, the comparisons are based on the external L-valve aeration for temperature effect. Solid circulation results measured in the pilot and prototype are plotted versus fluidization number of the external gas injection into the L-valve in Figure 3.22. The curves in the basis of fluidization number become closer to each other and the difference between them contracts. This demonstrates that the minimum fluidization velocity is once more a useful comparison basis not only for the solid properties but also variation of the gas properties. U_{mf} at high temperatures were experimentally measured in reactor R1 of the pilot plant. However, calculation of the U_{mf} at superambient temperatures is a tricky task [240-242]. Increase of temperature is known to increase the ε_{mf} [240,241]and decrease the U_{mf} [240-242]. Therefore, the temperature effect is not only due to the gas property variation but also effect of the change of the bed voidage in the standpipe. It should be mentioned that reduction of U_{mf} at higher temperatures can reduce the maximum solid flow rate in the L-valve by lowering the maximum allowable slip velocity in the standpipe which is U_{mf}.

Comparing the solid flux results at high temperature with the ambient temperature illustrates that all solids have similar slope versus variation of the external aeration rate in terms of fluidization number (U/U_{mf}). The major difference is in the onset point of the solid flow. The onset point decreases as the size of the particles reduces. This effect explains partially the reason why the 403 °C curve remains slightly above the 705 °C curve as the particles in the first case have smaller average diameter.

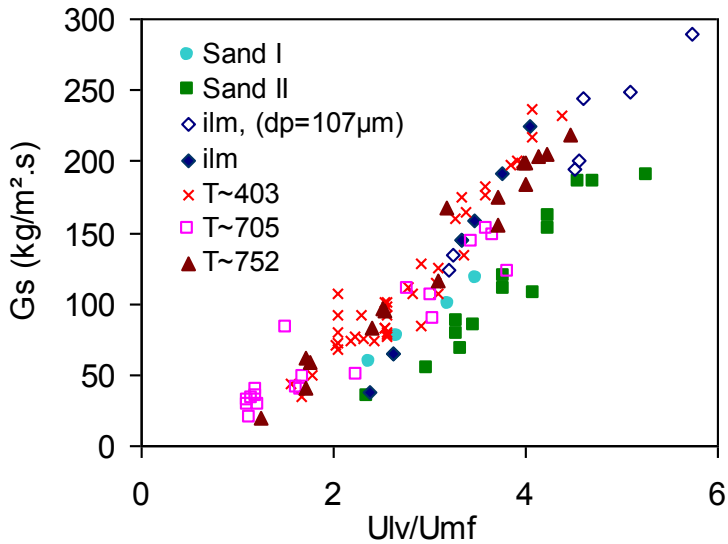

Figure 3.22: Effect of temperature on the solid flux in the L-valves of the cold flow model with three solids in the ambient conditions and the hot pilot plant with oxygen carrier particles at two temperatures. The size of the particles were modified between the pilot tests, with dp = 168 µm at 403 °C and 201 µm at 705 °C.

The results demonstrated significant effect of the temperature on the solid flow rate actuated in the L-valve. Temperature influences the solid flow through two properties of gas, density and viscosity. Solid flow rate was shown to increase in higher temperature due to the decrease of the gas density (gas expansion). However, the increase of solid flow rate due to the temperature is more than what expected only by gas expansion. This was shown to be due to the increase of the gas viscosity by comparing the high temperature results with L-valve operation with Helium.

3.1.9 L-valve Limiting Operation

The L-valve operation is reported to be limited due to different phenomena including: fluidization of standpipe [93], limit of solid flow rate into the L-valve [243], or unstable operation in the inclined section of the L-valve [95] (in case of hybrid standpipe as in the current configuration). However, these limits depend on the pressure drop across the standpipe of the L-valve which is a dependent variable. Accordingly, the upper operation limit of the L-valve can be adjusted depending upon the operating conditions. Two test series were carried out to investigate limiting L-valve operation in batch and continuous operations.

A batch test was carried out to investigate different limiting operations in the L-valve based on the pressure drop in the standpipe. The reactor R1 was initially filled with a high solid height of about 0.9 m. A constant external aeration of 0.36 m/s (equivalent to $5.3*U_{mf}$) was then applied to the L-valve (lv1) while the second L-valve was not operating. Therefore, the solid inventory in the R1 started to decrease. The resulting variation of the pressure drop and the downwards gas flow in the standpipe are illustrated in Figure 3.23 for this test. Different zones can be distinguished as indicated in the figure:

- t = 0 second: The external L-valve aeration was adjusted to 0.36 m/s ($5.3*U_{mf}$).
- t = 0 – 50 seconds: Pressure drop across the standpipe increases rapidly to a maximum level of about 60 mbar where the solid column gets fluidized. Increase of pressure drop reduced downward gas flow rate progressively down to zero. Gas flow in the horizontal section of the L-valve then reduced continuously, resulting in a reduction of the solid flux.
- t = 60-110 seconds: Solid in the standpipe is fluidized. Standpipe pressure drop reached its maximum value and remained constant while at the same time, pressure drop in the reactor was reducing continuously. Solid flow rate reduced continuously indicating that more gas was flowing upwards and gas flow around the bend was reducing. Upward gas flow opposed solid flow into the L-valve and reduced solid flow rate from the reactor into the L-valve. Accordingly, less solid was entering the L-valve compared to the solid outflow. Therefore, the height of the solid column in the standpipe descended gradually. As solid height decreases, more gas tends to flow upward in the standpipe; consequently, gas flow in the horizontal section of the L-valve reduced more. Therefore, solid flow rate actuated in the L-valve reduced. Thus, the height of solid in the standpipe reduced to a minimum level where it stabilized for a moment and then started to rise. The minimum solid height is equivalent to the point where solid flows in and out of the L-valve are equal.
- t = 110 – 140 seconds: solid height started to rise and standpipe was filled again with solids. Upward gas flow started to form bubbles in the standpipe, causing fluctuations in pressure drop.
- t = 140 – 180 seconds: Gas bubbles enlarged in size gradually, resulting in formation of plugs of solid and gas in the standpipe. High upward gas flow rate in the standpipe and low pressure drop across the reactor reduced solid flow into the L-valve to a very low quantity. Solid flow in the L-valve was finally stopped due to insufficient pressure drop in the reactor and high upward gas flow rate in the standpipe.

This experimental test illustrates different possible operation regimes in the L-valve for a constant external aeration. Therefore, the pressure drop across the standpipe in the L-valve has to be selected appropriately to avoid the standpipe to become empty of solids or to avoid bubble formation.

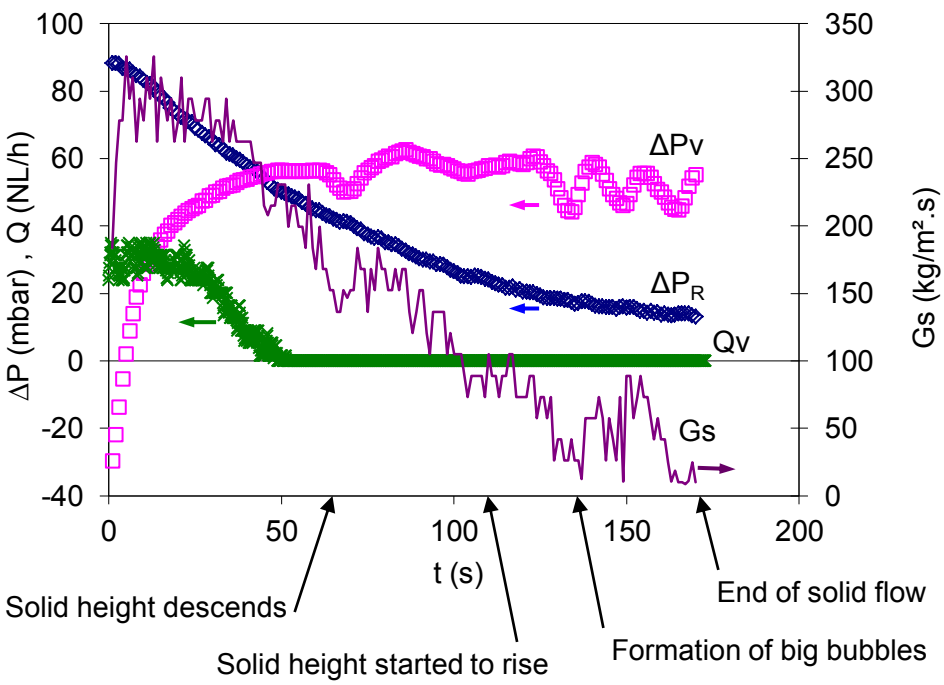

Figure 3.23: The measure pressure drop and the measured gas flow rate in the L-valve for a batch operation with Q_{lv} = 0.29 Nm3/h (U_{lv} = 0.355 m/s).

A second test was carried out to investigate continuous operation of the L-valve in limiting conditions. The external gas flow rate was set to a high value of 0.416 m/s (6.2 U_{mf}). The resulting pressure drop variation and gas flow in the standpipe are illustrated in Figure 3.24. An oscillatory behavior of the pressure drop and gas flow was observed in the system. Moreover, the height of moving bed in the standpipe was also behaving in an oscillatory mode. Once the L-valve was opened, solid height started to gradually decrease while pressure drop was increasing across the standpipe. The solid height finally get to a minimum level where it started to rise again. The solid height then increased till it reached the top of the L-valve where the solid height started to descend again. This unsteady phenomenon repeated itself in an oscillatory mode as illustrated in Figure 3.24.

When a very high gas flow rate is injected into the L-valve, a high solid flow rate is actuated in the L-valve exit (W_s) higher than solid flow entering into the L-valve (W_{in}). The solid height in the standpipe (H_s) then reduces, resulting in an increase of pressure drop per unit height in the standpipe ($\Delta P/H_s$). Consequently, the downward gas flow rate in the standpipe (U_v) reduces gradually, gets to zero and finally gas flows upwards in the standpipe. Accordingly, U_H reduces, resulting in a reduction of solid flow rate actuated in the L-valve. The solid inventory in the reactor then increases. Consequently, pressure drop in the reactor increases, resulting in reduction of the total pressure drop in the standpipe. As the solid flow rate reduces, W_{in} exceeds W_{out} and standpipe starts to fill again. As the solid height in the standpipe increases, $\Delta P/H_s$ reduces. Therefore, more gas passes downwards, and the solid flow rate increases gradually. This pattern continues until solid height reaches its maximum once the standpipe is filled with the solid and again W_{out} exceeds W_{in}. Once more, the same cycle starts to repeat again. This operation is in fact the condition of the second operation regime of Figure 3.23 (t = 60 -110) where the system can not stabilize around a stable point. This behavior is similar to the operation called the automatic operation of the L-valve described by Knowlton in [108].

During this test, the second L-valve (lv2) was operating normally with an average solid flow rate similar in average to the flow in the first L-valve (lv1), while the first L-valve was operating in an unstable mode. The stable operation of the second L-valve was due to proper adjustment of external aeration and pressure drop along the standpipe. The external air flow velocity was set to 0.381 m/s (compared to 0.416 m/s in the lv1) and the pressure drop in the reactor was slightly higher in the

reactor R2 compared to R1. This illustrates the importance of proper selection of the operating conditions in high solid flow rate operations to avoid possible instabilities. This is of particular interest for design purposes when a high solid circulation rate is expected between two reactors to transfer the required oxygen for combustion.

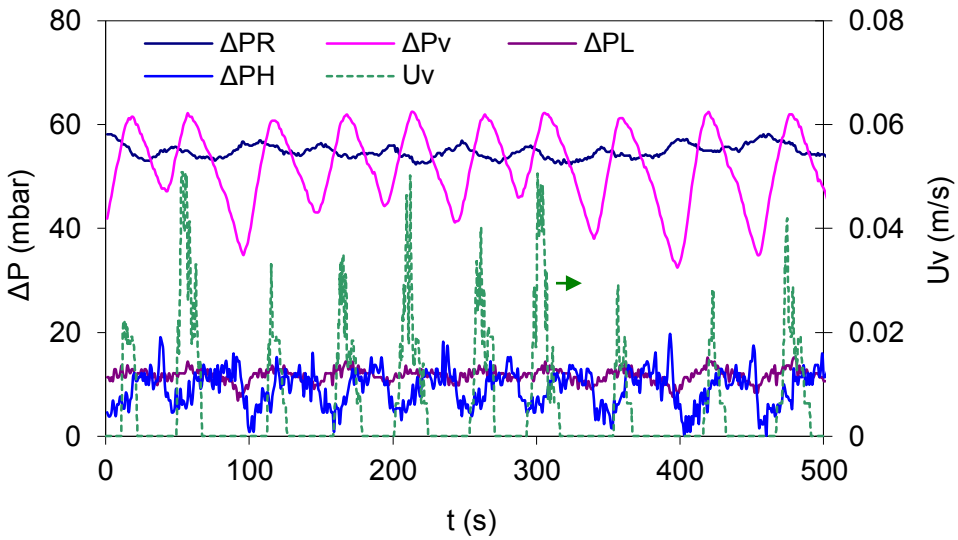

Figure 3.24: The measured pressure drop and the gas flow rate in the oscillatory operation of the L-valve in limiting condition with Q_{lv} = 0.34 Nm^3/h (U_{lv} = 0.381 m/s) for sand particles.

Some important conclusions can be deduced from the above two limiting operations of the L-valve:

- The batch circulation test demonstrates that different operational regimes are possible in the L-valve as a result of pressure drop variation across the reactor. Therefore, in case of high solid flow rate, while high external gas flow rate is necessary, sufficient pressure drop upstream of the L-valve is required.
- In continuous solid circulation test, two valves were operating with identical solid flow rates. Proper set of external gas injection and pressure drop adjustment resulted in stable operation of an L-valve in one case, while the other L-valve was operating in unstable mode.
- Standpipe of the L-valve acts as an auto-adjusting element to maintain pressure balance and solid flow rate. This adjusting phenomenon is carried out through two mechanisms:
    - In non-fluidized operations, the relative solid gas velocity changes pressure drop along the standpipe.
    - In operations with fluidized solid flow in the standpipe, pressure drop across the unit length of the solid column is constant. Therefore, standpipe pressure drop adjusts itself by variation of the height of the solid column in the standpipe similar to the loop-seal.
- A L-valve can be considered as a solid conveying device with two adjustable restrictions to control solid flow rate (Figure 3.25):
    1. The horizontal section of the L-valve controls solid flow rate as a function of the quantity of the gas passing through the element.
    2. Solid entrance into the L-valve which acts similarly to an orifice and limits solid flow rate as a function of the pressure drop and gas flow rate across the element.

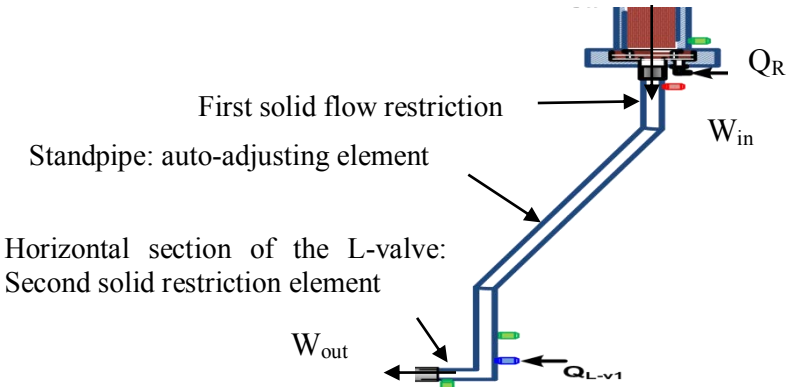

Figure 3.25: Schematic representation of the L-valve. Main restricting and adjusting elements are indicated in the figure.

3.2 Loop-seal Operation

Solid flow into the reactors could carry gases into the reactor resulting in gas leakage. To minimize this possibility, loop-seals are employed in the solid entrance into the reactor. Loop-seals are commonly used in the circulating fluidized beds to ensure gas tightness of the solid flow into a riser. In the current design, loop-seals are used for solid flow into the dense phase of a bubbling fluidized bed (Figure 3.26). Accordingly, solid height in the reactor affects considerably the operation of the loop-seal through the imposed back pressure on the loop-seal. Loop-seal minimizes gas leakage into the reactors according to the siphon principle. Formation of a solid column in the recycle chamber with positive pressure drop, prevents free gas flow into the reactor. Therefore, formation and control of solid column and associated gas flow rate in the supply chamber is an important factor in proper operation of loop-seal. Dependency of the solid column height (H_{sc}) in the supply chamber of the loop-seal to different operating parameters in the current CLC prototype is illustrated in the Figure 3.27.

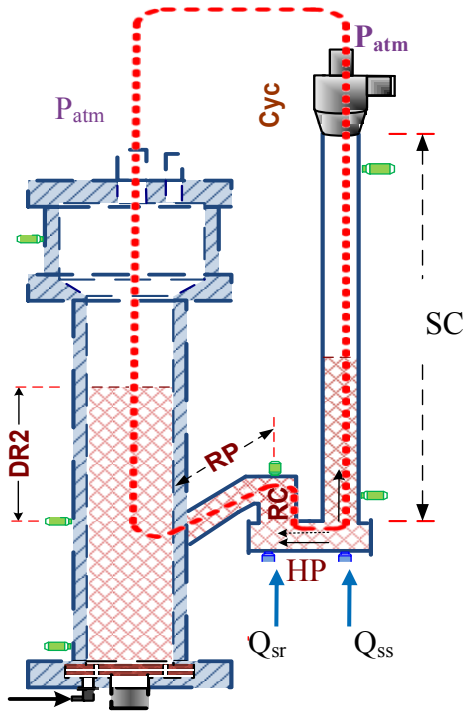

Figure 3.26: Schematic representation of the loop-seal and associated pressure balance loop. Abbreviations used for different sections are indicated in the scheme, meaning: Cyc: cyclone, SC: supply chamber, HP: horizontal pipe, RC: recycle chamber, RP: recycle pipe, DR: fraction of solid bed above the loop-seal solid injection point into the reactor, Qss: first external gas injection into the loop-seal under the supply chamber, and Qsr: the second external gas injection into the loop-seal under the supply chamber.

$$
\text{Hsc} \propto \begin{cases} Q_{sc} = \text{sum of} \begin{cases} Q_{ss} \\ -\,Q_{HP} \end{cases} \\ \Delta Psc \propto \Sigma\Delta P \text{ sum of} \begin{cases} \Delta P_{Cyc} \propto G_s,\ Q_L \\ \Delta P_{HP} \propto G_s \\ \Delta Prc \propto G_s,\ Qrc \\ \Delta P_{RP} \propto G_s,\ Q_{RP} = Q_{RC} \\ \Delta P_{DR2} \propto M_R \end{cases} \end{cases}
$$

Figure 3.27: Dependence of height of the solid column in the supply chamber of the loop-seal to different operating parameters of the system.

There are geometrical and operational similarities between the L-valve and the loop-seal in the current design. In both elements, pressure drop of the moving bed in the standpipes (SC in the loop-seal) is developed as results of the relative solid and gas flow and is a function of the overall pressure balance. In the L-valve, however, solid flow rate varies as a function of the aeration gas while the height of the solid column in the standpipe remains constant. In the loop-seal, solid flow rate is constant (in the current system) while height of the moving solid column varies. Gas flow in the horizontal section of the L-valve is supplied from the external L-valve aeration, Q_{lv}, and standpipe gas flow, Q_{sp}. Likewise, gas flow in the horizontal pipe of the loop-seal is supplied from the loop-seal external aeration in Q_{ss} and gas flow in the supply chamber Q_{sc}. Two cases are possible in loop-seal based on the external gas injection, Q_{ss}:

1. Condition I (Q_{HP} > Qss): in this case, the external gas flow of Q_{ss} is not sufficient for solid flow in the horizontal pipe of the loop-seal. Therefore, the deficient gas flow required for horizontal solid flow ($Q_{HP} - Q_{SS}$) will be supplied from the gases carried down by the solid flow. Q_{SC} will have a positive sign and gases leak into the reactor with solid flow.

2. Condition II ($Q_{HP} < Q_{SS}$): in this case, the external gas flow of Q_{ss} is more than required gas flow to convey solid particles in the horizontal pipe of the loop-seal. Therefore, surplus of the aeration gas, $Q_{SS} - Q_{HP}$, flows into the supply chamber. Q_{SC} will then be negative. Therefore, gas flow in the supply chamber is upwards and best gas tightness is achieved.

3.2.1 Pressure Drop in the Loop-Seal

Formation of the solid column in the supply chamber (SC) of the loop-seal is mainly a function of: the loop-seal pressure balance, loop-seal aeration in Q_{Ss} and solid flow rate. Relevant pressure balance to consider for loop-seal in the present system in the cold flow model is the pressure difference between the cyclone atmospheric gas discharge and the atmospheric discharge of the reactor. This pressure loop is illustrated in Figure 3.26 as:

$$\Sigma P_{ls} = \Delta P_{Cyc,g-s} + \Delta P_{SC} + \Delta P_{HP} + \Delta P_{RC} + \Delta P_{RP} + \Delta P_{DR2} = 0 \qquad \textbf{Eq. 3.3}$$

Similar to the standpipe of the L-valve, the supply chamber of the loop-seal is a non-fluidized or fluidized standpipe, the pressure drop of which depends on the pressure drop across the other elements of the system. ΔP_{SC} varies to adjust the overall pressure balance in the circulation loop. This phenomenon is well demonstrated in Figure 3.28 where solids are circulated in batch operation with constant flow rate from R1 to R2. Pressure drop in the reactor (ΔP_{R2}) was continuously increased. Therefore, pressure drop in the standpipe followed the pressure variation imposed by the reactor pressure drop (ΔP_{R2}). Pressure drops in the other elements of the loop-seal are function of solid and gas flow rates and remain constant regardless of pressure variation across the circulation loop.

Build up of a minimum pressure drop at the loop-seal outlet was necessary to form a solid column in the supply chamber. Therefore, a minimum solid height in the reactor above the loop-seal entrance point was necessary to form a stable solid column in the SC. The main reason for the required

minimum reactor pressure drop was to overcome the pressure drop imposed by cyclone on the loop-seal. Therefore, the downstream pressure in the loop-seal should increase above the upstream loop-seal pressure (cyclone in this case) for the solid column in the supply chamber to form.

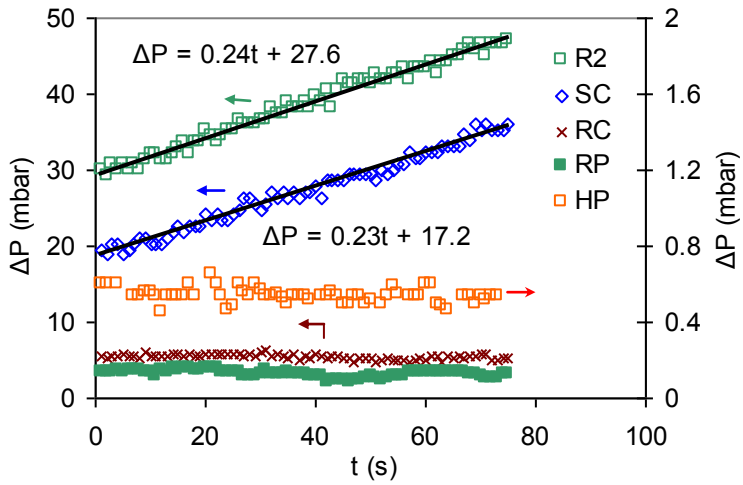

Figure 3.28: Evolution of pressure drop in the loop-seal components for a batch process with G_s=85 kg/h and Q_{Ss}=0.21 Nm^3/h in the cold flow prototype with sand II particles.

The pressure drop variation across the recycle chamber (ΔP_{RC}) of the loop-seal was investigated in terms of the solid properties, solid flux and gas flow rate. Experimental results of this study in the cold flow prototype are presented in Figure 3.29 and Figure 3.30. ΔP_{RC} increases linearly as the solid flux increases with similar trend for all three solids. Figure 3.29 illustrates three test series for sand 2 particles with second loop-seal aeration (Q_{sr}) of 0 to 0.45 Nm^3/h, and variable Qsr. Comparison of these series demonstrates that ΔP_{RC} depends strongly on the gas flow rate across the recycle chamber. Higher gas flow rate decreases the pressure drop across the recycle chamber. Figure 3.30 illustrates this dependency on the gas flow rate. Ilmenite particles in the Figure 3.30 show less sensibility to gas flow rate. This is mostly due to the high gas flow rate in the RC compared to the U_{mf} for ilmenite particles (U_{RC} > 10 U_{mf}). The variation of the pressure drop in the recycle chamber can be explained based on the change of the voidage of the fluidized bed in this element. Increase of the solid flow rate or decrease of the gas flow rate across the recycle chamber reduces the bed voidage which in turn increases the pressure drop.

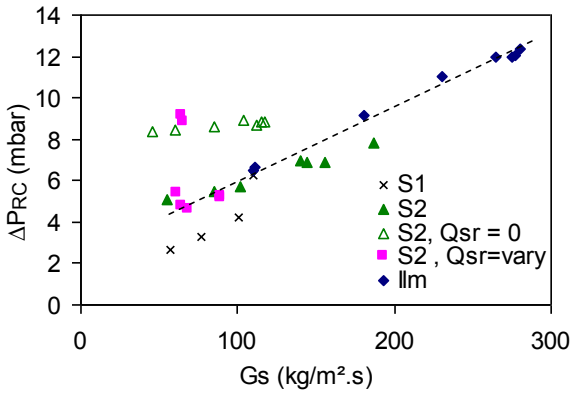

Figure 3.29 : Pressure drop variation in the recycle chamber (RC) of the loop-seal versus solid flux in the cold flow prototype. The second loop-seal aeration (Qsr) was 0.41, 0.45 and 0.29 Nm^3/H for sand 1, sand 2 and ilmenite particles.

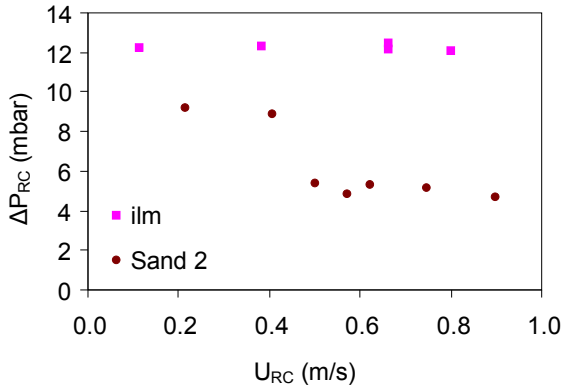

Figure 3.30 : Pressure drop variation in the recycle chamber of the loop-seal (Q_{RC}=Q_{HP} +Q_{sr}) versus gas flow velocity in the cold flow prototype. The solid flux was 66 kg/m².s for sand 2 and 280 kg/m².s for ilmenite particles.

Pressure drop variation across the recycle pipe (ΔP_{RP}) of the loop-seal was investigated in the cold flow prototype (Figure 3.31 and Figure 3.32). Similar to the recycle chamber, pressure drop in the

recycle pipe increases linearly as the solid flux increases. However, the ΔP_{RP} does not show a strong dependency on the solid properties or the gas flow rate contrary to the recycle chamber. This relies on the special gas-solid flow in the recycle pipe where solids flow by gravity co-current with gas. Regarding the slow gas velocity, the solid weight should be the main pressure drop source in this element. Accordingly, solid flux, which is closely related to the solid weight in the recycle pipe, is the main pressure drop influencing parameter.

The pressure drop variation in different elements of the loop-seal were analysed as function of gas and solid flow rate and pressure balance. The results illustrate that the pressure drop in the horizontal pipe, recycle chamber and recycle pipe are function of solid and gas flow rate but not the pressure balance loop. On the other hand, pressure drop in the supply chamber depends strongly on the pressure balance across the solid circulation loop. These results are used in the development of solid circulation model discussed in the chapter 4.

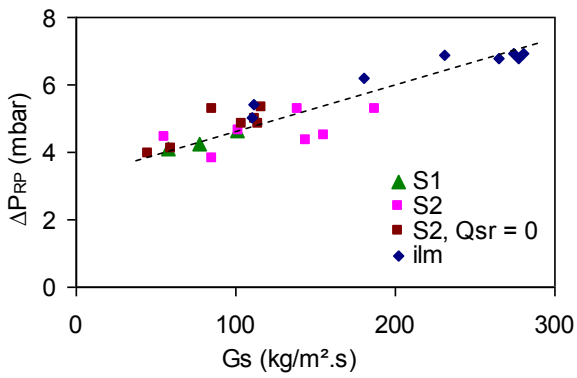

Figure 3.31 : Variation of the pressure drop in the recycle pipe of the loop-seal in the cold flow prototype. The second loop-seal aeration (Qsr) was 0.41, 0.45 and 0.29 Nm³/H for sand 1, sand 2 and ilmenite particles.

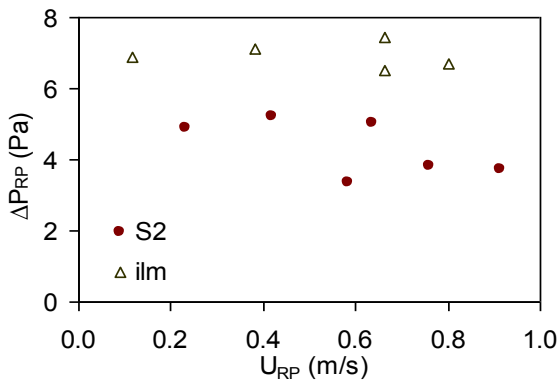

Figure 3.32 : Variation of the pressure drop in the recycle pipe of the loop-seal in the cold flow prototype as a function of gas velocity in RP measured by tracing. The solid flux was 66 and 280 kg/m².s for sand 2 and ilmenite particles.

3.3 Loop-seal Gas Tracing Study

Gas flow pathway and solid flow behavior in the loop-seal were studied using gas tracing investigation. Three Helium injection – detection configurations of 4, 6, 7 in Table 2.3 were employed to investigate different phenomena in the loop-seal.

3.3.1 Effect of the Loop-seal Aeration, Qss

Gas injection under supply chamber of loop-seal (Q_{ss}) is the principal external gas injection of the loop-seal. Q_{ss} supplies the gas flow required to convey solids horizontally in the horizontal pipe (HP). Moreover, it controls the gas flow in the supply chamber (Q_{sc}). Three experimental configurations of 5, 6 and 7 of Table 2.3 were employed to investigate the effect of Q_{ss}. This enables the study of the gas flow in the supply chamber in both downward and upward direction.

3.3.1.1 Effect of Qss on the Downward Gas Flow in the Supply Chamber

Effect of first loop-seal aeration (Qss) on the downward gas flow in the supply chamber was investigated first. Helium was injected in the lift and detected in the exit of the reactor R2. This configuration permits to measure downward gas flow in the supply chamber. Qsc was then measured for different tests in steady state solid circulation between the two reactors. Qss is the only parameter changed between two points while other parameters were constant. Figure 3.33 illustrates variation of

the gas flow velocity in the supply chamber versus first external gas injection into the loop-seal (Qss). External gas injection is expressed in terms of the fluidization number, this permits to present ilmenite and sand II results in the same graph. Therefore:

$$N_f = \frac{U_{g,ss}}{U_{mf}} = \frac{Q_{SS}/A_{SC}}{U_{mf}} \qquad \textbf{Eq. 3.4}$$

Results demonstrate that increasing the external gas injection reduces the downwards gas flow in the supply chamber. Detected downwards gas flow rate gets to a minimum value of about zero for ilmenite and sand particles. This happens once the external injected gas flow of Qss is higher than the required horizontal gas flow of Q_{HP}. The surplus of the gas required for horizontal pipe, flows into the supply chamber in counter direction of solid particles.

The variation of the pressure drop and height of solid column versus the external gas flow of Qss is illustrated in Figure 3.34 for sand particles for the same experimental series above. Increase of external gas injection (Uss) reduces slightly the pressure drop in the supply chamber. However, Hsc reduces significantly as Uss increases. This change is relied on the variation of the gas - solid slip velocity in the supply chamber. While solid velocity is constant, downward gas velocity decreases in the supply chamber. Therefore, gas – solid slip velocity increases, resulting in augmentation of pressure drop per unit of solid column height. Hence, height of solid column decreases according to:

$$H_{sc} = \frac{\Delta P_{SC}}{\Delta P \text{ per unit height of solid in } SC} \qquad \textbf{Eq. 3.5}$$

Consequently, total height of solid column in the supply chamber decreases. The variation of the pressure drop per unit length is limited to fluidization of the solid column. Thereafter, height of solid column does not vary anymore if the slip velocity increases more. This variation can be well observed in the Figure 3.34 where Hsc remains constant after getting to a minimum solid height.

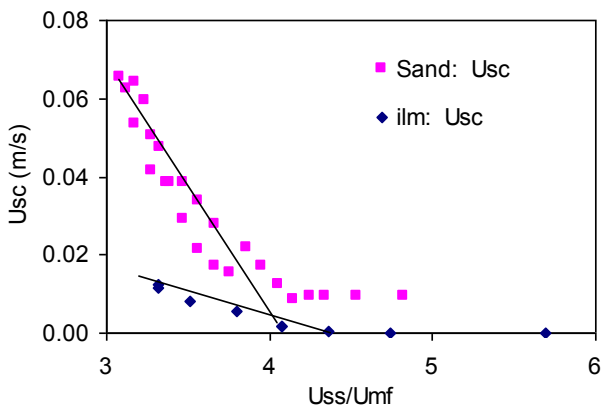

Figure 3.33: Effect of gas injection rate below the standpipe of the loop-seal on the quantity of the gas passing through the supply chamber with Gs = 118 kg/m².s for sand particles and Gs = 122 kg/m².s for ilmenite particles. Gas injection is expressed in terms of the injection velocity (Uss = Qss/Asc) divided by Umf for ilmenite and sand particles.

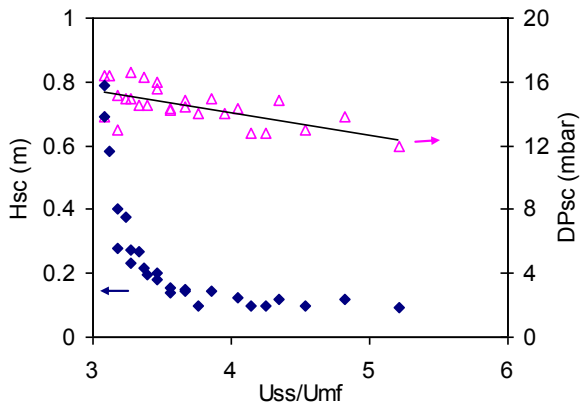

Figure 3.34: Effect of the aeration rate below the supply chamber of the loop-seal ($U_{ss} = Q_{ss} / A_{sc}$) on the visually measured height of the solid column (H_{sc}) and pressure drop across the supply chamber (ΔP_{sc}) with Gs = 118 kg/m².s for sand particles.

3.3.1.2 Effect of the Loop-seal Aeration (Qss) on Upward Gas Flow in the Supply Chamber

Effect of the first loop-seal aeration of Qss on the upward gas flow rate in the supply chamber was investigated in the cold flow prototype. Helium was injected into the loop-seal aeration in Qss. Gas analyzer was installed at the gas exit of the cyclone (configuration 7 of Table 2.3). Therefore, upward gas flow in the supply chamber was measured. Figure 3.35 illustrates experimental results for ilmenite

and sand particles. Comparing the results with Figure 3.33 demonstrates that for both cases with loop-seal gas injection of about 4*Umf, gas flow direction in the supply chamber changes to upward direction. Thereafter, upward gas flow rate in the supply chamber increases as the gas injection into the loop-seal increases.

Solid flow in the supply chamber with upwards gas flow rate was rather difficult to stabilize in case of sand particles compared to ilmenite particles. Upward gas flow destabilized solid flow out of the cyclone and in some cases solids were leaving out of the system through cyclone gas exit. This problem was not encountered with ilmenite particles where solid flow was stable even at high upward gas flow and fluidized solid column in the supply chamber.

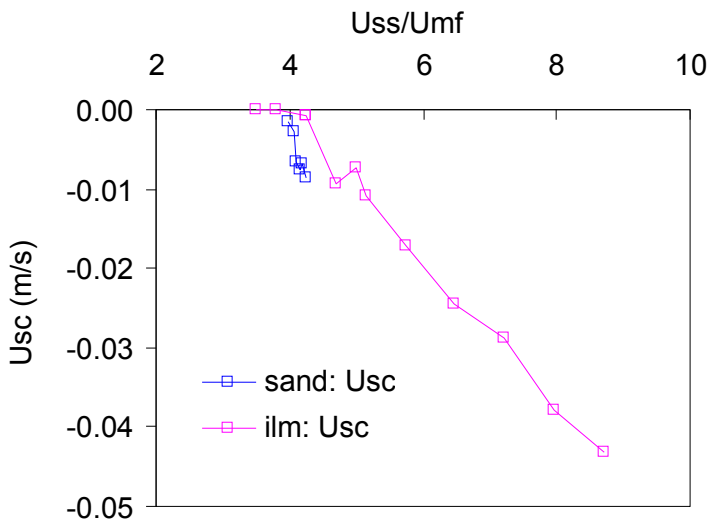

Figure 3.35: Variation of upward gas velocity in the supply chamber due to the increase of the external gas inflow, Uss = Qss/Asc. Ilmenite particles with H_R = 0.5m, and Gs = 70 kg/m².s and sand particles with H_R = 0.5 m, and Gs = 104 kg/m².s. Positive direction is solid flow direction (downward).

The presented results illustrate that the increase in the first external gas injection (Qss) reduces the downward gas flow in the supply chamber and favours upward flow. The gas – solid slip velocity increases in this case, resulting in descent of height of the solid column in the supply chamber. The variation of H_{SC} is limited to the fluidization of the solid column. In case of fluidized bed, the pressure drop per unit of length may even decrease due to the formation of bubbles. Moreover, the fluidization of the solid bed in the supply chamber can result in instability problems as in case of sand II particles presented above.

3.3.2 Effect of Loop-Seal Aeration, Qsr

Second loop-seal aeration (Qsr) is applied to ease solid flow through recycle chamber by fluidizing the solid column in this section. Gas flow necessary in the horizontal pipe of the loop-seal in the current installation is always above minimum fluidization gas required in the recycle chamber. Accordingly, loop-seal can be operated without extra gas injection in the Qsr. However, to avoid any possible malfunctioning or instability in the loop-seal, Qsr is better to be applied so that gas velocity in the supply chamber be higher than U_{mf} of bigest particles in the system [119,244].

A series of steady state tests were carried out to study the effect of the second aeration in the loop-seal (Qsr) on gas flow rate in the supply chamber (Qsc). Qsr was varied between different experimental points from 0 to 0.56 Nm^3/h while other operating parameters were constant. Gas flow rate and height of solid column in the supply chamber were then measured. Results are presented in the Figure 3.36 in

terms of the velocity of external gas injection ($Usr = Qsr/A_{RC}$) and total gas flow rate in the recycle chamber which is the sum of gas flow in the horizontal pipe and the external gas flow rate ($U_{g,RC} = (Qsr + Q_{HP})/A_{RC}$).

Results of the Figure 3.36 illustrate that H_{SC} decreases slightly by increasing the second gas flow rate in the loop-seal (Qsr). This can be explained based on the pressure drop balance across the solid circulation loop. Increasing gas flow rate in the recycle chamber (Qsr), increases gas voidage in the recycle chamber. Consequently, pressure drop in this element decreases. Therefore, overall pressure drop in the solid circulation loop decreases. Supply chamber then needs to recover less pressure. Consequently, $_{HSC}$ decreases. However, gas flow rate through the supply chamber remains fairly constant since solid flux and Qss were constant. This behavior is illustrated in the Figure 3.37 for this experimental series.

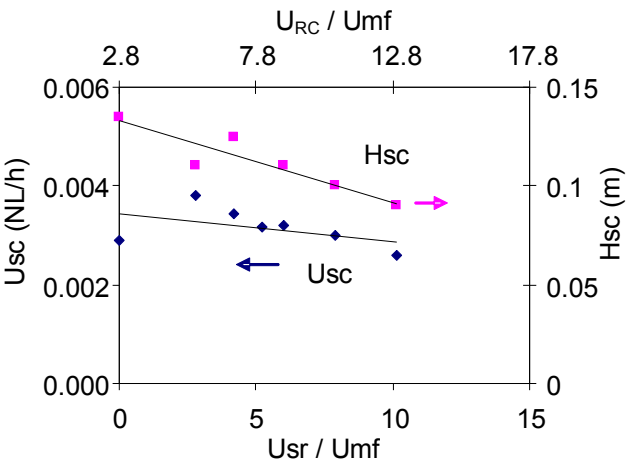

Figure 3.36: Effect of the second loop-seal aeration (Qsr) on the gas flow velocity in the supply chamber (Usc), and height of solid column in the supply chamber (H_{sc}) for sand particles with Q_{ss} = 0.175 Nm^3/h, and Gs = 83 $kg/m^2.s$. Primary x-axis is the external gas injection ($U_{sr} = Q_{sr}/A_{RC}$) and the secondary x-axis is the total gas flow in the recycle chamber ($U_{RC} = (Qsr + Q_{HP})/A_{RC}$).

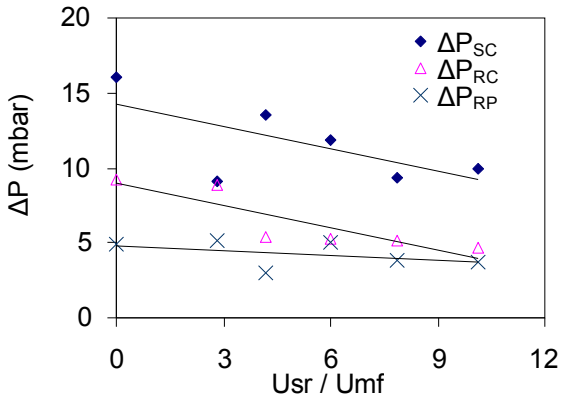

Figure 3.37: Variation of the pressure drop in the supply chamber for the experimental series presented in the Figure 3.36.

3.3.3 Effect of Solid Flow Rate

Solid flow rate can change the gas flow rate in the supply chamber through two phenomena: increase of pressure drop and increase of the required gas flow in the horizontal pipe (Q_{HP}). Effect of solid flux on pressure drop (ΔP_{sc}), gas flow rate (Q_{sc}) and height of solid column (H_{sc}) in the supply chamber for ilmenite and sand particles were experimentally investigated. Helium was injected into the lift with 0.6 vol% concentration. Gas detector was installed at the gas exit of the reactor R2 (configuration 4 of Table 2.3). This configuration permits to measure downward gas flow rate in the supply chamber. Measurements were carried out for series of steady state solid circulation between two reactors. Solid circulation rate was the only parameter changed between each two experimental points while other operating parameters were kept constant.

Experimentally measured gas flow rate and pressure drop variation across the supply chamber are plotted in Figure 3.38 for the experiments explained above. Pressure drop across the supply chamber did not vary significantly with solid flux variation. It should be noted that the slight change observed for ilmenite particles was due to the variation of solid height in the reactor and not the solid flow rate variation. Nevertheless, gas flow velocity in the supply chamber ($U_{sc} = Q_{sc}/A_{sc}$) was considerably affected by solid flow rate variation. Higher solid fluxes favor downwards gas flow in the supply chamber.

Downwards gas flow rate in the supply chamber increases with increasing solid flux in the supply chamber. This phenomenon is relied on the gas flow rate through the horizontal pipe of the loop-seal (Q_{HP}). In the region of low solid flow in the loop-seal (Figure 3.38), external gas injection of Qss is higher than the gas flow rate required for the solid flow rate. Surplus gas then flows into the supply chamber in upward direction and minimizing gas leakage into the reactor. This illustrates the reason why in the first region no gas was detected in the reactor exit. As solid flow rate is increased, higher gas flows into the horizontal pipe of the loop-seal until a limit is reached where Q_{HP} is higher than Qss. This limit is about 85 kg/m².s for sand particles and 70 kg/m².s of ilmenite according to the Figure 3.38. Higher increase of solid flow rate requires the deficient horizontal gas flow to be carried by the solids flow through the supply chamber. Consequently, lift gas leaks into the reactor and tracer gas can be detected in the reactor gas exit.

Variation of the height of solid column in the supply chamber versus gas flux in the loop-seal is plotted in the Figure 3.39 for sand particles in the same experimental test series. H_{sc} increases considerably as solid flux augments. This variation is due to the change of gas flow rate across the supply chamber and its effect on gas – solid slip velocity. Increase of solid flow rate decreases the slip velocity through reduction of upward gas flow in the supply chamber. Consequently, pressure drop per unit height of solid column decreases. Height of the solid column then increases to recover the pressure drop necessary to balance the pressure across the solid circulation loop.

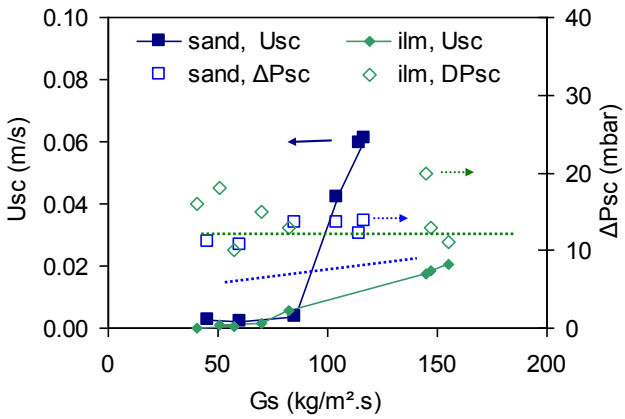

Figure 3.38: Measured gas flow rate and pressure drop in the supply chamber (SC) of the loop-seal versus solid flux. Reactor height is about 0.5 m and Uss = 0.038 m/s for ilmenite and Uss = 0.228 m/s for sand particles.

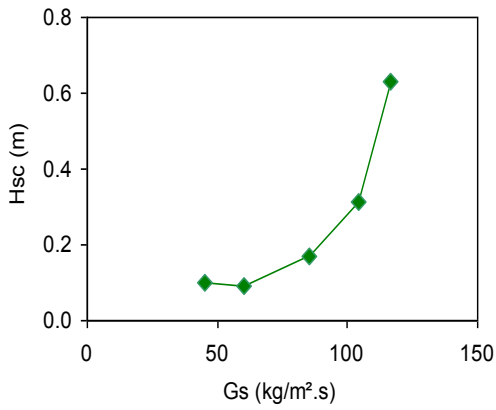

Figure 3.39: Measured height of solid column in the supply chamber of the loop-seal for sand particles with Uss = 0.228 m/s.

These results illustrates that the increase in solid flow rate augments the required gas flow rate in the horizontal pipe of the loop-seal. Accordingly, for a constant external gas injection, downward gas flow rate in the supply chamber increases, resulting in reduction of relative gas – solid slip velocity. Thus, height of solid column in the supply chamber increases to account for the reduction of the slip velocity.

3.3.4 Effect of the Pressure Drop across the Supply Chamber

Supply chamber of loop-seal is a standpipe, conducting particles separated in the cyclone into the horizontal pipe. Solids flow in non-fluidized mode in this element. Pressure drop in the supply chamber is a variable parameter changing to adjust overall pressure balance across the solid circulation loop. Pressure adjustment in the loop-seal is developed through two mechanisms: relative solid – gas velocity (slip velocity) and height of the solid column. Pressure balance loop for the loop-seal in the current installation is illustrated in the Figure 3.26. Pressure drop in the supply chamber in the current system is:

$$\Delta P_{SC} = -\Delta P_{Cyc} + \Delta P_{HP} + \Delta P_{RC} + \Delta P_{RP} + \Delta P_{DR2} \qquad \textbf{Eq. 3.6}$$

Pressure drops in the HP, RC and RP are function of the external gas injection into the loop-seal and of the solid flow rate. Pressure drop in the reactor is only a function of solid inventory (height of the solid bed) in the reactor. Therefore, change of the height of the solid bed in the reactor (H_R) changes the pressure drop across the supply chamber for a fixed solid and external gas flow rates.

Experimental tests were carried out to study effect of the variation of the pressure drop across the supply chamber (ΔP_{SC}) on the gas flow rate (Q_{SC}) and height of the solid column (H_{SC}) in the supply chamber. Testes were carried out for a constant solid flow rate and constant external gas injection into the loop-seal. Pressure drop across the supply chamber was varied by changing the solid inventory in the reactor R2. Variation of gas flow rate in the supply chamber was studies for upwards and downwards gas flow rate in the supply chamber.

Direction of gas flow in the supply chamber was controlled by applying proper external gas injection into the loop-seal in the gas flow rate below the supply chamber (Q_{SS}). Downward gas flow was achieved by injecting Q_{SS} less than required minimum Q_{HP} for the solid flow rate. Upward gas flow in the supply chamber was attained by injecting Q_{SS} higher than the required Q_{HP}.

3.3.4.1 Effect of ΔP_{SC} on Downward Gas Flow Rate in the Supply Chamber

Effect of the pressure drop across the supply chamber (ΔP_{SC}) on the downward gas flow rate in the supply chamber was investigated for both ilmenite and sand particles. Helium was injected into the Lift air with 0.01% volume concentration. Gas analyzer was installed at the gas out flow of the reactor R2 (configuration 4 of Table 2.3). Height of solid column, gas flow rate and pressure drop in the supply chamber were measured. Measurements were carried out during steady state operations with different solid heights in the reactor for each test. Variation of solid inventory in the reactors changes the solid flow rate actuated in the L-valves (section 3.1.3). External L-valve aeration was consistently modified to compensate this effect. However, small variation in the solid flow rate between different test points was inevitable. Figure 3.40 and Figure 3.41 illustrates results of the test for downward gas flow in the supply chamber for ilmenite and sand particles.

Pressure drop of the supply chamber follows linearly pressure drop of the reactor as presented in the Figure 3.40. Increasing the pressure drop in the reactor for 26 mbar augmented ΔP_{SC} by 25 mbar for ilmenite particles. Similarly, 32 mbar variation of ΔP_{R2}, increased the ΔP_{SC} by 32 mbar for sand particles. This behavior is due to the fact that solid column in the supply chamber acts as an adjusting standpipe to balance the pressure drop across the solid circulation loop as discussed above. Pressure drop in the supply chamber is recovered by two mechanisms of change of slip velocity and variation of the height of solid column. Both mechanisms are measured and discussed for these experimental series.

Downward superficial gas velocity in the supply chamber (U_{SC}) is plotted in Figure 3.40. Results demonstrate that U_{SC} decreases slightly as the pressure drop in the supply chamber increases. This change is about 0.004 m/s for sand particles and 0.003 m/s for ilmenite particles. This variation is partly due to the change of solid flow rate due to the variation of the solid inventory in the reactors. Variation of the solid inventory in the reactor changed the solid flux about 4.2 kg/m².s for ilmenite particles and about 5 kg/m².s for sand particles. This variation is the reason for gas velocity reduction of about 0.001 m/s for ilmenite and 0.004 m/s for sand particles. Therefore, the gas flow variation due to the ΔP_{SC} change is insignificant in the experimental results presented**.** The reason for the negligible variation of U_{SC} is the fact that extra pressure drop developed in the reactor is absorbed through variation of height of the solid column in the standpipe. Since solid flow rate and external aerations remained constant, solid – gas slip velocity in the element did not vary significantly.

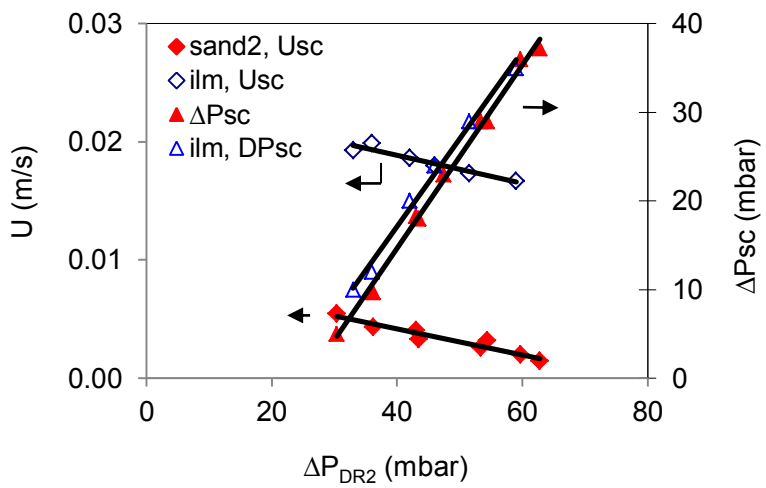

Figure 3.40: Effect of the height of the fluidized solid bed in the reactor (pressure drop above the loop-seal injection point in the reactor) on the quantity of the gas passing through the supply chamber (SC) with Uss = 0.038 m/s and Gs ~ 135 kg/m².s for ilmenite particles and Uss = 0.228 m/s and Gs ~ 87 kg/m².s for sand II particles.

The gas-solid slip velocity did not vary significantly in the experimental tests presented above. This relays on the fact that solid flow rate and external gas injection remained constant. Therefore, the only pressure balance mechanism for the supply chamber is the variation of the height of the solid column (H_{SC}). Variation of the height of the solid column (H_{SC}) versus pressure drop in the reactor is plotted in the Figure 3.41 for the experimental tests of Figure 3.40. Increase in the reactor pressure drop increases linearly the pressure drop in the supply chamber and consequently height of solid column.

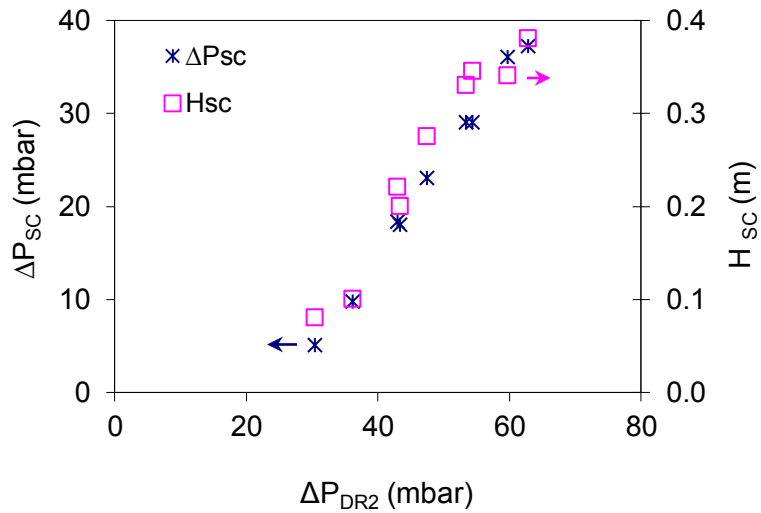

Figure 3.41: Variation of the height of the solid column in the supply chamber visually measured (H_{SC}) versus pressure drop in the supply chamber of the loop-seal for sand particles. Results are corresponding to the same experimental series presented in the Figure 3.40.

3.3.4.2 Effect of ΔP_{SC} on Upward Gas Flow Rate in the Supply Chamber

Effect of pressure drop in the reactor on the upward gas flow rate in the supply chamber was investigated using configuration 6 of Table 2.3. Helium was injected into the first external gas injection of the loop-seal (Q_{SS}) and gas analyzer was installed at the gas exit of the cyclone. Therefore, upward gas flow rate in the supply chamber was measured. Gas flow rate below the standpipe of the

loop-seal (Qss) and solid flow rate were constant while pressure drop in the reactor was being changed for different tests.

Figure 3.42 illustrates the experimental results on the upward gas flow for ilmenite particles. Similar to the downward gas flow condition, increase in the reactor pressure drop increases the pressure drop and height of solid column in the supply chamber. Upwards gas flow velocity was reduced insignificantly by about 0.0012 m/s. Moreover, the solid inventory variation was equivalent to 5 kg/m².s, corresponding to 0.001 m/s reduction of upward gas flow velocity in the supply chamber. Considering both gas flow variation, total velocity variation for this case is about 0.0022 m/s reduction of upward gas flow velocity, as pressure drop in the supply chamber increases.

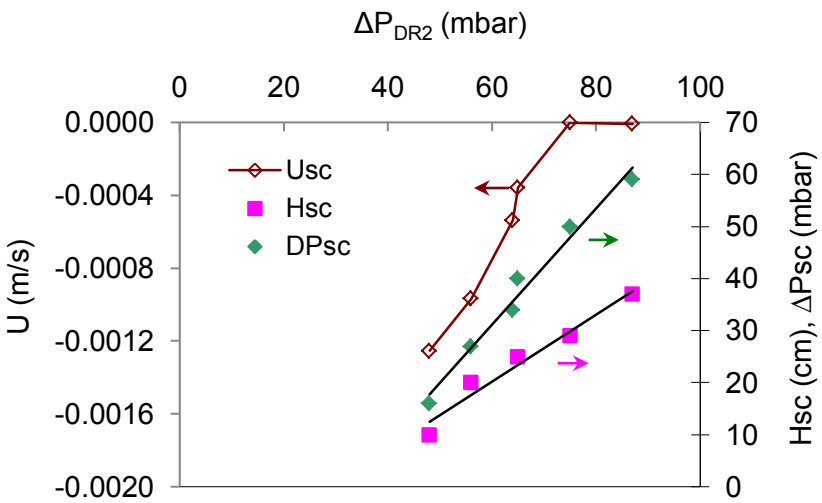

Figure 3.42: Variation of gas flow velocity in the supply chamber (SC) of the loop-seal due to the pressure drop variation cross the SC for ilmenite particles with Uss = 0.06 m/s and Gs ~ 100 kg/m².s.

The experimental results demonstrate that the pressure drop downstream of the loop-seal (in the reactor) changes significantly the pressure drop and height of solid bed in the supply chamber. This is in agreement with the batch results presented in the section 3.2.1. The relative gas - solid velocity decreases both in downward and upward gas flow through the supply chamber. It appears that the horizontal gas flow rate increases slightly as pressure drop downstream of the loop-seal increases. However, this variation is negligible compared to the total horizontal gas flow rate. Therefore, it can be concluded that the extra pressure drop is principally absorbed through the variation of solid height in the supply chamber rather than the relative gas-solid velocity.

3.3.5 Flow in the Horizontal Pipe of the Loop-seal

Horizontal pipe connects the supply chamber into the recycle chamber in the loop-seal. To convey solids horizontally through this section, a minimum gas flow rate is required in this pipe. Gas flow in the horizontal pipe is composed of sum of the external loop-seal gas injection (Qss) and the gas flow rate in the supply chamber (Q_{SC}). As explained above, two operational conditions are possible based on the quantity of the external gas injection (Qss) compared to the horizontal gas flow rate (Q_{HP}):

- Case I: external injection gas is in deficit compared to the required horizontal gas (Q_{HP} > Qss).
- Case II: external injection gas is in surplus compared to the required horizontal gas (Q_{HP} < Qss).

Flow behaviors in each of these two conditions are discussed below.

3.3.5.1 Horizontal Gas Flow in the Loop-seal, Case I (QHP > Qss)

Variation of gas flow rate in the horizontal pipe was experimentally investigated for the condition where external gas injection is less than the minimum gas required in the horizontal pipe. Helium was injected into the lift with concentration of 0.6 vol%. Gas analyzer was installed at the gas exit of the reactor (configuration 4, Table 2.3). This permitted to measure downward gas flow rate in the supply chamber. Gas flow rate in the horizontal pipe (Q_{HP}) was therefore sum of the downward gas flow in the supply chamber and external gas injection, as:

$$Q_{HP} = Q_{SC} + Q_{SS} \qquad and \qquad U_{HP} = \frac{Q_{HP}}{A_{HP}} \qquad \textbf{Eq. 3.7}$$

Variation of the gas flow velocity in the horizontal pipe of the loop-seal (U_{HP}) versus the first external gas injection into the loop-seal is plotted in the Figure 3.43 for ilmenite and sand particles. Results demonstrate that horizontal gas flow rate remains fairly constant for constant solid flow rate regardless of the external gas injection variation. This suggests that increasing the first external gas injection (Qss) reduces the downward gas flow rate in the supply chamber according to the Eq. 3.7 as gas flow rate in the horizontal pipe (Q_{HP}) is constant. This conclusion is in agreement with the effect of Qss on the gas flow rate in the supply chamber discussed in the section 3.3.1 (Figure 3.33).

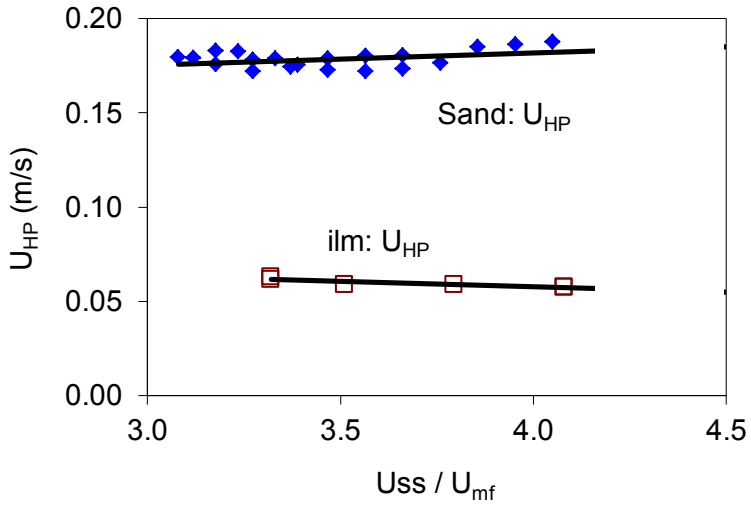

Figure 3.43: Variation of gas flow velocity in the horizontal pipe of the loop-seal versus change of the external gas flow injection in the Qss (Uss = Qss /A_{SC}). Gas flow rate in the supply chamber is downwards for entire experimental series. Sand particles with: H_{R2} = 0.5 m, Gs = 118 kg/m².s and ilmenite particles with: H_{R2} = 0.51 m, Gs = 120 kg/m².s.

3.3.5.2 Horizontal Gas Flow in the Loop-seal, Case II (QHP < Qss)

Gas flow rate in the horizontal pipe was also investigated for the condition where the external gas injection into the loop-seal is higher than the gas required for the horizontal solid flow in the horizontal pipe (HP). As discussed in the section 3.3, extra gas injected into the loop-seal flows upward through the supply chamber (Figure 3.35). Associated gas flow rate in the horizontal pipe is discussed in this section.

Helium was injected into the loop-seal external gas injection (Qss). Gas analyzer was installed at the gas exit of the reactor. Accordingly, gas flow rate in the horizontal pipe of the loop-seal sourced from the Qss was measured. Resulting measured horizontal gas flow velocity versus the external gas injection variation is plotted in Figure 3.44. Accordingly, gas flow velocity in the horizontal pipe increases linearly as the external gas injection into the loop-seal increases. These results are different

from the horizontal gas flow rate measured in the last section, case I, where gas flow rate was constant for constant solid flow rate.

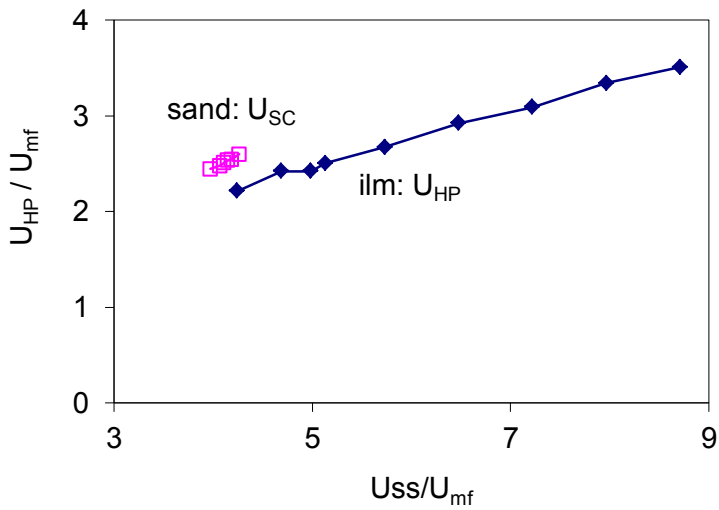

Figure 3.44: Variation of gas flow velocity in horizontal pipe (U_{HP} = Q_{HP}/A_{HP}) of the loop-seal due to the variation of the loop-seal aeration below the supply chamber (Uss=Qss/A_{SC}) for ilmenite particles with Gs = 70 kg/m².s. Associated gas flow rate in the supply chamber for this case is illustrated in the Figure 3.35.

Gas flow rate in the horizontal pipe for the two possible cases of surplus and deficient external gas injection into the loop-seal were discussed above. Results demonstrate that the gas flow rate in the horizontal section remains fairly constant for a given solid flow rate in the case where the external gas injection into the loop-seal is less than the required Q_{HP}. Condition with surplus external gas flow was discussed next. Accordingly, Q_{HP} was not constant in this region and increases as external gas injection into the loop-seal (Qss) increases. Therefore, one can conclude that the Q_{HP} measured in the condition of case I (deficient external gas injection) is the minimum gas required for horizontal solid flow in the loop-seal. Measured gas flow rate in the horizontal pipe versus solid flux in the loop-seal is plotted in Figure 3.45. Measurements are carried out in the case I explained above (deficient external gas injection). Therefore, gas flow velocities correspond to minimum gas required in the horizontal pipe of the loop-seal.

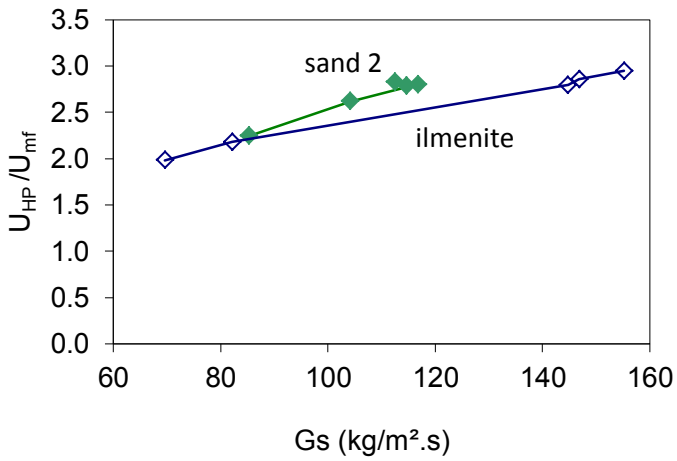

Figure 3.45: Gas flow velocity in the horizontal pipe versus solid flux in the loop-seal for sand and ilmenite particles. H_{R2} = 0.5 m and Uss = 0.228 m/s = 3.4*Umf for sand particles and Uss = 0.038 m/s = 2.9*Umf for ilmenite particles.

The experimentally measured gas flow velocities in the horizontal section of the L-valve and horizontal pipe of the loop-seal are compared for both ilmenite and sand II particles in Figure 3.46 and Figure 3.47. The gas flow in the horizontal section of the L-valve is presented for two tests with variable and constant external gas injection correspondingly with constant and variable solid height in the reactor. The loop-seal results are with constant external gas injection below the supply chamber (Qss) and variable solid flow rate with downwards gas flow rate in the supply chamber. Results demonstrate that the solid flow rate in both L-valve and loop-seal has a similar behavior. This similarity is based on the similitude of the design of these elements as discussed above.

The characteristic curves presented above have similar slopes but different intercepts. The difference of the x-axis intercept can be related to the difference in the geometry of these elements. The horizontal section in the L-valve has a smaller diameter but longer length compared to loop-seal. Longer length of the horizontal section in the L-valve imposes higher gas velocity for the solid to start to circulate. Therefore, the onset point of circulation in the L-valve is displaced rightwards in the graph indicating higher initial gas flow. This effect will be discussed in more details in the next chapter in development of a correlation for this section.

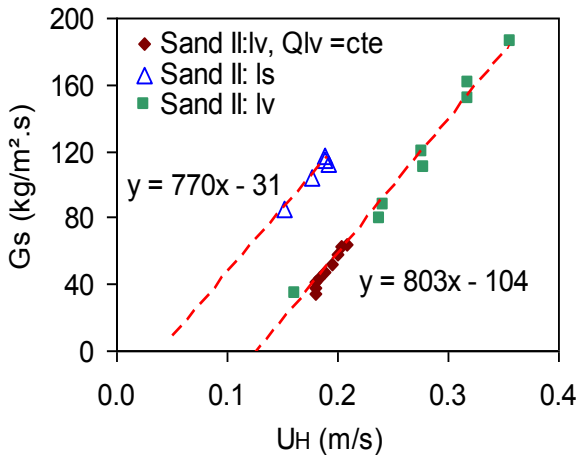

Figure 3.46: Comparison of the horizontal gas flow rate in the L-valve and loop-seal for sand II particles with H_{R2} = 0.5 m and Uss = 0.228 m/s = 3.4*U_{mf}.

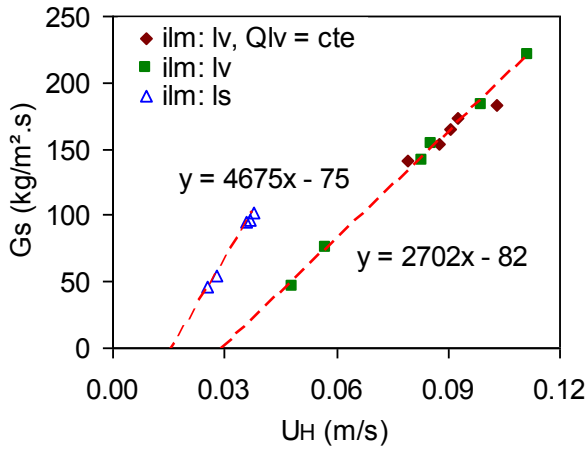

Figure 3.47: Comparison of the horizontal gas flow rate in the L-valve and loop-seal for ilmenite particles with Uss = 0.038 m/s = 2.9*U_{mf}.

According to the presented results, the required gas flow rate in the horizontal pipe of the loop-seal for a specific solid flow rate remains constant in the case of downward gas flow in the supply chamber. This relation was shown to be regardless of the first external gas injection (Qss) as in Figure 3.43. The relation of the solid flux and gas velocity was then shown to be similar between L-valve and loop-seal in this condition (Figure 3.46 and Figure 3.47). However, in the condition with upwards gas flow rate in the supply chamber ($Q_{SS} > Q_{HP}$), the gas flow rate in the horizontal pipe varies by change of the first external gas injection (Qss) as presented in Figure 3.44.

3.4 Global Gas Tightness between the Reactors

In order to detect net gas leakage between two reactors a series of tests were carried out where reactor R1 was fluidized with 100% Helium. The gas at the exit of the second reactor was then analyzed to measure the quantity of the gas of the R1 which have flowed into the R2 with solid flow. The results demonstrate that the gas leakage increases with increasing solid flow rate. Moreover, the curves illustrate the efficiency of the aeration rate of Qss in control of the gas leakage into the reactor.

Measured gas concentration at the exit of R2 is very low in all cases (less than 25 ppmV). This is a characteristic of the current CLC system where there exist three elements reducing the gas leakage between reactors. First element is the standpipe of the L-valve which is a non-fluidized solid flow. Therefore, gas flow through this element is limited and gas can not flow freely along the standpipe. Second element is the dilution of the gas flow in the Lift. Gas flow leaked from the reactor enters into the lift where gas flow rate is considerably higher than the gas flow in the standpipe. Finally, the third element is the loop-seal. Non-fluidized solid column in the loop-seal prevents free gas flow into the reactor. These elements explain why the detected overall gas leakage in the current system is very low.

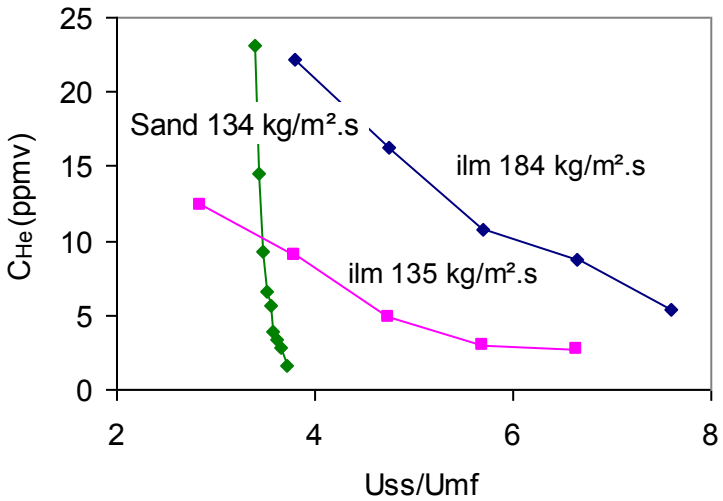

Figure 3.48: Gas leakage from the reactor R1 into the reactor R2 expressed as the Helium concentration in the gas exit stream of the R2 for ilmenite and sand particles as a function of the first aeration in the loop-seal. Ilmenite particles with: H_R = 0.5 m, U_{R1} = 0.036 m/s of He and U_{R2} = 0.08 Nm^3/h. Sand particles with: H_R = 0.5 m, U_{R1} = 0.078 m/s, U_{R2} = 0.067 m/s.

3.5 Steady State Operation

Continuous steady state operations were successfully carried out both in the cold flow prototype and high temperature pilot. The system demonstrated stable operation where pressure drops and solid inventories in the reactors remained constant in the course of the operation for several consecutive hours. In a stable solid circulation operation, pressure variation is balanced over the circulation loop. In the cold flow prototype, the pressure balance is:

$$\Sigma\Delta P = \Delta P_{R1} + \Delta P_{lv,v} + \Delta P_{lv,H} + \Delta P_L + \Delta P_{Tb} + \Delta P_{HC} + \Delta P_{Cyc,s} + \Delta P_{SC} + \Delta P_{HP} + \Delta P_{RC} + \Delta P_{RP} + \Delta P_{DR2} = 0 \quad \textbf{Eq. 3.8}$$

Where ΔP is positive if pressure increases along the element and is negative if pressure decreases, with reference positive sense is solid flow direction. Variation of the gauge pressure across the solid circulation loop versus height of each element is plotted in this section. The pressure loop is presented for the pressure drop variation from the bottom of the reactor R1 to the bottom of the reactor R2. The reason for this choice is the fact that the solid circulation loops have identical dimensions. Therefore, in a continuous solid circulation operation with identical solid inventories in each reactor, the pressure drops are identical for different lines from one reactor to the other. Therefore, the pressure drop variation across one line is presented in the following figures.

Evolution of gauge pressure over the entire pressure loop due to the change of solid flow rate is illustrated in Figure 3.49 for sand II. Pressure drop variation across the standpipe of the L-valve demonstrates most obvious variation for different solid flow rates. This is due to the fact that this element absorbs the pressure drop variation in all other solid conveying elements, as explained

previously. Therefore, in the case of change in pressure drop of other elements, standpipe pressure drop varies automatically. Supply chamber of the loop-seal has similar function in adjustment of the overall pressure balance and therefore recovers the extra pressure produced in the loop. Pressure drop in other solid circulation elements is a function of the element geometry and solid and gas flow rates.

The pressure drop for all three solid flow rates is practically identical at the solid exit of the cyclone (P10 in Figure 2.1). This phenomenon is due to the fact that the cyclone is connected to the atmosphere thought the gas exit pipe. The pressure drop at this point is then the pressure difference between the gas exit and solid exit in the cyclone. This is created by gas reversal and exit contraction pressure drop in the cyclone which are two phenomena depending on gas flow rate. Therefore, solid flow rate does not directly affect the pressure drop in this section (indirect effect is due to the variation of the solid volume in the cyclone which reduces the available space for gas and increases slightly gas flow rate in the cyclone). This phenomenon provides a physical basis for the idea of using two separate pressure drop loops in the current CLC by breaking the Eq. 3.1 into two sections. This is developed in Chapter 0 as the basis of the circulation modeling developed in this study.

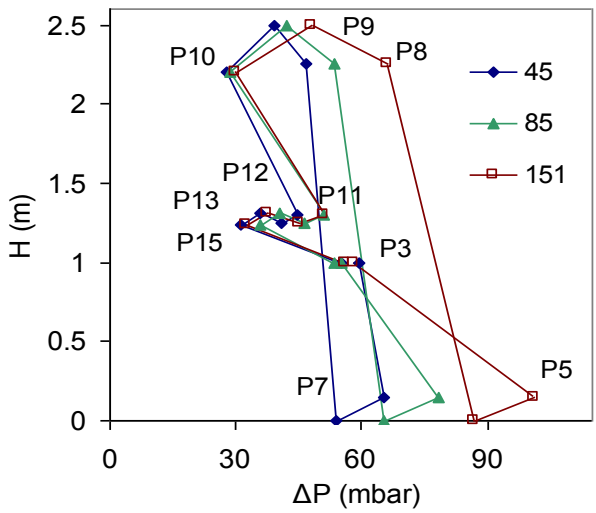

Figure 3.49: Pressure drop variation in the solid circulation loop for different heights in the reactor for sand II. Indicated pressures refer to the pressure tabs noted in Figure 2.1.

Figure 3.50 illustrates pressure drop variation across the solid circulation loop for three solids with similar solid fluxes in the cold flow prototype. In all three cases, the height of the solid bed in the reactor was 0.5 m. The solid density of the ilmenite particles (4750 kg/m^3) is about two times higher than density of the sands (2650 kg/m^3). Therefore, the pressure drop of the ilmenite bed in the reactor (P3) is about two times higher than the sands I and II. An initial pressure drop difference that changes the behavior of the whole circulation loop.

The difference of pressure drop in the supply chamber of the loop-seal is another observation on the Figure 3.50. As explained in section 3.2, pressure drop in this section is a dependent parameter relying on the pressure drop across the solid circulation loop. The pressure drop in the reactor above the entrance point of particles into the reactor was determined to be one of the most important affecting parameters. Accordingly, this difference could be explained based on the difference in density of the ilmenite and sands, and different bed voidage in each case.

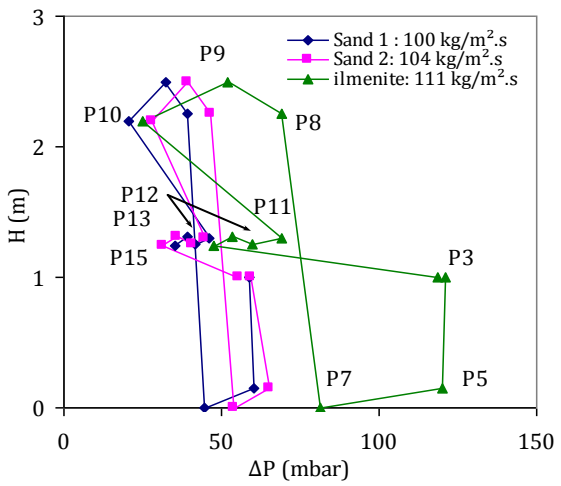

Figure 3.50: Pressure drop evolution over the entire solid circulation loop for three solids with similar solid flow rates. The pressure reference points are indicated in Figure 2.1.

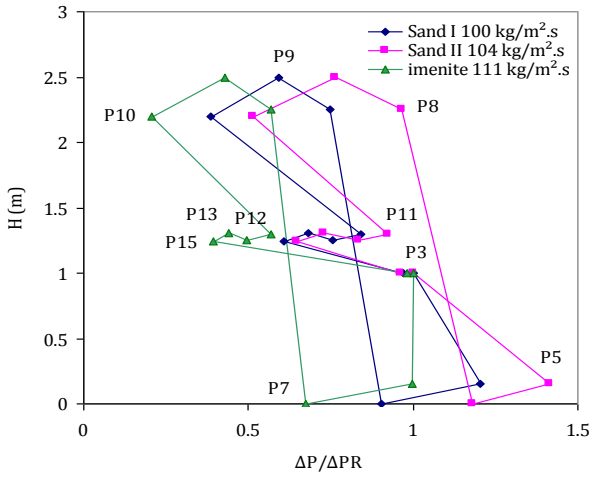

Figure 3.51: Normalized pressure drop evolution over the entire solid circulation loop for three solids with similar solid flow rates. The pressure reference points are indicated in Figure 2.1.

Figure 3.51 illustrates the normalized pressure drop variation loop of three solids for similar solid fluxes. Pressure drop in each element is divided by the pressure drop in the reactor to have the same departure point for all three solids. The most visible difference in the figure between the solids is the difference in pressure drop along the standpipe of the L-valve (P5-P3). Ilmenite shows minimum pressure drop in $\Delta P_{lv,v}$ which is mostly due to the higher pressure drop in the reactor for ilmenite particles with higher density. However, the difference between sand I and sand II is only in particle size and different gas velocity in the lift aeration, Q_L. Therefore, pressure drop in the solid conveying lines are higher in the case of sand II, resulting in higher imposed pressure drop across the $\Delta P_{lv,v}$.

Similar gauge pressure balance loops were developed for the high temperature pilot plant. The number of the installed pressure measurement gauges was less than the cold flow prototype. Therefore, a detailed pressure variation study was not possible in this case. Figure 3.52 illustrates the pressure loop for three solid fluxes in about 390 °C. Moreover, two pressure variation curves for 397, and 737 °C are plotted in the Figure 3.53. The pressure variation illustrates similar trend as cold flow prototype with the standpipe of the L-valve showing highest variation.

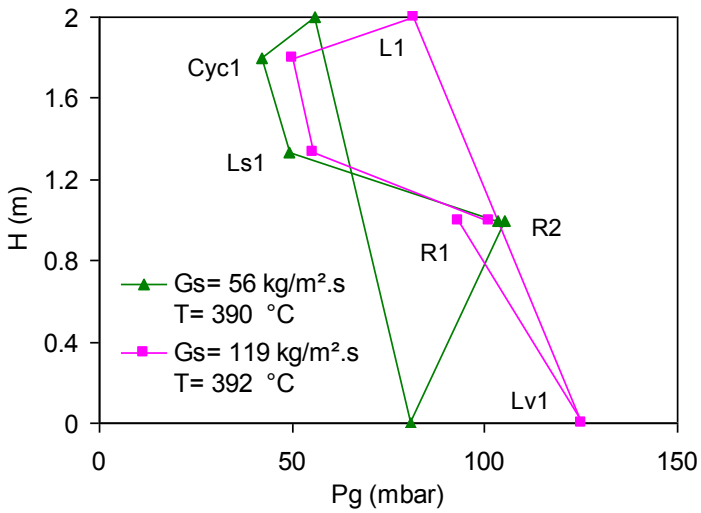

Figure 3.52: Pressure balance loop across the solid circulation line from R1 to R2 in high temperature pilot plant for two solid fluxes in the lift with U_L = 5.4 m/s.

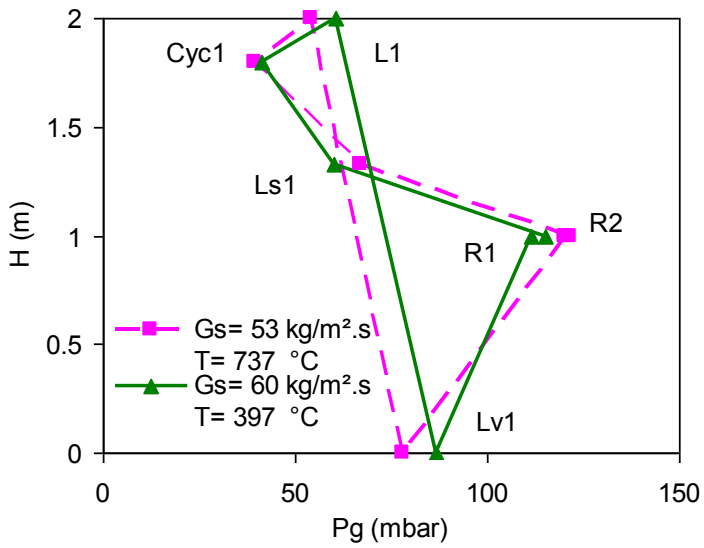

Figure 3.53: Pressure balance loop across the solid circulation line from R1 to R2 in high temperature pilot plant for two temperatures with U_L = 5.3 m/s.

3.6 Geometrical Parameters of the Loop-seal and the L-valve

Geometry of L-valve and loop-seal has been subject of various researches to date [93,97,112]. In the current design, the external aeration point into the L-valve was placed in $1.5D_{lv}$ from the center line of the horizontal pipe according to the design criteria proposed by Knowlton and Hirson [93]. Placing the aeration close to the elbow results in:

- Reduction of pressure drop in the L-valve, downstream of the aeration point.
- Increase of the total length of the standpipe which increases the pressure drop absorption span in the standpipe.

Moreover, the length of the horizontal section was minimised in the current study to minimize the pressure drop in this section [97]. Accordingly an inclined section was added to the standpipe to convey solids horizontally along the distance imposed by size of the thermal insulations around the system.

Different aeration points were tested in the loop-seal for Qss and Qsr as shown in Figure 3.54. The Qsr location did not have a significant effect on the solid circulation. However, the location of Qss had an important influence on the solid circulation and stability of the loop-seal. The optimum location was on the bottom of the horizontal pipe below the supply chamber, adjacent to the internal wall of the supply chamber. Placing the aeration in the horizontal pipe maximises the length of the standpipe. Therefore, the pressure drop operation margin of the standpipe maximises. Placing the aeration close to the internal wall of the supply chamber, minimises the stagnant solid formation in the bottom of the supply chamber and increases the operation window for solid flow rate in this section.

The length of the horizontal pipe (HP) in the loop-seal should be minimized according to Basu and Butler [112]. This minimises pressure drop in the HP, increases solid flow rate and decreases required external aeration. The length of the horizontal pipe in the current study was designed to be as small. The final length was imposed by the thickness of the thermal insulation employed in the high temperature pilot plant.

The current study was mostly focused on the comprehension of the solid circulation and associated phenomena. Scale effect and more precise geometrical studies are still required to be conducted in order to have the knowledge necessary for large size industrial scale CLC process.

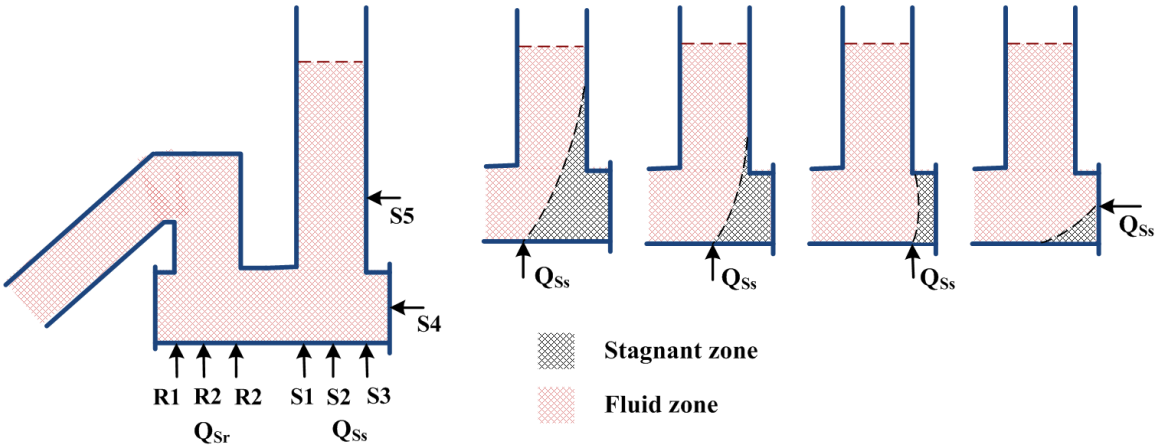

Figure 3.54 : Different possible aeration points in the loop-seal. Stagnant zones are illustrated in the figure by grey hatched zone.

3.7 Conclusion

The hydrodynamics of solid circulation in the current CLC system was experimentally investigated. The main conclusions can be outlined as:

- A wide range of solid flow rate control was achieved by aid of L-valves with solids of different size and density. The solid flow rate was demonstrated to be a function of the gas flow rate around the elbow of the L-valve.
- The external aeration was the main solid flow rate controlling parameter while the pressure drop across the solid circulation loop demonstrated to have a significant effect on the flow rate and stability of the L-valve. It was demonstrated that the solid flow rate can be varied by change of the pressure drop across the solid circulation loop while the external L-valve aeration was constant.
- The particles properties were demonstrated to have a significant effect on the solid circulation in the L-valve. Particle size had the most important effect. The smaller sized particles required less gas injection for a given solid flow rate compared to bigger particles. Increase of solid density also resulted in higher solid flow rate achieved. Moreover, solid density influences the solid flow rate indirectly by change of pressure drop across the solid circulation loop for instance in the reactor.
- Voidage of the moving solid bed in the standpipe of the L-valve was calculated based on the gas tracer experimental results. The linear voidage correlation proposed by Knowlton [235] resulted in closest prediction compared to the experimental results.
- Volumetric gas flow rate (velocity) around the elbow is the solid flow controlling parameter in a geometrically defined L-valve. Gas density was shown to have negligible effect on the solid flow rate in the L-valve. However, high temperature results indicated that increase of gas viscosity increases the actuated solid flow rate.
- Loop-seal was shown to be an effective measure to prevent gas leakage into the reactors. The main operating parameter in gas leakage minimisation in the loop-seal was the first gas injection into the loop-seal below the supply chamber (Qss). Qss acted similar to the L-valve external aeration (Qlv) with the difference that Qss controls height of the solid column in the supply chamber of the loop-seal rather than solid flow rate control.

The aim of this study was to develop an understanding of the L-valve and loop-seal behaviour and their operation limits. Scale up and effect of the size of different system components on their behaviour is another important parameter to be investigated for development of the industrial sized installations.

Chapter 4.

Solid Circulation Investigations: Modeling

4.1 MODELLING APPROACH 101

4.2 FIRST MODEL SECTION 103

4.3 SECOND MODEL SECTION 104

4.4 PRESSURE DROP MODELLING 105

4.4.1 Pressure Drop in the Reactor 106

4.4.2 Pressure Drop in the Standpipe of the L-valve 106

4.4.3 Pressure Drop in the Lift 107

4.4.4 Pressure Drop in the Horizontal Conveying Line and the Blinded Tee Bend 109

4.4.5 Cyclone Pressure Drop 110

4.4.6 Pressure Drop in the Supply chamber of the Loop-Seal 111

4.4.7 Recycle Chamber Pressure Drop 112

4.4.8 Recycle Pipe Pressure Drop 114

4.4.9 Solid Flow in the L-valve and the Loop-Seal 115

4.4.10 Pressure Drop in Horizontal Flow 118

4.5 MODEL VALIDATION 119

4.5.1 Model Results, Solid Flow Rate 119

4.5.2 Model Results, Height of Solid Column in the Supply Chamber of the loop-seal 121

4.5.3 Model Results, Pressure Variation Loop 122

4.6 SENSITIVITY ANALYSIS 126

4.7 CONCLUSION 127

4. Solid Circulation Investigations: Modeling

Experimental investigations in the previous chapter have highlighted that solid circulation in L-valve and loop-seal depend on the gas flow rate around the elbows of these elements. The amount of gas flow in these sections is a function of the amount of gas injected through external aerations but also on the amount of gas coming from the standpipe (supply chamber in loop-seal). Moreover, the gas flow rate in the standpipe/supply chamber depends on the pressure balance around solid circulation loop.

Prediction of solid circulation rate is essential for design and control of operation in the CLC process. Therefore, in order to get a good representation of solid circulation in the present system, it is essential to represent not only the L-valves and loop-seals, but to account for all pressure drop terms around the system. This results in a good prediction of the pressure balance loop.

In this chapter, a model is developed to predict solid circulation rate in the current CLC system both for cold flow prototype and high temperature pilot. The main outputs of the model are solid flow rate actuated in the L-valve and the height of solid bed in the supply chamber of the loop-seal (loop-seal stability). First, the principles of the employed modelling approach are described. Two pressure balance loops are considered in the system; around the L-valve and loop-seal separately. Pressure drop in each of the constituting elements of the system are calculated to complete the pressure balance loops. The employed methods and hypothesis to calculate pressure drop in different sections of the system are presented in detail. Some correlations are developed to model the solid flow rate in the L-valve, voidage of the fluidized bed in the recycle chamber of the loop-seal and the friction factor in the recycle pipe. The calculated pressure drop in each section is compared with the experimental results to validate the applicability of the employed equations. Next, the overall model results are compared with the experimental results obtained with the cold flow prototype and high temperature pilot plant. A sensitivity analysis is finally carried out using the developed model to investigate the effect of different parameters on the solid flow rate and solid bed in the supply chamber of the loop-seal.

4.1 Modelling Approach

The current CLC system includes an L-valve and a loop-seal in series, a configuration that makes the system to be specific compared to the other existing systems. During a stable solid circulation operation, pressure is balanced over solid circulation loop. The current CLC system is composed of two (three in hot pilot plant) identical conveying lines between the reactors. A pressure balance over one line is valid for the other one. The pressure loop from atmospheric pressure above the first reactor to the atmospheric pressure above the second reactor can be written as:

$$P_1 + \Delta P_{R1} + \Delta P_{lv,v} + \Delta P_{lv,H} + \Delta P_L + \Delta P_{Tb} + \Delta P_{HC} + \Delta P_{Cyc,s} + \Delta P_{SPs} + \Delta P_{HP} + \Delta P_{RC} + \Delta P_{RP} + \Delta P_{DR2} + P_2 = 0 \quad \textbf{Eq. 4.1}$$

Where P_1 and P_2 are respectively pressure values at the top of reactor R1 and R2 with the hypothesis that $P_1 = P_2$ in the cold flow prototype (Figure 4.1). Similar equation applies to the high temperature pilot plant with a difference that P_1 and P_2 are pressure drop at the exit of reactors, upstream of particles filters. Cyclone has a gas exit into the atmosphere; therefore, equation 1 could be broken into two parts. First split including the L-valve is:

$$\Sigma P_{lv} = \Delta P_{R1} + \Delta P_{lv,v} + \Delta P_{lv,H} + \Delta P_L + \Delta P_{Tb} + \Delta P_{HC} + \Delta P_{Cys,g} = 0 \quad \textbf{Eq. 4.2}$$

And the second part including the loop-seal is:

$$\Sigma P_{ls} = \Delta P_{Cyc,g-s} + \Delta P_{SPs} + \Delta P_{HP} + \Delta P_{RC} + \Delta P_{RP} + \Delta P_{DR2} = 0 \quad \textbf{Eq. 4.3}$$

Where ΔP is positive if pressure increases along the element and is negative if pressure decreases. And reference positive direction is solid flow direction. These two equations are employed separately to predict solid flow rate actuated in the L-valve, and the loop-seal operation. The division of the solid circulation line into two subsections is the basis of the circulation model. Figure 4.1 illustrates this

principle on a circulation line between two reactors R1 to R2. The known and unknown variables in each section of the system and employed key equations are listed in Table 4.1.

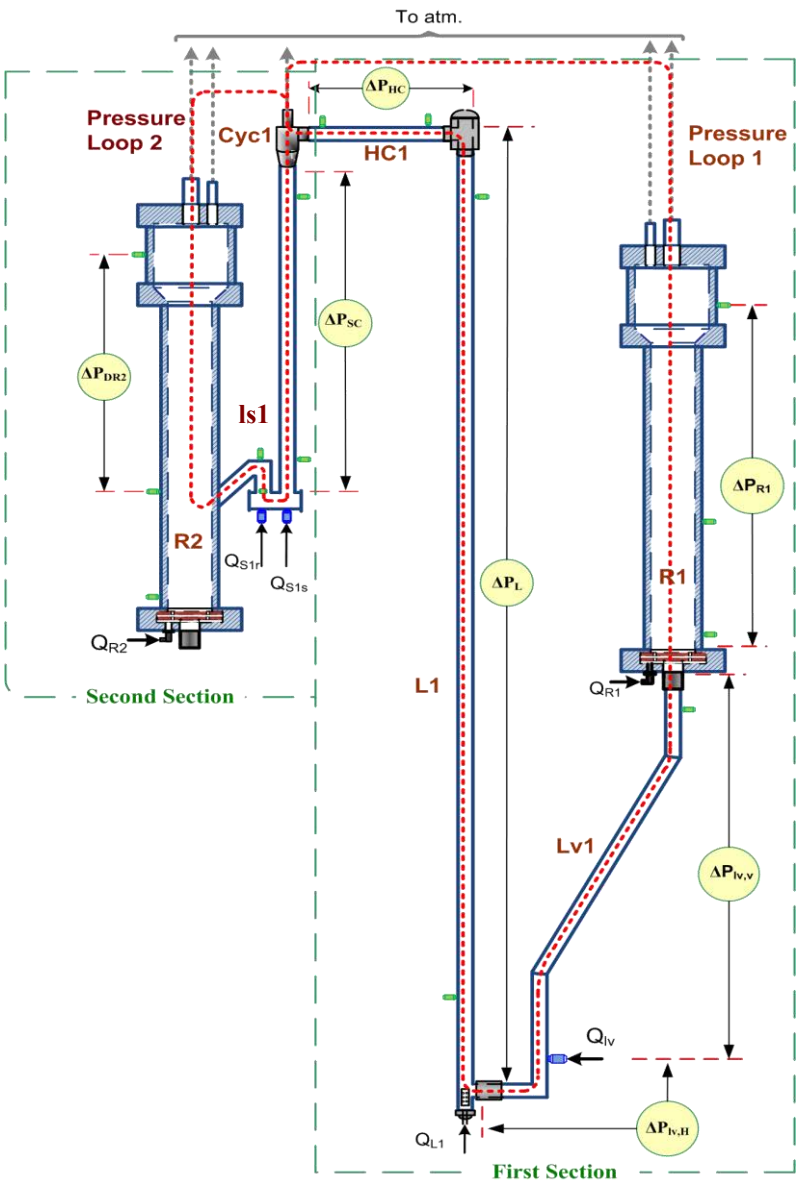

Figure 4.1: Pressure drop indications around the solid circulation loop including pressure drop in reactor (ΔP_{R1}), standpipe of the L-valve ($\Delta P_{lv,v}$), horizontal section and vertical section below the aeration point of L-valve ($\Delta P_{lv,H}$), lift (ΔP_L), Horizontal conveying line and T-bend (ΔP_{HC}), supply chamber (ΔP_{SC}), second reactor above the loop-seal entrance (ΔP_{DR2}). Two modeling sections used in the model are indicated in the scheme by red dashed lines as Pressure Loop 1 and 2. The scheme stands for both cold flow prototype and high temperature pilot plant.

Table 4.1: List of known and unknown variables in the model and the key equations used.

	Unknown variables	Known variables	Key Equations
Section 1	G_s , δ_{lv}	Q_{lv} , M_{R1} , Q_{R1} , Q_L	$\Sigma\Delta P_{lv}= 0$ $G_s = f(U_{lv,H})$
Section 2	L_{SC} , δ_{ls}	G_s , Q_{Ss} , Q_{Sr} , Q_{R2} , M_{R2}	$\Sigma\Delta P_{ls}=0$ $G_s = f(U_{HP})$

4.2 First Model Section

The solid flow rate in the CLC system is controlled in the L-valve where the total quantity of the gases passing through the elbow ($Q_{lv,H}$) determines the solid flow rate. Figure 4.2 illustrates schematically the L-valve used in the current system. As discussed in chapter 3, the quantity of $Q_{lv,H}$ depends on the external L-valve aeration (Q_{lv}) and the gas flow in the standpipe ($Q_{lv,v}$).Therefore:

$$Q_{lv,H} = Q_{lv} + Q_{lv,v} \qquad \textbf{Eq. 4.4}$$

Gas flow rate in the standpipe ($Q_{lv,v}$) could be either upwards (negative sign) or downwards (positive sign). The standpipe gas flow fraction compared to the external aeration is calculated as:

$$\delta_{lv} = \frac{Q_{lv,v}}{Q_{lv}} \qquad \textbf{Eq. 4.5}$$

lv can be either positive or negative depending on gas flow direction in the standpipe. The gas flow in the standpipe depends on pressure balance and is not known initially. Therefore, the model uses an iterative procedure to calculate solid flow rate in the L-valve. Knowing aeration rate into the L-valve, an initial value of 0 is set for the gas fraction factor (δlv). Solid flow rate is then calculated, using the horizontal solid flow rate correlation. Pressure drop in different sections of the system are then calculated, based on the solid flow and gas flow rates in various sections of the system. The sum of the pressure drop across the first section of the transport line (ΣΔPlv) is then calculated using equation 2. If ΣΔPlv equals to zero, the results are considered as the final results. Otherwise δlv is increased by an incremental value as:

$$\delta_{lv,1} = \delta_{lv,0} + d\delta_{lv} \qquad \textbf{Eq. 4.6}$$

$\Sigma\Delta P_{lv}$ is then calculated for the new δ_{lv} and it is checked if the pressure drop sum equals zero. In the case that $\Sigma P_{lv} \neq 0$, a new δ_{lv} is set and the procedure continues until pressure drop sum equals zero. The results are then considered as the final values and used as an input for the second section of the model including loop-seal.

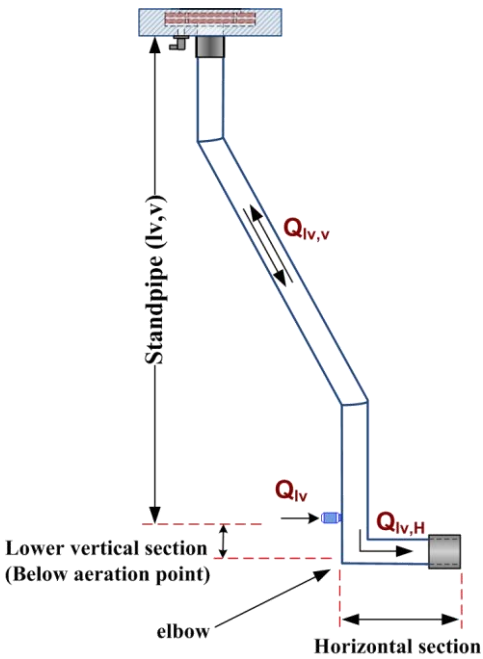

Figure 4.2: Scheme of the L-valve and its main constituting elements.

4.3 Second Model Section

The second section of the pressure drop loop is illustrated in Figure 4.3. Solid particles separated in the cyclone flow downwards to the loop-seal through standpipe by the effect of gravity. Air injected in the loop-seal under the supply chamber (standpipe) conveys solids through the horizontal pipe (HP) towards the recycle chamber (RC). In the recycle chamber, a second air injection is applied to transport solids into the reactor through the recycle pipe (RP).

As indicated in Table 4.1, the gas fraction factor (δ_{ls}) and solid height in the supply chamber of the loop-seal (H_{SC}) are to be found in this section. Solid height in the supply chamber is calculated from the pressure drop in this element. The pressure drop in the supply chamber is then calculated from the second pressure balance loop, Eq 4.3. Indeed, solid flow rate is a known parameter in this section. Accordingly, horizontal gas flow in the horizontal pipe of the loop-seal is found from the horizontal flow correlation. The gas flow rate in the supply chamber is the difference of the external aeration (Qss) and the horizontal gas flow rate. The gas fraction factor (δ_{ls}) between standpipe and the horizontal pipe is calculated as:

$$\delta_{ls} = \frac{Q_{SC}}{Q_{SS}} = \frac{Q_{HP} - Q_{SS}}{Q_{SS}} \qquad \textbf{Eq. 4.7}$$

This procedure is explained in details in the section 4.4.6. The flow chart of the current model is illustrated in Figure 4.4.

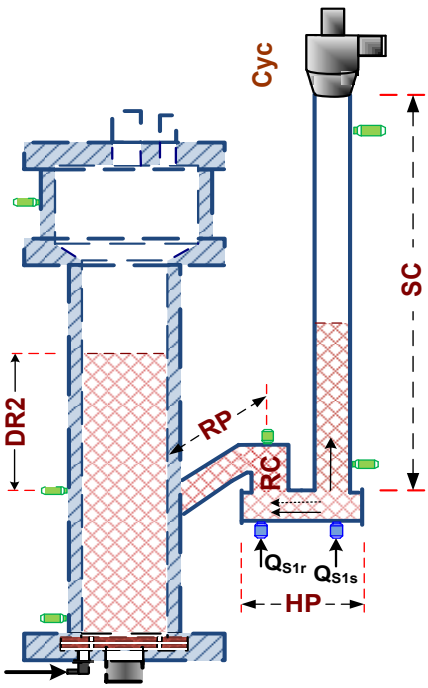

Figure 4.3: Scheme of the second part of the solid flow line.

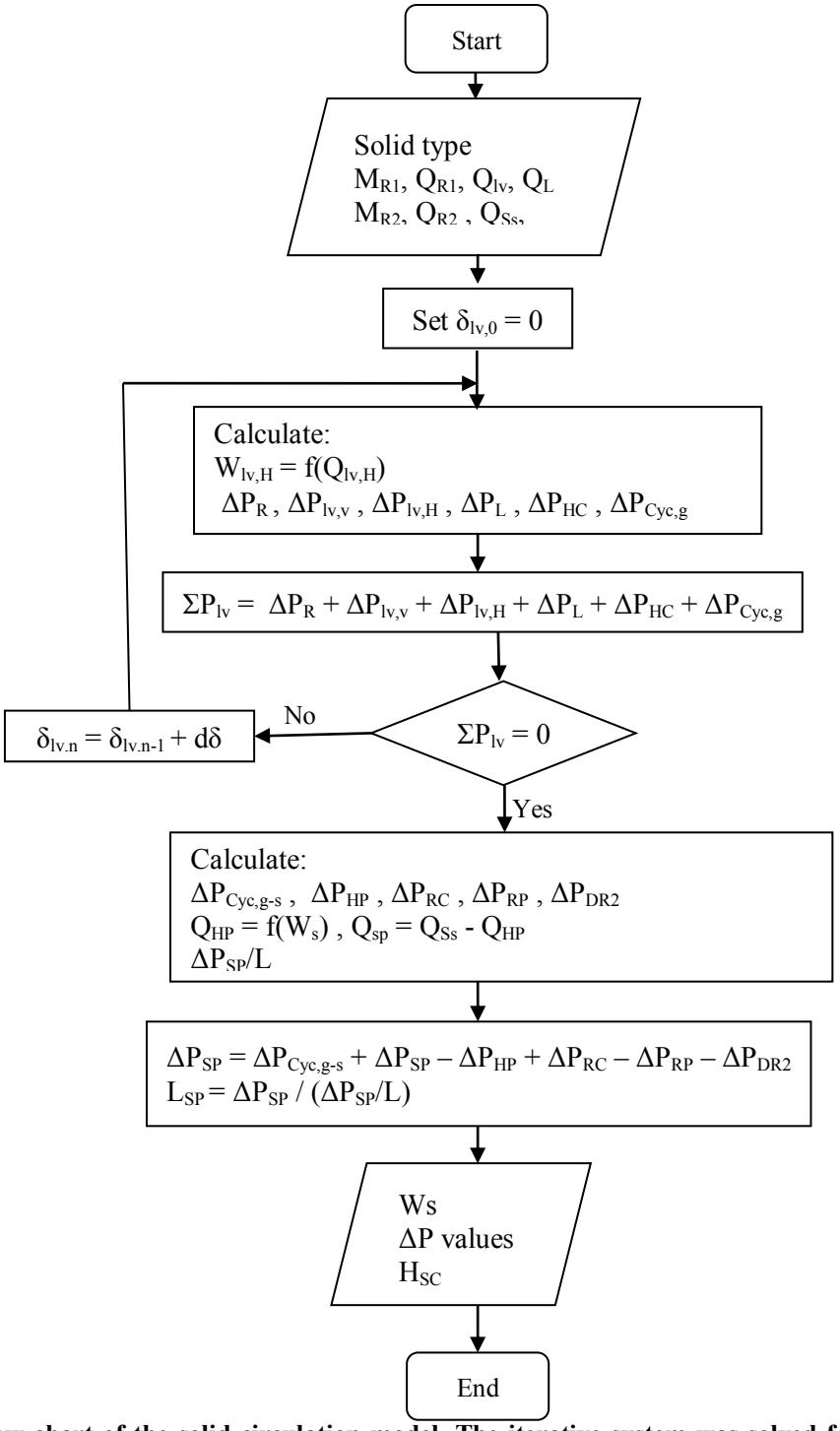

Figure 4.4: Flow chart of the solid circulation model. The iterative system was solved for δ_{lv} by use of VBA solver in excel.

4.4 Pressure Drop Modelling

Pressure drops in each section of the system have to be calculated in order to complete pressure balance equations discussed above. The different correlations used to describe each section and the hypotheses taken into account are discussed below.

4.4.1 Pressure Drop in the Reactor

The reactors in the current installation are in bubbling fluidized bed mode. Therefore, the gas velocity in the bed lays in the limits of minimum bubbling velocity (U_{mb}) and minimum slugging velocity (U_{ms}) [230]. These limiting conditions are calculated in the model with the procedure presented in the appendixes 5. The pressure drop of the fluidized bed in this condition is constant and can be calculated from the weight of solids in the reactor (neglecting gas weight). The weight of the solids in the reactor is calculated taking into account the quantity of solid in the L-valve (M_{lv}), transport lines (M_{tl}) and loop-seal (M_{ls}). Therefore:

$$M_R = M_T - (M_{lv} + M_{tl} + M_{ls})$$ **Eq. 4.8**

The particles in the lift, horizontal conveying line and cyclone were ignored due to dilute solid flow in these elements compared to L-valve and loop-seal. Solid weight is calculated for each section by:

$$M_s = V_i \times \rho_s \times (1 - \varepsilon_i)$$ **Eq. 4.9**

Where ε_i and V_i stand for the voidage and volume of the element whose particle content is to be calculated. The pressure drop in the reactor is calculated based on the solid inventory in the reactor as:

$$\Delta P_R = M_R g / A_R$$ **Eq. 4.10**

The pressure drop above the loop-seal entrance in the reactor is calculated as:

$$\Delta P_{DR} = \rho(1 - \varepsilon_R) g (H_R - 0.3)$$ **Eq. 4.11**

Where 0.3 is the height of the loop-seal entrance into the reactors (both installations) and ε_R is bed voidage. The height and the voidage of the solid bed in the reactor is calculated by use of a simplified procedure based on the two phase model [153] in a bubbling fluidized bed. The detailed procedure is developed in the appendixes. 6 The resulting calculated height of solid bed in the reactor is compared with the experimental results in Figure 4.5.

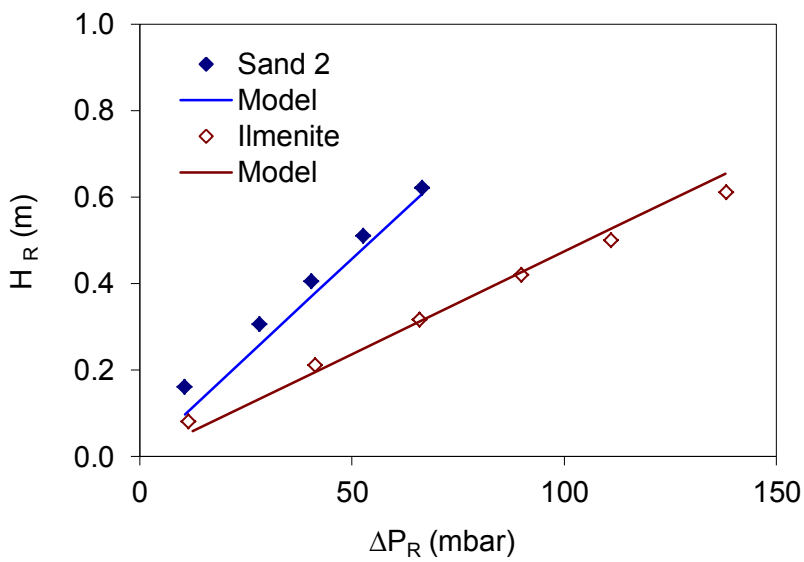

Figure 4.5: Prediction of the height of the solid bed in the reactor versus the experimental results in the cold flow prototype.

4.4.2 Pressure Drop in the Standpipe of the L-valve

The pressure drop across the standpipe of the L-valve ($\Delta P_{lv,v}$) is a dependent parameter. It changes to adjust the overall pressure balance across the solid circulation line [93]. Therefore, $\Delta P_{lv,v}$ can be calculated from the pressure balance as:

$$\Delta P_{lv,v} = -(\Delta P_{R1} + \Delta P_{lv,A-H} + \Delta P_L + \Delta P_{Tb} + \Delta P_{HC} + \Delta P_{Cyc,g} + \Delta P_{piping})$$ **Eq. 4.12**

The pressure drop is then used to calculate the gas flow rate across the standpipe. Solid flow in the standpipe of the L-valve is in the form of a moving packed bed. Ergun equation [94] is used to the governing relation in this section. The general form of the Ergun equation [94] for superficial gas velocity U_g in a fixed bed of solids is:

$$\frac{\Delta P}{L} = 150.\frac{\mu_g U_g}{(\phi.d_p)^2}.\frac{(1-\varepsilon)^2}{\varepsilon^3} + 1.75.\frac{\rho_g U_g^{\ 2}}{\phi.d_p}.\frac{(1-\varepsilon)}{\varepsilon^3}$$ **Eq. 4.13**

The equation is to be modified by substituting the interstitial gas – solid slip velocity (v_{sl}) into the equation as:

$$v_{sl} = \frac{U_{sl}}{\varepsilon}$$ **Eq. 4.14**

The result is Ergun equation used in a moving packed bed:

$$\frac{\Delta P}{L} = 150.\frac{\mu_f v_{sl}}{(\phi.d_p)^2}.\frac{(1-\varepsilon)^2}{\varepsilon^2} + 1.75.\frac{\rho_f v_{sl}^{\ 2}}{\phi.d_p}.\frac{(1-\varepsilon)}{\varepsilon}$$ **Eq. 4.15**

Where v_{sl} stands for relative slip velocity between gas and solids in the standpipe and can be calculated as:

$$v_{sl} = v_g - v_s = \frac{Q_{lv,v}/A_{SP}}{(1-\varepsilon_{lv,v})} - \frac{G_{lv,v}/\rho_S}{\varepsilon_{lv,v}}$$ **Eq. 4.16**

Where the direction of the solid flow is considered as reference sense (positive velocity). $Q_{lv,v}$ is the gas flow rate through the standpipe and Gs is the solid flux. The voidage of the moving solid bed is in the packed bed mode is considered as the tapped bed voidage. The voidage in the transitional packed bed mode is calculated using the linear relation proposed by Knowlton and Hirsan [93] as:

$$\varepsilon_{lv,v} = \varepsilon_s + \frac{(\varepsilon_{mf} - \varepsilon_s)}{v_{mf}} v_{sl}$$ **Eq. 4.17**

Where v_{mf} stands for the interstitial minimum fluidization velocity (U_{mf}/ε_{mf}). The choice of this methodology was discussed in the chapter 3 based on the experimental gas tracer study.

4.4.3 Pressure Drop in the Lift

The size of the lift (vertical dilute phase conveying pipe) in this installation (0.021 m ID) is small with a relatively high gas flow rate. Moreover, no significant radial profile variation or descending solid films was observed in the experimental tests. Thus, the voidage (ε_L) is considered as an average value along the lift by neglecting axial and radial variation of the voidage. The pressure drop across the lift is modelled using a conventional pressure drop correlation for vertical dilute phase conveying. Accordingly, pressure drop is composed of the weight of the gas and solid in the line, gas and solid friction and acceleration terms as [152]:

$$\left(\frac{dP}{dz}\right)_{RC} = \left(\frac{dP}{dz}\right)_{gravity} + \left(\frac{dP}{dz}\right)_{friction} + \left(\frac{dP}{dz}\right)_{acceleration}$$ **Eq. 4.18**

Where, the gravity pressure drop in the integrated form is [153]:

$$\frac{\Delta P_{gravity}}{L} = g.(1-\varepsilon).\rho_s + g\varepsilon\rho_g$$ **Eq. 4.19**

The average gas voidage in the lift is calculated by [245]:

$$\varepsilon = 1 - \frac{Gs}{\rho_S . v_P}$$ **Eq. 4.20**

Where v_P stands for the average real particle velocity and is calculated using the slip velocity, as:

$$v_s = v_g - v_{sl}$$ **Eq. 4.21**

The slip velocity (v_{sl}) for a single particle in an infinite space is the terminal velocity (u_t). However, particle - particle and particle – wall effects causes the slip velocity to be higher than the terminal velocity. Various works has been carried out to calculate the slip velocity [246-250]. In the current study, the v_{sl} calculated according to the correlation developed by Sankar and Smith [247], as:

$$\left(\frac{v_{sl}}{v_t}\right) = 0.011\left(\frac{Ws}{Q_L \rho_g}\right)^{-0.1}\left(\frac{v_g}{v_t}\right)^{1.34}\left(\frac{d_P}{D_L}\right)^{0.56}\left(\frac{\rho_S}{\rho_g}\right)^{0.68}$$ **Eq. 4.22**

The empirical correlation developed by Patience et al. [250] had a better prediction result for Sand 2 and ilmenite particles while it overestimated for the sand 1 particles. This relation is:

$$\left(\frac{U_{lift}/\varepsilon}{v_P}\right) = 1 + \frac{5.6}{Fr} + 0.47 Fr_t^{0.41}$$ **Eq. 4.23**

Where Fr and Fr_t are respectively the Froude number based on superficial gas velocity in the lift and particle terminal velocity. The terminal velocity (v_t) is calculated from the equation presented by Kunii and Levenspiel [153]. The friction is composed of two components from gas and solid flow [245]:

$$\frac{\Delta P_f}{L} = \frac{2 f_s v_s^2 (1-\varepsilon)\rho_s}{D} + \frac{2 f_g v_g^2 \varepsilon \rho_g}{D}$$ **Eq. 4.24**

Gas friction factor is calculated as [153]:

$$f_g = 0.0791\,\mathrm{Re}^{-0.25} \qquad for \qquad 3\times10^3 < \mathrm{Re} < 10^5$$ **Eq. 4.25**

And

$$f_g = 0.0008 + 0.0552\,\mathrm{Re}^{-0.237} \qquad for \qquad 10^5 < \mathrm{Re} < 10^8$$ **Eq. 4.26**

Where Re is calculated as: $Re = U_g.D_L/\nu$. Solid friction factor is calculated using Konno and Saito [251] correlation:

$$f_S = 0.0285\frac{\sqrt{g.D_P}}{v_p}$$ **Eq. 4.27**

The acceleration pressure drop is especially important in the systems which are short in length [152] as in the current installations. Acceleration pressure drop is consisted of two terms of solid and gas acceleration. The gas acceleration is assumed to happen in the initial expansion of the gas at the exit of the bubble cap gas distributor. This section is not in the pressure drop loop of the system as illustrated in Figure 4.1. Accordingly, the gas pressure drop is omitted from the overall pressure drop term. Therefore, the acceleration term is consisted of solid acceleration as [153]:

$$\Delta P_{acceleration} = G_s . v_s$$ **Eq. 4.28**

The resulting pressure drop prediction based on this method is compared with the existing experimental results in the cold flow prototype in Figure 4.6. The two methods explained above are used to calculate the solid velocity in the lift. As in the figure the method of the Patience results in a better pressure drop prediction in the case of the ilmenite particles.

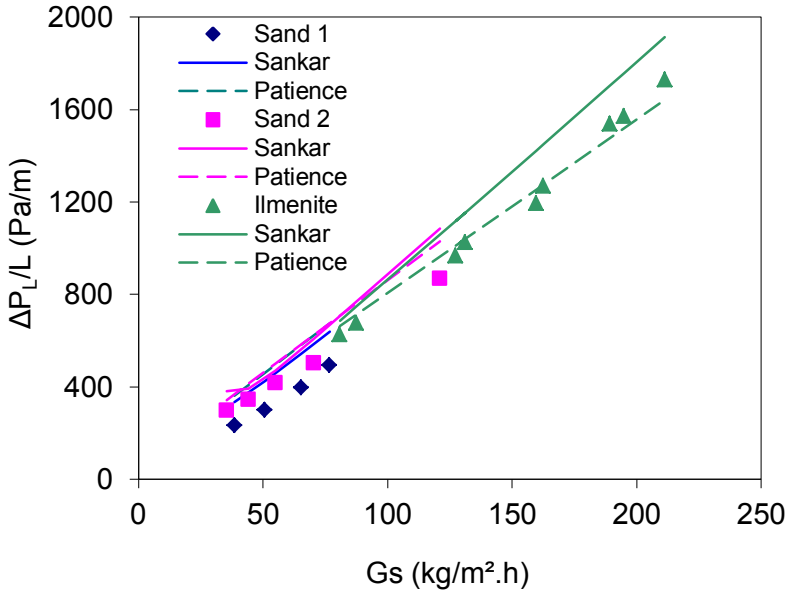

Figure 4.6: Comparison of the model pressure drop prediction versus the experimental results obtained in the cold flow prototype with the solid velocity calculated by correlations of Sankar and Smith [247] and Patience et al. [250].

4.4.4 Pressure Drop in the Horizontal Conveying Line and the Blinded Tee Bend

Solids leaving the lift are lead to a horizontal dilute phase conveying line through a blinded tee bend (T-Bend). The phenomenon in the T-Bend is an initial vertical deceleration and then an horizontal reacceleration of the solid particles [252]. There exist different correlations to describe bends pressure drops in the literature [253-255]. Different existing correlations were tested in the current study. The simple relation developed by reference demonstrated a good fit with the experimental results:

$$\Delta P_b = 2 f_b \overline{\rho} U_g^2 \qquad \textbf{Eq. 4.29}$$

The value for f_b factor was given as a function of the curvature ration (ratio of bend radius to pipe diameter). No factor was available for T-bend. Therefore, f_b was calculated based on the least square curve fitting method. The resulting factor was 0.495 compared to 0.375 for a radius bend with a curvature ratio of 2. This seems reasonable since the T-bend has a higher curvature compared to the radius bends. The pressure drop in the horizontal conveying line is then calculated as:

$$\frac{\Delta P_{HC}}{L} = \frac{2 f_s v_s^2 (1-\varepsilon)\rho_s}{D} + \frac{2 f_g v_g^2 \varepsilon \rho_g}{D} \qquad \textbf{Eq. 4.30}$$

The solid real velocity was then calculated based on the equation proposed by IGT [246]:

$$\frac{V_P}{V_g} = 1 - 0.68 d_P^{0.92} D^{-0.54} \rho_P^{0.5} \rho_g^{-0.2} \qquad \textbf{Eq. 4.31}$$

The solid and gas friction factors (f_s and f_g) were calculated similar to the lift (see section 4.4.3). The resulting pressure drop predictions versus the experimental results are illustrated in the Figure 4.7.

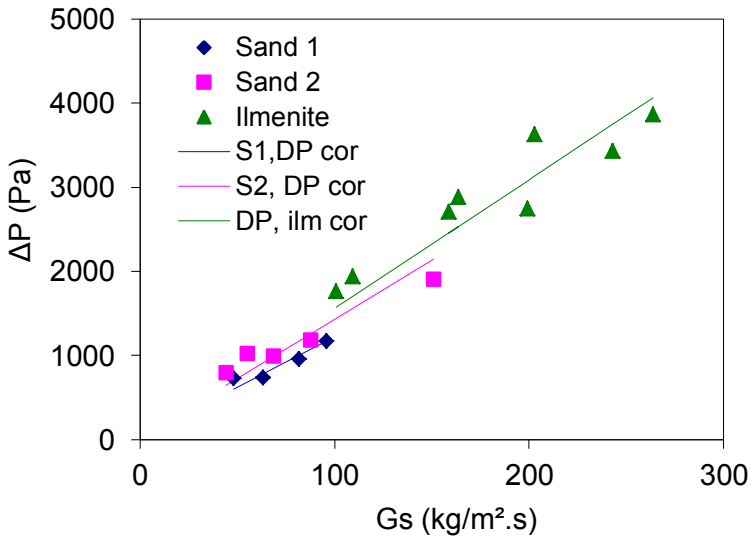

Figure 4.7: The comparison of the pressure drop prediction in the T-bend and the horizontal conveying line versus experimental results ($R^2 = 0.98$).

4.4.5 Cyclone Pressure Drop

Pressure drop in the cyclone is the result of different physical phenomena happening in the cyclone. According to Knowlton [256] these phenomena include: gas contraction ($\Delta P_{(f\text{-}i)g}$), solid acceleration ($\Delta P_{(f\text{-}i)p}$), barrel friction (ΔP_{bf}), gas reversal (ΔP_r) and gas contraction at the cyclone exit (ΔP_o). The formulas and correlations to calculate each of these terms are listed in appendixes 7. Cyclone pressure drop can be calculated for different pathways in the cyclone as illustrated in Figure 4.8. Proper pressure drop terms should be taken into account in each case. Pressure drop between solid entrance and exit is:

$$\Delta P_{Cyc,s} = \Delta P_{(f-i)g} + \Delta P_{(f-i)p} + \Delta P_{bf} \qquad \textbf{Eq. 4.32}$$

For gas entrance and exit:

$$\Delta P_{Cyc,g} = \Delta P_{(f-i)g} + \Delta P_{(f-i)p} + \Delta P_{bf} + \Delta P_r + \Delta P_o \qquad \textbf{Eq. 4.33}$$

And pressure drop between gas and solid exit of cyclone is:

$$\Delta P_{Cyc,g-s} = \Delta P_o + \Delta P_r \qquad \textbf{Eq. 4.34}$$

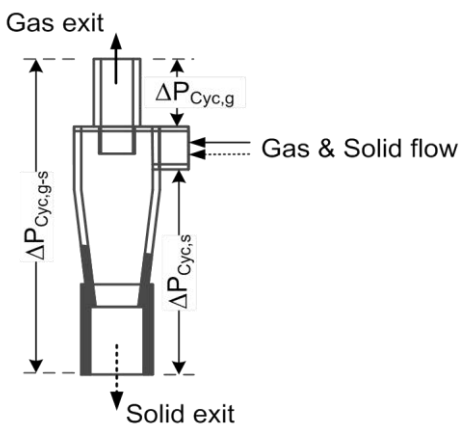

Figure 4.8: Flow of solid and gas in the cyclone and different possible pressure drops.

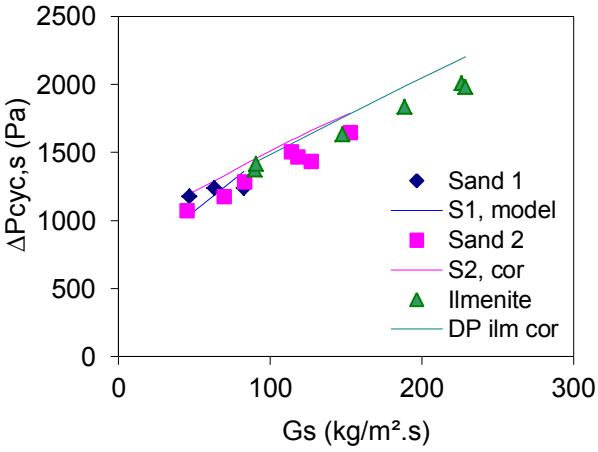

Figure 4.9: Comparison of the experimental and model pressure drop prediction for the solid exit of the cyclone in the cold flow prototype.

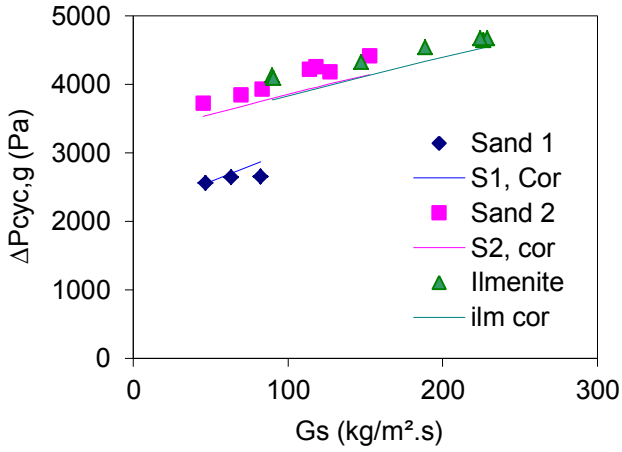

Figure 4.10: Comparison of the experimental and model pressure drop prediction for the gas exit of the cyclone in the cold flow prototype.

4.4.6 Pressure Drop in the Supply chamber of the Loop-Seal

Pressure drop across the supply chamber (standpipe) in the loop-seal is a dependent variable similar to the standpipe of the L-valve. A non-fluidized solid bed is formed in the supply chamber to balance the pressure across the solid-circulation loop. The height of this bed is adjusted, based on the imposed pressure drop on the standpipe and the relative gas-solid slip velocity. The bed of the solids creates a barrier against the gas flow and results in the gas-tightness. Solid flow in the supply chamber of the loop-seal is similar to the L-valve. The only difference is the height of the solid bed which is fixed in the L-valve and variable in the loop-seal. According to the pressure balance Equation (4.3), pressure drop across the supply chamber in the loop-seal is:

$$\Delta P_{SC} = -(\Delta P_{Cyc,g-s} + \Delta P_{HP} + \Delta P_{RC} + \Delta P_{RP} + \Delta P_{DR2}) \qquad \textbf{Eq. 4.35}$$

In a stable operation, pressure drop along the supply chamber is positive, i.e. the pressure is higher in the bottom of the supply chamber. This pressure difference across the supply chamber results in formation of a solid bed the result of which is gastightness.

The gas flow in the horizontal pipe (Q_{HP}) is calculated from the correlation between the solid and gas flow in the horizontal section of the loop-seal (see section 4.4.9). Therefore:

$$Q_{HP} = f(Gs) \qquad \textbf{Eq. 4.36}$$

The gas flow rate through the supply chamber is then calculated by a simple material balance around the elbow of the loop-seal, as:

$$Q_{SC} = Q_{HP} - Q_{Ss} \qquad \textbf{Eq. 4.37}$$

Therefore, the gas fraction coefficient in the loop-seal (δ_{ls}) is:

$$\delta_{ls} = \frac{Q_{SC}}{Q_{Ss}} \qquad \textbf{Eq. 4.38}$$

The value of δ_{ls} could be either negative or positive depending on the gas flow direction in the supply chamber. Therefore, δ_{ls} is calculated for each specific condition in this model. However, Cheng and Basu [257] considered a fixed value of 0.095 for δ_{ls}.

The height of the solid bed in the supply chamber is then calculated from the pressure drop and gas flow rate. Ergun equation modified for slip velocity is used to calculate the pressure drop per unit length of the solid bed in the supply chamber. Therefore:

$$\frac{\Delta P}{L} = 150.\frac{\mu_f v_{sl}}{(\phi.d_p)^2}.\frac{(1-\varepsilon)^2}{\varepsilon^2} + 1.75.\frac{\rho_f v_{sl}^{\ 2}}{\phi.d_p}.\frac{(1-\varepsilon)}{\varepsilon} \qquad \textbf{Eq. 4.39}$$

Then, the height of the solid column is:

$$L_{SC} = \frac{\Delta P_{SC}}{\Delta P_{SC}/L} \qquad \textbf{Eq. 4.40}$$

4.4.7 Recycle Chamber Pressure Drop

Solid particles in the recycle chamber are in bubbling/ slugging fluidization regime with the gas velocity above the minimum fluidization velocity of the biggest particles in the system according to [244]. Therefore, solid flow in this element is a vertical dense phase pneumatic conveying [152]. Pressure drop in the recycle chamber is composed of the four main elements already explained for vertical dilute phase conveying (section 4.4.3). However, frictional pressure drops can be neglected in this system with voidage below 0.85 [258]. The acceleration terms are also negligible due to small velocities. Consequently, the dominant pressure term is the gravity forces due to particles weight. Therefore, in integrated form:

$$\Delta P_{RC} = \rho(1-\varepsilon_{RC})gh_{RC} \qquad \textbf{Eq. 4.41}$$

Basu and Fraser [259] have considered a constant voidage of 0.5 in this section. This can represent pressure drop if gas flow velocity in the recycle chamber remains close to minimum fluidization conditions. However, in the current study a constant gas flow rate was applied in the recycle chamber regardless of variation of the solid flow rate. It was observed that pressure drop is a strong function of the solid flow rate in the current system, as presented in the chapter 3. This indicates dependence of the voidage of the fluidized bed in the recycle chamber to solid flux. Monazam et al. [123] have developed a correlation between the pressure drop and solid flux in the recycle chamber for group B particles. However, this correlation failed to predict the pressure drop in the current system. Accordingly, the variation of the bed voidage in the supply chamber was correlated based on the experimental results in the current study.

Results of this study demonstrate a dependence of the pressure drop on the solid flow rate. Increase of solid flow rate increased the pressure drop in the recycle chamber suggesting a decrease of the bed voidage in this section. Different possibilities were considered to model the bed voidage variation in the recycle chamber. First, two phase theory of the bubbling fluidized bed [153,169] was employed using the Werther equation [260] for bubble size diameter and slugging bubble rise velocity calculated either by Davidson (bubbling bed) or Steward and Davidson (slugging bed) [261]. However, this method failed to well predict the pressure drop variation in the recycle chamber as illustrated in the Figure 4.11. This approach is highly dependent on the gas flow rate in the recycle chamber which does not correspond to present experimental findings. Moreover, the loop-seal in the current system has a small diameter. This limits the bubble diameter and can have considerable effect on the regime change in the recycle chamber. The slugging regime is highly probable in this section based on the criteria explained in the appendix 5. The turbulent regime is less probable according to Bi and Grace [230]. However, the visual observations during the experiential test revealed behaviour similar to bubbling to turbulent fluidized compared to the slugging system.

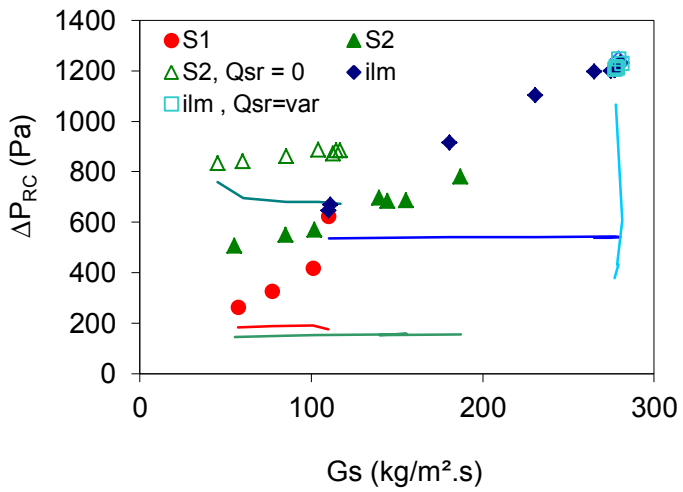

Figure 4.11: Modelling result for pressure drop in the recycle chamber based on the two phase theory to calculate the bed voidage.

A specific correlation was therefore developed based on the experimental results to model the voidage of the fluidized bed in the recycle chamber as a function of the solid flow rate across it:

$$\varepsilon_{RC} = 1 - 0.171\varepsilon_{mf} - 0.918\frac{U_s}{\sqrt{g.D}} \qquad \textbf{Eq. 4.42}$$

Using this correlation, pressure drop is calculated as in the section 4.4.8. The resulting pressure drop prediction is illustrated in Figure 4.12. The correlation results are acceptable for a wide range of pressure drop variation for sand 2 and ilmenite. However, the results for the sand 1 overestimate the experimental results for about 20%. This is however acceptable in the current study regarding uncertainties imposed by experimental conditions of sand 1 particles and the small contribution of this term in the overall pressure balance.

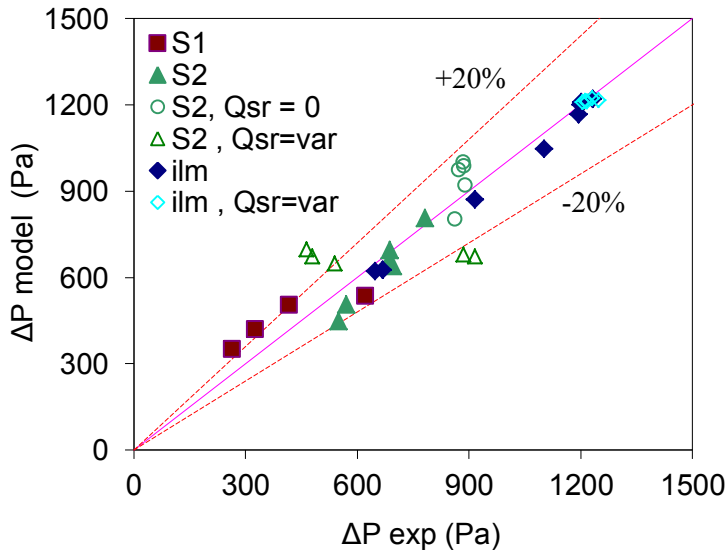

Figure 4.12: Pressure drop prediction in the recycle chamber using the variable voidage described by correlation 4.42.

4.4.8 Recycle Pipe Pressure Drop

Recycle pipe leads the overflow of solids from the recycle chamber into the fluidized solid bed in the reactor. The solid flow in this section has a complex behavior due to specific aspects of the recycle pipe flow as: low gas velocity, inclined pathway of pipe, effect of the gravity and friction, high solid saltation on the bottom of pipe, short flow pathway and non uniform solid feeding into the pipe (over flow from recycle chamber). The pressure drop in the recycle pipe can be calculated based on the conventional pressure drop in the downers [118,262,263]. Therefore:

$$\left(\frac{dP}{dz}\right)_{RC} = \left(\frac{dP}{dz}\right)_{gas-wall\ friction} + \left(\frac{dP}{dz}\right)_{solid-wall\ friction} + \left(\frac{dP}{dz}\right)_{acceleration} - \left(\frac{dP}{dz}\right)_{gravity} \quad \textbf{Eq. 4.43}$$

Acceleration and gravity terms are composed of two terms for gas and solid phase. However, due to low gas velocity and short transport distance, gas acceleration and gravity terms can be neglected. Therefore, the integrated form of this equation is:

$$\Delta P_{RC} = \frac{2 f_g \rho_g U_g^2 L_{RP}}{D_{RC}} + \frac{2 f_s G_s U_s L_{RP}}{D_{RC}} + G_s u_s - \rho_s (1-\varepsilon) g L_{RP} \sin\theta \quad \textbf{Eq. 4.44}$$

Gas friction factor is calculated using equations given by Kunii and Levenspiel [153] similar to the lift, Eq. 4.25 and Eq. 4.26. To find a relation between the gas – solid velocity, a simple force balance equation on a single particle was developed as [262]:

$$\Sigma F = m_P.a_P = \rho_p.Vol_P \frac{\partial V_P}{\partial t} = \frac{1}{2}\rho_g \left|V_g - V_P\right|\left(V_g - V_P\right) A_X C_D + (\rho_P - \rho_g).Vol_P.g \quad \textbf{Eq. 4.45}$$

With [264]:

$$C_D = \frac{18.5}{\mathrm{Re}_P^{0.6}} \quad \textbf{Eq. 4.46}$$

The average solid velocity was calculated based on this force balance for a solid at height of H/2. Cheng and Basu [257] have used a constant value of 2.9 as a best fitted value for the solid friction factor. However, in this study, a friction factor correlation was developed based on the general form proposed by Weber [265]. It should be noted that this procedure does not take into account all the involving phenomena in the recycle pipe for calculation of the solid velocities. The solid – wall and friction effect and solid – solid interaction effects has to be taken into account for a better estimation. However, it was assumed that the developed solid friction factor will take into account this shortage.

The experimental results presented in the chapter 2 suggest that the pressure drop in the recycle pipe is not a function of the solid properties neither gas flow rate across the recycle chamber. However, solid flux across the recycle pipe demonstrated to affect the pressure drop. Based on these results, a novel solid friction factor was developed. Weber [265] proposed a general form of friction factor as:

$$f_s = K\mu^a Fr_g^b Fr_s^c \left(\frac{D}{d_P}\right)^d \quad \textbf{Eq. 4.47}$$

Where μ stands for solid loading factor (kg solid divided by kg gas), Fr_g and Fr_s are the Fraud numbers calculated respectively for gas and solid superficial velocities. The final friction correlation based on the general form is:

$$f_s = 0.35\mu^{-0.17} Fr_s^{-1.8} \quad \textbf{Eq. 4.48}$$

Using this friction factor, the resulting pressure drop calculation is illustrated in Figure 4.13.

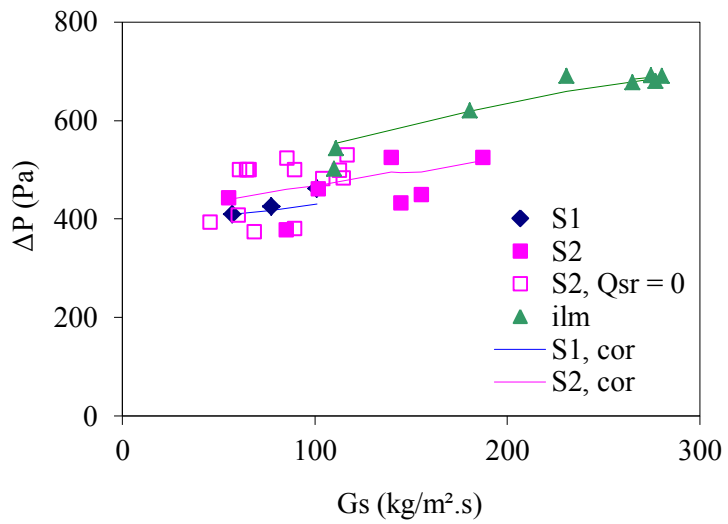

Figure 4.13: Comparison of the experimental and predicted pressure drop in the recycle pipe of the loop-seal for different particles in the cold flow prototype.

4.4.9 Solid Flow in the L-valve and the Loop-Seal

Solid flow rate correlations available in the literature for horizontal solid flow in the L-valve are listed in Table 1.3. Figure 4.14 illustrates the solid flux calculation results of the existing correlations with closest prediction for the current study. Most of the presented correlations are developed based on the L-valve external aeration except the correlation of Yang and Knowlton [102] who consider no slip condition (U_{sl} =0) in the standpipe. This assumption improves prediction. However, this assumption is limited to the high flux operations. In cases of low solid fluxes or high pressure across the standpipe, especially for particles of large size, this hypothesis is less convincing. Moreover, results of the current study demonstrated that the quantity of the gas in the standpipe of the L-valve can change considerably for a given L-valve external aeration rate. In the other hand, empiricism in the development of the correlations requires cautiousness in application in the ranges other than their original development conditions.

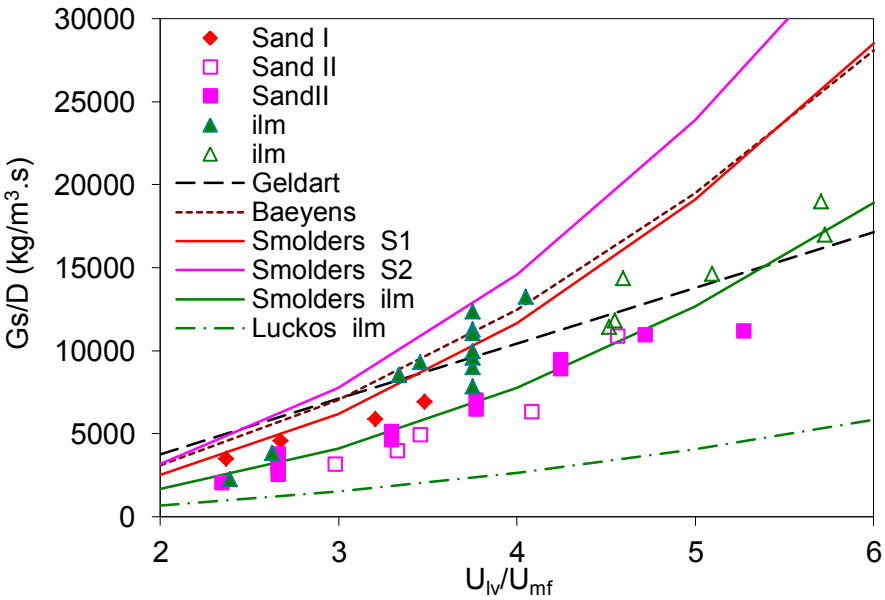

Figure 4.14: Prediction of the experimental solid flow rate with correlations developed by Baeyens [98] Geldart [92], Smolders [97], and Luckas [100] (Luckas correlation for the sand 1 & 2 are not presented in the graph since the correlation considerably overestimated the results).

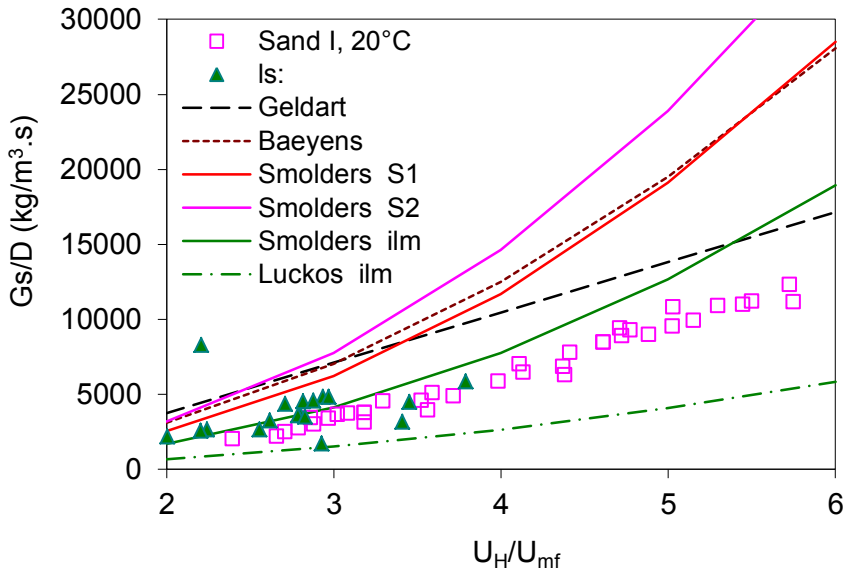

Figure 4.15: Prediction of the experimental solid flow rate with correlations developed by Baeyens [98], Geldart [92], Smolders [97], and Luckas [100] versus gas flow velocity around the bend of the L-valve (Luckas correlation for the sand 1 & 2 are not presented in the graph since the correlation considerably overestimated the results).

The correlations developed by Smolders [97] and Geldart [92] result in closest predictions to the current experimental results. Comparison of Figure 4.14 and Figure 4.15 illustrates that expressing results for gas flow rate around the elbow of the L-valve shrinks the experimental results on the same curve. Accordingly, a novel correlation was developed in the current study based on the actual gas flow around the elbow of L-valve. This correlation is not depending upon pressure balance. Different possible influencing parameters were identified from references [90,92,93,97,104] and proper dimensionless parameters were formed considering the π-theorem [266], as:

$$Re_{pipe}\,,\ Fr_g,\ Fr_s,\ Ar,\ \frac{\rho_s}{\rho_g}\,,\ \frac{d_p}{D}\,,\ \frac{U_g}{U_{mf}}\,,\ \frac{U_g}{U_t}\,,\ \frac{G_s}{\rho_s U_{mft}} \qquad \textbf{Eq. 4.49}$$

Most of the literature correlations are based on the Gs/D_{lv} versus U_g/U_{mf} [92,97-100]. This approach was verified in this study by comparing the different terms listed above and it was found to be the best relation**.** The solid flux versus the gas flow normalized to Umf around the elbow of the L-valve and the loop-seal are plotted in Figure 4.16 and Figure 4.17. These illustrate that plotting the flux versus the fluidization number in the elbow (horizontal section), shrinks the curves of different solids on an identical line. The results show a linear relation between the flux and the fluidization number (U/Umf) in the horizontal section rather than quadratic relation developed in some of the literatures [97,98,100]. It should be noted that the configuration of the experimental system effects the L-valve operation, as discussed previously.

Comparison of the results in Figure 4.16 and Figure 4.17 illustrate that the correlations in the L-valve and the loop-seal are not identical while both have similar trends. The solid flux divided by the diameter of the L-valve or loop-seal (Gs/D) is plotted in Figure 4.18. The resulting correlation show similar trend and this plotting method does not show a significant amelioration. The final correlation used in the current model was a linear relation similar to the correlation of Geldart and Jones [92]:

$$G_s = 48.1\left(\frac{U_{lvH}}{U_{mf}}\right) - 83.6 \qquad \textbf{Eq. 4.50}$$

Linear form of the solid flux (Gs= a (U/Umf)+b) with an intercept, b, seems to be physically close to what happens in the L-valve. The external aeration into the L-valve needs to be superior to a minimum threshold value for the solid flow to initiate. This can be explained based on the force balance.

Particles start to move once the gas – solid friction force overcomes the static shear force between the particles and walls. Equally this can be explained based on the angle of internal friction of the solid particles in the L-valve. The length of the horizontal section in the L-valve is longer than the distance freely covered by the particles. Therefore, an external aeration is required to decrease this angle and let particles to move along the horizontal section. This phenomenon can be well observed in the Figure 4.16 and Figure 4.17 for the L-valve and the loop-seal. The longer length of the horizontal section and smaller pipe diameter results in higher threshold value for the L-valve compared to the loop-seal. The literature results demonstrate that this threshold value increases with increase of particle diameter [90,92,104], higher particle density [90,104], increase of diameter of vertical section, slight effect diameter of horizontal section and negligible effect of horizontal section length [90].

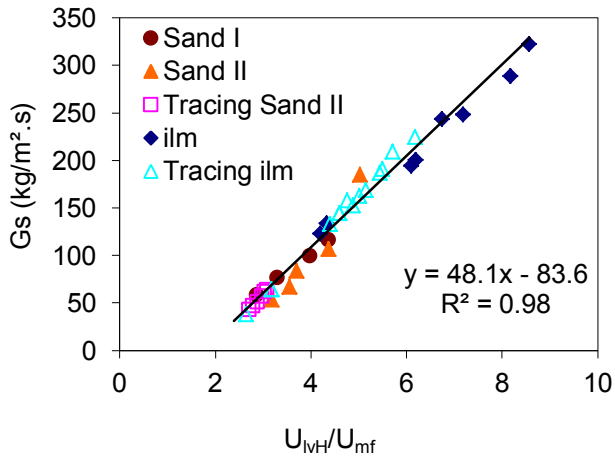

Figure 4.16: Solid flux versus the gas flow rate around the elbow of the L-valve for three solids in the cold flow prototype.

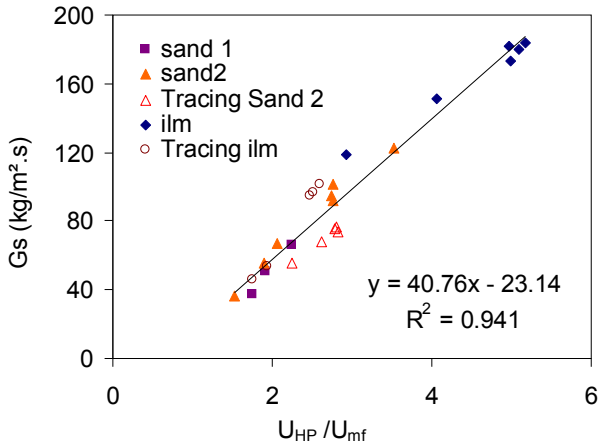

Figure 4.17: Solid flux versus the gas flow rate in the horizontal pipe of the loop-seal for three solids in the cold flow prototype.

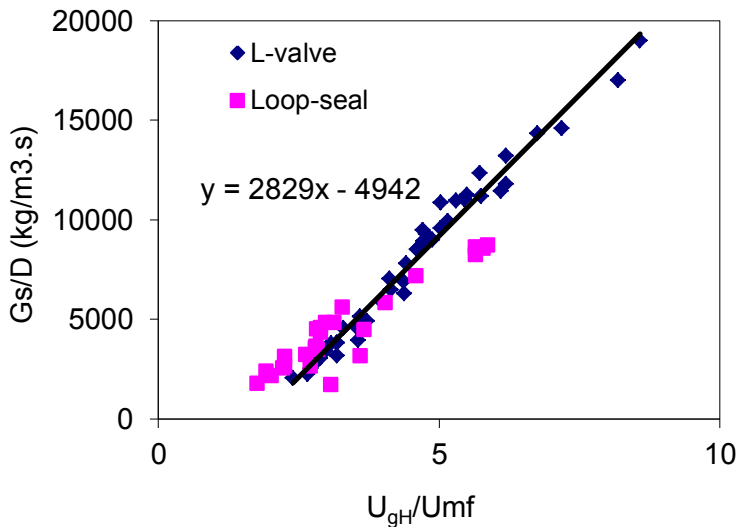

Figure 4.18: Solid flux divided by diameter versus the fluidization number in the horizontal sections of the loop-seal and the L-valve.

4.4.10 Pressure Drop in Horizontal Flow

The solid flow in the horizontal sections of the L-valve and the loop-seal is in dense phase horizontal pneumatic conveying mode. Several correlations have been developed to predict the pressure drop in this kind of flows [130]. Moreover, different researches have been carried out to correlate the pressure drop in the horizontal section of the L-valve. List of some of the existing correlations applicable to this section are tabulated in the Table 1.4. Figure 4.19 illustrates the prediction result of some of the existing correlation compared to the experimental results obtained in the current study. As shown in Figure 4.19, the range of prediction is wide from one correlation to another. Based on our results, the best correlations are the ones proposed by Werner [267], Luckos [100], and Arena et al. [104].

The pressure drop in the horizontal section of the loop-seal was also compared with the existing correlations. The results are illustrated in Figure 4.20. More dispersion is observed in this case compared to the L-valve. Based on the current results, the best correlations are those proposed by Werner [267], Luckos [100], and Arena et al. [104]. However, the accuracy of these correlations is not as good for the loop-seal compared to the L-valve. Luckos equation has a dimensional form including effect of solid flux, particle diameter and density as:

$$\frac{\Delta P_{lv,H}}{L_{lv,H}} = 0.115 \frac{Gs^{0.137}}{\rho_b^{0.131} d_P^{0.64}} \qquad \textbf{Eq. 4.51}$$

And the Werner equation [267] is an dimensionless equation developed for the solid flow rate in an horizontal pipe as:

$$\frac{\Delta P_{lv,H}}{L_{lv,H}} = \left(\frac{1}{1 + \frac{\rho_s C_{mk}}{\mu \rho}} \right) \rho_s g(\lambda + \sin\theta) \qquad \textbf{Eq. 4.52}$$

Where θ stands for the inclination of the pipe ans:

$$\lambda = (0.25 + 7.82 \times 10^{-5} \mu Fr_s) \left(\frac{d_m}{D} \right)^{C1} \left(\frac{d_s}{d_m} \right)^{C2} \qquad \textbf{Eq. 4.53}$$

And

$$C_{mk} = 921 (\mu Fr_s)^{-0.59} \left(\frac{d_m}{D} \right)^{C3} \left(\frac{d_s}{d_m} \right)^{C4} \qquad \textbf{Eq. 4.54}$$

With the Ci exponents being the adjusting parameters with the values of -0.15, 1.043, 0.3 and -0.2 in the current model compared to the original published values of -0.3, 0.2, 0.3, and -0.2.

The principle of the solid circulation model and the employed equations to model behaviour of each section of model was presented above. The literature equations were compared with experimental results of the current study to select the best equation available in each case. Moreover, some correlations were developed in this study to model the variation of the bed voidage in the recycle chamber, friction factor in the recycle pipe and solid flow rate in the L-valve and loop-seal versus gas flow rate around the elbow of the L-valve.

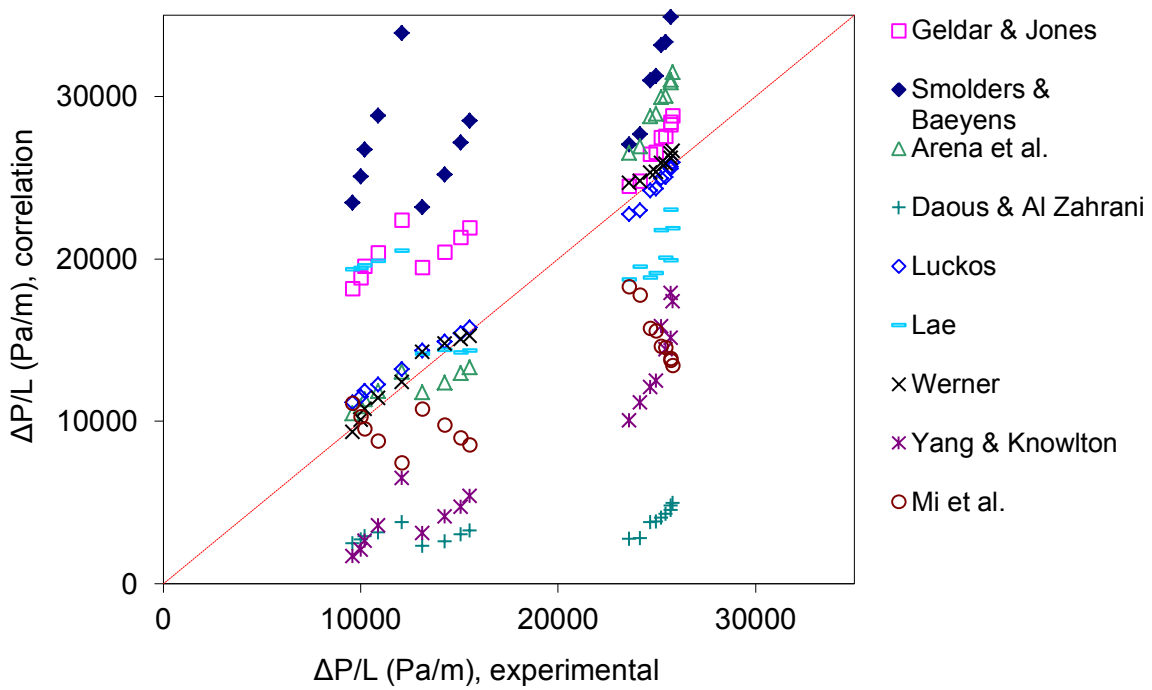

Figure 4.19: Prediction of the pressure drop in the L-valve by correlations of Geldart [92], Arena et al. [104], Smolders and Baeyens [237], Daous [268], Luckas [100], Lae F. [105], Werner [267], Yang and Knowlton [102], and Mi et al. [269].

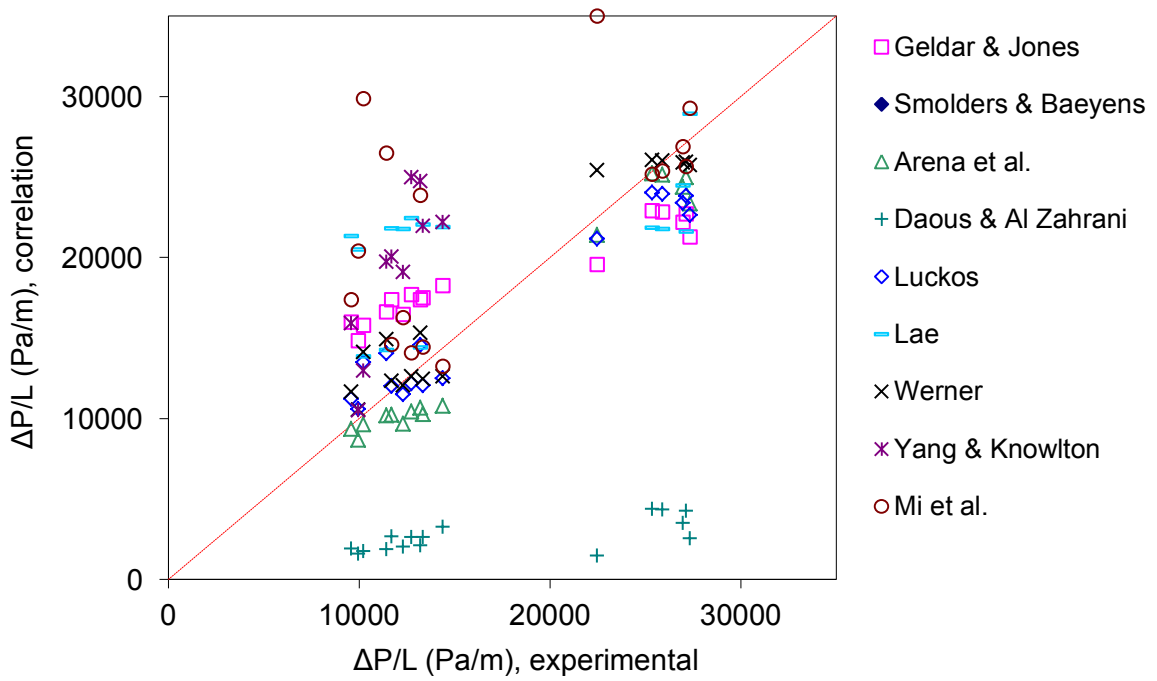

Figure 4.20: Pressure drop prediction in the horizontal pipe of the loop-seal by different existing correlation listed in the figure.

4.5 Model Validation

4.5.1 Model Results, Solid Flow Rate

Model predictions of solid flow rate for three solids in the cold flow prototype are compared with experimental results in Figure 4.21. The model demonstrates an acceptable prediction with an error less than 15%. It should be noted that the key parameter in solid flow rate prediction is the solid flow

rate correlation for the horizontal section of the L-valve and calculation of the quantity of the gas passing through this section. Therefore, the more accurate the correlations, the better the prediction result of the model.

Similarly, the modelling results are compared with experimental results obtained in the high temperature pilot plant with oxygen carriers at 390 °C and 750 °C. The model results in a reasonable prediction. However, the modelling results are more sensitive to temperature variation compared to the experimental findings. As explained above this is mostly related to the solid flow rate correlation in the L-valve and effect of U_{mf} which is the only variable to take into account the parameters variation.

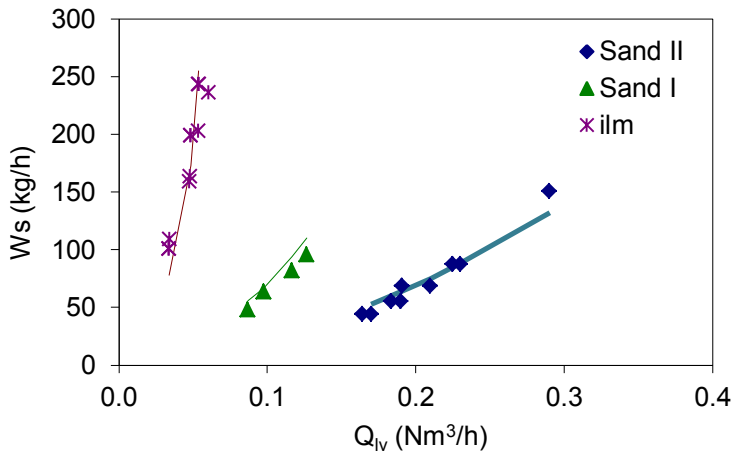

Figure 4.21: Solid flow rate prediction of the model for different aeration rates of the L-valve, with H_R = 0.5 m. The other operating conditions are listed in the Table 4.2.

Table 4.2: Operating conditions of the experimental tests presented in Figure 4.21.

	Sand I		Sand II		ilmenite	
	Q (mn3/h)	**U (m/s)**	**Q (mn3/h)**	**U (m/s)**	**Q (mn3/h)**	**U (m/s)**
R1	2.10	0.074	3.59	0.127	1.68	0.059
R2	2.05	0.072	3.58	0.126	1.61	0.057
L1	6.78	5.4	8.46	6.8	8.46	6.8
L2	6.62	5.3	8.54	6.9	8.54	6.9
S1r	0.43	0.131	0.43	0.131	0.289	0.088
S2r	0.41	0.126	0.45	0.137	0.287	0.088

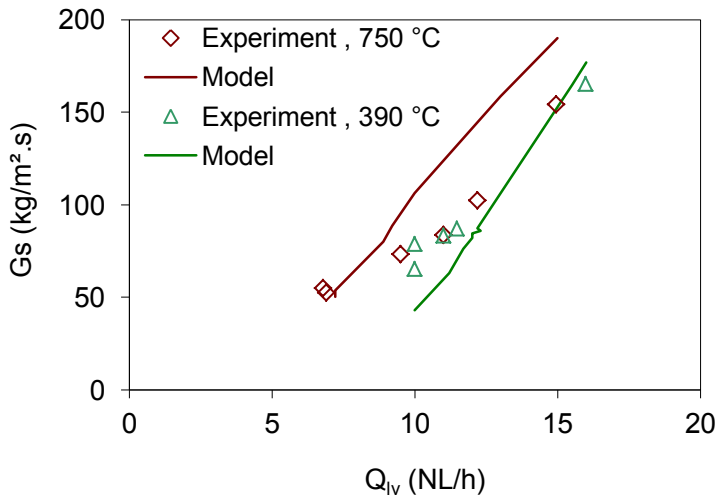

Figure 4.22: Model prediction of the solid flow rate actuated in the high temperature pilot plant at 390 °C, and 750 °C.

Table 4.3: Operating conditions of the pilot plant corresponding to the results presented in Figure 4.22, identical aerations were applied for all three circulation lines.

	390 °C		750 °C	
	Q (Nm^3/h)	U (m/s)	Q (Nm^3/h)	U (m/s)
R1	0.5	0.025	0.5	0.039
R2, R3	0.5	0.043	0.5	0.066
L1, L2, L3	2.5	5.37	1.6	5.30
S1r, S2r, S3r	0.1	0.38	0.1	0.59

4.5.2 Model Results, Height of Solid Column in the Supply Chamber of the loop-seal

Calculation of the solid height in the supply chamber of the loop-seal is highly sensitive to the quantity of the gas passing thought this section. Gas velocity in this section affects directly the pressure drop per unit length calculated by Ergun equation. In addition, it affects the pressure drop indirectly through variation of the solid bed voidage which is a function of gas – solid slip velocity. The key relation to calculate the gas flow rate in the supply chamber is the correlation between solid and gas flow rate in the horizontal pipe as explained in the section 4.3.

The model prediction of the height of the solid column in the supply chamber of the loop-seal is illustrated in the Figure 4.23. The model gives a reasonable prediction versus the experimental results with sand 2 and ilmenite. The experimental results of the solid height in the recycle chamber for sand I have not been considered since they are not reliable enough to make a conclusion. This was mostly due to the strong electrostatic effects observed during the experiments. This imposed an oscillatory solid level in the supply chamber and made it impossible to find a constant solid height.

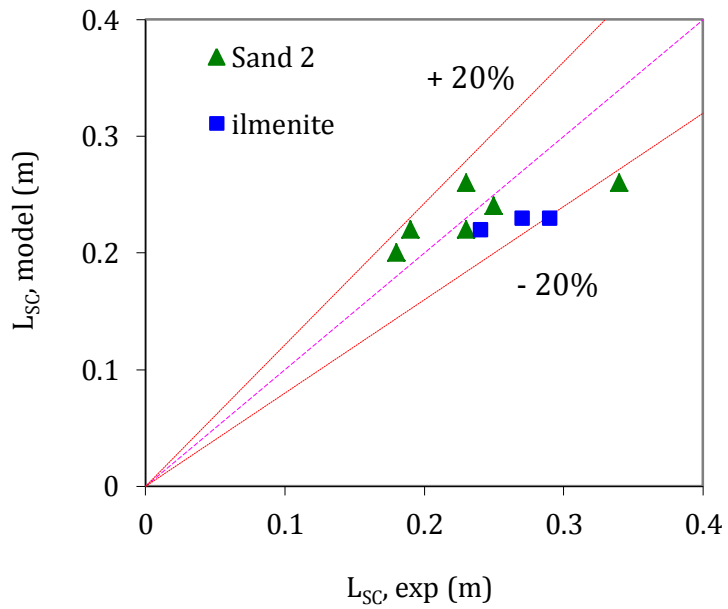

Figure 4.23: Prediction of the solid height in the standpipe of the loop-seal by model. Model results were obtained while all affecting parameters were adjusted to be identical with experimental results including: solid flow rate, solid height in the reactor and aeration rate into the loop-seal.

4.5.3 Model Results, Pressure Variation Loop

Model prediction results for gage pressure variation across the solid circulation loop are presented in this section both for the cold flow prototype and the high temperature pilot plant. Experimental and corresponding modelling results are illustrated in Figure 4.24 to Figure 4.28. The most significant differences observed between model and experiment is for sand 1 particles in the cold flow prototype. This is probably due to the electrostatic effects which are ignored in the model. It should be noted that errors are accumulative in this kind of curves; the error in each point is sum of the individual errors in the preceding points.

The modelling and experimental pressure variation loops in the cold flow prototype are illustrated in Figure 4.24 to Figure 4.26 for sand I, sand II and ilmenite. Experimental results in the cold flow prototype were obtained during two successive experimental runs, due to a limited number of pressure gauges available. In a first run, eight pressure drop for the first loop were measured with a given gas flow rate into the L-valve. In a second run, the pressure measurement gauges were connected into the second loop and pressure drops were measured for identical operating conditions. While the operating conditions were controlled to be similar during the two corresponding runs, changes in results were unavoidable. Therefore, a difference up to 8 % existed in experimental solid mass flow rate between corresponding runs. This was more noticeable in the case of ilmenite with rather low aeration rates (Q_{lv}=0.03 - 0.06m^3/h). In this case, a small change in aeration could result in a considerable variation in solid circulation rate. However, for sand 2 particles, the impact of the experimental procedure was less significant due to the higher aeration flow rates in the L-valve (Q_{lv}=0.15 – 0.3m^3/h).

The modelling versus experimental pressure loop results for the high temperature pilot plant are illustrated in Figure 4.27 and Figure 4.28 with NiO/NiAl2O4 particles. It should be mentioned that less pressure measurement gauges were installed in the pilot. Moreover, all of the measurements were carrier simultaneously during a steady state operation. According to the presented results, model provides an acceptable prediction. The comparison of the experimental and modelling results were based on the solid flow rate in the system and not the external L-valve aeration. Therefore, in each case L-valve aeration in the model was adjusted in a manner to have identical solid flow rates with the experimental results.

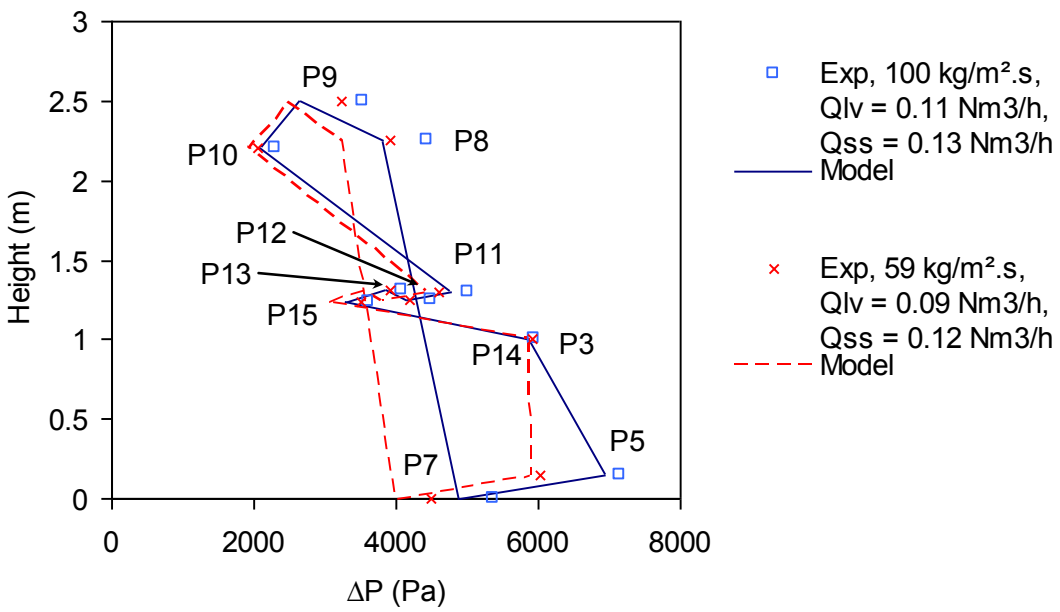

Figure 4.24: Experimental and modelling results of gage pressure variation across the solid circulation line from reactor R1 to R2 in the cold flow prototype for sand 1 particle. The pressure drop measurement points are illustrated in Figure 2.1.

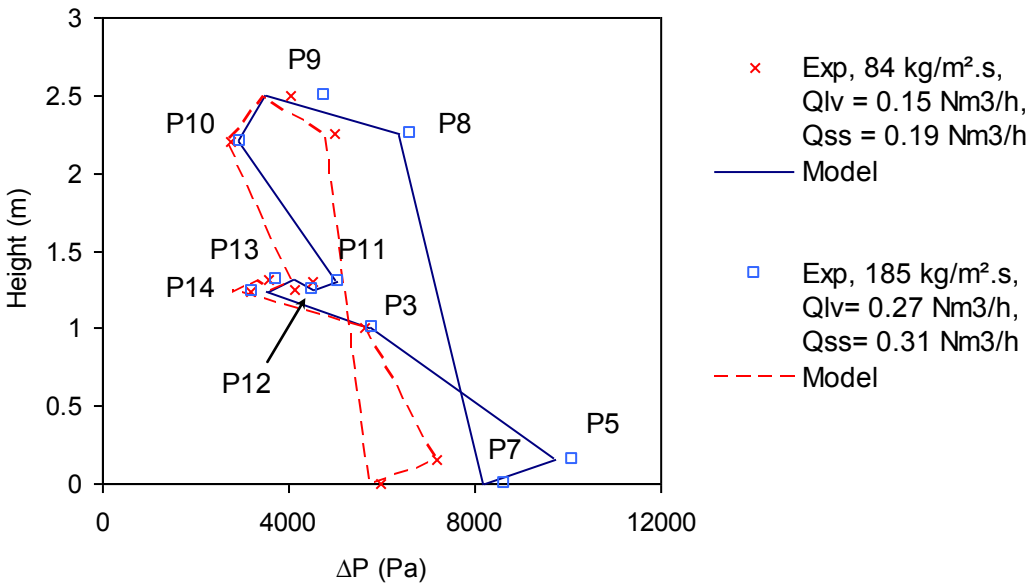

Figure 4.25: Modelling and experimental results of pressure variation loop across the cold flow prototype for sand 2 particles in the cold flow prototype. The pressure drop measurement points are illustrated in Figure 2.1.

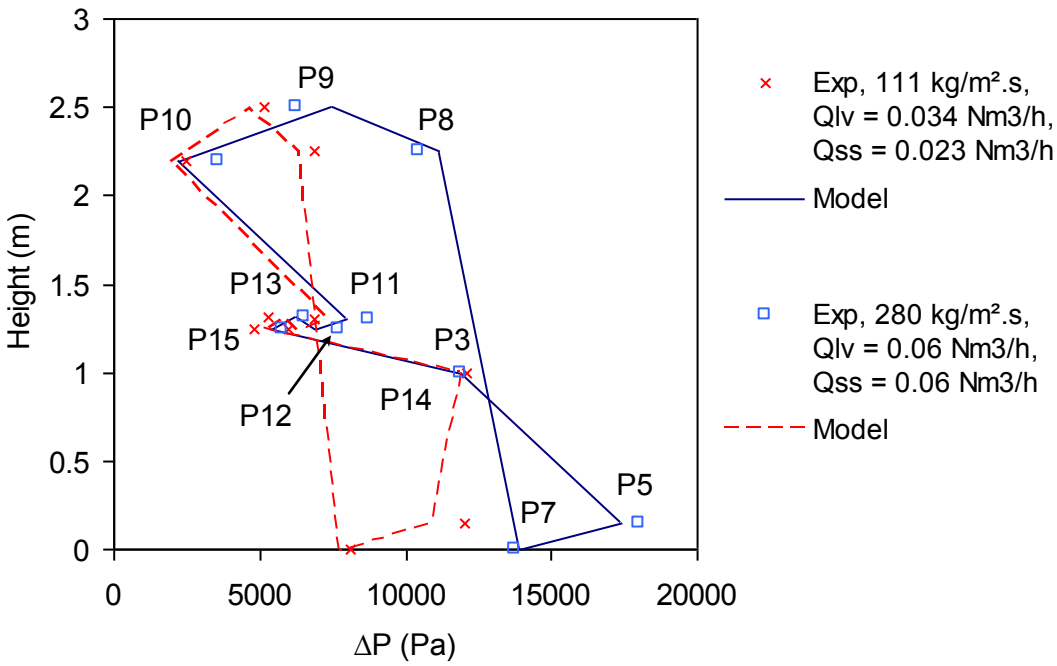

Figure 4.26: Pressure loop variation across the solid circulation loop predicted by model versus experimental results for ilmenite particles in the cold flow prototype. The pressure drop measurement points are illustrated in Figure 2.1.

Table 4.4: Operating conditions for Figure 4.24 to Figure 4.26.

	Ilmenite	Sand 2	Sand 1
Q_R (Nm^3/h)	1.68	3.59	2.1
Q_L (Nm^3/h)	8.46	8.46	6.8
Q_{Sr} (Nm^3/h)	0.29	0.43	0.43

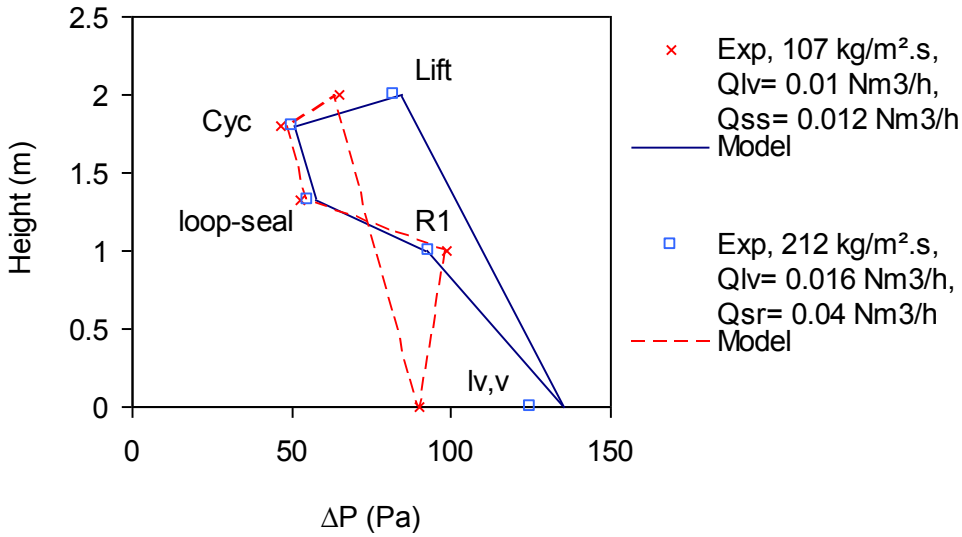

Figure 4.27 : Modelling and experimental results of pressure variation loop across the high temperature pilot plant for Nickel based oxygen carriers at about 400°C, Q_L = 2.5 Nm^3/h, Q_{R1} = 0.5 Nm^3/h, Q_{sr} = 0.1 Nm^3/h.

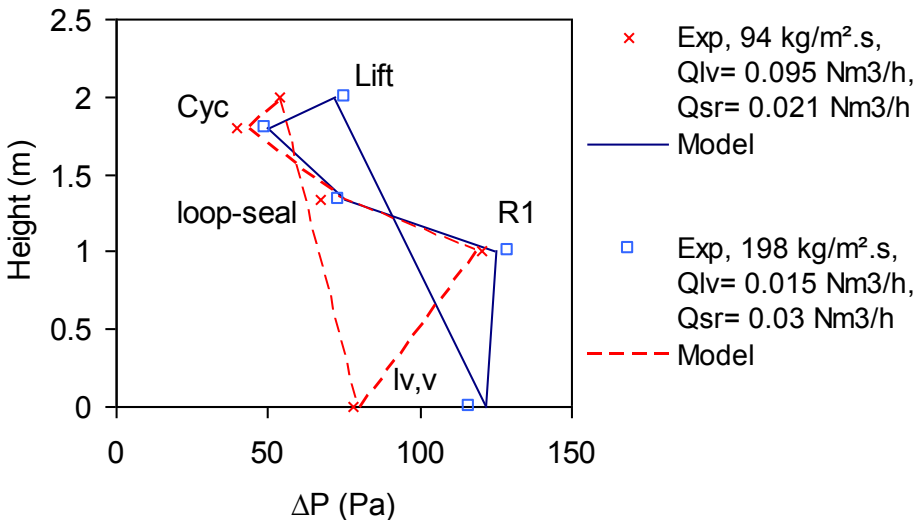

Figure 4.28 : Modelling and experimental results of pressure variation across the high temperature pilot plant for Nickel based oxygen carriers at about 750 °C, Q_L = 1.6 Nm^3/h, Q_{R1} = 0.5 Nm^3/h, Q_{sr} = 0.1 Nm^3/h.

Experimental results presented in chapter 3 illustrated that the pressure drop in the reactor have a significant effect on solid flow rate actuated in the L-valve of the current system. Accordingly, model response to the variation of pressure drop in the reactor was investigated. Figure 4.29 to Figure 4.32 present the comparison of the modeling versus the experimental results in the cold flow prototype for sand 2 and ilmenite particles.

Comparison of the measured and predicted pressure drop in the standpipe of the L-valve illustrates that model predicts well the variation trend. However, it underestimates the exact pressure drop for both sand and ilmenite particles. It should be noted that the pressure drop in the standpipe is a dependent variable which is function of the pressure loop across the system. Therefore, the main reason for this difference is in the pressure drop prediction of the other elements which overestimate the pressure drop in total. This difference in the $\Delta P_{lv,v}$ imposes an error in the prediction of the gas

flow rate across the standpipe and solid flux. The overall model respond is acceptable, confirming the modeling approach selected in this study.

Concerning the gas flow in Figure 4.30, the experimental results present only the downward gas flow rate. Therefore, zero gas flow rate in the graph signifies upward gas flow rate in the standpipe. Consequently, modeling prediction of upward gas flow rate is correct while its trend can not be directly compared with the current measured gas flow rate results. However, regarding the observed change in the pressure drop and solid flow rate which follow similar trend in both sections, the predicted gas flow rate by model should be similar to the real trend in the standpipe.

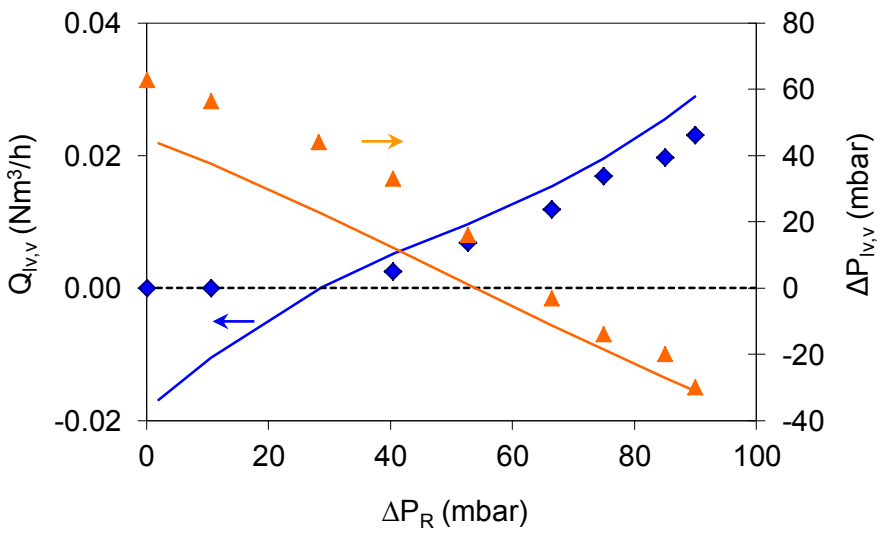

Figure 4.29 : Comparison of the modelling (lines) and experimental results (points) for the effect of pressure drop variation in the reactor on the pressure drop and the gas flow rate in the standpipe of the L-valve for sand 2 particles with Q_{lv} = 0.15 Nm³/h. Consequent variation of the solid flux is illustrated in the Figure 4.30.

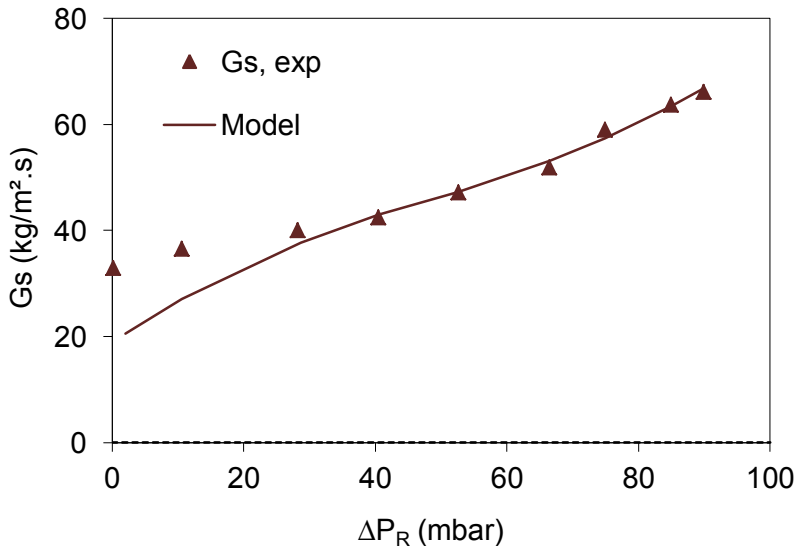

Figure 4.30 : Comparison of the modelling and experimental result of the reactor pressure drop effect on the solid flux in the L-valve corresponding to Figure 4.29.

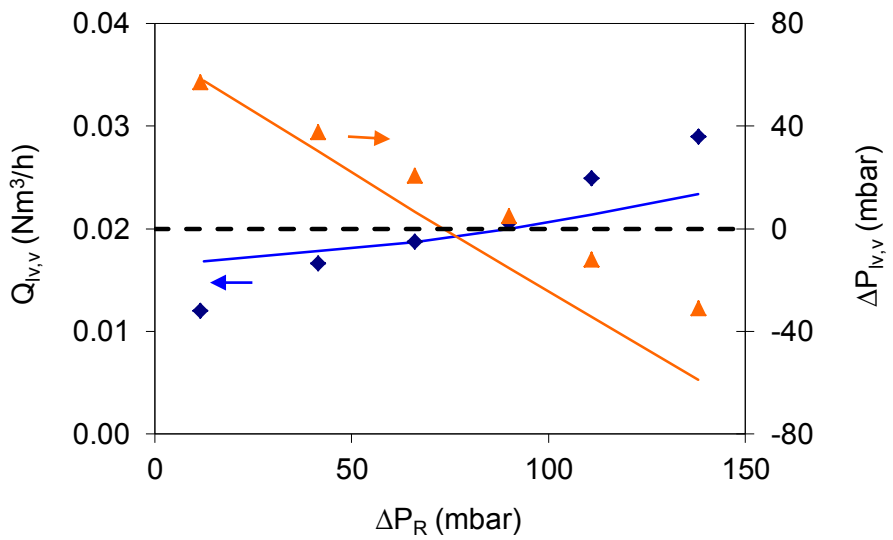

Figure 4.31 : Modelling versus experimental results for the effect of pressure drop variation in the reactor on the pressure drop and gas flow rate in the standpipe of the L-valve for ilmenite particles with Q_{lv} = 0.055 Nm³/h. Consequent variation of the solid flux is illustrated in Figure 4.32.

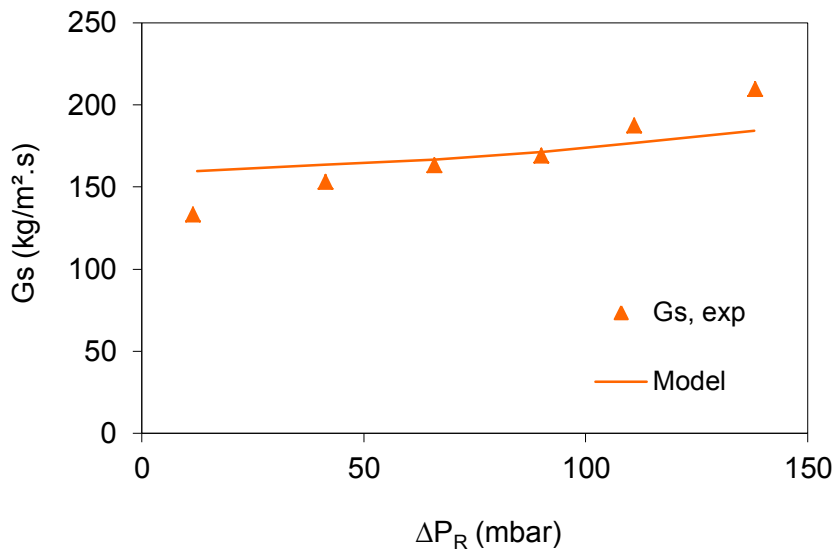

Figure 4.32 : Comparison of modelling and experimental results for the effect of the reactor pressure drop on the solid flux in the L-valve for the test conditions of Figure 4.31.

4.6 Sensitivity Analysis

Solid flow rate and height of the solid column in the standpipe of the loop-seal are the main parameters calculated by the proposed model. The sensitivity of these parameters towards the operational conditions and the solid properties was analyzed. Table 4.5: lists the solid flow variation for ± 10 % change in the reference parameters presented in the table. Particle size (d_P) demonstrate to have the most significant effect on the solid flow rate. This effect is not linear as decrease of the diameter has higher effect on the flow rate then increase in d_p for the current reference case. L-valve aeration demonstrates a linear effect on the solid flow rate. Solid density increases the solid flow rate with the same order as density change. Variation of the cyclone pressure drop, lift aeration, and reactor solid height demonstrate the impact of pressure balance. The reactor and the cyclone pressure drops which are considered as independent variables have less effect while variation of lift pressure drop imposes the highest variation.

Sensibility of the solid height in the supply chamber of the loop-seal is presented in Table 4.6. Aeration rate below the standpipe of the loop-seal and particle size demonstrated the most significant effect in a nonlinear manner. Solid grain density and solid height in the reactor have an important influence on the resulting solid height in the standpipe. The height of the solid column in the standpipe of the loop-seal is highly sensitive to the solid inventory in the reactor. This was well observed in the experiments, where the height of the solid column was following the solid height in the reactor. Model shows the same behaviour and solid height in the standpipe of the loop-seal follows the height of the solid in the reactor.

Table 4.5: Solid flow rate sensitivity analysis based on the developed solid circulation model.

	W_s (kg/h)	Q_{lv} (Nm^3/h)	Q_L (Nm^3/h)	$\Delta P_{cyc,exit}$ (mbar)	H_R (m)	d_P (µm)	ρ_P (kg/m^3)
Reference value	103	0.22	8.5	18.5	0.5	321	2650
Ws with – 10% of ref.		-17%	6%	2%	-3%	30%	-9%
Ws with + 10% of ref.		17%	-8%	-1%	3%	-19%	9%

Table 4.6: Sensitivity of the height of solid column in the standpipe of the loop-seal to the variation of the operational parameters and solid properties.

	L_{SP} (m)	Q_{Ss} (Nm^3/h)	ΔP_{cyc} (mbar)	Ws (kg/h)	H_R (m)	d_P (µm)	ρ_P (kg/m^3)
Reference value	0.252	0.22	18.5	103	0.5	321	2650
L_{SP} with - 10% of ref.		58%	13%	-15%	-25%	-34%	30%
L_{SP} with + 10% of ref.		-27%	-13%	17%	29%	86%	-24%

4.7 Conclusion

The steady state solid circulation model developed in the current study was presented in this chapter. The model predicts the solid circulation rate actuated in the L-valve, height of the solid bed in the supply chamber of the loop-seal and pressure drop variation in different elements of the system. The model is based on the balance of pressure drop across the solid circulation loop. Therefore, careful calculation of the pressure drop across the individual system elements is an essential task. Due to lack of suitable correlations in the available literature, some relations were developed based on the experimental results including: the solid flow rate in the L-valve, variation of voidage of the fluidized bed in the recycle chamber of the loop-seal and friction factor in the recycle pipe of the loop-seal.

The prediction of the model was compared with the experimental results. The model demonstrated acceptable prediction compared to the experimental results obtained in both the cold flow prototype and the high temperature pilot plant. Moreover, the model demonstrated a good agreement with the experimentally measured effect of solid inventory in the reactor on the solid flow rate actuated in the L-valve.

The sensitivity analysis based on the model demonstrated that the solid flow rate is highly sensitive to the particles diameter. Particle density and gas flow rate in the riser were the other influencing parameters. The solid height in the supply chamber of the loop-seal was more sensitive to parameter variation compared to L-valve. The external gas injection below the supply chamber, particle diameter and particle density had the most influencing effect. Pressure drop in the reactor and cyclone and solid flow rate also were the other influencing parameters on the solid height in the supply chamber.

The developed model is a useful tool for the scale up purposes for similar designs containing L-valve and/or loop-seal. However, more investigations are required to include effect of scale variation on the behaviour change of different components and to validate or modify calculation methods employed in the current study.

Chapter 5
Reactor Study: Hydrodynamics

5.1 EXPERIMENTAL RTD INVESTIGATION 131
5.2 RTD MEASUREMENT INPUT FUNCTION 132
5.3 GAS SAMPLING 135
5.4 RTD SIGNAL TREATMENT 136
5.4.1 Linear Residence Time (RT) Treatment 136
5.4.2 Analysis of Signal Dispersion 137
5.5 INTERFERING SIGNALS MEASUREMENT 137
5.6 EFFECT OF OPERATING PARAMETERS ON RT 138
5.6.1 Effect of the Fluidized Bed Height 138
5.6.2 Effect of the Gas Velocity on the Residence Time (RT) 139
5.6.3 Effect of Solid Flow Rate on Residence Time (RT) 140
5.7 BUBBLING FLUIDIZED BED MODEL 140
5.8 MODELING OF THE SYSTEM COMPONENTS 145
5.9 MODEL RESULTS 147
5.9.1 Bubble Size Correlations 147
5.9.2 Gas Dispersion in Emulsion Phase 148
5.9.3 Model Validation 150
5.9.4 Sensitivity Analysis 153
5.10 CONCLUSION 155

5. Reactor Study: Hydrodynamics

The solid circulation in the current CLC system was experimentally investigated and modeled as presented in the previous chapters. This helped to attain two of the principal objectives of the current study in understanding the control of solid circulation and gas leakage in the current system. Nevertheless, analysis of the performance of the CLC system requires a more accurate understanding of the phenomena in the reactors. Therefore, the next principal objective of the current study is to investigate reactors performance in more details. This requires characterization of the hydrodynamics and kinetics phenomena in the reactors and development of a reactor model capable of predicting reactor behaviors.

A reactor model is composed of a reaction mechanism and a hydrodynamic platform on which the model is constructed. Hydrodynamics of a chemical reactor plays an important role to explain its performances, especially in case of a fluidized bed reactor. In this chapter, experimental and modeling works related to the characterization of the fluidized bed hydrodynamics are presented.

Hydrodynamics of the fluidized bed reactors used in the current design was experimentally investigated in the cold flow prototype with ilmenite particles. The gas phase residence time distribution method was employed for this purpose by use of air as main fluidization gas with Helium as the tracer gas. The employed experimental investigation is first discussed including the signal treatment methods. The impact of operating parameters on the mean gas residence time is then discussed including effects of height of fluidized bed, gas flow rate, and the solid circulation flow rate.

A hydrodynamic model is then developed based on the two phase model of the bubbling fluidized bed [153]. Regarding the dispersion of the existing models in the literature [153,170,172,175,177,270], the experimental results are used to best select the governing material balance models in each phase for the current reactor design. Therefore, axial dispersion – plug flow model is chosen for the gas flow in the emulsion phase and a plug flow for the bubble phase. The axial dispersion coefficient of the gas in the emulsion phase is then selected based on the experimental findings. The developed model is finally used to analyze sensitivity of the mean gas residence time in the reactor for different operating parameters.

Solid phase was considered to be homogeneous in the current study (CSTR model). Therefore, solid phase residence time distribution tests were not conducted. The main reasons for this selection will be discussed in the next chapter.

5.1 Experimental RTD Investigation

The experimental tests were carried out in the reactor R1 of the cold flow prototype (R1 and R2 are identical in the cold flow model). The configuration of the injection and detection system used for this study is described in details in the chapter 2. A short description of the system is illustrated in Figure 5.1 with indication of the different terms used in the current report. The tests were carried out with ilmenite particles. Helium was used as the tracer gas with air as the main fluidization gas. A mass spectrometer detector was used to measure the Helium concentration sucked into the device through a capillary sniffer. An on/off electromechanical valve was used to control the tracer gas flow rate. All data were automatically registered on a computer

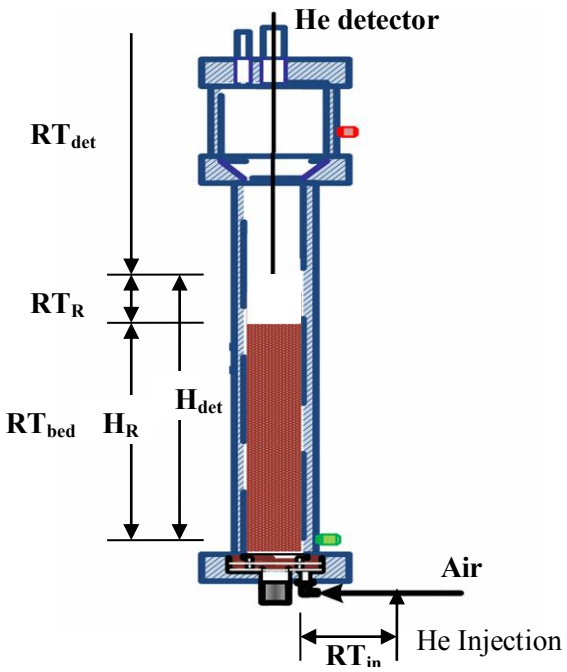

Figure 5.1: The principal injection and detection system components. Nomenclature of different residence times and heights used in this report are illustrated in the figure. Dimensions of different parts are listed in the appendix 1.

5.2 RTD Measurement Input Function

Proper tracer injection is an essential part of RTD study to obtain a suitable input function. Different possible tracer input functions discussed in chapter 1 were tested during the residence time distribution (RTD) study. The first tracer input function tested was a positive step change. Production of a controlled input step function was however a technical challenge. Higher pressure in the Helium injection line compared to the gas feed of the reactor caused an initial impulse behavior as shown in the Figure 5.2. Different configurations were therefore tested to solve this problem. The best solution tested was to use a purge line in the helium feeding line. The pressure in the helium injection line was then purged just before the tracer injection. This resulted in production of proper response function as illustrated in Figure 5.3.

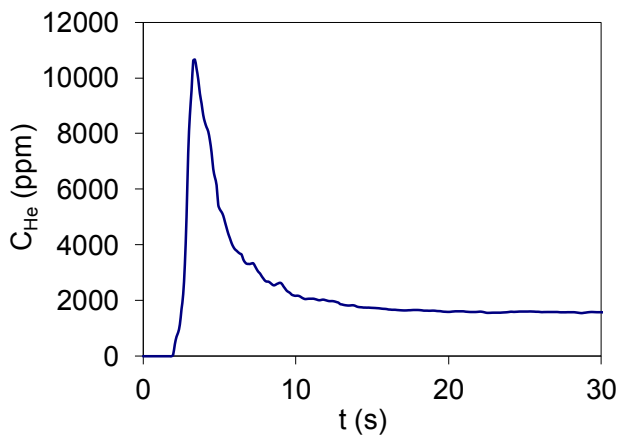

Figure 5.2: Example of a faulty step input function due to the pressure difference in injection line. Helium is injected upstream of the distributor and measured above the fluidized bed with height of H_R=0.5 m and U_R = 0.067 m/s.

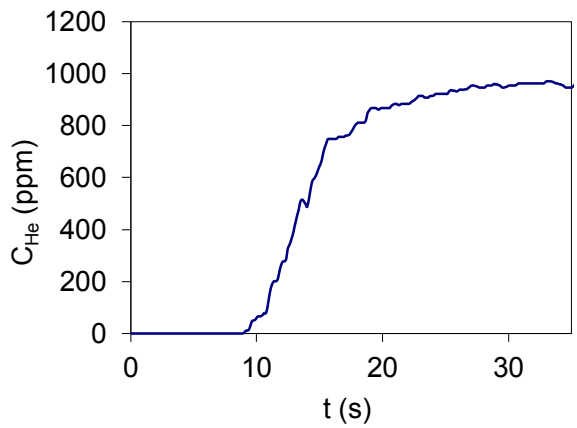

Figure 5.3: Example of a positive step change input function for 0.3 m height of fluidized bed in the reactor, U_R = 0.067 m/s (5.2 times Umf) and t_{first} = 8.97 s.

Impulse injection of the tracer was the next input function tested. An Impulse input peak can be easily produced. However, reproducibility of identical impulse functions was difficult because of a poor control of pressure difference between the injection line and the distributor. This phenomenon is illustrated in Figure 5.4 where two consecutive impulse functions result in different output behavior in terms of maximum concentration. This is however improved when normalized input function E(t) is calculated in each case (Figure 5.5).

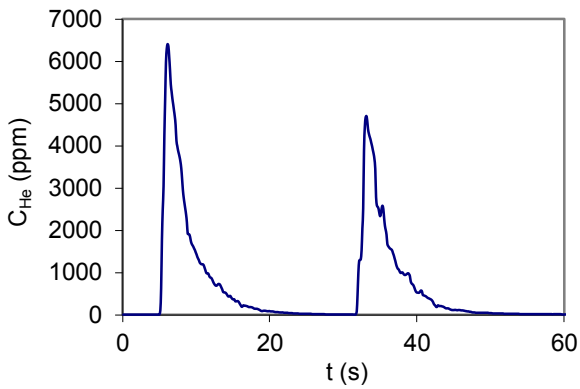

Figure 5.4: Resulting concentration output for two consecutive impulse input functions. The gas injection and measurement is according to the configuration of Figure 5.1.

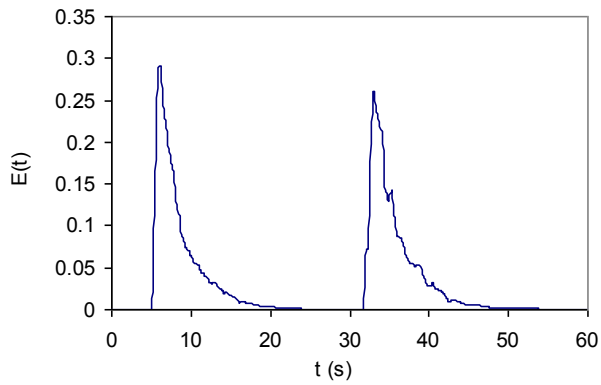

Figure 5.5: E(t) function for the experimental of Figure 5.4.

The last tested tracer input function was negative impulse change to zero (also called "wash out function"). Production of this injection mode is easier than the two other functions discussed above. The initial tracer concentration (C_0) is a well known value; resulting from stable continuous Helium injection. And the final concentration (C_∞) is zero. Moreover, this function was easily reproducible since the stop of the small flow of Helium did not affect significantly pressure in the lines. An example of the wash out tracer injection function is illustrated in the Figure 5.6. W(t) is calculated as the tracer concentration normalized to the initial tracer concentration, $W(t) = C/C_0$.

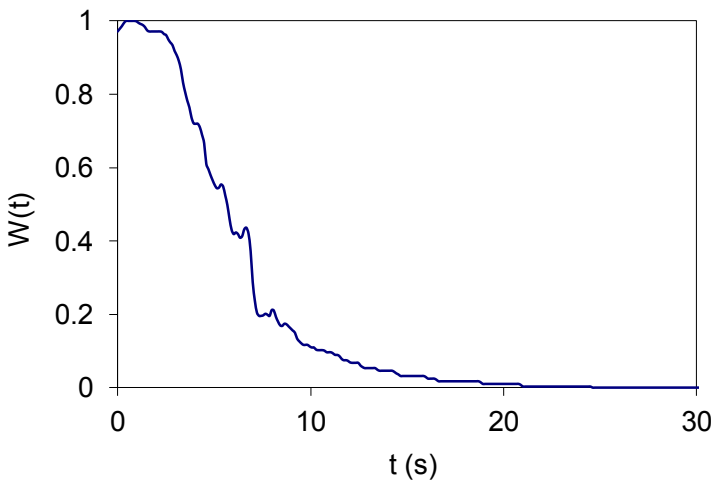

Figure 5.6: Output resulting function for an input of wash out function for a bed height of 0.1 m and U_R = 0.067 m/s (5.2 U_{mf}).

Reproducibility of the experimental results was studied by repeating the experiment several times for each tested condition. Figure 5.7 illustrates three experimental runs conducted with a bed height of 0.3 m and a fluidization flow rate of Q_R = 1.89 Nm^3/h in the reactor. This demonstrates acceptable reproducibility of the experimentations.

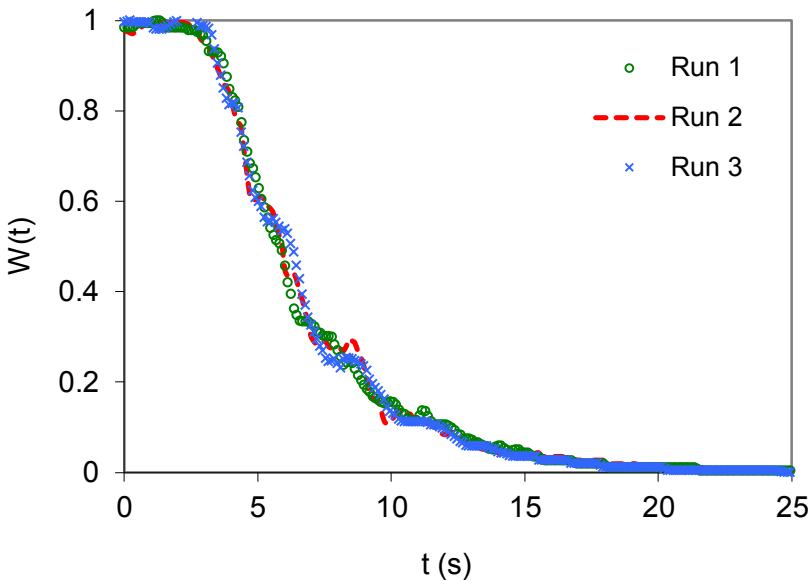

Figure 5.7: Results of three experimental runs for height of reactor bed 0.3 m and Q_R = 1.89 Nm3/h.

Values of the residence time and the variance are calculated numerically based on the method explained in the chapter 0 for a wash out function [155]. Therefore, using trapezoidal numerical integration:

$$\bar{t} = \int_0^{\infty} W(t)dt = \sum_{i=1}^{\infty}\left(\frac{W(i-1)+W(i)}{2}\Delta t\right) \qquad \textbf{Eq. 5.1}$$

And

$$\sigma^2 = \frac{\mu_2'}{\bar{t}^2} = \frac{2\sum_{i=1}^{\infty}\left(\frac{t(i-1)W(i-1)+t(i)W(i)}{2}\Delta t\right)}{\bar{t}^2} - 1 \qquad \textbf{Eq. 5.2}$$

First appearance time, t_{first}, presents the shortest residence time in a system. t_{first} can be calculated with different methods. Considering the fractional tubularity model it can be determined from the slope of the ln(W(t)) versus time which is $1/(\bar{t} - t_{first})$ for $t>t_{first}$ [154]. Tubularity parameter can also be found from [154]:

$$\tau_p = t_{first}/\bar{t} = 1 - \sigma \qquad \textbf{Eq. 5.3}$$

Another method is to find the t_{first} directly from the experimental results as illustrated in Figure 5.8. In this method t_{first} is calculated as the interception of a straight line as extrapolation of the linear section of the W(t) function with highest initial value of the W(t) function. First appearance time calculated with these two methods results in similar values. The last approach is therefore used in the current study to calculate t_{first}.

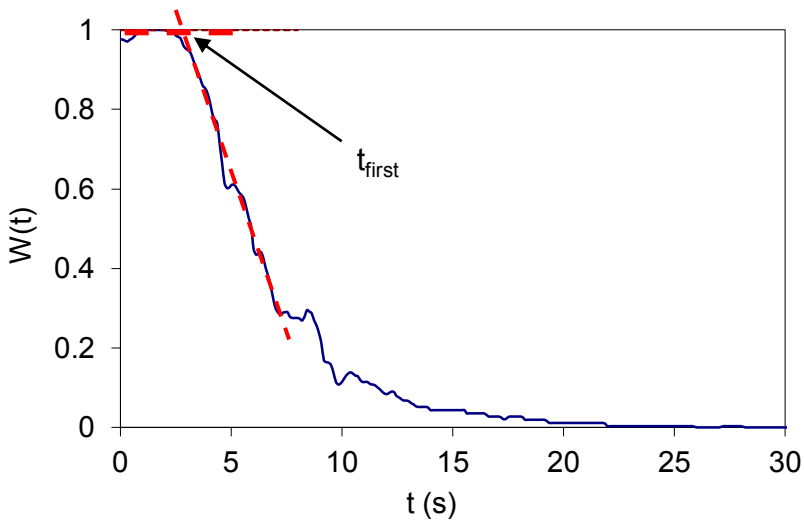

Figure 5.8: Example of first appearance time calculation based on the experimental results, for a solid height of 0.3 m in the reactor and U_R = 0.067 m/s. Resulting t_{first} is 2.8 s.

5.3 Gas Sampling

Gas sampling in a fluidized bed can result in misleading information due to hydrodynamic factors, biased sampling from the dense phase and radial gradients. Grace et al. [271] have listed different measurement pitfalls in fluidized beds. The main error sources can come from the different gas concentrations in the bubble and dense phase, radial concentration gradient, hydrodynamic interference of the gas sampling line, and the adsorption and trapping of the gas. The error sources, most relevant to the current study can be listed as: the difference of concentration between gas in the bubble and emulsion phases, and the radial concentration gradient in the reactor. These two phenomena are closely related especially in the current RTD test where no reaction takes place.

The gas flow in the bubbles is considerably faster than gas flow rate of the emulsion phase in the current fluidized bed. Moreover, the bubbles transport particles upwards in the bubble wake [153]. This imposes a downward solid flow near the reactor walls, resulting in a complicated solid flow pattern in the bed. This difference between the bubble and the solid flow results in a radial concentration profile in the gas phase. The gas concentration variation inside and above the bed has been investigated by different researchers [272,273]. The results illustrate that the gas variation across the bed can be considerable.

In the current study, mean gas residence time was measured in two extreme radial positions on the bed surface: one adjacent to the reactor wall and the other in the reactor center. The detector was placed adjacent to the surface of the fluidized bed in both cases (H_R = 0.51m, Ur=0.068m/s). Average measured residence time when detector was located on the center was 3.65s. The average measured residence time increased to 5.32s when the detector was located adjacent to the wall. These show the difference of two extreme cases of gas flow in the reactor. Bubbles tend to flow along the center line of the fluidized bed; therefore, the tracer gas measured at the center is mostly carried out through bubbles which have a fast velocity. On the other hand, the gas flow near the reactor walls is mostly conveyed through the interstitial space between the fluidized particle with a velocity much less than bubbles. Moreover, the downward solid flow near the reactor walls tends to further reduce gas flow rate in this region.

5.4 RTD Signal Treatment

Measured residence time response function includes not only the response of the fluidized solid bed but also some interfering components illustrated in the Figure 5.1. The measured residence time response includes:

- RT_{in}: Residence time of the gas injection line.
- RT: Residence time of the solid bed which is aim of the measurement.
- RT_R: Residence time of the empty space above the bed
- RT_{det}: Including the residence time of the detector and the capillary sniffer tube of the detector. This residence time is fairly constant regarding the fact that internal gas flow rate inside the detector is controlled with an internal vacuum pump.

In the current tests the injection and detection system were installed to minimize the interfering effects on the output signal. However, the effect of these interfering signals can not be neglected. Therefore, two methods were employed to treat the experimental results:

- Residence time values are treated considering linear relation between different RT values based on mean residence times (section 5.4.1).
- The interfering system elements are modeled based on the chemical reactor characteristics and their response is convoluted with the fluidized bed response in the fluidized bed model.

A series of blank tests were carried out to measure separately RTD of Helium detector, injection facilities and the empty reactor. The resulting values are listed in the appendixe 8 and are used below to characterize system components.

5.4.1 Linear Residence Time (RT) Treatment

Linear residence time treatment method involve assumption of independence of individual RT in each component [217]. Accordingly, the residence time of the solid bed can be calculated as:

$$RT = RT_t - RT_{\det} - RT_{in} - RT_R \qquad \textbf{Eq. 5.4}$$

The different notations used above are illustrated in the Figure 5.1. Residence time of the gas flow between the fluidized bed and the detector tube is calculated as:

$$RT_R = (H_R - H_{\det})\frac{(\Delta RT_{R\,empty})}{\Delta H_{\det}} \qquad \textbf{Eq. 5.5}$$

Where $\Delta RT_{R\ empty}$ stands for the residence time of the gas in the empty reactor for a height of ΔH_{det} calculated from blank tests listed in the appendixe 8. The experimental values for blank tests ($RT_{R\ empty}$ and RT_{in}) were measured for a reference gas flow rate in the reactor. These values were modified in case of experimental test with different gas flow rate other than the reference rate measured in the blank test series. Therefore:

$$RT_{in} = RT_{in0}\frac{Q}{Q_0} \qquad \textbf{Eq. 5.6}$$

Where $RT_{in,0}$ stands for the gas residence time of the injection system for the reference gas flow rate measured in blank test experiments. And similarly:

$$RT_R = RT_{R,0}\frac{Q}{Q_0} \qquad \textbf{Eq. 5.7}$$

Where $RT_{R,0}$ stands for the gas residence time between the bed surface and the detector for the reference gas flow rate measured in blank test experiments. This approach does not take into account the gas dispersion measured by RTD output function. Therefore, an additional analyzing method is employed in this study to investigate overall gas dispersion in the current fluidized bed.

5.4.2 Analysis of Signal Dispersion

The dispersion of the residence time distribution output function (represented by dimensionless variance ζ^2) can not be calculated with a linear treatment as presented above. The output RTD signals can be analyzed based on two possible methods: mathematical approach and chemical reactor modeling approaches. The mathematical approach involves use of deconvolution method. In fact, the measured output signal of the reactor (f_{out}) includes the bed response function (f_{bed}) convoluted with the response of the system parts other than the fluidized bed (f_{in}). Therefore:

$$f_{in} * f_{bed} = f_{out} \qquad \textbf{Eq. 5.8}$$

Accordingly, the interfering signal should be deconvoluted from total system response function in order to obtain the real response of the fluidized bed from the experimental response signal. Figure 5.9 illustrates schematically additional dispersion caused by the interfering system components other than fluidized bed. This method involves calculation of the real input signal into the bed from the known system output signal (f_{out}) and the measured interfering signal (f_{in}). It uses specific mathematical signal treatment procedures. However, the interfering signal should be known in each experimental condition since there is no modeling of the interfering functions involved.

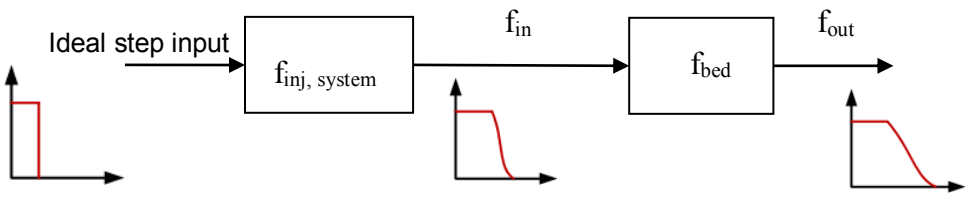

Figure 5.9: The signal deformation in different system components.

The chemical reactor modeling approach involves modeling of whole system components including not only the fluidized bed but also the injection system, detector and measurement parts. Therefore, the total system is broken down to a series of ideal reactors, depending on their specificities. The advantage of this method is the physical sense of the treatment method. Moreover, once the system is calibrated for a reference operating condition, it is expected to reliably predict the system behavior in other operating conditions. Therefore, this method was selected as the preferred signal treatment approach in this study.

5.5 Interfering Signals Measurement

In order to identify extra gas dispersion caused by system components other than the fluidized bed, a series of experimental tests were carried out. Therefore, response functions to input wash out signal were determined for the three system interfering parts, as shown in Figure 5.10. Output signal of the detector alone shows a minimum dispersion of signal with $\zeta^2 = 0.084$ and RT = 1.72 s. Comparing the output signal of the detector and the detector and injection line together demonstrates that Helium injection system causes an extra dispersion of $\zeta^2 = 0.51$ and RT = 2.15 s. Reproducibility is shown here since all three responses represented give similar results. Moreover, response function of the injection line, distributor, and Helium detector together is presented in Figure 5.10. The dispersion caused by these elements is $\zeta^2 = 0.6$ and RT = 3.91 s. The resulting output signal demonstrates that gas distributor and the injection line causes a significant dispersion of the input function.

These results are used to calibrate the reactor model for each component of the system. The RTD signal of the interfering parts (injection system, distributor and detector) was measured for Q_R = 1.92 Nm^3/h which is the gas flow rate used in the investigation of effect of the solid height and circulation flow rate investigations.

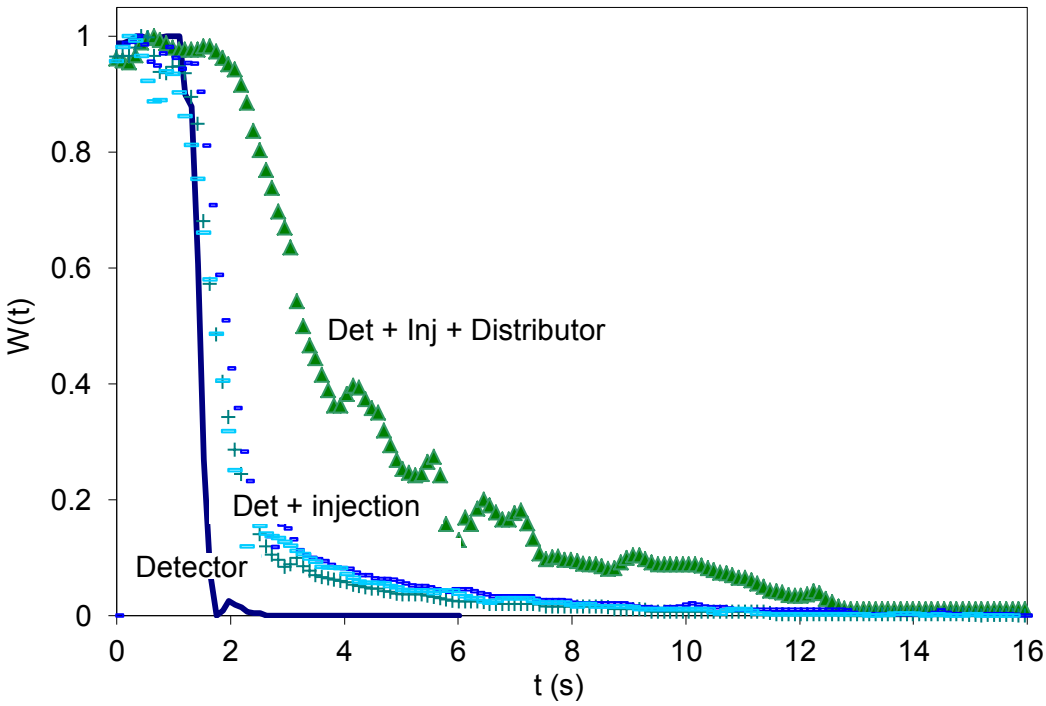

Figure 5.10: Response functions of different system components to a wash out input function for injection system, distributor and the Helium detector for C_{He0} = 0.05 vol. % and Q_R = 1.92 Nm^3/h. Response functions of the total injection, distribution and the detector were measured with the detector sniffer immersed in a fluidized bed of H_R = 0.51 m.

5.6 Effect of Operating Parameters on RT

The effect of three parameters on the residence time of gas in the reactor was studied including: height of the solid bed (H_R), gas velocity in the bed (UR), and solid circulation rate (Ws). The residence time values are all calculated from the washout function regarding the advantages associated with this function as discussed above. The residence time values presented in sections 5.6.1 - 5.6.3 are all calculated according to the linear signal treatment method explained in the section 5.4.1 where:

$$RT = RT_t - RT_{\det} - RT_{in} - RT_R \qquad \textbf{Eq. 5.9}$$

The experimental results will be then treated based on the chemical reactor modeling analysis method in the section 5.9.3.

5.6.1 Effect of the Fluidized Bed Height

An increase of the fluidized bed height increases the length of the gas trajectory along the reactor. In a fluidized bed, due to the effect of bubbles and variation of bubble size and velocity residence time could have a behavior different from conventional reactors such as plug flow reactors. Two experimental test series were carried out. First, the residence time of the gas phase in the reactor was measured for three different solid heights of 0.3, 0.5 and 0.7 m with detector being placed about 0.1 m above the surface of the fluidized bed. In a second test series, the gas residence time was measured for a given constant height of the fluidized bed while the detector was placed at different heights inside the fluidized bed. The fluidized bed RT results for these two experimental series are presented in the Figure 5.11. Results demonstrate that the residence time increases rather linearly as the height of the solid bed increases.

A slight difference can be observed between two series in terms of RT_t in Figure 5.11. This relays on the fact that the detector is placed with a distance above the bed with the second test series as explained above. This adds a small additional residence time which is eliminated for the RT curves.

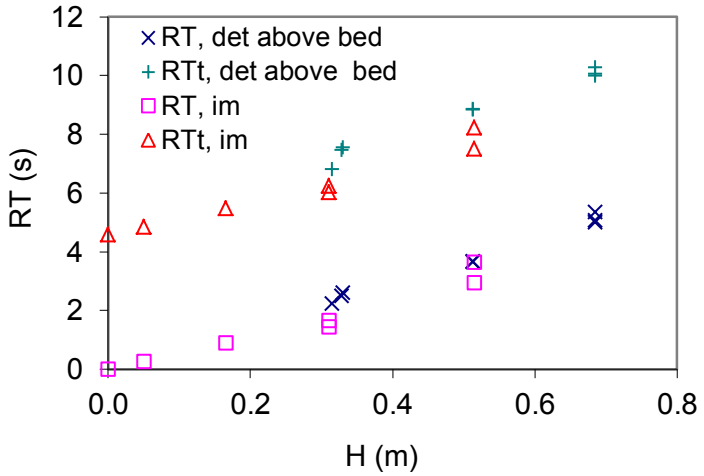

Figure 5.11: The variation of the experimentally measured bed residence time (RT) and total system residence time (RTt) for two test series: first series represents fluidized bed with fixed height of 0.51 m and variable detector height inside the bed (Δ, □), and the second series with variable height of the solid bed with detector being placed about 0.05 m above the bed surface (x,+). Vsg = 0.068 m/s (5.26 Umf), and Ws = 0.

5.6.2 Effect of the Gas Velocity on the Residence Time (RT)

The impact of the gas fluidization flow rate on the RT was experimentally investigated. The gas flow velocity was varied in a range of 2 – 12 times U_{mf}, covering a wide range of the bubbling fluidization. The resulting mean RT variation is illustrated in Figure 5.12. Variation of the gas flow rate in the reactor changes the height of the solid bed as illustrated in Figure 5.12. Residence time decreases rather linearly up to 6 U_{mf} above which the variation flattens. It should be pointed out that the height of the fluidized bed in the reactor was changing due to bed expansion caused by higher aeration rate (illustrated in Figure 5.12).

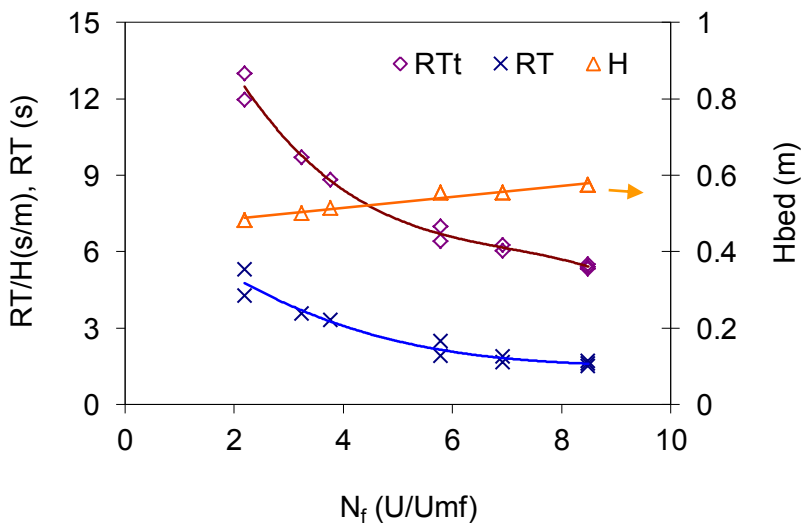

Figure 5.12: Variation of the experimentally measured residence time and height of the fluidized solid bed in the reactor for different aeration gas velocities in the reactor for a bed with constant mass and no solid circulation.

5.6.3 Effect of Solid Flow Rate on Residence Time (RT)

Effect of the solid flow rate on the residence time of the reactor was the last parameter to be studied. The tests were carried out with continuous solid circulation between two reactors with constant height of solid bed in each reactor. The resulting residence time values are presented in Figure 5.13. Residence time increases slightly for higher solid flow rates but the trend is almost negligible. In average, solid flow rate imposes an additional downwards solid flow rate on the solid bed in the reactor. However, regarding the diameter of the reactor, the imposed additional solid velocity is negligible compared to the bubble velocity which is the main influencing parameter in the residence time. For instance, a solid flow rate of 120 kg/h, in solid bed of 0.5 m, results in an average solid flow rate of 0.00089 m/s compared to the bubble average velocity of about 0.4 m/s based on the simplified two-phase model [153]. The imposed solid flow rate is even less than the downward solid flow imposed by the bubble movements in the bed. The average downward solid velocity caused by bubbles is expected to be about 0.0097 m/s considering a wake to bubble ratio of fw = 0.22 and average bubble fraction of $\delta = 0.113$ in the bed for $U_R = 0.067$ [160].

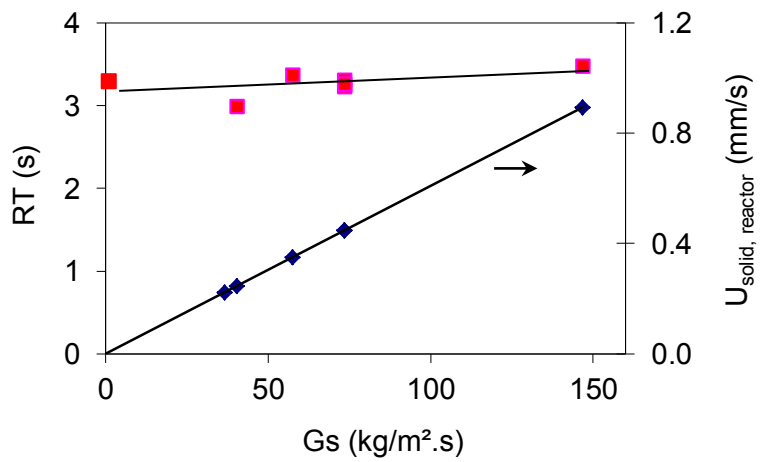

Figure 5.13: Effect of the solid flow rate on the residence time of the gas phase in the reactor with solid height of the 0.5 m and superficial gas velocity of 0.067 m/s (5.2 Umf).

Results of experimental investigations on the variation of the mean gas residence time in the fluidized bed reactor of the current CLC system was presented above. Increase of the height of the fluidized bed was shown to increase linearly the gas residence time in the bed. Fluidization gas flow rate had a significant effect on the mean gas residence time. RT decreased sharply as the gas flow rate was increased. Finally, it was shown the solid circulation flow rate has a negligible impact on the gas residence time in the reactor. The experimental results were only analysed regarding average gas phase residence time. The investigation of gas dispersion requires development of a model for treatment of the results. This will be discussed in the following sections.

5.7 Bubbling Fluidized Bed Model

Hydrodynamic model is an essential part in development of the overall reactor model, especially for fluidized beds. The hydrodynamic of the bubbling fluidized bed employed in the current CLC system was experimentally investigated. In the following sections a hydrodynamic model is developed to describe the fluidized beds of the current CLC system based on literature findings. The model is then validated using the experimental results obtained with the cold flow prototype.

Various hydrodynamic modeling methods of bubbling fluidized beds have been developed to date as discussed in chapter 1. The principal aim of the current study is to adopt one of the available modeling

procedures which best fits the experimental data and could be reliable for scale up to the hot pilot plant conditions. Consequently, the modified two phase bubble - emulsion model proposed by Toomey and Johnstone [169] and Wen and Fan [170] was used in the current study. The main hypotheses of the developed model are:

- Fluidized bed is consisted of two phases: bubble and emulsion.
- All particles are in the emulsion phase and the bubble phase contains no particles.
- The gas in the bubble phase is in the plug flow mode with gas interchange with the emulsion phase.
- In the emulsion (dense) phase:
    - Solids are stagnant (no solid circulation in average) and the gas flows with a constant velocity of U_e.
    - Solid phase is homogeneously mixed (CSTR). This hypothesis will be discussed in details in the next chapter.
    - Axial dispersion with convection is considered as the material balance equation of the gas in emulsion phase.

Fast bubble rise velocity along the reactor with absence of reaction in this phase suggests use of a plug flow model as the governing equation in this phase. Accordingly, the material balance equation for component "i" in the bubble phase is:

$$\frac{\partial C_i^b}{\partial t} = -\frac{1}{\varepsilon_{gb}} \cdot \frac{\partial}{\partial z}\left(u_{gb} . \varepsilon_{gb} . C_i^b\right) - K_{be} . \left(C_i^b - C_i^d\right) \qquad \textbf{Eq. 5.10}$$

Where i stands for CH_4, H_2, N_2, CO, H_2O, CO_2, and O_2 (in the air reactor). The term in the left hand side of the equation stands for dynamic variation of concentration of different components. The right side terms stand respectively for convection and bubble – emulsion gas exchange.

The selection of material balance equation for the gas flow in the emulsion phase is less obvious compared to the bubble phase. Three possible models are tested in the current study including: plug flow (PF), CSTR, and axial convection – dispersion model. The final selection of the governing equation is made based on the experimental results. The selection procedure is explained in details in the section 5.9.2. The axial convection, dispersion model used in the gas emulsion phase can be written as:

$$\frac{\partial C_i^d}{\partial t} = \frac{D_{axg}}{\varepsilon_{gd}} \cdot \frac{\partial}{\partial z}\left(\varepsilon_{gd} . \frac{\partial C_i^d}{\partial z}\right) - \frac{1}{\varepsilon_{gd}} \cdot \frac{\partial}{\partial z}\left(u_{gd} . \varepsilon_{gd} . C_i^d\right) + K_{be} . \frac{\varepsilon_{gb}}{\varepsilon_{gd}} . \left(C_i^b - C_i^d\right) \qquad \textbf{Eq. 5.11}$$

Where i stands for CH_4, H_2, N_2, CO, H_2O, CO_2, and O_2 (in the air reactor). The left hand side term accounts for the dynamic concentration variation. The terms in right present axial dispersion, convection, and emulsion – bubble gas exchange. Similar relation was used to present the plug flow model by Dawg = 0. Alternatively, the CSTR model tested for this phase is:

$$H_R \varepsilon_{gdt} \frac{\partial C_i^d}{\partial t} = \varepsilon_{gd} . u_{gd,in} . C_{i,in}^d - \varepsilon_{gd} . u_{gd,out} . C_i^d + \int_0^H K_{be} . \varepsilon_{gb,i} . \left(C_i^b - C_i^d\right) dz \qquad \textbf{Eq. 5.12}$$

Where ε_{gdt} stands for fraction of the fluidized bed occupied by the gas in the emulsion phase. $U_{gd,in}$, $U_{gd,out}$ are respectively gas velocity entering the emulsion phase and leaving the emulsion phase. The overall calculation procedure employed in the model is illustrated in a simplified flowchart in Figure 5.15.

The partial differential equations were solved using the explicit finite volume method. The reactor was discretized into definite differential segments (cells) along the vertical axis. The sizes of the segments (dz) were selected small enough to reliably consider constant hydrodynamic properties in each cell. The size of the cells was selected small enough to ensure no effect on the numerical solution of the differential equations. Accordingly, dz was smaller than the maximum cell size below which all the

equations converge to a unique stable solution FORTRAN was used as the programming language. The equations in the time space were solved by use of a FORTRAN package named LSODES (Livermore solver for ordinary differential equations) [274].

The boundary conditions were selected for time and space. The reactor concentration at the time t = 0 was considered equal to the input gas concentration into the reactor, then:

$$C_i^d = C_i^b = C_{in} \quad at \quad t = 0 \qquad \textbf{Eq. 5.13}$$

Regarding the z-axis, no axial dispersion is considered at the entrance into the reactor in the dense phase, therefore:

$$\frac{\partial C^d}{\partial z} = 0 \quad at \quad z = 0 \qquad \textbf{Eq. 5.14}$$

And similarly axial dispersion is considered to be zero at the top surface of the bed in the dense phase:

$$\frac{\partial C^d}{\partial z} = 0 \quad at \quad z = H_{bed} \qquad \textbf{Eq. 5.15}$$

The model was to be compared with the experimental RTD results for validation and choice of most suitable hydrodynamic equations such as bubble diameter and gas exchange coefficients.

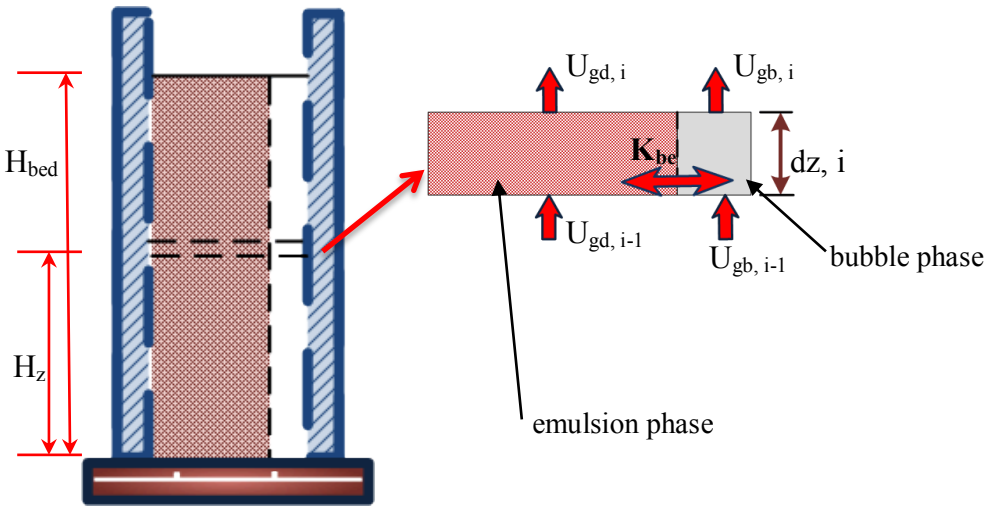

Figure 5.14: Schematic representation of the two phase model and different relations employed to calculate bed properties [153].

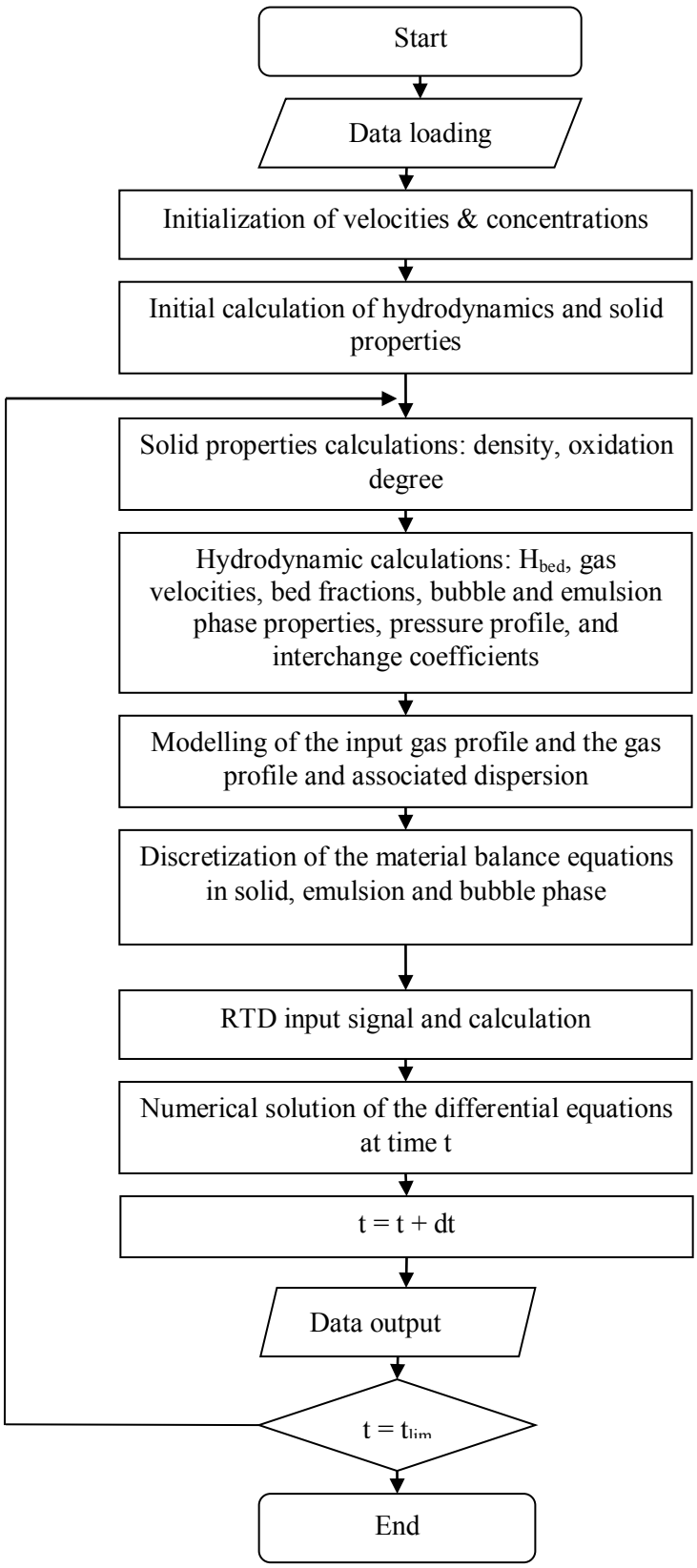

Figure 5.15 : Simplified flow chart of the Hydrodynamic model.

The basic equation for the gas distribution in the fluidized bed can be developed from mass balance at a certain height as:

$$Vsg = U_{gd}(1-\varepsilon_{gb}) + \frac{Q_b}{A} + U_{tf}\varepsilon_{gb} + \frac{Q_v}{A} \qquad \textbf{Eq. 5.16}$$

Where U_{gd}, Q_b and U_{tf} respectively stand for gas velocity in the emulsion phase, visible bubble flow rate, gas through flow. The gas velocity in the emulsion phase is assumed to be equal to the minimum fluidization velocity. Qv presents the net flow of gases entrained inside the particles pores. This term is zero in the current model considering no net particle up or down flow. The bubble fraction in the bed can be calculated as:

$$\varepsilon_{gb} = \frac{Q_b / A}{U_{gb}} \qquad \textbf{Eq. 5.17}$$

The visible bubble flow rate is calculate as [275]:

$$Q_b / A_R = \varphi(Vsg - U_{mf}) \qquad \textbf{Eq. 5.18}$$

Where θ is the fraction of visible bubble:

$$\varphi = 1.45Ar^{-0.18} \qquad 10^2 < Ar < 10^4 \qquad \textbf{Eq. 5.19}$$

With θ being 0.8 outside this boundary. The gas through flow is therefore calculated as:

$$U_{tf} = (1-\varphi).(Vsg - U_{mf}) \qquad \textbf{Eq. 5.20}$$

The bubble rise velocity is calculated as:

$$U_{gb} = Q_b / A_R + \alpha 0.711\sqrt{g.d_b} \qquad \textbf{Eq. 5.21}$$

Here, θ is a parameter taking into account the deviation of bubbles from a single bubble rising velocity calculated as [275]:

$$\alpha = \begin{cases} 1.01 & D_R < 0.1m \\ 3.2\sqrt{D_R} & 0.1m \le D_R \le 1.0m \\ 3.2 & D_R > 1.0m \end{cases} \qquad \textbf{Eq. 5.22}$$

The bubble size variation along the height of the fluidized bed is calculated using Mori and Wen relation [276] as:

$$d_b = 8.53\times10^{-3}\sqrt[3]{1+27.2(U-U_{mf})}(1+6.48h-h_0-h_{jet})^{1.21} \qquad \textbf{Eq. 5.23}$$

Here, h_0 stands for the height above the distributor plate where the bubbles are as large as those formed by commercial plates and h_j is the jet length at the distributor. h_0 and h_{jet} are considered to be zero this reduces the equation to that of a pores plate. The bubble growth equation selection will be discussed below, in section 5.9.1 where RTD results are used to find the best equation. The bubble – emulsion gas exchange coefficient is calculated according to [159,277]:

$$K_{be} = 1/K_{bc} + 1/K_{ce} \qquad \textbf{Eq. 5.24}$$

With bubble – cloud gas exchange coefficient of:

$$K_{bc} = 4.50\left(\frac{U_{mf}}{d_b}\right) + 5.85\left(\frac{D^{0.5}g^{1/4}}{d_b^{5/4}}\right) \qquad \textbf{Eq. 5.25}$$

And cloud – emulsion exchange of:

$$K_{ce} = 6.77\left(\frac{\varepsilon_{mf}\, DU_{br}}{d_b^3}\right)^{1/2} \qquad \textbf{Eq. 5.26}$$

The exchange coefficient and its effect on the residence time will be discussed below in section 5.9.4. The height of the fluidized bed (H_R) is calculated based on material balance at hegiht H of the bed as:

$$H_{bed} = H_{mf} + H_{bubble} = \frac{M_{bed}}{A_R \rho_s (1-\varepsilon_{mf})} + \int_0^{Hbed} \varepsilon_{gb}.dz \qquad \textbf{Eq. 5.27}$$

H_{mf} and H_b stand for height of the bed in the emulsion and bubble phase separately.

5.8 Modeling of the System Components

As discussed in section 5.5, the experimental results demonstrated that the dispersion imposed by the current RTD study system is not negligible compared to the fluidized bed effect. Deformation of the signals through injection system, distributor and detectors are indeed significant. Therefore, the model has to include all of the system elements; otherwise a considerable error will be introduced while comparing modeling and experimental results. The main gas tracer injection and detection components of the experimental installation are illustrated in the Figure 5.1. All interfering component, upstream and downstream of the fluidized bed, were modeled. Therefore, the overall model includes a series of six reactors including the fluidized bed, as shown in Figure 5.16. For each interfering section, a physical model was selected based on the nature and dimensions of different components to best fit the experimental results. The governing material balance equations used in each system component is listed in the Table 5.1.

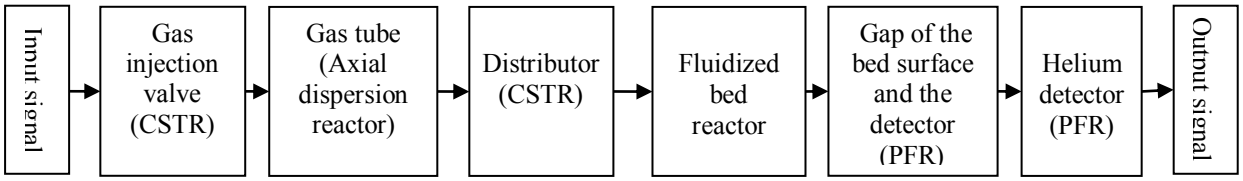

Figure 5.16: Scheme of the whole system divided into six reactors in series including the fluidized bed.

Table 5.1: The governing equations used in each of the system components.

Component	Governing equation	Comment	
On/off injection valve	$C = C_0 \exp(-(t-t_0)/\tau_v)$	$\tau_v = 2.8$ curve fitting result	**Eq. 5.28**
Gas injection tube	$\frac{\partial C_t^i}{\partial t} = D_{axt}\frac{\partial^2 C_t^i}{\partial x^2} + U_x \frac{\partial C_t^i}{\partial x}$ $\frac{1}{Pe} = \frac{D_{axt}}{uD_{tube}} = \frac{3.10^7}{\mathrm{Re}^{2.1}} + \frac{1.35}{\mathrm{Re}^{0.125}}$	L_{inj} = 0.35 m in the model based on the system geometry	**Eq. 5.29** **Eq. 5.30**
Distributor	$\frac{\partial C_{dis}^i}{\partial t} = \frac{U_x}{\tau_{dis}}(C_{in} - C_{dis}^i)$	$\tau_{dis} = Vol_{dis}/Q = 2.3$ (curve fitting result)	**Eq. 5.31**
Bed – detector gap	$\frac{\partial C_{b-d}^i}{\partial t} = U_b \frac{\partial C_{b-d}^i}{\partial z}$	The z value are experimental values	**Eq. 5.32**
Detector	$\frac{\partial C_{\det}^i}{\partial t} = U_{\det}\frac{\partial C_{\det}^i}{\partial x}$	L_{det} = experimental length of the sniffer of the Helium detector.	**Eq. 5.33**

The model geometrical values were used directly from the system dimensions for injection line, the detector response, and the gap between the bed surface and the sniffer. Gas injection valve has an on/off control mode with a rather complex response. It was simulated using the analytically resolved CSTR reactor response function with an average lag time (t_0) as presented in Table 5.1. The reason for introduction of t_0 was to take into account the transitional concentration variation inside the valve dead volume. The Helium concentration is initially 100% in this volume and gradually reduces to zero due to the dilution effect of the air flow in the main injection line. Otherwise, the injection system can be modeled with a CSTR in parallel with and plug flow reactor as explained by Levenspiel [217].

Gas flow from the injection valve to the distributor was modeled using a conventional convection, axial dispersion model. The geometrical dimensions were identical to the measured values. The gas distributor was modeled using and CSTR reactor model. The time constant of the distributor model (τ_{dis}) was fitted in the model based on the experimental results. The model value was 2.3 compared to the geometrical value of about 0.1 (calculated for an ideal flow). This difference is mostly due to the use of a static gas mixer (0.1m) in the gas injection line which introduces an additional dispersion which is not taken into account by the axial dispersion model of the gas injection tube.

The gas flow from the top of the bed into the detector was modeled using an ideal plug flow model. In reality there is some gas dispersion associated in this section due to the bubbles disruptions in the surface and particles presence above the bed. However, theses effects were ignored in the current tests as compared to the dispersion introduced through the CSTR model of the gas distributor. The detector sniffer was similarly modeled by a plug flow model. This assumption is in agreement with experimental results which illustrate a limited dispersion caused by sniffer line.

The model prediction results for the residence time distribution of the system elements other than the fluidized bed are presented in Figure 5.17. The proposed model predicts well the experimental results presented.

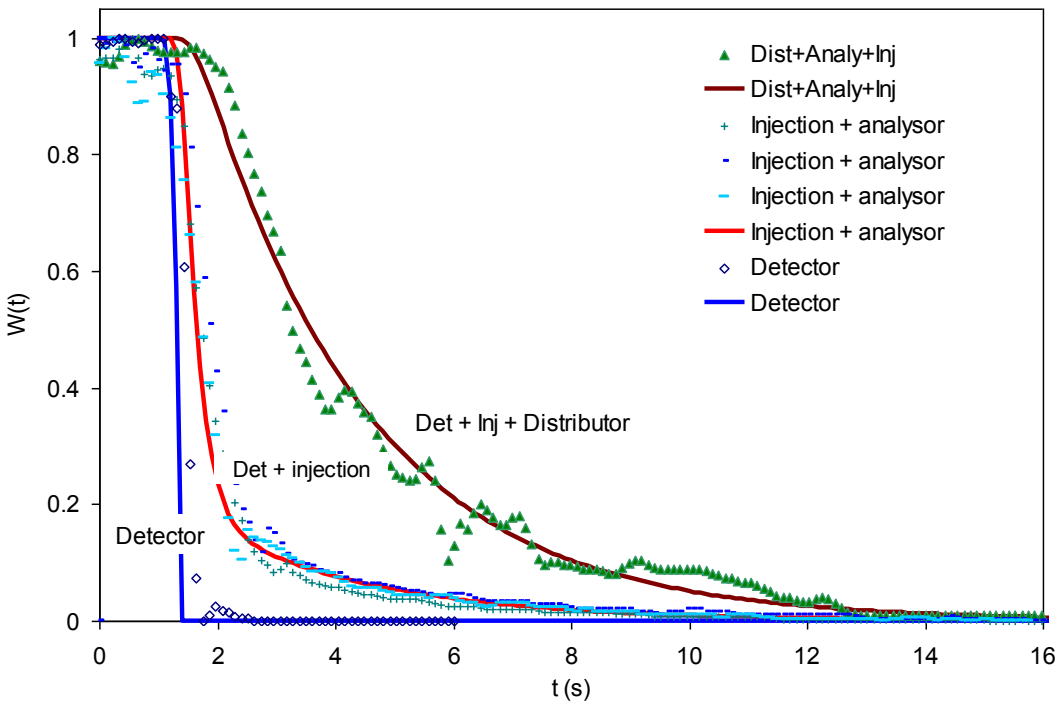

Figure 5.17: Modeling of the residence time distribution of different system components other than the fluidized bed for U_R =0.071 m/s. The RTD of the "Det+inj+Distributor" was measured in a bed of 0.5m height with the sniffer immersed into the bed just above the distributor with Ws = 0 kg/h.

5.9 Model Results

Experimental residence time distribution measurements and basis of a hydrodynamic model were discussed in this chapter. In the following sections, the experimental results are used to select a relation for the size of the bubbles in the fluidized bed and an appropriate model to describe gas flow in the emulsion phase. The hydrodynamic model was then compared with the experimental date for the impact of height of the fluidized bed, fluidization gas injection flow rate, and solid circulation flow rate. Finally, sensitivity of the gas phase residence time was analyzed based on the developed model for the most important hydrodynamic parameters.

5.9.1 Bubble Size Correlations

Proper selection of the bubble size correlation is essential in the bubbling fluidized bed hydrodynamic model. Bubble size affects the bubble velocity and therefore changes the bubble hold-up and gas residence time in the reactor. Moreover, bubble size affects the gas exchange between bubble and emulsion phase. Therefore, it influences the overall reaction conversion in the reactor. Moreover, bubble velocity causes gas dispersion along the fluidized bed due to the difference of gas flow velocity in the bubble and emulsion phase. Baeyens and Wu [239] have compared more than a dozen of the bubble size correlations in the literature. They concluded that the equations stress the fact that the mean bubble size depends only upon $U - U_{mf}$, H, and area of distributor orifice, whereas particle size has no effect.

Different bubble diameter correlations [276,278-280] were tested in the current study to find the one most adapted to the experimental RTD results. The comparison is made by considering a plug flow of gas in the emulsion phase (Daxg = 0). Figure 5.18 illustrates comparison of the modeling and experimental results for four bubble diameter correlations. The sum of least square of errors for each modeling curve is presented in the figure. Accordingly, the relation of Darton [276] resulted in the best fit. The bubble size calculated with Darton [276] equation has the largest size compared to other cases and therefore results in faster bubble rise velocity. It should be noted that the bubble rise velocity and the gas dispersion in the emulsion phase are closely related. This relation and its influence on the selection of bubble diameter correlation will be discussed in the next section.

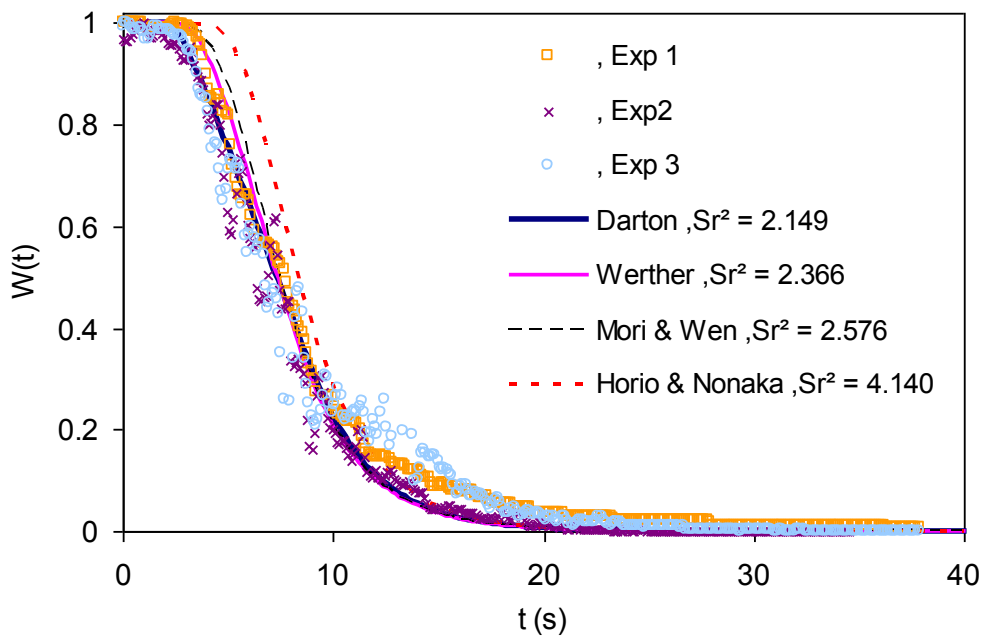

Figure 5.18: Comparison of experimental RTD results and modelling results with various bubble diameter correlations. The sum of least square of errors of model and average experimental results are listed in the figure.

Table 5.2: The bubble diameter expressions presented in the Figure 5.18.

Author	Expression
Darton et al. [278]	$d_b = \frac{0.54(U-U_{mf})^{0.4}(h+4\sqrt{A_0})^{0.8}}{g^{0.2}}$
Werther [281]	$d_b = 8.53\times10^{-3}\sqrt[3]{1+27.2(U-U_{mf})}(1+6.48h-h_0-h_{jet})^{1.21}$ d_0: Height above the distributor plate where the bubbles are as large as those formed by commercial plates. d_j: jet length at the distributor.
Mori and Wen [276]	$d_{b,\max} = 0.65(A_R(Vsg-U_{mf}))^{0.4}$ $d_{b,0} = 1.3/g^{0.2}((Vsg-U_{mf})/N_{or})^{0.4}$ $d_b = d_{b,\max} - \exp(-0.3H/D_R)(d_{b,\max}-d_{b,0})$
Horio and Nonaka [280]	$d_b = \left[0.46\frac{(U_R-U_{mf})^{0.5}H}{g^{0.25}} + d_{b0}^{1.25}\right]^{4/3}$ $d_{b0} = \frac{3.77(U_R-U_{mf})^3}{g}$

5.9.2 Gas Dispersion in Emulsion Phase

The gas flow in the bubble phase is assumed to have a plug flow behavior in the current model. This choice seems reasonable considering fast upward rise of the bubbles in the bed. Identical choice has been made by various authors [153,172,175,270]. However, the choice of the gas flow model in the emulsion phase is less obvious. Gas flows upwards in this phase with a relatively slow velocity. Moreover, bubbles flow causes a considerable mixing in the emulsion phase in different radial and axial directions [282]. Various methods have been proposed in the literature [153,159,170,175] to model the emulsion phase, as presented in chapter 1. Different possibilities are tested in the current study to select the most adopted model based on the experimental results.

Gas flow in the emulsion phase is encountered with two gas dispersing phenomena. First is the upwards gas dispersion caused by fast bubbles flow parallel with the emulsion phase. Two way gas exchange between bubble and emulsion phase results in upwards gas dispersion along the reactor. Gases at height H can enter into the bubble, move rapidly upwards and then re-enter into the emulsion phase in a height above the actual height of the original emulsion gas flow. Moreover, a very small portion of the gas in the emulsion phase can be trapped into the bubbles wakes and moved upwards. The second gas dispersion phenomenon is related to the particles movement. Particles have a downward movement in the emulsion phase, as discussed previously. Therefore, particles can drag a part of gas downwards relative to the emulsion phase gas flow direction. This results in downward gas dispersion. Therefore, these mixing mechanisms have ordered directions which make them more similar with axial dispersion model rather than CSTR system.

Three models were tested in the current study to describe gas flow in the emulsion phase including: plug flow, CSTR, and axial convection – dispersion model. The correlation of Darton et al. [278] was first used to calculate the bubble size in the model. Resulting RTD curves are presented in the Figure 5.19 for each case and compared with the experimental results. The plug flow model (Daxg = 0 m²/s) slightly overestimates the results in the beginning and underestimates the experimental results for the second half of the curve. On the other hand, the CSTR model largely overestimates the

experimental results. Accordingly, none of the ideal PFR or CSTR models can best predict the gas dispersion in the emulsion phase. Axial dispersion model was tested as an intermediate modeling solution. The resulting predicted curves demonstrate that the axial dispersion model gives the best fit result with Daxg of 0.008 m²/s.

Correlation of Werther [281] was next used in the model to calculates RTD results similar to the procedure explained with Darton equation. The results are plotted in the Figure 5.20. The best modeling result was obtained with axial convection – dispersion model with Daxg of 0.068 m²/s. The Daxg in this case is one order of magnitude higher than the Daxg obtained with Darton equation. This result is in agreement with the above made discussion about the sources of dispersion for gas in the emulsion phase. Identical dispersion results are achieved here either by small Daxg and fast bubble rise velocity (big bubble diameter), or by higher gas dispersion and slower bubble rise velocity.

The correlation developed by Werther [281] was used in the rest of this study. The main reason for this selection was the fact that the Daxg with Werther equation was relatively higher than Daxg with Darton equation. This results in a repartition of gas dispersion between both bubble rise velocity and solid movement in the emulsion phase. However, optimum selection of bubble size correlation requires measurement of the bubble size in the fluidized bed. However, this measurement was not carried out in the current investigation. Therefore, an exact selection of a bubble size correlation is not possible.

Comparison of the gas axial dispersion coefficients in the literature illustrates that the main parameters influencing Daxg are gas velocity and reactor diameter. The influence of these parameters on axial dispersion will be discussed in more details in the following sections.

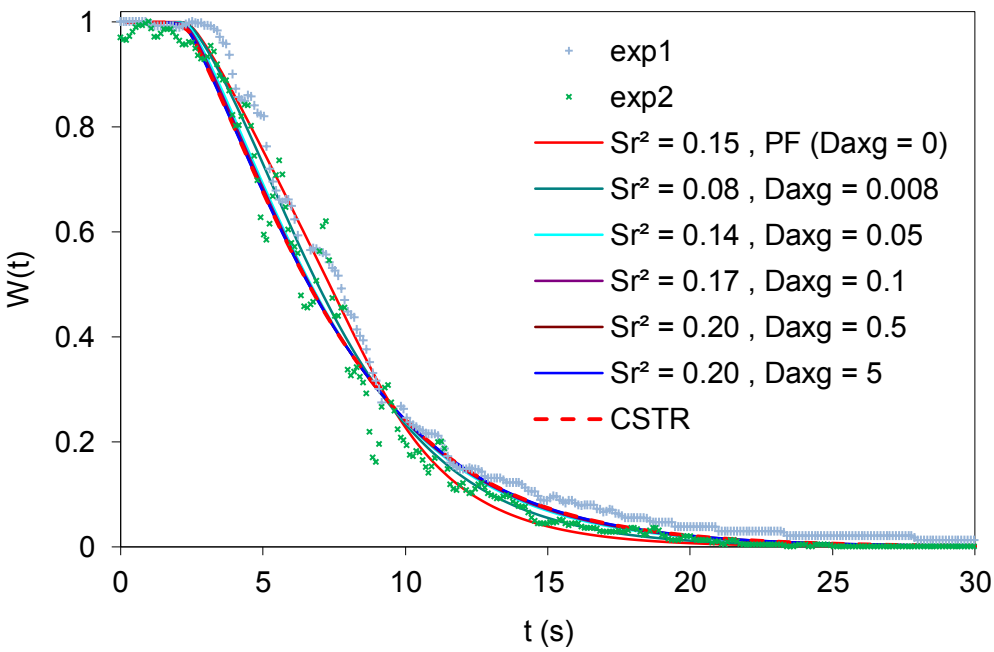

Figure 5.19: Comparison of different possible models for the gas in the emulsion phase with H_R = 0.50 m, U_R = 0.068 m/s (5.26 U_{mf}), and Ws = 0. The sums of least square errors are listed in the figure compared with the experimental results of identical conditions. The experimental values are not plotted for a better distinction between model results. Darton's correlation [276] is used to calculated the bubble size in all modeling results.

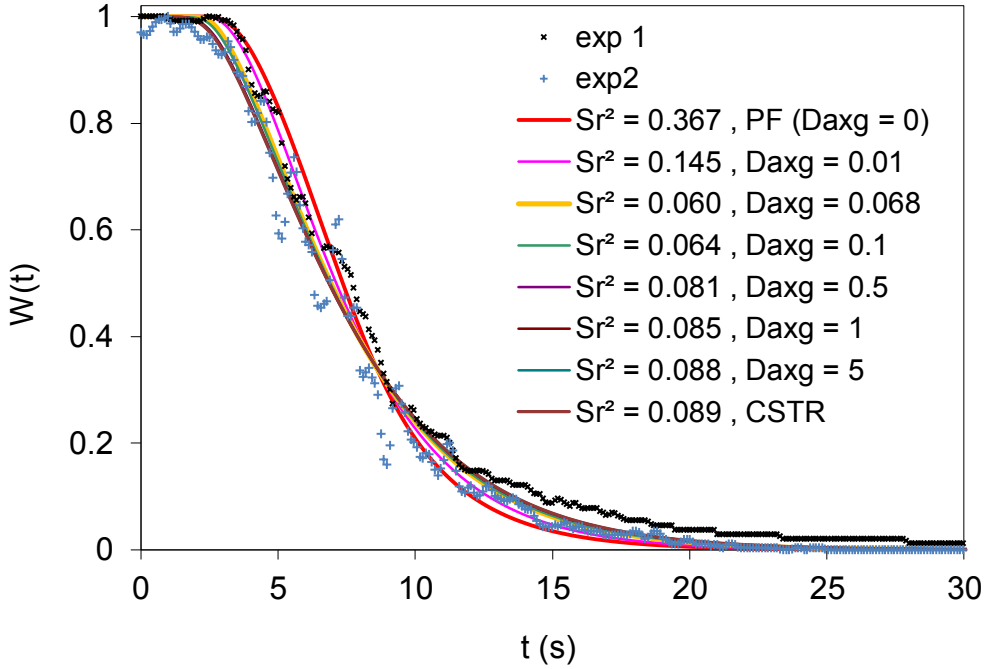

Figure 5.20: Comparison of different possible models for the gas in the emulsion phase with H_R = 0.50 m, U_R = 0.068 m/s (5.26 U_{mf}), and Ws = 0. The sums of least square errors are listed in the figure compared with the experimental results of identical conditions. The experimental values are not plotted for a better distinction between model results. Werther [281] correlation is used to calculated the bubble size in all modeling results.

Material balance model for the gas in the emulsion phase was investigated in this section. Two sources of gas dispersion were identified in the emulsion phase including: fast bubble rise velocity and downward solid flow. The convection – axial dispersion model was found to be the best material balance equation representing gas flow in the emulsion phase. The bubble diameter correlation developed by Werther [281] was selected to be used in the model with a constant axial dispersion coefficient of 0.068 m²/s.

5.9.3 Model Validation

In this section, the developed hydrodynamic model of the bubbling fluidized bed is compared with the experimental RTD results obtained in the cold flow prototype. As discussed before, effects of three operating parameters on the residence time distribution were investigated in this study including: height of fluidized bed, gas fluidization velocity, and solid flow rate.

First, the modeling and experimental results are compared with various fluidized bed height (solid inventory) in the reactor. The experimental tests were carried out with constant fluidization gas injection and no solid circulation. The height of the fluidized bed was changed from 0.05 m to 0.5 m. The detector sniffer was placed inside the bed for most of the measurement heights for these tests. This eliminates the interference of the RT_R (see Figure 5.1) in the experimental results. Only in the last experimental test with bed height of 0.068 the sniffer was placed 0.02 m above the bed in the freeboard.

Experimental and model output functions are compared in Figure 5.21 to evaluate the impact of the variation of fluidized bed height. The average residence times of whole system (RT) and dimensionless variances (ζ^2) are plotted in Figure 5.22 for the same experimental and modeling tests. Accordingly, modeling and experimental gas dispersion results show a good agreement in this case. This implies that axial gas dispersion is not a strong function of height of the solid bed in the current conditions.

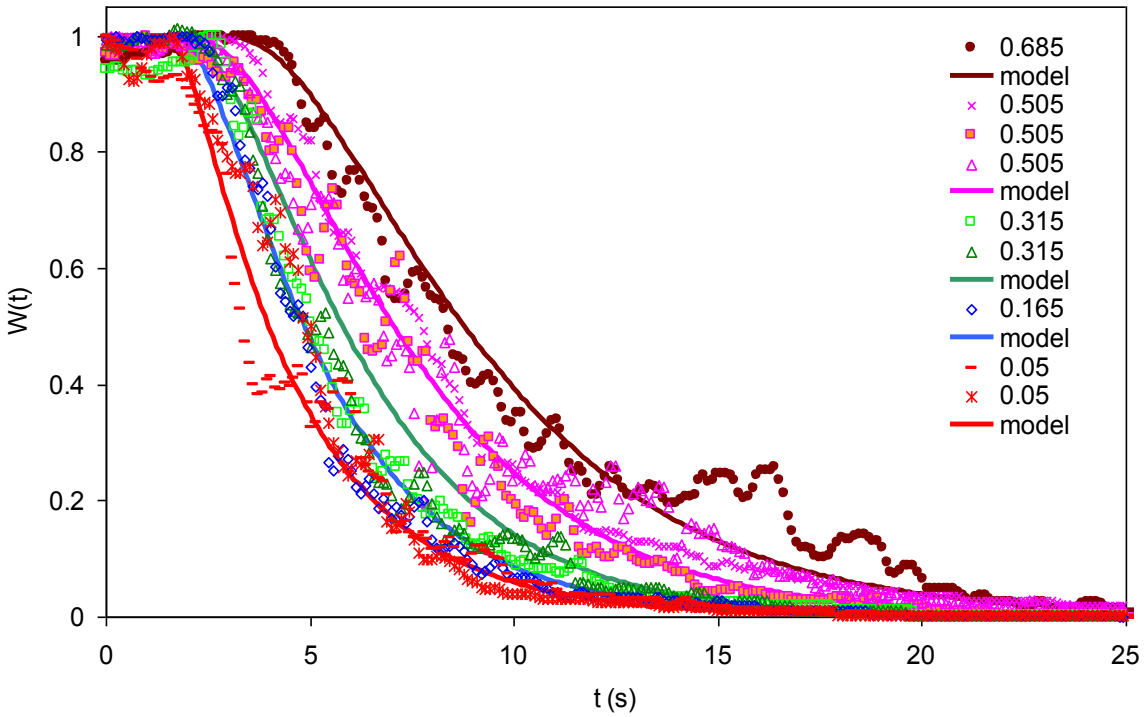

Figure 5.21: Model prediction compared to the experimental results for different solid heights in the reactor. The response function is plotted for the whole injection, reactor and detection system with Q_R = 1.92 Nm^3/h, and no solid circulation. The detector sniffer is placed inside the fluidized bed. Therefore, there exist no additional distance between point of measurement and the detector

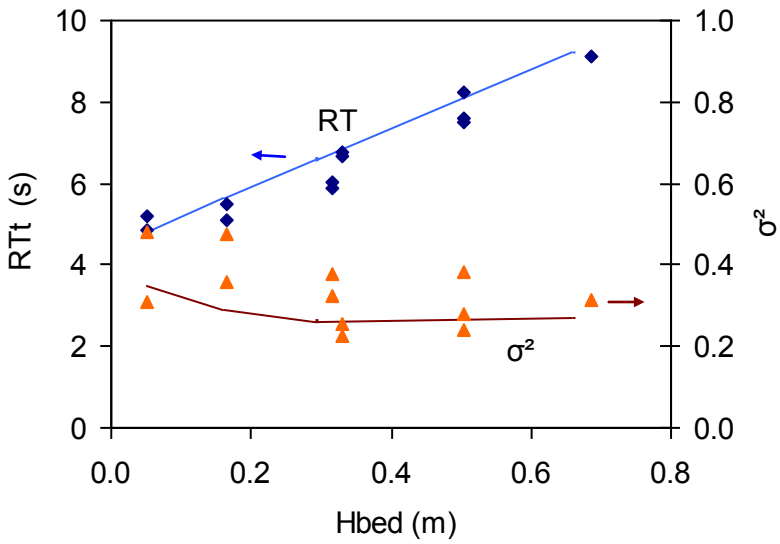

Figure 5.22: Model prediction results versus the experimental results of the residence time for whole system (injection, reactor and detection).

Variation of the residence time distribution due to change of the gas fluidization velocity in the reactor was investigated next. The fluidization gas was changed from 0.03 m/s ($2.6U_{mf}$) to 0.16 m/s ($12.2U_{mf}$) with a constant solid inventory and no solid circulation. Figure 5.23 illustrates the modeling and experimental residence time distribution results. While the model predicts well the gas distribution for

moderate flow rates, it fails to properly simulate the gas distribution for high gas velocities. The model overestimates the residence time especially at high gas flow rates. This difference probably relies on the limit of the models for the system components other than fluidized bed. The most susceptible region is the distance between the surface of the fluidized bed and the detector sniffer ($\Delta H_{sniffer}$) due to the influence of bubbles rupture on the bed surface. This effect is more significant with higher gas flow rates due to more violent bubble behavior and higher $\Delta H_{sniffer}$ chosen in the experimental tests. It should be mentioned that this gap did not exist in the experimental tests with variable height of fluidized bed presented above.

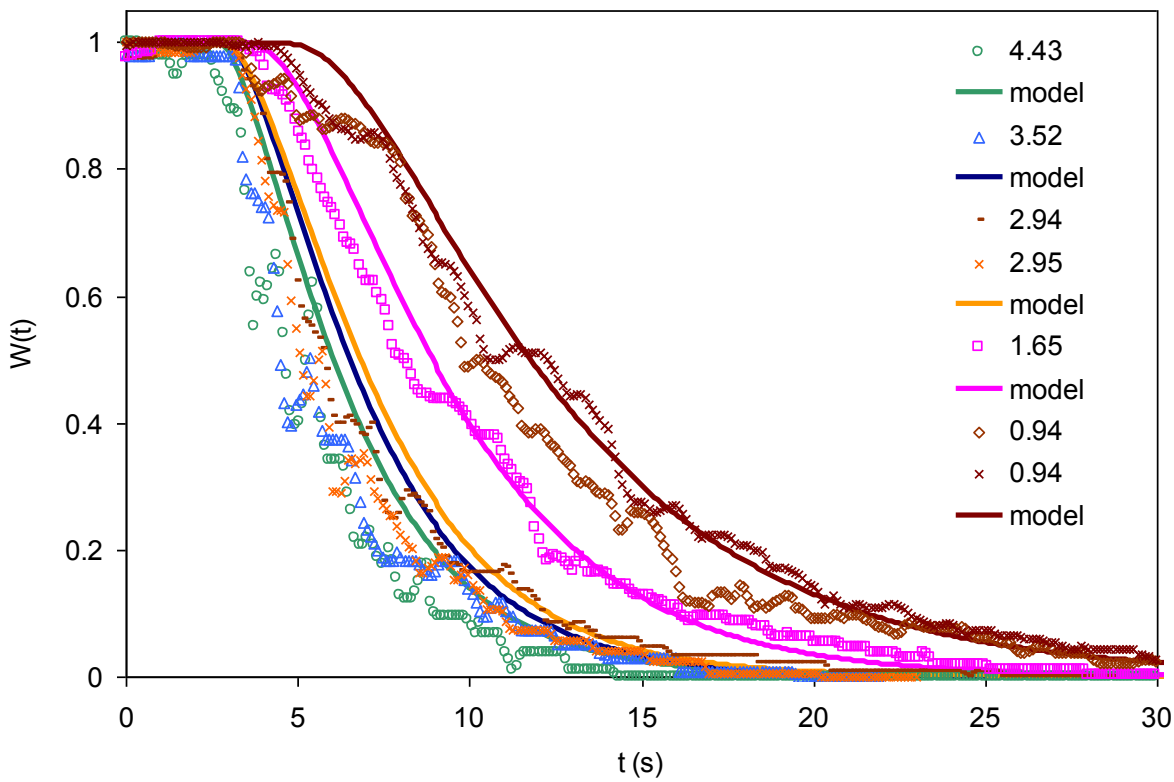

Figure 5.23: Comparison of the model and the experimental results for the effect of gas velocity on the residence time distribution of the whole system (injection, reactor and detection).

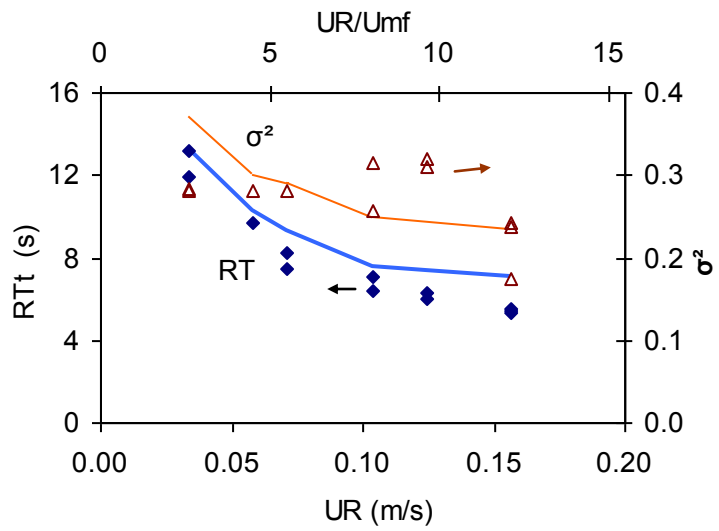

Figure 5.24: Comparison of the model and experimental results of RT and ζ^2 for different gas flow rates. The residence time values are the whole system response including injection, reactor and detection parts.

The modeling results were finally compared with the experimental results with variation of solid circulation flow rate. The resulting wash out function for a solid flow rate of 33 kg/h to 120 kg/h is illustrated in Figure 5.25. The plotted curves confirm the results previously presented in section 5.6.3. The solid flow rate does not have a significant effect on the gas residence time in the fluidized bed. The model response plotted in Figure 5.25 is simulated for identical condition but with no solid circulation. These results confirm hypothesis of neglecting effect of solid flow rate in the reactor on the gas residence time. The main reason for this behavior is the influence of bubbles in the fluidized bed as discussed in section 5.6.3.

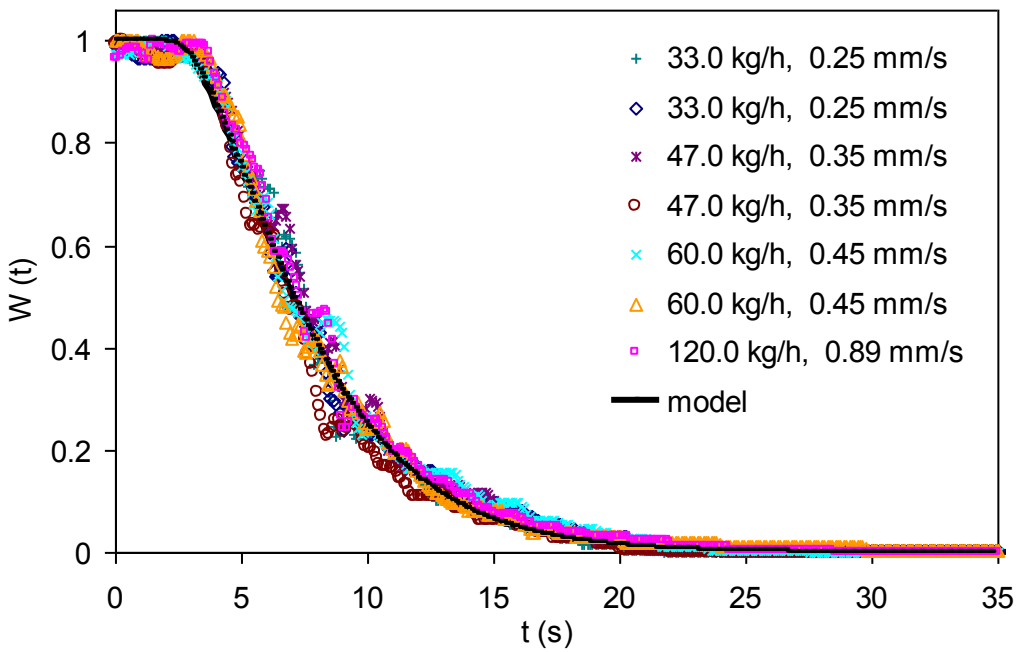

Figure 5.25: Experimental RTD results for solid flow rate variation with H_R = 0.5 m, and Q_R = 1.65 Nm^3/h. The solid velocity is calculated as the superficial solid velocity in the reactor. There is no solid circulation in the model.

Comparison of the modelling and experimental results illustrated that the emulsion phase is best modelled by an axial dispersion – plug flow model. A fixed value of 0.1 m^2/s was selected for the dispersion coefficient of gas flow in the emulsion phase in the current study based on the experimental RTD results. Comparison of the modelling results and the experimental findings demonstrated that the model predicts well the effect of variation of solid height in the reactor while it has a less precision regarding the impact of the gas flow rate variation especially for high gas flow rates. The solid flow rate was illustrated to have a negligible impact on the overall gas residence time in the reactor.

5.9.4 Sensitivity Analysis

Mean gas residence time sensibility was investigated using the developed model. The investigated parameters include variation of bubble diameter, bubble raise velocity, gas velocity in the emulsion phase, and bubble – emulsion gas exchange coefficient. The resulting parameter sensitivity is plotted in Figure 5.26.

Gas velocity in the emulsion phase (U_e) affects the RT value linearly. However, the impact is relatively small on the gas residence time; for instance 50% change of the U_e, results in less than 5%

variation of the RT. Indeed most of the gas flows in the form of bubbles in the fluidized bed. Therefore, the flow rate variation in the emulsion phase is not the main parameter contributing to RT.

Mean gas residence time sensibility to the bubble raise velocity in the bed is also plotted in the Figure 5.26. The resulting curve demonstrates considerable importance of the bubble velocity in the bed. As the bubble raise velocity increases, more gas passes through the bubble phase compared to the emulsion phase. However, this impact decreases as the bubble velocity increases. It should be noted that the bubble raise velocity is a function of the bubble diameter in the bed. This can be well deduced from the sensibility results of the bubble diameter illustrated in Figure 5.26. The gas residence time in the bed demonstrates similar sensibility to the variation of the bubble diameter as the bubble raise velocity.

Another important parameter in the bubbling fluidized bed is the gas exchange between the emulsion and the bubble phases (K_{be}). Effect of variation of the K_{be} on the residence time in the reactor is illustrated in the Figure 5.26. Accordingly, gas exchange coefficient does not have a significant effect on the residence time for the range of ±90% in the current test conditions. It should be noted that exchange coefficient have a significant importance if reactions are taken into account. Since the reactions are carried out only in the emulsion phase in the current model while most gases flow in the bubble phase. Therefore, exchange of the gas between these two zones has a significant importance on the overall reaction conversion.

The impact of the gas dispersion on the average gas residence time can be deduced from the Figure 5.19. Gas residence time increases as gas dispersion increases with the smallest residence time for plug flow conditions and highest for CSTR gas model in the emulsion phase. This impact relies on the nature of these type of reactors and the fact that higher dispersion causes gas to disperse along the reactor and therefore have a higher residence time.

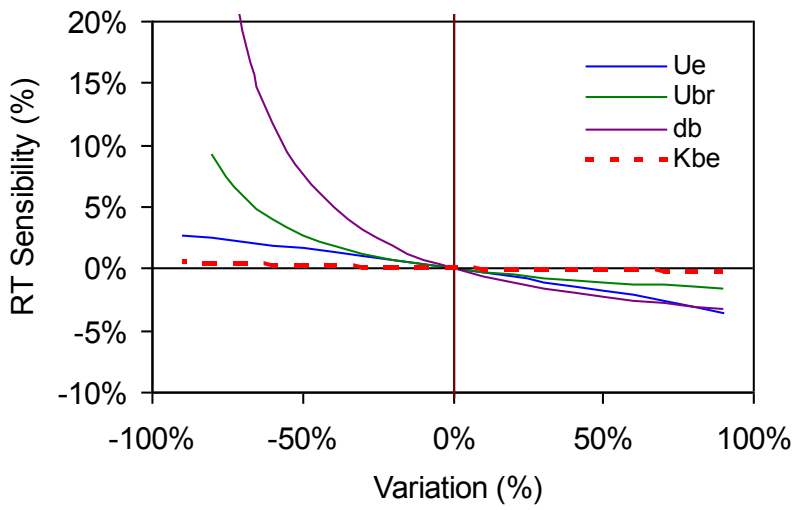

Figure 5.26: Sensibility of the gas residence time (RT) in the bed for variation of the U_{br}, U_{mf}, d_b, and K_{be}. The reference condition is H_R = 0.5 m, U_R = 0.07 m/s.

According to the presented results, the mean gas residence is very sensitive to the variation of bubble size and bubble raise velocity. These two parameter are closely related as bigger bubbles has a higher gas velocity in the reactor [277,278]. Velocity of the gas flow in the emulsion phase was shown to have a linear effect on the residence time. RT increases as the U_e decreases. However, this impact is not significant compared to the bubbles influence. The emulsion – bubble gas exchange coefficient had the less significant effect on the mean gas residence time.

5.10 Conclusion

The current chapter presented the experimental and modeling hydrodynamic investigations carried out on the bubbling fluidized bed reactor of the cold flow prototype. The main conclusions from this study can be listed as:

- A wash out input tracer function was best adapted to experimental investigation of the mean gas residence time distribution in the reactor.
- The experimental results demonstrated that the extra dispersion caused by the system components other than the fluidized bed was considerable compared to the RTD results of the bed. Therefore, the output signals were treated carefully to avoid errors introduced by these extra elements. Two signal treatment methods were employed:
    - Simple linear treatment to analyze the mean residence time values.
    - Development of a reactor model including all system elements including the whole injection, distribution and detection system in addition to the fluidized bed itself for gas dispersion analysis.
- Experimental investigations illustrated that gas residence time increases rather linearly with increase of the height of the fluidized bed. Increase of the gas flow rate decreases mean gas residence time with a sharp effect for low gas flow rate and less significant effect for higher gas flow rats. The solid flow rate was shown to have a negligible effect on the mean gas residence time.
- A hydrodynamic model was developed based on the two phase theory of bubbling fluidized bed. A plug flow reactor was selected for the gas in the bubble phase and an axial dispersion – plug flow model for the gas in the emulsion phase. A fixed axial dispersion coefficient of 0.1 m^2/s was selected based on the fitting of the experimental results.
- A sensitivity analysis was carried out based on the developed model. It demonstrates that the mean residence time is very sensible to the variation of the bubble raise velocity and the bubble diameter with less sensitivity to the gas flow velocity in the emulsion phase.

The developed hydrodynamic model is used in the next chapter to develop a reactor model by including the kinetic mechanisms and reaction effects such as gas expansion, and influence of oxygen carriers.

Chapter 6

Reactor Study: Methane Combustion

6.1 EXPERIMENTAL RESULTS 159

6.1.1 Data Evaluation 159

6.1.2 Continuous and Transitional Steady State Test 161

6.1.3 Batch tests 167

6.1.4 Oxidation Reactor 170

6.1.5 CO_2 Capture Efficiency 172

6.1.6 Attrition and Particle Aging 173

6.1.7 Agglomeration 177

6.2 REACTOR MODEL 178

6.2.1 Modeling of the System Components 178

6.2.2 Reaction Mechanism 180

6.2.3 Kinetic Rate Equations 181

6.2.4 Heat Transfer 183

6.2.5 Gas Phase Reaction and Expansion 184

6.2.6 Solid Phase Material Balance 185

6.3 MODEL VALIDATION 186

6.4 CONCLUSION 189

6. Reactor Study: Methane Combustion

The principal purpose of the current system is to provide a flexible experimental device to investigate various influencing CLC parameters including: different oxygen carriers, reaction mechanisms, and contact of oxygen carrier with fuel and air. As discussed previously, a great emphasis was given to carefully control operating parameters including independent solid circulation, gas flow rates, solid inventory distribution between the reactors, and leakages.

This chapter presents the last parts of the current work which is dedicated to the combustion investigations in reference conditions.Ni/$NiAl_2O_4$ particles were used as reference oxygen carriers with methane as reference fuel. The reference condition permits to develop a simple experimental basis both for comparison with exiting experimental literature data as well as the future developments both in terms of oxygen carrier and feedstock. It should be mentioned that the current study was limited in terms of experimental time since the pilot plant was then modified for other feeds and OCs.

Current pilot plant is designed for steady state continuous operations. However, batch and transitional continuous tests were also conducted. Impacts of operation temperature, solid circulation rate, fuel flow rate, and oxygen carrier conversion were investigated in continuous operations. The transitional tests were carried out with a continuous and steady solid circulation between all three reactors with only one operating parameter being changed. Thereby, impacts of solid inventory in the fuel reactor and fuel injection flow rate on gas conversion were studied. In batch operations, a fixed quantity of oxygen carriers was placed inside the fuel reactor without solid circulation. Methane was then injected during a determined time period to measure variation of different parameters including solid inventory, temperature and fuel injection flow rate. Oxidation of oxygen carriers in the air reactor was also investigated. All three types of tests explained above were used for this purpose. The main investigated parameters in solid oxidation are: effect of solid inventory and air flow rate.

The experimental results of methane combustion in the high temperature pilot plant are first presented in this chapter for all three types of tests. Thereafter, the essay continues with a discussion on the experimental oxidation tests. The effect of long term operation on the oxygen carriers are then briefly discussed in terms of: attrition resistance, surface modification and porosity variation. Furthermore, the observed agglomeration during the experimental period is briefly reported.

A hydrodynamic model for bubbling fluidized bed was developed in the previous chapter. This model is further developed in this chapter to include the effect of gas expansion and solid phase material balance. A kinetic model is adapted from the available literature to model the kinetics of methane reduction on NiO/NiAl2O4 in the current system. The model includes both gas phase and solid phase models to cover different reaction aspects. Finally, the modeling results are compared with the experimental results to validate the developed model.

6.1 Experimental Results

6.1.1 Data Evaluation

Some specific terms are used in the current study to ease the comparison and investigation of the obtained data. The most common term is the oxidation degree of the oxygen carrier (OC). This stands for the ratio of the actual available oxygen in the OC compared to the total available oxygen in fully oxidized state. Oxidation degree is defined as [68]:

$$X = \frac{m - m_{red}}{m_{ox} - m_{red}} \qquad \textbf{Eq. 6.1}$$

Where, m is the actual mass of the particles, m_{red} and m_{ox} are correspondingly mass of sample in fully reduced and oxidized states. The oxygen ratio is defined as the maximum oxygen transfer capacity of the oxygen carried defined as [68]:

$$R_0 = \frac{m_{ox} - m_{red}}{m_{ox}} \qquad \textbf{Eq. 6.2}$$

R_0 depend on the active metal used in the oxygen carrier as well as the amount of inert in the particle. The oxygen ratio is 12.85 % for the oxygen carrier used in the current study. The flue gas at the outlet of the fuel reactor contains some nitrogen from the loop-seal. As explained in previous chapters, this amount can vary as a function of solid flow rate. To avoid results dispersion by nitrogen, the gas fractions are normalized to nitrogen free gas fraction as:

$$Y_i = \frac{Y_i}{Y_{CO2} + Y_{CO} + Y_{CH4} + Y_{H2}} \qquad \textbf{Eq. 6.3}$$

Where i stands for CH_4, CO, and H_2. The gas yield is defined as the fraction of methane that has been fully oxidized to CO_2 compared to a complete combustion and calculated as:

$$\gamma_{red} = \frac{Y_{CO2}}{Y_{CO2} + Y_{CO} + Y_{CH4}} \qquad \textbf{Eq. 6.4}$$

Combustion efficiency is another term used in some publications to assess the combustion conversion. This is defined by the ratio of the oxygen consumed by the gas leaving the reactor to the oxygen consumed by the gas if it is completely burned to CO_2 and H_2. Therefore:

$$\eta_C = \frac{(2C_{CO2} + C_{CO} + C_{H2O})Q_{R,out}}{4C_{CH4}Q_{CH4,in}} \qquad \textbf{Eq. 6.5}$$

The other useful term is the CO_2 capture efficiency (η_{CO2}) standing for the ratio of the CO_2 in the flue gas of the fuel reactor to the total CO_2 leaving the system. Therefore:

$$\eta_{CO2} = \frac{Q_{R2,out}C_{CO2}}{\sum Q_{out}C_{CO2}} \qquad \textbf{Eq. 6.6}$$

The gases at the exit of each reactor pass through a series of conducting tubes and treatment systems as explained in chapter 2 before reaching the analyzers. This distance between the reactor gas exit and analyzers imposes a lag time (Δt_{lag}) between the real gas concentration at the exit of the reactor and the measured concentrations by analyzers. This lag time is a function of gas flow rate, for instance it is about 200 s for injection of 0.5 Nm^3/h of CO_2 compared to about 110 s for combustion of 0.75 Nm^3/h of CH_4. Response time of thermocouples was almost instantaneous and about 20 s for the pressure measurement gauges.

The concentration measurement lag time does not introduce any interference in interpretation of continuous operation results regarding the fact that the final values in steady operations were select once the system had got to a stable level. Transitional test were carried out during rather long time periods of about 60 minutes. Therefore, the lag time does not have a significant influence on the measured concentrations. However, for each transitional test the Δt_{lag} is measured and the final measured concentration signals are corrected by $t = t_0 - \Delta t_{lag}$. In other words, the concentration curves are shifted backwards in terms of time by Δt_{lag} compared to temperature and pressure measurements. This lag time presents a considerable influence in case of the batch tests regarding the short overall experimental time. Therefore, it has to be taken into consideration in modeling and interpretation of batch tests. This interference in batch tests is discussed in more details in section 6.1.3.

Carbon balance on the carbon could be performed based on the outlet gas flow rate measured by means of a flow meter installed at the exit of the fuel reactor, downstream of the primary condenser. The condenser got saturated after an operation of 2 to 3 hours, and could not remove all of the water vapor produced during the combustion. Therefore, the measured dry gas flow rate was most of the times containing some water vapor. Hence, an excess of 5 – 10 % of carbon was measured in the flue gas compared to the inlet flow in most of the tests with a random nature in this interval. It should be

mentioned that a second condenser was installed at the inlet of the analyzers controlled with a sensor to ensure dehumidification of the analyzed gas. The lack of carbon mass balance is not a primary concern in the current study regarding the fact that no carbon deposition was observed during the tests and minimum gas leakage out of the fuel reactor (section 6.1.5). In this study the comparisons are based on the yield and gas concentrations to avoid erroneous conclusions.

6.1.2 Continuous and Transitional Steady State Test

The procedure of a typical steady state test in the high temperature pilot plant is explained in the chapter 2. First, a steady state solid circulation with constant pressure drop and desired solid inventory in each reactor was set. In this step the fuel reactor and lifts were fluidized with Nitrogen while air was injected into the air reactor to ensure complete oxidation of oxygen carriers. Once the steady circulation was achieved, Nitrogen was replaced with natural gas in the reactor and combustion starts.

Figure 6.1 illustrates a typical combustion test with injection of methane. The concentration measurements for the steady state tests were conducted once the exit results were reasonably stable for example with t > 7000 s in the current test. The results are average of the concentration output during a period of about 5 min which is well above the gas residence time and comparable with solid residence time in the reactor. Since there is only one gas analyzer available for the two air reactors, oxygen concentration was first measured at the outlet of the reactor R2 till all oxygen is consumed. Thereafter, the analyzer is shifted to the exit of the reactor R3 to measure the excess of oxygen as indicated in the Figure 6.1.

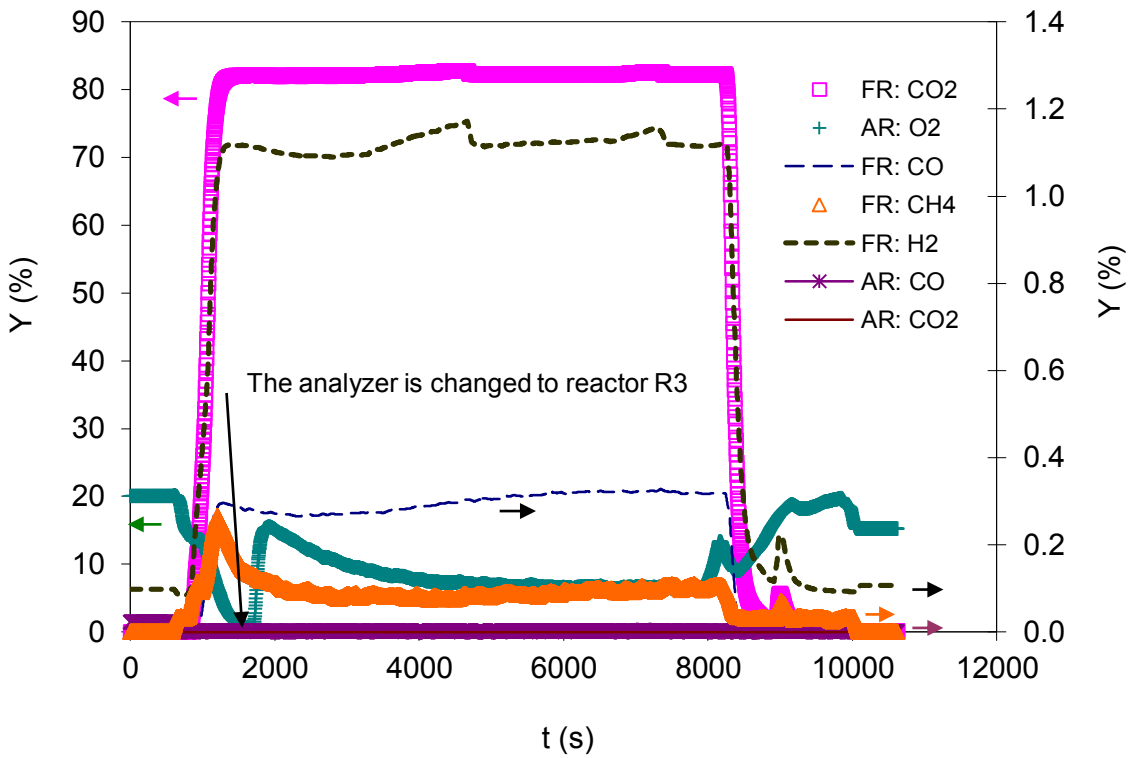

Figure 6.1: A typical continuous combustion test in the high temperature pilot plant with H_{R1} = 0.51 m, and Ws = 45 kg/h, Q_{CH4} = 0.5Nm^3/h, inlet U_{CH4} = 0.066 m/s, U_R = 0.2 m/s for reacted gases, ΔX = 25%, Q_{lv} = 7.5 NL^3/h, Qss = 0.1 NL^3/h.

The pressure drop and temperature in main sections of the system are plotted in Figure 6.2. The supposed steady state region is illustrated by use of dashed lines in the figure. Stability of pressure

drop in lifts shows that the solid flow rates are fairly unchanged. Pressure drop in reactors remain fairly constant indicating steady state operation. It should be noted that a small difference in the solid flow rate can result in slight variation of solid height in the reactors. This was controlled by manually adjusting the L-valves flow rate during tests to achieve a condition in which solid heights remained constant to the desired levels. This can be distinguished in the figure where the heights of three reactors get the same level at the end of the run.

The solid flow rate was measured at the end of each test by stopping one of the L-valves. Therefore, solid flow rate is measured from the accumulation of solids in reactors. Temperature variations in all reactors are also plotted. Temperature has inertia much higher than other parameters to be stabilized. In terms of the carbon balance, an excess of 9% was measured in this test. As explained above this difference is due to the presence of water vapor in the measured dry air flow rate.

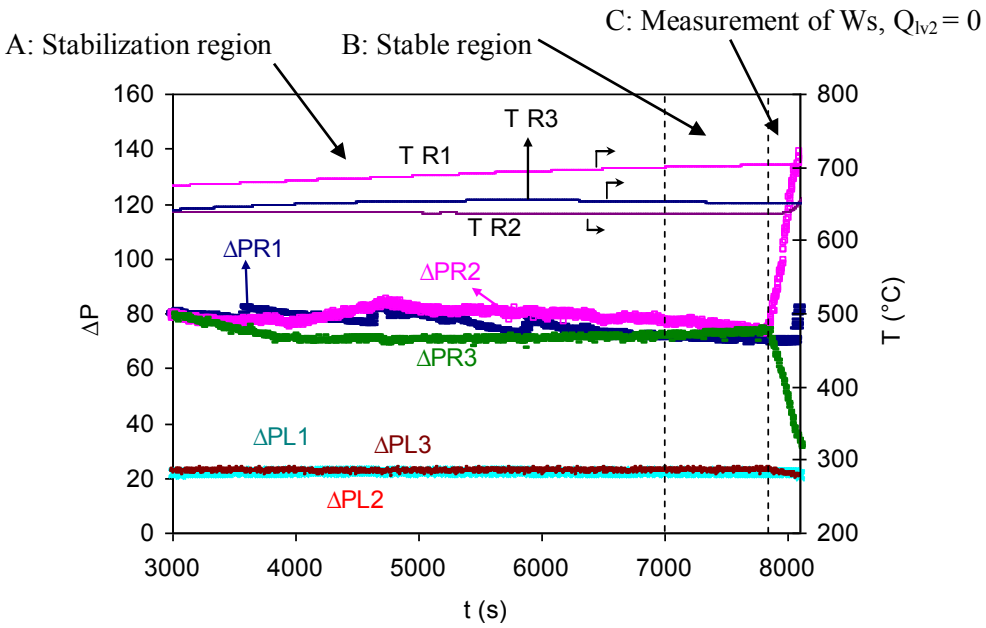

Figure 6.2: Pressure and temperature variation in the reactors of the high temperature pilot plant for the experimental test presented in Figure 6.1.

Effect of temperature on the combustion conversion was investigated in the pilot plant. The other operating conditions were kept constant including solid flow rate in the range of 40±5 kg/h, CH_4 injection flow rate of 0.5 Nm^3/h, and height of solid bed of 0.5 ±5 m. The resulting ΔX (based on total methane conversion) was about 28 %. Figure 6.3 illustrates the resulting variation of the combustion conversion and gas fractions (Yi) of CO, CH4 and H2 in a temperature range of 620 – 830 °C. All over the measurement temperature range, the CH_4 conversion remains very high above 99.4 %. As temperature increases, CO_2 conversion decreases slightly by about 0.3 %, CO concentration increases by 0.24%. The concentration of CH_4 and H_2 show a very narrow increase in the same temperature range. These results are consistent with the thermodynamic analysis carried out by Mattisson et al. [199] based on the minimization of Gibbs free energy. These results suggest that the reactions involved in the reactions involved in the current tests have been fast enough for the flue gas to get to the equilibrium state. Furthermore, it can be concluded that the increase of temperature results in the reduced methane conversion by current oxygen carrier.

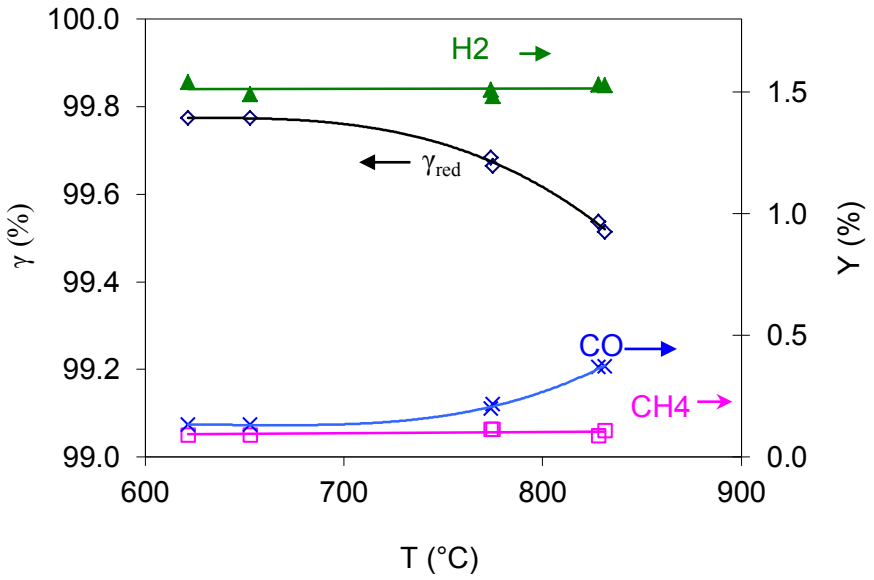

Figure 6.3: The effect of temperature on the combustion yield in the fuel reactor with Q_{CH4} = 0.5 Nm^3/h, H_R = 0.5 ± 5 m, Ws = 40±5 kg/h, ΔX = 28 %, inlet U_{CH4} = 0.066 m/s, and U_R = 0.2 m/s for reacted gases.

Effect of solid – gas contact time on the gas conversion was investigated in steady state continuous experimental tests. Gas conversion and concentration of gases at the flue gas are illustrated in Figure 6.4. Height of the fluidized bed was varied from 0.12 m to 0.55 m. The operating conditions were maintained constant with CH_4 injection flow rate of 0.5 Nm^3/h, temperature of 800±15 °C, solid flow rate of 800±15 °C, and oxygen carrier conversion of 28 %. As height of the fluidized bed increases, the solid – gas contact time raises. Therefore, reaction conversion tends to the equilibrium state. Gas yield increases rather linearly as height of the bed increases. Consequently, CH_4 exit concentration decreases linearly. H_2 goes through a rather rapid concentration reduction up to a bed height of 0.3 m above which its concentration remains constant. Similarly, Concentration of CO increases rapidly till H_R = 0.3 m, above this limit it remains almost constant.

It should be noted that all over the presented range gas yield remains high, above 99%. This illustrates the very fast reactions involved in the combustion of CH_4 by $Ni/NiOAl_2O_4$. The average residence time of the gas in the fluidized bed can be calculated using the hydrodynamic model described in the chapter 5. The resulting average gas phase residence time in the reactor is about 0.83 s for HR = 0.12 m and about 1.63 s with H_R = 0.3. This illustrates that the required residence time for the methane in the reactor to achieve a conversion of above 99.4 is in order of 1 to 2 s with the current OC. This implies that other forms of the fluidized bed reactors can be satisfactorily used in methane combustion. This result is in accordance with the literature results in terms of reactor operation regime selection [77,223]. Furthermore, the presented results demonstrate a good gas exchange between the bubble and emulsion phase. This will be discussed in more details below in section 6.3

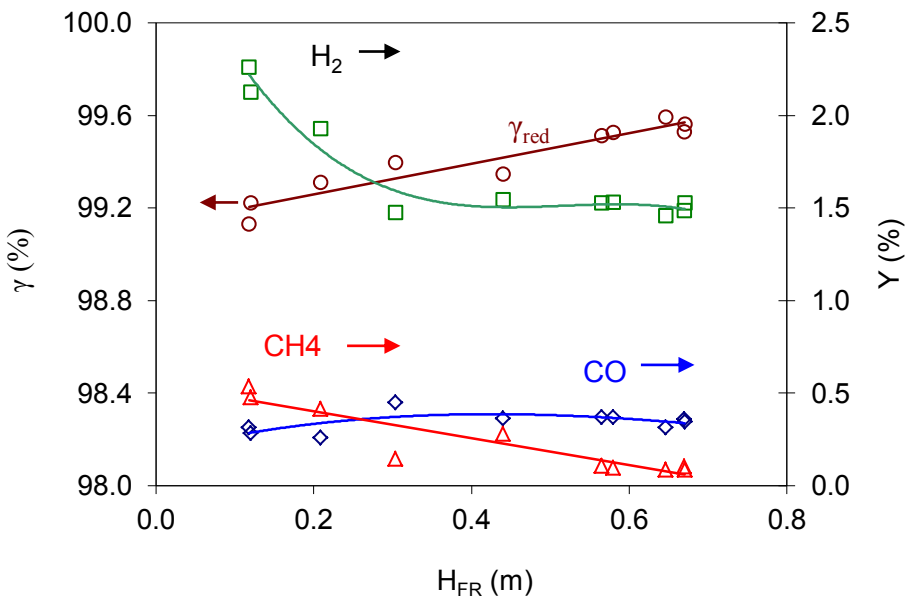

Figure 6.4 : Effect of the solid bed height in the reactor on the combustion yield with Q_{CH4} = 0.5 Nm^3/h, T_{R1} = 800±15 °C, Ws = 40±5 kg/h, ΔX = 28 %, inlet U_{CH4} = 0.066 m/s, and U_R = 0.2 m/s for reacted gases.

The impact of the fluidized bed height in the fuel reactor on the gas conversion was also investigated in transient conditioned. First, a steady state solid circulation was set in the pilot plant with constant solid circulation rate of 45 kg/h. The height of solid bed in the fuel reactor was initially set to 0.45 m with 800 °C and 0.5 Nm^3/h of CH_4. The outlet solid flow rate from the fuel reactor was then slightly increased above the incoming solid flow rate. As a consequence, the height of the solid bed started to decrease gradually. This permits to investigate the effect of variation of the gas – solid contact time in a continuous transitional test. The resulting variation of the exit gas concentration and H_R is illustrated in Figure 6.5. Different regions can be observed as function of the height of the solid bed as:

1. H_R > 0.26 m: variation of the H_R does have no significant effect on the conversion (CO_2 concentration of 99.4%).
2. 0.26m > H_R > 0.1 m: a gradual reduction of conversion due to decrease of solid – gas contact time is observed. However, the effect remains negligible in this region with final CO_2 concentration of 99.07%.
3. 0.1m > H_R > 0.02m: The height of the fluidized bed is less than the bed diameter of the reactor in this region. Reduction rate of the gas conversion increases slightly. However, the variation remains relatively small. CO_2 concentration drops to 97.8% at 0.02 m.
4. 0.02 m > H_R: The gas passes across the solid bed as a jet with very limited contact time between two phases. CO_2 yield decreases drastically in this region down to 65 % with rapid increase of H_2 to 75%, CO_2 to 71%, CO of 16%, and non-reacted CH_4 of up to 18%. CO2 still remains at a rather high value, suggesting a methane conversion of 83 % and CO_2 yield of 68%.
5. H_R ≈ 0: CO_2 fraction is still in the range of 60%, despite the fact that there is no remaining fluidized bed. Reaction can only be explained here by a solid – gas contact in dilute region resulting from the fall of particles from loop-seal entry into the reactor till the L-valve exit in bottom of the reactor. The gas conversion stabilizes to its limiting values as presented in the Figure 6.5. The rather high CO_2 fraction (corresponding to about 80 % CH_4 conversion and a CO_2 yield of 62%) is surprising since the fall of oxygen carrier in the dilute phase is not aimed to result in a homogenous contact here.

These results indicate importance of reaction in the dilute region in the freeboard of the fluidized bed and confirms similar result obtained by Abad et al. [163] by their developed CLC model discussed in chapter 1.

During operations with height of the fluidized bed less than 0.3 m, the surface of the fluidized bed is below the solid entrance point into the reactor. Therefore, there is an initial solid – gas contact in this zone where downward flowing fresh particles meet upward flowing gases above the fluidized bed (with H_R <0.3m). This contact becomes more important as the height of the solid bed decreases. This contact accounts for an important overall contact time in the reactor especially when bed height disappears, as in the region 5 of Figure 6.5 ($H_R \approx 0$). Exact effect of this region on the reaction requires development of a model with this region included. A simple calculation based on the velocity of free falling particles suggest an contact time of about 0.35 s for particles falling freely from the loop-seal outlet into the reactor bottom. Once more, the activity in this region suggests that the methane combustion with NiO/NiAl2O4 is very rapid.

Similar transitional test was carried out in a lower temperature range of 645±10 °C as presented in Figure 6.6. Comparison of the results of the two tests illustrates that CO_2 conversion starts to decrease earlier in lower temperatures. Moreover, there is a higher fraction of non-reacted CH_4 in lower temperature (48% at 645 °C compared to 20% at 790 °C).

Concerning the temperature, two measured T are plotted in the Figure 6.5 and Figure 6.6. The temperature of particles in the reactor is measured at a height of 0.1 m. Therefore, once the height of the bed descends below 0.1 m the particles temperature is not measured. Accordingly, the temperature of particles measured at the blinded T-bend is reported. This is a measure of particle temperature at the exit of the reactor.

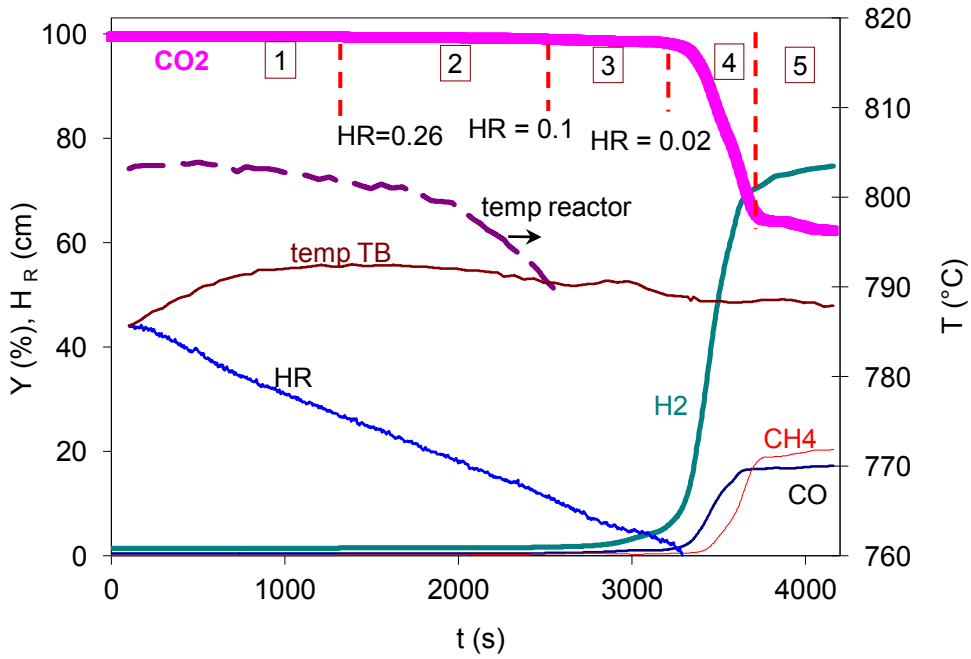

Figure 6.5: Transitional combustion of CH_4 in the reactor R1 with Q_{CH4} = 0.5 Nm^3/h, U_{CH4} = 0.066 m/s (U_R = 0.2 m/s of reacted gases). The height of the solid bed in the reactor was reduced continuously from 0.44m to 0 m, and Ws_1 = 45 kg/h into reactor R2.

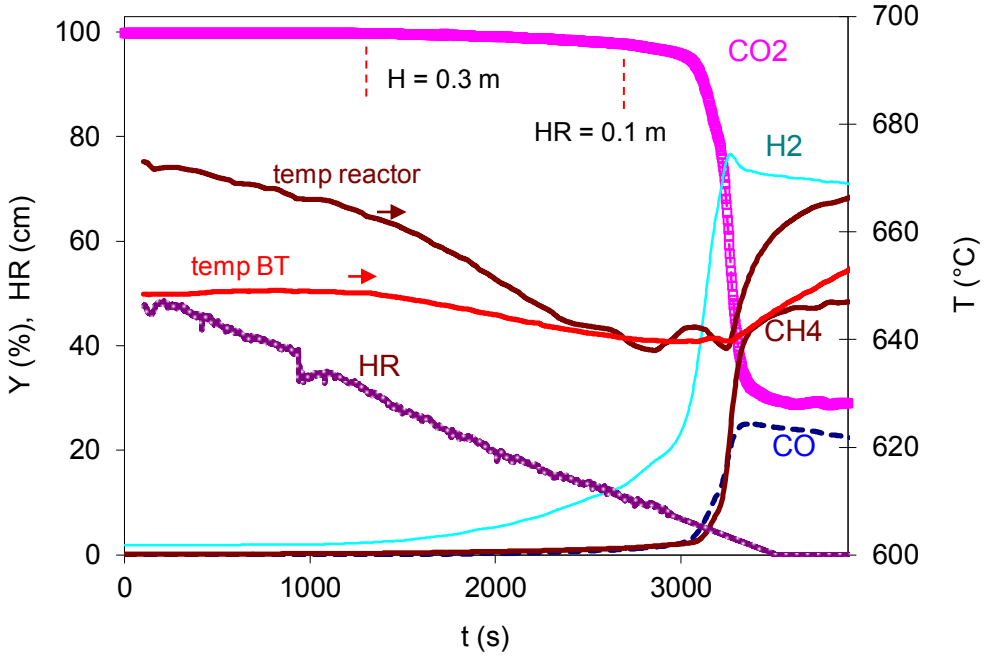

Figure 6.6: Combustion of methane in the reactor R1 in a transitional test with variable height of solid bed from 0.44m to 0 m, Q_{CH4} = 0.5 Nm^3/h, U_{CH4} = 0.066 m/s (U_R = 0.2 m/s of reacted gases), and Ws = 54 Kg/h into reactor R1.

The effect of the oxidation degree (ΔX) of the oxygen carrier on the combustion reaction was investigated in a transient test presented in Figure 6.7. Initially a steady state solid circulation was set between all three reactors. The height of the fluidized bed was 0.22 m, constant solid circulation of 50 kg/h, and initial temperature of 767 °C and 0.5 Nm^3/h of CH_4. Once steady conditions attained, the methane injection flow rate was started to increase gradually to 1 Nm^3/h. Accordingly, as solid flow rate is unchanged, the oxidation degree of the oxygen carriers start to decrease.

Figure 6.7 illustrates that the concentration of combustion gases remains fairly constant up to ΔX = 30 % (t ≈ 1000 s). This is consistent with previous results already published [84] which were obtained in the pilot plant with another $NiO/NiAl_2O_4$ material. However, with ΔX above 30% the exit concentration of methane decreases while CO and H_2 increase slightly in concentration. CO_2 yield remains constant at about 99.4% all along the test. This change in behavior is likely related to the increase of the Ni concentration in the oxygen carrier which has a catalytic effect of converting CH_4 to CO and H_2. This effect is not due to temperature as the temperature was decreasing slightly (by 25 °C) along the test. As discussed above lower temperature has an inverse effect by increasing CH_4 and decreasing CO and H_2. The principal reason for descent of temperature is the fact that as more gas is injected, more oxygen is consumed and therefore more heat is absorbed. These results illustrate flexibility of the operation with Ni based oxygen carrier in terms of the reduction degree.

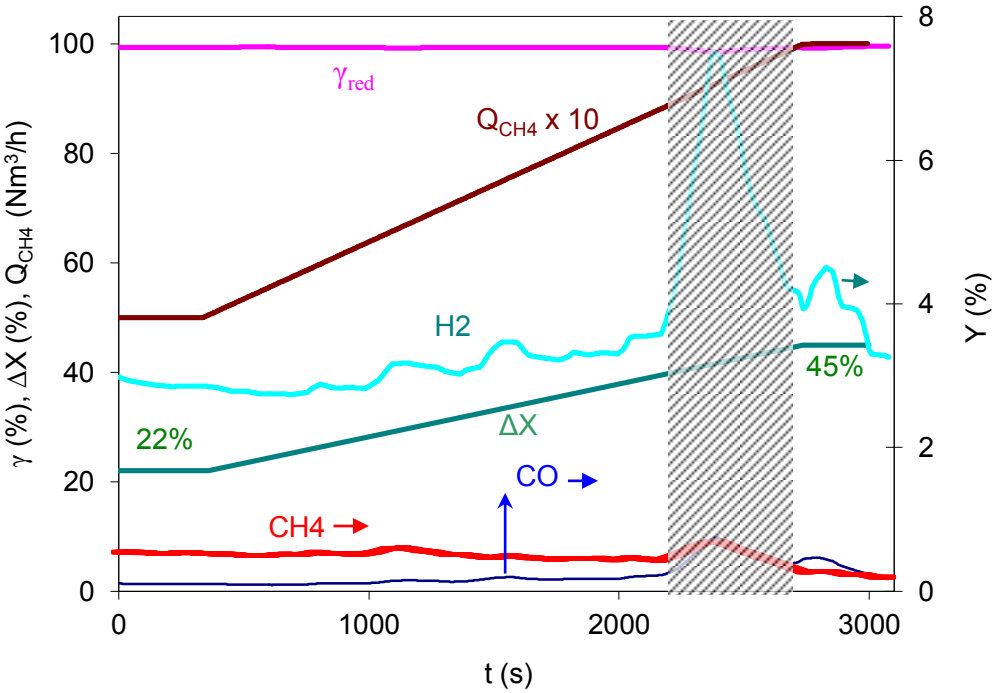

Figure 6.7: Combustion of methane in the reactor R1 in a transitional test with variable CH_4 injection (variable ΔX). H_{R1} = 0.22 m, Ws = 50 kg/h, and T = 767 – 742 °C. The experimental results in shadowed zone were altered due to a temporary blockage in the filter down stream of the reactor due to accumulated water caused by increase of methane injection.

Combustion of methane in the high temperature pilot plant in continuous steady state and transitional tests were discussed above. The effect of temperature on the reaction follows thermodynamic expectations. This implies fast reaction rates which results in a flue gas with concentrations close to the thermodynamic equilibrium. The effect of gas - solid contact time was investigated in transitional and steady state tests. Both results indicate small variation of gas concentration for bed height of above 0.1 m with concentrations variation of less than 1%. Once more, this indicates very fast reaction rate between methane and current oxygen carrier. Finally it was illustrated that oxidation degree has no visible effect for ΔX less than 30%. Above this limit a negligible gas concentration variation can be seen in transitional tests.

6.1.3 Batch tests

A series of batch combustion tests were carried out in the high temperature pilot plant. The main purpose of these tests was to supply a transient kinetic bench mark to evaluate the combustion model presented in the second half of the current chapter. In these tests, a known quantity of totally reduced oxygen carriers were transferred into the fuel reactor. Gas injections in the loop-seal and L-valve of the reactor were stopped to prevent any possible solid circulation. Nitrogen injections in the connecting lifts were also stopped to prevent dilution of the flue gas. Moreover, in the case of tests with height of the bed below the loop-seal entrance, the gas outlet of the connected cyclone was closed to avoid gases leaving the reactor through exists other than that of the reactor connected to the gas analyzers. Once temperature is stabilized to the expected value, methane was then injected into the bed with a constant flow rate during a determined time interval to achieve the aimed ΔX.

The resulting variation of gas concentrations at the exit of the fuel reactor for a series of 5 tests are illustrated in Figure 6.8 to Figure 6.10. An important observation in all batch tests is the variation of CH_4 concentration. It increases initially to a maximum values and then drops to a very small concentration. This phenomenon has been observed in small scale batch combustion tests as well [165]. This behavior is probably due to the formation of catalytic Ni sites in the oxygen carriers.

Initially only NiO is present in the oxygen carrier. Accordingly, the initial reaction is the CH_4 oxidation by NiO. As time passes, some Ni sites are formed on the oxygen carrier. This will catalyze CH_4 to CO which have a faster reaction rate with NiO. Accordingly, the CH_4 concentration will decrease as ΔX increases. This hypothesis was verified by injection of CH_4 to a reactor with the oxygen carriers partially oxidized. This was affirmed as no CH_4 peak was observed. T. Mattisson et al. [199] had observed similar phenomena and related it to same mechanism. This phenomenon is discussed in more details in section 6.2.3 in a development kinetic scheme for reactor modeling.

Figure 6.8 illustrate results of batch combustion of 0.5 Nm^3/h of CH_4 with two different height of the fluidized oxygen carrier bed. Accordingly, CO_2, CO and H_2 demonstrate identical behavior. This is in agreement with the previous findings of fast reactions rates involved for these gases as increase of contact time (H_R) does not have any significant impact on these gases. On the other hand, the peak of CH_4 concentration decreases as height of the fluidized bed increase. This implies the fact that the direct reaction of CH_4 and NiO is slow. Therefore, increase of contact time increases CH_4 conversion through this reaction.

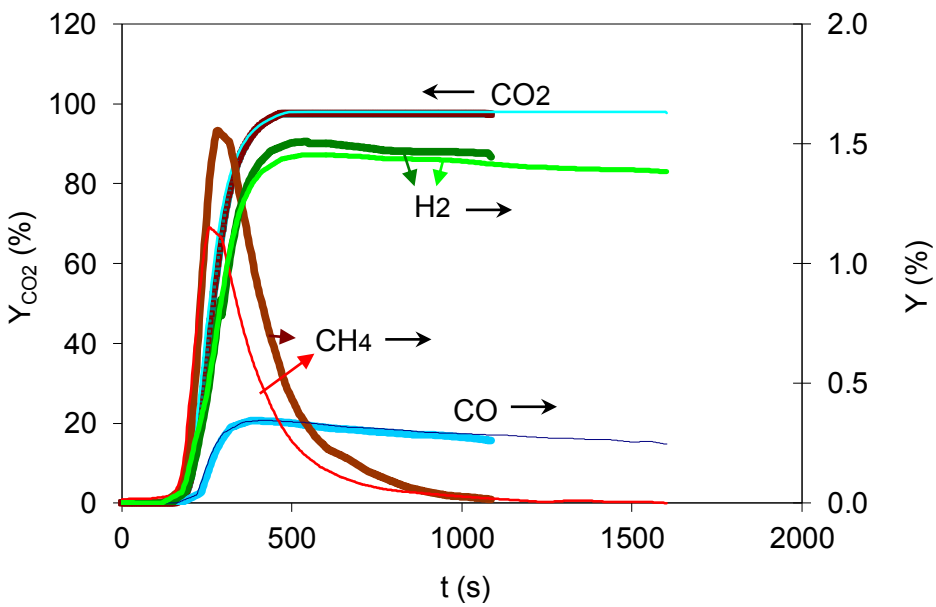

Figure 6.8: Batch combustion (no solid circulation) of CH_4 in the reactor R1 of the pilot. The solid line presents H_{R1} = 0.33m, Q_{CH4} = 0.5 Nm^3/h, T = 750 – 698 °C, injection time = 948 s, and ΔX= 0 -35 %. and the bold line with H_{R1} = 0.51 m, Q_{CH4} = 0.5 Nm^3/h, and T = 754 – 705 °C, injection time = 1482 s, and ΔX= 0 – 37%. The CH_4 is injected in both case at t = 0 s.

Figure 6.9 illustrates the batch combustion tests for two CH_4 injection rates of 0.5 Nm^3/h and 0.75 Nm^3/h. In both tests the height of the fluidized bed was about 0.33 m and initial temperature was set about 750 °C. Both tests illustrate similar behaviors in terms of H_2, CO_2 and CO. However, the peak of CH_4 varies between two tests. Similar reason stands for this behavior as discussed for H_R. The slow direct reaction of CH_4 with NiO explains this difference. As injection flow rate of methane increases, contact time decreases, accordingly the observed methane peak increases.

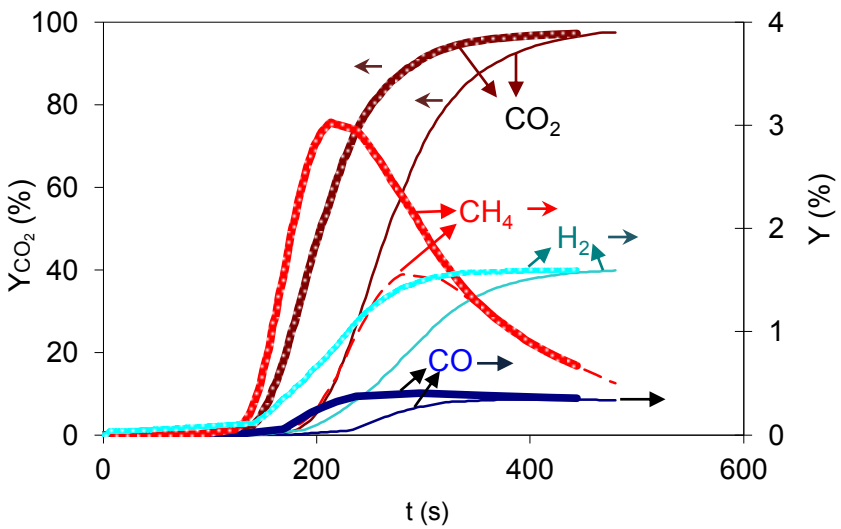

Figure 6.9: Comparison of batch combustion (no solid circulation) of CH_4 in the reactor R1 of the pilot for two CH_4 injections. Solid line presents 0.5 Nm^3/h of CH_4, H_{R1} = 0.33m, Q_{CH4} = 0.5 Nm^3/h, T = 750 – 698 °C, injection time = 948 s, and ΔX= 0 -35 % (The same test as solid narrow lines in Figure 6.8). The bold lines present 0.75 Nm^3/h of CH_4 with H_{R1} = 0.33 m, T = 748 – 696 °C, injection time= 584 s, and ΔX = 0 – 34%. The CH_4 is injected in both case at t = 0 s.

Figure 6.10 illustrates the impact of variation of the methane flow rate on the flue gas concentrations with a small solid inventory. Two methane flow rate of 0.75 Nm^3/h and 1.0 Nm^3/h are tested with H_R = 0.15 m, and initial temperature of about 75. °C. Compared to the above presented results, CH_4 peak increases to 4.2 % for 1.0 Nm^3/h and 3.2 % for 0.75 Nm^3/h. The resulting CO and H_2 concentration increases significantly compared to the previous results. The reaction between the CH_4 and Ni is considerably fast. Therefore, the CH_4 consumption remains high even with limited solid inventory. However, due to limited oxygen stock in the reactor, only a portion of the produced gases is converted to CO_2 and H_2O. This effect increases as available oxygen decreases with time. These results are consistent with the transient continuous tests regarding the effect of ΔX. In both cases the most significant concentration variation happens for ΔX of above 30% (Figure 6.10).

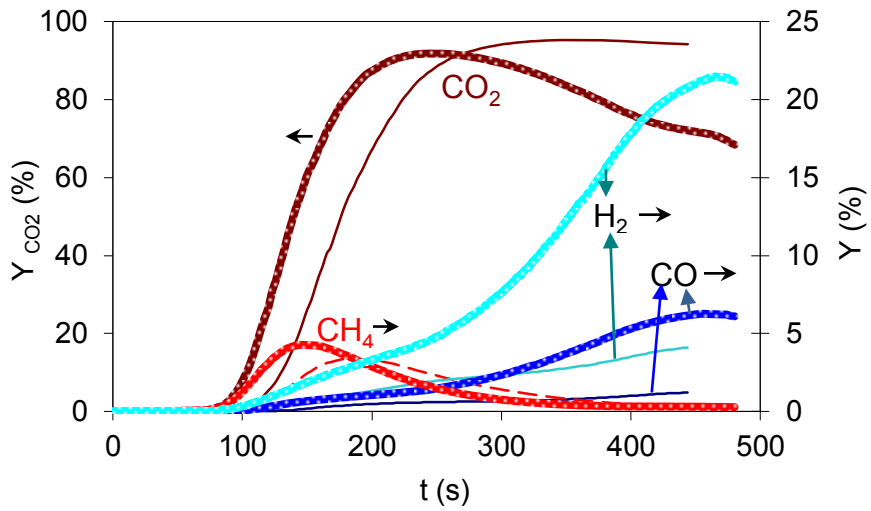

Figure 6.10: Comparison of batch combustion (Ws=0 kg/h) of CH4 reactor R1 of the pilot for two methane flow rate. The thin solid line presents 0.75 Nm^3/h CH_4, T = 756 – 684 °C, H_R = 0.15m, and injection time = 360 s, and ΔX= 0 – 46%. The bold solid line represents Q_{CH4} = 1.0 Nm^3/h, T = 740 – 657 °C, H_R = 0.15m, and injection time = 357 s, and ΔX= 0 – 60%. CH_4 injection time is at t = 0 s for both cases.

An inconvenience in the gas concentration measurement in large units is the dispersion caused by the conducting flue gas line into the analyzers as discussed in the previous section. This was measured in the current system by aid of blank tests in which CO_2 was injected into the fuel reactor in form of a step function. The analyzer respond was then measured to be used in the reactor model. Two respond functions of this type are illustrated in Figure 6.11. These results are used in the modeling section to take into account both the imposed lag time and the gas dispersion.

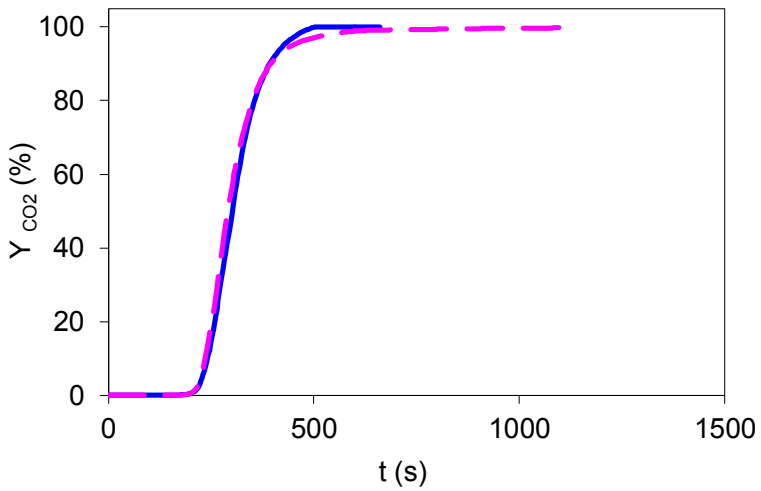

Figure 6.11: Two analyzer respond functions for a step function of Q_{CO2} = 0.5 Nm^3/h injected at t=0 with T = 750 °C and H_R = 0.15 m.

6.1.4 Oxidation Reactor

Oxidation of the reduced oxygen carrier in the air reactor was also studied in the pilot plant similar to the reduction reactions presented above. Transient and batch oxidation tests are presented in this section. Effect of the fluidized bed height in the air reactor (R2) on the oxidation reaction was investigated in a continuous transient test (Figure 6.12). Similar to the transient combustion tests, first a steady state continuous operation was set in the pilot plant. Once the system achieved the steady condition, the solid flow rate out of the air reactor, R2, was slightly increases. Therefore, height of the solid bed in the reactor was continuously decreasing. Similar to the combustion reaction, different zones can be distinguished based on the solid height.

- H > 0.22 m: all air oxygen is consumed indicating sufficient residence time in the reactor for the oxidation reaction.
- 0.22 m > H > 0.05 m: The residence time is less than the required reaction time. Therefore, the concentration of the oxygen at the out let of the air reactor starts to increase gradually. 92 % of the injected air oxygen is consumed by particles.
- 0.05 m > H: The concentration of unreacted oxygen at the exit of the reactor increases exponentially. The height of the gas jet above the distributor is probably higher than the height of solid bed causing some gases to bypass the solid bed without efficient gas – solid contact.
- H ≈ 0 m: The unreacted oxygen concentration gets to stable level of 12.2 vol. % (36% of injected air oxygen is consumed). The reaction is carried out in the limited contact time between the particles entrance into the bed through the loop-seal and their exit at the bottom of the reactor through the L-valve.

The temperature of the fluidized bed in the air reactor at the height of 0.1 m above the distributor is plotted in the Figure 6.12. While the released energy was constant in the bed, the quantity of the oxygen carriers, and the surface of heat transfer with the reactor walls was decreasing. Therefore, the temperature of the bed was increasing during the test.

These results demonstrate that the oxidation of the $NiO/NiAl_2O_4$ particles is a rapid reaction. The average residence time of the gas phase is about 1.2 s with H_R = 0.22 m. This is calculated based on the depleted air velocity by aid of the hydrodynamic model presented in the last chapter. The superficial air velocity at the distributor (before reaction) is 0.51 m/s (23 U_{mf}) and the superficial velocity of the depleted air is 0.4 m/s (18.4 U_{mf}). This demonstrates that the oxidation reaction can be well accomplished in the circulating or turbulent beds similar to the existing designs as in references [69,74]. It should be noted that the selection of the oxidation reactor technology is independent of the system fuel contrary to the fuel reactor.

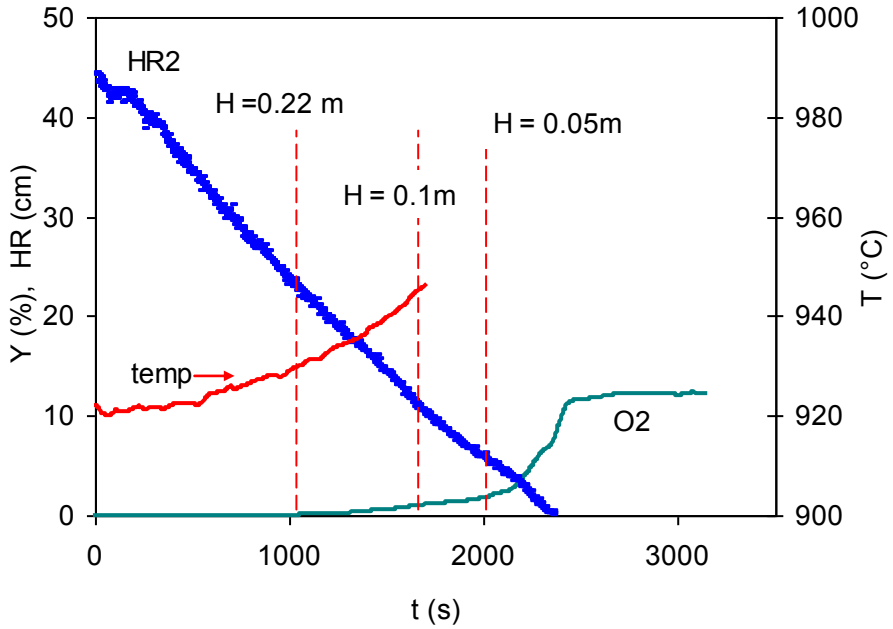

Figure 6.12: Transitional oxidation reaction in the air reactor R2 with variable height of the solid bed from 0.44 to 0 m, Q_{air} = 3.5 Nm^3/h, Ws = 45 kg/h, and Q_{CH4} = 0.5 Nm^3/h. At the same time, the combustion was stable in the fuel reactor with γ_{CO2} = 99.5 % equivalent to ΔX = 25%.

Batch oxidation tests were also conducted in the air reactor (R2) by fully oxidizing a known quantity of partially reduced particles. The resulting oxygen concentration at the exit of the air reactor is illustrated in Figure 6.13. Two factors are analysed in these tests: effect of height of the fluidized bed, and the gas injection flow rate. Three oxidation phases can be well distinguished in all cases:

- 0 – t_1; Initial oxidation which is very fast and all of the injected oxygen are consumed. With solid height above 0.31 the oxygen in depleted air appears for oxidation degree of below 24 %. However, this limit increases as the height of the bed decreases or as the air injection rate increases.
- t_1 – t_2: Second phase where a part of the injected oxygen leaves the reactor unreached. Accordingly, the reaction rate is less than the first phase.
- t_2 < t Third phase where the oxidation of the particles approaches to final completion. The reaction rate decreases in this case and much more time is required to end the oxidation to 100%.

Similar to the combustion tests, blank experiments were carried out at the end of each test with identical operating condition. Therefore, once the oxygen carriers were fully oxidized, the air was purged with nitrogen and then air was injected to measure the respond time of the analyzers. The four blank tests plotted in Figure 6.13 overlap indicating identical analyser respond time for all tests.

Variation of the bed temperature measured at 0.1 m above the distributor is also plotted in Figure 6.13 for the presented batch tests. In all cases temperature increases by about 150 °C and then decreases to its initial values. The main reasons for initial increase are: high exothermal nature of oxidation, limited heat transfer exchange surface, and lack of solid circulation as a heat sink. As reaction reaches near complete conversion the temperature decreases due to the reduction in the reaction rate, heat transfer by injection air and to the reactor walls.

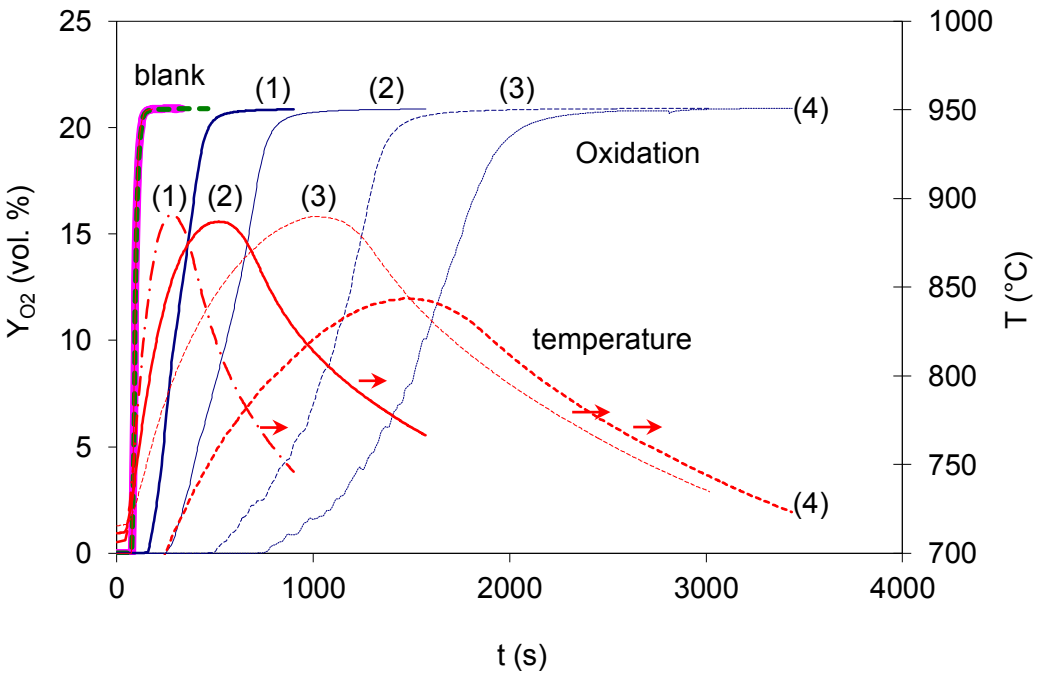

Figure 6.13: Results of batch oxidation tests (Gs = 0) in the reactor R2 of high temperature pilot plant with the operating conditions listed in the Table 6.1. All 4 blank tests overlap.

Table 6.1: The operating conditions and results of the plotted series in Figure 6.13.

No	HR (m)	Qair (Nm^3/h)	Uair,in (m/s)	ΔX (%)	t_1 (s)*	ΔX_{t1} (%) #	t_2 (s)
(1)	0.15	4.99	0.64	50%	117	43.0%	362
(2)	0.13	2.5	0.32	49%	249	34.7%	672
(3)	0.31	2.5	0.32	39%	372	24.5%	1254
(4)	0.45	2.5	0.32	40%	717	23.1%	1788

*** Time at which the unreacted oxygen appears at the outlet of the bed, the lag time is excluded.**
 # The oxidation degree at which the unreacted oxygen appears at the outlet of the bed.

The results of the oxidation tests illustrate a fast reaction rate between oxygen and the oxygen carrier. The transitional tests illustrate that all of the air oxygen is consumed with fluidized bed higher than 0.22 m. Three phases can be distinguished in batch oxidation of the oxygen carriers. The reaction rate is high in the first two phases. The reaction rate decreases in the final phase. This illustrates the fact that the complete re-oxidation of the particles may require a considerable contact time to be achieved. The oxidation reaction is a very exothermic reaction. Therefore, the reactor temperature increased more than 150 °C for very high air flow rates in batch tests.

6.1.5 CO_2 Capture Efficiency

The captured CO_2 in the fuel reactor can leak out of the reactor in two forms: gas or coke. The gas leakage can only happen through the L-valves due to solid circulation. Moreover, carbon deposition on the surface of the oxygen carriers [165,199] (coking) results in leakage. The gas leakage was

investigated in the cold flow prototype and demonstrated to be a function of pressure drop across the system. However, the total quantity of the gas flow through the L-valve is much less than the total gas flow in the reactor. This indicates that the capture efficiency in the current system is considerably high. As an example, in case of 0.5 Nm^3/h of CH_4 combustion with solid circulation rate of 50 kg/h, the gas out flow through the L-valve is less than 0.008 Nm^3/h. Accordingly, the capture efficiency is above 98.4 % in this case depending on the pressure balance across the system.

Gas leakage into the air reactor or formation of carbon deposits on the surface of oxygen carriers was possible to be measured thanks to a CO_2 and CO analyzer coupled with the oxygen analyzer in the air reactor. However, no CO or CO_2 was measured at the air reactor exit in all tests. This indicates absence of notable leakage or carbon deposition.

The gas leakage into the fuel reactor could happen through the gas flow into the reactor from the loop-seal. All of the gases injected into the loop-seal below the recycle chamber (Qsr) end its way into the reactor. This explains the maximum CO_2 concentration of about 83% in the Figure 6.1 with Q_{sr} = 0.1 Nm^3/h. The CO_2 concentration was increased to 91% in following tests by reducing the second loop-seal aeration (Q_{sr}) to 0.05 Nm^3/h for Q_{CH4} = 0.75 Nm^3/h. This dilution effect was possible to be further minimized as the second aeration in the loop-seal is not necessary in the current system as explained in the chapter 3. Moreover, replacement of the Nitrogen with water vapor or CO2 results in total elimination of this dilution effect. Moreover, the current system is in a small laboratory scale which requires relatively higher gas flow in loop-seal compared to system capacity. Therefore, increase of the system scale can result in improvement in this regard. These results indicate that a high CO_2 capture above 90% is easily possible in the current system.

6.1.6 Attrition and Particle Aging

Particle attrition and entrainment are main sources of oxygen carrier lost in the CLC systems. In the current configuration, the main attrition sources are gas jets above the distributor, T-bends, cyclones, and probable rapid change of temperature [283]. To reduce the attrition at the distributors, a shroud was added concentric to the jet hole. This configuration decreases the gas velocity before entering the bed while maintaining required pressure drop in the distributors. T-bend is reported to trigger an attrition rate similar to that of radius bends while it entails an erosion effect much less than that of radius bends [284]. Cyclone separation efficiency increases by increasing the gas entrance velocity and decreasing barrel diameter [226]. However, modification of these two factors increases the solid velocity and hence increases attrition inside the cyclone. Therefore, these parameters were selected to meet the required separation efficiency while minimizing the particle attrition in the current design.

The oxygen carriers employed in the current study have undergone about 200 hours of circulation and 63 hours of combustion in the current experimental campaign (at 400 °C to 900 °C). This is equivalent to 330 cycles of solid circulation at an average of 50 kg/h. The total initial mass of the oxygen carrier was 50 kg with 8.8 % (4.4 kg) of particles with diameter less than 100 µm. The initial Sauter diameter of the oxygen carriers was 200 µm.

At the end of the experimental campaign, the solids were conveyed out of the system through a tube at the bottom of reactor R1. A total of 40 kg of oxygen carrier was finally gathered with 6 kg of particles with particle size less than 100 µm and an average Sauter diameter of 240 µm. The difference between the initial and final solid inventory was mainly due to some solids remained inside the system or in the conveying lines downstream of the reactors, and probable agglomerated particles at the bottom of the reactor or in the bends of the L-valves and loop-seals.

An attrition test was carried out on the fresh and used oxygen carriers to investigate the effects of operation on the mechanical resistance of the materials. The oxygen carriers were first tested in a Grace–Davison jet cup attrition test system [285]. There exist some critics to this kind of methods in the literature regarding the difference between attrition mechanism in this test compared to real industrial processes and formation of stagnant region [283,286]. Accordingly, the conical jet cup system proposed by PSRI [286] was used to measure the mechanical resistance of oxygen carriers.

Repetition of the test on similar samples proved reproducibility of the test results with this system. In addition, this new test method may produce results closer to real systems [286,287].

The particle size distributions of tested samples before and after attrition test are illustrated in Figure 6.14 and Figure 6.15. Comparison of the fresh and used materials before attrition test illustrates that the particle size distribution of the used particles has shrank to a smaller span compared to the fresh particles. It should be mentioned that especially in the beginning of the experimental operations a fraction of particles had left the system through cyclones due to some instabilities in the loop-seal operations. This instability happened a few times and was mostly due to the filter blockages by condensed water at the exit of R1 (this problem was solved later on). The particles that left the system were gathered in a reservoir and sent back to the system. However, the particles with diameter smaller than 100 µm were screened out before sending the particles back into the system. Accordingly, this screening phenomenon has played an important role in the change of the particles size distribution before and after tests. Also some fine particles left the system through the cyclones or the reactors exit which do not have any cyclone. These particles were collected on the filters downstream of each cyclone or reactor. Therefore, a direct conclusion can not be made based on the initial particle distributions.

Abrasion effect can be well observed with the fresh particles in the attrition tests results of fresh particles in Figure 6.14. Abrasion has resulted in a small peak of fine particles of about 5 µm in the graph according to criteria by Werther and Reppenhagen [288]. Fragmentation effect can also be distinguished in the fresh particles through the leftward shift of the particle distribution curve. Similarly, both abrasion and fragmentation can be observed in the test results of the used oxygen carriers but in much smaller extend (Figure 6.15). This illustrates that after long term operation in the high temperature pilot plant; only the most resistant particles are left over.

Gayán et al. [289] have presented the measured solid lost due to attrition for several Ni based particles. Their results show a high solid lost in the first 20 cycle above which the rate of attrition lost decreases considerably. They relate this behavior to the rounding effects on the irregularities of the particles and because of the fines stuck to the particles during their preparation. Similar observations have been made in FCC process where a part of the fresh catalyst attrite and leave the system early after being introduced into the reactor. The remaining particles are much more resistant in this case.

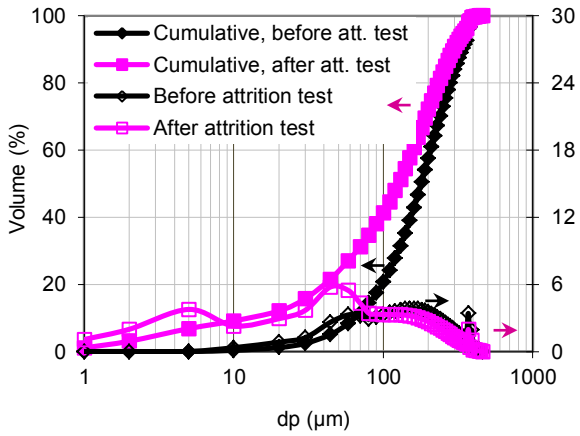

Figure 6.14 : Fresh particles, comparison of the particle size distribution before and after attrition tests with test duration of 3h, ambient temperature, U_{in} = 137 m/s, AI(44) = 16.5%, AI(100) = 41%.

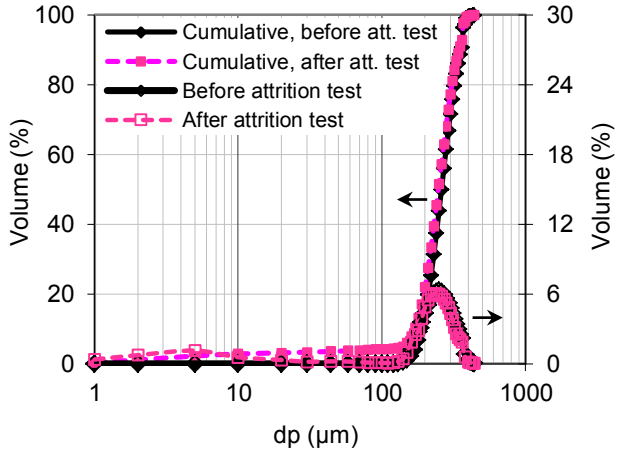

Figure 6.15 : Used particles, comparison of the particle size distribution before and after attrition tests with test duration = 3h, ambient temperature, U_{in} = 137 m/s, AI(44) = 3.5%, AI(100) = 4%.

The SEM image of the fresh and used oxygen carriers are illustrated in Figure 6.16 and Figure 6.17. Cracks can be observed on the surface of fresh oxygen carriers. The propagation of these cracks can results in abrasion or fragmentation of particles due to different types of the stresses exercised on the

particles during operation. Particles with crack have less mechanical strength and will have a higher attrition. Fewer particles with cracks were observed among the used oxygen carriers (Figure 6.17). This is probably due to the fact that the cracked particles have been more vulnerable to attrition. Particles with signs of fractures can be distinguished among the used oxygen carriers. These could be results of the fracture of particles with surface cracks. It is likely that the particle attrition rate can be reduced with increasing the quality of the oxygen carriers manufacturing.

A considerable amount of irregular particles can be observed in both the fresh and used particles. Therefore, the regularity of the particles has not changed considerably during the operations in the pilot plant.

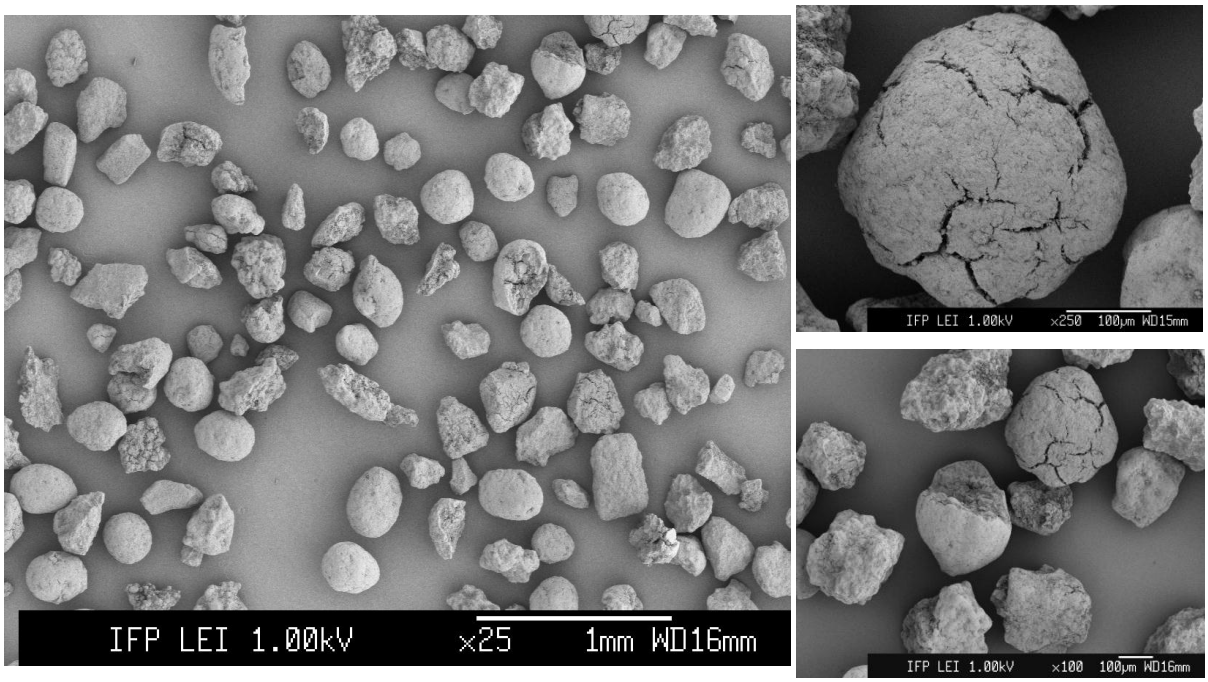

Figure 6.16 : SEM images of the fresh oxygen carriers before screening and tests in the pilot plant.

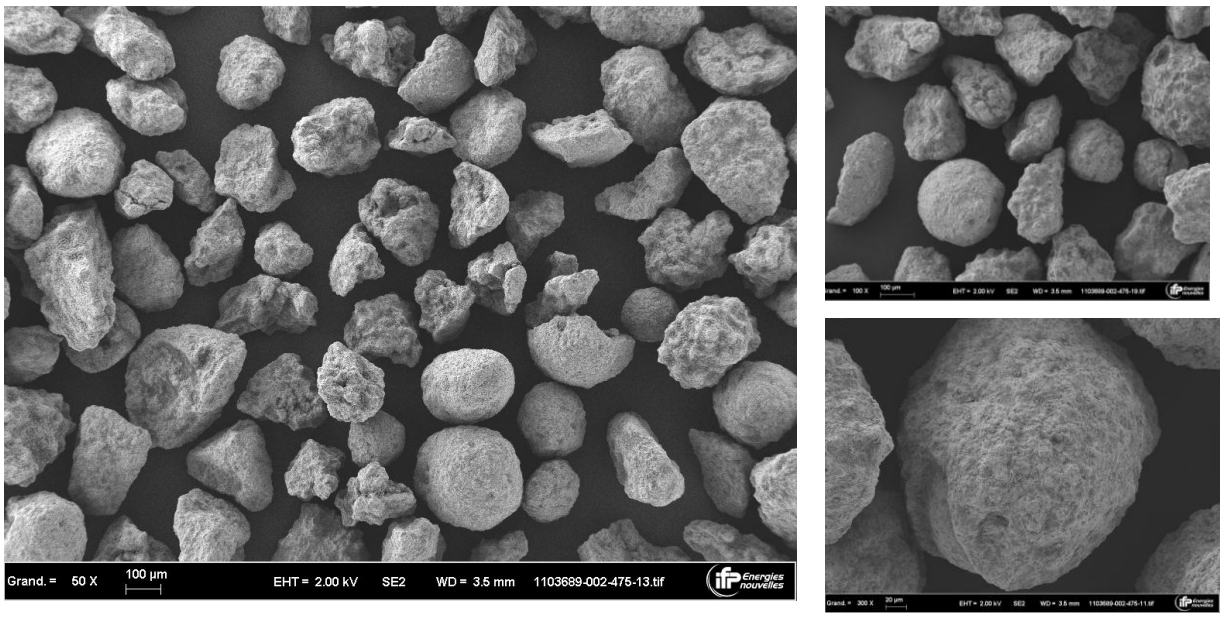

Figure 6.17 : SEM images of the used oxygen carriers after circulation in the pilot plant.

The porosity of the particles was measured using mercury porosimetry. Results are presented in Figure 6.18 for both fresh and used oxygen carriers. Three distinguishable regions in the graph correspond to:

(1) Size of 10 ~ 100 µm: entrance of the fluid into interparticular space which is higher for the used particles due to the presence of less fine particles. Fine particles enter into the space between the bigger particles and can reduce the overall porosity.

(2) Size of 0.1 ~ 10 µm: fluid enters into the big pores and the big surface cracks. Fresh particles have more mercury displaced in this section indicating existence of more surface cracks and defaults.

(3) Size less than 0.1 µm: mercury enters into the smaller pores. Comparison of the dVol/dD curve illustrates that more small pores exist in the fresh particles compared to the used ones. This indicates that the operation in the pilot plant at high temperature has closed some of the small pores inside the particles. This can be an effect of sintering which has enlarged some of the bigger pores and closed smaller pores in the used oxygen carriers.

The measured bulk density was 2670 kg/m^3 for fresh particles and 2370 kg/m^3 for used particles. The reduction is probably due to decrease of fine particles which enter into interparticular space and reduce bed voidage as explained above.

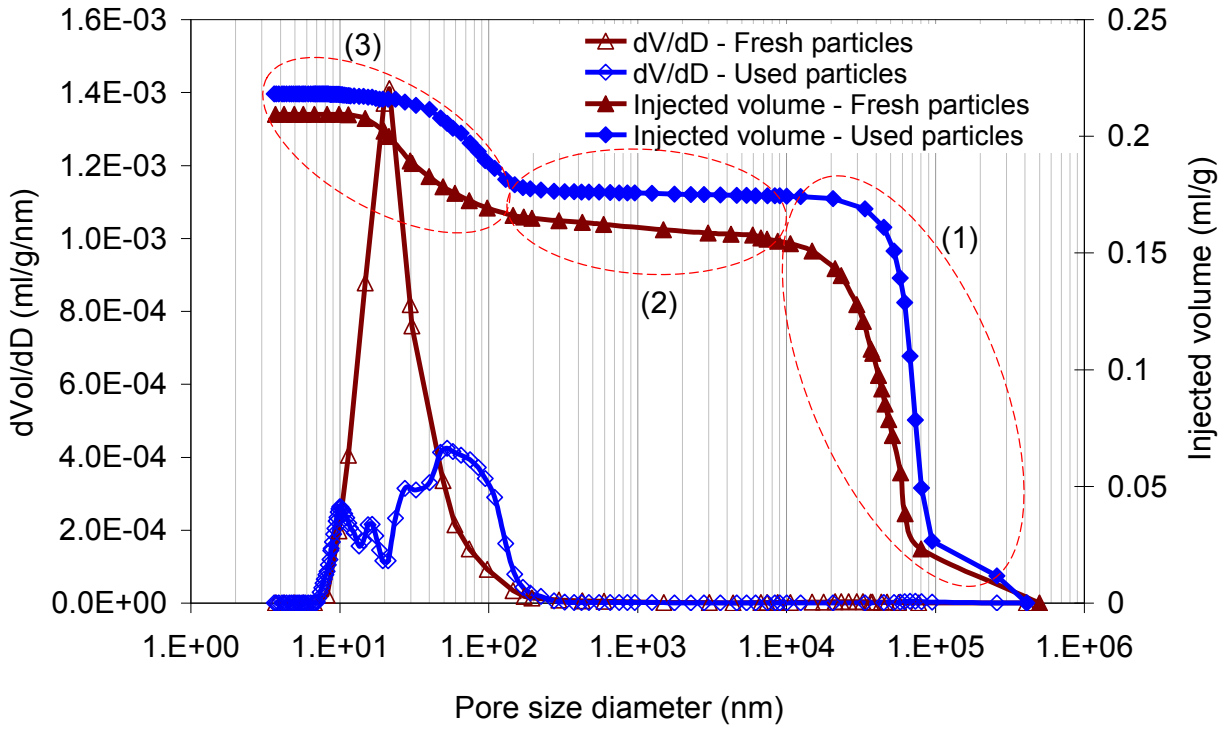

Figure 6.18 : Mercury porosimetry results of the fresh and used oxygen carriers. The apparent density was 2670 kg/m^3 for fresh particles and 2370 kg/m^3 for used particles.

The aged particles used in the above tests were sampled from the oxygen carriers recovered from the pilot after operations. However, a more detailed study is required to compare the attrition results obtained from the particles circulation inside the CLC system compared with the attrition tests results. These results can then be coupled with attrition models to better understand the attrition phenomenon in CLC system as well as scale up possibilities [164].

The discussion made in this section illustrated that the attrition was a main source of oxygen carrier loss in the current study. The attrition test results demonstrated that only the particles with high mechanical strength were left in the system after long term operation. The SEM results illustrated presence of surface defaults and crack on the initial particles. The remaining particles in the system after circulation tests had less surface crack indicating elimination of the defaulted materials during the operation either by fragmentation or abrasion. The quantity of fine particles was also decreased during operation. Moreover, high temperature operation has resulted in elimination of some of small pores (~20 nm) while the bigger pores (~100 nm) had grown in size.

6.1.7 Agglomeration

Agglomeration was not observed in the current study while the system was in circulation. However, it was sometimes difficult to start up solid circulation in the L-valve (lv1) located below the fuel reactor after long standby periods. The cause of this problem was not so clear, but it could be due to the formation of agglomerates. The supposed agglomerates were loose enough to be broken only by increasing the pressure drop in the reactor above the L-valve and minimizing the pressure drop in the lift downstream of the L-valve.

Agglomeration in the fluidized bed can be detected by a sharp decrease in the bed pressure drop caused by particles sticking and defluidization [290]. This was never observed in the current study even with very high reduction degree of the oxygen carriers. Similar observation have been reported in other works with the Nickel based oxygen carriers [289,291].

At the end of the experimental campaign, an endoscopic visual inspection of the interior of emptied system was carried out. Figure 6.19 illustrates the formation of agglomerates at the bottom of the fuel reactor. Some agglomerates were also found deposited at the walls of the L-valve standpipe near the angled sections of pipe. These zones are the region where particles are stagnant and not well fluidized. Moreover, presence of reduced particles in the reduction reactor had favored agglomeration at the exit of this reactor.

According to these results, the agglomerate formation is favored in dead zone with presence of highly reduced oxygen carriers. Maintaining solids in circulation is probably a good way to limit agglomeration in the system.

Agglomerates formed in the stagnant region at the bottom of the reactor with limited fluidization

Figure 6.19: Visual inspection of the rector interior by use of an endoscope at the end of the experimental tests.

6.2 Reactor Model

As discussed previously, one of the aims of this study is to develop a reactor model capable of representing the performance of the current CLC system. A hydrodynamic model was developed based on the experimental residence time distribution results as presented in the last chapter. In order to fully represent the fuel reactor, the model requires some modifications to include reaction kinetics and mass balance considerations.

The following sections present the additional development of the reactor model to include the reactional aspects of the fuel reactor. A simple model is first developed to represent the lag time and dispersion introduced by the system components other than the fluidized bed.

The reaction mechanisms chosen and kinetic rate equations are presented first. Mass balance equations are then discussed for the gas phase to account for molar gas expansion resulting from combustion reaction in the reduction reactor. Moreover, the mass balance equation used in the solid phase is presented to account for oxygen release. Finally, the model prediction is compared with the experimental results obtained from the high temperature pilot plant combustion tests.

6.2.1 Modeling of the System Components

The distance between the reactor exit and the gas analyzers is relatively long as illustrated in the Chapter 1. This results in time lag responses to be accounted for when comparing model predictions to experimental results. Furthermore, this distance introduces some additional dispersion as discussed in section 6.1.3. Similar to the RTD modeling, this interference was taken into account by modeling individual elements of the system. Table 6.2 presents a list of the simulated elements as well as the employed governing equations and geometrical properties of the fuel reactor R1.

The gas injection line upstream of the reactor is modeled using an axial dispersion – convection model. The flue gas conducting lines from the reactor to the analyzers are modeled by use of simple plug flow models based on the geometrical data from the pilot plant. CSTR models are used to model the particle filter, primary and secondary condensers. These elements have a rather complicated geometry. Therefore, the apparent volume of the filter and primary condenser were used in the current model as the geometrical data. To match experimental signals in order to ensure proper description of the global system components, the volume of the secondary condenser and length of the analyzer conducting line were adjusted by fitting the modeling and experimental blank test results. This was supposed to take into account the geometrical complexities not included in the model as well as the dispersion effects caused by distributor and gas injection valves not included directly in the current model. Both fitted and apparent size of these elements is listed in Table 6.2. In both cases the fitted value is about 3 times bigger than the measured apparent size. This difference seems reasonable regarding the overall system complexity.

Figure 6.20 illustrates the modeling versus experimental blank test in the high temperature pilot for a step input function. In these tests, the fuel reactor was initially fluidized by N_2. The fluidization gas was then replaced by CO_2 at time t = 0 s. Comparison of the modeling and experimental results illustrate a good agreement in this case due to the fitting of the conducting line geometry. This model remains empirical since the exact description of system components is only partly conducted. However, the only expectation here is to properly represent time lag and dispersion changes as a function of operating condition changes.

Table 6.2: Scheme of the whole system divided into six reactors in series including the fluidized bed.

Input gases ⇩	
Gas injection line	Axial dispersion – convection model: $\frac{\partial C_i}{\partial t} = D_{axial}\frac{\partial^2 C_i}{\partial x^2} + U\frac{\partial C_i}{\partial x}$ $\frac{1}{Pe} = \frac{D_{axial}}{uD_{tube}} = \frac{3\times10^7}{\mathrm{Re}^{2.1}} + \frac{1.35}{\mathrm{Re}^{0.125}}$ D = 0.004, L_{inj} = 6.0 m , P_{inj} = 1.5 bar, T_{inj} = 300 °C
Reactor	The developed fluidized bed model.
Free board in the reactor	Axial dispersion – convection model. H_{top} = 1.0 - H_R, D = D_R = 0.13 m, P= 1 atm
Particles filter	CSTR model: $\frac{\partial C_i}{\partial t} = \frac{U}{\tau_{dis}}(C_{in} - C_i)$ Volume = 4.5e-3 m^3, T = 20 °C
Conducting lines	Plug flow model: $\frac{\partial C_i}{\partial t} = U_{gas}\frac{\partial C_i}{\partial z}$ D = 0.015 m, L = 6.0 m, P = 1 atm, T = 20 °C
Primary condenser	CSTR model: $\frac{\partial C_i}{\partial t} = \frac{U}{\tau_{dis}}(C_{in} - C_i)$ Volume = 2.0e-3 m^3, T = 20 °C
Analyzer conducting line	Plug flow model: $\frac{\partial C_i}{\partial t} = U_{gas}\frac{\partial C_i}{\partial z}$ D= 0.015m, L = 10.0 m
Secondary condenser	CSTR model: $\frac{\partial C_i}{\partial t} = \frac{U}{\tau_{dis}}(C_{in} - C_i)$ Volume = 1.2 m^3 fitted value (real volume = 0.5e-3 m^3)
Conducting line ⇩	Plug flow model: $\frac{\partial C_i}{\partial t} = U_{gas}\frac{\partial C_i}{\partial z}$ D= 0.004m, L = 10.0 m fitted (the real line is about 3.0 m)
Analysers	

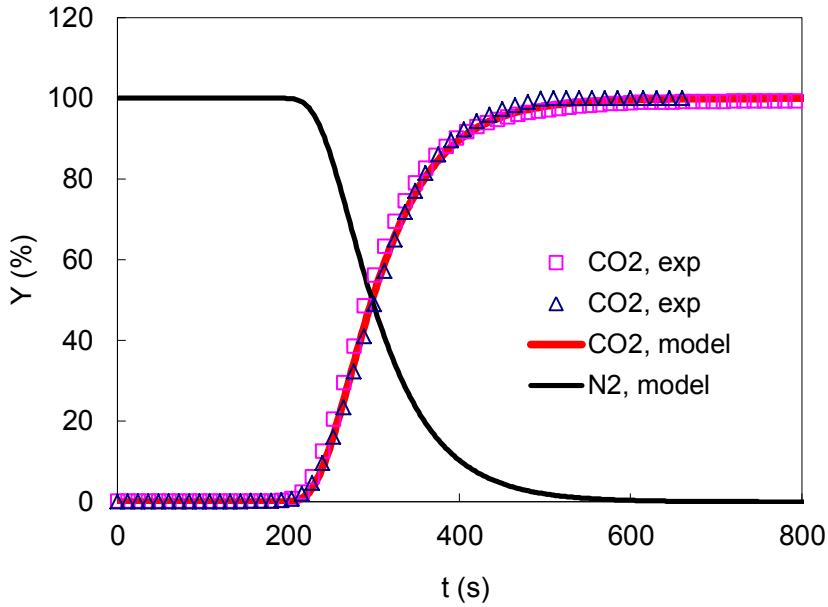

Figure 6.20 : The experimental and model respond to a unit step CO_2 input into the system in the fuel reactor.

6.2.2 Reaction Mechanism

The reaction path considered for the CH_4 reaction with the oxygen carriers is based on two different kinds of reaction mechanisms following the approach proposed by Iliuta et al. [165]. First non-catalytic direct reaction between reactive gases (CH_4, CO and H_2) and NiO are presented. Next a series of catalytic reactions enhanced due to the presence of Ni on the oxygen carriers are considered. The non-catalytic reactions [165,218-220] involved are the reduction of NiO by CH_4 as

$$CH_4 + NiO \rightarrow Ni + 2H_2 + CO \qquad \textbf{Eq. 6.7}$$

The reduction of NiO by CO:

$$CO + NiO \rightarrow Ni + CO_2 \qquad \textbf{Eq. 6.8}$$

The reduction of NiO by H_2:

$$H_2 + NiO \rightarrow Ni + H_2O \qquad \textbf{Eq. 6.9}$$

These reactions involve transfer of oxygen from the NiO to the reacting gases and are considered thermodynamically irreversible for practical purposes. The catalytic reactions considered, based on the literatures [165,214,219,220] are: consisted of methane steam reforming :

$$CH_4 + H_2O \xleftrightarrow{Ni} CO + 3H_2 \qquad \textbf{Eq. 6.10}$$

Methane reforming with carbon dioxide:

$$CH_4 + CO_2 \xleftrightarrow{Ni} 2CO + 2H_2 \qquad \textbf{Eq. 6.11}$$

Methanation of carbon monoxide:

$$CO + 3H_2 \xleftrightarrow{Ni} CH_4 + H_2O \qquad \textbf{Eq. 6.12}$$

Water gas shift (WGS) reaction:

$$CO + H_2O \xleftrightarrow{Ni} CO_2 + H_2 \qquad \textbf{Eq. 6.13}$$

The oxidation reaction is simply considered as:

$$2Ni + O_2 \xleftrightarrow{Ni} 2NiO \qquad \textbf{Eq. 6.14}$$

Carbon deposition and subsequent reactions were not included in the current model. Indeed, no CO2 emission was observed in the air reactor even with NiO conversion up to 50%., as shown before. Ishida et al. [206] have demonstrated negligible coke formation with H_2O to CO ratio of above 1. In the current tests this condition was almost always met. This can be deduced from the fact that two H_2 atoms are formed for each CO produced through reaction Eq7. Considering fast reaction of H_2 with oxide to form H_2O, the H_2O partial pressure will be always superior to CO unless the oxygen carriers are highly reduced. However, this is not within the scope of the current model, since most of the experimental tests cover ΔX in the range of 0 to 40 %.

6.2.3 Kinetic Rate Equations

The kinetic rate reaction in the current study is consisted of two elements. The first one is the chemical reaction rate equation (r_0) based on the concentration of the reactants. The second element is the available active sites on the oxygen carriers (α). Therefore, the overall reaction rate equation can be written as:

$$r = r_0 \alpha \qquad \textbf{Eq. 6.15}$$

As presented in the experimental batch tests results, reduction of oxygen carriers by CH_4 goes through an initial activation step. As discussed in chapter 1, this behavior is a common phenomenon in the solid phase reaction in which the active sites (nuclei) are formed during an initial slow step followed by an induction and then acceleration reaction region. This behavior is taken into account by special rate laws developed for solid phase reaction which count up to more than 20 laws [209]. The oxygen carrier reductions in the CLC application have been modeled using different existing solid models [165,216,292]. Different models were tested in the current study. The model did not have significant effect on the direct reaction of reactive gases with NiO. However, the form of the selected model influences significantly the total reaction conversion through change of the catalytic reaction effect.

Richardson et al. [210] used X-ray diffraction to study nickel oxide reduction by hydrogen. They found that the reduction follows a series of steps: (1) initial induction period with formation of Ni metal clusters; (2) acceleration of reduction rate as size of clusters increase; and (3) pseudo-first-order advance of reaction. This illustrates change of the behavior during reduction reaction, indicating limited use of single classical models for whole range. Kruggel-Emden et al. [216] have proposed to use empirical equations which are sum of different exponential and polynomial terms to cover variation of the behavior through whole reduction path. In the current study, the oxygen carrier was never reduced to 100% and most of the studies were limited to the conversion of 30%. Accordingly, a single classical two dimensional nuclei growth Avrami rate law was employed to model reduction progress (Ni growth) as:

$$\alpha = 1 - \exp(-k_t t^m) \qquad \textbf{Eq. 6.16}$$

Where m = 2 for a two dimensional growth and $k_t = 1.1\times10^{-6}$ calculated in this study by optimization based on the experimental batch results. Accordingly, this expression was added to the kinetic rate laws of catalytic reactions to take into account the initial oxygen carrier activation step as:

$$r = r_0 \alpha = r_0 (1 - \exp(-k_t t^m)) \qquad \textbf{Eq. 6.17}$$

Therefore, the rate expression depends not only on the concentration of the gases in the reactor but also on the availability of the active catalytic Ni sites on the oxygen carrier. Accordingly, the rate equation for the non-catalytic reaction Eq. 1.10 is:

$$r_1 = k_1 \exp(E_1 / RT) C_{CH4} C_{NiO} (1 - \alpha) \qquad \textbf{Eq. 6.18}$$

Here, the activation energy is E_1 = 23660 J/mol [165], and $k_1 = 1.09\times10^{-6}$ ($l/\cdot mol^{-1}\cdot s^{-1}$) obtained by curve fitting. The rate equation for the reaction Eq. 1.11 is:

$$r_2 = k_2 \exp(E_2 / RT) C_{CO} C_{NiO} (1 - \alpha) \qquad \textbf{Eq. 6.19}$$

The activation energy is E_2 = 26410 J/mol [165], and $k_2 = 4.6\times10^{-6}$ ($l/\cdot mol^{-1}\cdot s^{-1}$) from curve fitting. The rate equation for the reaction Eq. 1.12:

$$r_3 = k_3 \exp(E_3 / RT) C_{H2} C_{NiO} (1-\alpha) \qquad \textbf{Eq. 6.20}$$

The activation energy is E_3 = 26500 J/mol [165], and k_3 = 5.7×10^{-3} (l/·mol^{-1}·s^{-1}) from curve fitting. The pre-exponential constants (k_i) are apparent chemical kinetic constant taking into account the total active sites, diffusion limits, and reaction. The values of these constants were fitted in the model to predict the catalytic reactions play an important role in the reduction reaction with the current oxygen carriers due to presence of Ni active site in the reduced particles. Therefore, proper selection of the rate equations for these reactions is an essential task. Iliuta et al. [165] have selected a series of relevant rate equations available in the literature based on the reduction experimental results from a fixed bed micro-reactor. Similar modeling strategy is employed in this study where the reaction equations of the catalytic reactions are adopted mostly from methane reforming investigations results.

Despite comprehensive investigations on the methane steam reforming process, no generalized kinetic is developed yet to be used for different catalysts [220]. An important point about use of the existing equations is the fact that the change of catalyst composition changes not only the values of the parameters of the kinetic model, but it may also change the structure of the kinetic model via changes in the mechanism [293]. Therefore, use of the reaction equations based on these studies should be with sufficient caution with respect to the applicability of the models. In the current model, the reaction equations capable of best predicting current results were chosen.

The kinetics model developed by Hou and Hughes [220] is used for methane steam reforming and water gas shift reactions. The model was developed for a commercial Ni/Al_2O_3 catalyst based on the mechanism that both methane and steam are adsorbed on the catalyst with dissociation, and the surface reaction between adsorbed species as rate controlling step. Kinetic rate equations have been developed based on the Langmuir–Hinshelwood–Hougen–Watson (LH–HW) approach and Freundlich's adsorption concept. The equation for the reforming is:

$$r_4 = \frac{k_4 \exp(-E_4 / RT)(P_{CH4} P_{CH4}^{0.5} / P_{H2}^{1.25})(1-(P_{CO} P_{H2}^3 /(K_{P4} P_{CH4} P_{H2O}))}{(1+K_{CO} P_{CO} + K_H P_H^{0.5} + K_{H2O}(P_{H2O} / P_{H2}))^2} .\alpha \qquad \textbf{Eq. 6.21}$$

With the reaction equilibrium constant of:

$$K_{P4} = 1.198 \times 10^{17} \exp(-26830/T) \quad , \quad Pa^2 \qquad \textbf{Eq. 6.22}$$

And the water gas shift equation:

$$r_5 = \frac{k_5 \exp(-E_5 / RT)(P_{CO} P_{H2O}^{0.5} / P_{H2}^{0.5})(1-(P_{CO2} P_{H2} /(K_{P5} P_{CO} P_{H2O}))}{(1+K_{CO} P_{CO} + K_{H2} P_{H2}^{0.5} + K_{H2O}(P_{H2O} / P_{H2}))^2} .\alpha \qquad \textbf{Eq. 6.23}$$

With the reaction equilibrium constant of:

$$K_{P5} = 1.767 \times 10 \exp(4400/T) \quad , \quad Pa^0 \qquad \textbf{Eq. 6.24}$$

The other reaction constants used in these equations are listed in Table 6.3.

Table 6.3: Activation energies, adsorption enthalpies and pre-exponential factors for Eq. 6.21 and Eq. 6.23 from reference [220] with $K_i = K_{i,r} \exp(-\Delta H_i/R/T)$

E_1 (kJ/mol)	E_2 (kJ/mol)	ΔH_{CO} (kJ/mol)	ΔH_H (kJ/mol)	ΔH_{H2O} (kJ/mol)
209.2	15.4	-140.0	- 93.4	15.9
$K_{1,r}$	$K_{2,r}$	$K_{CO,r}$	$K_{H,r}$	$K_{H2O,r}$
5.922×10^8	6.028 × 10^{-4}	5.127 × 10^{-13}	5.68 × 10^{-10}	9.251

Reforming of methane with carbon dioxide on the nickel based catalyst has been subject of many investigations to date [294-298]. The literature results are not consistent in regard of the limiting step depending on the test conditions [295]. The rate expression developed by Wang and Lu [295] with Ni/γ-Al_2O_3 is chosen in the current study. It supposes that both methane and CO_2 are adsorbed on the catalyst followed by methane dissociation with surface reaction between adsorbed C and CO_2 being the rate controlling step. The rate equation in a Langmuir Hinshelwood mechanism was written as:

$$r_6 = \frac{k_6 \exp(-E_6 / RT) P_{CH4} P_{CO2}}{(1 + K_{rf,CH4} P_{CH4})(1 + K_{rf,CO2} P_{CO2})} .\alpha \approx \frac{k_6 \exp(-E_6 / RT) P_{CH4} P_{CO2}}{(1 + K_{rf,CO2} P_{CO2})} .\alpha \qquad \textbf{Eq. 6.25}$$

The simplification above is made regarding the low concentration of CH_4 which results in $K_{61}P_{CH4} << 1$. Here E_6 = 77500 J/mol [165], and k_6 = 1.107e-7 from curve fitting. And:

$$K_{mC} = 2.4 \times 10^{-8} \exp(-9920 / RT) \quad , \quad Pa^{-1} \qquad \textbf{Eq. 6.26}$$

The kinetic of carbon monoxide methanation has been modeled based on power law [299,300] and Langmuir adsorption isotherms [301]. The kinetic model developed by Klose and Baerns [301] is used in the current model. It assumes that the reaction between surface carbon and two surface hydrogen atoms resulting from dissociatively adsorbed carbon monoxide and hydrogen to a carbene (H_2C:) species is the rate-limiting step. Therefore:

$$r_7 = \frac{k_7 \exp(-E_7 / RT) K_{mC} K_{mH}^2 P_{CO}^2 P_{H2}}{(1 + K_{mC} P_{CO}^{0.5} + K_{mH} P_{H2}^{0.5})^3} .\alpha \qquad \textbf{Eq. 6.27}$$

With k_7 = (1.33±0.58)x10^{-4}, and E_7 = 103±2 kJ/mol, and:

$$K_{mC} = (5.8 \pm 3.8) \times 10^{-6} \exp((-42 \pm 3) \times 10^3 / RT) \quad , \quad Pa^{-0.5} \qquad \textbf{Eq. 6.28}$$

And

$$K_{mC} = (1.6 \pm 1.3) \times 10^{-4} .\exp((-16 \pm 3) \times 10^3 / RT) \quad , \quad Pa^{-0.5} \qquad \textbf{Eq. 6.29}$$

As explained previously the kinetic scheme and reaction rate depend on the oxygen carriers properties especially in case of catalytic reactions. Accordingly, to achieve a confident kinetic model it is appreciated to separate experimental tests in well controlled hydrodynamic conditions, for instance in a batch micro fixed bed as in some literature works [165]. However this was not possible in the frame of the present study. Therefore, the available batch fluidized bed experiments on the pilot plant were used to verify the kinetic model.

6.2.4 Heat Transfer

High heat transfer coefficient and uniform temperature is one of the main features of fluidized beds [302]. Vigorous motion of particles results in a nearly isothermal bed while the freeboard can show a substantial temperature gradient [303]. In the current CLC system, the reactor is relatively small and well isolated. Moreover, the gas velocity is well above U_{mf} resulting in bubbling flow with good particle mixing in the reactor. Accordingly, the bed temperature is considered to be identical all over the reactor. This hypothesis is well confirmed with experimental axial temperature data where the temperature difference between two axial points of 0.1 m is less than 5 °C.

As presented previously, the temperature of the fluidized bed was not constant during the experimental tests in batch mode. A complete heat balance around the fluidized bed would be required to predict temperature evolution in the bed. However, this is a complex modeling in the pilot plant because heat losses and compensations are significant and have to be accounted for. Therefore, in this case, the temperature variation is simply taken into account by imposing a linear temperature variation in the model based on the experimental results for batch tests. Therefore, the system temperature is calculated as:

$$T = T_0 + m_T t \qquad \textbf{Eq. 6.30}$$

Where T_0 stands for the initial solid bed temperature and m_T presents the slope of experimental temperature variation. This model section can be more developed by including heat transfers from the bed to the reactor walls and the effect of the heating system in addition to the reaction heats and convective flux in the heat balance equations. The current model does not include thermal heat balance. The addition of heat equations into the model is an important further modification to be considered. This is of particular interest in case of industrial reactors were the conditions are closer to adiabatic rather than isothermal as studied here.

6.2.5 Gas Phase Reaction and Expansion

The material balance equations for gas in bubble and emulsion phases were presented in chapter 0. As discussed previously all reactions occur in emulsion phase in the current model. Therefore, the reaction term is required to be added to the material balance equation of gas in the emulsion phase. Therefore, the equation becomes:

$$\frac{\partial C_i^d}{\partial t} = \frac{D_{axg}}{\varepsilon_{gd}} \cdot \frac{\partial}{\partial z}\left(\varepsilon_{gd} \cdot \frac{\partial C_i^d}{\partial z}\right) - \frac{1}{\varepsilon_{gd}} \cdot \frac{\partial}{\partial z}\left(u_{gd} . \varepsilon_{gd} . C_i^d\right) + K_{be} . \frac{\varepsilon_{gb}}{\varepsilon_{gd}} . \left(C_i^b - C_i^d\right) + \rho_s . \varepsilon_s . \sum_j \mu_{ij} . r_j \qquad \textbf{Eq. 6.31}$$

Here the last additional term in the right of the equations takes into account the variation of concentration of component "i" in all individual reaction "j". The material balance equation for gas in bubble phase remains identical as there is no reaction taking place in this phase.

The combustion of methane involves a considerable gas expansion due to formation of novel molecules as presented above. This expansion was taken into account in the current model by relating the material balance and pressure variation in each cell of the model. The sum of concentrations of all gases in the bubble phase of a given height in the reactor is related to the pressure as:

$$\Sigma C_i^b = \frac{P_b}{RT} = \frac{P_t}{RT} \qquad \textbf{Eq. 6.32}$$

Where P_t is the gas pressure in the given height which is considered identical radial in the reactor. Similarly for the dense phase:

$$\Sigma C_i^d = \frac{P_d}{RT} = \frac{P_t}{RT} \qquad \textbf{Eq. 6.33}$$

Therefore, the pressure can be substituted in the sum of the material balance equations in bubble and emulsion phases. By considering that $\partial P/\partial t = 0$, the final equation in the bubble phase is:

$$\frac{\partial((U_{gb} + U_{ft})\varepsilon_{gb} . P_t)}{\partial z} = \varepsilon_{gb} \frac{P_t}{T} \frac{\partial(.T)}{\partial t} \qquad \textbf{Eq. 6.34}$$

This equation equal to zero in isothermal conditions. Similarly for the dense phase:

$$\frac{\partial(U_{gd}\varepsilon_{gd} . P_t)}{\partial z} = \varepsilon_{gd} \frac{P_t}{T} \frac{\partial(T_t)}{\partial t} + D_{ax} . \frac{\partial}{\partial z}\left(\varepsilon_{gd} . \frac{\partial P_t}{\partial z}\right) + RT\rho_s\varepsilon_s \sum_i \sum_j \mu_{ij} . r_j \qquad \textbf{Eq. 6.35}$$

Where for isothermal conditions the term including $\partial T/\partial t$ will be omitted. And the pressure drop variation across the reactor height is:

$$\frac{\partial P_t}{\partial z} = -\rho_s . g . \varepsilon_s \qquad \textbf{Eq. 6.36}$$

The new gas velocity in bubble and dense phase is calculated from the equations above. The total gas expansion is calculated as:

$$Vsg = \varepsilon_{gb}(U_{gb} + U_{ft}) + \varepsilon_{gb} U_{gd} \qquad \textbf{Eq. 6.37}$$

And the gas flow rate is calculated as Qg = Vsg.A. Figure 6.21 illustrates the variation of different hydrodynamic parameters of the fluidized bed during combustion of 0.5 Nm^3/h of methane as an example. The effect of gas expansion can be well distinguished in the Figure 6.21. The gas velocity increases due to the combustion reaction particularly in the first 0.1 m of the bed. Similarly, size of the bubbles increases as well as bubble fraction along the bed height both due to the gas expansion and bubble growth.

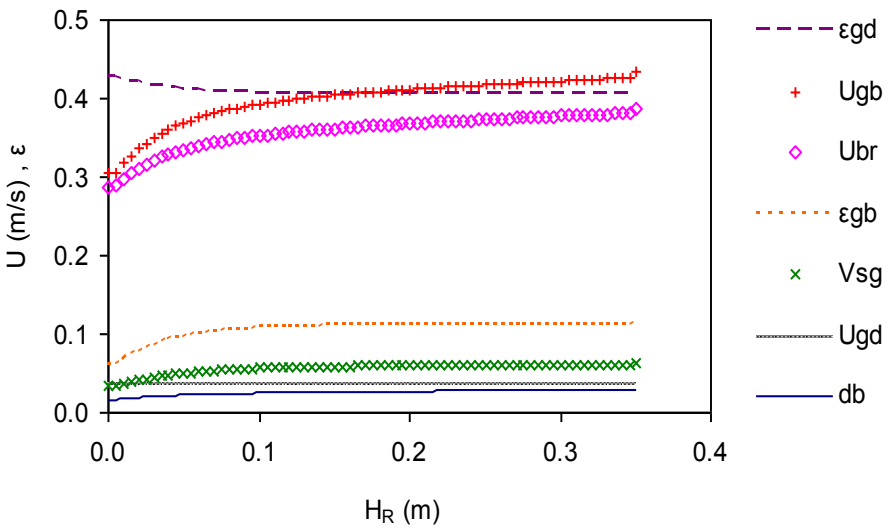

Figure 6.21: Variation of different hydrodynamic parameters across the reactor height with Q_{CH4} = 0.5 Nm^3/h, ΔP_R = 55 mbar, and T = 700 °C.

6.2.6 Solid Phase Material Balance

Solid in the emulsion phase can be either modeled with an axial dispersion or a CSTR model. The CSTR model is selected in the current study to represent solid phase. This is a common choice in modeling of bubbling fluidized beds [163-165]. The main reasons for this choice are:

- The reactors are operated with the gas flow rate well above the U_{mf} in the bubbling regime. Therefore, the solid mixing in the reactor is considerable and particles are mixed along the reactor due to the bubbles effect [153,304] and not in the short and random manner which is characteristic of an axial dispersion model.
- Reaction rate between the NiO and CH_4 is considerably high. Moreover, oxygen is always available in the oxygen carrier as the oxidation degree (ΔX) normally doest not exceed 30%. Accordingly, most of the reaction will occur in the bubbles cloud region. Therefore, the main restriction should be the gas transfer between the bubble and the emulsion phase and not the solid mixing.
- Residence time of solid particles is large (5 – 18 min) compared to the gas phase residence time (5 -12s).

Therefore, the material balance equation for component "i" in the solid phase is:

$$H_{bed}\varepsilon_{s,av}\frac{\partial C_i^s}{\partial t}=\frac{G_s}{\rho_{s,0}}C_{i,0}^s-\frac{G_s}{\rho_{s,av}}C_i^s+\rho_{s,av}.\varepsilon_{s,av}.\sum_j \mu_{ij}.r_j \qquad \textbf{Eq. 6.38}$$

Where "i" stands for Ni and NiO concentration in the oxygen carrier. The left hand side term represents concentration variation with time. The right hand side terms stand for solid influx into the reactor, solid flux out of the reactor, and the concentration variation due to sum of individual reactions "j". The oxidation degree of the oxygen carrier is the calculated as:

$$X=\frac{C_{NiO}M_O}{R_0\rho_{oxide}} \qquad \textbf{Eq. 6.39}$$

Where M_O stands for the oxygen molar weight, and ρ_{oxide} for the density of fully oxide particle. The reduction of the oxygen carriers changes the total mass of the particles in side the bed compared to the fresh entering particles. In the current model the volume of the particles is assumed to remain constant after reduction reaction. Therefore, the effect of oxygen consumption is considered to change only the particle density as:

$$\rho = \rho_0 (1 - (1 - X) R_0) \qquad \textbf{Eq. 6.40}$$

Where ρ is the density of particle with oxidation degree of X and ρ_0 is the density of fully oxide oxygen carriers.

6.3 Model Validation

Experimental results presented previously are used to validate the model and to perform the necessary modifications. Figure 6.22 compares the model and experimental results of batch combustion of 0.5 Nm^3/h of CH_4 with H_{R1} = 0.33m (corresponding to Figure 6.8). The results show that a larger portion of the injected CH_4 leaved the reactor compared to the experimental results. This unreacted portion increased by increasing the CH_4 injection rate or decreasing the height of the fluidized bed. Moreover, it was independent of the reaction rate in the model as increase of reaction rates did not modified the behavior. Comparison of the gas concentration in bubble and emulsion phase showed that the bubble – emulsion gas exchange rate is the principal source of this difference. As explained previously, the oxygen carriers used in this study have a porous nature with a very high reactivity. According to Kunni and Levenspiel [153], the bubble emulsion gas exchange rate is upto one order of magnitude higher for the adsorbing particles compared to non-adsorbing particles. They have introduced a new gas exchange coefficient (K_d) which takes into account both transfer across the bubble – cloud boundary, as well as exchange due to the particles dispersed in the bubbles. Accordingly:

$$K_d = \gamma_b \frac{6(Sh^*)D}{\phi_s d_P^2 y} \eta_d + K_{be} \qquad \textbf{Eq. 6.41}$$

Where γ_b stands for the volume fraction of particles in the bubble, considered 0.005. y is the logarithmic mean fraction of the inert or non-diffusing component, assumed to be H_2O and CO_2 in this model. η_d is the fitted adsorption efficiency which is 0 for non-adsorbing particles and 1 for highly adsorbing particles. Sh* is [305]:

$$Sh^* = 2 + 0.6\,\mathrm{Re}^{1/2}\, Sc^{1/3} \qquad \textbf{Eq. 6.42}$$

Here, Re is calculated for mean particles size and reactor superficial velocity and Sc = μ/ρ.Dg where Dg is the gas phase diffusion coefficient.

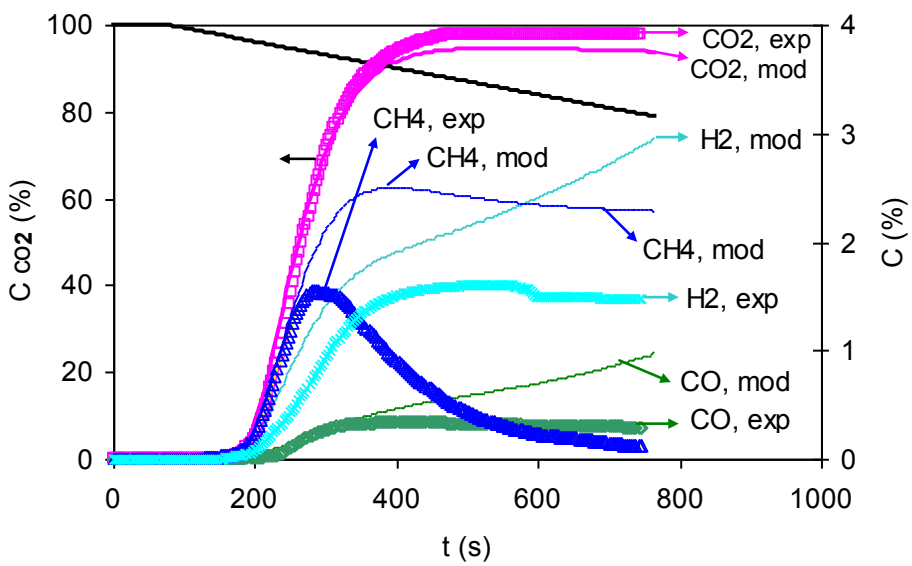

Figure 6.22: Comparison of modelling and experimental results with 0.5 Nm^3/h of CH_4, H_{R1} = 0.33m (corresponding to Figure 6.8) with K_{be} of non-adsorbing particles.

Figure 6.23 and Figure 6.24 illustrate the modeling results after modification of the gas exchange coefficient. Accordingly, the model produces the CH_4 peak in a satisfactory manner for different gas flow rates. CO_2 concentration is well predicted particularly due to high CO_2 concentration compared to other gases. These results illustrate that the model sensibility to the variation of the fuel flow rate is satisfying compared to the experimental results. However, calculated H_2 concentration does not follow exactly the experimentally observed behavior. This can be modified by taking into account the thermodynamic limitation of H_2 combustion with NiO. In the current model a direct reaction of H_2 and NiO is considered which results in such a concentration profile.

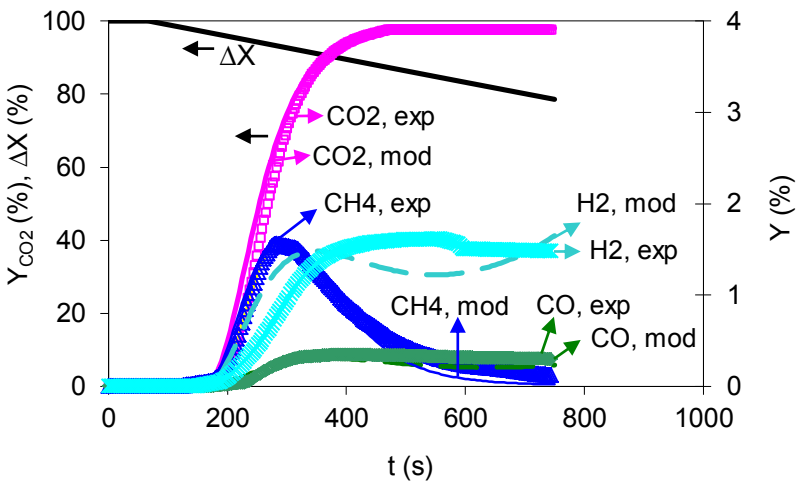

Figure 6.23: Comparison of modelling (narrow lines) and experimental results (thick lines) with 0.5 Nm^3/h of CH_4, H_{R1} = 0.33m (corresponding to Figure 6.8), dT/dt = -0.055 °C/s.

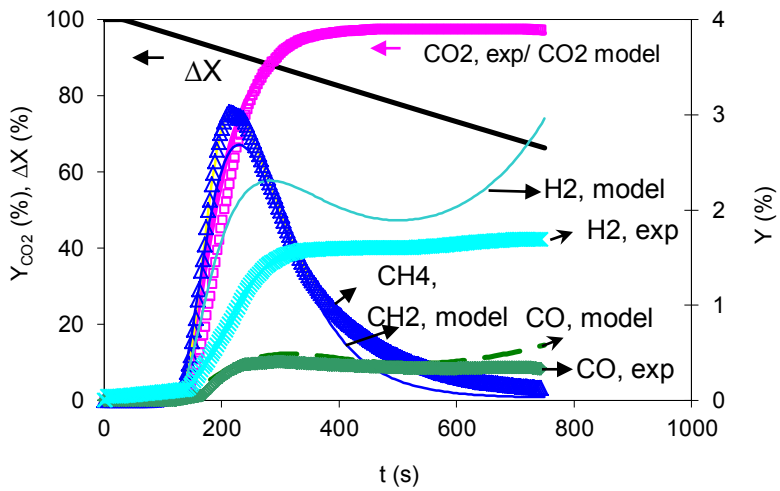

Figure 6.24: Comparison of modelling (narrow lines) and experimental results (thick lines) with 0.75 Nm^3/h of CH_4, H_{R1} = 0.33m, and dT/dt = -0.06 °C/s.

The experimental and model sensibility to variation of the fluidized bed height (contact time) is then investigated. Figure 6.25 illustrates comparison of the model and experimental results for combustion of 0.5 Nm^3/h of CH_4 with H_R = 0.55 m (compared to H_R = 0.33 m in Figure 6.23). Accordingly, CH_4, CO, and H_2 conversion is higher in the model than the experimental results. Regarding CO and H_2 a solution is to consider thermodynamic limitations. However, the main reason for this difference is probably the freeboard and particularly grid region effect. Freeboard region is less dependent to the bed height therefore it decreases the observed difference. The grid region is probably more important. It has been reported that the mass transfer in the grid region can be about 40 to 60 times higher than the bubbling region in the bed [306]. The gas exchange coefficient proposed by Sit and Grace [307]

can be used in this region by applying an appropriate jet length correlation. In this case a higher portion of the reactions will be in the grid region. Therefore, decrease of bed height above the jet height will have less influence on the conversion. Moreover, this explains high gas conversion with very low solid height observed in the transient tests presented in section 6.1.2.

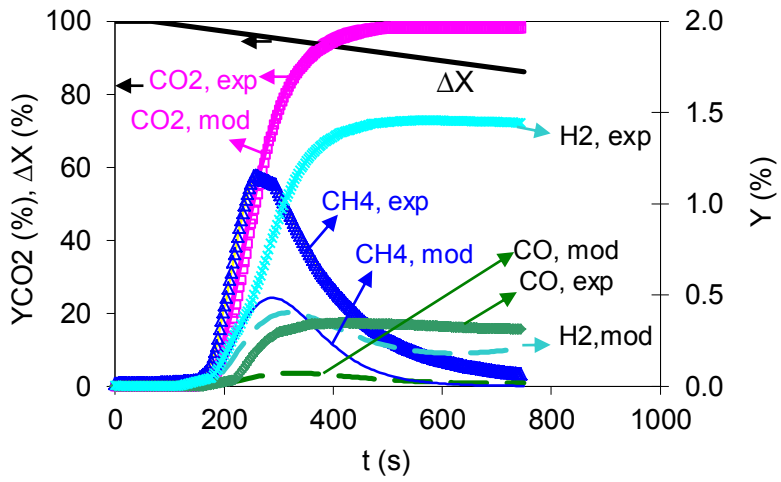

Figure 6.25: Comparison of modelling and experimental results with 0.5 Nm^3/h of CH_4, H_{R1} = 0.55 m.

The model was then compared with the experimental steady state methane combustion. Figure 3.26 illustrates the CO_2 yield in terms of fluidized bed height in the fuel reactor. The model fails to well predict the yield with solid height below 0.2 m. Similar explanation is valid in this case as the batch results for effect of the H_R. The observed difference is mainly due to the elevated bubble – emulsion phase gas exchange in the grid region. Moreover, with H_R less than 0.3 m, the bed surface is below the loop-seal entrance into the bed (as discussed in section 6.1.2). Therefore, freeboard of the fluidized bed has a high particle concentration which affects the gas conversion considerably. Similar trend can be observed for prediction of the gas concentrations by the model (Figure 6.27). The model fails to predict appropriately the gas concentrations at low and high heights of the bed due to the same causes explained above. A possible modification is to consider thermodynamic limitations in the combustion of CO, and H_2 as explained previously. This will results in better model prediction with high height of the fluidized bed where current model predict nearly complete conversion for these gases.

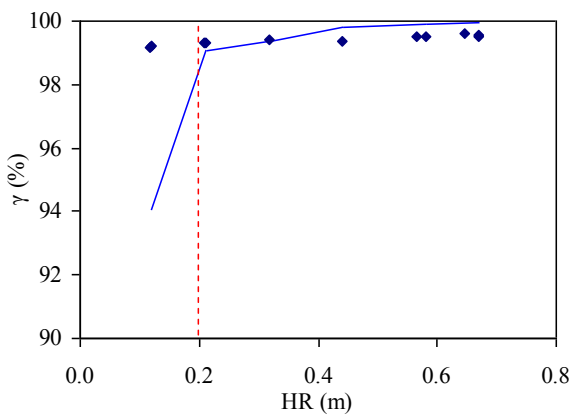

Figure 6.26: Comparison of the modeling (solid line) and experimental (points) CO_2 yield results in terms of the height of the fluidized bed in the fuel reactor with T_R = 750 ± 02 °C, Q_{CH4} = 0.5 Nm^3/h.

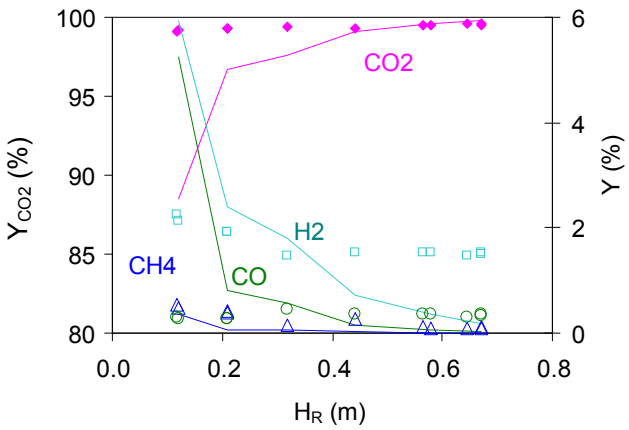

Figure 6.27: Comparison of the modeling (solid lines) and experimental (points) methane combustion in the fuel reactor at with various heigh of fluidized bed, T_R = 750 ± 20 °C, and Q_{CH4} = 0.5 Nm^3/h.

The effect of temperature on the model prediction in the steady state tests is next investigated. Figure 6.28 illustrates the predicted CO_2 yield versus experimental results. The yield results are satisfactorily close to the experimental results. However, the model fails to produce proper prediction in terms of gas concentrations (Figure 6.29). This is partly related to the activation energies in the reaction constants which were selected from literature in the current model. Moreover, consideration of appropriate thermodynamics limitations can improve the model prediction in this case.

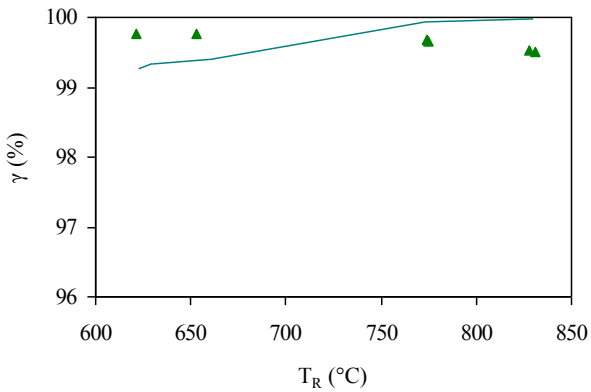

Figure 6.28: Comparison of the modeling (solid line) and experimental CO_2 yield (points) in the fuel reactor at different temepratures with H_R = 0.42 ± 0.5 m, and Q_{CH4} = 0.5 Nm^3/h.

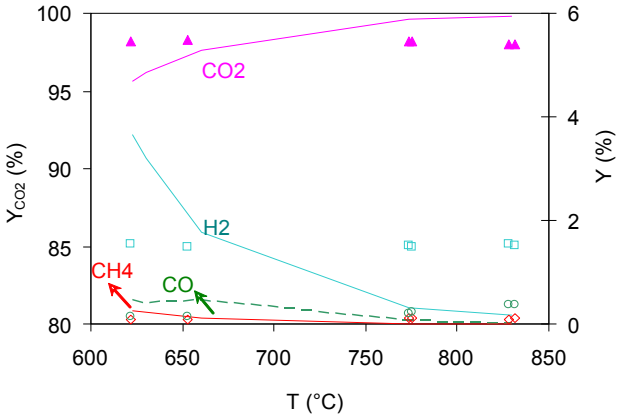

Figure 6.29: Comparison of the modeling (solid line) and experimental (points) methane combustion in the fuel reactor at different temepratures with H_R = 0.42 ± 0.5 m, and Q_{CH4} = 0.5 Nm^3/h.

Comparison of the model and experimental results in this section illustrate importance of the grid and freeboard region in the current CLC system. Moreover, the results illustrate that the selected reaction kinetic rates need to be modified for a better kinetic prediction. An important modification is consideration of thermodynamics regarding fast reaction rates observed.

It should be noted that a detailed kinetic study was not the aim of the current work. This requires methane combustion in reactors with well controlled hydrodynamics (fixed bed) and analyses of different gases as CO, H_2, H_2O, and CH_4 to better identify kinetic of each reactions. The oxidation reactor was not modeled in the current study. The principal reason was the fact that in the current tests oxidation was carried out in bubbling fluidized beds which are not of interest with the current oxygen carriers with high oxidation rate.

6.4 Conclusion

Experimental and modeling results of methane combustion were presented in this chapter. Experimental combustion tests were conducted in the high temperature pilot plant using $NiO/NiAl_2O_4$ oxygen carriers. A dynamic model was developed based on hydrodynamic model developed in the previous chapter by introducing solid phase material balance and a reaction scheme. The principal conclusions can be listed as:

- The experimental methane combustion results illustrated very high reactivity of the particles with CH_4. However, the CO_2 yield was thermodynamically limited. The fast reaction rates imply that other types of reactors could be used for CH_4 and $NiO/NiAl_2O_3$ system such as turbulent or dilute phase reactors.

- The oxidation of the oxygen carriers was also investigated in the pilot plant. The $NiO/NiAl_2O_4$ particles demonstrated a high oxidation rate similar to the reduction reaction. Therefore, other types of reactors can be used for oxidation reaction with current oxygen carrier. This can be studied in the current system by injecting air in the lifts in place of Nitrogen.
- In the current CLC pilot, gas leakage out of the fuel reactor was due to the gas flow through the L-valve which is very low compared to the total gas injected into the system. The other carbon leakage mechanism is through carbon deposition on the oxygen carrier particles leaving the fuel reactor. Carbon deposition was not observed in this study. Accordingly, current system provides elevated capture efficiency above 98.4 %. The main gas dilution was caused by the Nitrogen injection into the loop-seal. This can be easily minimised by injection of either CO_2 or water vapour in the loop-seal.
- The oxygen carriers have gone through an initially high attrition rate. The particles left over in the system after long term operation had a high resistance toward attrition.
- The employed modeling method was able to produce the CH_4 peak and H_2 and CO exit concentrations for different gas flow rates. However, the model was not able to predict properly effect of the fluidized bed height in the reactor (solid – gas contact time).The bubble – emulsion gas exchange coefficient was modified in the model to take into account the gas exchange imposed by dispersed particles in the bubble phase.
- The results revealed importance of grid region and freeboard in the gas conversion in the current system. Grid region has reported to have a very high gas exchange coefficient between the emulsion and jet phase. This increases the reaction conversion in this zone compared to the rest of the bed as observed in the current experimental tests. Increase of bubble size and velocity raises gas bypassing along the fluidized bed as the height increases.
- The employed kinetic model was able to produce the trend of experimental results reasonably in batch and steady state tests. However, it failed to properly present the effect of the fluidized bed height. This can be modified by including freeboard and grid region as well as including thermodynamic limitations.

Conclusions

Conclusions

Chemical looping combustion (CLC) was investigated in a novel 10 kW_{th} experimental configuration. The system is based on the interconnected bubbling fluidized bed principle. Solid flow rate control is achieved by use of non-mechanical L-vales while loop-seals are used to minimize gas leakage into the reactors. The purpose of the design was to investigate CLC in a wide range of operating conditions under steady state.

This work was carried out in two principal phases. The first part focused on the study of solid circulation, particularly on the role of L-valve and loop-seal. The principal conclusions of this part of study can be listed as:

- Stable solid circulation was easily achieved with the current configuration both at ambient and high temperature conditions. Various particles were used with average diameters ranging from 107 µm to 368 µm and densities of 2650 kg/m^3 to 4750 kg/m^3.
- L-valves proved to be an effective device to control solid flow rate with particles of group B in a wide range of temperatures. The external L-valve aeration was the main solid flow rate controlling parameter. Moreover, the pressure drop across the solid circulation loop demonstrated to have a significant effect on the flow rate and stability of the L-valve.
- L-valves provided a solid flow control independent of the gas flow rate in the reactors. This increases the system operation flexibility. Moreover, use of multiple L-valves in the current system resulted in control of solid inventory distribution between reactors. This provides an additional flexibility of the system, interesting for laboratory studies.
- Volumetric gas flow rate (velocity) around the elbow is the solid flow controlling parameter in a geometrically defined L-valve. Gas density was shown to have negligible effect on the solid flow rate in the L-valve. However, high temperature results indicated that an increase of gas viscosity increases the actuated solid flow rate.
- Loop-seals are shown to be efficient means to prevent gas leakage into the reactors. Careful attention should be given to pressure drop across the solid circulation path for loop-seal stability. The first external aeration below the supply chamber was proven to be a critical element both in control of circulation stability and leakage minimization.
- A zero order steady state solid circulation model was developed based on the pressure balance principle. The model provides acceptable solid flow rate and pressure drop prediction across the system based on the operating conditions including solid inventory and external gas injection rates. Scale-up effects remain to be included.

The second part of the work focused on the characterisation of the reactors employed in the current system. The principal conclusions of this phase can be listed as:

- The hydrodynamic of the bubbling fluidized bed was experimentally studied using the residence time distribution (RTD) method in the cold flow prototype. A hydrodynamic model was developed based on the two phase model of bubbling fluidized beds. The experimental RTD results provided a benchmark to select critical relation required in the hydrodynamic model including the bubble size correlation and gas dispersion in the emulsion phase.
- The experimental combustion results revealed a fast reaction rate of $NiO/NiAl_2O_4$ both with methane and oxygen. This suggests possible use of turbulent and dilute phase reactors with such a combustion system. The reaction with methane is however limited thermodynamically and complete conversion is not possible.

- In the current CLC pilot, gas leakage out of the fuel reactor was due to the gas flow through the L-valve which is very low compared to the total gas injected into the system. The other carbon leakage mechanism is through carbon deposition on the oxygen carrier particles which was not observed in this study. Accordingly, current system provides elevated capture efficiency above 98.4 %. The main gas dilution was caused by the Nitrogen injection into the loop-seal. This can be easily minimised by injection of either CO_2 or water vapour in the loop-seal.

The principal interest of the current CLC system was development of a tool to conduct laboratory scale investigations. Therefore, the design was aimed to achieve operation flexibility, maximum solid flow rate control and minimum gas leakage. This provides flexibility in terms of oxygen carriers and gas feed used. Another outcome is a large operation span permitting easier modification of the system in terms of the feed and oxygen carriers.

The study was carried out with Nickel based oxygen carriers ($NiO/NiAl_2O_4$) and CH_4 feed. This provided an essential understanding of the system and a standard benchmark for planned further developments. Moreover, this study provided a supplementary understanding on solid circulation control and gas leakage minimisation through L-valves and Loop-seals. These are important parameters in CLC process development regardless of the feed, system scale or used oxygen carrier. The developed solid circulation model provides a useful development tool while additional scale effects remain to be considered.

Various studies are required to be conducted to achieve feasible industrial CLC process. In this perspective, development of the oxygen carriers is an essential task to meet the required reactional, mechanical and safety aspects. Investigation of liquid and solid feedstock is another possible research theme, possible to be investigated in the current CLC pilot plant. It should be noted that the design depends on the nature of the fuel and associated reactional mechanisms. Therefore, some modifications are required to be carried out in each case.

The main challenge with the liquid feeds is fuel injection into the fuel reactor. Heavy liquid fuels are of more interest in this regard. However, this involves some new phenomena to be considered including: carbon deposition, presence of sulphur and heavy metals.

Combustion of solid fuels is another research topic in CLC development field. This involves a wide range of fuels such as Petroleum coke, coal, and biomasses. Combustion of solid fuels involves a series of phenomena including volatilisation, gasification and combustion. Gasification is the limiting step in this case. Therefore, specific reactor design and fuel injection systems are required. Another important technological challenge to be addressed is the solid – solid separation to avoid unburned solids to enter into the air reactor and to extract ashes out of the system.

Scale-up and design of industrial CLC process is the aim of R&D efforts. This adds effect of size to the above mentioned challenges. For this purpose appropriate designs should be developed taking into account material limitations. Experimental study of intermediate sizes is an essential step in this case. This helps to understand the governing phenomena and their evolution in terms of size. Detailed circulation, combustion and CFD modelling is a useful extrapolation tool for CLC process development.

Refrences

References

[1] Hansen J., Ruedy R., Sato M., Imhoff M., Lawrence W., Easterling D., Peterson T., and Karl T., J. Geophys. Res., 106 (2001) 23947-23963.

[2] Jones P.D. and Moberg A., J. Climate, 16 (2003) 206-223.

[3] IPCC. Summary for Policymakers. In: Climate Change 2007: The Physical Science Basis. Contribution of Working Group I to the Fourth Assessment Report of the Intergovernmental Panel on Climate Change. Solomon, S., Qin D., Manning M., Chen Z., Marquis M., Averyt K.B., Tignor M., and Miller H.L. 2007. Cambridge, United Kingdom, Cambridge University Press.

[4] IPCC. 2001c: Climate Change 2001: the Scientific Basis. Contribution of Working Group I to the Third Assessment Report of the Intergovernmental Panel on Climate Change. J.T.Houghton, Y.Ding, D.J.Griggs, M.Noguer, P.J.van der Linden, X.Dai, K.Maskell, and C.A.Johnson. 2001. Cambridge, UK, Cambridge University Press.

[5] Mann M.E., Bradley R.S., and Hughes M.K., Geophys. Res. Lett., 26 (1999) 759-762.

[6] Vaclav Smil, The Earth's Biosphere: Evolution, Dynamics, and Change, MIT Press, Cambridge, Massachusetts, USA 2003.

[7] National Research Council, Solar Influences On Global Change, National Academy Press, Washington, D.C. 1994.

[8] Usoskin I.G., Schussler M., Solanki S.K., and Mursula K., Solar Activity over the Last 1150 years: Doest it Correlates with Climate?, 2005, pp. 19-22

[9] Solomon S., Qin D., Manning M., Marquis M., Averyt K., Tignor M., and Chen Z., Climate Change 2007, The Physical Science Basis, Cambridge University Press, 2007.

[10] Hansen J., Sato M., and Ruedy R., J. Geophys. Res., 102 (1997) 6831-6864.

[11] Levitus S., Antonov J.I., Boyer T.P., and Stephens C., Science, 287 (2000) 2225-2229.

[12] Hansen J., Sato M., Ruedy R., Lacis A., Asamoah K., Beckfor K., Borenstein S., Brown E., Cairns B., and Carlson B., J. Geophys. Res., 1997 (1997) 25679-25720.

[13] Hansen J., Sato M., Ruedy R., Lacis A., and Oinas V., Global warming in the twenty-first century: An alternative scenario, PNAS, 97 (2000) 9875-9880.

[14] Meehl G.A., Washington W.M., Ammann C.A., Arblaster J.M., Wigleym T.M.L., and Tebaldi C., Combinations of Natural and Anthropogenic Forcings in Twentieth-Century Climate, Journal of Climate, 17 (2004) 3721-3727.

[15] Rhode R.A. Climate Change Attribution. 2006. 2011. http://www.globalwarmingart.com/wiki/File:Climate_Change_Attribution_png

[16] IPCC, 2007: Summary for Policymakers. In: Climate Change 2007: The Physical Science Basis. Contribution of Working Group I to the Fourth Assessment Report of the Intergovernmental Panel on Climate Change . Solomon, S., Qin D., Manning M., Chen Z., Marquis M., Averyt K.B., Tignor M., and Miller H.L. 2007. Cambridge University Press, Cambridge, United Kingdom and New York, NY, USA.

[17] Mauna Loa Observatory: NOAA-ESRL. Earth's CO2 Home Page. 2011. http://co2now.org/

[18] Bernstein L., Christ R., Davidson O., Hare W., Bosch P., Canziani O., Chen Z., and et. Climate Change 2007: Synthesis Report. Abdelkader Allali, Roxana Bojariu Sandra Diaz Ismail Elgizouli Dave Griggs David Hawkins Olav Hohmeyer Bubu Pateh Jallow Luc4ka Kajfez4-Bogataj Neil Leary Hoesung Lee David Wratt. 2007.

[19] IPCC. Climate Change: The IPCC Scientific Assessment. Houghton J.T., Jenkins G.J., and Ephraums J.J. 199. Cambridge University Press, Cambridge, Great Britain. http://www.ipcc.ch/publications_and_data/publications_and_data_reports.shtml

[20] Unietd Nations. The United Nations Framework Convention on Climate Change. 1992. http://unfccc.int/resource/docs/convkp/conveng.pdf

[21] UNITED NATIONS. Kyoto Protocol to the United Nations Framework Convention on Climate Change. 1998.

[22] Baumert K.A., Herzog T., and Pershing J. Navigating the Numbers Greenhouse Gas Data and International Climate Policy. 2005. Washington, DC, Word Resources Institute.
[23] European Commission. The EU climate and energy package. 2008. http://ec.europa.eu/clima/policies/package/index_en.htm
[24] IEA. Energy Technology Perspectives 2008 - Scenarios and Strategies to 2050. 2008. Paris, France, IEA. http://www.iea.org/w/bookshop/add.aspx?id=330
[25] IEA. Clean Energy Progress Report, IEA Input to the Clean Energy Ministerial. 2011. Paris, France, OECD/IEA.
[26] Metz B., Davidson O., de Coninck H., Loos M., and Meyer L., IPCC Special Report on Carbon Dioxide Capture and Storage, Cambridge University Press, Cambridge 2005.
[27] Summary for Policymakers, Climate Change 2001: Mitigation, A Report of Working Group III of the Intergovernmental Panel on Climate Change. 2001. http://www.ipcc.ch/ipccreports/tar/wg3/pdf/WG3_SPM.pdf
[28] M. Ranjan and H. J. Herzog, Feasibility of air capture, Energy Procedia, 4 (2011) 2869-2876.
[29] An Assessment of Carbon Capture Technology and Research Opportunities. 2005. STANFORD UNIVERSITY, Global Climate & Energy Project.
[30] G. Scheffknecht, L. Al-Makhadmeh, U. Schnell, and J. Maier, Oxy-fuel coal combustionGÇöA review of the current state-of-the-art, International Journal of Greenhouse Gas Control, 5, Supplement 1 (2011) S16-S35.
[31] M. B. Toftegaard, J. Brix, P. A. Jensen, P. Glarborg, and A. D. Jensen, Oxy-fuel combustion of solid fuels, Progress in Energy and Combustion Science, 36 (2010) 581-625.
[32] J. D. Figueroa, T. Fout, S. Plasynski, H. McIlvried, and R. D. Srivastava, Advances in CO2 capture technologyGÇöThe U.S. Department of Energy's Carbon Sequestration Program, International Journal of Greenhouse Gas Control, 2 (2008) 9-20.
[33] Doctor R. and et al. IPCC Special Report on Carbon dioxide Capture and Storage, Ch. 4.: Transport of CO2. Pichs-Madruga R. and Timashev S. 2011. New York, USA, Cambridhe University Press.
[34] The Parliamentary Office of Science and Technology, CO2 Capture, Transport and Storage, postnote, 335 (2009).
[35] K. Lackner and S. Brennan, Envisioning carbon capture and storage: expanded possibilities due to air capture, leakage insurance, and C-14 monitoring, Climatic Change, 96 (2009) 357-378.
[36] IPCC. Special report on previous termcarbonnext termprevious termcapturenext term and previous termstoragenext term. Metz, B. and t al. 2005. New York, Cambridge University Press. Working group III of the Intergovernmental Panel on Climate Change.
[37] J. C. M. Pires, F. G. Martins, M. C. M. Alvim-Ferraz, and M. Sim+Áes, Recent developments on carbon capture and storage: An overview, Chemical Engineering Research and Design, 89 (2011) 1446-1460.
[38] B. van der Zwaan and K. Smekens, CO2 Capture and Storage with Leakage in an Energy-Climate Model, Environmental Modeling and Assessment, 14 (2009) 135-148.
[39] S. Solomon, M. Carpenter, and T. A. Flach, Intermediate storage of carbon dioxide in geological formations: A technical perspective, International Journal of Greenhouse Gas Control, 2 (2008) 502-510.
[40] Orr F.M.Jr, Storage of Carbon Dioxide in Geologic Formations. SPE paper 88842, JPT, (2004) 90-97.
[41] John Barry and Graeme S.S.Sweeney, Role of CO2 EOR in Progressing Carbon Capture and Storage Worldwide, Oil and Gas Innovation in the Fossil Fuel Future, 2006,
[42] Gozalpour F., Ren S.R., and Tohidi B., CO2 EOR and Storage in Oil Reservoirs, Oil & Gas Science and Technology - Rev. IFP, 60 (2011) 537-546.
[43] Brendan B., CCS Technology: Capture, Transpot and Storage of CO2, CCS Africa, 2007,
[44] Bachu S., Shaw J.C., and Pearson R.M., Estimation of Oil Recovery and CO2 Storage Capacity in CO2 EOR Incorporating the Effect of Underlying Aquifers. SPE Paper 89340, SPE/DOE 14th Symposium on Improved Oil Recovery, 2004,
[45] SBI Energy. EOR Enhanced Oil Recovery Worldwide. 2010. Rockville, USA, SBI Reports.

[46] Lemaire E., Le Captage et le Stockage du CO2, Formation de Captage et Stockage de Dioxyde de Carbon, 2010,
[47] IEA. CO2 capture as a factor in power station investment decisions. 2006/8. 2006. International Energy Agency.
[48] M. Rydén, A. Lyngfelt, and T. Mattisson, Synthesis gas generation by chemical-looping reforming in a continuously operating laboratory reactor, Fuel, 85 (2006) 1631-1641.
[49] H. J. Ryu and G. T. Jin, Chemical-looping hydrogen generation system: Performance estimation and process selection, Korean Journal of Chemical Engineering, 24 (2007) 527-531.
[50] T. Mattisson, A. Lyngfelt, and H. Leion, Chemical-looping with oxygen uncoupling for combustion of solid fuels, International Journal of Greenhouse Gas Control, 3 (2009) 11-19.
[51] Naqvi R., Wolf J., and Bolland O., Part-load analysis of a chemical-looping combustion (previous termCLC)next term combined cycle with CO2 capture, Energy, 32 (2007) 360-370.
[52] C. Ekstrom, F. Schwendig, O. Biede, F. Franco, G. Haupt, G. de Koeijer, C. Papapavlou, and P. E. Rokke, Techno-Economic Evaluations and Benchmarking of Pre-combustion CO2 Capture and Oxy-fuel Processes Developed in the European ENCAP Project, Energy Procedia, 1 (2009) 4233-4240.
[53] M. Ishida and H. Jin, A Novel Chemical-Looping Combustor without NOx Formation, Industrial & Engineering Chemistry Research, 35 (1996) 2469-2472.
[54] Hossain M.M. and de Lasa H.I., Chemical-looping combustion (CLC) for inherent CO2 separations—a review, Chemical Engineering Science, 63 (2008) 4433-4451.
[55] Lyngfelt A., Johansson M., and Mattisson T., Chemical Looping Combustion - Status of Development, 9th International Conference on Circulating Fluidized Beds (CFB-9), 2008,
[56] T. Mattission, A. Lyngfelt, and P. Cho, The use of iron oxide as an oxygen carrier in chemical-looping combustion of methane with inherent separation of CO2, Fuel, 80 (2001) 1953-1962.
[57] E. Jerndal, T. Mattisson, and A. Lyngfelt, Thermal analysis of chemical-looping combustion, Chemical Engineering Research and Design, 84 (2006) 795-806.
[58] Kronberger B., Johansson E., Löffler G., Mattisson T., Lyngfelt A., and Hofbauer H., A Two-Compartment Fluidized Bed Reactor for CO2 Capture by Chemical-Looping Combustion, Chemical Engineering & Technology, 27 (2004) 1318-1326.
[59] Gayan P, Abad A, Ada´nez J, de Diego LF, and Garcý´a-Labiano F, Reduction and oxidation kinetics of a copper-based oxygen carrier prepared by impregnation for chemical-looping combustion, Ind Eng Chem Res, 43 (2004) 8168-8177.
[60] Johansson E., Lyngfelt A., Mattisson T., and Johnsson F., Gas leakage measurements in a cold model of an interconnected fluidized bed for chemical-looping combustion, Powder Technology, 134 (2003) 210-217.
[61] Lewis W. and Gilliland E. Production of pure carbon dioxide. [2,665,972]. 1954. US patent.
[62] Richter H.J. and Knoche K., Reversibility of combustion processes, efficiency and costing, Second law analysis of processes, ACS symposium series 235, 1983, pp. 71-85
[63] Ishida M. and Jin H., A Novel Combustor Based on Chemical-Looping Reactions and Its Reaction Kinetics, Journal of Chemical Engineering of Japan, 27 (1994) 296-301.
[64] Noorman S., van Sint Annaland M., and Kuipers H., Packed Bed Reactor Technology for Chemical-Looping Combustion, Ind. Eng. Chem. Res., 46 (2009) 4212-4220.
[65] Noorman S., Packed Bed Reactor Technology for Chemical Looping Combustion, International Oxy-Combustion Research Network, 2007,
[66] Dahl Ivar M., Bakken Egil, Larring Yngve, Spjelkavik Aud I., Håkonsen Silje Fosse, and Blom Richard, On the development of novel reactor concepts for chemical looping combustion, Energy Procedia, 1 (2009) 1513-1519.
[67] Ishida M., Zheng D., and Akehata T., Evaluation of a Chemical-Looping Combustion Power-Generation System by Graphic Exergy Analysis, Energy, 12 (1987) 147-154.
[68] Lyngfelt A., Leckner Bo, and Mattisson T., A Fuidized-bed combustion process with inherent CO2 separation; application of chemical-looping combustion, Chemical Engineering Science, 56 (2001) 3101-3113.
[69] Lyngfelt Anders and Thunman Hilmer, Construction and 100 h of Operational Experience of A 10-kW Chemical Looping Combustor, in: Thomas D.C. and Benson S.M. (Eds.), Carbon

Dioxide Capture for Storage in Deep Geologic Formations, Vol. 1. Elsevier Ltd., 2005, pp. 625-645.

[70] Ryu H.J., Jin G.T., and Yi C.K., Demonstration of Inherent CO_2 Separation and No NOx Emission in a 50kW Chemical-Looping Combustor: Continuous Reduction and Oxidation Experiment, in: Morris T., Gale J., and Thambimuthu K. (Eds.), Vol. II. Elsevier Ltd., 2005, pp. 1907-1910.

[71] Shen Laihong, Wu Jiahua, Gao Zhengping, and Xiao Jun, Reactivity deterioration of NiO/Al2O3 oxygen carrier for chemical looping combustion of coal in a 10 kWth reactor, Combustion and Flame, (2009).

[72] Shen Laihong, Wu Jiahua, and Xiao Jun, Experiments on chemical looping combustion of coal with a NiO based oxygen carrier, Combustion and Flame, 156 (2009) 721-728.

[73] de Diego L.F., García-Labiano F., Gayan P., Celaya J., Palacios J.M., and Adanez J., Operation of a 10 kWth chemical-looping combustor during 200 h with a CuO.Al2O3 oxygen carrier, Fuel, 86 (2007) 1036-1045.

[74] Pröll T., Rupanovits K., Kolbitsch P., Bolhàr-Nordenkampf J., and Hofbauer H., Cold Flow Model Study on a Dual Circulating Fluidized Bed System for Chemical Looping Processes, Chem. Eng. Technol., 32 (2009) 418-427.

[75] Kronberger Bernhard, Lyngfelt Anders, Lo1 ffler Gerhard, and Hofbauer Hermann, Design and Fluid Dynamic Analysis of a Bench-Scale Combustion System with CO2 Separation-Chemical-Looping Combustion, Ind. Eng. Chem. Res., 44, (2005) 546-556.

[76] Forero C.R., Gayán P., de Diego L.F., Abad A, García-Labiano F., and .Adánez J, Syngas combustion in a 500 Wth Chemical-Looping Combustion system using an impregnated Cu-based oxygen carrier, Fuel Processing Technology, 90 (2009) 1471-1779.

[77] Kolbitsch P., Pröll T., Bolhar-Nordenkampf J., and Hofbauer H., Design of a Chemical Looping Combustor using a Dual Circulating Fluidized Bed Reactor System, Chem. Eng. Technol., 32 (2009) 398-403.

[78] Ryu H.J., Jo S.H., Park Y.C., Bae D.H., and Kim S.D., Long term operation experience in a 50 kWth chemical looping combustor using natural gas and syngas as fuels, Les Rencontres Scientifiques de l'IFP: 1st International Conference on Chemical Looping, 2010,

[79] Andrus H.E., Chiu J.H., Thibeault P.R., and Brautsch A., Alstom's Calcium Oxide Chemical Looping Combustion Coal Power Technology Development, The 34th International Technical Conference on Clean Coal & Fuel Systems, 2009,

[80] A. Charitos, C. Hawthorne, A. R. Bidwe, L. Korovesis, A. Schuster, and G. Scheffknecht, Hydrodynamic analysis of a 10kWth Calcium Looping Dual Fluidized Bed for post-combustion CO2 capture, Powder Technology, 200 (2010) 117-127.

[81] Shimizu T., Takahashi T., Narisawa H., Li L., and Kim H., CO2 Looping Cycle for CO2 Separation, Engineering Conferences International, New York, USA, 2011,

[82] Abad A., Mattisson T., Lyngfelt A., and Rydén M., Chemical-looping combustion in a 300 W continuously operating reactor system using a manganese-based oxygen carrier, Fuel, 85 (2006) 1185.

[83] S. R. Son and S. D. Kim, Chemical-Looping Combustion with NiO and Fe2O3 in a Thermobalance and Circulating Fluidized Bed Reactor with Double Loops, Industrial & Engineering Chemistry Research, 45 (2006) 2689-2696.

[84] S. Rifflart, A. Hoteit, M. M. Yazdanpanah, W. Pelletant, and K. Surla, Construction and operation of a 10kW CLC unit with circulation configuration enabling independent solid flow control, Energy Procedia, 4 (2011) 333-340.

[85] M. M. Yazdanpanah, A. Hoteit, A. Forret, A. Delebarre, and T. Gauthier, Experimental Investigations on a Novel Chemical Looping Combustion Configuration, Oil Gas Sci. Technol. Rev. IFP Energies nouvelles, 66 (2011) 265-275.

[86] Real Son Sung, Kim Sang Done, and Lee Jea-Keun, Continuous and Semi-Continuous Operations of Chemical-Looping Combustion in an Annular Fluidized Bed Reactor with Solids Circulation, 2007 ECI Conference on The 12th International Conference on Fluidization - New Horizons in Fluidization Engineering, Vancouver, Canada, 2007., http://services.bepress.com/eci/fluidization_xii/118/.

[87] Berguer N. and Lyngfelt A., Design and operation of a 10 kWth chemical-looping combustor for solid fuels - Testing with South African coal, Fuel, 87 (2008) 2713-2726.
[88] Béal C., Epple B., Lyngfelt A., Adanez J., Larring Y., Guillemont A., and Anheden M., Development of metal oxides chemical looping process for coal-fired power plants, Les Rencontres Scientifiques de l'IFP: 1st International Conference on Chemical Looping, 2010., http://www.ifpenergiesnouvelles.com/actualites/evenements/nous-organisons/rs-chemical-looping.
[89] Merrow E., Linking R & D to Problems Experienced in Solids Processing, Chem. Eng. Processing, (1985) 14-22.
[90] Knowlton T.M. and I. Hirsan, L-valve Characterized for Solids Flow, Hydrocarbon Processing, 57 (1978) 149-156.
[91] Gauthier T., Bayle J., and Leroy P., FCC: Fluidization Phenomena and Technologies, Oil & Gas Science and Technology - Rev. IFP, 55 (2000) 187-207.
[92] Geldart D. and P. Jones, The behaviour of L-valve with granular solids, Powder Technology, 67 (1991) 163.
[93] Knowlton T.M. and Hirsan I., Solids Flow Control using a Nonmechanical L-valve, Ninth Synthetic Pipeline Gas Symposium, 1997,
[94] Ergun S., Fluid flow through packed columns, Chemical Engineering Process, 48 (1952) 89.
[95] Knowlton T.M., Standpipes and Nonmechanical Valves, in: W.-C. Yang (Ed.), Handbook of Fluidization and Fluid-Particle Systems, Marcel Dekker, Inc, New York, 2003, p. 576.
[96] P. H. Luong and S. C. Bhattacharya, A study of solid circulation rate in a circulating fluidized bed, Int. J. Energy Res., 17 (1993) 479-490.
[97] Smolders K. and Baeyens J., The operation of L-valves to control standpipe flow, Advanced Powder Technology, 6 (1995) 163-176.
[98] Baeyens J., Van Rompay P., and Smolders K, Operation of Standpipes and L-valves, CHISA 93, 1993,
[99] Daous M.A. and Al-Zahrani A.A., Modeling solids and gas flow through an L-valve, Powder Technology, 99 (1998) 86-89.
[100] Luckos A. and den Hoed P., A study into the hydrodynamic behaviour of heavy minerals in a circulating fluidized bed, IFSA 2005, Industrial Fluidization South Africa, South African Institute of Mining and Metallurgy, 2005, pp. 345-355
[101] T. Y. Yang and L. P. Leu, Multi-resolution analysis of wavelet transform on pressure fluctuations in an L-valve, International Journal of Multiphase Flow, 34 (2008) 567-579.
[102] W. C. Yang and T. M. Knowlton, L-valve equations, Powder Technology, 77 (1993) 49-54.
[103] D. Geldart and S. J. Ling, Dense phase conveying of fine coal at high total pressures, Powder Technology, 62 (1990) 243-252.
[104] Arena U., Langeli C.B., and Cammarota A., L-valve Behavior with Solids of Different Size and Density, Powder Technology, 98 (1998) 231.
[105] Lae F. Etude Experimentale et Modelisation du Fonctionnement d'un Lit Circulant. 2000. l'Université de Technologie de Compiégne.
[106] S. M. Yoon and D. Kunii, Gas Flow and Pressure Drop through Moving Beds, Industrial & Engineering Chemistry Process Design and Development, 9 (1970) 559-565.
[107] Rhodes M.J. and Laussmann P., A Study of the Pressure Balance Around the Loop of a Circulating Fluidized Bed, Can. J. Chem. Eng., 70 (1992) 625.
[108] Knowlton T.M., Solid Transfer in Fluidized Systems, in: Geldart D. (Ed.), Gas Fluidization Technology, John Wiley & Sons, Chichester, 1986, pp. 341-414.
[109] D. Geldart, Use of non-mechanical valves at high temperature: A case study, Can. J. Chem. Eng., 86 (2008) 605-607.
[110] Johansson A., Johnsson F., and Andersson B.A., The Performance of a Loop Seal in a CFB Boiler, Journal of Energy Resources Technology, 128 (2006) 135-142.
[111] Basu P., Chandel M., Butler J., and Dutta A., An Investigation Into the Operation of the Twin-Exit Loop-Seal of a Circulating Fluidized Bed Boiler in a Thermal Power Plant and Its Design Implication, Journal of Energy Resources Technology, 131 (2009) 041401-1-041401-8.
[112] Basu P. and Butler J., Studies on the operation of loop-seal in circulating fluidized bed boilers, Applied Energy, 86 (2009) 1723-1731.

[113] Butler J.W. and Basu P., Effect of Horizontal Passage Length on the Solid Recycle through a Loop Seal in a Circulating Fluidized Bed, 2007 ECI Conference on The 12th International Conference on Fluidization - New Horizons in Fluidization Engineering, 2007, pp. 153-160
[114] Basu P., Luo Z.Y., Boyd M., Chen L.M., and Cen K.F., An experimental investigation into a loop seal in a circulating fluidized bed, 6th Inter Conf on Circulating Fluidized Beds, 1999, pp. 805-810
[115] Basu P., Chen K.F., Cheng L.M., Boyd M., and Luo Z.Y., Experimental investigation into a loop seal in an atmospheric pressure circulating fluidized bed, The 6th Int. Conf. on Circulating Fluidized Beds, 1999,
[116] Basu P. and Chen L., An Analysis of Loop Seal Operations in a Circulating Fluidized Bed, Trans IChemE, 78, PartA (2000).
[117] Botsio E. and Basu P., Experimental Investigation into the Hydrodynamics of Flow of Solids through a Loop Seal Recycle Chamber, Can. J. Chem. Eng., 83 (2005) 554-558.
[118] Cheng L., Basu P., and Cen K., Solids Circulation Rate Prediction in a Pressurized Loop-Seal, Trans IChemE, 76, Part A (1998) 761-763.
[119] Cheng L. and Basu P., Effect of pressure on loop seal operation for a pressurized circulating fluidized bed, Powder Technology, 103 (1999) 203-211.
[120] Kim S.W., Namkung W., and Kim S.D., Solid Flow Characteristics in Loop-Seal of a Circulating Fluidized Bed, Korean J. Chem. Eng., 16 (1999) 82-88.
[121] Kim S.W., Kim S.D., and Lee D.H., Pressure Balance Model for Circulating Fluidized Beds with a Loop-seal, Ind. Eng. Chem. Res., 41 (2002) 4949-4956.
[122] Kim S.W. and Kim S.D., Effects of particle properties on solids recycle in loop-seal of a circulating fluidized bed, Powder Technol, 124 (2002) 76-84.
[123] Monazam E.R., Shadle L.J., and Mei J.S., Impact of the Circulating Fluidized Bed Riser on the Performance of a Loopseal Nonmechanical Valve, Ind. Eng. Chem. Res., 46 (2007) 1843-1850.
[124] Kim S.W., Namkung W., and Kim S.D., Solid Recycle Characteristics of Loop-seals in a Circulating Fluidized Bed, Chem. Eng. Technol., 24 (2001) 843-848.
[125] Lim K.S., Peerler P., Close R., and Joyce T., Estimation of Solids Ciculation Rate in CFB from Pressure Loop Profiles, 6th International Conference on Circulating Fluidized Beds, DECHEMA e. V., Germany, 1999, p. 819
[126] Basu P. and Fraser S.A., Circulating Fluidized Boilers, Design and Operations, Butterworth-Heinemann, 1991.
[127] Rudolph V., Chong Y.O., and Nicklin D.J., Standpipe Modeling for Circulating Fluidized Beds, CFB Technol. Ill, Pergamon Press, New York, 1991, p. 49
[128] Kojabashian C. Properties of dense-phase fluidized solids in vertical downflow. 1958. Massachusetts Inst. of Technology.
[129] J. Y. Zhang and V. Rudolph, Transitional packed bed flow in standpipes, Can. J. Chem. Eng., 69 (1991) 1242-1246.
[130] Klinzing G.E., Rizk F., Marcus R., and Leung L.S., Pneumatic Conveying of Solids: A Theoretical and Practical Approach, Springer, New York 2010.
[131] Li Y., Lu Y., Wang F., Han K., Mi W., Chen X., and Wang P., Behavior of gas-solid flow in the downcomer of a circulating fluidized bed with a V-valve, Powder Technology, 91 (1997) 11-16.
[132] Chan C.W., Seville J., Fan X., and Baeyens J., Solid particle motion in a standpipe as observed by Positron Emission Particle Tracking, Powder Technology, 194 (2009) 58-66.
[133] Li Y., Hydrodynamics, in: Kwauk M. (Ed.), Fast Fluidization, Academic Press, San Diego, CA, 1994, pp. 110-111.
[134] Yagi S., Chemical Machinery, Japon, (1952) 307.
[135] Knowlton T.M., Hirsan I., and Leung L.S., The effect of aeration tap location on the performance of a J-valve, in: Davidson J.F. and Keairns D.L. (Eds.), Fluidization, Cambridge University Press, 1978, pp. 128-133.
[136] Yagi S., Chemical Machinery, Japon, 16 (1952) 307.
[137] H. Li, The dynamics of non-fluidized gas-particle flow, Powder Technology, 73 (1992) 147-156.

[138] Bai D., Issangya A.S., Zhu J.X., and Grace J.R., Analysis of the Overall Pressure Balance around a High-Density Circulating Fluidized Bed, Ind. Eng. Chem. Res., 36 (1997) 3898-3903.
[139] Breault R.W. and Mathur V.K., High-velocity fluidized-bed hydrodynamic modeling. 2. Circulating bed pressure drop modeling, nd. Eng. Chem. Res., 28 (1989) 688-693.
[140] Rhodes M.J. and Geldart D., A Model for the Circulating Fluidized Bed, Powder Technology, 53 (1987) 155-162.
[141] K. Smolders and J. Baeyens, Hydrodynamic modeling of circulating fluidized beds, Advanced Powder Technology, 9 (1998) 17-38.
[142] Wu S., Alliston M.G., Kwauk M., and Li J., Circulating Fluidized Bed Technology V. Science Press., Beijing, 1996, pp. 158-163
[143] Knowlton T.M., Non-mechanical solid feed and recycle devices for CFB, Ciculating Fluidized Bed Technology II, Pergamon Press, Oxford, 1988, pp. 31-42.
[144] Knowlton T.M. Feeding and Discharge of Solids Using Nonmechanical Valves. Institute of Gas Technology . 1988. Chicago, Illionois, Institute of Gas Technology.
[145] Burkell J.J., Grace J.R., Zhao J., and Lim C.J., Circulating Fluidized Bed technology II, Pergamon, Oxford, 1988, pp. 501-509
[146] Couturier M.F., Stevens D., and Razbin V., 12th Int Conf. Fluidized Bed Combustion, ASME, 1993, pp. 869-875
[147] Dry R.J., White R.B., and Joyce T., Circulating Fluidized Bed Technology IV, AIChE., 1994, pp. 621-627
[148] Patience G.S., Chaouki J., and Grandjean B.P.A., Solids flow metering from pressure drop measurement in circulating fluidized beds, Powder Tech., 61 (1990) 95-99.
[149] Davies C.E. and Harris B.J., Fluidization VII, Engineering Foundation, New York, 1992, pp. 741-748
[150] Dybeck K., Nagel R., Schoenfelder H., Werther J., and Slnger H., Fluidizatin VII, Engineering Foundation, New York, 1995, pp. 9-16
[151] Lech M., Mass flow rate measurement in vertical pneumatic conveying of solid, Powder Technology, 114 (2001) 55-58.
[152] Klinzing G.E., Marcus R.D., Rizk F., and Leung L., Pneumatic Conveying of Solids: A Theoretical and Practical Approach, Chapman & Hall, London 1997.
[153] Kunii Daizo and Levenspiel Octave, Fluidization Engineering, Butterworth-Heinemann, Boston 1991.
[154] Nauman E.B., Chemical Reactor Design, Optimization, and Scaleup, McGRAW-HILL, New York 2002.
[155] Nauman E.B., Handbook of Industerial Mixing Science and Practice, JOHN WILEY & SONS, INC., Hoboken, New Jersey 2004.
[156] E. B. Nauman and C. N. Collinge, The theory of contact time distributions in gas fluidized beds, Chemical Engineering Science, 23 (1968) 1309-1316.
[157] Pustelnik P. and Nauman E.B., Contact time distributions in a large fluidized bed, AIChE Journal, 37 (1991) 1589-1592.
[158] D. Christensen, J. Nijenhuis, J. R. van Ommen, and M. O. Coppens, Residence times in fluidized beds with secondary gas injection, Powder Technology, 180 (2008) 321-331.
[159] Davidson J.F. and Harrison D.H., Fluidised Particles, Cambridge University Press, Cambridge 1963.
[160] P. N. Rowe and B. A. Partridge, Trans. I. Chem. E., 43 (1965) 157.
[161] Shakourzadeh K., Calcul des réacteurs à lits fluidisés, Techniques de l'Ingenieur, (1992).
[162] Grace R., Fluidized Bed Hydrodynamics, CFB10 Short Course, PSRI, 2011,
[163] Abad A, Adanez J., Garcia-Labiano F., L. F. de Diego, and Gayan P., Modeling of the chemical-looping combustion of methane using a Cu-based oxygen-carrier, Combustion and Flame, 157 (2010) 602-615.
[164] Kramp M., Thon A., Hartge E.-U., Heinrich S., and Werther J., The Role of Attrition and Solids Recovery in a Chemical Looping Combustion Process, Oil Gas Sci. Technol. - Rev. IFP Energies nouvelles, (2011).
[165] Iliuta I., Tahoces R., Patience G.S., Rifflart S., and Luck F., Chemical-looping combustion process: Kinetics and mathematical modeling, AIChE Journal, 56 (2010) 1063-1079.

[166] MAY W.G., Chem. Eng. Prog, 55 (1959) 49.
[167] Gilliland E.R. and Knudsen C.W., Chem. Eng. Prog. Symp. Ser., 67 (1971) 168.
[168] E. B. Nauman and C. N. Collinge, Measurement of contact time distributions in gas fluidized beds, Chemical Engineering Science, 23 (1968) 1317-1326.
[169] Toomey R. and Johnstone H.P., Chemical Engineering Progress, 48 (1952) 220-226.
[170] Wen C.Y. and Fan L.T., Models for Flow Systems and Chemical Reactors, Marcel Dekker, New York 1975.
[171] Ho T.C., Modelling, in: Yang W.C. (Ed.), Handbook of Fluidization and Fluid-Particle Systems, Marcel Dekker, Inc, New York, 2003.
[172] Orcutt J.C., Davidson J.F., and Pigford R.L., Chem. Eng. Prog. Sym., 58 (1962) 1.
[173] Werther J., Chemical Engineering Science, 5(1-2) (1980) 372-379.
[174] Higbie R., Trans. Am. Inst. Chem. Eng., 31 (1935) 365.
[175] Kunii D. and Levenspiel O., Bubbling bed model for kinetic processes in fluidized beds, I & EC Process Design and Development, 7 (1968) 481-492.
[176] Harrison D., Davidson J.F., and De Kock J.W., On the nature of aggregative and particulate fluidisation, Trans Inst Chem Engrs, 39 (1961) 211.
[177] Kato K. and Wen C.Y., Bubble assemblage model for fluidized bed catalytic reactors, Chem Eng Sci, 24 (1969) 1351-1369.
[178] J. M. van Baten and R. Krishna, Eulerian simulations for determination of the axial dispersion of liquid and gas phases in bubble columns operating in the churn-turbulent regime, Chemical Engineering Science, 56 (2001) 503-512.
[179] Deen N.G., Mudde R.F., Kuipers J.A.M., Zehner P., and Kraume M., Bubble Columns, in: Bohnet M. and et al. (Eds.), Ullmann's Encyclopedia of Industrial Chemistry, Wiley, Weinheim, 2010.
[180] R. Krishna, Urseanu M.I., J. M. van Baten, and Ellenberger J., Influence of scale on the hydrodynamics of bubble columns operating in the churn-turbulent regime: experiments vs. Eulerian simulations, Chemical Engineering Science, Chemical Engineering Science, 54 (1999) 4903-4911.
[181] Baird M.H.I. and Rice R.G., Axial dispersion in large unbaffled columns, Chem. Eng J., 9 (1975) 171-174.
[182] Riquarts H.P., Chemie Ingenieur Technik, 52 (1980) 777-862.
[183] Mangartz K.H. and Pilhofer T., Verfahrenstechnik, 1 (1980) 40-44.
[184] Bi H.T., Ellis N., Abba I.A., and Grace R., A state-of-the-art review of gas-solid turbulent fluidization, Chemical Engineering Science, Chemical Engineering Science, 55 (2000) 4789-4825.
[185] Lee G.S. and Kim S.D., Axial mixing of solids in turbulent fluidized beds, The Chemical Engineering Journal, 44 (1990) 1-9.
[186] Geun S. and Sang D.K., Axial Mixing of Solids in Turbulent Fluidized Beds, The Chemical Engineering Journal, 44 (1990) 1-9.
[187] Lee G.S., Kim S.D., and Baird M.H.I., Axial mixing of fine particles in fluidized bed, Chem. Eng. J., 47 (1991).
[188] T. Miyauchi, S. Furusaki, S. Morooka, and Y. Ikeda, Transport Phenomena and Reaction in Fluidized Catalyst Beds, in: B. D. Thomas (Ed.), Advances in Chemical Engineering, Academic Press, 1981, pp. 275-448.
[189] A. Lyngfelt, Oxygen Carriers for Chemical Looping Combustion - 4 000 h of Operational Experience, Oil Gas Sci. Technol. Rev. IFP Energies nouvelles, 66 (2011) 161-172.
[190] Liu J.A. Kinetics, catalysis and mechanism of methane steam reforming. 2006. Worcester Polytechnic Institute.
[191] S. Wang and G. Q. M. Lu, CO2 reforming of methane on Ni catalysts: Effects of the support phase and preparation technique, Applied Catalysis B: Environmental, 16 (1998) 269-277.
[192] H. Jin and M. Ishida, A new type of coal gas fueled chemical-looping combustion, Fuel, 83 (2004) 2411-2417.
[193] Bolhár-Nordenkampf J., Proll T., Kolbitsch P., and Hofbauer H., Performance of a NiO-based oxygen carrier for chemical looping combustion and reforming in a 120 kW unit, Energy Procedia, 1 (2009) 19-25.

[194] K. E. Sedor, M. M. Hossain, and H. I. De Lasa, Reactivity and stability of Ni/Al2O3 oxygen carrier for chemical-looping combustion (CLC), Chemical Engineering Science, 63 (2008) 2994-3007.
[195] P. Gayan, C. Dueso, A. Abad, J. Adanez, L. F. de Diego, and F. Garcia-Labiano, NiO/Al2O3 oxygen carriers for chemical-looping combustion prepared by impregnation and deposition coprecipitation methods, Fuel, 88 (2009) 1016-1023.
[196] C. Dueso, A. Abad, F. Garcia-Labiano, L. F. de Diego, P. Gayan, J. Adanez, and A. Lyngfelt, Reactivity of a NiO/Al2O3 oxygen carrier prepared by impregnation for chemical-looping combustion, Fuel, 89 (2010) 3399-3409.
[197] P. Cho, T. Mattisson, and A. Lyngfelt, Comparison of iron-, nickel-, copper- and manganese-based oxygen carriers for chemical-looping combustion, Fuel, 83 (2004) 1215-1225.
[198] T. Mattisson, A. J+ñrdn+ñs, and A. Lyngfelt, Reactivity of Some Metal Oxides Supported on Alumina with Alternating Methane and OxygenApplication for Chemical-Looping Combustion, Energy Fuels, 17 (2003) 643-651.
[199] T. Mattisson, M. Johansson, and A. Lyngfelt, The use of NiO as an oxygen carrier in chemical-looping combustion, Fuel, 85 (2006) 736-747.
[200] R. Villa, C. Cristiani, G. Groppi, L. Lietti, P. Forzatti, U. Cornaro, and S. Rossini, Ni based mixed oxide materials for CH4 oxidation under redox cycle conditions, Journal of Molecular Catalysis A: Chemical, 204-205 (2003) 637-646.
[201] H. Jin, T. Okamoto, and M. Ishida, Development of a Novel Chemical-Looping Combustion: the Synthesis of a Solid Looping Material of NiO/NiAl2O4, Industrial & Engineering Chemistry Research, 38 (1998) 126-132.
[202] M. Johansson, T. Mattisson, and A. Lyngfelt, Creating a Synergy Effect by Using Mixed Oxides of Iron- and Nickel Oxides in the Combustion of Methane in a Chemical-Looping Combustion Reactor, Energy Fuels, 20 (2006) 2399-2407.
[203] M. Ishida, H. Jin, and T. Okamoto, A Fundamental Study of a New Kind of Medium Material for Chemical-Looping Combustion, Energy Fuels, 10 (1996) 958-963.
[204] H. J. Ryu, D. H. Bae, and G. T. Jin, Effect of temperature on reduction reactivity of oxygen carrier particles in a fixed bed chemical-looping combustor, Korean Journal of Chemical Engineering, 20 (2003) 960-966.
[205] H. J. Ryu, D. H. Bae, and G. T. Jin, Effect of temperature on reduction reactivity of oxygen carrier particles in a fixed bed chemical-looping combustor, Korean Journal of Chemical Engineering, 20 (2003) 960-966.
[206] M. Ishida, H. Jin, and T. Okamoto, Kinetic Behavior of Solid Particle in Chemical-Looping Combustion: Suppressing Carbon Deposition in Reduction, Energy Fuels, 12 (1998) 223-229.
[207] Adanez J., de Diego L.F., Garcia-Labiano F., Gayan P., Abad A., and Palacios J.M., Selection of Oxygen Carriers for Chemical-Looping Combustion, Energy Fuels, 18 (2004) 371-377.
[208] Q. Zafar, T. Mattisson, and B. Gevert, Integrated Hydrogen and Power Production with CO2 Capture Using Chemical-Looping ReformingRedox Reactivity of Particles of CuO, Mn2O3, NiO, and Fe2O3 Using SiO2 as a Support, Industrial & Engineering Chemistry Research, 44 (2005) 3485-3496.
[209] House James E, Principles of Chemical Kinetics, Academic Press, New York 2007.
[210] J. T. Richardson, R. Scates, and M. V. Twigg, X-ray diffraction study of nickel oxide reduction by hydrogen, Applied Catalysis A: General, 246 (2003) 137-150.
[211] J. T. Richardson, R. M. Scates, and M. V. Twigg, X-ray diffraction study of the hydrogen reduction of NiO/[alpha]-Al2O3 steam reforming catalysts, Applied Catalysis A: General, 267 (2004) 35-46.
[212] O. Dewaele and G. F. Froment, TAP Study of the Mechanism and Kinetics of the Adsorption and Combustion of Methane on Ni/Al2O3 and NiO/Al2O3, Journal of Catalysis, 184 (1999) 499-513.
[213] M. Zanfir and A. Gavriilidis, Catalytic combustion assisted methane steam reforming in a catalytic plate reactor, Chemical Engineering Science, 58 (2003) 3947-3960.
[214] P. Gayan, L. F. de Diego, F. Garcia-Labiano, J. Adanez, A. Abad, and C. Dueso, Effect of support on reactivity and selectivity of Ni-based oxygen carriers for chemical-looping combustion, Fuel, 87 (2008) 2641-2650.

[215] J. E. Readman, A. Olafsen, J. B. Smith, and R. Blom, Chemical Looping Combustion Using NiO/NiAl2O4 Mechanisms and Kinetics of Reduction Oxidation (Red-Ox) Reactions from In Situ Powder X-ray Diffraction and Thermogravimetry Experiments, Energy Fuels, 20 (2006) 1382-1387.
[216] H. Kruggel-Emden, F. Stepanek, and A. Munjiza, A comparative study of reaction models applied for chemical looping combustion, Chemical Engineering Research and Design, In Press, Corrected Proof.
[217] Levenspiel O., Chemical Reaction Engineering, John Wiley & Sons, New York 1999.
[218] B. r. Christian Enger, R. L°deng, and A. Holmen, A review of catalytic partial oxidation of methane to synthesis gas with emphasis on reaction mechanisms over transition metal catalysts, Applied Catalysis A: General, 346 (2008) 1-27.
[219] H. Jin and M. Ishida, Reactivity Study on Natural-Gas-Fueled Chemical-Looping Combustion by a Fixed-Bed Reactor, Industrial & Engineering Chemistry Research, 41 (2002) 4004-4007.
[220] K. Hou and R. Hughes, The kinetics of methane steam reforming over a Ni/[alpha]-Al2O catalyst, Chemical Engineering Journal, 82 (2001) 311-328.
[221] P. Cho, T. Mattisson, and A. Lyngfelt, Carbon Formation on Nickel and Iron Oxide-Containing Oxygen Carriers for Chemical-Looping Combustion, Industrial & Engineering Chemistry Research, 44 (2005) 668-676.
[222] J. Bolhár-Nordenkampf, T. Proll, P. Kolbitsch, and H. Hofbauer, Comprehensive Modeling Tool for Chemical Looping Based Processes, Chemical Engineering & Technology, 32 (2009) 410-417.
[223] Kolbitsch P., Bolhar-Nordenkampf J., T. Proll, and Hofbauer H., Design of a Chemical Looping Combustor Using a Dual Circulating Fluidized Bed (DCFB) Reactor System, 9th Int. Conf. on Circulating Fluidized Beds, 2008,
[224] Kolbitsch P., Tobias P., and Hermann H., Modeling of a 120kW chemical looping combustion reactor system using a Ni-based oxygen carrier, Chemical Engineering Science, 64 (2008) 99-108.
[225] A. Abad, Mapping of the range of operational conditions for Cu-, Fe- and Ni- based oxygen carriers in chemical looping combustion, Chem. Eng. Sci., 62 (2007) 533-549.
[226] Basu P., Combustion and Gasification in Fluidized Beds, CRC Press, Taylor & Francis Group, Boca Raton 2006.
[227] Haider A. and Levenspiel O., Drag coefficient and terminal velocity of spherical and nonspherical particles, Powder Tech., 58 (1989) 63-70.
[228] C. Y. Wen and Y. H. Yu, A generalized method for predicting the minimum fluidization velocity, AIChE Journal, 12 (1966) 610-612.
[229] PSRI, Desktop Design Manual, Particulate Solid Research, Inc., Chicago 1994.
[230] Bi H.T. and Grace J.R., Flow regime diagrams for gas-solid fluidization and upward transport, International Journal of Multiphase Flow, 21 (1995) 1229-1236.
[231] PSRI, Desktop Design Manual, Particulate Solid Research, Inc., Chicago 1994.
[232] Wu S. and Alliston M.G., Circulating Fluidized Bed Technology V, Science Press, Beijing, 1996, pp. 158-163
[233] P. M. Herbert, T. A. Gauthier, C. L. Briens, and M. A. Bergougnou, Application of fiber optic reflection probes to the measurement of local particle velocity and concentration in gasGÇösolid flow, Powder Technology, 80 (1994) 243-252.
[234] Aubert E. 1993. Institut Français du Pétrole, ENSPM, Paris.
[235] Knowlton T.M. and I. Hirsan, L-valve Characterized for Solids Flow - Design Parameters Examined for Valve Use in Coal Gasification, Hydrocarbon Processing, 57 (1978) 149.
[236] Knowlton T.M. and I. Hirsan, L-Valve Characterized for Solids Flow - Design Parameters Examined for Valve Use in Coal Gasification, Hydrocarbon Processing, 57 (1978) 149.
[237] K. Smolders and J. Baeyens, The Operation of L-valve to Control Standpipe Flow, Advaced Powder technology, 6 (1995) 163.
[238] D. Geldart, Use of non-mechanical valves at high temperature A case study, Can. J. Chem. Eng., 86 (2008) 605-607.
[239] Baeyens J. and Wu S.Y., Bed expansion and the visible bubble flow rate in gas fluidized beds, Advanced Powder Technology, 3 (1992) 163-189.

[240] B. Formisani, R. Girimonte, and L. Mancuso, Analysis of the fluidization process of particle beds at high temperature, Chemical Engineering Science, 53 (1998) 951-961.
[241] K. Svoboda and M. Hartman, Influence of temperature on incipient fluidization of limestone, lime, coal ash, and corundum, Industrial & Engineering Chemistry Process Design and Development, 20 (1981) 319-326.
[242] J. G. Yates, Effects of temperature and pressure on gas-solid fluidization, Chemical Engineering Science, 51 (1996) 167-205.
[243] H. Li, The dynamics of non-fluidized gas-particle flow, Powder Technology, 73 (1992) 147-156.
[244] Cheng L., Basu P., and Cen K., Solid Circulation Rate Prediction in a Pressurized loop-Seal, Trans IChemE, 76, Part A (1998) 761-763.
[245] Klinzing G.E., Dilute-Phase Pneumatic Conveying, in: W.-C. Yang (Ed.), Handbook of Fluidization and Fluid-Particle Systems, Marcel Dekker, Inc, New York, 2003.
[246] Institute of Gas Technology (IGT). Dept. of Energy Contract, FE 2286-32. 1978.
[247] S. R. Sankar and T. N. Smith, Slip velocities in pneumatic transport part II, Powder Technology, 47 (1986) 179-194.
[248] Yang W.C., A unified theory in dilute phase pneumatic transport, Int. Powder and Bulk Solids Handling and Processing Conf., 1976,
[249] Matsen J., AIChE Annual Meeting, 2011,
[250] G. S. Patience, J. Chaouki, F. Berruti, and R. Wong, Scaling considerations for circulating fluidized bed risers, Powder Technology, 72 (1992) 31-37.
[251] Konno H. and Saito S.J., Pneumatic conveying of solids through straight pipes, Chem. Eng. Japan, 2 (1969) 211-217.
[252] Rose H.E. and Duckworth R.A., Transport of solid particles in liquids and gases, The Engineer, 227 (1969) 392-396.
[253] Engineers Equipment Users Association, Pneumatic Handeling of Powdered Materials, Constable and Company, London 1963.
[254] M. A. Westman, E. E. Michaelides, and F. A. Thompson, Pressure Losses Due to Bends in Pneumatic Conveying, J. of Pipelines, 7 (1987) 15.
[255] A. Chambers and RD. Marcus, Pneumatic Conveying Calculations, Second International Conference on Bulk Materials Storage, Handling and Transportation, 1986,
[256] Knowlton K., Cyclone Separators, in: Yang Wen-Ching (Ed.), Handbook of Fluidization and Fluid-Particle Systems, Marcel Dekker, New York, 2003.
[257] Cheng Leming and Basu Parbir, Effect of pressure on loop seal operation for a pressurized circulating fluidized bed, Powder Technology, 103 (1999) 203-211.
[258] C. E. Capes and K. Nakamura, Vertical pneumatic conveying: An experimental study with particles in the intermediate and turbulent flow regimes, Can. J. Chem. Eng., 51 (1973) 31-38.
[259] Basu P. and Fraser S.A., Circulating Fluidized Boilers, Design and Operations, Butterworth-Heinemann, 1991.
[260] Werther J., Influence of the Distributor Design on Bubble Characteristics in Large Diameter Gas Fluidized Beds, Fluidization, (1978).
[261] P. S. B. Stewart and J. F. Davidson, Slug flow in fluidised beds, Powder Technology, 1 (1967) 61-80.
[262] Bolkan-Kenny Y.G., Pugsley T.S., and Berruti F., Computer Simulation of the Performance of Fluid Catalytic Cracking Risers and Downers, Industrial & Engineering Chemistry Research, 33 (1994) 3043-3052.
[263] Y. Bolkan, F. Berruti, J. Zhu, and B. Milne, Modeling circulating fluidized bed downers, Powder Technology, 132 (2003) 85-100.
[264] R. B. Bird, W. E. Stewart, and E. N. Lightfoot, Transport Phenomena, Wiley, New York 1960.
[265] M. Weber, Friction of the air and the air/solid mixture in pneumatic conveying, Bulk Solids Handling, 11 (1991).
[266] PETER L., TEA JR., CASTELLI V., URDOCK J.W., and MEIROVITCH L., Mechanics of Solids and Fluids, in: AVALLONE E.A., BAUMEISTER T., and ADEGH A.M. (Eds.), Marks' Standard Handbook for Mechanical Engineers, McGraw-Hill, New York, 2007.

[267] Werner D., Influence of Particle Size Distribution during Pneumatic Dense Phase Conveying in Vertical and Horizontal Pipes, Bulk Solids Handling, 3 (1983) 351-359.
[268] Daous M.A. and Al-Zahrani A.A., Modeling solids and gas flow through an L-valve, Powder Technology, 99 (1998) 86-89.
[269] B. Mi and P. W. Wypych, Investigations into wall pressure during slug-flow pneumatic conveying, Powder Technology, 84 (1995) 91-98.
[270] J.Werther, Chemical Engineering Science, 5(1-2) (1980) 372-379.
[271] J. Grace, H. Bi, and Y. Zhang, Pitfalls in gas sampling from fluidized beds, Chemical Engineering Science, 64 (2009) 2522-2524.
[272] Li Tingwen, Y. Zhang, J. Grace, and X. Bi, Numerical Investigation of Gas Sampling from Fluidized Beds, The 13th International Conference on Fluidization - New Paradigm in Fluidization Engineering, ECI Engineering Conferences International, 2010, pp. 137-144., http://services.bepress.com/eci/fluidization_xiii/.
[273] R. Solimene, A. Marzocchella, R. Ragucci, and P. Salatino, Flow Structures and Gas-Mixing Induced by Bubble Bursting at the Surface of an Incipiently Gas-Fluidized Bed, Ind. Eng. Chem. Res., 43 (2004) 5738-5753.
[274] Radhakrishnan K. and Radhakrishnan A.C. Description and Use of LSODE, the Livermore Solver for Ordinary Differential Equations. LLNL report UCRL-ID-113855. 1993.
[275] Werther J. and Wein J., Expansion Behavior of Gas Fluidized Beds in the Turbulent Regime, Aiche Symposium Series, 301 (1994) 31-44.
[276] S. Mori and C. Y. Wen, Estimation of bubble diameter in gaseous fluidized beds, AIChE Journal, 21 (1975) 109-115.
[277] Kunii D. and Levenspiel O., Bubbling Bed Model, Ind Eng Chem Fund, 7 (1968) 446-452.
[278] Darton R.C., LaNauze R.D., Davidson J.F., and Harrison D., Bubble growth due to coalescence in fluidized beds, Trans. Inst. Chem. Eng., 55 (1977) 274-280.
[279] Werther J., in: Davidson J.F. and Keairns D.L. (Eds.), Fluidization, Cambridge University Press, London, 1978.
[280] Horio M. and Nonaka A., A generalized bubble diameter correlation for gas-solid fluidized beds, AICHE J., 33 (1987) 1865-1872.
[281] Werther J., Chem. Ing. Tech., 49 (1977) 777-785.
[282] J. A. Valenzuela and L. R. Glicksman, An experimental study of solids mixing in a freely bubbling two-dimensional fluidized bed, Powder Technology, 38 (2003) 63-72.
[283] J. Werther and J. Reppenhagen, Catalyst attrition in fluidized-bed systems, AIChE Journal, 45 (1999) 2001-2010.
[284] Bonder S., 1982,
[285] Weeks SA and Dumbill P., Method speeds FCC catalyst attrition resistance determinations, OIL & GAS JOURNAL, 88 (1990) 38-40.
[286] R. Cocco, Y. Arrington, R. Hays, J. Findlay, S. B. R. Karri, and T. M. Knowlton, Jet cup attrition testing, Powder Technology, 200 (2010) 224-233.
[287] R. Cocco, Y. Arrington, R. Hays, J. Findlay, S. B. R. Karri, and T. M. Knowlton, Jet cup attrition testing, Powder Technology, 200 (2010) 224-233.
[288] Werther J. and Reppenhagen J., Attrition, in: W.-C. Yang (Ed.), Handbook of Fluidization and Fluid-Particle Systems, Marcel Dekker, Inc, New York, 2003, p. 576.
[289] P. Gayín, L. F. de Diego, F. Garcia-Labiano, J. Adanez, A. Abad, and C. Dueso, Effect of support on reactivity and selectivity of Ni-based oxygen carriers for chemical-looping combustion, Fuel, 87 (2008) 2641-2650.
[290] L. F. de Diego, P. Gayan, F. Garcia-Labiano, J. Celaya, A. Abad, and J. Adanez, Impregnated CuO/Al2O3 Oxygen Carriers for Chemical-Looping Combustion: Avoiding Fluidized Bed Agglomeration, Energy Fuels, 19 (2005) 1850-1856.
[291] C. Dueso, F. Garcia-Labiano, J. Adanez, L. F. de Diego, P. Gayan, and A. Abad, Syngas combustion in a chemical-looping combustion system using an impregnated Ni-based oxygen carrier, Fuel, 88 (2009) 2357-2364.
[292] S. R. Son and S. D. Kim, Chemical-Looping Combustion with NiO and Fe2O3 in a Thermobalance and Circulating Fluidized Bed Reactor with Double Loops, Industrial & Engineering Chemistry Research, 45 (2006) 2689-2696.

[293] M. A. Soliman, A. M. Adris, A. S. Al-Ubaid, and S. S. E. H. El-Nashaie, Intrinsic kinetics of nickel/calcium aluminate catalyst for methane steam reforming, J. Chem. Technol. Biotechnol., 55 (1992) 131-138.
[294] S. Wang, G. Q. Lu, and G. J. Millar, Carbon Dioxide Reforming of Methane To Produce Synthesis Gas over Metal-Supported Catalysts:GÇë State of the Art, Energy Fuels, 10 (1996) 896-904.
[295] S. Wang, A Comprehensive Study on Carbon Dioxide Reforming of Methane over Ni/+¦-Al2O3 Catalysts, Industrial & Engineering Chemistry Research, 38 (1999) 2615-2625.
[296] M. C. J. Bradford and M. A. Vannice, Catalytic reforming of methane with carbon dioxide over nickel catalysts II. Reaction kinetics, Applied Catalysis A: General, 142 (1996) 97-122.
[297] Y. Schuurman, V. C. H. Kroll, P. Ferreira-Aparicio, and C. Mirodatos, Use of transient kinetics techniques for studying the methane reforming by carbon dioxide, Catalysis Today, 38 (1997) 129-135.
[298] A. K. Avetisov, J. R. Rostrup-Nielsen, V. L. Kuchaev, J. H. Bak Hansen, A. G. Zyskin, and E. N. Shapatina, Steady-state kinetics and mechanism of methane reforming with steam and carbon dioxide over Ni catalyst, Journal of Molecular Catalysis A: Chemical, 315 (2010) 155-162.
[299] S. i. Fujita, M. Nakamura, T. Doi, and N. Takezawa, Mechanisms of methanation of carbon dioxide and carbon monoxide over nickel/alumina catalysts, Applied Catalysis A: General, 104 (1993) 87-100.
[300] S. S. Randhava, E. H. Camara, and A. Rehmat, Methanation of Low Levels of Carbon Monoxide over Nickel Catalyst, Product R&D, 8 (1969) 347-352.
[301] J. Klose and M. Baerns, Kinetics of the methanation of carbon monoxide on an alumina-supported nickel catalyst, Journal of Catalysis, 85 (1984) 105-116.
[302] A. Stefanova, H. T. Bi, J. C. Lim, and J. R. Grace, Local hydrodynamics and heat transfer in fluidized beds of different diameter, Powder Technology, 212 (2011) 57-63.
[303] Grace J.R., Heat Transfer, CFB10 Short Course, PSRI, Sunriver, Oregon, USA, 2011,
[304] K. S. Lim, V. S. Gururajan, and P. K. Agarwal, Mixing of homogeneous solids in bubbling fluidized beds: Theoretical modelling and experimental investigation using digital image analysis, Chemical Engineering Science, 48 (1993) 2251-2265.
[305] Froessling N., The evaporation of falling drops, Beitr. Geophysik, 52 (1938) 170.
[306] Behie L.A. and Kehoe P., The grid region in a fluidized bed reactor, AICHE J., 19 (1973) 1070-1072.
[307] Sit S.P. and Grace J.R., Interphase mass transfer during bubble formation in fluidized beds, 46, Engineering Foundation, New York, 1986, p. -39
[308] Hilal N., Ghannam M.T., and Anabtawi M.Z., Effect of Bed Diameter, Distrubutor and Inserts on Minimum Fluidization Velocity, Chemical Engineerin Technology, 24 (2001) 161-165.
[309] Clift R., Hydrodynamics of Bubbling Fluidized Beds, in: Geldart D. (Ed.), Gas Fluidization Technology, John Wiley & Sons, Chichester, 1986, p. 88.
[310] Baeyens M.M. and Geldart D., Chemical Engineering Science, 29 (1974) 255.
[311] Stewart P.S.B. and Davidson J.F., Slug flow in fluidized beds, Powder Technology, 1 (1967).
[312] S. Mori and C. Y. Wen, Estimation of bubble diameter in gaseous fluidized beds, AIChE Journal, 21 (1975) 109-115.

Appendixes

1. PHOTO OF THE CLC COLD FLOW PROTOTYPE 213
2. PARTICLES PROPERTY MEASUREMENT METHODS 215
2.1. Density Measurement 215
2.2. Sphericity 216
2.3. Minimum Fluidization Velocity 216
2.4. Particle Size Distributions 218
3. HELIUM DETECTOR CHARACTERISTICS 221
4. CALIBRATION OF ROTAMETERS 222
5. BUBBLING FLUIDIZATION REGIME 223
6. CALCULATION OF THE SOLID BED HEIGHT AND VOIDAGE IN THE REACTOR 224
7. CYCLONE PRESSURE DROP TERMS 225
8. LIST OF EXPERIMENTAL RTD RESULTS 226

Appendixes

1. Photo of the CLC Cold Flow Prototype

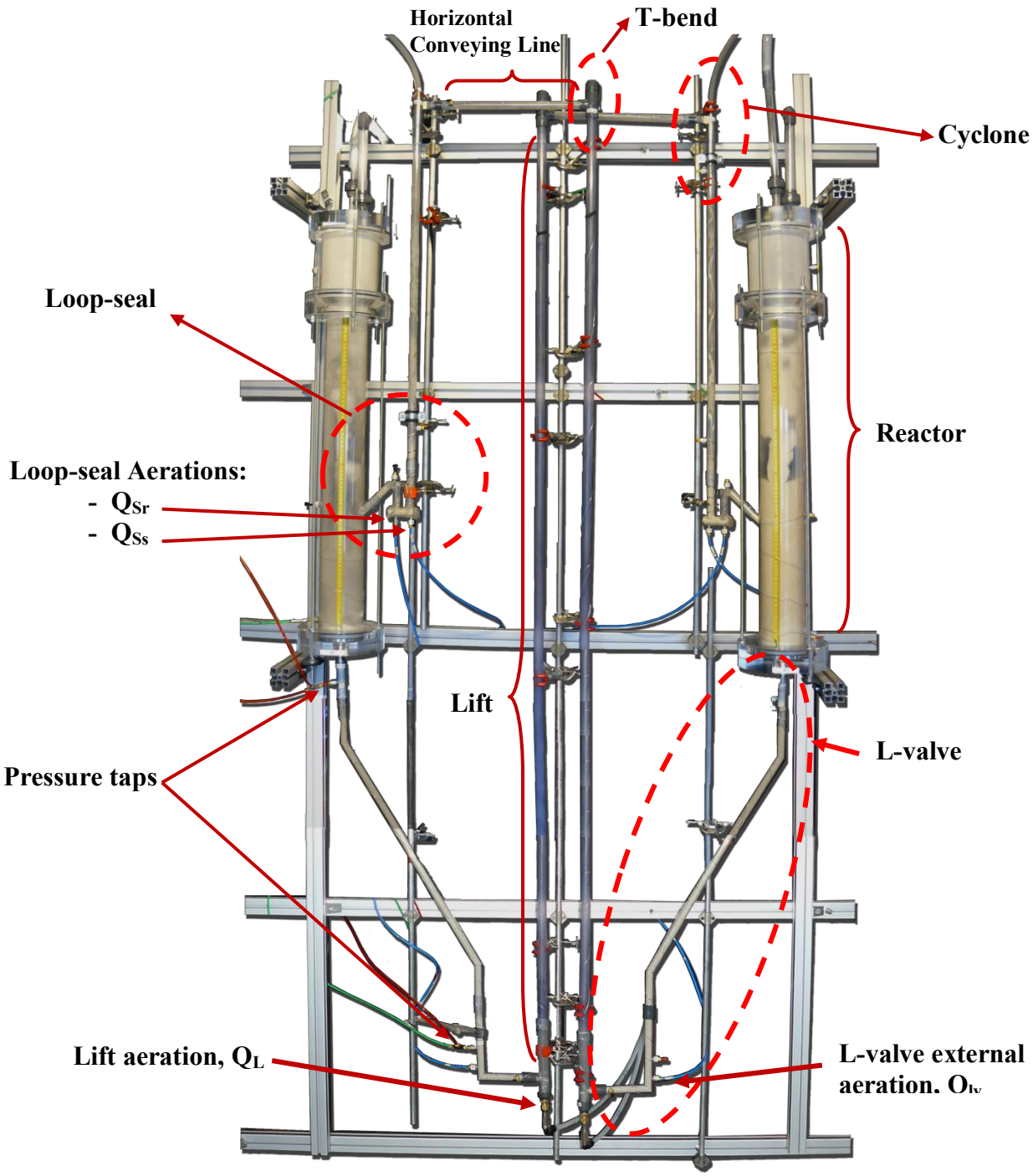

Figure 1: Photo of the cold prototype installations at IFP Energies nouvelles.

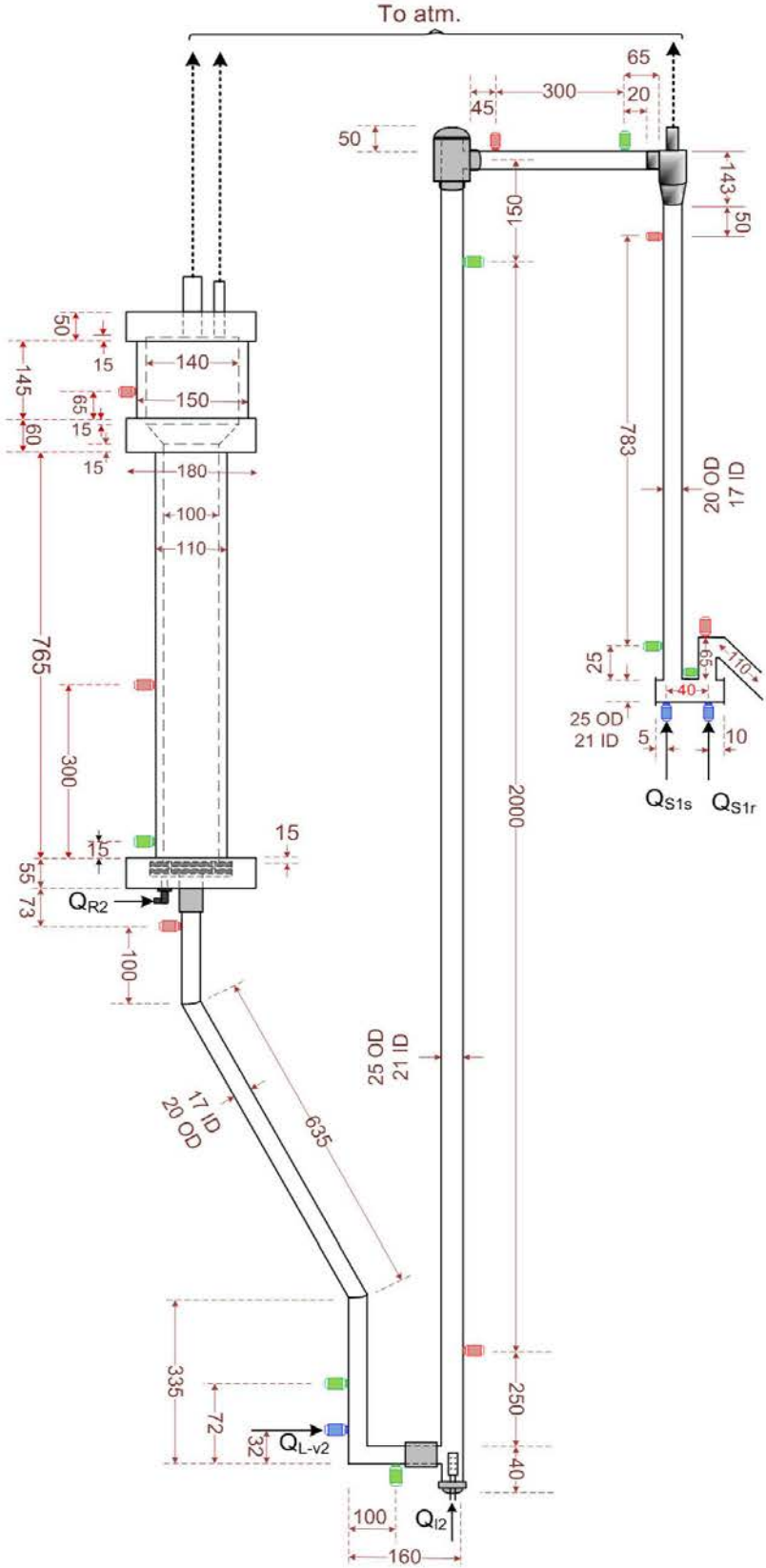

Figure 2: Dimensions of the cold flow prototype. The sizes are identical for both transfer lines.

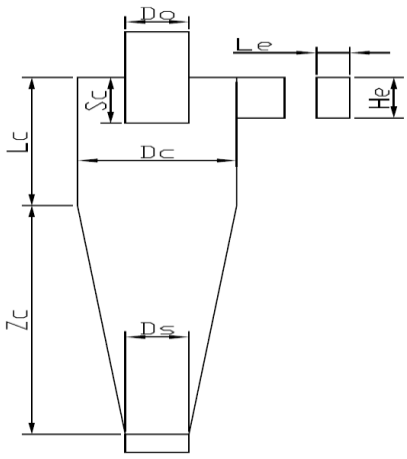

Element	Dimension (m)
He	0.015
Le	0.006
Do	0.009
Dc	0.029
Sc	0.018
Lc	0.0406
Zc	0.0754
Ds	0.012

Figure 3: Dimensions of cyclones used in the installations.

2. Particles Property Measurement Methods

2.1. Density Measurement

Bulk density of solid bed was measured by weighting a free settled bulk of solids in a 0.5 liter cylinder. Therefore:

$$\rho_b = \frac{Mass\,of\ the\ solid\ bed}{Vol.of\ cylinder} \qquad \textbf{Eq. 6.43}$$

The measurement was repeated three times for each solid to minimize human errors involved in the measurement.

Density of the solid particles was measured using a volumetric flask of 0.5 L and water as the displacement liquid. The measurement procedure and employed notations are illustrated in the Figure 4. The solid density was calculated as:

$$\rho_S = \frac{Mass\,of\ solid\ particles}{Vol\,of\ particles} = \frac{M_S}{Vol_S} = \frac{M_S}{Vol_{flask} - Vol_L} = \frac{M_S}{Vol_{flask} - M_L/\rho_L} \qquad \textbf{Eq. 6.44}$$

The voidage of free settled bed of solids were also calculated from these results by knowing the solid grain density. Therefore:

$$\varepsilon_b = \frac{Vol\ occupied\ by\ particles}{Vol.of\ cylinder} = \frac{Mass\,of\ the\ solid\ bed\ /\ \rho_s}{Vol.of\ cylinder} \qquad \textbf{Eq. 6.45}$$

This method was used for the non-porous materials i.e. sand I, sand II, and ilmenite, but not for NiO based oxygen carriers.

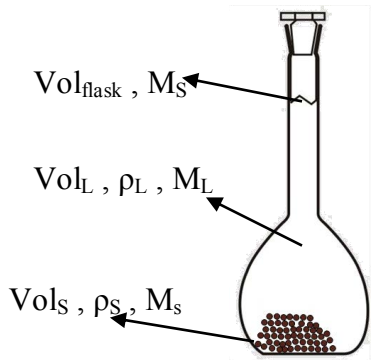

1. Measure the mass of the empty flask (M_{flask})
2. Place a specified mass of solids inside the flask (M_s).
3. Fill the flask with water of density ρ_L.
4. Weight the mass of water inside the flask M_L.
5. Empty the flask and fill it with water to measure the water density: $\rho_L = M_L/Vol_{flask}$

Figure 4: Experimental procedure of solid particle density measurement.

2.2. Sphericity

Sphericity of particles was measured using the method suggested by Kunii and Levenspiel [153]. Pressure drop was measured across a fixed bed of solids for different gas velocities. Bed voidage was varied for each gas velocity by vibrating the reactor which forced the particles to settle closer. The voidage variation was calculated from variation of the solid height as:

$$\varepsilon_n = 1 - \frac{H_0}{H_n}(1-\varepsilon_0) \qquad \textbf{Eq. 6.46}$$

Where ε_n is the bed voidage with height of H_n. while ε_0 and H_0 are known voidage and height of free settled initial solid bed. Ergun equation [94] correlates the pressure drop across a fixed bed of solids and different solid and fluid properties. The solid sphericity is calculated in this equation through fitting the experimental and equation results by adjusting the sphericity. The results for sand II is illustrated in Figure 5 demonstrating a good agreement between the equation and the experimental results. The measured sphericity in this method is an effective sphericity and may differ from the real sphericity of the particles.

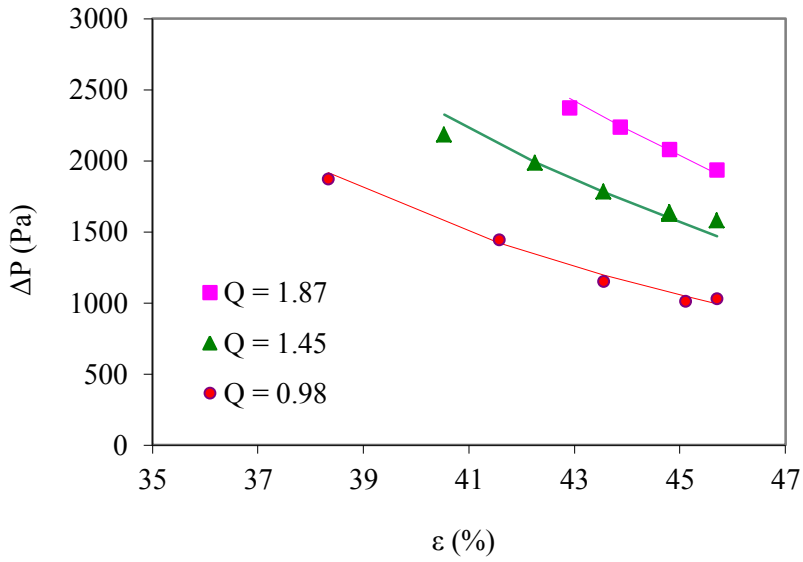

Figure 5: Variation of the pressure drop across the fixed solid bed with initial height of the 0.2 m for different aeration flow rate in Nm^3/h indicated in the graph. Solid lines represent the Ergun equation fitted for the experimental results represented by points in the figure.

2.3. Minimum Fluidization Velocity

Minimum fluidization velocity (U_{mf}) was measured for the particles in the reactor R1 of the installations according to the method by Kunii and Levenspiel [153] (Figure 6 -Figure 8). U_{mf} is calculated for the red points in the figures which represent the decreasing gas velocity. Hilal N. et al. [308] reported that U_{mf} depends on reactor diameter and gas distribution configuration. Smaller diameters increase the U_{mf} value. Therefore, the U_{mf} values may slightly differ in loop-seal and L-valve compared to the experimental values. Minimum fluidization velocity was also measured in the

high temperature pilot plant for different temperatures. Results, illustrated in Figure 9, show that increase of temperature decreases the U_{mf} as expected.

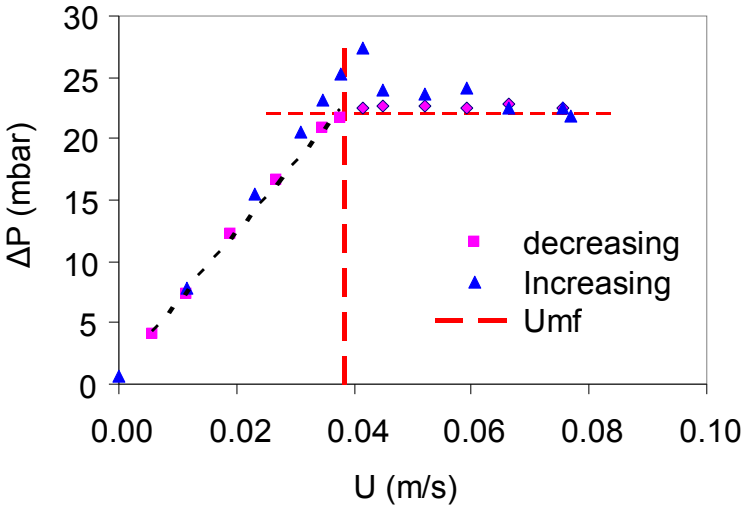

Figure 6: Minimum fluidization velocity of sand 1 particles measurement in the reactor R1 of the installation for a free settled solid height of 0.2 m. Pressure drop is shown for Increasing and decreasing velocities.

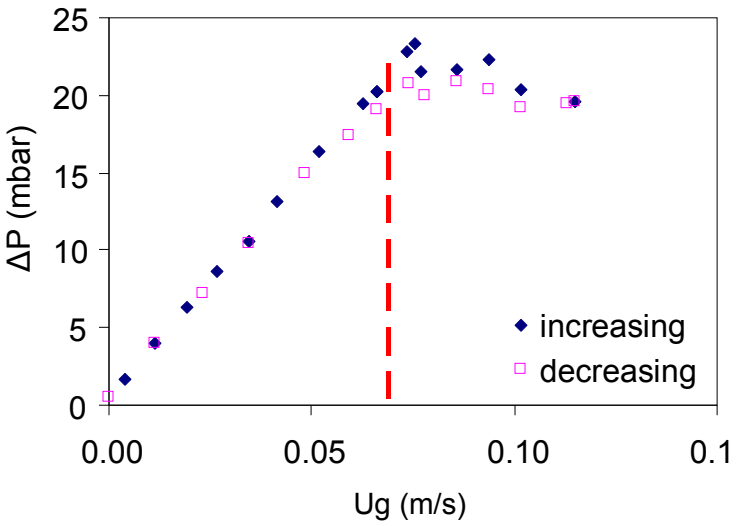

Figure 7: Minimum fluidization velocity of sand 2 particles measurement in the reactor R1 of the installation for a free settled solid height of 0.2 m. Pressure drop is shown for Increasing and decreasing velocities.

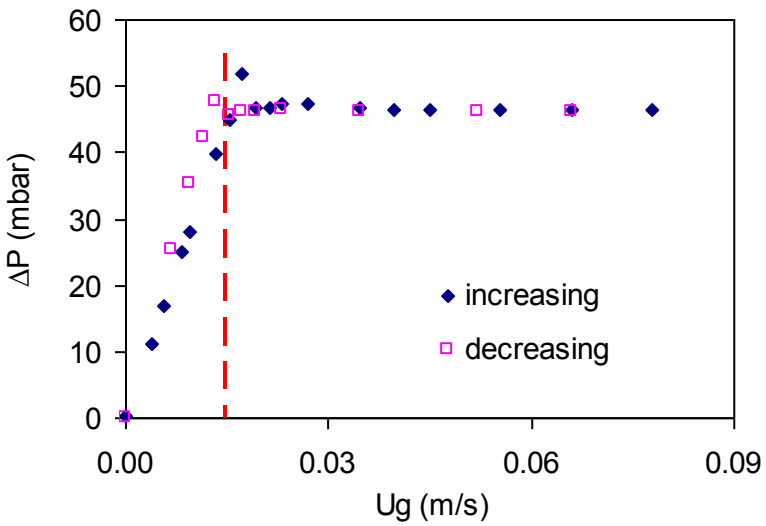

Figure 8: Minimum fluidization velocity of ilmenite particles measurement in the reactor R1 of the installation for a free settled solid height of 0.2 m. Pressure drop is shown for Increasing and decreasing velocities.

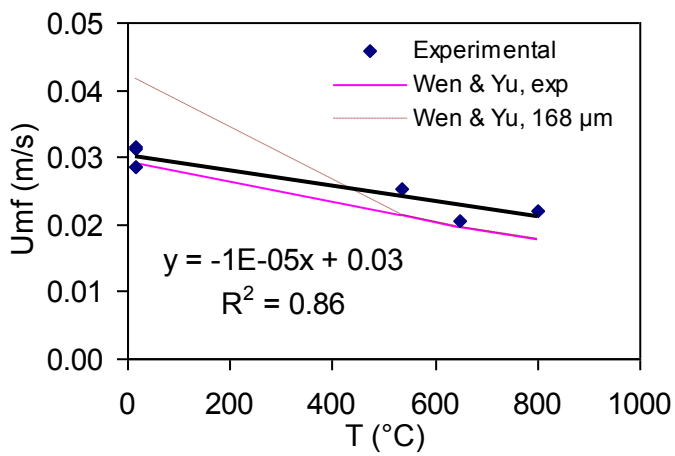

Figure 9: Variation of the minimum fluidization velocity by temperature, measured in the reactor R2 of high temperature pilot plant with $NiO/NiAl_2O_4$ oxygen carriers. The particle size was 168 for ambient temperature tests, and 201 μm for higher temperature tests.

2.4. Particle Size Distributions

Particle sizes were measured with laser granolometry analysis for ilmenite and sand particles. Fractional and accumulative distribution results are presented in the figures below.

Table 1: Size characteristics of sand particles measured by laser particle size distribution measurement.

Property	Sand I	Sand II	ilmenite	OC1	OC2
Volume weighted mean	283	402	138	215	
Surface weighted mean	253	368	127	168	240
d (0.1)	172	260	92	105	190
d (0.5)	268	384	132	201	260
d (0.9)	415	568	190	347	360

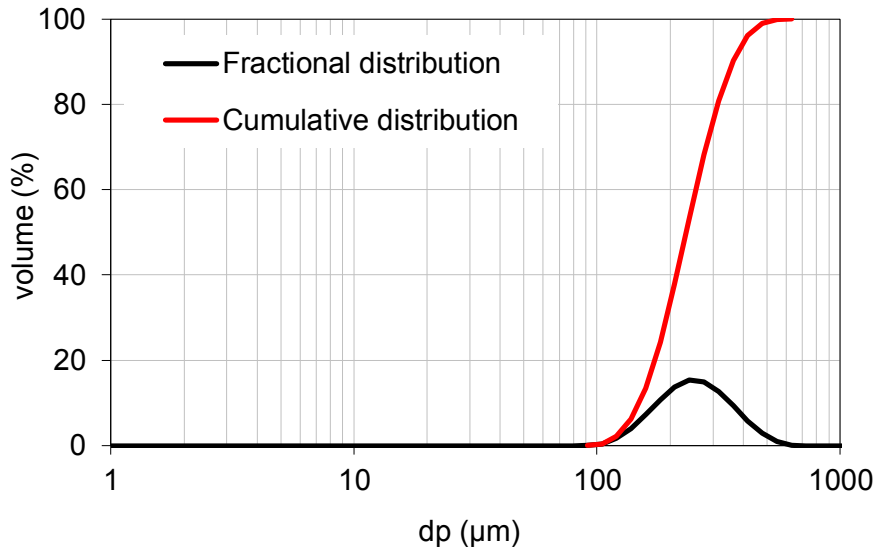

Figure 10: Particle size distribution for sand I particles.

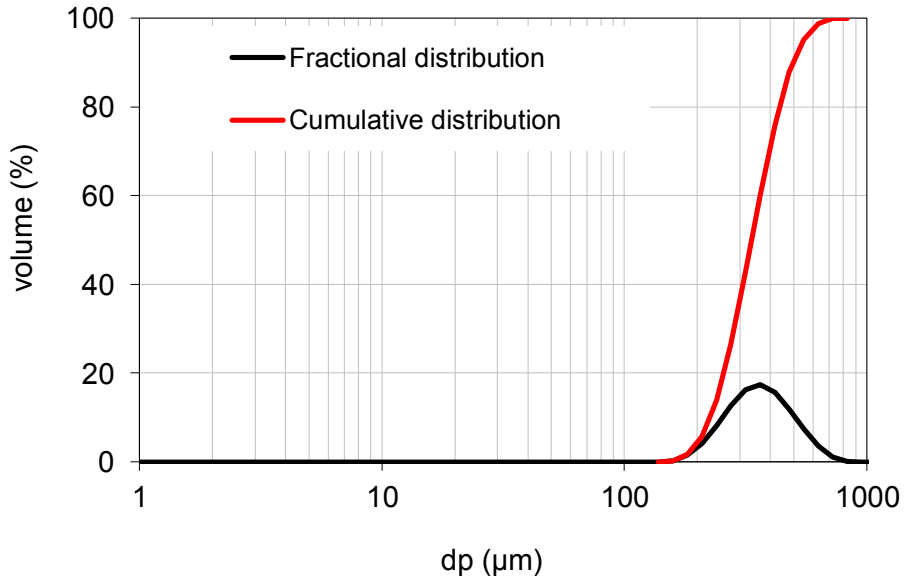

Figure 11: Particle size distribution for sand II particles

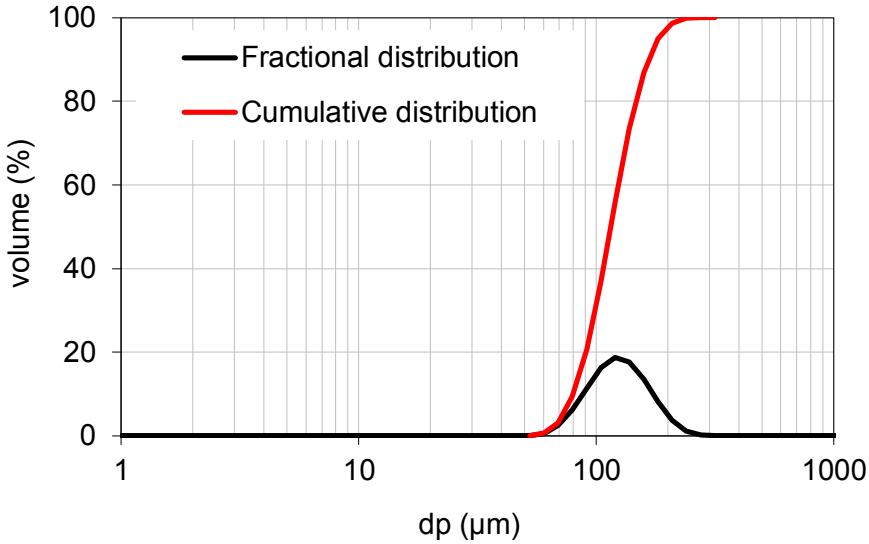

Figure 12: Particle size distribution of the ilmenite particles, result of laser granolometry.

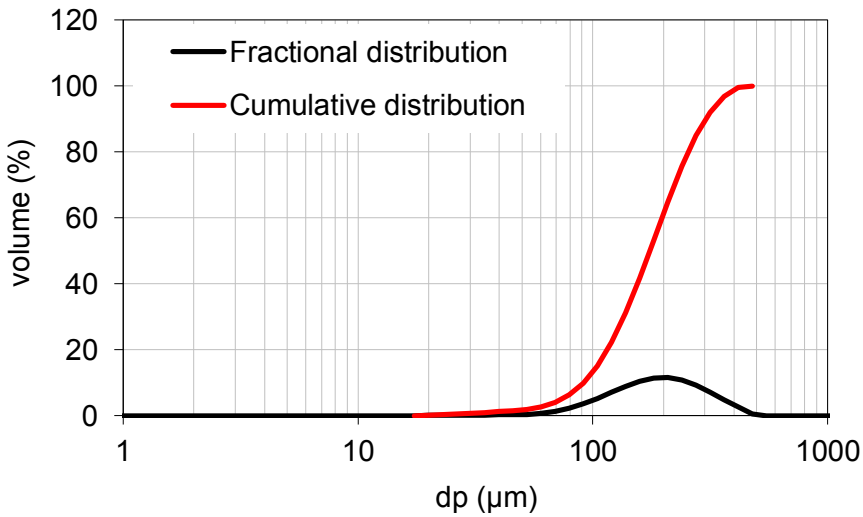

Figure 13: Particle size distribution of the initial Ni based oxygen carriers (OC1) used in the solid circulation tests.

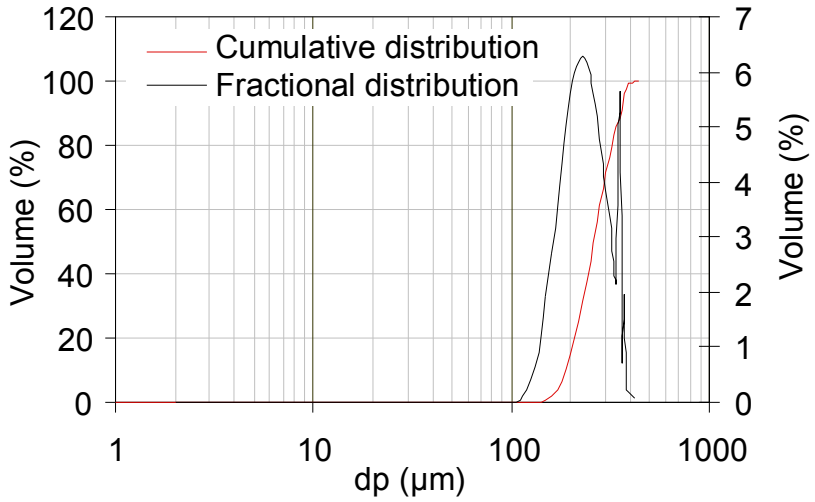

Figure 14: Particle size distribution of the oxygen carriers (OC2) used in the combustion tests measured after the end of the experimental tries.

3. Helium Detector Characteristics

Principal characteristics of the Helium detector used in the current study are presented **Error! eference source not found.**. Moreover, Figure 15 illustrates results of calibration of the apparatus.

Table 2: Technical data of the He detector.

Lowest detectable leak rate	4 x 10^{-7} mbar.l.s^{-1}
Measurement range	6 decades
Mass spectrometer	Quadrupole mass spectrometer
Ion source-cathode	Iridium with yttrium oxide coating
Time constant of leak rate signal	< 1 s
Gas flow through the capillary	60 – 90 sccm
Time until ready for operation	< 3 min

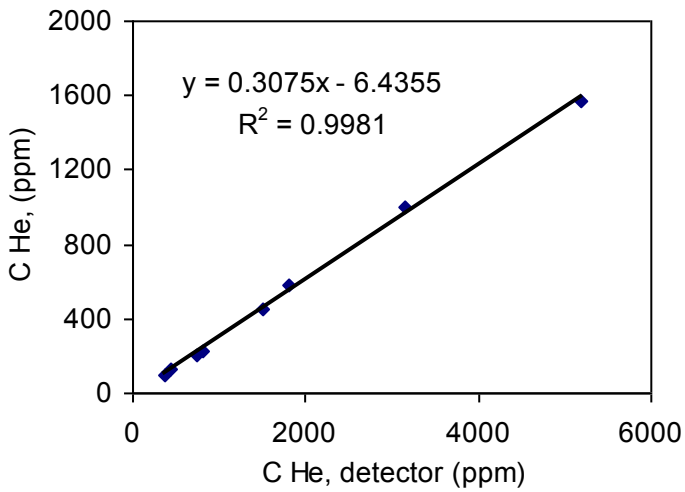

Figure 15: Helium detector calibration curve.

4. Calibration of Rotameters

The rotameter used for the Helium flow control was calibrated using a Definer™ 220 volumetric flow meter device with volumetric accuracy of ± 0.75 % of reading. The calibration device works based on the positive displacement principle. The resulting calibration curves for two different pressures across the rotameter are illustrated in Figure 16 All of the Rotameters used in this study were similarly calibrated as illustrated in Figure 17 to Figure 19.

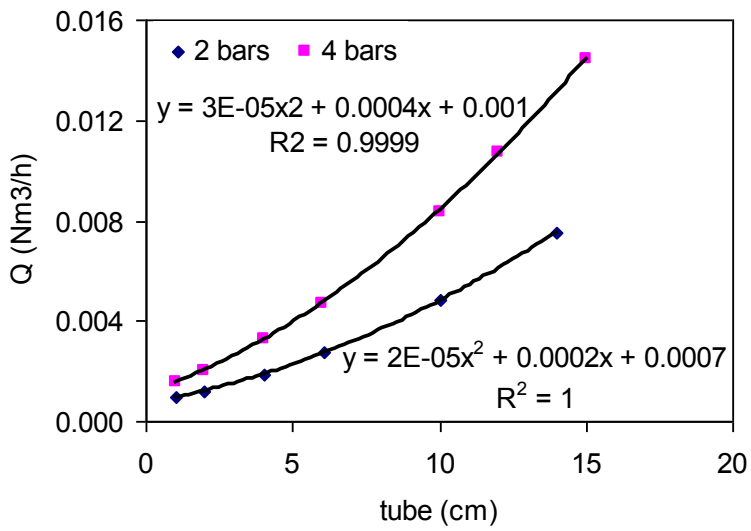

Figure 16: Calibration curves of the Helium injection rotameter. The device is calibrated for two constant pressures of 2 and 4 bars fixed with a pressure regulator.

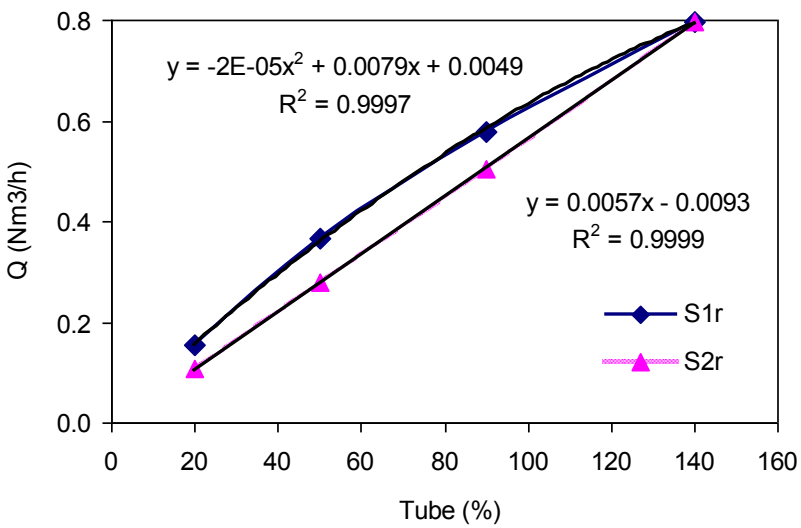

Figure 17: Calibration curve of the loop-seal Rotameters.

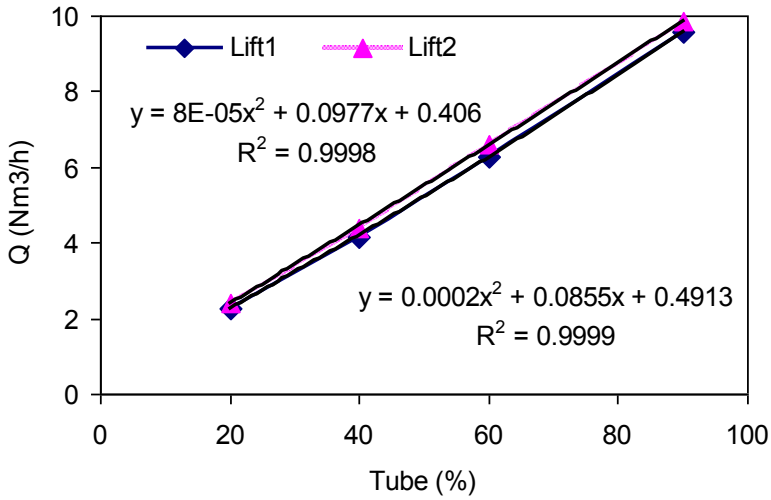

Figure 18: Calibration curve of the lifts Rotameters.

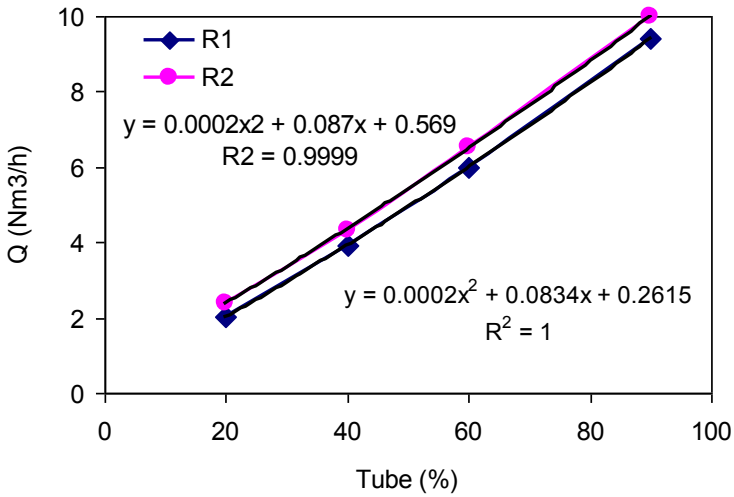

Figure 19: Calibration curve of the reactors Rotameters.

5. Bubbling Fluidization Regime

Bubbling fluidization regime happens for the gas velocity limit of U_{mb} (=U_{mf} for group B) and U_s (slugging velocity). Slugging happens only if some essential criteria are met in the bed. A necessary condition for slug flow is that the bubble diameter should be bigger than $0.6D_b$ as described by Clift R.[309]. This depends on solid properties, gas velocity and bed height. Limiting bubble size ($d_{b,max}$) for a deep bed is given by equation (8.11). Moreover, Yang's criterion describes possibility of slug formation for the condition when:

$$Fr_t^2 = \frac{U_t^2}{gD} \geq 0.123 \qquad \textbf{Eq. 6.47}$$

U_{mb} for group B particles is practically U_{mf} and U_{ms} could be found from correlation developed by Baeyens and Geldart [310]:

$$U_{ms} = U_{mf} + 0.07\sqrt{gD_b} + 0.16(1.34D_b^{0.174} - H_{mf})^2 \qquad \textbf{Eq. 6.48}$$

In the case that $H_{mf} > 1.34D^{0.174}$, third term is omitted and equation reduces to Stewart and Davidson correlation for deep beds [311].

6. Calculation of the Solid Bed Height and Voidage in the Reactor

The height of the bed is then obtained from expression developed by Davidson and Harrison [159]:

$$\frac{H - H_{mf}}{H_{mf}} = \frac{U - U_{mf}}{U_{bm}} \qquad \textbf{Eq. 6.49}$$

Using voidage value at minimum fluidization condition (ε_{mf}), H_{mf} is calculated by:

$$H_{mf} = \frac{M_R}{A_b \rho_s (1 - \varepsilon_{mf})} \qquad \textbf{Eq. 6.50}$$

And average bubble velocity (U_{bm}) is assumed as a constant mean bubble velocity in the bed and calculated as[153]:

$$U_{bm} = U - U_{mf} + u_{bs,ave} \qquad \textbf{Eq. 6.51}$$

Where average single bubble rise velocity ($u_{bs,ave}$) is considered as rise velocity for an bubble with average diameter in the bed and obtained from [153]:

$$u_{bs,ave} = 0.711\sqrt{g d_{b,ave}} \qquad \textbf{Eq. 6.52}$$

Considering average bubble diameter to be the arithmetic mean diameter of smallest and larges bubble diameter ($d_{b,min}$ and $d_{b,max}$) in the bed, as:

$$d_{s,ave} = \frac{d_{b,\min} + d_{b,\max}}{2} \qquad \textbf{Eq. 6.53}$$

The minimum bubble diameter is considered as initial bubble diameter (d_{b0}) and obtained from the equations developed by Kunii and Levenspiel[153]. The expression for law gas flow rate ($d_{b0} \leq l_{or}$) is:

$$d_{b0} = \frac{1.30}{g^{0.2}}\left[\frac{u_0 - u_{mf}}{N_{or}}\right]^{0.4} \quad \text{for} \quad d_{b0} \leq l_{or}, \quad \text{(cm)} \qquad \textbf{Eq. 6.54}$$

and for high gas flow rates ($d_{b0} > l_{or}$):

$$d_{b0} = \frac{2.78}{g}(u_0 - u_{mf})^2 \quad \text{for} \quad d_{b0} > l_{or}, \quad \text{(cm)} \qquad \textbf{Eq. 6.55}$$

Maximum bubble size in the equation 57 is considered as bubble size in the bed surface obtained from correlation developed by Mori and Wen [312]for group B and D particles:

$$\frac{d_{b,\max} - d_b}{d_{b,\max} - d_{b0}} = \exp\left(-\frac{0.3Z}{D}\right) \qquad \textbf{Eq. 6.56}$$

Where d_{b0} is initial bubble size calculated from equation 58 or 59, z is bed height $_{HR}$ and d_{bm} is the limiting bubble size which for a deep bed is given by Kunii and Levenspiel [153] as:

$$d_{b,\max} = 0.65\left[\frac{\pi}{4} d_t^{\,2}(U - U_{mf})\right]^{0.4}, \quad \text{(velocities in cm/s)} \qquad \textbf{Eq. 6.57}$$

The conditions where the correlation is developed for are: $D \leq 1.3$, $0.5 \leq u_{mf} \leq 20$ cm/s, $60 \leq d_p \leq 450$ µm and $U_o - U_{mf} \leq 48$ cm/s. Bed voidage is then calculated from the pressure drop correlation where:

$$\Delta P_R = \rho g H_R (1 - \varepsilon) = M g A_R \qquad \textbf{Eq. 6.58}$$

Thus:

$$\varepsilon = 1 - \frac{M}{A_R \rho H_R} \qquad \textbf{Eq. 6.59}$$

7. Cyclone Pressure Drop Terms

Cyclone pressure drop was calculated by summing several individual types of pressure-drop terms as explained by Knowlton [256].

The pressure drops include:

1. Contraction Pressure Drop

$$\Delta P_{(f-i)g} = 0.5\rho_g (U_i^2 - U_f^2 + K_{fi} U_i^2) \qquad \textbf{Eq. 6.60}$$

K_{fi} is the contraction coefficient due to gas flowing from a larger area to a smaller area and could be find in reference[256].

2. Acceleration of Solids Pressure Drop.

$$\Delta P_{(f-i)p} = L U_{pi} (U_{pi} - U_{pf}) \qquad \textbf{Eq. 6.61}$$

3. Barrel Friction Pressure Drop.

$$\Delta P_{bf} = \frac{2 f \rho_g U_i^2 \pi D_b N_s}{d_{hi}} \qquad \textbf{Eq. 6.62}$$

Where f is fanning friction factor calculated from correlation given by Kunni and Levenspiel [153] (equations 4.25 and 4.26) and N_s is the number of effective spiral paths taken by the gas in the outer vortex of the cyclone find from a graph in reference [256].

4. Gas Reversal Pressure Drop, as:

$$\Delta P_r = \frac{\rho_g U_i^2}{2} \qquad \textbf{Eq. 6.63}$$

5. Outlet Exit Contraction Pressure Drop:

$$\Delta P_o = 0.5\rho_g (U_o^2 - U_b^2 + K_o U_o^2) \qquad \textbf{Eq. 6.64}$$

K_0 is contraction coefficient and could be find in reference[256] for ratio of the outlet to the inlet area of cyclone $(D_o/D_b)^2$.

8. List of Experimental RTD results

Table 3: Experimental results of RTD study.

H_R (m)	Q_R (Nm^3/h)	N_f (U_R/U_{mf})	H_d (m)	Gs ($kg/m^2.s$)	RT (s)	RT bed (s)	ζ^2	t first (s)
Blank tests								
			line		1.72		0.084	
			line		2.29		0.20	0.96
	2.01		0	0	8.81		0.67	
	2.01		0.3	0	10.30	1.48	0.43	
	2.01		0.5	0	11.7	2.89	0.35	
	2.01		0.7	0	14.57	5.75	0.26	
Effect of solid bed height								
0.31	2.01	6		0	6.80	2.23	0.29	
0.33	2.01	6	0.385	0	7.46	2.61	0.26	3.40
0.33	2.01	6	0.385	0	7.55	2.71	0.23	3.54
0.513	2.01	6	0.6	0	8.84	3.84	0.37	
0.513	2.01	6	0.6	0	8.83	3.83	0.38	3.34
0.685	2.01	6	0.735	0	10.3	5.45	0.22	4.55
0.685	2.01	6	0.745	0	10.05	5.18	0.30	
0.685	2.01	6	0.745	0	9.98	5.11	0.31	4.03
0.515	2.01	6	0.57	0	7.90	3.06	0.33	4.70
0.515	2.01	6	0.57	0	8.19	3.34	0.29	4.27
0.515	2.01	6	0.515	0	8.22	3.65	0.39	2.52
0.515	2.01	6	0.515	0	7.51	2.94	0.28	2.15
0.515	2.01	6	0.31	0	6.02	1.45	0.38	2.45
0.515	2.01	6	0.31	0	6.23	1.66	0.27	2.94
0.515	2.01	6	0.165	0	5.48	0.90	0.36	2.42
0.52	2.01	6	0.165	0	5.12	0.55	0.48	1.70
0.515	2.01	6	0.05	0	4.84	0.26	0.48	1.34
0.515	2.01	6	0	0	4.57	0	0.60	1.88
Effect of gas velocity								
0.482	1.12	3	0.6	0	13.18	5.73	0.28	4.47
0.502	1.65	5	0.6	0	9.70	4.01	0.28	3.74
0.515	2.01	6	0.57	0	8.19	3.34	0.29	4.07
0.555	2.75	8	0.62	0	6.44	2.32	0.25	3.14
0.555	3.33	9	0.66	0	6.14	2.18	0.29	2.63
0.575	4.32	12	0.675	0	5.46	1.92	0.16	2.88
Effect of solid flow rate								
0.505	2.01	6	0.6	40	8.0	2.99	0.23	2.3
0.515	2.01	6	0.6	37	7.6	2.61		2.3
0.518	2.01	6	0.6	58	8.4	3.37	0.25	3.0
0.505	2.01	6	0.6	80	8.4	3.31	0.30	2.8
0.515	2.01	6	0.6	80	8.2	3.23		3.8
0.52	2.01	6	0.6	80	8.2	3.27		3.5
0.52	2.01	6	0.6	147	8.4	3.48	0.27	3.8

Résumé étendu

1. INTRODUCTION 229
2. LES INSTALLATIONS 231
2.1. Maquette froide 231
2.2. Le pilote chaud 233
3. LA CIRCULATION DES PARTICULES 235
3.1. Opération du siphon 238
4. MODELE DE CIRCULATION 239
4.1. La premier section du modèle 240
4.2. La deuxième section du modèle 241
4.3. Validation du modèle 242
5. HYDRODYNAMIQUE DU REACTEUR 244
5.1. La validation du modèle 245
6. LA COMBUSTION DU METHANE 246
6.1. La modélisation du réacteur 249
7. CONCLUSIONS 249

Résumé étendu

1. Introduction

La température globale de la terre est généralement fonction de la différence d'énergie reçue du soleil et de l'énergie réfléchie dans l'espace environnant. L'atmosphère de la Terre agit comme un bouclier couvrant qui capture une partie de cette énergie radiative. Cela maintient une température assez haute pour la vie sur la terre. Cet effet est appelé l'effet de serre, qui existe grâce à la présence de certains gaz naturellement présents dans l'atmosphère comme H_2O, CO_2, CH_4, N_2O et O_3. Toutefois, depuis la révolution industrielle, l'homme a exploité des combustibles fossiles qui ont été conservés sous terre pendant des millions d'années, pour les brûler et les émettre dans l'atmosphère. En conséquence, des milliards de tonnes de gaz à effet de serre, notamment de CO_2, ont été émis dans l'atmosphère à partir de sources souterraines. Par ailleurs, l'humanité n'a cessé d'affecter les puits naturels de ces gaz en particulier par la déforestation. Ces actions anthropiques ont ajouté une contrainte supplémentaire considérable sur le climat de la terre, causant une grande menace de vie appelée «réchauffement climatique».

Différentes mesures ont été proposées pour lutter contre les effets indésirables du réchauffement climatique. Le captage et stockage du dioxyde de carbone (CCS) ont été largement considérés comme un moyen de réduire les émissions des gaz à l'effet de serre. Par ailleurs, le captage de CO_2 peut présenter un double avantage, environnemental et économique. Ceci peut être réalisé si le CO_2 est utilisé dans certaines applications industrielles, après avoir été capté. Le procédé CO2-EOR (récupération améliorée du pétrole en injectant du CO2 dans les réservoirs du pétrole) est l'une des applications industrielles potentielles du CO2 pour augmenter la production de pétrole. Ce procédé est utilisé commercialement depuis environ 40 ans (avec le CO_2 principalement comme source naturelle) et sa faisabilité a bien été reconnue en ce qui concerne le transport et l'injection de CO_2. La partie principale manquante de la chaîne de CCS est un système de captage du CO_2 à faible coût. Dans ce procédé, le combustible fossile est exploité à partir des gisements, son énergie utilisée, et les composés à effet de serre, produits par l'usage du combustible, sont ré-injectés à leur place initiale où ils ont été depuis des millions d'années.

Dans le système de circulation sanguine du corps humain, les globules rouges agissent comme transporteurs d'oxygène, intermédiaire entre l'air et les cellules du corps. Par conséquent, la production d'énergie dans les cellules se fait sans contact direct entre l'air et les cellules. Un système similaire est utilisé dans la combustion en boucle chimique (CLC). Un transporteur d'oxygène (principalement un oxyde de métal) transporte l'oxygène de l'air à un "réacteur de combustion" (FR) où il délivre de l'oxygène à un combustible. Par conséquent, les gaz de combustion produits sont exempts d'azote et riches en CO_2. Autrement dit, le CO_2 est un produit intrinsèque du procédé CLC, rendant ce procédé de captage du CO_2 efficace et à coût réduit. Le transporteur d'oxygène est alors envoyé dans le "réacteur à air" où il est réoxydé.

Une attention croissante est portée sur la combustion en boucle chimique depuis le début du ce siècle. Plusieurs groupes académiques et industriels travaillent actuellement sur ce sujet dans le monde entier. La recherche et le développement dans le domaine de CLC peuvent être divisés en deux catégories principales. Le premier est le développement des transporteurs d'oxygène efficaces concernant les aspects économique, technique, environnemental et de sécurité. Le deuxième axe concerne le développement du procédé industriel fiable. Différents pilotes à l'échelle du laboratoire ont été développés avec des capacités allant de 0,3 kW_{th} à 1 MW_{th}. La combustion en lit fluidisé circulant (CFB) et le craquage catalytique (FCC) sont deux des principaux procédés industriels matures impliquant la circulation de particules fluidisés. Ces systèmes, en particulier la CFB, ont servi de base pour le développement du procédé CLC. L'extrapolation du procédé à l'échelle industrielle nécessite néanmoins encore des efforts en R&D, notamment pour la conception de systèmes de plus grande capacité.

Le procédé de combustion en boucle chimique a l'avantage d'être flexible en termes de choix du combustible. Différents types de gaz, combustibles liquides et solides ont été testés. Une attention particulière a tout d'abord été portée sur les charges gazeuses. Des études complémentaires sont encore nécessaires pour le développement des transporteurs ainsi que pour l'adaptation du procédé selon chaque type de combustible à l'échelle industrielle.

La circulation des particules solides est un facteur clé dans le développement de procédés de combustion en boucle chimique, le solide transportant l'oxygène nécessaire à la combustion du combustible. En outre, la circulation des solides est un paramètre crucial pour l'équilibre thermique dans l'ensemble du système, en particulier dans le cas où la différence entre la chaleur de réaction d'oxydation et celle de réduction est significative. Le contrôle de la circulation des particules permet d'ajuster correctement le débit du solide, et de réaliser la distribution de la chaleur nécessaire. Cela donne également une certaine flexibilité en termes de capacité de production d'énergie, et de choix du transporteur d'oxygène ou de combustible.

L'étanchéité des réacteurs est un autre facteur important dans le dimensionnement du procédé CLC. Les particules circulant entre les réacteurs peuvent entraîner du gaz et provoquer des fuites de gaz entre les réacteurs. La fuite de gaz hors du réacteur à combustible génèrera une perte de CO_2 séparé et réduirait l'efficacité de captage. Par ailleurs, la fuite de gaz du FR vers l'AR induirait un contact direct entre l'air et le combustible. Cela entraînerait une combustion exothermique vigoureuse qui pourrait entraîner des problèmes de sécurité et des dommages matériels. La fuite de gaz dans le réacteur fuel entraînerait une dilution du flux de CO2 produit avec de l'azote, ce qui réduirait l'efficacité de séparation. Ce problème peut être résolu par un design appropriée du système et en utilisant des organes étanches au gaz tel que le siphon.

Différentes approches de contrôle du débit du solide ont été employées dans les pilotes CLC existants. Une méthode possible est l'utilisation de vannes pneumatiques comme le siphon ou la vanne-en-L. Malgré l'utilisation de ce type d'organes dans les systèmes industriels comme la combustion en lit fluidisé circulant, des investigations complémentaires sont nécessaires pour une utilisation optimale de ces dispositifs dans le procédé CLC. L'effet de la température et des propriétés du gaz sur le fonctionnement de ces dispositifs sont particulièrement étudiés ainsi que leurs éventuelles limites opérationnelles.

La modélisation du système CLC est une étape importante, à la fois pour mieux comprendre le procédé ainsi que pour pouvoir extrapoler le système aux échelles supérieures. La modélisation peut être divisée en deux parties. La première concerne la modélisation de la circulation du solide et de la variation de perte de charge. Ce modèle permet de mieux comprendre les phénomènes associés à la circulation des particules. En outre, elle fournit un outil pour prédire l'effet des principaux paramètres opératoires sur les régimes de circulation, notamment l'effet de la température et de la taille des particules. La seconde partie de la modélisation concerne la cinétique des réacteurs du CLC, qui permet de choisir les schémas réactionnels les plus appropriés. Le modèle hydrodynamique couplé à la cinétique est un outil indispensable pour l'extrapolation du procédé à taille industrielle.

Un point important à considérer dans la modélisation des procédés en lit fluidisé est la base de données utilisée pour ajuster le modèle. Une large plage de conditions opératoires doit être balayée afin d'éviter qu'en cas d'augmentation d'échelle, le modèle ne soit plus représentatif de certains phénomènes. En conséquence, il est toujours recommandé d'utiliser à la fois les études expérimentale et de modélisation dans le développement d'un procédé. Manifestement, cela implique des études scientifiques complètes dans chaque étape de développement en termes d'études expérimentales et de modélisation.

IFP Energies nouvelles et Total travaillent actuellement sur un projet commun de développement sur la combustion en boucle chimique. L'objectif principal du projet est de développer un procédé de CLC à l'échelle commerciale. Elle implique des études CLC à différents stades, de l'ATG (analyse thermogravimétrique) à l'échelle de 1 MW_{th}, appliqués aux combustibles gazeux, liquides et solides. La thèse actuelle a été définie dans le cadre de ce projet, incluant les études expérimentales et de modélisation dans une maquette froide de compréhension et un pilote chaud de 10 kW_{th} de capacité thermique. L'objectif du pilote est d'étudier les réactions CLC dans des conditions bien définies et

contrôlées, afin de tester différents transporteurs d'oxygène. Le pilote est à l'origine construit pour différents types de charges gazeuses (CH_4, CO, H_2) avec une possibilité de passage aux charges liquides et solides après modifications.

Le système 10 kW_{th} actuel est basé sur le principe de lits fluidisés interconnectés. Les réacteurs à lit fluidisé bouillonnant sont utilisés comme réacteur à air et réacteur à combustible. Les solides circulent entre les réacteurs grâce à des lignes de transport. Chaque ligne est composée d'une série d'éléments pneumatiques pour transporter les particules vers le réacteur suivant. Le débit du solide est contrôlé par l'utilisation des vannes-en-L installées à la sortie en bas de chaque réacteur. À la sortie de chaque vanne-en-L, les solides sont transportés verticalement à travers un riser. Un coude (Blinded T-bend) détourne les particules via une ligne horizontale de transport des solides vers un cyclone. Les solides séparés quittent le cyclone via un siphon qui les transporte vers le réacteur suivant. Les siphons sont utilisés pour assurer l'étanchéité au gaz de chaque réacteur.

L'étude actuelle peut être divisée en deux parties principales: la circulation solide à température ambiante et des études de réacteur à haute température impliquant des réactions. L'hydrodynamique de la circulation du solide a été étudiée dans une maquette froide aux conditions ambiantes. Le fonctionnement de la vanne-en-L et le siphon pour le contrôle de la circulation du solide et l'étanchéité au gaz ont été les objectifs principaux de cette étude. Un modèle de circulation a ensuite été développé sur la base des résultats expérimentaux en utilisant le principe de l'équilibre de pression. L'hydrodynamique des réacteurs à lit fluidisé bouillonnant a été étudiée expérimentalement par l'utilisation de la méthode de distribution du temps de séjour (DTS) dans la maquette froide.

La deuxième partie de l'étude concerne l'étude de combustion en boucle chimique dans le pilote chaud en utilisant $NiO/NiAl_2O_4$ comme transporteurs d'oxygène et le méthane comme charge. La principale raison de ce choix est l'existence d'une littérature fournie sur des systèmes similaires. Cela aide à mieux comprendre et vérifier le fonctionnement du système CLC actuel. La circulation solide à haute température et les réactions d'oxydation et de réduction ont été étudiées dans cette phase. Les résultats ont ensuite été utilisés pour confirmer le mode de circulation des solides à haute température. Par ailleurs, un modèle de combustion a été développé pour prédire la conversion du gaz dans le "réacteur fuel" basé sur un schéma réactionnel adapté de la littérature.

Ce travail consiste à mieux comprendre le système CLC actuel en termes de circulation solide, et de cinétique (réactions de combustion et d'oxydation). Cela constitue une base solide pour le développement ultérieur de systèmes alternatifs avec différents transporteurs d'oxygène et/ou différentes charges.

2. Les Installations

2.1. Maquette froide

Une maquette froide a été utilisée pour étudier la circulation solide et l'hydrodynamique des réacteurs fluidisés. La maquette a été construite avec du plexiglas (transparent) qui permet l'observation visuelle des différents phénomènes dans le système. Par ailleurs, cela facilite les modifications, si nécessaire. La Figure 1 montre le schéma de la maquette froide avec l'indication des éléments essentiels du système et les abréviations correspondantes utilisées dans ce rapport.

La maquette froide est composée de deux réacteurs interconnectés à lit fluidisé bouillonnant, R1 et R2 à section circulaire de 0,1 m de diamètre et 1 m de hauteur. Le gaz est injecté au bas des réacteurs à travers des plaques perforées de quatre trous d'injection identiques avec une densité de trous de 509 orifice / m². Dans la maquette froide, l'air est utilisé comme gaz de fluidisation dans les deux réacteurs. La gamme de vitesse superficielle du gaz s'étend de 0,035 m/s à 0,35 m/s. Dans la partie supérieure du réacteur, le diamètre est augmenté afin de réduire la vitesse du gaz et de limiter l'entrainement des particules. Les gaz à la sortie des réacteurs et les cyclones sont évacués vers un filtre afin de recueillir les fines, ainsi qu'un stockage de sécurité pour collecter les particules qui quittent le système au cours d'éventuelles opérations instables. Le raccordement de toutes les sorties de gaz au même filtre induit

des pressions de sortie identiques à tous ces éléments. La sortie des gaz du filtre de collecte est ensuite reliée à un filtre électrostatique avant le rejet à l'atmosphère.

Les lits fluidisés sont interconnectés avec deux lignes de circulation identiques composées d'une vanne-en-L, un coude-en-T, un cyclone et un siphon. Les vannes-en-L pneumatiques de 0.017 m de diamètre intérieur et 1 m de hauteur sont utilisées pour contrôler le débit solide. Les particules à la sortie des vannes-en-L sont transportées à travers une ligne de transport en phase diluée verticale (lift) de 0,021 m de diamètre intérieur et 2,25 m de hauteur. La vitesse superficielle du gaz dans le lift varie de 1,5 à 8,0 m/s. Un coude-en-T est utilisé pour détourner le flux de particules vers une conduite de transport horizontale en phase diluée de 0,017 m de diamètre intérieur et 0,365 m de longueur. La séparation des gaz et des solides est effectuée dans un cyclone où les solides séparés sont conduits vers un siphon situé au bas de la jambe de retour du cyclone (dipleg). Les particules sont ensuite ré-envoyées vers le premier réacteur à travers une seconde ligne de transport identique.

Les expériences ont été réalisées aux conditions ambiantes en utilisant l'air sec comme gaz de fluidisation. Les flux de gaz pour les vannes-en-L et les siphons sont contrôlés par des débitmètres massiques connectés à un ordinateur pour l'acquisition des données. Les débits de gaz dans les lifts et les réacteurs sont contrôlés par des vannes manuelles et les débits sont mesurés à l'aide de rotamètres à pression constante. Les pertes de charge ont été mesurées par des capteurs de pression numériques et ont été automatiquement enregistrées sur un ordinateur avec une fréquence réglable. Plusieurs prises de pression sont situées dans l'installation pour mesurer les pertes de charge dans différentes sections de l'installation. Les prises de pression sont schématisées dans la Figure 1 par des prises vertes.

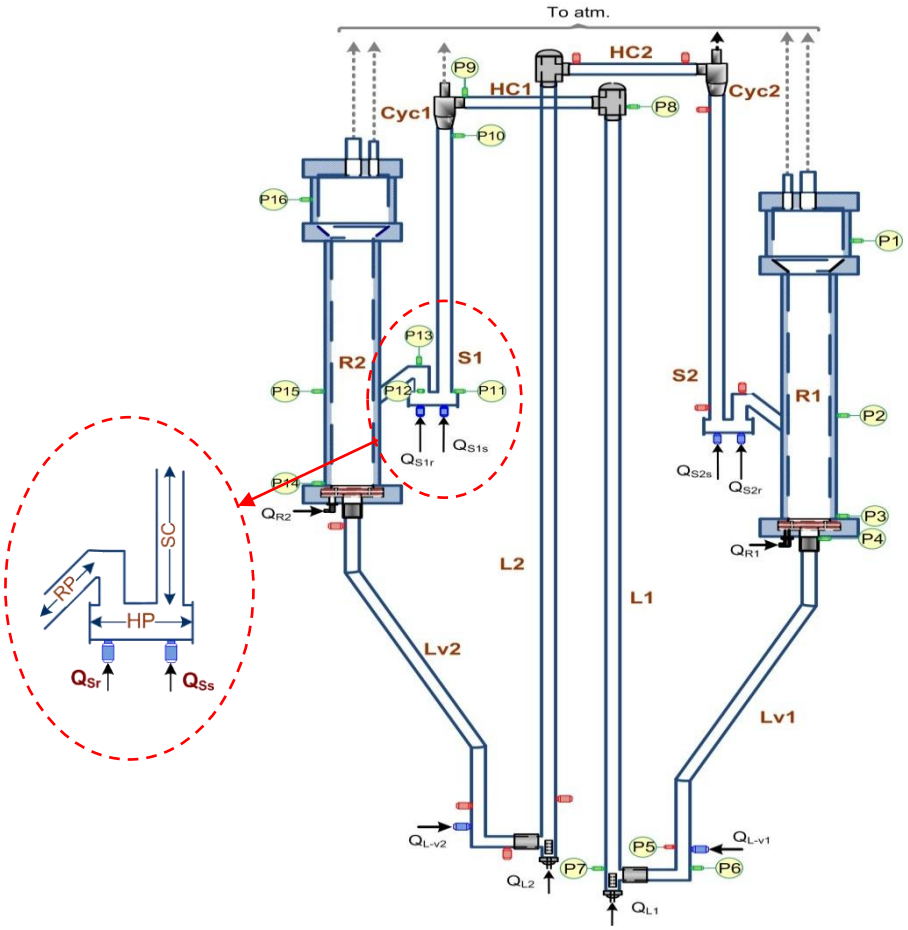

Figure 1: Le schéma de la maquette froide de CLC installée à l'IFP Énergies nouvelles. les prises bleues représentent les points d'aération et les prises rouges sont les prises utilisées sur l'installation pour la mesure de pression. Les abréviations utilisées dans la figure sont: R: réacteur, lv: vanne-en-L, lvH: section horizontale de la vanne-en-L, L: lift, HC: transport horizontal, Cyc: cyclone.

2.2. Le pilote chaud

Un pilote chaud a été construit avec des principes identiques que la maquette froide, et avec des dimensions similaires. La configuration du pilote chaud est montrée dans la Figure 2. La différence principale entre la maquette froide et le pilote chaud est le nombre de réacteurs interconnectés qui est de trois dans le pilote par rapport aux deux de la maquette froide. Le réacteur R1 (0,13 m id, et 1 m de haut) est le réacteur de fuel (FR) avec possibilité d'injection de CH_4 et/ou de N_2. Les deux autres réacteurs, R2 et R3 (0,1 m id, et 1 m de haut), sont les réacteurs d'oxydation (AR) avec la possibilité d'injection d'air et /ou d'azote. Le pilote a été construit avec un alliage spécifique de RH-120 qui offre une excellente résistance à haute température jusqu'à 1095 ° C. L'injection des gaz dans les réacteurs est effectuée à travers des plaques perforées avec quatre trous identiques (densité de trous de 509 orifice / m²).

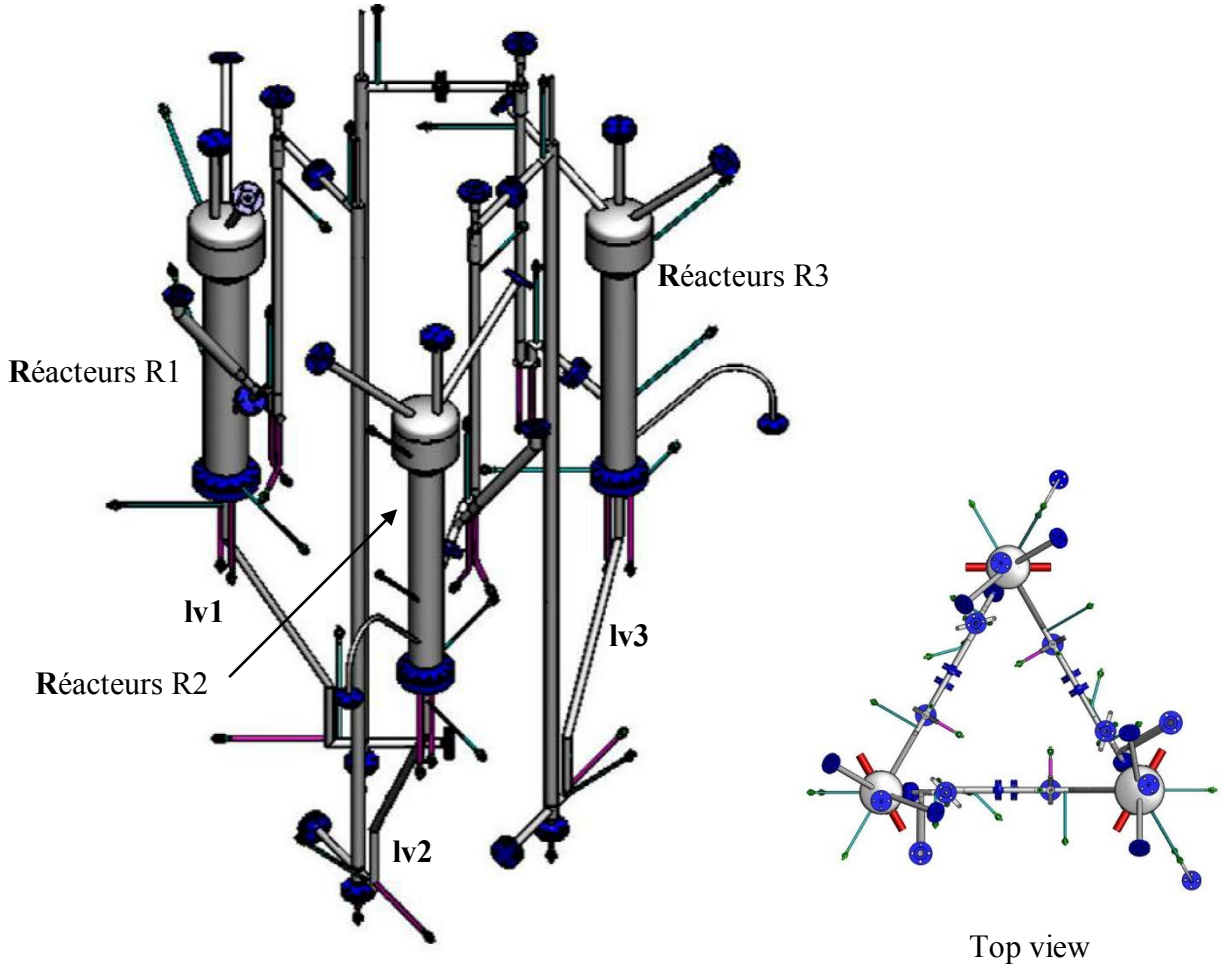

Figure 2: Le schéma du pilote chaud avec trois réacteurs interconnectés.

Le pilote chaud est composé de trois réacteurs à lit fluidisé bouillonnant interconnecté. Le réacteur de fuel (R1) a un diamètre intérieur de 0,13 m tandis que les réacteurs de l'air ont diamètres identiques de 0.1m. Les particules quittent les réacteurs à travers un standpipe relié à une vanne-en-L de 0,017 m du diamètre et 1,1 m de la hauteur. Les solides à la sortie des vannes-en-L sont transportés par un lift de 0,02 m du diamètre et 2,25 m du haut. Un coude-en-T est utilisé pour détourner le flux des particules vers une conduite horizontale. La séparation des solides et du gaz est réalisée dans un cyclone où les particules séparées sont amenées à un siphon situé en bas de la jambe de retour du cyclone. Les particules sont ensuite transférées vers le second réacteur d'air (R3). Les particules circulent de la même façon entre R3 et R1.

L'air sec est fourni à partir d'un réseau d'air comprimé avec une pression constante. L'azote a été utilisé comme le gaz de fluidisation lorsque les gaz réactifs ne sont pas injectés dans le système. L'azote et le méthane (CH4) proviennent de bouteilles fournies par Air Liquide. Le gaz de fluidisation dans chaque composant du système et les débits d'injections correspondants sont listés dans le Tableau 1. Les débits de gaz dans le système sont contrôlés par des débitmètres massiques pilotés à partir d'un ordinateur. Les pertes de charge ont été mesurées par des capteurs de pression numériques et ont été automatiquement enregistrés sur un ordinateur avec une fréquence réglable. Les prises de pression installée dans le pilote sont montrées dans la Figure 2.3 pour une ligne de transport entre deux réacteurs. Les emplacements des prises de pression sont identiques pour les deux autres lignes. La température du système est contrôlée par les chauffages électriques installés autour des réacteurs et des lignes de transfert du solide. Les températures sont mesurées par des thermocouples de type K.

Les gaz de combustion à la sortie du réacteur du fuel ont été déshumidifiés par les condenseurs refroidis à l'eau. Le débit de l'air sec a été mesuré par un débitmètre et enregistrés dans un ordinateur. Une fraction constante des gaz de combustion est échantillonnée en continu et envoyée vers les analyseurs pour mesurer les concentrations de H_2, CO, CO_2, CH_4 et N_2.

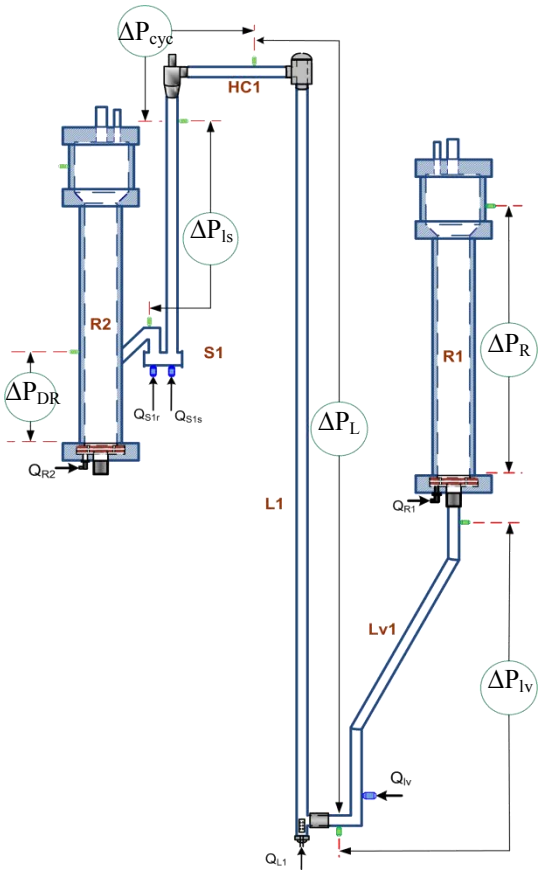

Figure 3: Les prises de la pression installées sur le pilote chaud.

Les propriétés des particules sont des paramètres importants pour le fonctionnement de la circulation du solide. Par conséquent, la caractérisation appropriée des particules utilisées est essentielle pour la compréhension et la modélisation du système actuel. L'étude hydrodynamique a été réalisée dans la maquette froide en utilisant trois solides : sand I, sand II, et ilmenite. Des particules de $NiO/NiAl_2O_4$ (60/40) sont utilisées comme transporteur d'oxygène dans le pilote chaud. Ce transporteur d'oxygène a été fabriqué par Marion Technologies (France) et préparé par précipitation. Les propriétés principales de ces particules sont listées dans le Table 2.2. La capacité théorique de transfert d'oxygène (R_0) est 12.8 % correspondant à la réduction de NiO à Ni.

Tableau 1: Les débits d'injection dans le pilote chaud.

Élément	Gaz de fluidisation	Débit (Nm^3/h)
Réacteur du fuel (R1)	Azote CH_4	0 – 0.5 0 – 1.0
Réacteur d'oxydation (R2)	Air Azote	0 – 3.5 0 – 0.5
Réacteur d'oxydation (R3)	Air Azote	0 – 2.5 0 – 0.5
Lift (L1, L3)	Azote	0 – 3.0
Lift (L2,)	Air Azote	0 – 3.0 0 – 3.0
Siphon (1, 2, 3)	Azote	0 – 0.5

Tableau 2: Les propriétés des particules utilisées dans la maquette froide et le pilote chaud. Les propriétés sont mesurées expérimentalement à la température ambiante sauf exception.

Property	Value			
Solid	**Sand I**	**Sand II**	**ilmenite**	**OC1**
ρ_s (kg/m^3)	2650	2650	4750	3250
d_p (µm)	253	368	107 [c]	168
d_{50} (µm)	268	384	132	201
U_{mf} (m/s)	0.038	0.068	0.0147	0.03 [b]
U_t (m/s)	1.37 [a]	1.95 [a]	0.82 [a]	1.22 [a]
U_{ch} (m/s)	3.8 [e]	4.4 [e]	3.4 [e]	3.6 [e]
ε_{mf}	0.513	0.514	0.455	0.48
ε_s (free settled)	0.463	0.457	0.434	
ε_{st} (tapped)	0.398	0.404	0.396	
Φ	0.86	0.76	0.64	

[a] Calculée par la corrélation de Haider et Levenspiel [227].
[b] Calculée par la corrélation de Wen et Yu [228]
[C] Les particules utilisées pour les essais de traçage et DTS ont été tamisés à 50 µm avec d_P déplacé à 128 µm.
[e] Calculée par la corrélation de PSRI [229].

3. La circulation des particules

Les études de la circulation des solides sont focalisées principalement sur le fonctionnement de la vanne-en-L et le siphon en tant qu'éléments critiques du système. Les vannes-en-L permettent de contrôler le débit de solide et la répartition d'inventaire entre différents réacteurs. Par conséquent, une compréhension suffisante de fonctionnement de la vanne-en-L est essentielle dans le système CLC actuel. En plus, le travail actuel visait à comprendre le fonctionnement optimal du siphon en termes de la minimisation de la fuite du gaz et de la conception. En ce qui concerne la fuite de gaz, le débit de gaz hors des réacteurs à travers les vannes-en-L est un paramètre important à étudier et minimiser si possible. Cela a été étudié par la mesure de perte de charge et le traçage gaz pour les fuites hors des réacteurs. La circulation des solides et les études hydrodynamiques ont été principalement menées dans la maquette froide grâce à la facilité d'utilisation, possibilité d'observations visuelles et la facilité des modifications si nécessaire.

La perte de charge dans la jambe dite standpipe de la vanne-en-L est un paramètre qui change pour ajuster la balance de pression à travers la boucle de circulation du solide [93,235]. La boucle de pression autour de la vanne-en-L dans la maquette froide est la suivante:

$$\Sigma \Delta P = \Delta P_{R1} + \Delta P_v + \Delta P_{lvH} + \Delta P_L + \Delta P_{Tb} + \Delta P_{HC} + \Delta P_{Cys,g} = 0 \qquad \textbf{Eq. 665}$$

Afin d'étudier le comportement de la perte de charge dans la vanne-en-L, la variation de perte de charge dans le standpipe a été mesurée lors d'une expérience en batch dans la maquette froide. Les

particules ont été transportées avec une aération constante de la vanne-ne-L (Q_{lv1}) alors que la circulation a été interrompue en lv2 ($Q_{lv2} = 0$). Les résultats de ces essais sont montrés dans la Figure 4 et la Figure 5.

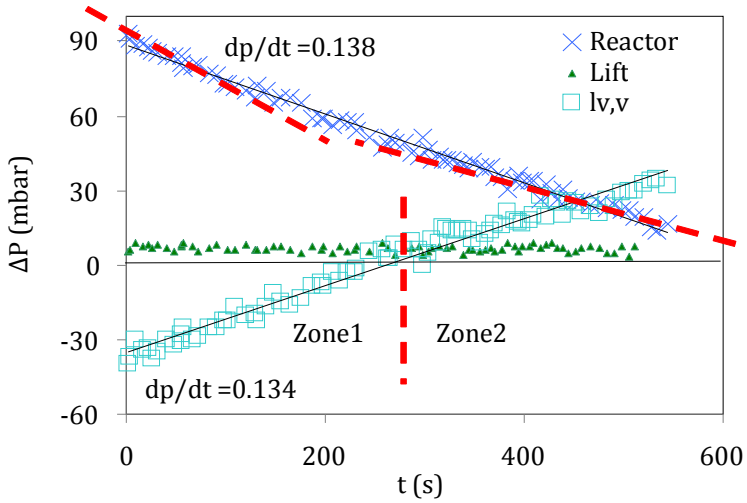

Figure 4 : La perte de charge dans le standpipe de la vanne-en-L (lv,v) pour une circulation du solides en batch du réacteur R1 vers R2 avec Q_{lv1} = 0.08 Nm3/h, et Gs = 49 kg/m².s.

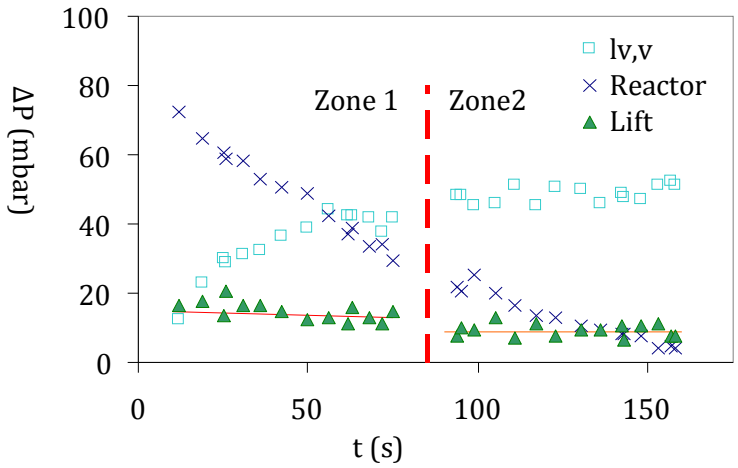

Figure 5: La perte de charge dans le standpipe de la vanne-en-L (lv,v) pour une circulation des solides en batch du réacteur R1 vers R2 avec Q_{lv1} = 0.18 Nm3/h, Gs = 196 kg/m².s dans la zone 1 et 98 kg/m².s dans la zone 2.

Comme illustré dans la Figure 3.2, la variation de la pression dans la jambe standpipe suit la variation de la pression du réacteur, mais en sens inverse. La variation de la perte de charge dans le standpipe suggère différents régimes de fonctionnement dans le standpipe de la vanne-en-L, énumérés dans le Table 3.1. Ces différents régimes peuvent être brièvement expliqués comme:

- Régime 1 : La perte de charge dans le standpipe est négative dans le cas de perte de charge élevée dans le réacteur.
- Régime 2 : Baisse de la perte de charge dans le réacteur (ou un autre élément dans la boucle de la pression) augmente la perte de charge dans le standpipe. Au-dessous d'une certaine perte de charge dans le réacteur, la perte de charge du standpipe (ΔP_v) devient positive.
- Régime 3 : correspond à la condition où la perte de charge dans le standpipe est suffisamment élevée pour imposer une vitesse de glissement de gaz - solides supérieure à la vitesse des solides. Dans ce cas, le gaz commence à monter au long du standpipe à contre-courant du sens

d'écoulement des particules. Le régime 3 pourrait arriver après les régimes 4 ou 5 en fonction des propriétés des particules.

- Régime 4 : La perte de charge le longe de standpipe peut augmenter jusqu'à une limite qui est la fluidisation de la vanne-en-L, correspondant à une vitesse de glissement supérieur à la vitesse minimale de fluidisation [235]. Par conséquence, la perte de charge atteint sa valeur maximale et standpipe ne peut pas absorber plus de pression.
- Régime 5 : Transition vers le régime bouillonnant provoque une perturbation considérable de flux solide. Dans cette condition, le débit solide diminue en raison de la formation de bulles de gaz qui augmente la porosité des particules dans le standpipe. Par conséquent, la quantité des particules dans la vanne-en-L diminue, ca qui provoque une chute de pression du standpipe. Ce phénomène est bien démontré dans la Figure 3.3 où le flux chute brusquement de 196 kg/m².s à 98 kg/m².s. Par conséquent, l'opération d'une vanne-en-L avec une standpipe fluidisé n'est pas recommandée.

Comme mentionné dans le Tableau 3, il existe différents régimes d'écoulement du solide et du gaz dans le standpipe de la vanne-en-L. Le régime d'écoulement peut être déduit à partir du débit solide et la perte de charge dans le standpipe. Les régimes 1 -3 avec un standpipe non-fluidisé sont les zones d'opérations les plus courants de vanne-en-L comme. En conséquence, le comportement des écoulements dans ces régimes ont été étudiés en plus des détails dans ce travaille comme présenter dans le manuscrit principal de la thèse.

Tableau 3: Les diffèrent régimes opérations dans le standpipe de la vanne-en-L.

Regime	ΔP_v = P5-P4	$V_r = V_s - V_g$	U_g	Scheme	Reference	Comment
1	négative	négative	descendant	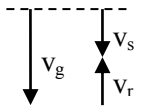	Figure 3.2 – Zone 1	moving Packed bed
transition	0	0	$U_g = U_s$			
2	positive	positive	descendant	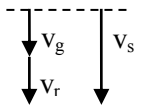	Figure 3.2 – Zone 2	Transitional packed bed
transition	positive	$v_r = v_s$	$v_g = 0$			
3	positive	$v_r > v_s$	ascendant	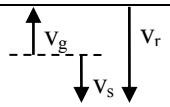	Figure 3.3 – Zone 1	
transition	$\Delta P_{SP} = \Delta P_{mf}$	$v_r = v_{mf}$	asc. / des.			
4	$\Delta P_{SP} = \Delta P_{mf}$ = cte	$v_r > v_{mf}$	asc. / des.		Figure 3.3 – Zone 2	Écoulement fluidisé
transition	$\Delta P_{SP} = \Delta P_{mb}$	$v_r = v_{mb}$	asc. / des.			
5	$\Delta P_{SP} < \Delta P_{mf}$	$v_r > v_{mb}$	asc. / des.			
	$\Delta P_{SP} = \Delta P_t$	$v_r = v_t$	asc.			arrêt d'écoulement

3.1. Opération du siphon

L'écoulement des particules entre les réacteurs peut transporter le gaz d'un réacteur vers l'autre et génère un transfert (fuite) de gaz. Cela peut diluer le flux de CO_2 capturé ou diminuer l'efficacité de captage de CO_2. Pour réduire cette fuite indésirable, le système actuel utilise des siphons à l'entrée de chaque réacteur. Les siphons sont normalement utilisés dans les lits fluidisés circulants afin d'éviter le retour des gaz de combustion vers le riser. Dans le système actuel les siphons sont utilisés pour l'écoulement des particules vers un lit fluidisé dense (Figure 6). Par conséquent, la hauteur du lit fluidisé dans le réacteur affecte considérablement l'opération du siphon en imposant une pression en sortie du siphon.

Le siphon minimise la fuite de gaz en formant une colonne des particules dans le standpipe du siphon (SC) avec une perte de charge positive qui empêche l'écoulement libre du gaz vers le réacteur. Donc, la formation et la maitrise de la colonne des particules dans le standpipe du siphon est un facteur important dans l'opération de cet élément. Le Figure 7 montre différents paramètres qui influencent la hauteur de la colonne des particules dans le standpipe (H_{SC}) de la configuration actuelle.

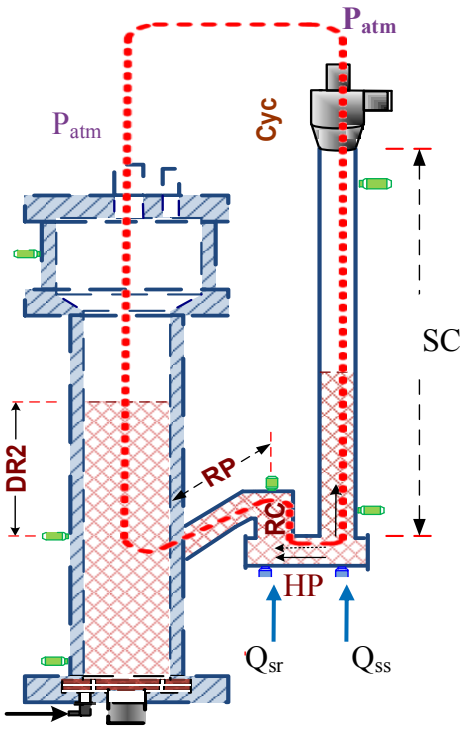

Figure 6: Schéma du siphon et les différents éléments utilisé dans le système CLC actuelle.

$$\text{Hsc } \alpha \begin{cases} Q_{sc} = \text{sum of} \begin{cases} Q_{ss} \\ -\,Q_{HP} \end{cases} \\ \Delta Psc\ \alpha\ \Sigma\Delta P \text{ sum of} \begin{cases} \Delta P_{Cyc}\ \alpha\ G_s,\ Q_L \\ \Delta P_{HP}\ \alpha\ G_s \\ \Delta Prc\ \alpha\ G_s\ ,\ Qrc \\ \Delta P_{RP}\ \alpha\ G_s,\ Q_{RP} = Qrc \\ \Delta P_{DR2}\ \alpha\ M_R \end{cases} \end{cases}$$

Figure 7: Dépendance de la hauteur de la colonne des particules dans le standpipe du siphon en fonction des paramètres opératoires.

La vanne-en-L et le siphon dans le système actuel sont en partie similaires : dans les deux éléments, la perte de charge dans les standpipes est une fonction de la vitesse de glissement et du bilan de pression

dans la boucle de circulation des particules. Cependant, les variables principales dans ces deux éléments sont le débit de la circulation des particules dans la vanne-en-L et le débit du gaz dans le standpipe du siphon. Le débit de solide est fixé dans la vanne-en-L et le siphon ne le change pas dans le système actuel. Le débit solide dans la vanne-en-L est fonction du débit gaz dans la section horizontale de la vanne-en-L. Cela est la somme de l'aération externe de la vanne-en-L et le débit gaz dans le standpipe. De la même façon, le débit gaz dans le standpipe du siphon (Q_{SC}) est fonction de l'écoulement de gaz dans la section horizontale du siphon (Q_{HP}) qui est la somme de l'aération externe Q_{Ss} et du débit gaz dans le standpipe du siphon (Q_{SC}). Deux cas sont possibles dans le fonctionnement du siphon :

a. $Q_{HP} > Q_{SS}$: Dans ce cas, l'aération externe du siphon (Q_{SS}) ne suffit pas pour l'écoulement horizontal des particules. Par conséquence, un parti du débit horizontal requis ($Q_{HP} - Q_{SS}$) sera fourni par le gaz porté par les particules dans le standpipe du siphon (Q_{SC}). Donc, cette flux de gaz vas arriver au réacteur et provoque un fuit.

b. $Q_{HP} < Q_{SS}$: Dans ce cas, l'aération externe du siphon (Q_{SS}) est plus élevé que le débit horizontal requis. Donc, l'excédent du gaz d'aération ($Q_{SS} - Q_{HP}$) va remonter dans le standpipe. Q_{SC} est négatif dans ce cas, et la meilleure étanchéité est réalisée.

4. Modèle de circulation

Un modèle de la circulation est développé pour le système de CLC actuel, la maquette froide et le pilote chaud. Les résultats principaux de ce modèle sont le débit de solide dans la vanne-en-L et la fuite de gaz dans le siphon. Le principe du modèle de la circulation est expliqué dans ce rapport, les détails et les résultats sont présentés dans le rapport principal de la thèse.

Le système CLC de cette étude utilise une vanne-en-L et un siphon en série, une configuration qui rend le système différent des autres systèmes existants. Le modèle développé est basé sur le principe du bilan de pression. Etant donné que les lignes de transport des particules sont identiques dans ce système, le bilan de la pression pour une ligne est valide pour les autres. Le bilan de pression pour la ligne de transport du réacteur R1 vers le réacteur R2 est :

$$P_1 + \Delta P_{R1} + \Delta P_{lv,v} + \Delta P_{lv,H} + \Delta P_L + \Delta P_{Tb} + \Delta P_{HC} + \Delta P_{Cyc,s} + \Delta P_{SPs} + \Delta P_{HP} + \Delta P_{RC} + \Delta P_{RP} + \Delta P_{DR2} + P_2 = 0 \quad \textbf{Eq. 66}$$

La P_1 et la P_2 sont respectivement les pressions aux sorties gaz des réacteurs R1 et R2. Cette équation est valable pour la maquette froide et le pilote chaud. Concernant le fait que le cyclone a une sortie atmosphérique, cette équation peut être divisée en deux parties. La première partie via la vanne-en-L est :

$$\Sigma P_{lv} = \Delta P_{R1} + \Delta P_{lv,v} + \Delta P_{lv,H} + \Delta P_L + \Delta P_{Tb} + \Delta P_{HC} + \Delta P_{Cys,g} = 0 \quad \textbf{Eq. 67}$$

Et la deuxième partie via le siphon est :

$$\Sigma P_{ls} = \Delta P_{Cyc,g-s} + \Delta P_{SPs} + \Delta P_{HP} + \Delta P_{RC} + \Delta P_{RP} + \Delta P_{DR2} = 0 \quad \textbf{Eq. 68}$$

ΔP est positive si la pression augmente le long de l'élément et négative si la pression diminue. Ces deux équations sont utilisées séparément pour prédire le débit de la circulation et la fuite dans le siphon. La division du bilan de la pression en deux parties est la base du modèle actuel. La Figure 8 montre ce principe dans une ligne de la circulation entre les réacteurs R1 et R2. Les variables connues et inconnues dans chaque section du modèle et les équations clés utilisées sont listés dans le Tableau 4.

Tableau 4: La liste des variables connues et inconnues et les équations clés utilisées dans le modèle.

	Variables inconnues	Variables connue	Equations clés
Section 1	G_s , δ_{lv}	Q_{lv} , M_{R1} , Q_{R1} , Q_L	$\Sigma\Delta P_{lv} = 0$ $G_s = f(U_{lv,H})$
Section 2	Q_{SC} , H_{SC}	G_s , Q_{Ss} , Q_{Sr} , Q_{R2} , M_{R2}	$\Sigma\Delta P_{ls}=0$ $G_s = f(U_{HP})$

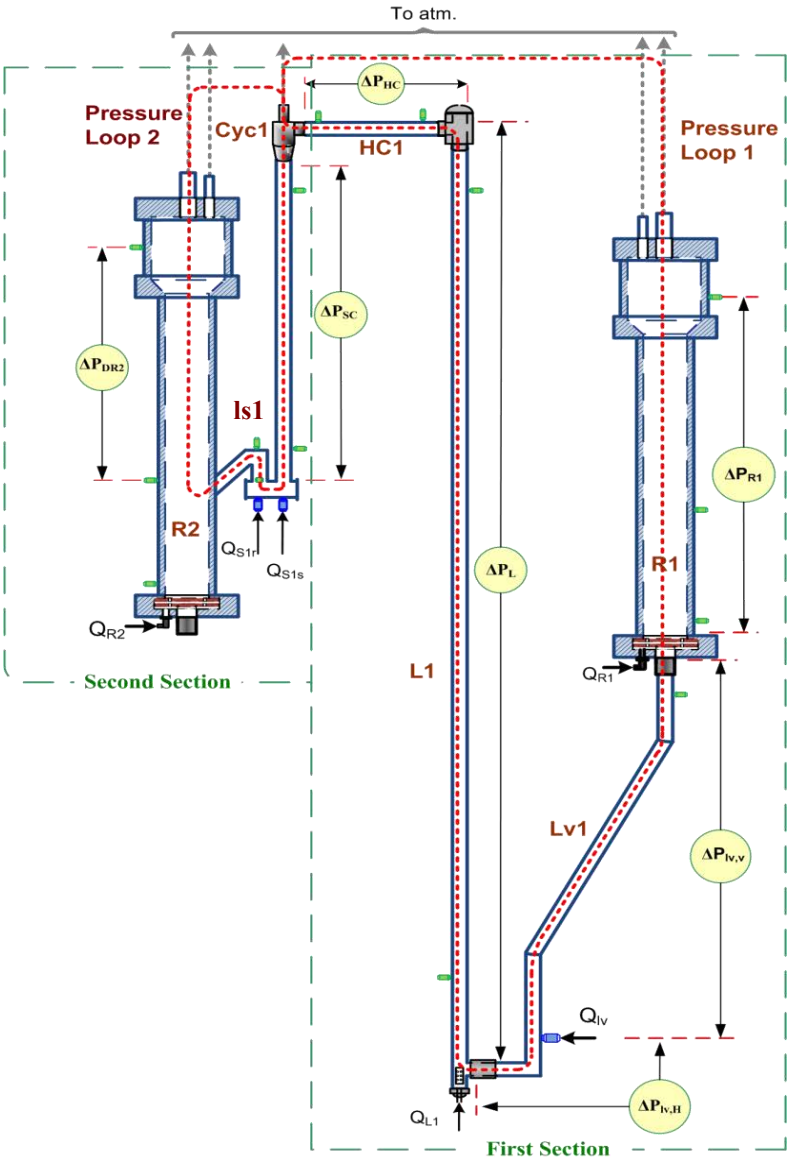

Figure 8: Les deux bilans de pression utilisés dans le modèle de circulation.

4.1. La premier section du modèle

Le débit de solide dans le système actuel est contrôlé dans la vanne-en-L où la quantité totale du débit de gaz dans la section horizontale ($Q_{lv,H}$) détermine le débit de solide. La Figure 4.2 montre la configuration de la vanne-en-L du système CLC actuel. Comme expliqué précédemment, le débit gaz dans la section horizontale de la vanne-en-L est :

$$Q_{lv,H} = Q_{lv} + Q_{lv,v} \qquad \textbf{Eq. 69}$$

Le débit de gaz dans le standpipe ($Q_{lv,v}$) peut être vers le haut (signe négatif) ou vers le bas (positif). Le ratio du débit de gaz dans le standpipe par rapport à l'aération externe est :

$$\delta_{lv} = \frac{Q_{lv,v}}{Q_{lv}} \qquad \textbf{Eq. 70}$$

δ_{lv} peut être positif ou négatif correspondant à la direction d'écoulement du gaz. Le débit de gaz dans le standpipe dépend du bilan de pression. Une procédure itérative est utilisée dans le modèle pour calculer le débit de solide. Une valeur du zéro est initialement désignée à δ_{lv}. Donc, le débit de gaz

dans le standpipe est zéro et le débit de gaz horizontal ($Q_{lv,H}$) égal à l'aération externe. Le débit de solide est calculé en fonction de $Q_{lv,H}$. Les pertes de charge dans différentes sections du système sont ensuit calculés. Le bilan de pression dans la première partie de la maquette est calculé en utilisant l'équation 3.2. Si le bilan est bouclé ($\Sigma\Delta P_{lv}$=0), les résultats sont considérés comme les résultats définitifs. Sinon δ_{lv} est augmenté par une valeur incrémentale :

$$\delta_{lv,1} = \delta_{lv,0} + d\delta_{lv} \qquad \textbf{Eq. 71}$$

$\Sigma\Delta P_{lv}$ est ensuit calculée en fonction de la nouvelle fraction δ_{lv}. Si le bilan boucle, le résultat est considéré comme résultat définitif. Sinon, la valeur de δ_{lv} est augmentée et la procédure est répétée pour trouver $\Sigma\Delta P_{lv}$=0 et le débit de solide correspondant.

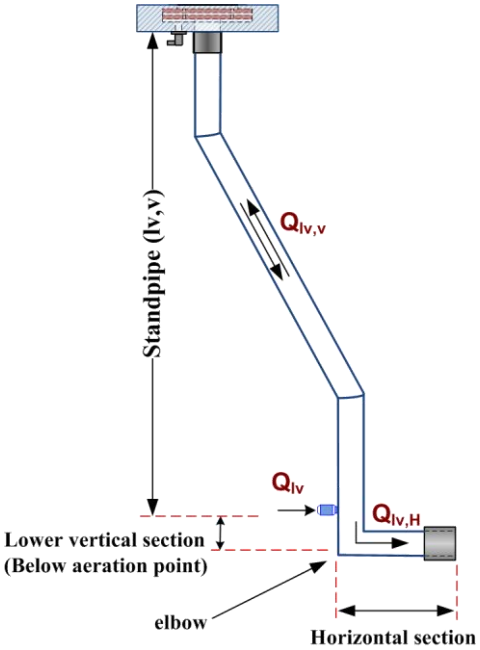

Figure 9: Le schéma de la vanne-en-L et les éléments principaux.

4.2. La deuxième section du modèle

La deuxième section du bilan de pression est montrée dans la Figure 10. Les particules séparées dans le cyclone s'écoulent vers le bas à travers le standpipe par gravité. L'injection de l'air en bas du siphon aide à l'écoulement des particules à travers la section horizontale (HP) vers le tuyau de retour (RC) ou l'écoulement des particules est assisté par une deuxième aération extérieure. Le but du modèle est de trouver le débit de gaz (Q_{SC}) et la hauteur de la colonne des particules (H_{SC}) dans le standpipe du siphon.

Le débit de la circulation des particules est une variable connue qui est précédemment calculé dans la vanne-en-L. Le débit de gaz dans la section horizontale (Q_{HP}) est calculé en utilisant la corrélation entre le débit de solide et le débit de gaz dans la section horizontale. Donc, le débit de gaz dans le standpipe du siphon est :

$$Q_{SC} = Q_{HP} - Q_{SS} \qquad \text{Eq. 72}$$

La hauteur de la colonne des particules dans le standpipe est calculée en utilisant la perte de charge dans cette section (ΔP_{SC}). La perte de charge du standpipe (ΔP_{SC}) est une fonction du bilan pression, l'équation 3.3. Par la suit, la hauteur de la colonne des particules est calculée à l'aide de l'équation d'Ergun [94].

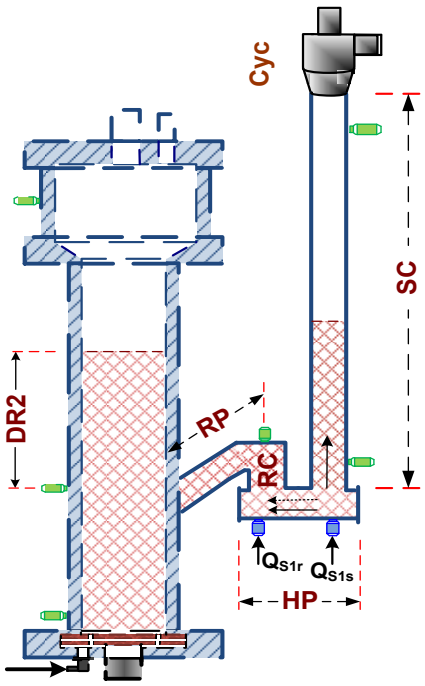

Figure 10: Le schéma de la deuxième section du modèle.

4.3. Validation du modèle

Les résultats de la modélisation ont été ensuite comparés avec les résultats expérimentaux pour valider le modèle. La Figure 11 et la Figure 12 comparent la prédiction du débit de solide par le modèle avec les résultats expérimentaux. Le modèle prédit bien le débit de la circulation aux conditions ambiantes. Cependant, dans les conditions de haute température le modèle est moins précis. Cela est principalement dû à la corrélation du débit de solide dans la section horizontale de la vanne-en-L.

La Figure 13 et la Figure 14 comparent les résultats de la modélisation avec les résultats de la perte de charge dans la maquette froide. Donc, le modèle prédit bien la perte de charge dans le système actuel. Les descriptions détaillées de la modélisation et la comparaison détaillée avec les résultats expérimentaux sont présentés dans le manuscrit de la thèse.

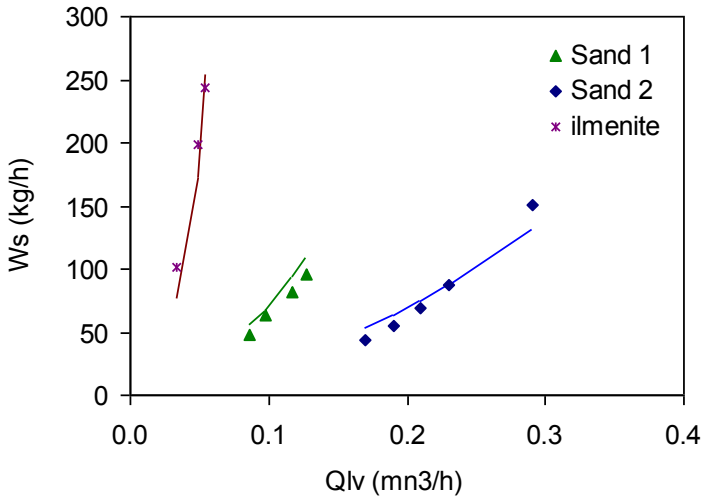

Figure 11: La comparaison de la prédiction du débit de solide par le modèle avec les résultats expérimentaux dans la maquette froide avec H_R = 0.5 m.

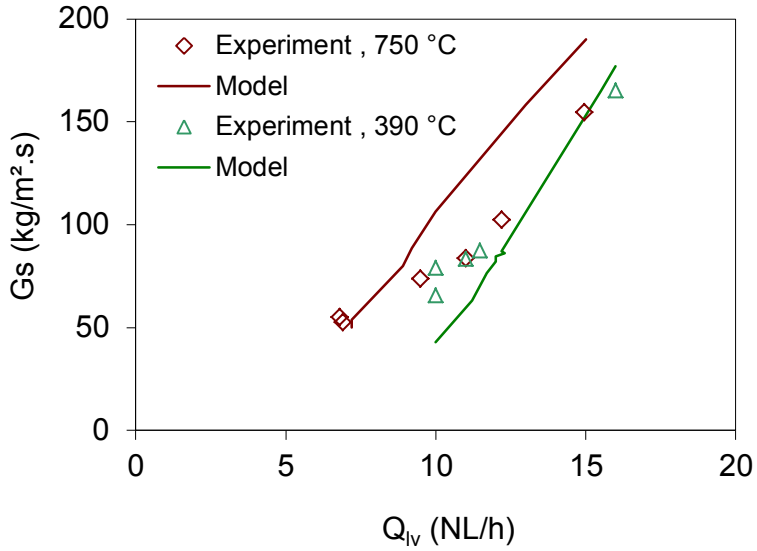

Figure 12: La comparaison de la prédiction du débit de solide par le modèle avec les résultats expérimentaux du pilote chaud avec H_R = 0.5 m, T = 390 °C, et 750 °C.

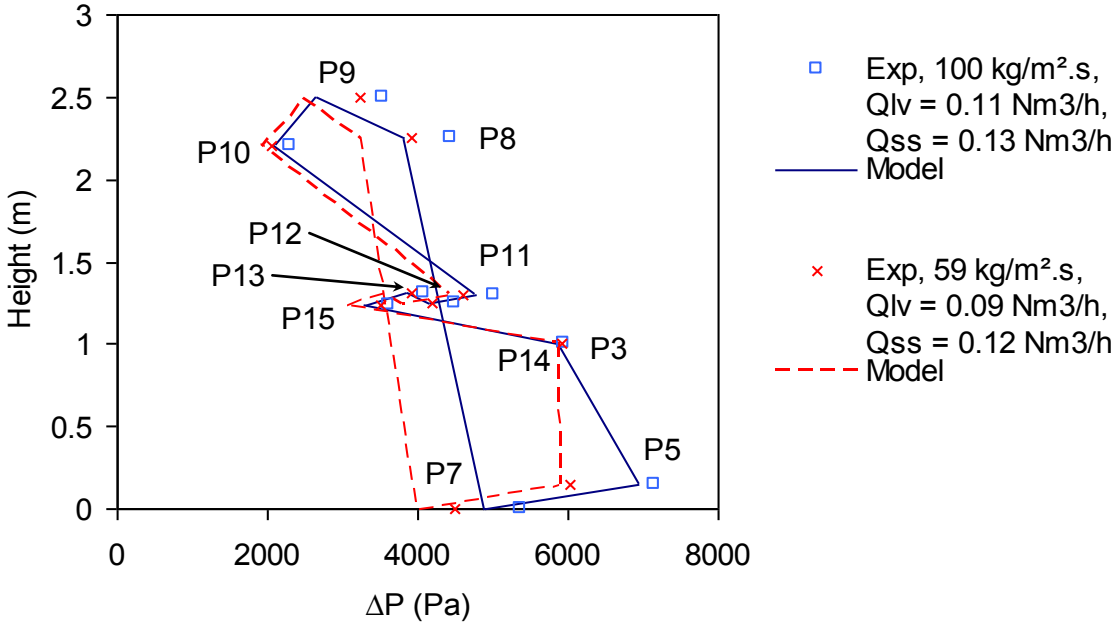

Figure 13: La comparaison de la prédiction de la perte de charge par le modèle avec les résultats expérimentaux dans la maquette froide pour le sable I (sand I).

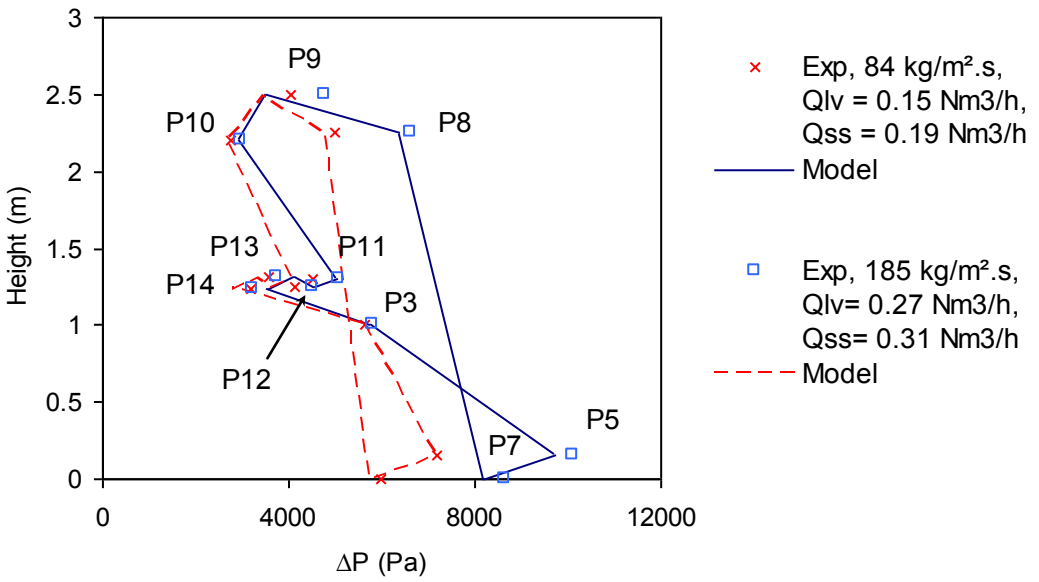

Figure 14: La comparaison de la prédiction de la perte de charge par le modèle avec les résultats expérimentaux dans la maquette froide pour le sable II (sand II).

5. Hydrodynamique du réacteur

La circulation des particules et la fuite du gaz entre les réacteurs ont été étudiées expérimentalement. Un modèle a été également développé basé sur le principe du bilan de pression. Néanmoins, les phénomènes hydrodynamiques et cinétiques dans les réacteurs doivent être étudiés afin d'obtenir une meilleure compréhension du procédé de CLC. Donc, le reste de cette étude a été focalisé sur la performance du lit fluidisé bouillonnant qui se trouve dans les réacteurs du fuel et de l'air.

La modélisation est une étape nécessaire pour la compréhension et le développement d'un procédé. Un modèle du réacteur est au moins composé d'un mécanisme réactionnel et une base hydrodynamique. L'hydrodynamique du réacteur joue un rôle important dans sa performance, particulièrement pour un lit fluidisé. Cette partie de la thèse a été consacrée à la caractérisation hydrodynamique du réacteur avec les analyses expérimentales et la modélisation. L'hydrodynamique du lit fluidisé utilisé dans le système actuel a été étudiée expérimentalement dans la maquette froide avec l'ilménite. La méthode de la distribution de temps de séjour a été utilisée à cette fin en utilisant l'Hélium comme le traceur gaz. L'impact des principaux paramètres opératoires ont été étudiés, y compris : le niveau du lit dans le réacteur, le débit de gaz, et le débit de la circulation des particules.

Un modèle hydrodynamique a été développé basé sur la model du lit fluidisé en deux phases de la bulle et de l'émulsion [153]. Tenant compte de la diversité des modèles de la littérature [153,170,172,175,177,270], les résultats expérimentaux ont été utilisés pour sélectionner les meilleures relations et corrélations dans différentes parties du modèle.

Le but principal de cette étude est d'adapter un des modèles de la littérature en bon accord avec les résultats du système actuel. Ce modèle doit être fiable pour l'extrapolation des résultats à des températures plus élevées et des échelles plus importantes. Donc le modèle à deux phases de Toomey et Johanstone [169] et Wen et Fan [170] a été utilisé. Les hypothèses principales de ce modèle sont :

- Le lit fluidisé est composé de deux phases: bulle et émulsion.
- Toutes les particules sont dans la phase d'émulsion et la phase bulle ne contient pas des particules.

- Le flux de gaz dans la phase bulle est modélisé par un modèle de piston avec un terme d'échange gaz avec la phase d'émulsion.
- Dans la phase d'émulsion :
  - Les particules sont stagnantes (pas d'écoulement en moyenne).
  - L'écoulement de la phase gaz est avec une vitesse constante égale à la vitesse minimale de la fluidisation.
  - Le model de la phase gaz est un modèle de dispersion axiale – piston.
  - Les particules sont mélangés de une façonne homogène donc un modèle de réacteur parfaitement agité est utilisé pour cette phase.

Les résultats de l'étude expérimentale de la distribution de temps de séjour ont été utilisés pour trouver les meilleures relations et coefficients pour les termes de l'échange, du coefficient de la dispersion, et de la taille des bulles.

5.1. La validation du modèle

Le modèle hydrodynamique a été validé en utilisant les résultats expérimentaux de la distribution de temps de séjour (DTS). La Figure 15 montre la comparaison entre le modèle et l'expérimentation pour l'effet du niveau du lit fluidisé dans le réacteur (H_R). Le modèle prédit bien l'impact de niveau des particules dans le réacteur. L'impact du débit de gaz a été ensuite comparé avec le modèle (Figure 16). Le modèle prédit bien les résultats pour les débits faibles et moyens. Cependant, le modèle surestime les résultats expérimentaux pour les débits de gaz élevés. Cela est probablement lié à la corrélation de la taille des bulles qui joue un rôle important dans le temps de séjour de la phase gaz. Finalement, le modèle est validé en fonction de l'effet du débit de solide (Figure 17). Les résultats montrent bien que le débit de solide a un effet minimal sur le temps de séjour de la phase gazeuse. La raison principale de cette observation est le fait que la vitesse des bulles est beaucoup plus élevée que la vitesse des particules. Donc, la variation imposée par les particules sur le temps de séjour est négligeable.

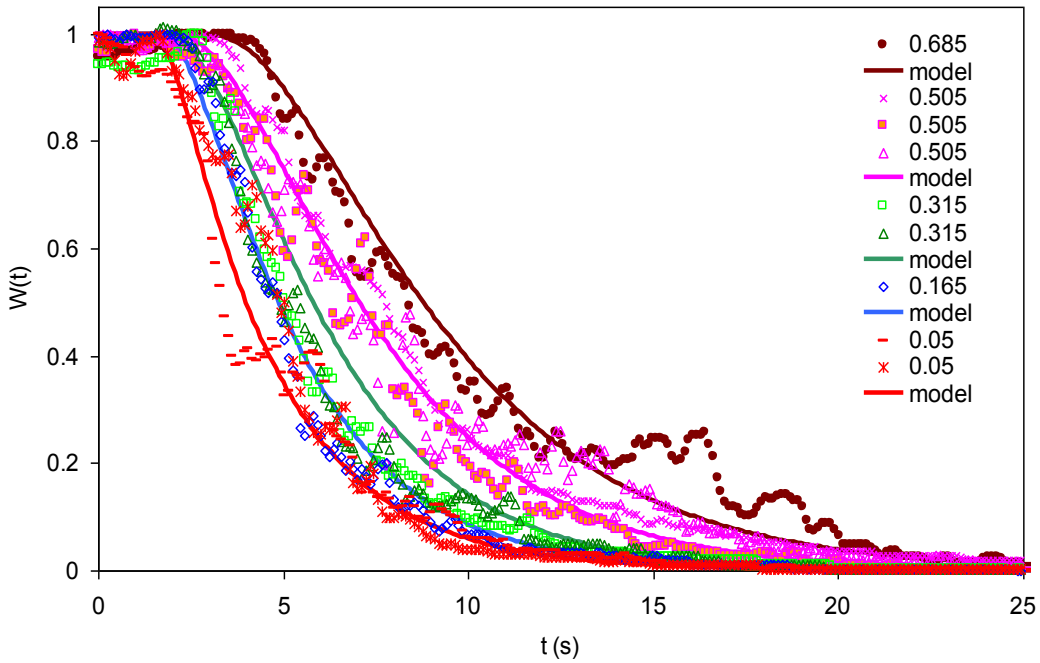

Figure 15: La comparaison des résultats de la model avec les résultats expérimentaux pour l'effet du niveau du lit fluidisé dans le réacteur (Q_R = 1.92 Nm^3/h, W_s = 0 kg/h).

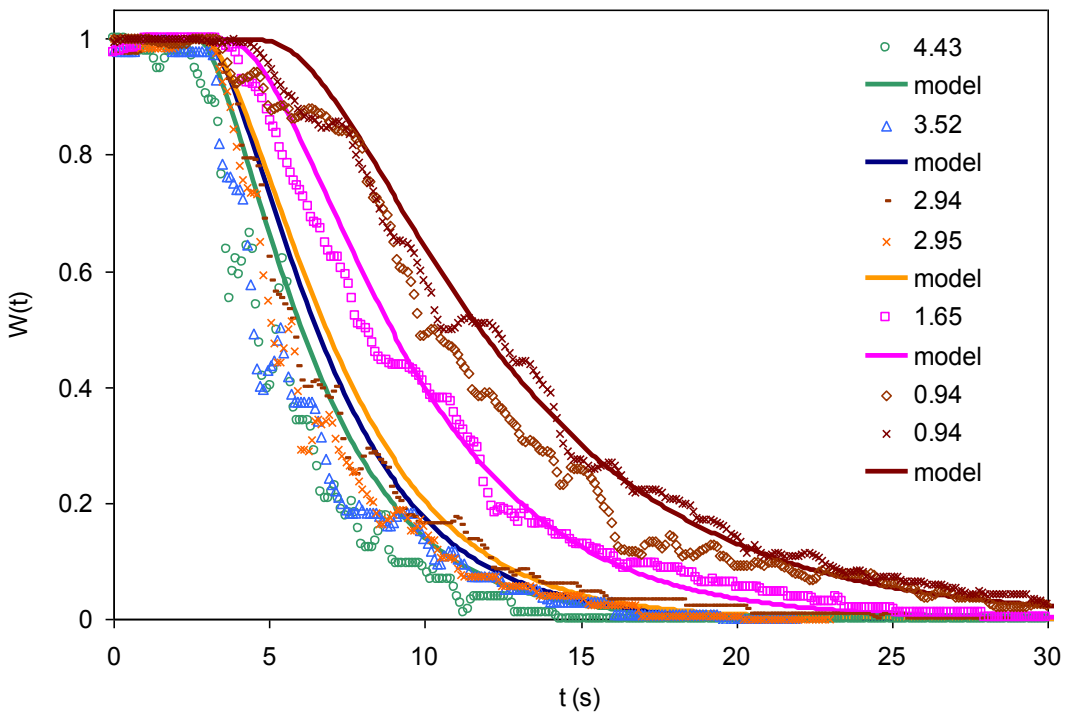

Figure 16: La comparaison des résultats du modèle avec les résultats expérimentaux pour l'effet du débit d'injection du gaz dans le réacteur (Q_R = 1.92 Nm^3/h, W_s = 0 kg/h).

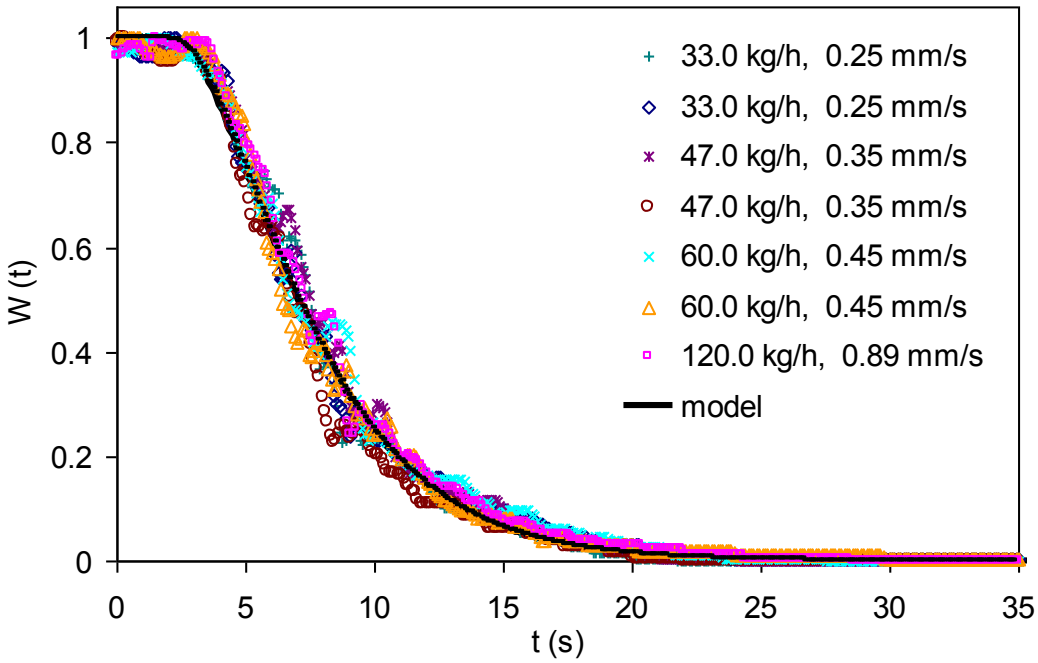

Figure 17: La comparaison des résultats du modèle avec les résultats expérimentaux pour l'effet de débit de la circulation des particules (Q_R = 1.92 Nm^3/h).

6. La combustion du méthane

Le but principal du système actuel est de fournir un dispositif expérimental pour étudier les paramètres importants de CLC, notamment : le transporteur d'oxygène, les mécanismes réactionnels, et le temps de contact nécessaire dans les réacteurs de fuel et de l'air. Une grande importance a été accordée à la

maitrise du fonctionnement, dont le débit de la circulation des particules, les inventaires dans chaque réacteur, et les fuites de gaz.

La combustion de méthane avec les transporteurs d'oxygène ($Ni/NiAl_2O_4$) a été étudié dans la dernière partie de cette thèse. Le pilote chaud est construit pour les opérations en régime stationnaire. Cependant, des essais complémentaires ont été réalisés en régime transitoire et en batch. Les paramètres les plus importants étudiés dans ces essais sont les impacts de la température, du débit de la circulation des particules, de la conversion du transporteur d'oxygène, et du débit d'injection de méthane et de l'air.

Le Figure 18 montre un essai typique en régime établi pour obtenir un point de mesure réalisé suivant plusieurs étapes :

1. La première étape est d'établir une circulation stable des particules entres les trois réacteurs.
2. Une fois que l'opération stable est établie, le méthane et l'air sont injectés pour commencer la combustion.
3. Les mesures sont prises quand les paramètres opératoires (les températures, les concentrations, et les pertes de charges) restent stables.
4. A la fin de l'essai, le méthane est remplacé par l'azote. La circulation est arrêtée une fois que toutes les particules sont totalement oxydées.

La Figure 19 montre l'impact de la température sur la combustion du méthane en régime établi dans le réacteur combustible. Les résultats démontrent que les réactions parviennent quasiment à l'état d'équilibre thermodynamique. Cela montre que les réactions de la combustion sont très rapides dans le système actuel.

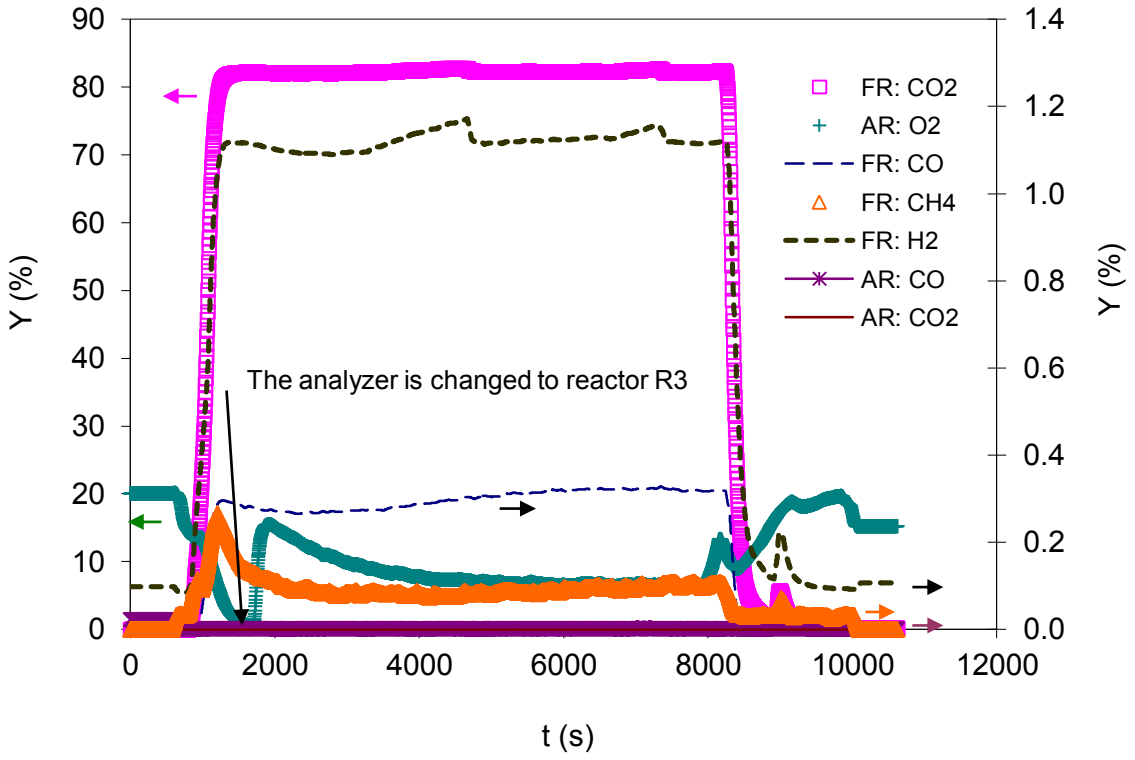

Figure 18: Un essai typique de combustion dans le pilote chaud avec H_{R1} = 0.51 m, Ws = 45 kg/h, Q_{CH4} = 0.5Nm^3/h, U_{CH4} = 0.066 m/s, U_R = 0.2 m/s pour le gaz de combustion, ΔX = 25%, Q_{lv} = 7.5 NL^3/h, Qss = 0.1 NL^3/h.

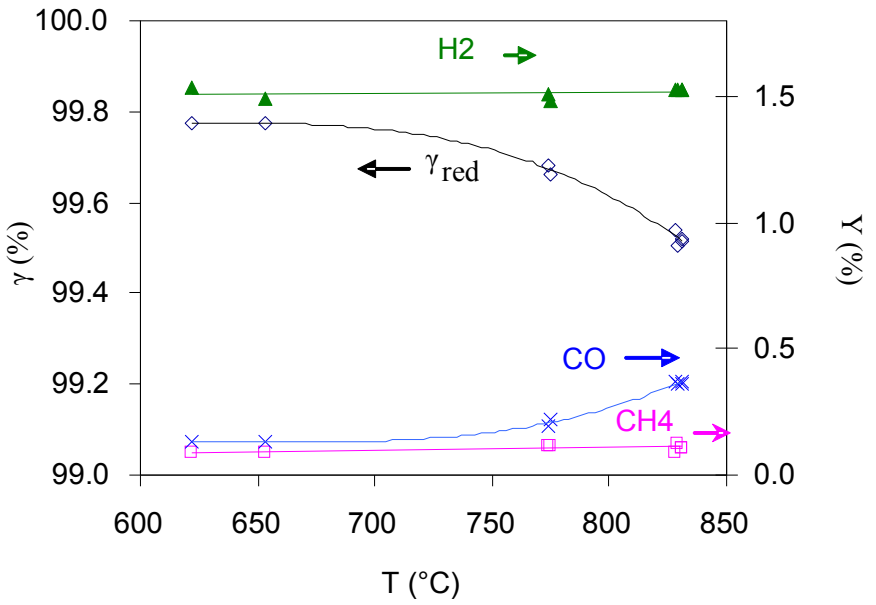

Figure 19: L'impact de la température sur la combustion du méthane dans le réacteur combustible avec Q_{CH4} = 0.5 Nm^3/h, H_R = 0.5 ±5 m, Ws = 40±5 kg/h, ΔX = 28 %, U_{CH4} = 0.066 m/s à l'entrée, and U_R = 0.2 m/s pour le gaz de combustion.

Les essais transitoires ont été réalisés en utilisant le pilote chaud. Dans ce type des essais, le régime établi est d'abord atteint. Ensuite, un seul paramètre opératoire est modifié entre deux limites de fonctionnement. Le comportement du système au niveau des différentes variables est observé en détail pour identifier les différentes régions d'opération possible. La Figure 20 montre un essai transitoire pour étudier l'effet du niveau du lit fluidisé sur la combustion. Le niveau du lit (H_R) est varié de 0.45 m à 0 m. Différentes régions sont ensuite identifiées. Ces résultats sont démontrés en détail dans le manuscrit de la thèse.

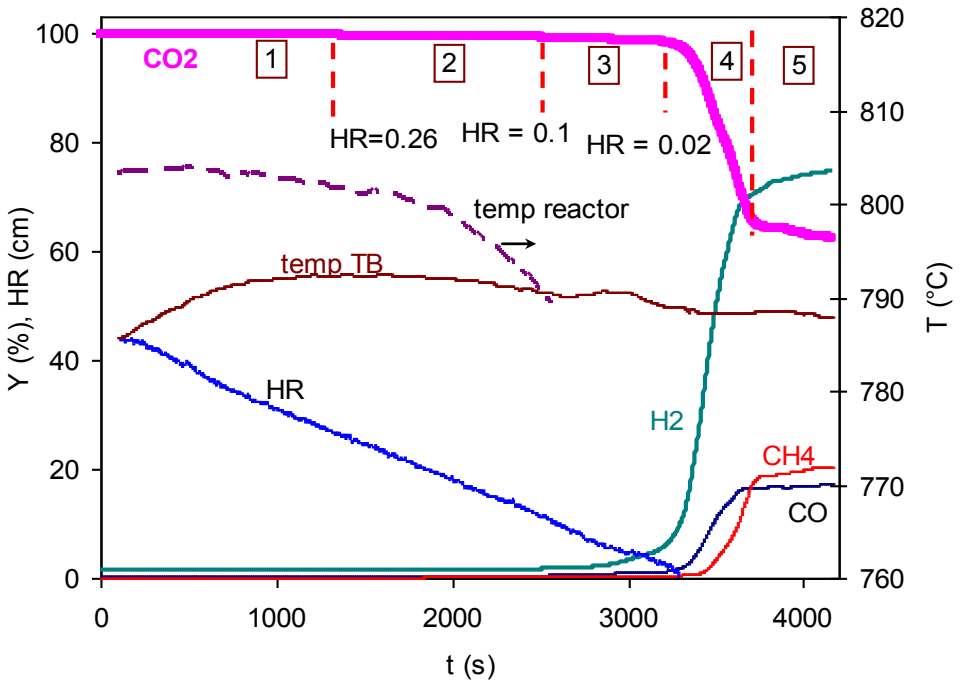

Figure 20: L'impact du niveau du lit fluidisé (H_R) sur la combustion dans le réacteur de fuel (R1) avec Q_{CH4} = 0.5 Nm^3/h, U_{CH4} = 0.066 m/s (U_R = 0.2 m/s pour les gaz de combustion).

Dans les opérations en batch, une quantité fixe de transporteur d'oxygène est placé dans un réacteur sans circulation. Le méthane ou l'air est ensuite injecté pendant une période de temps déterminée afin de mesurer la variation des différents paramètres. Ces résultats sont démontrés en détails dans le manuscrit de la thèse.

6.1. La modélisation du réacteur

Un modèle hydrodynamique a été développé précédemment en utilisant les résultats des essais de distribution de temps de séjour (DTS). Ce modèle a été modifié pour prendre en compte les réactions chimiques, l'expansion du gaz, et le bilan matière pour la phase solide. Un schéma cinétique est adapté de la littérature pour modéliser les réactions de la combustion du méthane sur NiO/NiAl2O4. Le modèle inclut à la fois les réactions directes entre NiO et les gaz réactifs et également les réactions catalytiques dues au Nickel. La Figure 21 compare la prédiction du modèle avec les résultats expérimentaux de la combustion en batch. Les descriptions détaillées de la modélisation et la comparaison avec les résultats expérimentaux sont présentés dans le manuscrit de la thèse.

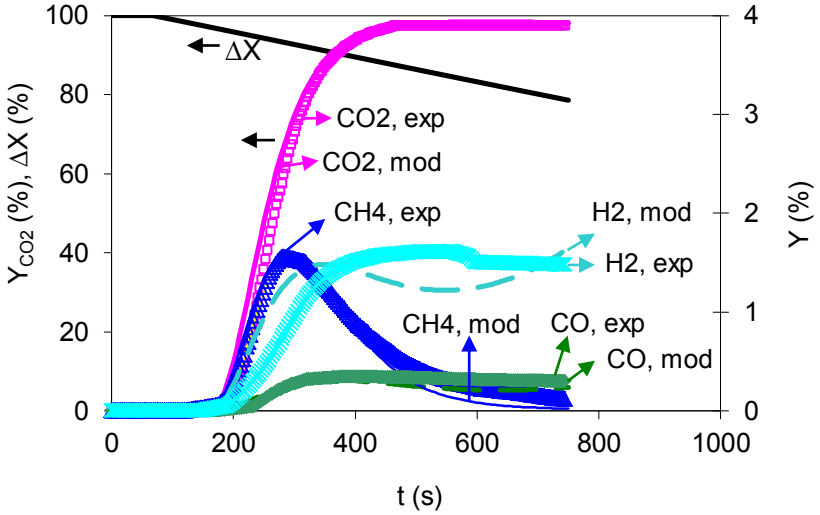

Figure 21: La comparaison des résultats de la modélisation et les résultats expérimentaux avec 0.5 Nm^3/h du CH_4, H_{R1} = 0.33m, et dT/dt = -0.055 °C/s.

7. Conclusions

La combustion en boucle chimique (CLC) a été étudiée en utilisant une nouvelle configuration expérimentale de 10 kW thermique, en maquette froide pour les aspects hydrodynamiques et en pilote chaud pour les aspects cinétiques. Le but principal de ces installations est de développer des dispositifs expérimentaux afin d'étudier la combustion en boucle chimique dans une gamme importante des variables. Ce système est basé sur le principe des lits fluidisés interconnectés. Le débit de la circulation des particules est contrôlé par l'utilisation des vanne-en-L, et les fuites du gaz entres les réacteurs sont minimisées en utilisant les siphons.

Ce travail est divisé en deux parties principales. La première partie se focalise sur l'étude de la circulation des particules, en particulier sur l'opération de la vanne-en-L et du siphon. Les principales conclusions de cette partie de l'étude peuvent être énumérées comme suit :

- Une circulation stable des particules entre les réacteurs a été atteinte avec la configuration actuelle aux conditions ambiantes et aux températures élevées (jusqu'à 900°C). Différentes

particules ont été utilisées avec des tailles moyennes allant de 107 µm à 368 µm et des densités de 2650 kg/m^3 à 4750 kg/m^3.

- La vanne-en-L a montré un contrôle efficace du débit de la circulation des particules pour les particules de groupe B dans une large gamme de température. L'aération externe de la vanne-en-L est le paramètre principal du contrôle du débit des particules. Aussi, la perte de charge dans la jambe « standpipe » de la vanne-en-L démontre avoir un effet important sur le débit de solide et la stabilité de la circulation.
- La vanne-en-L permet un contrôle du débit de solide indépendamment du débit de gaz dans les réacteurs. Cela augmente la flexibilité du fonctionnement du système actuel. Par ailleurs, l'utilisation de plusieurs vannes-en-L dans le système actuel permet de maîtriser la distribution de l'inventaire solide dans chaque réacteur. Ceci fournit une flexibilité supplémentaire au système, intéressant pour les études laboratoires.
- Le débit volumique de gaz dans le coude de la vanne-en-L est le paramètre qui contrôle le débit de solide dans une vanne-en-L d'une géométrie définie. La densité du gaz a un effet négligeable sur le débit de solide dans la vanne-en-L. Cependant, les résultats à haute température ont démontré que l'augmentation de la viscosité du gaz augmente le débit de solide. Le siphon est un moyen efficace pour réduire les fuites de gaz entre les réacteurs. Une attention particulière devrait être accordée à la perte de charge dans la boucle de pression pour la stabilité de la circulation. La première aération externe du siphon est le paramètre le plus important pour la stabilité du siphon et également pour la minimisation des fuites.
- Un modèle en régime stationnaire a été développé, basé sur le principe d'équilibre de pression dans la boucle de circulation des particules. Le modèle prédit bien les résultats expérimentaux de la perte de charge et du débit de circulation des particules, même si il reste à intégrer les effets de taille dans le modèle.

La deuxième partie de ce travail a porté sur la caractérisation des réacteurs utilisés dans le système actuel. Les principales conclusions de cette phase d'étude peuvent être énumérées comme suit :

- L'hydrodynamique du lit fluidisé bouillonnant a été expérimentalement étudiée en utilisant la méthode de distribution de temps de séjour (DTS) dans la maquette froide. Un modèle hydrodynamique a été développé basé sur le modèle des lits fluidisés à deux phases. Les résultats expérimentaux de DTS ont fourni un repère pour choisir les relations critiques hydrodynamiques, notamment la corrélation de la taille des bulles et la dispersion du gaz dans la phase émulsion.
- Les résultats expérimentaux de combustion ont démontré que les réactions entre le transporteur d'oxygène et le CH_4 ou l'air sont très rapides. Ceci suggère la possibilité d'utiliser des réacteurs en régime turbulent ou dilué pour le système actuel. Cependant, la réaction de $Ni/NiOAl_2O_4$ avec le méthane est thermodynamiquement limitée et la conversion totale n'est pas possible.
- Grace à l'utilisation des siphons et des vannes-en-L, les fuites sont minimisées dans la configuration actuelle de CLC. Ainsi, une efficacité de captage de CO_2 supérieure à 98.4 % a été atteinte.

L'intérêt principal du système actuel CLC a été le développement d'un outil pour mener des essais à l'échelle laboratoire. Le système a été construit de façon à avoir une large flexibilité d'opération, le contrôle d'une gamme importante de débit de solide et la minimisation des fuites de gaz. Ceci peut permettre l'utilisation de différents transporteurs d'oxygène et de divers combustibles.

L'étude actuelle a été réalisée avec des transporteurs d'oxygène à base de Nickel ($NiO/NiAl_2O_4$) et CH_4 comme combustible. Cela a permis de comprendre le fonctionnement fondamental du système, notamment sur le contrôle de la circulation des particules et la minimisation des fuites du gaz entre les réacteurs, et donne une référence pour les futurs développements prévus.

Résumé

La combustion en boucle chimique (CLC) est une nouvelle technologie prometteuse, qui implique la séparation inhérente du dioxyde de carbone (CO_2) avec une perte minimale d'énergie. Un transporteur d'oxygène est utilisé pour le transfert de l'oxygène en continu du "réacteur air" vers le "réacteur fuel" où l'oxygène est apporté au combustible. Ainsi, le contact direct entre l'air et le combustible est évité. Le gaz résultant est riche en CO_2 et n'est pas dilué avec de l'azote. Le transporteur d'oxygène réduit est ensuite transporté vers le "réacteur air" afin d'être ré-oxydé, formant ainsi une boucle chimique.

Ce manuscrit présente des études conduites en utilisant une nouvelle configuration de CLC de 10 kW_{th} construite pour étudier une large gamme de conditions opératoires. Cette unité met en œuvre le concept des lits fluidisés interconnectés en utilisant des vannes-en-L pour contrôler le débit de solide et des siphons pour minimiser les fuites de gaz. L'hydrodynamique de la circulation de solide a été étudiée sur une maquette froide et un pilote chaud. Un modèle de la circulation du solide a ensuite été développé sur le principe du bilan de pression.

L'hydrodynamique de la phase gaz dans le réacteur a été étudiée expérimentalement en utilisant la distribution des temps de séjour (DTS). Un modèle hydrodynamique a été développé sur le principe du lit fluidisé bouillonnant à deux phases. La combustion du méthane a été étudiée avec $NiO/NiAl_2O_4$ comme transporteur d'oxygène. De bonnes performances de combustion et de captage de CO_2 ont été atteintes. Un modèle de réacteur a été finalement mis au point en utilisant le modèle hydrodynamique du lit fluidisé bouillonnant développé précédemment et en adaptant un schéma réactionnel à cette configuration.

Mots clés: Captage CO_2, Combustion en boucle chimique, Modelisation, Lit fluidisé, Vanne-en-L, Siphon.